



*minerals*

# Mineralogical Approaches to Archaeological Materials

## Technological and Social Insights

---

Edited by  
Daniel Albero Santacreu,  
José Cristóbal Carvajal López and Adrián Durán Benito

Printed Edition of the Special Issue Published in *Minerals*

**Mineralogical Approaches to  
Archaeological Materials:  
Technological and Social Insights**





# **Mineralogical Approaches to Archaeological Materials: Technological and Social Insights**

Editors

**Daniel Albero Santacreu**

**José Cristóbal Carvajal López**

**Adrián Durán Benito**

MDPI • Basel • Beijing • Wuhan • Barcelona • Belgrade • Manchester • Tokyo • Cluj • Tianjin



*Editors*

Daniel Albero Santacreu  
Historical Sciences and  
Arts Theory  
University of the  
Balearic Islands  
Palma  
Spain

José Cristóbal Carvajal López  
School of Archaeology &  
Ancient History  
University of Leicester  
Leicester  
UK

Adrián Durán Benito  
Department of Chemistry  
University of Navarra  
Pamplona  
Spain

*Editorial Office*

MDPI  
St. Alban-Anlage 66  
4052 Basel, Switzerland

This is a reprint of articles from the Special Issue published online in the open access journal *Minerals* (ISSN 2075-163X) (available at: [www.mdpi.com/journal/minerals/special\\_issues/maamtsi](http://www.mdpi.com/journal/minerals/special_issues/maamtsi)).

For citation purposes, cite each article independently as indicated on the article page online and as indicated below:

LastName, A.A.; LastName, B.B.; LastName, C.C. Article Title. <i>Journal Name</i> <b>Year</b> , Volume Number, Page Range.
--

**ISBN 978-3-0365-5678-9 (Hbk)**

**ISBN 978-3-0365-5677-2 (PDF)**

Cover image courtesy of Daniel Albero Santacreu

© 2022 by the authors. Articles in this book are Open Access and distributed under the Creative Commons Attribution (CC BY) license, which allows users to download, copy and build upon published articles, as long as the author and publisher are properly credited, which ensures maximum dissemination and a wider impact of our publications.

The book as a whole is distributed by MDPI under the terms and conditions of the Creative Commons license CC BY-NC-ND.



# Contents

<b>About the Editors</b> . . . . .	vii
<b>Preface to "Mineralogical Approaches to Archaeological Materials: Technological and Social Insights"</b> . . . . .	ix
<b>Masanori Kurosawa, Masao Semmoto and Toru Shibata</b> Mineralogical Characterization of Early Bronze Age Pottery from the Svilengrad-Brantiite Site, Southeastern Bulgaria Reprinted from: <i>Minerals</i> <b>2022</b> , <i>12</i> , 79, doi:10.3390/min12010079 . . . . .	1
<b>Daniel J. Alberó Santacreu, Jose C. Carvajal López and Alejandro Ramos Benito</b> Technological Characterization of Almohad Pottery Glazes from SW Mallorca (Balearic Islands, Spain) Reprinted from: <i>Minerals</i> <b>2022</b> , <i>12</i> , 106, doi:10.3390/min12010106 . . . . .	19
<b>Roberta Montesana, Anno Hein, Marisol Madrid i Fernández, Vassilis Kilikoglou and Jaume Buxeda i Garrigós</b> Think Globally, Act Locally: Global Requirements and Local Transformation in Sugar Pots Manufacture in Sicily in the Medieval and Post-Medieval Periods Reprinted from: <i>Minerals</i> <b>2022</b> , <i>12</i> , 423, doi:10.3390/min12040423 . . . . .	35
<b>Gilda Russo, Emanuela Ceccaroni, Aida Maria Conte, Laura Medeghini, Caterina De Vito and Silvano Mignardi</b> Archaeometric Study on Roman Painted Terracottas from the Sanctuary of Hercules in Alba Fucens (Abruzzo, Italy) Reprinted from: <i>Minerals</i> <b>2022</b> , <i>12</i> , 346, doi:10.3390/min12030346 . . . . .	73
<b>Pía Sapiains, Valentina Figueroa, Frances Hayashida, Diego Salazar, Andrew Menzies and Cristián González et al.</b> Supergene Copper and the Ancient Mining Landscapes of the Atacama Desert: Refining the Protocol for the Study of Archaeological Copper Minerals through the Case Study of Pukara de Turi Reprinted from: <i>Minerals</i> <b>2021</b> , <i>11</i> , 1402, doi:10.3390/min11121402 . . . . .	85
<b>Joshua Emmitt, Andrew McAlister and Jeremy Armstrong</b> Pitfalls and Possibilities of Patinated Bronze: The Analysis of Pre-Roman Italian Armour Using pXRF Reprinted from: <i>Minerals</i> <b>2021</b> , <i>11</i> , 697, doi:10.3390/min11070697 . . . . .	113
<b>Michela Botticelli, Laura Calzolari, Caterina De Vito, Silvano Mignardi and Laura Medeghini</b> <i>Aqua Traiana</i> , a Roman Infrastructure Embedded in the Present: The Mineralogical Perspective Reprinted from: <i>Minerals</i> <b>2021</b> , <i>11</i> , 703, doi:10.3390/min11070703 . . . . .	133
<b>Inês Coutinho, Isabel Cambil Campaña, Luís Cerqueira Alves and Teresa Medici</b> <i>Calle Horno del Vidrio</i> —Preliminary Study of Glass Production Remains Found in Granada, Spain, Dated to the 16th and 17th Centuries Reprinted from: <i>Minerals</i> <b>2021</b> , <i>11</i> , 688, doi:10.3390/min11070688 . . . . .	149
<b>Concetta Rispoli, Renata Esposito, Luigi Guerriero and Piergiulio Cappelletti</b> Ancient Roman Mortars from <i>Villa del Capo di Sorrento</i> : A Multi-Analytical Approach to Define Microstructural and Compositional Features Reprinted from: <i>Minerals</i> <b>2021</b> , <i>11</i> , 469, doi:10.3390/min11050469 . . . . .	169

<b>Iván Ruiz-Ardanaz, Esther Lasheras and Adrián Durán</b> Mineralogical Characterization of <i>Carreaux de Pavement</i> from Northern Spain (Tiebas, Navarre) Reprinted from: <i>Minerals</i> <b>2021</b> , <i>11</i> , 153, doi:10.3390/min11020153 . . . . .	<b>191</b>
<b>Ricardo Infante Gomes, António Santos Silva, Leandro Gomes and Paulina Faria</b> Fernandina Wall of Lisbon: Mineralogical and Chemical Characterization of Rammed Earth and Masonry Mortars Reprinted from: <i>Minerals</i> <b>2022</b> , <i>12</i> , 241, doi:10.3390/min12020241 . . . . .	<b>209</b>

# About the Editors

## **Daniel Albero Santacreu**

Dr Daniel Albero Santacreu is Lecturer at the Department of Historical Sciences and Arts Theory at the University of the Balearic Islands (Spain). His research involves archaeometric and technological analysis of archaeological materials such as pottery, clays, glazes and glass from diverse periods (Copper Age, Bronze Age, Iron Age, Islamic, Modern period, Contemporary era) and places (Balearic Islands, Sardinia, Andalusia, Ghana). He currently focuses on the role of technology in the interpretation of material culture and on the application of concepts such as agency, habitus, technological choices and identity in the study of ancient societies. He published *Materiality, Techniques and Society in Pottery Production* (De Gruyter Open, 2014).

## **José Cristóbal Carvajal López**

José C. Carvajal López did his undergraduate degree and his PhD in the University of Granada (Spain). He then held a Marie Curie Intra European Fellowship in the University of Sheffield (UK), became lecturer of Islamic Archaeology in UCL Qatar, and since 2018 is a lecturer of Historical Archaeology at the University of Leicester (UK). His specialist field as an archaeologist is pottery and material culture in general, primarily in Iberia, but he also has experience in landscape and architectural archaeology. He focuses on archaeological study of the Islamic culture, mainly in the process of Islamization and in interactions of Islam with other cultures. He searches for approaches that combine anthropological theory on material culture and analyses with scientific techniques.

## **Adrián Durán Benito**

Dr Adrian Duran Benito is Professor in the Department of Chemistry at the University of Navarra (Spain). He has published more than 75 papers in journals indexed in the Web of Science and his H-index is 25. His research involves materials science studies. His investigation in archaeometry and cultural heritage has been centered in materials such as paintings on canvas, polychromed sculptures, wall paintings, illuminated manuscripts, parchments, pottery, glazes and metals from diverse periods (from the Prehistoric age to the 20th century) and places (Andalusia, France and Navarra). He currently focuses on the technology and composition of medieval ceramics from Navarra and the historical evolution in the use of building mortars in Andalusia.





# Preface to “Mineralogical Approaches to Archaeological Materials: Technological and Social Insights”

Archaeometry is based on the necessary interdisciplinary relationship between diverse branches of the natural and social sciences. This relationship is essential in archaeology, since, from physical materials (objects), scholars have to face questions that go beyond the limits of the tangible and pertain instead to abstract and social concerns. Studies focused on archaeological materials have been substantially enriched by the application of techniques and methods from the natural sciences (e.g. physics, chemistry, geology, micropaleontology) and the implementation of chemical, physical and mineralogical analyses. Currently, archaeometric studies are fundamental to the accurate classification and characterization of archaeological materials, providing relevant data, among other aspects, about their production, function and social meaning.

Archaeometric studies have developed significantly since the 1960s and have enhanced the analytical tools and topics considered in the study of material culture. In this book, we present a set of papers that show the potential of mineralogical studies (e.g. petrography, mineral geochemistry, X-ray Diffraction) and multiproxy approaches to characterize the composition of a wide diversity of archaeological materials such as ceramics, terracotta, tiles, metals, glazes, glass and mortars related to several periods (Bronze Age, Roman, Middle Age, Modern period). These contributions conducted most of the archaeometric analyses usually applied in the study of material culture and demonstrate that the mineralogical characterization of these artifacts is crucial to address aspects related to the origin of the raw materials used in their manufacture and the technological processes applied by craftspeople.

In this sense, this book can be of interest for specialized researchers who seek specific case studies and are mainly concerned with certain kinds of materials, but also for those ones (e.g. students, researchers and professionals) who look for a practical overview of the chief methods that can be followed in the study of material culture. Last but not least, we would like to thank all the authors that participated in this project, as this book would not be possible without their contributions, time and effort.

**Daniel Albero Santacreu, José Cristóbal Carvajal López, and Adrián Durán Benito**

*Editors*





## Article

# Mineralogical Characterization of Early Bronze Age Pottery from the Svilengrad-Brantiite Site, Southeastern Bulgaria

Masanori Kurosawa <sup>1,\*</sup>, Masao Semmoto <sup>2</sup> and Toru Shibata <sup>3</sup><sup>1</sup> Faculty of Life and Environmental Sciences, University of Tsukuba, Tsukuba 305-8572, Japan<sup>2</sup> The Ancient Orient Museum, Tokyo 170-8630, Japan; semmoto@orientmuseum.com<sup>3</sup> Matsudo Museum, Matsudo 270-2252, Japan; s-toru@jcom.zaq.ne.jp

\* Correspondence: kurosawa@geol.tsukuba.ac.jp; Tel.: +81-29-853-6522

**Abstract:** Several pottery sherds from the Svilengrad-Brantiite site, Bulgaria, were mineralogically and petrographically analyzed. The aim was to add information to the very scarce material data available for Early Bronze Age pottery in the southeastern Thrace plain, Bulgaria, in order to examine a possible raw-material source of the pottery. The characterization techniques applied were optical microscopy (OM), petrographic microscopy (PM), scanning electron microscopy coupled with energy dispersive X-ray spectroscopy (SEM-EDS), X-ray fluorescence (XRF) spectroscopy, and X-ray diffraction (XRD). The pottery samples consisted of two typological groups: a local-made type and a cord-impressed decoration type influenced by foreign cultures. All of the samples were produced from fine clay pastes that had a quite similar composition, with abundant mineral grains of similar mineral composition and fragments of metamorphic and granitic rocks. The chemical compositions of each mineral in the grains and fragments were almost identical, and consistent with those from metamorphic and granitic rocks from the Sakar-Strandja Mountains near the study site. The clay paste compositions corresponded to those of illite/smectite mixed-layer clay minerals or mixtures of illite and smectite, and the clay-mineral species were consistent with those in Miocene–Pleistocene or Holocene sediments surrounding the site.

**Keywords:** petrographic analysis; rock fragment; pottery; ceramics; Early Bronze Age; Thrace

**Citation:** Kurosawa, M.; Semmoto, M.; Shibata, T. Mineralogical Characterization of Early Bronze Age Pottery from the Svilengrad-Brantiite Site, Southeastern Bulgaria. *Minerals* **2022**, *12*, 79. <https://doi.org/10.3390/min12010079>

Academic Editors: Daniel Albero Santacreu, José Cristóbal Carvajal López and Adrián Durán Benito

Received: 17 December 2021

Accepted: 5 January 2022

Published: 9 January 2022

**Publisher's Note:** MDPI stays neutral with regard to jurisdictional claims in published maps and institutional affiliations.



**Copyright:** © 2022 by the authors. Licensee MDPI, Basel, Switzerland. This article is an open access article distributed under the terms and conditions of the Creative Commons Attribution (CC BY) license (<https://creativecommons.org/licenses/by/4.0/>).

## 1. Introduction

The Upper Thracian Plain in southern Bulgaria is located between the Balkan Mountains and Rhodope Mountains (Figure 1). The plain underwent social, cultural, and economic transformation in the Early Bronze Age (EBA), from the fourth to the third millennium BCE, as a result of changes in livelihoods, migrations, and the spread of technological innovation. At the beginning of the third millennium BC, the Yamnaya group moved southwards into the plain from the North Pontic area, interacting with the sedentary groups and assimilating into their communities [1,2]. In connection with this issue, the presence of pottery with cord decoration has often been mentioned [2–7]. This pottery style is thought to have spread along with the migration of the Yamnaya groups across the West Pontic region from north to south [2,8], including the possibilities of the movement of potters or the transportation of pottery. This style of pottery, however, has been recovered more frequently from settlement sites other than Yamnaya-style burial mounds (kurgans) in the plain [4,9]; thus, some researchers have argued that indigenous groups in the plain adopted the locally unfamiliar technique of cord-impressed decoration and applied it to pottery [5,7], although the details of this adoption are still a matter of debate.



**Figure 1.** Location map of the Upper Thracian Plain and the Svilengrad-Brantiite site (solid circle) in Bulgaria; geological map of the area around the site (Figure 2) is shown as a dashed box.

Although various cultural and social issues in the plain have been discussed in the context of the typological and stylistic analysis of EBA pottery [10], mineralogical and petrographic analyses have been relatively sparse, except for a few studies of ceramic paste [11,12]. In addition, differences in clay pastes between the foreign-style pottery with cord decoration and local-style pottery have not been clarified. Mineralogical and geochemical analyses of EBA pottery, therefore, are expected to provide insights into the raw materials, provenance, and technology of ceramic manufacture in the area. For these reasons, we analyzed the mineralogical and chemical compositions of mineral grains, rock fragments, and ceramic paste in local- and foreign-style pottery from an EBA site at Svilengrad-Brantiite located in the southeastern part of the Upper Thracian Plain (Figure 1).

## 2. Materials and Methods

### 2.1. Materials

Thirty sherds of EBA pottery (samples SVL01 to SVL30) were selected from the flat settlement at Svilengrad-Brantiite based on their shape and decoration (Table 1). These were fragments of pots, shallow bowls, jars, and jugs. Seven of them (samples SVL24 to SVL30) were decorated with exotic cord impressions, and the remaining 23 (samples SVL01 to SVL23) were indicative of the local EBA2 pottery group. These pottery samples were provided by Dr. Nekhrizov at the National Institute of Archaeology and Museum, Bulgarian Academy of Sciences.

The Svilengrad-Brantiite site is located on a natural levee of the Maritsa River, 2 km southeast of modern Svilengrad, southeastern Bulgaria [13] (Figure 2). At the site, which has an area of approximately 1.5 ha, a series of rescue excavations were conducted between 2004 and 2006 prior to the construction of a railroad, and numerous pits dating to the EBA, Iron Age, medieval era, and Ottoman period were found [13–15]. Many pottery sherds were excavated from the EBA remains together with artifacts commonly found in other settlement sites, such as ground stone, flint tools, clay figurines, and spindle whorls [13–15]. The EBA pottery from the flat settlement at Svilengrad-Brantiite has typological characteristics (shapes and decoration) similar to those of cord-decorated vessels in the Upper Thracian Plain. Thus, the settlement can be dated to the second stage of the EBA (EBA2) in the first half of the third millennium BCE.

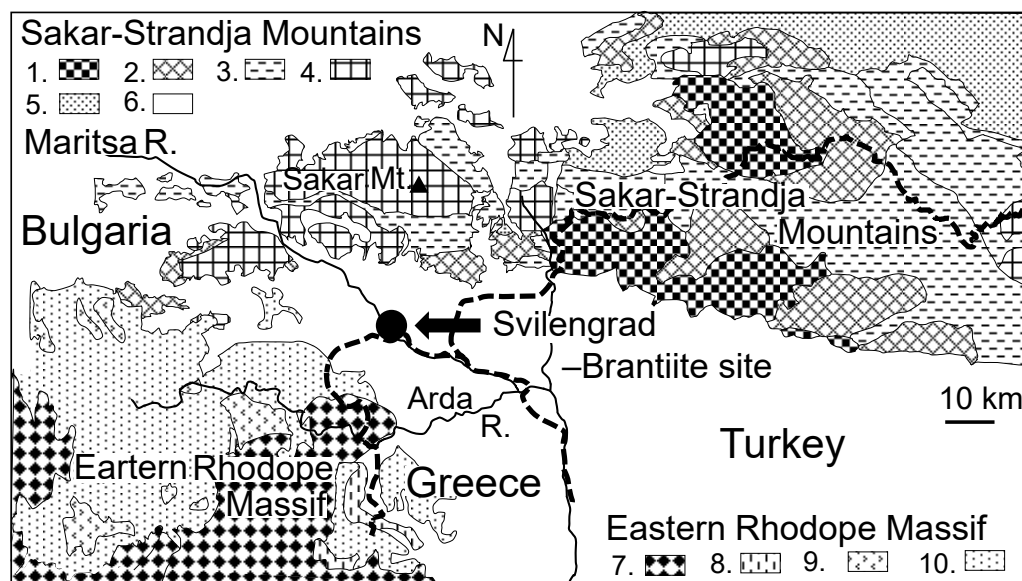
**Table 1.** Descriptions of pottery samples studied and mineral grains in the samples. Abbreviations: EBA2—local-made pottery at the second stage of the EBA (EBA2); Cord—pottery with cord decoration; Qtz—quartz; Kfs—potassium feldspar; Mc—microcline (potassium feldspar); Pl—plagioclase; Afs—alkali feldspar; Ms—muscovite; Ep—epidote; Bt—biotite; Opq—opaque minerals; Ttn—titanite; Am—amphibole; Grt—garnet; Chl—chlorite; St—staurolite.

Sample	Type (mm)	Thickness	Surface Color	Internal Color	Mineral Grains	Observed by Optical Microscope											
						Major Species						Minor Species					
						Qtz	Kfs	Mc	Pl	Afs	Ms	Ep	Bt	Opq	Ttn	Am	Grt
SVL01	EBA2	8	Dark brown	Dark brown	x x x x x x	x	x	x	x	x	x	x	x	x	x	x	x
SVL02	EBA2	7	Dark brown	Dark brown	x x x x x x	x	x	x	x	x	x	x	x	x	x	x	x
SVL03	EBA2	10	Dark brown	Dark brown	x x x x x x	x	x	x	x	x	x	x	x	x	x	x	x
SVL04	EBA2	6	Dark brown	Dark brown	x x x x x x	x	x	x	x	x	x	x	x	x	x	x	x
SVL05	EBA2	6	Dark brown	Dark brown	x x x x x x	x	x	x	x	x	x	x	x	x	x	x	x
SVL06	EBA2	7	Dark brown	Dark brown	x x x x x x	x	x	x	x	x	x	x	x	x	x	x	x
SVL07	EBA2	8	Dark brown	Dark brown	x x x x x x	x	x	x	x	x	x	x	x	x	x	x	x
SVL08	EBA2	7	Dark brown	Dark brown	x x x x x x	x	x	x	x	x	x	x	x	x	x	x	x
SVL09	EBA2	7	Dark brown	Dark brown	x x x x x x	x	x	x	x	x	x	x	x	x	x	x	x
SVL10	EBA2	7	Dark brown	Dark brown	x x x x x x	x	x	x	x	x	x	x	x	x	x	x	x
SVL11	EBA2	5	Dark brown	Light brown	x x x x x x	x	x	x	x	x	x	x	x	x	x	x	x
SVL12	EBA2	10	Dark brown	Light brown	x x x x x x	x	x	x	x	x	x	x	x	x	x	x	x
SVL13	EBA2	12	Dark brown	Light brown	x x x x x x	x	x	x	x	x	x	x	x	x	x	x	x
SVL14	EBA2	8	Dark brown	Dark brown	x x x x x x	x	x	x	x	x	x	x	x	x	x	x	x
SVL15	EBA2	8	Dark brown	Dark brown	x x x x x x	x	x	x	x	x	x	x	x	x	x	x	x
SVL16	EBA2	6	Dark brown	Dark brown	x x x x x x	x	x	x	x	x	x	x	x	x	x	x	x
SVL17	EBA2	7	Dark brown	Light brown	x x x x x x	x	x	x	x	x	x	x	x	x	x	x	x
SVL18	EBA2	7	Dark brown	Dark brown	x x x x x x	x	x	x	x	x	x	x	x	x	x	x	x
SVL19	EBA2	7	Dark brown	Dark brown	x x x x x x	x	x	x	x	x	x	x	x	x	x	x	x
SVL20	EBA2	8	Dark brown	Light brown	x x x x x x	x	x	x	x	x	x	x	x	x	x	x	x
SVL21	EBA2	7	Dark brown	Dark brown	x x x x x x	x	x	x	x	x	x	x	x	x	x	x	x
SVL22	EBA2	9	Dark brown	Light brown	x x x x x x	x	x	x	x	x	x	x	x	x	x	x	x
SVL23	EBA2	11	Dark brown	Dark brown	x x x x x x	x	x	x	x	x	x	x	x	x	x	x	x
SVL24	Cord	8	Dark brown	Light brown	x x x x x x	x	x	x	x	x	x	x	x	x	x	x	x
SVL25	Cord	10	Dark brown	Light brown	x x x x x x	x	x	x	x	x	x	x	x	x	x	x	x
SVL26	Cord	8	Dark brown	Light brown	x x x x x x	x	x	x	x	x	x	x	x	x	x	x	x
SVL27	Cord	10	Dark brown	Light brown	x x x x x x	x	x	x	x	x	x	x	x	x	x	x	x
SVL28	Cord	8	Dark brown	Light brown	x x x x x x	x	x	x	x	x	x	x	x	x	x	x	x
SVL29	Cord	9	Dark brown	Light brown	x x x x x x	x	x	x	x	x	x	x	x	x	x	x	x
SVL30	Cord	8	Dark brown	Light brown	x x x x x x	x	x	x	x	x	x	x	x	x	x	x	x

The Svilengrad–Brantiite site is located on the boundary between two different geological bodies: the Sakar–Strandja Mountains to the northwest and northeast side and the Eastern Rhodope massif to the southwest side (Figure 2). These geological bodies are important to consider when determining the major sources of mineral grains, rock fragments, and clay paste in the pottery samples.

The Sakar–Strandja Mountains are mainly composed of Paleozoic basement rocks (mica-schist, gneiss, migmatite, amphibolite, and metagranitoids), Paleozoic granitoids, Mesozoic granitoids, and a cover of Paleozoic to Mesozoic metamorphic rocks [16–20] (Figure 2). The basement rocks and the metamorphic rock cover near the site include muscovite, quartz, plagioclase, microcline, alkali feldspar, biotite, epidote, titanite, bluish-green amphibole, chlorite, opaque minerals, garnet, staurolite, zircon, and apatite [18,21–23]. The basement rocks, granitoids, and metamorphic rocks are overlain by Tertiary sediments (Eocene sedimentary rocks and upper Miocene to partially lowermost Pleistocene sediments [16,18,24,25]). The upper Miocene to Pleistocene sediments underlie and extend a few kilometers around the study site.





**Figure 2.** Simplified geology of the area around the Svilengrad–Brantiite site (modified after [17,18,26]). Sakar-Strandja Mountains: 1—Paleozoic basement; 2—Paleozoic granitoids; 3—Paleozoic–Mesozoic metamorphic rocks; 4—Mesozoic granitoids; 5—Late Cretaceous sedimentary rocks; 6—Tertiary sediments. Eastern Rhodope Massif: 7—Paleozoic basement; 8—Mesozoic low to medium-grade metamorphic rocks; 9—Tertiary volcanic rocks; 10—Tertiary volcano-sedimentary rocks.

The Eastern Rhodope massif consists mainly of Paleozoic basement rocks (metagranitoids, migmatite, and gneiss), medium- to high-grade metamorphic rocks (amphibolite, eclogite, metabasic rocks, and metaultrabasic rocks), and low-grade metamorphic rocks (greenschist, pelitic schist, phyllite, and marble) [27–30]. These metamorphic rocks include muscovite, quartz, plagioclase, microcline, alkali feldspar, biotite, epidote, titanite, amphibole, chlorite, opaque minerals, garnet, staurolite, and kyanite [27–31]. The basement rocks and metamorphic rocks are surrounded by Cretaceous to Paleogene volcanic and plutonic rocks [28,32,33] and Neogene volcano-sedimentary rocks [34].

The relatively high-grade metamorphic rocks at the Sakar Mountain area are very similar to the basement and metamorphic rocks in the Eastern Rhodope massif [18]. These geological bodies differ, however, in their maximum pressure conditions during metamorphism: ~8 k bar for Sakar Mountain [21,35] and ~13 k bar for the Rhodope massif [27,29,36,37]. Thus, the chemical compositions of their rock-forming minerals may also slightly differ. For this reason, we tried to elucidate the sources of the mineral grains and rock fragments derived from metamorphic rocks by using chemical analysis.

## 2.2. Methods

The pottery samples were cut into slices (approximately 20  $\mu\text{m}$  thick) and doubly polished for microscopic observations under polarized and reflected light. After the observations, the surfaces were coated with a carbon film to prevent electrostatic charging during the analyses with a scanning electron microscope equipped with an energy-dispersive X-ray spectrometer (SEM-EDS). In addition, 1.0 g of the representative samples was powdered for X-ray powder diffraction (XRD) and X-ray fluorescence (XRF) analyses.

Textural observations and chemical analyses of clay pastes and minerals in the samples were performed by using a SEM-EDS (JSM-6010LA, JEOL, Tokyo, Japan) with an accelerating voltage of 20 keV and a beam diameter of approximately 2  $\mu\text{m}$ . Measurement data were quantified by the ZAF method, and the quantified data were further corrected by using standard materials of albite, plagioclase, sanidine, biotite, chlorite, jadeite, Cr-diopside, diopside, rhodonite, kaersutite, almandine, and pyrope (Astimex Standards Ltd., Tronto, Canada). The quantified data were normalized to a total of 100 wt.%.

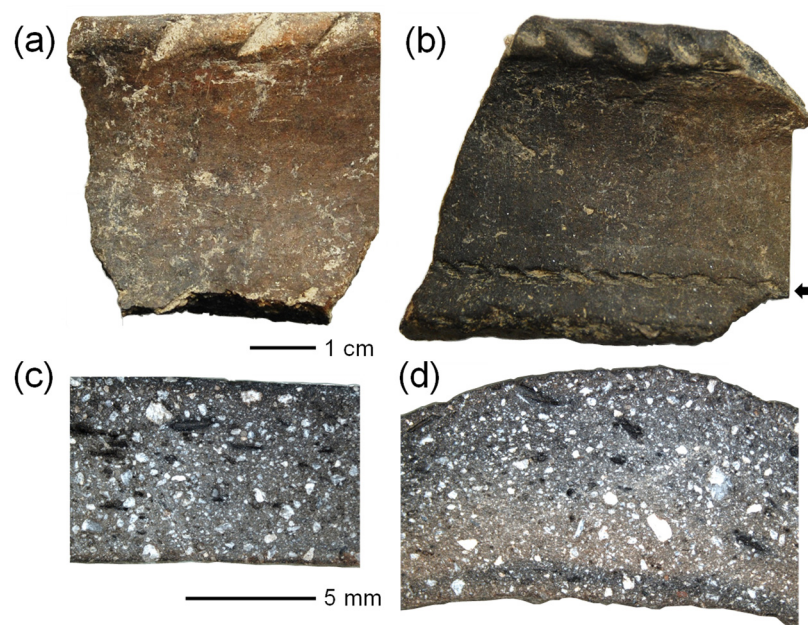
The major mineral compositions of the pottery samples were determined by using an X-ray diffractometer (MiniFlex600 D/teX Ultra, Rigaku, Tokyo, Japan) with a monochromized Cu K $\alpha$  X-ray (40 kV and 30 mA) and scintillation counter. The 2 $\theta$  scanning angle ranged from 3° to 65°, with 0.02° steps and a scanning speed of 2°/min.

Bulk chemical compositions of the pottery samples were also analyzed by a wavelength dispersive X-ray fluorescence spectrometer (MagiX PW2424, Philips, Eindhoven, Netherlands) using an Rh target X-ray tube operated at 2.4 kW (Paleo Labo Co., Ltd., Japan, Saitama, Japan). Glass-bead samples, fused with a mixture of a powdered specimen and Li<sub>2</sub>B<sub>4</sub>O<sub>7</sub>–LiBO<sub>2</sub> (1:5), were used for XRF analysis. We measured 10 major oxides (Na<sub>2</sub>O, MgO, Al<sub>2</sub>O<sub>3</sub>, SiO<sub>2</sub>, P<sub>2</sub>O<sub>5</sub>, K<sub>2</sub>O, CaO, TiO<sub>2</sub>, MnO, and FeO). The concentrations of these oxides were quantified by a calibration-curve method using 16 standard materials (reference rock powders JA-1, JA-2, JA-3, JB-1, JB-1a, JB-2, JB-3, JF-1, JF-2, JG-1a, JG-2, JG-3, JGb-1, JR-1, JR-2, and JP-1) of the Geological Survey of Japan (National Institute of Advanced Industrial Science and Technology, Tsukuba, Japan).

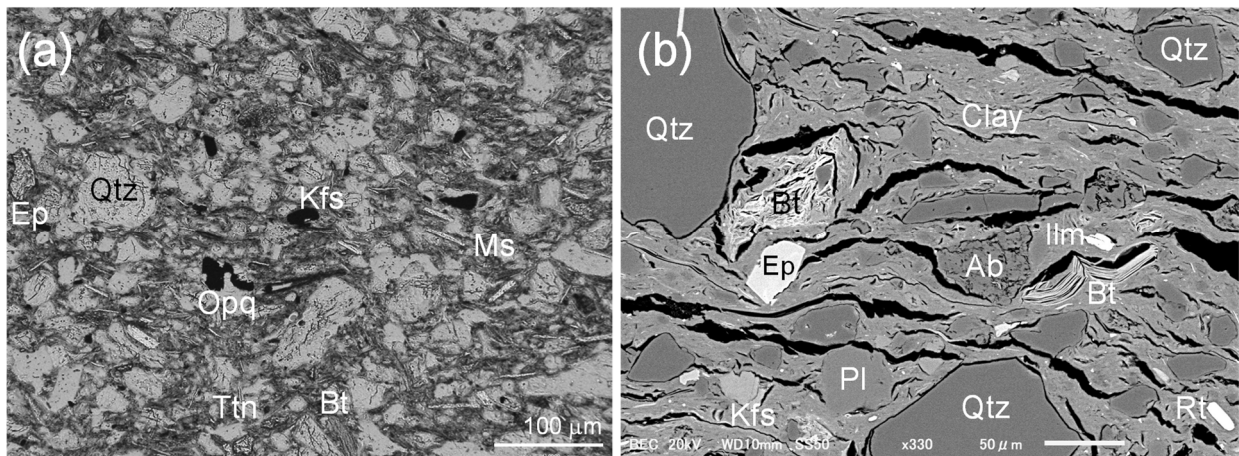
### 3. Results

#### 3.1. Features of Pottery Samples and Clay Paste

All of the pottery samples were about 7 mm thick (Table 1), and the surfaces were black to brown and were smoothed or burnished (Figure 3a,b). Cross sections of all of the samples were black to reddish-brown, and the samples were produced from fine clay with relatively large amounts of mineral grains and rock fragments (Figure 3c,d). A few elongated voids and rare clay pellets were observed; chaff and other impurities were absent. Minerals grains of muscovite and biotite showed a preferred orientation parallel to the pottery surface (Figure 4a), indicating that the clay paste was kneaded sufficiently during pottery making or possibly that a wheel-made production technique was used [38]. This preferred orientation was also observed for elongated voids in the pottery matrices (Figure 3c). In the SEM observations of the clay pastes in all the samples, the clay minerals showed good adhesion and no partial melting (Figure 4b).



**Figure 3.** (a) Local EBA2 pottery and (b) pottery with cord-impressed decoration (arrow). Scale bars are 1 cm. Cross sections of local EBA2 pottery (c) and pottery with cord-impressed decoration (d). White grains are mineral grains and rock fragments. Black elongated portions are pores. Scale bars are 5 mm.



**Figure 4.** (a) Photomicrograph of thin section for pottery sample (SVL24, plane-polarized light). Abbreviations: Qtz—quartz; Ep—epidote; Kfs—potassium feldspar; Ms—muscovite; Opq—opaque mineral (ilmenite); Ttn—titanite; Bt—biotite. (b) SEM image of pottery sample (SVL12). Abbreviations: Ilm—ilmenite; Ab—albite; Pl—plagioclase; Rt—rutile; Clay—clay minerals.

### 3.2. Mineral Grains

The polarized-microscopic observations and SEM-EDS analyses demonstrated that all of the samples included angular to sub-angular grains of dominant quartz, plagioclase, alkali feldspar, potassium feldspar, muscovite, and epidote; subordinate ilmenite, titanite, amphibole, chlorite, biotite, garnet, and staurolite; and trace amounts of zircon, apatite, and rutile. The qualitative volume ratios for the mineral grains were approximately 30 vol.% quartz, 15 vol.% feldspar, 5 vol.% muscovite, less than 1 vol.% other mineral grains and rock fragments, and 50 vol.% clay paste. All of the grains were euhedral in shape or fragmentary. Quartz grains often exhibited wavy extinction. Potassium feldspar and alkali feldspar grains demonstrated a microcline texture and a perthite texture, respectively. Biotite and chlorite were partially altered. Amphiboles were pleochroic and bluish-green and pale green under uncrossed polars.

In the SEM-EDS analyses, most of the plagioclases were found to be rich in sodium (Table 2). Muscovite was relatively enriched in Na and Mg, corresponding to the chemical composition of phengite, which is observed frequently in metamorphic rocks from the Sakar-Strandja Mountains [19,21] and the Eastern Rhodope massif [27,29,31]. Biotite was poor in potassium as a result of alteration (Table 2), and epidote was rich in iron and similar in composition to that from metamorphic rocks [19,29,30] or gabbro [33]. Amphibole exhibited chemical zoning, and its composition corresponded to calcic amphiboles (magnesiohornblende, edenite, ferroedenite, and rare pargasite). Garnet was enriched in iron, corresponding to almandine garnet. Opaque minerals were mostly ilmenite and rarely magnetite. Tiny grains, less than 10 μm in length, of zircon, apatite, and rutile were always observed, but their abundances varied across samples.

The mineral grains in all of the pottery samples showed the same combination of mineral species independent of grain size and grain amount, and the chemical compositions of each mineral were very similar among the samples. The major features of the grains were the similarity of mineral species, relatively large amounts of muscovite and epidote, and a lack of olivine or pyroxene, which are commonly found in igneous rocks. In addition, during the SEM observations, we observed an absence of minerals formed by high-temperature firing and a lack of textures associated with thermal decomposition and partial melting in the mineral grains. These features were identical in both the local EBA2 pottery and the cord-decorated pottery.

**Table 2.** Representative SEM–EDS analyses of minerals from pottery. Abbreviations: (g)—mineral grain; (f)—minerals in rock fragments. \* Numbers of ions in chemical formulae for potassium feldspar and plagioclase were calculated on an 8 oxygen basis, for muscovite and biotite on a 22 oxygen basis, for epidote on a 12.5 oxygen basis, for amphibole on a 23 oxygen basis, and for garnet on a 12 oxygen basis, respectively. Numbers of Fe<sup>3+</sup> in epidote and garnet were calculated based on Fe<sup>2+</sup> or Fe<sup>3+</sup> occupancies in the cation sites and the rest as Fe<sup>3+</sup> or Fe<sup>2+</sup> in the structural formulae. \*\* Numbers of ions in chemical formulae for titanite on a 5 oxygen basis, for staurolite on a 24 oxygen basis, for ilmenite on a 3 oxygen basis, for rutile on a 2 oxygen basis, for zircon and magnetite on a 4 oxygen basis, for apatite on a 26 oxygen basis, and for chlorite (chloritized biotite) on a 28 oxygen basis, respectively.

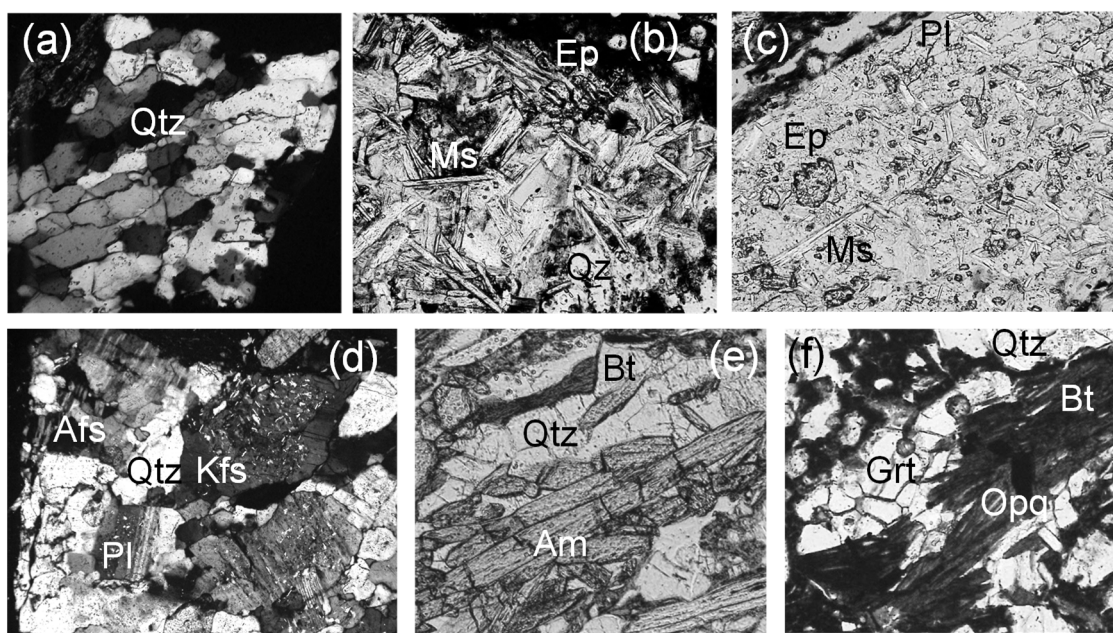
Potassium Feldspar + Al:R51		Plagioclase		Muscovite		Biotite		Epidote		Amphibole		Garnet		
Wt.%	(g)	(f)	(g)	(f)	(g)	(f)	(g)	(f)	(g)	(f)	(g)	(f)	(f)	
Na <sub>2</sub> O	0.91	0.74	9.36	9.42	Na <sub>2</sub> O	0.16	0.15	0.05	0.04	Na <sub>2</sub> O	2	1.77	Na <sub>2</sub> O	0.05
MgO	0.01	0.02	0	0	MgO	9.45	10.39	0.05	0.07	MgO	9.25	9.42	MgO	3.95
Al <sub>2</sub> O <sub>3</sub>	18.08	17.92	22.98	22.71	Al <sub>2</sub> O <sub>3</sub>	16.27	16.98	29.73	28.28	Al <sub>2</sub> O <sub>3</sub>	12.7	12.24	Al <sub>2</sub> O <sub>3</sub>	20.68
SiO <sub>2</sub>	65.28	65.31	62.98	63.32	SiO <sub>2</sub>	40.96	50.68	39.13	38.92	SiO <sub>2</sub>	44.78	44.75	SiO <sub>2</sub>	37.92
K <sub>2</sub> O	15.55	15.88	0.03	0.09	K <sub>2</sub> O	11.49	10.87	0	0	K <sub>2</sub> O	0.65	0.48	K <sub>2</sub> O	0.05
CaO	0.06	0	4.49	4.26	CaO	0.29	0	23.95	0	CaO	10.45	10.68	CaO	3.2
TiO <sub>2</sub>	0.04	0.12	0	0.11	TiO <sub>2</sub>	2.5	2.13	0.26	0.04	TiO <sub>2</sub>	0.56	1.03	TiO <sub>2</sub>	0.03
MnO	0	0	0.03	0	MnO	0.77	0.69	0.43	0.37	MnO	0.46	0.27	MnO	4.68
FeO	0.07	0.01	0.13	0.08	FeO	20.07	21.61	6.4	8.43	FeO	19.14	19.35	FeO	29.43
Total	100	100	100	100	Total	100	99.99	100	100	Total	99.99	99.99	Total	99.99
Numbers of ions in chemical formulae *														
T-site	3.009	3.014	2.802	2.938	T-site	5.909	5.657	3.006	3.022	T-site	6.577	6.572	T-site	3.055
Si	0.982	0.975	1.184	1.051	Si	2.091	2.343	2.692	2.589	Si	1.423	1.428	Si	1.946
Al	3.991	3.989	3.986	3.989	Al	8	8	0.016	0.002	Al	8	8	Al	0.002
(sum)					(sum)			0.411	0.547	(sum)	B-site+C-site		Fe <sup>3+</sup>	0.054
M-site	0.001	0.004	0.004	0.002	M-site	0.675	0.491	0	0	M-site	0.775	0.691	Fe <sup>3+</sup>	2
Ti	0.003	0	0.003	0.004	Ti	0.271	0.387	0.028	0.008	Ti	0.062	0.113	B-site	0
Fe	0	0	0	0	Fe	2.421	2.999	0.006	0.006	Fe	2.351	2.377	Fe <sup>2+</sup>	1.91
Mn	0	0	0	0	Mn	0.094	0.047	0	0.034	Mn	0.058	0.034	Mn	0.316
Mg	0.001	0.001	0	0	Mg	2.031	1.616	0.006	0.008	Mg	1.646	1.681	Mg	0.469
K	0.915	0.935	0.005	0.004	K	5.492	5.54	0.008	0.006	K	0.084	0.043	Na	0.008
Na	0.082	0.066	0.808	0.899	(sum)	1.753	1.952	1.971	1.984	(sum)	7.001	7	Ca	0.274
Ca	0.003	0	0.202	0.089	A-site	0.045	0.043	0	0	A-site	0.486	0.462	K	0.005
(sum)	1.005	1.007	1.022	0.998	K	0.045	0	2.013	2.023	Na	0.123	0.09	(sum)	2.912
Total	4.996	4.996	5.009	4.987	Ca	1.844	1.995	8.138	8.183	Total	0.609	0.552	Total	8.007
					(sum)	13.998	15.535			(sum)	15.61	15.552		
					Total					Total				

Table 2. Cont.

Titanite		Staurolite		Ilmenite		Rutile		Zircon		Apatite		Chlorite					
Wt. %	(g)	(f)	(g)	(f)	(g)	(f)	(g)	(f)	(g)	(f)	(g)	(f)	(g)				
Na <sub>2</sub> O	0.05	0	0	MgO	0	0	0	MgO	0	0	F	0	Na <sub>2</sub> O	3.64	2.76	0.14	0.16
MgO	0	0.02	2.16	Al <sub>2</sub> O <sub>3</sub>	0	0	0	Al <sub>2</sub> O <sub>3</sub>	0	0	Na <sub>2</sub> O	0	MgO	0.07	0.12	15.37	15.25
Al <sub>2</sub> O <sub>3</sub>	1.34	1.14	53.21	SiO <sub>2</sub>	0.21	0.16	0.2	SiO <sub>2</sub>	32.02	32.14	MgO	0	Al <sub>2</sub> O <sub>3</sub>	0.01	0	25.24	24.8
SiO <sub>2</sub>	32.42	32.05	29.03	CaO	0	0	0	CaO	0	0	Al <sub>2</sub> O <sub>3</sub>	0.06	SiO <sub>2</sub>	0.09	0.06	28.43	28.58
K <sub>2</sub> O	0.09	0.08	0	TiO <sub>2</sub>	52.4	52.61	98.2	TiO <sub>2</sub>	0	0	P <sub>2</sub> O <sub>5</sub>	42.92	K <sub>2</sub> O	42.52	42.92	0.08	0.06
CaO	26.77	27.13	0	MnO	6.61	7.57	0	MnO	0	0	Cl	0	CaO	0	0	0.36	0.02
TiO <sub>2</sub>	38.64	38.98	0.62	FeO	40.78	39.67	0.75	FeO	0	0	K <sub>2</sub> O	0.03	TiO <sub>2</sub>	0.04	0.03	0.15	0.08
MnO	0.14	0.07	0.03	Nb <sub>2</sub> O <sub>5</sub>	100	100	0.85	ZrO <sub>2</sub>	66.2	65.62	CaO	54.05	MnO	53.37	54.05	0.03	0.06
FeO	0.55	0.53	13.91	Total	100	100	100	HfO <sub>2</sub>	1.78	2.24	MnO	0.02	FeO	0	0.02	30.2	30.99
Total	100	100	99.99	Total	100	100	100	Total	100	100	FeO	0.03	Total	0.25	0.03	100	100
Numbers of ions in chemical formulae **																	
T-site	1.048	1.038	4	A-site	0.004	0.005	0.002	T-site	0.992	0.988	Ca-site	0.988	T-site	10.103	10.07	5.289	5.334
Si	0.051	0.043	0.17	Si	0.997	0.994	0.992	Si	0	0	Ca	0	Si	0	0.003	2.711	2.666
M-site	0.939	0.949	0.07	Ti	1.001	0.999	0.006	Al	0	0	Mg	0	Al	0	0.037	8	8
Al	0.015	0.014	8.965	(sum)	0.836	0.86	0	Fe	0	0	Fe	0	(sum)	0.004	0.019	0.021	0.011
Fe	0.004	0.002	9.123	B-site	0	0	0	Ti	0	0	Al	0	M-site	0.012	0	2.825	2.789
Mn	0	0.001	1.715	Al	0.162	0.141	0	Fe	0	0	(sum)	0	Al	0	0	0.021	0.011
Mg	0.003	0	0.002	Mn	0	0	0	Mg	0.988	0.996	P	0.996	Ti	10.12	10.129	4.7	4.836
Na	0.927	0.941	0.002	Mg	0	0	0	Zr	0.02	0.016	Mn	6.338	Fe	6.339	6.338	0.005	0.01
Ca	0.004	0.003	0.451	Ca	0	0	0	Hf	0	0	P	0	Mn	0.005	0.01	4.263	4.242
K	1.943	1.953	0	(sum)	0.998	1.001	1	Ca	1.008	1.012	F	2.03	Mg	1.525	2.03	0.019	0.014
(sum)	2.991	2.991	0	Total	1.999	2	2	(sum)	2	2	Cl	0	K	0	0	0.051	0.058
Total	2.991	2.991	0.044	0.044	1.999	2	2	Total	2	2	(sum)	1.012	Na	1.525	2.03	0.072	0.004
Ca	0	0	0.005	0.005	1.999	2	2	Total	2	2	Total	17.983	Ca	1.525	2.03	11.956	11.964
(sum)	2.172	2.172	15.328	15.328	1.999	2	2	Total	2	2	Total	18.497	(sum)	17.983	18.497	19.956	19.964

### 3.3. Rock Fragments

Rock fragments were angular to sub-angular, 0.1 mm to 2 mm in size, and variable in amount and size. Fifty mineral assemblages were distinguished in the fragments (Table 3). The most abundant rock fragments were polycrystalline quartz with undulatory extinction (Figure 5a), followed by assemblages of quartz + muscovite + epidote or plagioclase + muscovite + epidote with a schistose texture (Figure 5b,c). Metagranitoids and amphibolite with a deformed equigranular texture (Figure 5d,e) and garnet gneiss with a weak banded texture were also observed (Figure 5f).



**Figure 5.** Photomicrograph of rock fragments in pottery samples (plane-polarized polar). The vertical sizes are 200  $\mu\text{m}$ . (a) Fragment of quartz aggregate with undulatory extinction. (b) Pelitic or basic schist. (c) Pelitic or basic schist. (d) Metagranitoids or granitic rocks. (e) Basic schist or amphibolite. (f) Garnet gneiss. Abbreviations: Qtz—quartz; Ep—epidote; Ms—muscovite; Pl—plagioclase; Afs—alkali feldspar; Kfs—potassium feldspar; Bt—biotite; Am—amphibole; Grt—garnet; Opq—opaque.

The 50 mineral assemblages could be grouped into five assemblage types on the basis of the mineral species combinations (Table 3). These five mineral assemblage types were estimated to correspond to five kinds of original rock types based on the textures observed in the assemblages: pelitic or basic schist; metagranitoids or granitic rocks; amphibolite or basic schist; pelitic schist; and gneiss (Table 3). Because polycrystalline quartz is always present in these metamorphic rocks, it was considered to have originated from all five rock types. In addition, the chemical compositions of each mineral in the rock fragments were in good agreement with those of the mineral grains in the samples (Table 2), indicating that the mineral grains and rock fragments originated from the same source rocks.

### 3.4. Chemical Composition of Clay Paste

The chemical compositions of the clay pastes without mineral grains or rock fragments were analyzed with SEM-EDS, and average values for five-point analyses were obtained for 10 samples (Table 4).

All of the clay pastes were non-calcareous (<6 wt.% CaO [39]) and possessed relatively lower K<sub>2</sub>O contents than a typical illite [40,41]. The SiO<sub>2</sub> and Al<sub>2</sub>O<sub>3</sub> contents within each sample exhibited a narrow concentration range (Table 4), and the other elements except for CaO and P<sub>2</sub>O<sub>5</sub> showed similar tendencies. These narrow ranges demonstrate that the clay paste had a relatively homogeneous composition within each pottery sample. In addition, the pastes had a very similar oxide concentrations across all samples (Table 4), indicating

that all of the pottery samples had been produced from a clay paste with the same chemical composition. No systematic differences were observed in the chemical content between the local EBA2 group and the cord-decorated group.

**Table 3.** Mineral assemblages observed in rock fragments within pottery and the estimated rock type. Abbreviations: Afs—alkali feldspar; Am—amphibole; Ap—apatite; Bt—biotite; Chl—chlorite; Ep—epidote; Grt—garnet; Ilm—ilmenite; Kfs—potassium feldspar (or microcline); Mus—muscovite; Pl—plagioclase; Qtz—quartz; Rt—rutile; St—staurolite; Ttn—titanite; Zrn—zircon. \* Basic mineral assemblages were estimated based on combinations of the mineral assemblages. Rock types were estimated based on the basic mineral assemblages and textures observed in the assemblages.

Mineral Assemblages	Basic Mineral Assemblages and Estimated Rock Type *
Qtz (polycrystalline with undulatory extinction)	} Various metamorphic rocks
Qtz + Mus, Qtz + Ep	
Qtz + Mus + Ep	
Qtz + Mus + Ep + Bt	
Pl + Mus, Pl + Ep, Pl + Ilm	
Pl + Mus + Ep, Pl + Mus + Qtz, Pl + Ep + Qtz	
Pl + Ep + Bt	
Pl + Mus + Ep + Ilm	
Qtz + Ep + Afs, Mus + Ep + Afs	
Qtz + Pl + Ep + Afs, Qtz + Mus + Ep + Afs	
Chl + Pl, Chl + Ilm + Afs	
Qtz + Kfs, Qtz + Bt, Qtz + Pl	
Kfs + Mus, Kfs + Bt	
Qtz + Kfs + Mus, Qtz + Kfs + Bt,	} Type (2) Qtz + Kfs + Pl + Mus ± Bt ± Ttn ± Zrn ± Aπ : metagranitoids or granitic rocks
Qtz + Mus + Bt	
Mus + Bt + Ap	
Qtz + Kfs + Mus + Bt	
Qtz + Kfs + Pl + Zrn, Kfs + Pl + Zrn + Ap	
Qtz + Ttn, Pl + Ttn	
Qtz + Mus + Ttn, Pl + Mus + Ttn	
Qtz + Kfs + Mus + Bt + Ttn	
Qtz + Am, Am + Ilm, Am + Ep	
Qtz + Ilm, Ilm + Rt, Ilm + Zrn	
Qtz + Pl + Am, Pl + Am + Ilm, Ilm + Rt	} Type (3) : Qtz + Pl + Am + Ilm ± Afs ± Rt ± Zrn : amphibolite or basic schist
Qtz + Grt + St	
Qtz + Grt + St + Bt + Ilm	} Type (4) : Qtz + Grt + St ± Bt ± Mus ± Ilm ± Rt : pelitic schist
Qtz + St + Mus + Ilm + Rt	
Qtz + Bt + Grt, Qtz + Kfs + Grt	} Type (5) : Qtz + Bt + Kfs + Grt: gneiss

### 3.5. X-ray Fluorescence (XRF)

The bulk chemical composition of six pottery samples was analyzed by XRF. The oxide contents were very similar among the samples, and no systematic differences were observed between the pottery types (Table 4). The results for two major compounds, SiO<sub>2</sub> and Al<sub>2</sub>O<sub>3</sub>, agreed within approximately 7% among the samples (Table 4), but the values were higher than the corresponding SEM–EDS values of the clay pastes without mineral grains or rock fragments. The higher SiO<sub>2</sub> and Al<sub>2</sub>O<sub>3</sub> contents were thought to result from the contributions of quartz and feldspar as mineral grains and rock fragments. The average values for each compound were within one standard deviation of those estimated for an average mixture of clay paste and mineral grains (Table 4). The clay paste and the mineral grain values in the average mixture were selected from Tables 2 and 4, respectively. The mixture ratio was assumed to be 47.6 vol.% clay paste, 25.7 vol.% quartz grains, 16.4 vol.% plagioclase grains, 5.0 vol.% potassium feldspar grains, 4.2 vol.% muscovite grains, 0.8 vol.% ilmenite grains, and 0.3 vol.% apatite grains. The volume ratios of the major minerals were very close to those of the mineral grains observed with the optical microscope.



**Table 4.** Chemical compositions of clay pastes in pottery samples, bulk pottery samples, mixtures of clay paste and mineral grains, and Maritsa River sediments. \*1 Average value of the five-point analyses; standard deviations in parentheses. \*2 Pottery type: EBA2—local-made type; Cord—pottery with cord decoration. \*3 Average values for the results of 10 pottery samples; standard deviations in parentheses. \*4 Average values for the results of six pottery samples and standard deviations. \*5 Mixture composition estimated from the average clay paste composition and the chemical compositions of the mineral grains (Table 1). The mixing ratios were 47.6 vol.% clay paste, 25.7 vol.% quartz, 16.4 vol.% plagioclase, 5.0 vol.% potassium feldspar, 4.2 vol.% muscovite, 0.8 vol.% ilmenite, and 0.3 vol.% apatite. \*6 Average composition excluding water content of low-calcareous-content alluvial (flood-plain) sediments near the Maritsa River [42]; standard deviations in parentheses. –, Not analyzed.

Clay Paste Compositions (wt.% *1) Determined by SEM–EDS Analyses (without Mineral Grains or Rock Fragments)															
Sample	SVL01	SVL03	SVL04	SVL11	SVL12	SVL18	SVL23	SVL24	SVL25	SVL30	Average *3				
Type *2	EBA2	EBA2	EBA2	EBA2	EBA2	EBA2	EBA2	Cord	Cord	Cord		Cord			
Na <sub>2</sub> O	0.37 (0.08)	0.34 (0.15)	0.35 (0.06)	0.43 (0.21)	0.37 (0.16)	0.41 (0.15)	0.41 (0.10)	0.30 (0.05)	0.46 (0.18)	0.31 (0.12)	0.38 (0.04)				
MgO	2.51 (0.18)	2.75 (0.19)	2.55 (0.25)	2.48 (0.36)	2.06 (0.48)	3.26 (0.46)	2.34 (0.57)	3.03 (0.80)	2.50 (0.43)	2.63 (0.45)	2.61 (0.32)				
Al <sub>2</sub> O <sub>3</sub>	24.66 (1.35)	20.09 (1.39)	23.53 (0.84)	22.28 (1.56)	23.39 (1.86)	23.77 (1.68)	27.35 (1.35)	20.95 (2.13)	26.43 (0.84)	23.69 (0.75)	23.61 (2.11)				
SiO <sub>2</sub>	56.91 (1.45)	58.34 (2.29)	58.29 (1.45)	58.17 (1.43)	57.93 (2.48)	57.76 (1.44)	55.25 (1.24)	59.11 (2.97)	56.10 (1.21)	55.81 (1.20)	57.37 (1.18)				
P <sub>2</sub> O <sub>5</sub>	0.47 (0.18)	1.77 (0.52)	0.73 (0.11)	2.52 (0.42)	1.90 (0.47)	0.12 (0.06)	0.31 (0.09)	1.35 (0.17)	0.23 (0.14)	0.94 (0.56)	1.03 (0.71)				
K <sub>2</sub> O	3.61 (0.34)	3.58 (0.69)	3.11 (0.52)	2.74 (0.53)	2.77 (0.43)	2.87 (0.55)	2.64 (0.51)	3.45 (0.96)	2.10 (0.18)	3.07 (0.26)	2.99 (0.46)				
CaO	2.43 (0.42)	3.35 (1.20)	1.96 (0.16)	2.74 (0.47)	3.18 (0.61)	1.47 (0.22)	1.36 (0.52)	2.42 (0.32)	1.65 (0.69)	2.27 (0.95)	2.28 (0.65)				
TiO <sub>2</sub>	0.73 (0.38)	0.68 (0.08)	0.66 (0.10)	0.71 (0.19)	0.66 (0.19)	0.73 (0.12)	0.72 (0.12)	0.57 (0.10)	0.69 (0.15)	0.99 (0.21)	0.71 (0.14)				
MnO	0.04 (0.05)	0.03 (0.03)	0.03 (0.03)	0.04 (0.03)	0.05 (0.11)	0.05 (0.11)	0.08 (0.11)	0.01 (0.02)	0.03 (0.05)	0.04 (0.07)	0.04 (0.02)				
FeO	8.27 (2.31)	9.07 (0.56)	8.79 (0.99)	7.89 (0.91)	7.68 (0.92)	9.56 (1.03)	9.54 (0.62)	8.81 (0.75)	9.81 (1.10)	10.25 (1.15)	8.97 (0.91)				
Total	100.00	100.00	100.00	100.00	99.99	100.00	100.00	100.00	100.00	100.00	99.99				
Bulk compositions (wt.%) of pottery samples obtained by XRF analyses															
Mixture of clay and mineral grains *5															
Maritsa River sediments *6															
Sample Type	SVL01 EBA2	SVL04 EBA2	SVL11 EBA2	SVL12 EBA2	SVL24 Cord	SVL25 Cord	Average *4	Average clay paste composition + content of several mineral grains						Low-calcareous-content alluvial sediments (average)	
Na <sub>2</sub> O	1.51	1.9	1.7	1.6	2.22	1.6	1.76 (0.26)	1.77	1.65 (0.19)						1.65 (0.19)
MgO	0.94	1.58	1.22	0.92	1.69	1.04	1.23 (0.33)	1.33	1.82 (0.45)						1.82 (0.45)
Al <sub>2</sub> O <sub>3</sub>	14.88	18.2	16.12	15.86	16.52	16.1	16.28 (1.09)	17.22	16.63 (0.00)						16.63 (0.00)
SiO <sub>2</sub>	72.37	63.54	68.09	70.56	66.73	71.62	68.82 (3.35)	68.69	69.2 (0.83)						69.2 (0.83)
P <sub>2</sub> O <sub>5</sub>	0.22	0.88	1.24	0.7	0.48	0.12	0.6 (0.42)	0.62	–						–
K <sub>2</sub> O	3.04	3.09	2.57	2.68	2.85	2.58	2.8 (0.23)	2.69	2.29 (0.01)						2.29 (0.01)
CaO	1.68	2.56	2.32	1.82	2.5	1.35	2.04 (0.49)	1.99	1.56 (0.05)						1.56 (0.05)
TiO <sub>2</sub>	0.54	1.02	0.76	0.63	0.95	0.65	0.76 (0.19)	0.78	0.72 (0.01)						0.72 (0.01)
MnO	0.06	0.07	0.11	0.06	0.09	0.06	0.08 (0.02)	0.08	0.1 (0.01)						0.1 (0.01)
FeO	3.79	5.63	4.59	4.32	5.01	4.27	4.6 (0.65)	4.81	5.01 (0.21)						5.01 (0.21)
Total	99.03	98.48	98.71	99.15	99.04	99.38	98.97	99.98	98.98						98.98



In addition, the average XRF values agreed within one standard deviation with those of alluvial flood-plain sediments near the Maritsa River [42] (Table 4). The alluvial sediments include clay, mineral grains, and pebbles or gravel [42,43], as well as pebbles of metamorphic rocks [44]. Mineral grains in the sediments consist mainly of quartz, plagioclase, potassium feldspar, and muscovite; trace amounts of amphibole, epidote, titanite, zircon, opaque minerals; and variable amounts of calcite [42–44]. Calcite was not present in some layers of the sediments [42,43], and an assemblage of mineral grains excluding calcite was in good agreement with that of the mineral grains in the pottery samples. Therefore, the average chemical composition of the alluvial sediments in Table 4 was estimated based on the analytical data of low-calcareous sediments [42], excluding water contents.

### 3.6. X-ray Diffraction (XRD)

In six representative samples, major diffraction peaks of muscovite, quartz, and sodium-rich plagioclase (albite) were observed (Figure 6). Diffraction peaks of clay minerals and high-temperature firing minerals such as mullite were absent. The peak intensities of muscovite relative to those of other minerals were strongly lower in some samples, although the abundance of muscovite in the mineral grains was nearly constant in the clay pastes in the microscopic observations. Thus, the attenuation of the peak intensity in muscovite is thought to have originated from the deterioration of its crystal structure as a result of thermal alteration. A very weak peak of chlorite was also observed in one sample. Because chlorite was observed microscopically in many samples, the rare detection of a chlorite peak may also be the result of thermal decomposition.

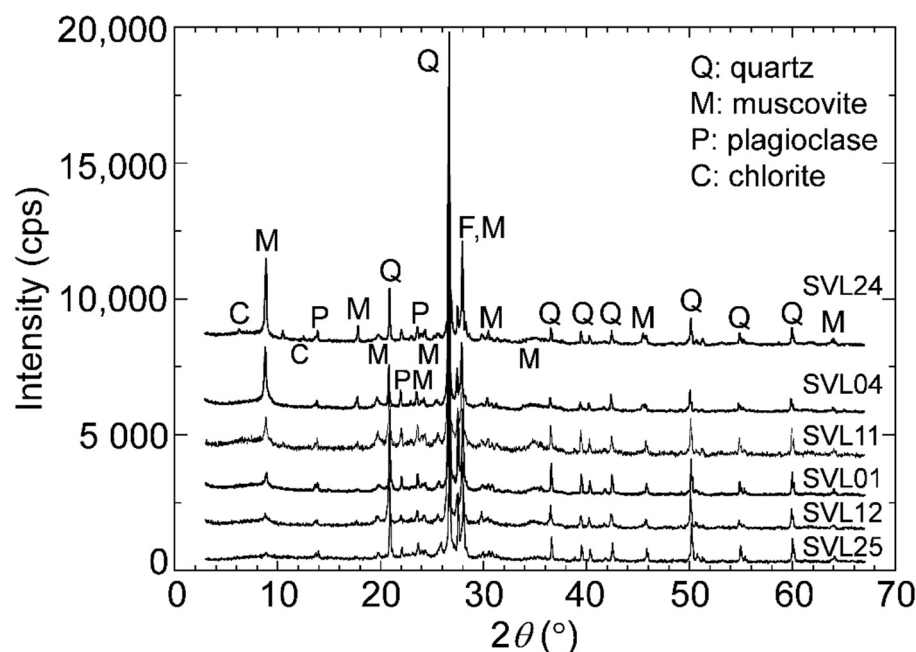


Figure 6. XRD patterns of pottery samples (SVL01, SVL04, SVL11, SVL12, SVL24, and SVL25).

## 4. Discussion

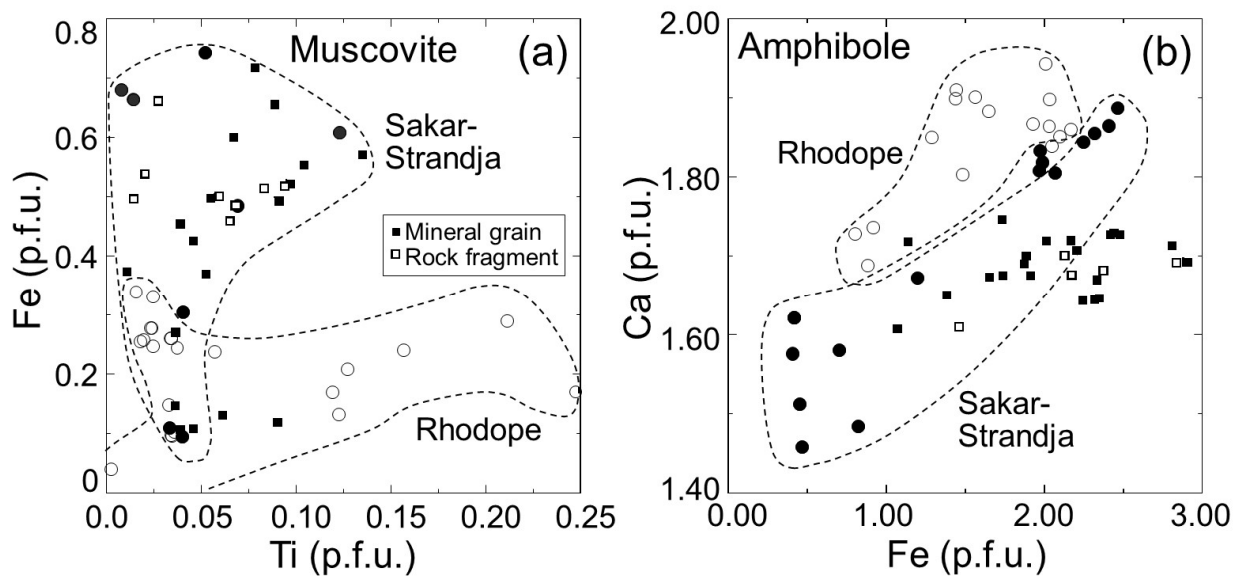
### 4.1. Origin and Source of the Mineral Grains and Rock Fragments

Both the rock fragments and the mineral grains in the pottery samples were inferred to have originated from metamorphic and metagranitoid or granitic rocks. Such metamorphic and granitic rocks are distributed widely in both the Sakar–Strandja Mountains and the Eastern Rhodope massif. Therefore, we examined the source area of the fragments and grains by comparing the mineral chemistry of the grains, fragments, and rocks in both areas using data from previous publications.

The atomic ratios of Ti/Fe in muscovite from metamorphic and granitic rocks exhibited different trends for the Sakar–Strandja Mountains and the Eastern Rhodope massif

(Figure 7a), and the majority of mineral grains and rock fragments plotted within the Sakar–Strandja region. The Ca/Fe atomic ratios in amphibole in the rocks also had different trends in the Sakar–Strandja and Rhodope areas (Figure 7b) and the grains and fragments plotted within the Sakar–Strandja region. These trends show that the mineral grains and rock fragments in the pottery originated from metamorphic and granitic rocks in the Sakar–Strandja Mountains. A similar trend was also observed in a Fe + Mg vs. Al plot for staurolite (not shown). These kinds of differences in correlations among elements, however, were unclear for plagioclase, alkali-feldspar, epidote, and garnet.

Upper Miocene to Pleistocene sediments (Ahmatovo Formation) are widely distributed from the southern slope of the Sakar-Strandja Mountains to the area surrounding the site [16]. The Ahmatovo Formation is also exposed within a few kilometers of the site; northwest of the site, it includes pebbles and gravel (up to boulder size) derived from metamorphic and granitic rocks of the Sakar-Strandja Mountains [24]. Typical raw-material sampling distances are thought to be within approximately 7 km of a given site [45], so the raw materials of the grains and fragments were probably derived from the Ahmatovo Formation. The alluvial sediments near the Maritsa River are also a possible raw-material source because sand grains occur in the same mineral assemblage as the pottery mineral grains and metamorphic rocks are present as pebbles [42–44]. Because the pottery mineral grains and rock fragments were angular to sub-angular, sub-angular sand grains and non-abraded pebbles in the sediments may have been the source material.

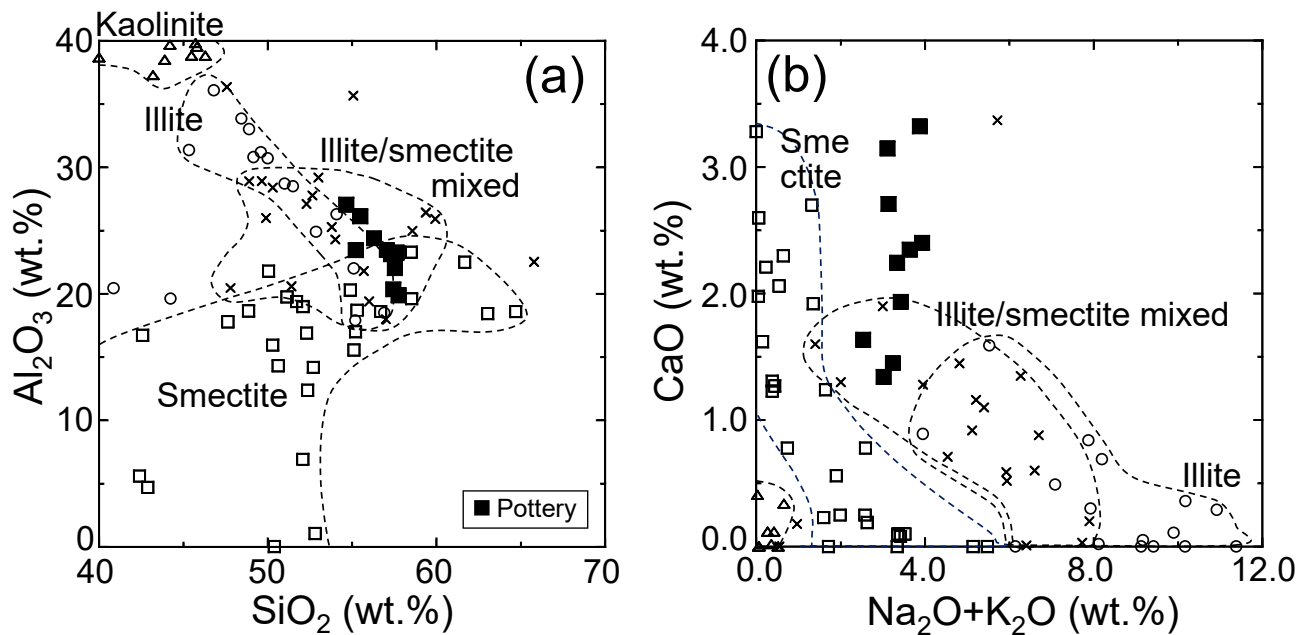


**Figure 7.** (a,b) Correlations of cations per formula unit (pfu) of minerals in mineral grains and rock fragments from pottery samples and metamorphic and igneous rocks from the Eastern Rhodope massif and Sakar–Strandja Mountains. (a) Ti vs. Fe in muscovite. Open circles, muscovite in gneiss and pelitic schists from the Eastern Rhodope massif [27,29,31]; solid circles, muscovite in gneiss and pelitic schists from the Sakar–Strandja Mountains [19,21]; closed squares, muscovite as mineral grains; solid squares, muscovite in rock fragments. (b) Fe vs. Ca in amphibole. Open circles, amphibole in schist, amphibolite, metamorphosed gabbro, and gabbro from the Eastern Rhodope massif [29,30,33,36]; solid circles, amphibole in amphibolite, metagranitoids, and gabbro from the Sakar–Strandja Mountains [19,46]; closed squares, amphibole as mineral grains; solid square, amphibole in rock fragments.

#### 4.2. Chemical Features of the Clay Paste

The chemical features of the clay pastes were examined by using oxide correlation plots based on the chemical compositions of representative clay minerals (kaolinite, illite, smectite, and illite/smectite mixed-layer clay minerals [41]) and the SEM-EDS results for the clay pastes without mineral grains or rock fragments (Table 4). In the SiO<sub>2</sub> vs. Al<sub>2</sub>O<sub>3</sub>

diagram (Figure 8a), the clay paste data were plotted in the compositional region between representative illite and smectite or representative illite/smectite mixed-layer clay minerals. In the  $\text{Na}_2\text{O} + \text{K}_2\text{O}$  vs.  $\text{CaO}$  diagram (Figure 8b), the clay pastes also fell within the region of the representative illite/smectite mixed-layer clay minerals, although some clay pastes demonstrated an excess of  $\text{CaO}$  content outside the range of the mixed-layer clay minerals. The excess  $\text{CaO}$  may have resulted from the presence of nano-sized fragments of calcite dispersed in the clay pastes. The compositions of the clay pastes are basically thought to correspond to those of illite/smectite mixed-layer clay minerals or a mixture of smectite and illite.



**Figure 8.** (a,b) Correlations of oxide contents in pottery clay pastes and representative clay minerals (kaolinite, illite, smectite, and illite/smectite mixed-layer clay minerals). Solid squares, clay paste from pottery samples; open triangles, kaolinite [41]; open circles, illite [41]; open squares, smectite [41]; crosses, illite/smectite mixed-layer clay minerals [41]. (a)  $\text{SiO}_2$  vs.  $\text{Al}_2\text{O}_3$  and (b)  $\text{Na}_2\text{O} + \text{K}_2\text{O}$  vs.  $\text{CaO}$ .

Illite/smectite mixed-layer clay minerals are often formed by the chemical weathering of basic schist [41,47]. On the eastern slope of the Sakar Mountain, mixed-layered illite/smectite and kaolinite were found to be the predominant clay minerals in clay from Miocene sediments corresponding to the Ahmatovo Formation [48]. Illite and smectite have also been identified in the clay sediments [48]. In addition, Holocene fluvial sediments from the Maritsa River consist mainly of clayey–silty sediments, sands, and gravels. Smectite is the principal clay mineral in the clayey–silty sediments (about 77%); illite (13%) and kaolinite (10%) are subordinate [43]. Thus, the outcrop area of the Ahmatovo Formation (i.e., the flood plains of the Maritsa River) was most likely the collecting site for the raw clay materials.

#### 4.3. Estimated Firing Temperature

Melting textures for the clay pastes and feldspar grains were not identified in the SEM observations. The starting points of melting for clay minerals are approximately 750–800 °C under reduced conditions and approximately 800–850 °C under oxidized conditions [39]; thus, the pottery samples were considered to have been fired at temperatures of less than 800 °C.

Some pottery samples demonstrated a marked decrease in the diffraction intensities of muscovite and chlorite (Figure 2), regarded as indicative of thermal decomposition

during pottery firing. The diffraction peak of muscovite in a clay matrix disappears at a temperature over 850 °C [49–51], and a decrease in the diffraction intensities is clearly observed at a temperature range of 700–800 °C [52]. Chlorite in a clay matrix is completely decomposed at a temperature of 750 °C under reduced or oxidized conditions [53,54]. Taking these factors into account, the firing temperature of the pottery is thought to have been 700–800 °C, which is close to the values of 750–850 °C reported for EBA pottery in northwestern Thrace, Bulgaria [55]. In addition, the existence of dark cores in the present samples indicates a firing of short duration or in an incomplete state of oxidation. Such firing conditions may be a feature of EBA pottery in the Thrace plain.

#### 4.4. Relationship between Petrographic and Typological Features of Pottery

The studied pottery samples contained chemically homogeneous clay pastes with rare clay pellets and without impurities. We presume that levigation was performed during the preparation of the clay raw materials. As a mixture of well-sorted clays and abundant angular mineral grains and rock fragments is exceptional in a naturally deposited clay bed, the mineral grains and rock fragments in the pottery samples are interpreted as artificially tempered materials introduced after the levigation step. The presence of artificially tempered materials in the samples appears to be consistent with the large volume ratios of tempered minerals and fragments observed under the microscope. Large volume ratios of mineral grains were also estimated in the calculations of the mixture compositions of clay paste and mineral grains (Table 4). The preferred orientation of muscovite grains and elongated voids in the clay pastes indicated that a high-skill technique was used during pottery making.

The techniques for pottery making, mineral species of the grains, rock types of the fragments, and chemical compositions of clay pastes were nearly the same in both the local EBA2 group pottery and the cord-decorated pottery. These results indicate that both pottery types were produced from the same raw materials and using the same production techniques. Thus, the cord-decorated pottery samples were probably local pottery made under the influence of a foreign culture.

## 5. Conclusions

The EBA pottery samples from the Svilengrad-Brantiite site in southeastern Bulgaria exhibited dark-colored surfaces and orange to reddish-brown cross sections with a dark core. The pottery was produced from non-calcareous clay pastes with abundant mineral grains and fragments of metamorphic and granitic rocks, was created using high-skill techniques, and was fired at moderate temperatures (700–800 °C). The two typological groups, local-made EBA2 and cord-decorated types, were quite similar in terms of mineral grains, rock fragments, clay pastes, and production techniques; thus, both types of pottery from Svilengrad-Brantiite are considered to be of the local style, most probably made by the inhabitants.

The mineral grains and rock fragments were inferred to have originated from metamorphic and granitic rocks in the Sakar-Strandja Mountains. Because fragments and separated grains of these rocks are present as gravel, pebbles, and sand in Neogene sediments and Maritsa River sediments, they were most likely collected from an area near the site. The clay materials were also likely to have been procured from river sediments or Tertiary sediments on the slopes of the Sakar-Strandja Mountains. The procurement of the raw materials near the site and the high-skill techniques used to make the pottery may be characteristic of EBA pottery from the southeastern part of the Upper Thracian Plain.

**Author Contributions:** Conceptualization, M.K. and M.S.; methodology, M.K. and T.S.; software, M.K.; validation, M.K. and M.S.; formal analysis, M.K. and T.S.; investigation, M.K., M.S. and T.S.; resources, M.K. and M.S.; data curation, M.K. and T.S.; writing—original draft preparation, M.K. and M.S.; writing—review and editing, M.K.; visualization, M.K.; supervision, M.K. and M.S.; project administration, M.K. and M.S.; funding acquisition, M.K. and M.S. All authors have read and agreed to the published version of the manuscript.

**Funding:** This study was supported in part by the Japan Society for the Promotion of Science Grants-in-Aid for Scientific Research (no. 18H05447 to M.K. and 19K13399 to M.S.).

**Data Availability Statement:** The dataset is presented directly in the present study. Additional data (unpublished) are available upon request from the corresponding author (M.K.).

**Acknowledgments:** The authors wish to thank G. Nekhrizov of the National Institute of Archaeology and Museum, Bulgarian Academy of Sciences, for provision of the pottery samples; K. Matsumoto of Tokai University, Japan, for sample preparation; and H. Takehara of Paleo Labo Co., Ltd., Japan, for conducting the XRF analyses. The authors would also like to thank the two anonymous reviewers for their useful comments that helped in the revision of this manuscript.

**Conflicts of Interest:** The authors declare no conflict of interest.

## References

1. RAnthony, D.W. *The Horse, the Wheel, and Language: How Bronze-Age Riders from the Eurasian Steppes Shapes the Modern World*; Princeton University Press: Princeton, NJ, USA, 2007.
2. Heyd, V. Yamnaya Groups and Tumuli west of the Black Sea. In *Ancestral Landscape. Burial Mounds in the Copper and Bronze Ages (Central and Eastern Europe–Balkans–Adriatic–Aegean, 4th–2nd millennium B.C.)*; Borgna, E., Müller-Celka, S., Eds.; Travaux de la Maison de l’Orient, TMO 58; Maison Orient: Lyon, France, 2011; pp. 535–555.
3. Georgiev, G. Beiträge zur Erforschung des Neolithikums und der Bronzezeit in Südbulgarien. *Arch. Austr.* **1967**, *42*, 90–144.
4. Roman, P.; Dodd-Oprîtescu, A.; János, P.; Hauptmann, H.; Schrickel, W. *Beiträge zur Problematik der Schnurverzierten Keramik Südosteuropas*; P. von Zabern: Mainz am Rhein, Germany, 1992.
5. Nikolova, L. Data about sea contacts during the Early Bronze Age in south-eastern Europe (c. 3500/3400–2350/2250 B.C.). *Thracia Pontica* **1994**, *5*, 57–86.
6. Lichardus, J.; Lichardus-Itten, M. Nordpontische Beziehungen während der frühen Vorgeschichte Bulgariens. *Thracia* **1995**, *11*, 31–62.
7. Leshtakov, K.; Tsirtsoni, Z. Caesurae in the Bronze Age chronology of Eastern Bulgaria. In *Der Schwarzmeerraum vom Neolithikum bis in Die Früheisenzeit (6000–600 v. Chr.). Kulturelle Interferenzen in der Zirkumpontischen Zone und Kontakte mit Ihren Nachbargebieten*; Nikolov, V., Schier, W., Eds.; Verlag Marie Leidorf GmH: Rahden, Germany, 2016; pp. 477–491.
8. Harrison, R.J.; Heyd, V. The transformation of Europe in the third millennium BC: The example of ‘Le Petit Chasseur I+III’ (Sion, Valais, Switzerland). *Praehist. Z* **2007**, *82*, 129–214. [CrossRef]
9. Semmoto, M. Chronology and Regional Interaction on Pottery in Early Bronze Age, Bulgaria: Focusing on Material Analysis of Tell Dyadovo. Ph.D. Thesis, Tokai University, Kanagawa, Japan, 2015.
10. Leshtakov, K. Troy and upper Thrace: What happened in the EBA 3? (Interrelations Based on Pottery Evidence). In *Early Bronze Age Troy: Chronology, Cultural Developments and Interregional Contacts*; Pernicka, E., Ünlüsoy, S., Blum, S., Eds.; Verlag Dr. Rudolf Habelt: Bonn, Germany, 2016; pp. 239–255.
11. Semmoto, M.; Kannari, T.; Shibata, T.; Leshtakov, K. Petrographic and Chemical characterization of Early Bronze Age pottery from Sokol Himitleyata in Nova Zagora Region: An interim report. *Stud. Archaeol. Univ. Serdicensis Diss. Ser.* **2018**, *6*, 153–167.
12. Leshtakov, K.; Machev, P.; Popova, T.; Vangelov, D.; Vangelova, V.; Stoilkova, T.; Petrova, V.; Ilieva, D.; Nikolova, N.; Chavdarova, S.; et al. Social dimensions of technology of ceramic production in southeast Bulgaria in 6th–2nd mill. BC. *Interdiscip. Stud.* **2019**, *26*, 33–106.
13. Nekhrizov, G.; Tzvetkova, J. Iron Age ritual pits near Svilengrad. In *Spasitelni Arheologicheski Razkopki po Traseto na Zhelezopatnata Liniya Plovdiv–Svilengrad Prez 2005 [Rescue Excavations along the Route of the Plovdiv–Svilengrad Railway in 2005]*; Nikolov, V., Nekhrizov, G., Tzvetkova, J., Eds.; Faber: Veliko Tarnovo, Bulgaria, 2008; pp. 331–493.
14. Nekhrizov, G. Iron Age pit sanctuary and Early Bronze Age settlement near the town of Svilengrad. In *Spasitelni Arheologicheski Razkopki po Traseto na Zhelezopatnata Liniya Plovdiv–Svilengrad Prez 2004 [Rescue Excavations along the Route of the Plovdiv–Svilengrad Railway in 2004]*; Nikolov, V., Nekhrizov, G., Tzvetkova, J., Eds.; Faber: Veliko Tarnovo, Bulgaria, 2006; pp. 397–548.
15. Valentinova, M.; Nenova, D. Early Bronze Age site near Svilengrad. In *Spasitelni Arheologicheski Razkopki po Traseto na Zhelezopatnata Liniya Plovdiv–Svilengrad Prez 2005 [Rescue Excavations along the Route of the Plovdiv–Svilengrad Railway in 2005]*; Nikolov, V., Nekhrizov, G., Tzvetkova, J., Eds.; Faber: Veliko Tarnovo, Bulgaria, 2008; pp. 494–526.
16. Kozhoukharov, D.; Boyanov, I.; Kozhoukharova, E.; Goranov, A.; Savov, S.; Shilyafov, G. *Explanatory Note to the Geological Map of Bulgaria on Scale 1:100000, Svilengrad Map Sheet*; Geology and Geophysics Corporation: Sofia, Bulgaria, 1995.
17. Okay, A.; Satir, M.; Tüysüz, O.; Akyüz, S.; Chen, F. The tectonics of the Strandja Massif: Late-Variscan and mid-Mesozoic deformation and metamorphism in the northern Aegean. *Int. J. Earth Sci.* **2001**, *90*, 217–233. [CrossRef]
18. Gerdjikov, I. Alpine metamorphism and granitoid magmatism in the Strandja Zone: New data from the Sakar Unit, SE Bulgaria. *Turkish J. Earth Sci.* **2005**, *14*, 167–183.
19. Sunal, G.; Satir, M.; Natal’in, B.A.; Topuz, G.; Vonderschmidt, O. Metamorphism and diachronous cooling in a contractional orogen: The Strandja Massif, NW Turkey. *Geol. Mag.* **2011**, *148*, 580–596. [CrossRef]
20. Machev, P.; Ganev, V.; Klain, L. New LA-ICP-MS U-Pb zircon dating for Strandja granitoids (SE Bulgaria): Evidence for two-stage late Variscan magmatism in the internal Balkanides. *Turkish J. Earth Sci.* **2015**, *24*, 230–248. [CrossRef]

21. Tzankova, N. Chemical characterization of garnets and P-T conditions of metamorphism of the Triassic rocks occurring to the south of Oreschnik, South-East Bulgaria. *Ann. Univ. Min. Geol. St. Ivan Rilski* **2005**, *48*, 155–160.
22. Tzankova, N.; Petrov, O. ICP AES, microprobe, and X-ray powder diffraction data for garnets from metamorphic rocks in the Sakar region, SE Bulgaria. *Geochem. Mineral. Petrol. Sofia* **2006**, *44*, 73–89.
23. Kamenov, B.K.; Vergilov, V.; Dabovski, C.; Vergilov, I.; Ivchinova, L. The Sakar batholith–petrology, geochemistry and magmatic evolution. *Geochem. Mineral. Petrol. Sofia* **2010**, *48*, 1–37.
24. Schaller, M.; Lachner, J.; Christl, M.; Maden, C.; Spassov, N.; Ilg, A.; Böhme, M. Authigenic Be as a tool to date river terrace sediments?—An example from a Late Miocene hominid locality in Bulgaria. *Quat. Geochronol.* **2015**, *29*, 6–15.
25. Ivanov, D.; Lazarova, M. Past climate and vegetation in Southeast Bulgaria—A study based on the late Miocene pollen record from the Tundzha Basin. *J. Palaeogeogr.* **2019**, *8*, 3. [CrossRef]
26. Caracciolo, L.; Orlando, A.; Critelli, S.; Kolios, N.; Manetti, P.; Marchev, P. The Tertiary Trace Basin of SE Bulgaria and NE Greece: A review of petrological and mineralogical data of sedimentary sequences. *Acta Vulcanol.* **2015**, *25*, 21–41.
27. Mposkos, E.; Liati, A. Metamorphic evolution of metapelites in the high-pressure terrane of the Rhodope zone, northern Greece. *Can. Mineral.* **1993**, *31*, 401–424. [CrossRef]
28. Marchev, P.; Raicheva, R.; Downes, H.; Vaselli, O.; Chiaradia, M.; Moritz, R. Compositional diversity of Eocene–Oligocene basaltic magmatism in the Eastern Rhodopes, SE Bulgaria: Implications for genesis and tectonic setting. *Tectonophysics* **2004**, *393*, 301–328. [CrossRef]
29. Nagel, T.J.; Schmidt, S.; Janák, M.; Froitzheim, N.; Jahn-Awe, S.; Georgiev, N. The exposed base of a collapsing wedge: The Nestos Shear Zone (Rhodope metamorphic province, Greece). *Tectonics* **2011**, *30*, TC4009. [CrossRef]
30. Bonev, N.; Ovtcharova-Schaltegger, M.; Moritz, M.R.; Marchev, P.; Ulianov, A. Peri-Gondwanan Ordovician crustal fragments in the high-grade basement of the Eastern Rhodope Massif, Bulgaria: Evidence from U-Pb LA-ICP-MS zircon geochronology and geochemistry. *Geodin. Acta* **2013**, *26*, 207–229. [CrossRef]
31. Mposkos, E. High-pressure metamorphism in gneisses and pelitic schists in the East Rhodope Zone (N. Greece). *Mineral. Petrol.* **1989**, *41*, 25–39. [CrossRef]
32. Yanev, Y.; Ivanova, R. Mineral chemistry of the collision-related acid Paleogene volcanic rocks of the Eastern Rhodopes, Bulgaria. *Geochem. Mineral. Petrol. Sofia* **2010**, *48*, 39–65.
33. Raicheva, R.; Marchev, P.; Georgiev, S.; Ichev, M. Geochemistry, mineral composition and conditions of crystallization of accessory-rich gabbro associated with adakitic rocks of the Drangovo pluton, Rhodope Massif. *C. R. Acad. Bulg. Sci.* **2018**, *71*, 220–229.
34. Caracciolo, L.; Orlando, A.; Marchev, P.; Critelli, S.; Manetti, P.; Raycheva, R.; Riley, D. Provenance of Tertiary volcanoclastic sediment in NW Thrace (Bulgaria): Evidence from detrital amphibole and pyroxene geochemistry. *Sediment. Geol.* **2016**, *336*, 120–137. [CrossRef]
35. Chavdarova, S.; Machev, P. Amphibolites from Sakar Mountain—geological position and petrological features. In Proceedings of the Bulgarian Geological Society, National Conference with International Participation “Geosciences 2017”, Sofia, Bulgaria, 7–8 November 2017; pp. 49–50.
36. Raeva, E.; Cherneva, Z. Metamorphic grade of the Madan unit in the southern part of the Central Rhodopes, Bulgaria. *Geochem. Mineral. Petrol. Sofia* **2009**, *47*, 135–161.
37. Moulas, E.; Schenker, F.L.; Burg, J.P.; Kostopoulos, D. Metamorphic conditions and structural evolution of the Kesebir-Kardamos dome: Rhodope metamorphic complex (Greece-Bulgaria). *Int. J. Earth Sci.* **2017**, *106*, 2667–2685. [CrossRef]
38. Braekmans, D.; Degryse, P. Petrography: Optical microscopy. In *The Oxford Handbook of Archaeological Ceramic Analysis*; Hunt, A.M.W., Ed.; Oxford University Press: Oxford, UK, 2016; pp. 233–265.
39. Maniatis, Y.; Tite, M.S. Technological Examination of Neolithic-Bronze Age pottery from central and southeast Europe and from the Near East. *J. Archeol. Sci.* **1981**, *8*, 59–76. [CrossRef]
40. Ionescu, C.; Hoeck, V.; Ghergari, L. Electron microprobe analysis of ancient ceramics: A case study from Romania. *Appl. Clay Sci.* **2011**, *53*, 466–475. [CrossRef]
41. Wilson, M.J. *Sheet Silicates: Clay Minerals, Rock-Forming Minerals*; The Geological Society of London: London, UK, 2013; Volume 3C.
42. Yaneva, M. Comparative sedimentologic characteristics of young sediments (Pliocene–Holocen) disturbed by Chirpan Fault. *Rev. Bulgarian Geol. Soc.* **2006**, *67*, 41–49.
43. Yaneva, M.; Lazarova, M. Preliminary sedimentological and palynological studies of Quaternary deposits from paleoseismological trench “Cherna Gora”, Chirpan district. *C. R. Acad. Bulg. Sci.* **2004**, *57*, 71–76.
44. Yaneva, M.; Todorova, N.; Katsarov, G.; Petrova, V.; Bacvarov, K. By the rivers of Nova Nadezhda: Dynamics of human–environment interaction at a prehistoric site in Upper Thrace. *Geol. Balc.* **2017**, *46*, 65–72.
45. Arnold, D. *Ceramic Theory and Cultural Process*; Cambridge University Press: Cambridge, UK, 1985.
46. Pristavova, S.; Tzankova, N.; Gospodinov, N.; Filipov, P. Petrological study of metasomatic altered granitoids from Kanarata deposit, Sakar Mountain, southeastern Bulgaria. *J. Mining Geol. Sci.* **2019**, *62*, 53–61.
47. Chamley, H. *Clay Sedimentation*; Springer: Berlin/Heidelberg, Germany, 1989.
48. Ilieva, A.; Milakovska, Z. Mineral composition of the clay fractions from sediments of Troianovo-North mine, East Maritza Basin (Bulgaria). In Proceedings of the Annual Scientific Conference of the Bulgarian Geological Society, GEOSCIENCES 2007, Sofia, Bulgaria, 13–14 November 2017; pp. 39–41.

49. Riccardi, M.P.; Messiga, B.; Duminuco, P. An approach to the dynamics of clay firing. *Appl. Clay Sci.* **1999**, *15*, 393–409. [CrossRef]
50. Hajjaji, M.; Kacim, S.; Boulmane, M. Mineralogy and firing characteristics of a clay from the valley of Ourika (Morocco). *Appl. Clay Sci.* **2002**, *21*, 203–212. [CrossRef]
51. Papadopouloul, D.N.; Lalia-Kantouri, M.; Kantiranis, N.; Stratis, J.A. Thermal and mineralogical contribution to the ancient ceramics and natural clays characterization. *J. Therm. Anal. Calorim.* **2006**, *84*, 39–45. [CrossRef]
52. Ortega, L.A.; Zuluaga, M.C.; Alonso-Olazabal, A.; Murelaga, X.; Alday, A. Petrographic and geochemical evidence for long-standing supply of raw materials in Neolithic pottery (Mendandia site, Spain). *Archaeometry* **2010**, *52*, 987–1001. [CrossRef]
53. Maniatis, Y.; Simopoulos, A.; Kostikas, A.; Perdikatsis, V. Effect of reducing atmosphere on minerals and iron oxides developed in fired clays: The role of Ca. *J. Am. Ceram. Soc.* **1983**, *66*, 773–781. [CrossRef]
54. Maggetti, M.; Neururer, C.; Ramseyer, D. Temperature evolution inside a pot during experimental surface (bonfire) firing. *Appl. Clay Sci.* **2011**, *53*, 500–508. [CrossRef]
55. Kostadinova-Avramova, M.; Jordanova, N.; Jordanova, D.; Grigorov, V.; Lesigyarski, D.; Dimitrov, P.; Bozhinova, E. Firing temperatures of ceramics from Bulgaria determined by rock-magnetic studies. *J. Archeol. Sci. Rep.* **2018**, *17*, 617–633. [CrossRef]

## Article

# Technological Characterization of Almohad Pottery Glazes from SW Mallorca (Balearic Islands, Spain)

Daniel J. Albero Santacreu <sup>1,\*</sup>, Jose C. Carvajal López <sup>2</sup> and Alejandro Ramos Benito <sup>3</sup><sup>1</sup> Department of Historical Sciences and Arts Theory, University of the Balearic Islands, 07122 Palma, Spain<sup>2</sup> School of Archaeology and Ancient History, University of Leicester, Leicester LE1 7RH, UK; jcl2@leicester.ac.uk<sup>3</sup> ArqueoUIB Research Group, University of the Balearic Islands, 07122 Palma, Spain; arbenito@outlook.com

\* Correspondence: d.albero@uib.es

**Abstract:** In this paper, we addressed the chemical composition and main features of a glazed Almohad ceramic assemblage recovered from Puig de Sa Morisca, a rural Islamic site located in southwest Mallorca. The glazes were analyzed by means of scanning electron microscope equipped with energy-dispersive spectrometer (SEM-EDS). The archaeometrical analysis conducted allowed us to characterize the technological choices applied by potters from the end of the 12th century and the beginning of the 13th century. The exclusive use of lead-silica glazes was confirmed, which in some cases was opacified with tin. We also established that some tableware vessels, which were imported to the island, have shown glazes with a particular composition within the analyzed record.

**Keywords:** pottery; Almohad period; Al-Andalus; lead glazes; tin glazes; SEM-EDS

**Citation:** Albero Santacreu, D.J.; Carvajal López, J.C.; Ramos Benito, A. Technological Characterization of Almohad Pottery Glazes from SW Mallorca (Balearic Islands, Spain). *Minerals* **2022**, *12*, 106. <https://doi.org/10.3390/min12010106>

Academic Editor: Marco Benvenuti

Received: 17 December 2021

Accepted: 13 January 2022

Published: 17 January 2022

**Publisher's Note:** MDPI stays neutral with regard to jurisdictional claims in published maps and institutional affiliations.



**Copyright:** © 2022 by the authors. Licensee MDPI, Basel, Switzerland. This article is an open access article distributed under the terms and conditions of the Creative Commons Attribution (CC BY) license (<https://creativecommons.org/licenses/by/4.0/>).

## 1. Introduction

Archaeometric methodologies are relatively recent in the study of Al-Andalus Almohad ceramics, but they have proved excellent for studying distribution networks and vessel technology elsewhere [1–6]. In addition, there are many analytical studies that have addressed the technology of Andalusian ceramic glazes, covering a broad chronology between the 10th and 15th centuries AD [7]. However, such works have been mainly focused on pottery assemblages from southern areas of the Iberian Peninsula associated with the early and late Islamic periods, related to the Nasrid kingdom period of Granada [3,8–11]. Some attention has also been paid to glazed ceramics recovered from archaeological sites located in the northeast of the Iberian Peninsula associated with the Taifa period (12th century AD) [12] and Hispano-Moresque glazed ceramics [13–16]. Although abundant information is available on the glaze recipes and the technological choices applied by Islamic potters related to diverse chronology and locations, few studies have addressed the compositional characterization of Almohad ceramic glazes and their connection to previous pottery productions.

In the case of Mallorca (Balearic Islands, Spain), the technological study of Islamic ceramics by means of archaeometric methods has only recently been implemented in relation to the petrographic study of pottery pastes [6,17]. Regarding the glazes of the vessels from this island, only the composition and technology of a very few samples ( $n = 6$ ) related to the Taifa period (11th century AD) have been characterized [7,16]. A specific and systematic study of the technological choices and recipes applied by the Almohad potters in the production of glazed ceramics has never been conducted on the island. In this paper, we carry out the archaeometric study by means of SEM-EDS of the chemical composition and technology of an Islamic glazed ceramic assemblage for the first time on the island. The pottery studied was retrieved from the Almohad rural site of Puig de Sa Morisca (Figure 1). In this sense, it must be highlighted too that this is also the first time that the composition



and technological features of a glazed ceramic assemblage recovered from a rural site of the Balearic Islands are studied.



**Figure 1.** Geographic location of Mallorca and the archaeological sites mentioned in the text (1, Puig de Sa Morisca; 2, Madīna Mayūrqa/Palma).

The research that we present here focuses on approaching the Islamic glazed ceramics found on this archaeological site with three objectives. First, we aim to continue with the analyses conducted by other scholars [7,18] and characterize the chemical composition and microstructure of late 12th and early 13th century glazes produced in the pottery workshops located in the main city of the island, Madīna Mayūrqa. Additionally, we will consider the features and particularities related to certain Islamic glazed ceramics that were imported to the island and subsequently distributed to some rural contexts. Finally, all this technological information will also be used to address the role played by the archaeological rural site of Puig de Sa Morisca during the Almohad period in order to provide a better understanding of the complexity of Islamic settlement before the Christian conquest of the island in 1229 [19].

## 2. Archaeological Context

The Islamic settlement at Puig de Sa Morisca is located in a rural area in southwest Mallorca (Balearic Islands, Spain). The Islamic site was built on top of an Iron Age site, reusing a prehistoric wall that protected the most accessible part of the 120 m hilltop where the site was placed. The rest of the 8500 m<sup>2</sup> settlement has abundant Islamic ceramics on the surface and is inaccessible due to the steep rock face. The earliest Islamic occupation included a hearth reoccupying a prehistoric tower in the fortified hill dated to 970–1160 Cal AD (UTC-10027), i.e., an early Islamic occupation corresponding to the Taifa period (1009–1115). However, the largest Islamic remains recovered up to now were located on the hilltop and included three rooms of Almohad date (1202–1229) organized around an Iron Age tower with abundant Islamic ceramics on the surface [20].

The excavations inside these rooms carried out between 2002 and 2007 yielded a large collection of domestic and utilitarian ceramics similar to other rural contexts [21]: pitchers, jugs, marmites, *ataifors* (serving dishes), large jars, lids, tripods, *alcadafes* (basins), oil lamps, etc. [22]. The typologies and decorative techniques, together with the simplification of the stamped decoration, evidenced that the majority of the ceramic production dated back to the 12th and beginning of the 13th century AD, corresponding to the Almohad period [20,22].

The petrographical and chemical analysis (WD-XRF) of the Islamic pottery recovered from the Almohad rural site of Puig de Sa Morisca [6,17] allowed us to identify the presence of a large set of ceramics, many of them glazed (Table 1), that were made with fine-textured calcareous clays with mudstones, calcimudstones, foraminifera and quartz (Petrofabric 1). The WD-XRF analysis conducted in 30 vessels from Petrofabric 1 allowed us to confirm the

presence in the archaeological site of a monogenic and chemically very homogeneous group with a very low total variation ( $vt = 0.29$ ), thus evidencing a common origin for all samples from this fabric. The petrographical features of the samples included in Petrofabric 1 and the study of the planktonic foraminifera present in the thin sections allowed us to relate the raw materials used in the production of these vessels to Pliocene clay deposits located on the Palma basin. Therefore, the archaeometric data available show that most of the vessels (78%) recovered from the rural site of Puig de Sa Morisca had a local origin and were possibly made in pottery workshops located in the urban center of Madīna Mayūrqa (current city of Palma, Figure 1).

In addition, the petrographical analysis allowed us to verify the existence of a limited number of glazed vessels related to loners with a particular mineralogical composition on the rural site. These petrofabrics include intermediate–felsic plutonic igneous rocks (Petrofabric 4), low-grade metamorphic rocks (Petrofabric 5) or have a distinctive amount of quartz and K-feldspar (Petrofabric 8). Given the calcareous nature of Mallorca and the absence of igneous and metamorphic formations in the local geology, it is clear that these vessels were imported to the island and subsequently consumed and deposited on the rural site under study.

**Table 1.** Typology, petrologic fabric and chemical composition of the glazes analyzed by means of SEM-EDS (wt%, normalized to 100%). n.d. = non-detected; \* = concentrations determined by means of WD-XRF [6].

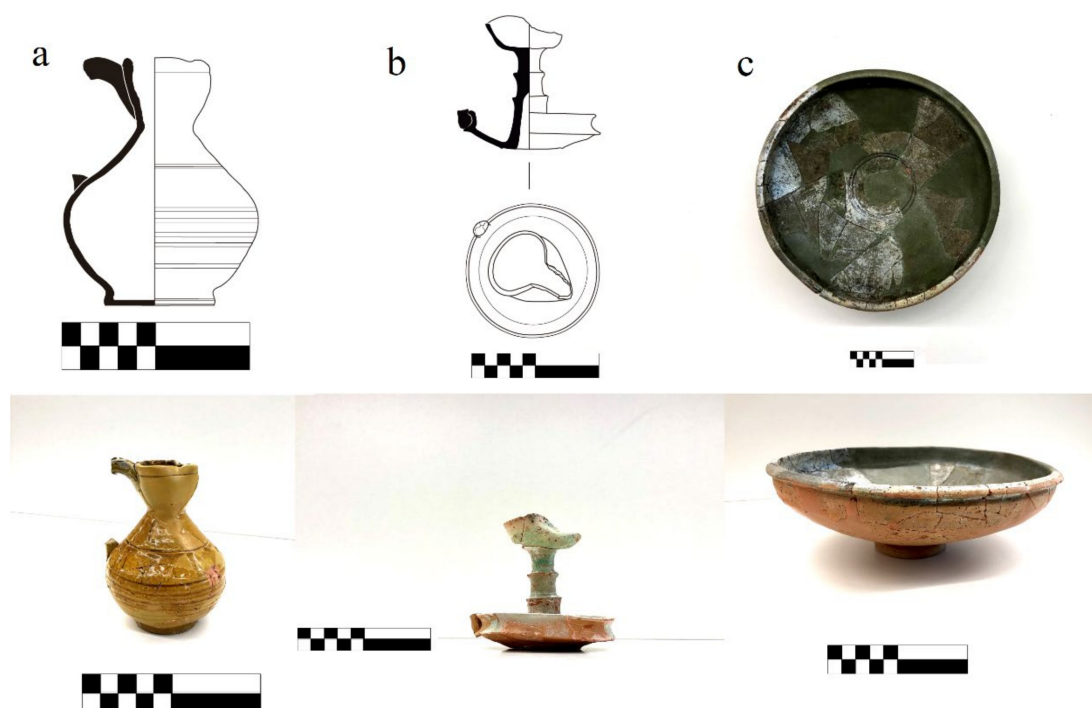
Sample	Typology	Petro Fabric	%CaO Body	Surface	Color	Na <sub>2</sub> O	MgO	Al <sub>2</sub> O <sub>3</sub>	SiO <sub>2</sub>	K <sub>2</sub> O	CaO	Fe <sub>2</sub> O <sub>3</sub>	CuO	PbO	SnO <sub>2</sub>
SM14	Tajen Lid	1	16.7 *	Outer	Green	n.d.	0.2	1.1	27.7	0.4	1.5	0.4	2	66.7	n.d.
SM21	Juglet	1	13.6 *	Outer	White	1	0.3	3.2	34.9	1.4	3	0.9	1	49.8	4.5
SM23	Atajfor	1	8.8	Inner	Green	n.d.	0.4	3.4	33.2	0.7	2.5	1	2.3	56.5	n.d.
SM28	Juglet	1	7.8 *	Outer	Green	n.d.	0.2	1.8	28.2	0.5	1.4	1.1	1.3	65.5	n.d.
SM29	Juglet	1	8.9	Outer	Green	n.d.	0.3	2.5	28.6	0.5	1.4	0.9	2.5	63.3	n.d.
				Inner	Colorless	n.d.	0.3	4	33.4	0.5	2.6	0.9	n.d.	58.3	n.d.
SM31	Orcita	1	8	Outer	White	1	n.d.	2.8	34.5	1.5	2	0.7	1.8	45.7	10
				Inner	Colorless	n.d.	0.3	3.5	26.5	0.4	1.3	0.8	n.d.	67.2	n.d.
SM32	Atajfor	1	9.4	Inner	Green	n.d.	0.6	5.5	38.4	1.7	3	1.7	2	47.1	n.d.
SM34	Juglet	1	13.3	Outer	White	1.8	0.4	3.6	32.6	1.8	2.6	1	1.1	52.2	2.9
SM36	Atajfor	1	12.2	Inner	Colorless	n.d.	0.6	5.1	27.2	1.1	4.8	3.7	n.d.	57.5	n.d.
SM37	Pitcher	1	10.7 *	Outer	Colorless	0.3	0.7	5.6	30.9	1.3	5.3	2.8	n.d.	53.1	n.d.
SM39	Atajfor	1	8.6 *	Inner	Yellow	n.d.	0.3	3.7	31.8	0.8	2.4	5.2	n.d.	55.8	n.d.
				Inner	Colorless	n.d.	0.3	3.1	34.6	0.9	3.1	1.2	n.d.	56.8	n.d.
SM40	Jar	1	12.3	Outer	Green	n.d.	0.4	5.7	33.4	1.1	4.8	1.7	2	50.9	n.d.
SM41	Large Storage Pot	1	6.2 *	Outer	Green	n.d.	0.2	2.3	29.2	0.4	1.1	0.9	0.6	65.3	n.d.
				Inner	Colorless	n.d.	0.2	1.9	29	0.3	1.3	0.8	n.d.	66.5	n.d.
SM42	Atajfor	1	17.5	Inner	White	1.5	0.3	3.7	34.4	1.5	2.6	1.1	1.7	49	4.2
SM43	Storage Pot	1	17.2	Outer	Green	n.d.	0.3	3.1	31.8	1.3	2.8	0.8	1	58.9	n.d.
SM44	Atajfor	1	11.9	Inner	White	1.5	0.2	2	34	0.9	1.8	0.9	0.6	53.7	4.4
SM47	Juglet	5	5.6	Outer	Colorless	0.3	0.6	5	35.9	1.1	1.1	2.7	n.d.	53.3	n.d.
SM48	Atajfor	1	9	Inner	White	1.2	0.3	2.9	34.9	1.2	1.7	0.8	1.3	50.4	5.3
SM49	Candle-Style Oil Lamp	1	10.3	Outer	Green	n.d.	0.3	3.1	33.9	0.7	2.3	0.9	2.4	56.4	n.d.

Table 1. Cont.

Sample	Typology	Petro Fabric	%CaO Body	Surface	Color	Na <sub>2</sub> O	MgO	Al <sub>2</sub> O <sub>3</sub>	SiO <sub>2</sub>	K <sub>2</sub> O	CaO	Fe <sub>2</sub> O <sub>3</sub>	CuO	PbO	SnO <sub>2</sub>
SM51	Oil Lamp	1	16.4	Outer	Colorless	n.d.	0.5	3.6	32.2	0.7	3.7	2.1	n.d.	57.2	n.d.
SM56	Ataifor	4	15.5	Inner	Green	1	0.3	1.3	29.3	1.1	2.3	0.8	1.7	62.2	n.d.
SM57	Ataifor	8	17.5	Inner Outer	Green Colorless	0.6 0.2	0.4 0.7	4.6 7.8	33.4 30.9	2 1.8	4.2 7.4	0.9 1.9	3 n.d.	50.9 49.3	n.d. n.d.
SM58	Ataifor	1	8.1	Inner Outer	Green Colorless	0.3 n.d.	0.6 0.5	2.2 3.4	28.7 33.9	0.9 0.9	4.2 3.7	0.9 1.2	2 n.d.	60.2 56.4	n.d. n.d.
SM59	Ataifor	5	15.5	Inner Outer	Green Yellow	n.d. n.d.	0.2 0.3	3.5 2.9	33.6 31.2	1.4 1.4	2.7 3.2	1 4.4	3 n.d.	54.6 56.6	n.d. n.d.

### 3. Materials and Methods

We analyze in this paper the chemical and mineralogical composition and the microstructure of 25 glazed ceramic samples that comprehend the wide typological diversity of glazed pottery identified on the archaeological site of Puig de Sa Morisca: pitchers, jugs, serving dishes, jars, lids, oil lamps, etc. (Table 1; Figure 2) [22]. The vast majority of the samples under study ( $n = 20$ ) were classified in Petrofabric 1 and are, therefore, related to local productions. In addition, the other five glazed ceramics, classified by their particular petrographic composition as loners and associated with imported wares, were also considered in the analysis (Table 1). The analysis of the glazes was conducted by cutting small fragments of the glazed pottery samples perpendicular to the glaze–body interface (including the body and the glazes located on the inner and outer surface of the vessels) with a diamond saw.



**Figure 2.** Photos and drawings of some of the glazed vessel typologies studied from Puig de Sa Morisca: (a) juglet (*redoma*), (b) candle-style oil lamp and (c) serving dish (*ataifor*). All the scale bars = 10 cm.

Polished cross-sections were prepared for examination in a JEOL JSM 6610 LV scanning electron microscope (SEM) (Jeol Ltd., Tokyo, Japan) equipped with an Oxford Instruments XMAXN 50 energy-dispersive spectrometer (EDS) (Oxford Instruments, Abingdon, United Kingdom). Quantitative analyses of the glazes were carried out using the EDS at 20 kV and scanning large areas of the glaze at  $2000\times$ , avoiding crystals related to the body–glaze interface, inclusions and any weathered or contaminated surface layers. However, sometimes evenly distributed inclusions, such as tin oxide particles, were necessarily included in the analysis. The reported values of the glazes are the averages of 10 analyses spread over the glaze layer in each sample.

Former WD-XRF data from Albero et al. [6] was used to record the CaO content of the ceramic body. However, not all the glazed samples analyzed in this study were formerly characterized by means of WD-XRF. In these cases, SEM-EDS scans of the clay matrix were also conducted in order to approach the calcareous/non-calcareous nature of the clay matrix. The CaO content of the matrix of each sample relates to the average of between

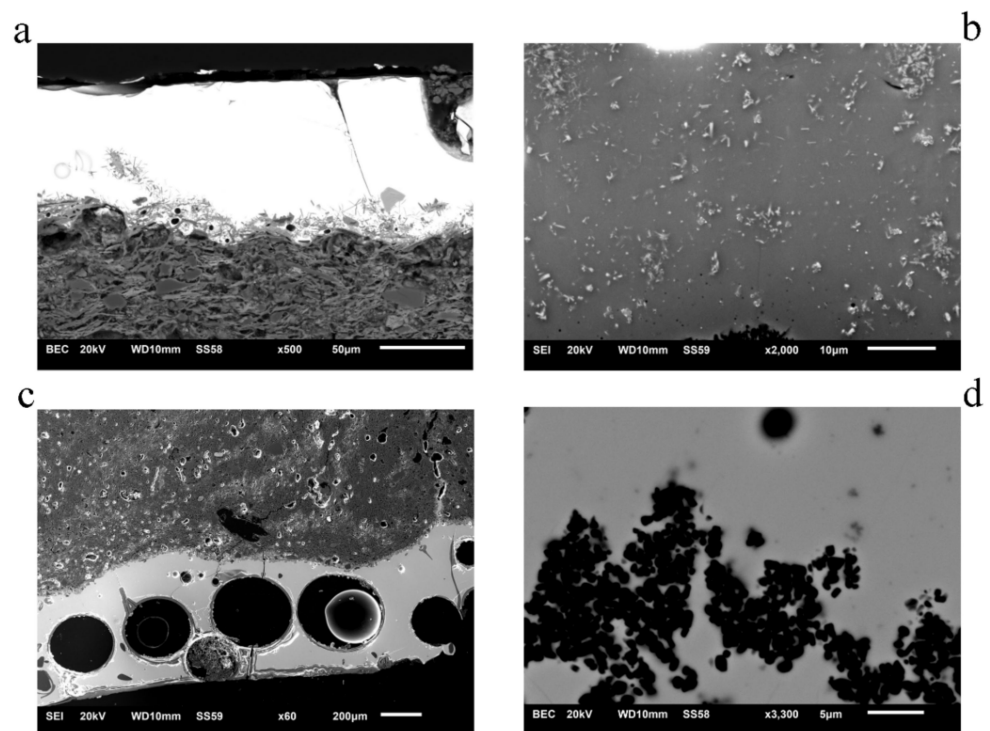
two and three microanalyses at  $2000\times$  magnifications, avoiding inclusions appearing on the clay body.

The analysis of the microstructure of the clay body was also carried out at  $2000\times$  magnifications using secondary electrons. The stability of the beam current during all these processes was monitored by calibrating against a cobalt standard. The accuracy and precision of the systems employed were checked against Corning B, C and D reference glasses. The limit of detection (LOD) of the instrument was only made possible to detect those elements with a weight greater than 0.2% of the total sample. All quantitative results of the glazes and clay matrix are reported as normalized weight per cent oxides with oxygen determined by stoichiometry.

## 4. Results

### 4.1. Local Pottery Production (Petrofabric 1)

The glazes identified in the archaeological vessels related to Petrofabric 1 are often slightly corroded, giving many samples a worn and dull appearance. The SEM-EDS analysis of the glazes provides evidence of the application of a vitreous layer between 60 and 200  $\mu\text{m}$  thick (although in some cases it can be up to 750  $\mu\text{m}$ ) generally rich in PbO (47–67%), thus suggesting the use of lead-silica glazes. The alkali content is low ( $\text{K}_2\text{O} < 2\%$  and  $\text{Na}_2\text{O} < 2\%$ ) and probably related to impurities present in the raw materials and chemical diffusion from the body paste during firing [7]. Therefore, lead is the main flux in these vitreous layers, many of them translucent (e.g., SM-36, SM-37, SM-51), since they did not incorporate colorants into their composition (Table 1; Figure 3a). However, most sherds under study show a green or greenish-white color on their surface.



**Figure 3.** (a) Back-scattered electron image showing a well-preserved thin glaze layer (SM-40), (b) Secondary electron image of cassiterite crystals in glaze of the sample SM-44, (c) Secondary electron image showing bubbles resulting from probably intentional gas release during the application of the glaze (SM-14), (d) Back-scattered electron image (BSEI) showing aggregates of equant pyroxene crystals in SM-14.

As could also be observed elsewhere and in other pottery samples from Al-Andalus [7,23,24], we identify the use of tin glazes in six ceramics. In our case, the glazes have a significant

PbO content (45.7–67.2%; average = 56.81%,  $\sigma$  = 6.31) and a lower amount of tin oxide (3–10%). Therefore, these are glazes made of lead, silica, a low amount of sodium-alkali fluxes and SnO<sub>2</sub> as opacifier. In these cases, the presence of SnO<sub>2</sub> in the glazes (Figure 3b)—probably related to the formation of cassiterite crystals [16]—allowed the potters to obtain a white opaque layer. These crystals are usually between 700–800 nm in size, although some of them can be up to 3.5  $\mu$ m. Generally, the crystals are heterogeneously distributed through the glass, greatly affecting the tin oxide concentrations recorded in different parts of the glaze. This variability can be clearly confirmed in the high standard deviation and coefficient of variation recorded for the SnO<sub>2</sub> values ( $\sigma$  = 1.45–7.15; c.v. = 0.33–0.71). The low amount of tin used (usually <5%) would not have been enough to successfully opacify the surface of the vessels. Therefore, semi-opaque glazes were obtained in which the color of the paste would have been slightly visible, providing a pinkish-greenish tone to the surface of the ceramics.

As observed in other tin-glazed Islamic ceramics from Mallorca [7], a small amount of copper (1–2%) was also added to the tin glazes analyzed (Table 1). This element would have generated a pale green-turquoise-colored glaze. As it is usual in this kind of tin glazes, the surfaces of the samples under study are highly corroded. As we previously noted, the loss of brightness and vitreous appearance is obvious even at the macroscopic level in these cases. The alkali (Na<sub>2</sub>O and K<sub>2</sub>O) and alumina content is less than 4%. The iron concentrations are up to 1.1%, which indicates that the ceramic body did not affect the chemical composition of the glass.

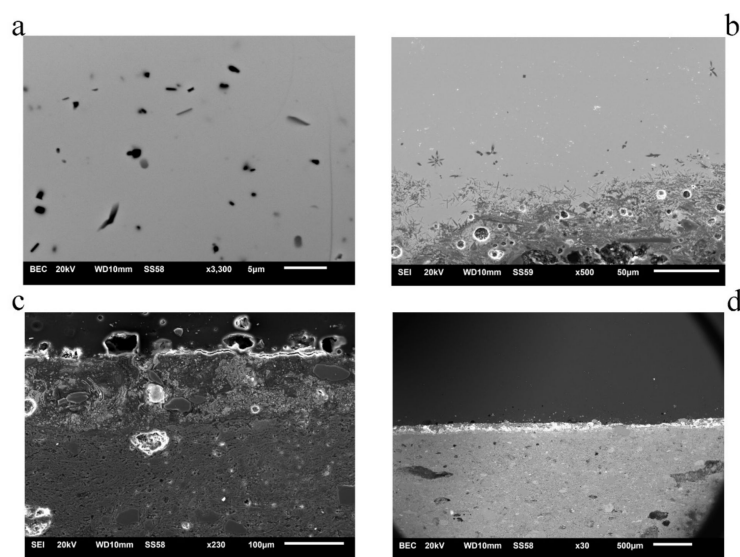
It is interesting to note that there is one case (SM-14) without tin in which we observe abundant microscopic bubbles (Figure 3c). These bubbles were formed by the occlusion of gases released in the molten glass from the decomposition of particles from the ceramic body (e.g., organic materials, carbonates, sulphates, hydrates) during the firing process. In normal conditions, these bubbles dissipate when the glazes are melted at a proper temperature. Once the cooling process starts, these bubbles cannot be eliminated. Therefore, the presence of these micro-bubbles in this glaze can be related to a lower firing temperature in this sample [25]. Other scholars recorded the presence of bubbles in ceramic glazes from Al-Andalus [7,9,26]. Their presence in the glazes seems to be associated with firing failures. Considering that this technological process has been identified (within the studied assemblage) only in this single vessel, we can point to a production failure in this case. However, we cannot dismiss that the formation of a significant amount of bubbles could also have been intentional in SM-14. It is well documented that Islamic potters also used gas bubbles locked in the glaze during the firing to reduce transparency and opacify the surface of the vessels [25,27].

The regular presence of crystalline silicates (sometimes forming aggregates) in the glazes studied, such as wollastonite (calcium silicate) or diopside (calcium magnesium silicate) (Figures 3d and 4a), which originated during the firing process, would also have contributed to opacifying the surfaces of the vessels [5,28].

It should also be noted that, as observed in other Islamic ceramics [7,29], there was a clear preference in all the samples analyzed (i.e., in both lead glazes and tin glazes) for using calcareous pastes to apply the glazes. The clay body of the local samples analyzed shows CaO concentration between 6.2–17.5%. According to Tite et al. [30], the coefficient of thermal expansion of calcite is very similar to that recorded in lead glazes. This aspect would have prevented the formation and propagation of cracks and fractures during the cooling and heating processes involved in pottery production. Moreover, the presence of iron (an element that is very common in calcareous pastes) would have promoted a higher degree of opacity in the tin glazes applied [31].

The thickness of the clay–glaze interface (Figures 3a and 4b)—usually of 5–10  $\mu$ m (<20  $\mu$ m)—and the limited development of Pb K feldspars suggest that glazes were applied in two separate firings in all samples analyzed [5,7,18]. Following the usual process of Al-Andalus pottery productions [32], a first firing process took place in order to fire the clay, while a second process was subsequently developed for glazing. In this sense, the use

of a double firing would have promoted more homogeneous and flawless surfaces. The diopside and wollastonite crystals identified in many samples would have been formed during the firing of the glaze [18].



**Figure 4.** (a) Back-scattered electron image (BSEI) showing acicular crystals of wollastonite (SM-28), (b) Secondary electron image showing the growth of sanidine crystals in the interface located between the glaze and the clay body (SM-37), (c) Secondary electron image showing the weathered alkaline glaze and the tin oxide layer identified in SM-38, (d) Back-scattered electron image taken at low magnifications showing the distribution of the tin oxide layer over the surface of the sample (SM-38).

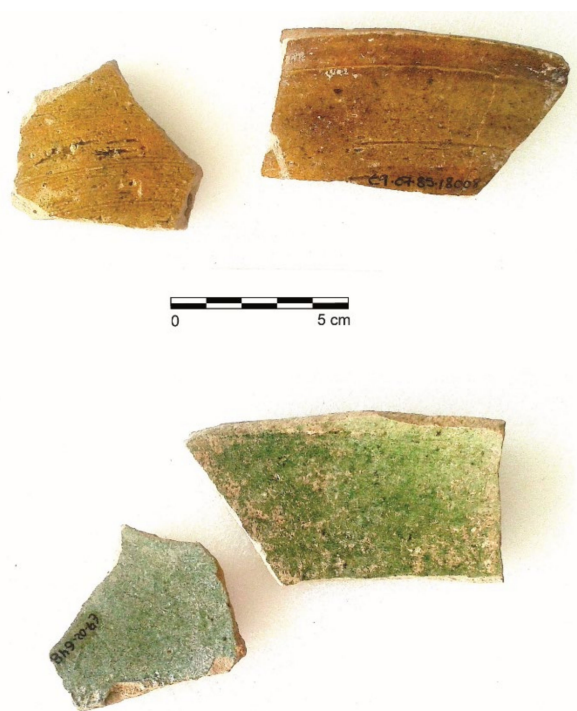
In addition, we identified five samples (a juglet/*redoma*, a small closed container/*orcita*, a jar/*jarro*, a serving dish/*ataifor* and a storage pot/*orza*) that are glazed on both the inner and the outer surfaces (Table 1). The glazes on each side show a different composition. One of them (usually the outer and most visible surface) has between 0.6% and 2.5% CuO, which is the amount necessary to provide a neutral green color to the glaze. In all these cases, the vessels were produced using lead-silica glazes, not tin glazes. Therefore, these ceramics have a translucent glaze on one of their surfaces, while the other one shows the addition of CuO with the aim to promote a green coloration [32]. These results demonstrate the use of different recipes to produce the inner and outer surfaces of the vessels. Furthermore, we document the addition of iron on the inner surface of the *ataifor* SM-39, probably with the aim to provide a yellowish-brown coloration [32]. In this case, the amount of iron (FeO = 5.2%) doubles the concentrations observed in the other samples.

#### 4.2. Imported Wares

The glazed imported wares consist mainly of serving dishes or *ataifor* ( $n = 4$ ) and a colorless juglet (*redoma*). Although these vessels are associated with different petrofabrics and origins [6], we document that almost all the glazes were applied following the same technological choices observed in the ceramic assemblage associated with local productions. On the one hand, we confirm the use of lead as the main flux in these vitreous layers (PbO = 49–62%) and a low alkali content ( $K_2O = <2\%$ ;  $Na_2O = <0.6\%$ ). On the other hand, the glazes were also applied on calcareous pastes (CaO = 5–17.5%). Finally, we also verify the addition of copper (CuO = 1.7–3%) on the glazes located on the inner surface of the serving dishes (*ataifor*) in order to provide their characteristic greenish color. In spite of these similarities, we observe that some of these imported vessels are singular within the ceramic assemblage under study. This is the case with the *ataifor* SM-59, which has the typical inner green glaze (CuO = 3%) but also the addition of iron (FeO = 4.4%) on the outer glazed layer, thus providing a yellowish coloration to the external surface of the vessel (Table 1; Figure 5). Therefore, we can conclude that this imported ceramic was produced



using more complex technological procedures and glazed recipes than the other vessels located on the site, as it incorporates two different colorants on its surfaces.



**Figure 5.** Photos of the inner and outer glaze layers of the imported sample SM-59.

We could not detect the use of tin to opacify the surfaces of the imported ceramics analyzed. However, we observed the use of a peculiar technological choice to opacify the surface of the vessel in one case. This is the case of the *ataifor* SM-38 (Figures 4 and 6), decorated with black strokes painted on a white background [33]. This pottery, which was imported to the island, is certainly particular within the ceramic assemblage studied for its decoration, typology, chronology (ca. late 10th century to 12th century AD) and technology. This sample is the only one that shows the application of an alkaline glaze. This glaze is completely degraded (Figure 3c), showing, as a result of corrosion, the presence of phosphates and carbonates. The high degree of corrosion prevents an accurate quantitative chemical analysis of this sample (this is the reason why SM-38 does not appear in Table 1). However, some interesting technological aspects can be pointed out from its study by means of SEM-EDS.

We are able to confirm that the presence of PbO in the glaze is much lower in this sample, evidencing that it is not related to a lead-silica glaze. In contrast, the amount of alkalis is significantly higher. Although we must consider that there could have been a loss of alkalis (such as Na<sub>2</sub>O) as a result of the degradation of the glaze, we observe that (in spite of being degraded) the K<sub>2</sub>O content is four times higher in this sample. The glaze located on the outer surface of the vessel shows a low amount of SnO<sub>2</sub>, which would have contributed to opacify the layer. The glaze applied on the inner surface of the pot has the same characteristics as the external one, but in this case, it is thicker (120 μm) and shows a layer very rich in SnO<sub>2</sub> between the glaze and the ceramic body (Figure 4d).

The location of this SnO<sub>2</sub> layer, together with the absence of the crystals usually observed in the tin glazes, suggests that the surface of this ceramic was opacified using a layer of powdered tin that was firstly applied to the ceramic body as a slip and was subsequently coated with a transparent alkaline glaze. The distinctive features of this glaze point to the use of a lead–tin alkaline frit [24]. Frequent rounded quartz grains of up to 50 μm are documented in this glaze. Such relic silicate inclusions in the glazes suggest the direct use of quartz-rich sand. As a consequence of the use of a high amount of tin oxide,

the inner surface of this vessel has a high degree of opacity, something advisable if black paint is going to be applied on such surface. While this technological choice to opacify the pottery surface is unique within the analyzed record, it has been documented in the Near/Middle East since the 8th century. It has been related to the deliberate application of a tin oxide slip [23] but also as a result of settling out of tin oxide due to deflocculation that occurs in a high-alkali glaze [23].



**Figure 6.** (a) Drawing of the imported *atai* for SM-38 and (b) photos of the white opaque glazed layer and the decorative motifs applied.

## 5. Discussion

The SEM-EDS analyses of the glazes associated with the local productions allegedly related to Madīna Mayūrqa pottery workshops demonstrate the use of the same recipe for vessels associated with a wide range of typologies. In this sense, we see how the amount of PbO used as flux is highly standardized (CV = 0.11) in the ceramics classified in the Petrofabric 1. This statement fits well with the high standardization and technical sophistication recorded in Almohad pottery productions [34], which are traditionally related to specialized productions developed in urban workshops [35]. In this sense, Almohad ceramics have been typically regarded as an improvement on previous surface treatments, indicating a sensible change in production strategies [36]. Nevertheless, the glazes studied in this research provide evidence that there is a clear compositional continuity with the glazed pottery productions developed in Palma in the 11th century AD [7], both with regard to the use of lead as flux, the addition of tin as opacifier and copper as colorant. The concentrations of these chemical elements (PbO, Sn<sub>2</sub>O and CuO), and of the alkaline elements recorded in the studied Almohad pottery glazes, fit well with the ranges observed in ceramics from Madīna Mayūrqa dating from the Taifa period (Table 2).

**Table 2.** Comparison of the chemical average concentrations (%wt) observed by means of SEM-EDS between Taifa and Almohad pottery glazes from Mallorca. \* = Values recorded from Molera et al. [7].

	Taifa Glazes * (11th Century)	Almohad Glazes (12–13th Centuries)
SiO <sub>2</sub>	31%	31.9%
PbO	54%	56.8%
Al <sub>2</sub> O <sub>3</sub>	3.2%	3.3%
SnO <sub>2</sub>	7–9%	5.2%
K <sub>2</sub> O	1.2%	0.9%
Na <sub>2</sub> O	1%	1%
CuO	1.6%	1.6%

Regarding the use of tin as opacifier, we see that this technological choice is usually related to tableware, mainly with *ataifors* (SM-42, SM-44, SM-48) and two small bottles (*redoma*). Likewise, the generation of bubbles, perhaps to provide an opaque surface, is also documented in a tableware vessel related to a lid or *tajeen* (SM-14). In addition, we also see some interesting correlations between the typology and the technology of certain glazed ceramics intended for the same function. This is the case with the oil lamps; we see how the oil lamp analyzed has a simple colorless glazed layer, while the candle-style oil lamp studied is associated with a more elaborated technique, since in this sample, CuO was added to the glaze in order to provide a greenish color to the outer surface of the vessel (Figure 2).

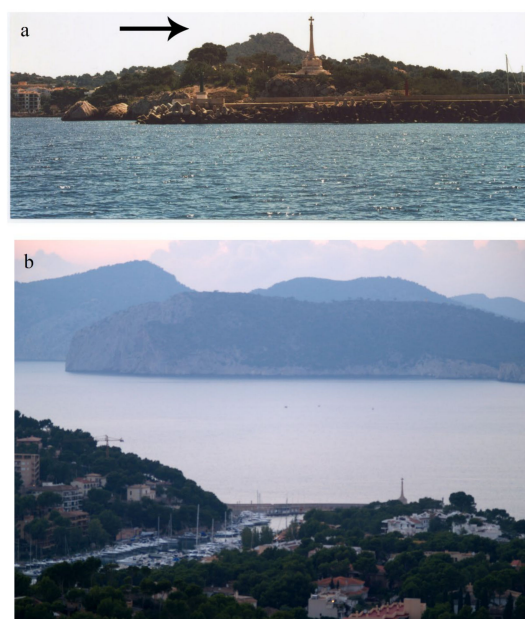
In agreement with the data available from other studies and diverse locations [7], the glazes of the imported ceramics recovered from the site show (except for sample SM-38) the same technical choices identified in the production of local pottery. This provides evidence of the high degree of standardization of the Al-Andalus ceramic productions as a whole, where the techniques applied were well established and shared among the different regions.

Despite the fact that most of the imported wares were made by means of the same technological procedures applied in the production of local glazed vessels, we also confirm that there are certain glazed samples that are unique within the analyzed ceramic assemblage. The decoration of these singular tableware potteries was clearly designed for exhibition and visualization. Such luxurious Islamic ceramics are usually found in urban contexts, being rather unusual on rural sites [37]. In this sense, two of the three bichrome serving dishes recovered from the rural archaeological site studied are related to ceramics that were imported to the island. Furthermore, one of them (SM-59) depicts higher technical complexity, since it is the only vessel analyzed that shows the application of different kinds of colorants on each of its surfaces.

The serving dish SM-38 is also unique within the ceramic assemblage studied, both due to its older chronology and the use of a layer very rich in tin to opacify the surface of the vessel. This ceramic represents a relic that clearly stands out among the Almohad pottery recovered from the rural site of Puig de Sa Morisca. The presence of this vessel—which is very unusual in rural contexts—on this site must be related to the owner’s interest in keeping and protecting this object over time, perhaps because of its distinctive foreign origin, its greater economic value or its social significance. In this sense, this vessel could have promoted a sense of belonging related to the owner’s life history. This type of *ataifor* can be related to the so-called *bacini*, which were imported to the Pisa area in Italy. The archaeometric analyses carried out on these types of luxurious, technically elaborated and exquisitely decorated masterpieces, suggest that they were imported from southern Al-Andalus [38].

In Islamic times, commerce was mainly articulated by coastal navigation, resorting to anchorage and coastal references [39]. In this sense, the geostrategic position of Puig de Sa Morisca—located in the main port to the west of the island (i.e., Santa Ponsa) and one of the most important references for coastal navigation in the region (Figure 7a)—could

have favored the distribution of some imported items towards this settlement. In this sense, given the strategic location of the Puig de Sa Morisca site in a coastal area with an intense commercial tradition [6,20], the arrival of these imported singular vessels on the site due to trade or plunder (activity well documented during the rule of Al-Muwaffaq and his son Ali Iqbāl al-Dawla) cannot be dismissed. Thus, we can suggest that this vessel could have been part of a larger set of ceramics, with its final destination being the ports of Tuscany, that ended up in the port of Madīna Mayūrqa or perhaps even in the port of Santa Ponsa [33].



**Figure 7.** Location of the archaeological site of Puig de Sa Morisca. (a) Views of the site from the sea (Source: ArqueoUIB research group) and (b) visual control of the coastal area and the port from the hilltop.

The presence of unique and more elaborated imported tableware such as this in non-urban contexts such as Puig de Sa Morisca allows us to perhaps rethink the role of this site, which could have gone beyond a mere fortified rural location (*hiṣn*) linked to the peasant communities that inhabited the area. In this sense, it can be suggested that, given its geostrategic position, Puig de Sa Morisca could have developed some kind of function as a coastal reference point for trade during the Islamic period and even for the visual control of one of the main landing ports of the island (Figure 7b). In this sense, it is worth highlighting that several Christian contingents landed in this area of the island during the 13th and 14th centuries AD [19]. It is necessary to conduct further archaeometric analysis and multiproxy approaches on rural ceramic assemblages and urban contexts from Mallorca in order to shed light and confirm the singular nature of the rural site of Puig de Sa Morisca and its role in the Islamic settlement pattern and trade networks.

## 6. Conclusions

The diverse recipes and techniques applied by Almohad potters from Mallorca to glaze the ceramics were identified by means of SEM-EDS. The technological choices recorded are in agreement with other pottery productions from Al-Andalus. The exclusive use of lead-silica glazes is verified, which in some cases were opacified by the addition of tin or, less commonly, by means of the generation of bubbles. In addition, the formation of crystalline silicates also contributed to opacifying the surface of the vessels. The addition of CuO and FeO to the glaze was also confirmed for the Almohad local productions of Mallorca. These materials were added with the aim to provide a neutral green and yellowish-brown color to the pottery surfaces, respectively. The thickness of the interface between clay and glaze,

together with the limited development of sanidine crystals, demonstrates that these glazes were applied in two firings and on calcareous ceramic pastes.

Finally, we confirm that some of the glazed ceramics that were imported to the island show certain particularities. Two of the imported *ataifors* recorded on the site are bichrome (one of them has a very high iron content), while another one features an alkaline glaze, very unique in the assemblage. The presence of these particular ceramics allows us to suggest that perhaps the site of Puig de Sa Morisca played a more complex role and carried out functions that went beyond the defense of a peasant group.

**Author Contributions:** Conceptualization: D.J.A.S., J.C.C.L. and A.R.B.; methodology: D.J.A.S. and J.C.C.L.; formal analysis: D.J.A.S. and A.R.B.; investigation: D.J.A.S.; resources: J.C.C.L.; writing—original draft preparation: D.J.A.S.; writing—review and editing: D.J.A.S., J.C.C.L. and A.R.B.; project administration: D.J.A.S.; funding acquisition: D.J.A.S. and J.C.C.L. All authors have read and agreed to the published version of the manuscript.

**Funding:** This research was funded by a José Castillejo grant CAS15/00052 (research mobility program for lecturers in foreign educational and research centers) from the Ministerio de Educación, Cultura y Deporte (Spain).

**Acknowledgments:** Preparation of samples and SEM-EDS analysis was carried out in the Laboratory of Archaeological Materials Science (University College London Qatar). We would like to thank Thilo Rehren and Myrto Georgakopoulou for giving us access to the facilities.

**Conflicts of Interest:** The authors declare no conflict of interest.

## References

- Bridgman, R. Re-examining Almohad economies in south-western Al-Andalus through petrological analysis of archaeological ceramics. In *Revisiting al-Andalus: Perspectives on the Material Culture of Islamic Iberia and beyond*; Anderson, G.D., Rosser-Owen, M., Eds.; Brill: Leiden, The Netherlands, 2007; pp. 143–166.
- Bridgman, R. Contextualising pottery production and distribution in South-Western al-Andalus during the Almohad period: Implications for understanding economy. In *Atti del IX Congresso Internazionale sulla Ceramica Medievale nel Mediterraneo*; All’Insegna del Giglio: Firenze, Italy, 2012; pp. 95–100.
- García Porras, A.; Capelli, C.; Cabella, R.; Romero, J.; Cardell, C. Ceramic production in Granada and in the southeast of the Iberian Peninsula during the late Middle Ages: Clays, tools and pots—Some preliminary notes. *Mediev. Ceram.* **2011**, *32*, 29–43.
- Pérez-Arantegui, J.; Hernández Pardos, A. Caracterización arqueométrica de la cerámica del castillo de Albarracín (Teruel, España) en la transición entre los siglos XII y XIII. *DigitAR* **2017**, *4*, 41–50. [CrossRef]
- Molera, J.; Pradell, T.; Merino, L.; García-Vallés, M.; García-Orellana, J.; Salvado, J.; Vendrell-Saz, M. La tecnología de la cerámica islámica y mudéjar. *Cesaraugusta* **1997**, *73*, 15–41.
- Albero Santacreu, D.; Mateu Vicens, G.; Ramos Benito, A.; Carvajal López, J.C.; Georgakopoulou, M. Pottery in the backyard: Almohad ceramic distribution networks in rural areas (SW Mallorca, Spain). *Archaeol. Anthropol. Sci.* **2019**, *11*, 4769–4788. [CrossRef]
- Molera, J.; Vendrell-Saz, M.; Pérez-Arategui, J. Chemical and textural characterization of tin glazes in Islamic ceramics from Eastern Spain. *J. Archaeol. Sci.* **2001**, *28*, 331–340. [CrossRef]
- González García, F.; González Rodríguez, M.; González Vilchez, C.; Vallejo Triano, A. Estudio arqueométrico de algunas cerámicas medievales de Madinat Al-Zahra (Córdoba). *Boletín de la Sociedad Española de Cerámica y Vidrio* **1992**, *31*, 491–498.
- Molera, J.; Carvajal López, J.C.; Molina, G.; Pradell, T. Glazes, colourants and decorations in early Islamic glazed ceramics from the Vega of Granada (9th to 12th centuries CE). *J. Archaeol. Sci. Rep.* **2018**, *21*, 1141–1151. [CrossRef]
- Salinas, E.; Pradell, T.; Tite, M.S. Tracing the tin-opacified yellow glazed ceramics in the western Islamic world: The findings at Madīnat al-Zahrā’. *Archaeol. Anthropol. Sci.* **2019**, *11*, 777–787. [CrossRef]
- Pradell, T.; Molina, G.; Molera, J.; Marinetto, P. Primeros resultados del estudio analítico de la cerámica vidriada decorada Nazari: La cerámica palatina (ss. XIV–XV). In *Actas del I Congreso Internacional Red Europea de Museos de Arte Islámico*; Universitat Politècnica de Catalunya: Barcelona, Spain, 2012; pp. 397–418.
- Pérez-Arantegui, J.; Marzo, P. Characterization of Islamic ceramic production techniques in Northeast Iberian Peninsula: The case of medieval albarracín (Spain). *Appl. Sci.* **2021**, *11*, 7212. [CrossRef]
- Molera, J.; Pradell, T.; Martínez, S.; Vendrell, M. The growth of sanidine crystals in the lead glazes of Hispano-Moresque pottery. *Appl. Clay Sci.* **1993**, *7*, 483–491. [CrossRef]
- Molera, J.; Vendrell-Saz, M.; García-Vallés, M.; Pradell, T. Technology and colour development of hispano-moresque lead-glazed pottery. *Archaeometry* **1997**, *39*, 23–39. [CrossRef]
- Pérez-Arantegui, J.; Larrea, A.; Molera, J.; Pradell, T.; Vendrell-Saz, M. Some aspects of the characterization of decorations on ceramic glazes. *Appl. Phys. A* **2014**, *79*, 235–239. [CrossRef]



16. Pradell, T.; Molina, G.; Molera, J.; Pla, J.; Labrador, A. The use of micro-XRD for the study of glaze color decorations. *Appl. Phys. A* **2013**, *111*, 121–127. [CrossRef]
17. Albero Santacreu, D.; Carvajal, J.C.; Mateu Vicens, G. Anàlisi petrològica preliminar de la ceràmica islàmica del Puig de sa Morisca (Calvià, Mallorca). In *VII Jornades d'Arqueologia de les Illes Balears*; Anglada, M., Riera, M., Martínez, A., Eds.; Consell Insular de Menorca: Maó, Spain, 2017; pp. 301–310.
18. Molera, J.; Pradell, T.; Salvadó, N.; Vendrell-Saz, M. Interactions between clay bodies and lead glazes. *J. Am. Ceram. Soc.* **2001**, *84*, 1120–1128. [CrossRef]
19. Albero Santacreu, D.; Calderón, M.; Calvo, M.; Gloaguen, E. Calvià y la conquista cristiana de Jaume I (1229). In *Patrimoni Cultural de Calvià (Vol. I)*; Calvo, M., Agualeles, A., Eds.; Ajuntament de Calvià, Mallorca: Calvià, Spain, 2011; pp. 177–186.
20. Albero Santacreu, D. Primeras aproximaciones a la organización del espacio rural durante época islàmica (902–1229) en Qalbiyān (SO de Mallorca). *Arqueología y Territorio Medieval* **2011**, *18*, 145–167. [CrossRef]
21. Malpica, A.; García Porras, A.; Álvarez, J.J.; Carta, R.; Carvajal, J.C.; Bonet, M.T.; Reyes, E. Planteamientos sobre las cerámicas urbanas y rurales del territorio granadino. In *La Cerámica en Entornos Urbanos y Rurales en el Mediterráneo Medieval*; García Porras, A., Villada, F., Eds.; Museo de Ceuta, Consejería de Educación, Cultura y Mujer: Ceuta, Spain, 2007; pp. 159–290.
22. Ramos, A. Primeres dades sobre la ceràmica andalusina del Puig de sa Morisca (Santa Ponça, Mallorca). In *VII Jornades d'Arqueologia de les Illes Balears*; Anglada, M., Riera, M., Martínez, A., Eds.; Consell Insular de Menorca: Maó, Spain, 2017; pp. 285–292.
23. Tite, M.; Pradell, T.; Shortland, A. Discovery, production and use of tin-based opacifiers in glasses, enamels and glazes from the late iron age onwards: A reassessment. *Archaeometry* **2008**, *50*, 67–84. [CrossRef]
24. Matin, M. Tin-based opacifiers in archaeological glass and ceramic glazes: A review and new perspectives. *Archaeol. Anthropol. Sci.* **2019**, *11*, 1155–1169. [CrossRef]
25. Gradmann, R. Analysis of Historical Islamic Glazes and the Development of a Substitution Material. Ph.D. Thesis, Institute of Geography and Geology, Department of Geodynamics and Geomaterial Research, Universität Würzburg, Würzburg, Germany, 2016.
26. Salinas, E.; Pradell, T.; Molera, J. Glaze production at an early Islamic workshop in Al-Andalus. *Archaeol. Anthropol. Sci.* **2019**, *11*, 2201–2213. [CrossRef]
27. Milwright, M. *An Introduction to Islamic Archaeology*; The New Edinburgh Islamic Surveys; Edinburgh University Press: Edinburgh, UK, 2010.
28. Mason, R.B.; Tite, M.S. The beginnings of tin-opacification of pottery glazes. *Archaeometry* **1997**, *39*, 41–58. [CrossRef]
29. Molera, J.; Pradell, T.; Salvadó, N.; Vendrell-Saz, M. Evidence of tin oxide recrystallization in opacified lead glazes. *J. Am. Ceram. Soc.* **1999**, *82*, 2871–2875. [CrossRef]
30. Tite, M.S.; Freestone, I.; Mason, R.; Molera, J.; Vendrell-Saz, M.; Wood, N. Lead glazes in antiquity. Methods of production and reasons for use. *Archaeometry* **1998**, *40*, 241–260. [CrossRef]
31. Vendrell, M.; Molera, J.; Tite, M.S. Optical properties of tin opacified glazes. *Archaeometry* **2000**, *42*, 325–340. [CrossRef]
32. Coll, J. Transferencias técnicas en la producción cerámica entre Al-Andalus y los reinos cristianos. El caso de Sharq Al-Andalus. In *Cerámicas Islámicas y Cristianas a Finales de la Edad Media. Influencias e Intercambios*; Museo de Ceuta, Consejería de Educación, Cultura y Mujer: Ceuta, Spain, 2003; pp. 301–366.
33. Ramos, A.; Albero, D.; Carvajal, J. Estudi tipològic i arqueomètric d'una safra singular recuperada a la Torre III del Puig de sa Morisca (Santa Ponça, Mallorca). In *VII Jornades d'Arqueologia de les Illes Balears*; Anglada, M., Riera, M., Martínez, A., Eds.; Consell Insular de Menorca: Maó, Spain, 2017; pp. 293–299.
34. Lafuente, P. Pottery and tiles. In *The Archaeology of Medieval Spain (1100–1500)*; Valor, M., Gutiérrez, A., Eds.; Equinox: Sheffield, UK, 2014; p. 82.
35. Coll, J.; García Porras, A. Tipologia, cronologia e produzione dei forni per ceramica in al-Andalus. In *Atti XLII Convegno Internazionale della Ceramica. Fornaci: Tecnologie e Produzione della Ceramica in Età Medievale e Moderna*; Centro Ligure per la Storia de la Ceramica: Savona, Italy, 2010; pp. 25–44.
36. González Navarro, E. *Tradición Tecnológica de la Cerámica de Cocina Almohade-Nazarí*; THARG: Granada, Spain, 2008.
37. García Porras, A. Caracterización de una producción cerámica comercializable: La cerámica almohade. In *A Ocupação Islâmica da Península Ibérica: Actas do IV Congresso de Arqueologia Peninsular*; Ferreira, N., Ed.; Centro de Estudos de Património, Universidade do Algarve: Faro, Portugal, 2008; pp. 139–155.
38. Baldassarri, M.; Berti, G. Nuovi dati sulle importazioni di ceramiche islamiche e bizantine a Pisa. In *Actas del VIII Congreso Internacional de Cerámica Medieval*; Zozaya, J., Retuerce, M., Hervás, M.A., de Juan, A., Eds.; AEAM: Ciudad Real, Spain, 2009; pp. 63–79.
39. Gutiérrez, J.A.; Valor, M. Housing and domestic life. In *The Archaeology of Medieval Spain (1100–1500)*; Valor, M., Gutiérrez, A., Eds.; Equinox: Sheffield, UK, 2014; pp. 73–99.





Article

# Think Globally, Act Locally: Global Requirements and Local Transformation in Sugar Pots Manufacture in Sicily in the Medieval and Post-Medieval Periods

Roberta Mentésana <sup>1,2,\*</sup> , Anno Hein <sup>3</sup>, Marisol Madrid i Fernández <sup>1,2</sup>, Vassilis Kilikoglou <sup>3</sup> and Jaume Buxeda i Garrigós <sup>1,2</sup> 

<sup>1</sup> Cultura Material i Arqueometria UB (ARQUB, GRACPE), Department d'Història i Arqueologia, Facultat de Geografia i Història, Universitat de Barcelona, 08001 Barcelona, Spain; mmadrid@ub.edu (M.M.i.F.); jbxeda@ub.edu (J.B.i.G.)

<sup>2</sup> Institut d'Arqueologia de la Universitat de Barcelona (IAUB), Facultat de Geografia i Història, Universitat de Barcelona, 08001 Barcelona, Spain

<sup>3</sup> National Centre of Scientific Research "Demokritos", Institute of Nanoscience and Nanotechnology, 15310 Athens, Greece; a.hein@inn.demokritos.gr (A.H.); v.kilikoglou@inn.demokritos.gr (V.K.)

\* Correspondence: r.mentésana@ub.edu

**Abstract:** Since medieval times, sugar production and consumption has had a huge impact on European social, cultural, and economic development. The introduction of sugar cultivation entailed knowledge transfer and new technological requirements, such as the manufacture of sugar pots used to crystallise sugar, which requires a specific design, and thermal and mechanical properties. This paper presents part of the results of the SPotEU project, funded under the Marie Skłodowska-Curie Actions, which explores the development and impact of sugar production in western Europe through the study of sugar pot manufacture from an interdisciplinary perspective, integrating archaeological and historical research with material science and material culture approaches. This paper focuses on sugar pots from Sicily, one of the main regions for sugar production in Western Europe in the 11–16th centuries A.D. Sugar pots were assessed from technological and performance points of view, aided by instrumental analysis (petrography, SEM, XRF, XRD, mechanical, and thermal property tests). The archaeological and analytical results are presented, revealing different centres of sugar pot production on the island, and specific choices in the design of the vessels and their properties. This allows us to discuss how craftspeople locally adapted their ceramic-making traditions to face the new product demands from the sugar production industry in the Mediterranean.

**Keywords:** ceramics; technological choices; petrography; SEM-EDX; WDXRF; PXRD; heat transfer properties; fracture strength

**Citation:** Mentésana, R.; Hein, A.; Madrid i Fernández, M.; Kilikoglou, V.; Buxeda i Garrigós, J. Think Globally, Act Locally: Global Requirements and Local Transformation in Sugar Pots Manufacture in Sicily in the Medieval and Post-Medieval Periods. *Minerals* **2022**, *12*, 423. <https://doi.org/10.3390/min12040423>

Academic Editors: Daniel Albero Santacreu, José Cristóbal Carvajal López and Adrián Durán Benito

Received: 25 February 2022

Accepted: 27 March 2022

Published: 30 March 2022

**Publisher's Note:** MDPI stays neutral with regard to jurisdictional claims in published maps and institutional affiliations.



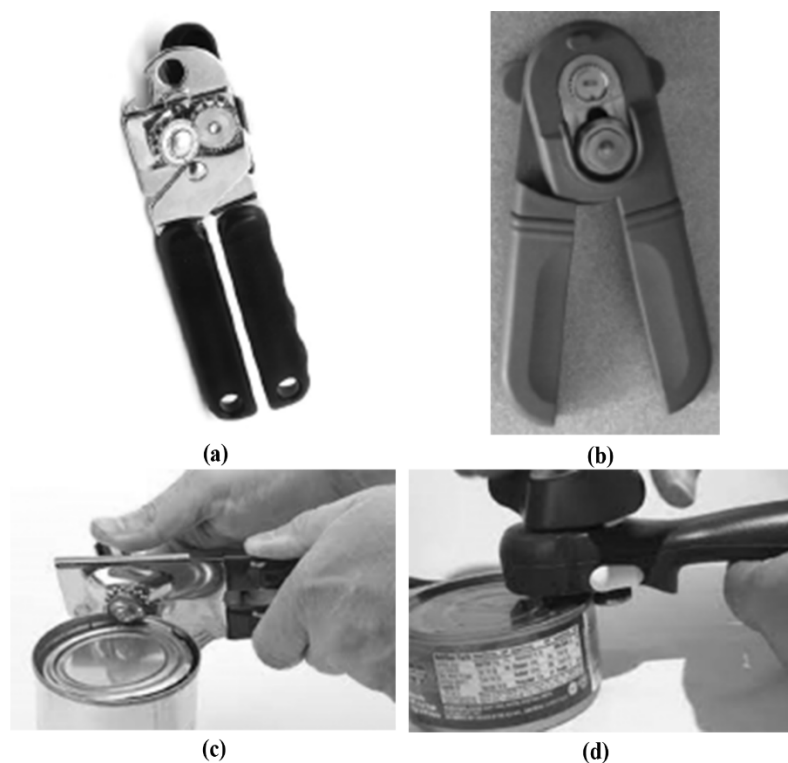
**Copyright:** © 2022 by the authors. Licensee MDPI, Basel, Switzerland. This article is an open access article distributed under the terms and conditions of the Creative Commons Attribution (CC BY) license (<https://creativecommons.org/licenses/by/4.0/>).

## 1. Introduction

In our industrialised and globalised world, separating the 'local' from the 'global' elements in the design and production of objects is a difficult matter. This is a difficulty that is not only practical but also emotional, as the concept of local is often paired with *tradition*, *identity*, *resilience*, and the *past*, while the global concept goes in the opposite direction [1]. Nevertheless, objects intended for the same function, produced industrially or not, tend to share strong similarities in design, although they probably will be highly varied if we can analyse their production sequence as we do with past material culture. If we can go beyond their common purpose and the impact this has on an object's appearance, we may discover that their production possibly involves raw materials, machinery, and product parts from different areas, and even different countries, and a blend of past and present design, but also different way of use. A can opener, now a common tool with the same functionality despite cultural or geographical contexts, embeds in its design and manufacture much more than what it may seem. If we compare a can opener sold in Italy and one sold in



the UK, they have commonalities, such as two rotating wheels (one cutting), two opposite levers, and a rotating handle. Probably both are ultimately made in Asia. The way these parts are combined creates two different objects, which imply a slightly different way of cutting: the first one cuts the can from the side (Figure 1a,c), whereas the other one from the top (Figure 1b,d). Neither of the two is technologically more advantageous (they are two of the multiple designs of the same object), and the first type was used in the UK until the 1980s, when the other type was invented and then rapidly adopted. One of the reasons for this may be that, in the UK, safety policy is included in everyday practices. This may have led to the acceptance of the top-cutting can opener, which allows opening a can without inserting the finger into the top part, risking cutting. Although familiar with the object *per se*, people living in the two countries may have difficulties in using a different type of can opener, because they would lack the body movement and mental structure required to operate it. Leaving aside the social acceptance factor, this example shows how similar objects, aimed at the same purpose, may have those small differences that tell us about product provenance, manufacturer design choices, and different mental attitudes and body gestures that required for operation. It tells us the ways in which a global requirement, i.e., opening a can, can be interpreted differently by manufacturers, even in our interconnected modernity, in response to different cultural attitudes.



**Figure 1.** Design and use of a side cutting can opener (a,c) and a top cutting opener (b,d). Modified after (a) Evan-Amos, Public domain, via Wikimedia Commons, (b) © Materials scientist at English Wikipedia, CC BY-SA 3.0 <https://creativecommons.org/licenses/by-sa/3.0> (accessed on 1 February 2022) via Wikimedia Commons, (c) © Whitestar1955 | Dreamstime.com <https://koit.com/96-5-koit-blog/youve-using-can-opener-wrong-whole-time/> (accessed on 1 February 2022), (d) © Susan Brown <https://www.youtube.com/watch?v=zePEyRB6Hqo> (accessed on 1 February 2022).

The SPotEU project (“Sugar Pot manufacture in Western Europe in the medieval and post-medieval period (11–16th centuries AD)”, funded under the Horizon 2020 Marie Skłodowska-Curie Actions (grant agreement: 797242)), of which this paper represents a part, was developed to explore the ways in which craftspeople faced the demands from the newly adopted sugar production in the Middle Ages. Although operating on a different scale than today, the Mediterranean has always been a medium for exchanging

materials, objects, and ideas, often transcending territorial political divisions and cultural differences [2,3]. Phenomena such as the production and consumption of sugar in the Middle Ages could be considered one of these pan-Mediterranean occurrences, which had, especially in the 14–16th century phases, a huge impact on European social, cultural, and economic development [4]. The chronology of the introduction of sugar cane into the Mediterranean suggests that it followed the Islamic expansion: it is documented in Egypt from the 8th century AD, and progressively in Cyprus, Crete, Sicily, the African coast, and the Iberian Peninsula by the 10th century AD [5]. However, what looks like a monolithic phenomenon linked with the movement of communities from the eastern Mediterranean may not have occurred in such a homogeneous way. Firstly, the ‘Arab agricultural revolution’, the label given to the set of intensive farming and irrigation technological novelties developed by Muslim groups [6], has lately been critically reviewed [7–9]. Moreover, it appears that in the Western Mediterranean, sugar production did not develop in the same way as in the Eastern Mediterranean. Regionally focused studies are now starting to reveal a more diversified picture of when and how the sugar industry was developed in each region, shedding light on local responses to the growing sugar demand [10–16]. Regarding commonalities, sugar production indeed required a specific sequence from its cultivation to processing, types of machinery (i.e., mill, a press, large firing installations), and objects having a specific purpose, such as cauldrons for sugar boiling and cone-shaped vessels for the crystallisation phase. Therefore, its introduction and cultivation entailed new technological requirements, and craftspeople and the local workforce needed to adapt or transform their skills and products to these new demands. Nevertheless, sugar production in the Western Mediterranean has often been observed from a top-down approach, from the point of view of merchant, landowner, royal, and ecclesiastical interests. Little is known about the role of craftspeople in the development of sugar production in modern Europe.

This paper explores the development and impact of sugar production in local craftsmanship, using one of the core crafts linked with sugar production as a baseline, i.e., the manufacture of sugar pots. These consist of a ceramic reversed cone with a hole at the bottom, where the liquid syrup is poured, and left to cool and crystallise, called the sugar mould cone (hereafter, *sugar cone*). They are often associated with molasses collecting jars (hereafter, *molasses jars*) where the liquid molasses, a discard of the first boiling of the sugar syrup, is collected when the sugar crystallised. The design and characteristics of this set of vessels (so-called *sugar pots*) developed explicitly for sugar production, and they are often the only archaeological evidence of past sugar production and consumption. Before the introduction of sugar pot manufacture, the design of these vessels was unknown to local potters, who faced several issues. First, the design of the sugar cone is dissimilar to that of other vessels: Ibn al-‘Awwām, in his handbook on agriculture, refers to the specific shape for the sugar to crystallise [17] (p. 393), but he does not provide further specifications. Moreover, the dimension of the sugar cones seems to be linked to specific product quality: the smaller the size, the more refined the sugar they contained [18] (p. 276) [13] (pp. 59–77). In addition, sugar pots had to exhibit sufficient material properties and design to withstand repeated thermal changes and mechanical stresses; they were intended to be repeatedly used before discard and, therefore, we may suppose they were made to last. Potters had also to contend with the high volume of ceramics required, as vessels were frequently broken during the process and, in some other cases, shipped with the sugar content [13] (pp. 76–77). All these features may have been shared with those operating in sugar production, as suggested by the similarities in sugar pots across time and space [13] (cf. pp. 59–77). However, as in the case of the can opener, potters also may have developed different manufacturing strategies and organisations to meet these new demands.

Following a similar approach as that applied for sugar production materials in the Near East [13,15], this paper focuses on Sicilian medieval archaeological evidence for sugar production. For the first time, sugar pots from this region were examined in such technological detail that allowed us to assess the places of production, movement, and material properties of sugar pots. Specifically, this paper focuses on the micro-scale of the

potters' community, and their technological choices in manufacturing sugar pots within their cultural context of manufacture. To explore this, we first needed to identify local production, aided by chemical and petrographic characterisation. We then examined the material properties by means of microstructure and textural analysis, and mineralogy, and how the materials affect the thermal and mechanical properties of the vessels [19–21]. This allowed us to discuss whether potters produced vessels with different characteristics. Considering their context of use, sugar pots require resistance to the thermal stresses of the boiling sugar syrup poured in to them (thermal shock resistance), but also must allow the dissipation of heat at a certain rate to allow the sugar to crystallise (heat transfer). In addition, sugar cones can be stacked directly on molasses jars or placed over a hole in a wooden bench, and were also frequently handled for production; in some cases, these pots travelled long distances, either empty or filled with sugar. Sugar pots, and specifically sugar cones, would need to withstand forces applied to them without failing (fracture strength and toughness). The mechanical and thermal properties were used as predictors of the performance of these vessels during use [22] because many parameters influence each other, and these parameters cannot be disentangled in archaeological ceramics, as can be done during experiments [23]. A further step, which will be published in another paper, simulated whether these vessels perform in the same way under similar use conditions [24,25]. This complex and multiphase set of examinations did not aim to assess functionality; rather, the objective was to explore the reasons for these choices, other than performance [23]. As well explained by Sillar and Tite [26] (p. 4), 'it is impossible to account for any of these choices without combining a consideration of both the material properties and the cultural context'.

## 2. Materials

According to the archive sources, authors have distinguished different phases in the sugar production on the island [18,27–29]. From the first acknowledgement in the mid-10th century until the beginning of the 13th century A.D., the production seemed concentrated in Palermo, and was small scale and mainly devoted to the consumption of the higher class and the pharmacopoeia. A crisis may have occurred before the 13th century if Frederick II had tried to reinstall Palermo's production. At the beginning of the 14th century, and particularly during this century, sugar production intensified. The number of sugar production centres increased considerably, leaving Palermo's walls and extending to the entire island. Sugar cane cultivation started taking up extensive portions of land, although co-existing with other crops. It was transformed into on-purpose large buildings (*trapetum,-*), involving several specialised workers, and exported to the whole European market. An economic crisis may have occurred between the end of the 15th century and the beginning of the 16th century, but sugar production flourished again in the mid-16th century until its final collapse in the mid-17th century. From this summary, it is clear that sugar production in Sicily had a long but discontinuous development. It could be wondered whether, during these phases, knowledge about sugar production and the manufacture of sugar pots was transmitted, and in which manner.

The archaeological evidence of sugar production on the island is concentrated in the north-western part of Sicily (Figure 2). A recent diachronic examination of the archaeological evidence [16] suggests that, despite the chronological issues, the design and volume of sugar pots changed with the phases noted above. However, they are also site-specific; that is, even sites of the same phase show differences in the design of the pots. Materials from some of these sites were studied and will be discussed extensively in a forthcoming publication [16], and are briefly presented here.



**Figure 2.** Map of Italy (a); western Sicily with the site discussed (b) (black dots: site sampled, black triangles: geological deposits sampled); and map of Palermo (c), with the sites discussed in the text. 1: Castello della Favara in Mareddolce, 2: Convento di Baida, 3: Palazzo Steri–Chiaramonte.

(1) The Castello della Favara in Mareddolce (MAR), in Palermo, was built with the artificial lake by the Norman king Roger II; in the 14–15th centuries, the building changed its function from residential to agricultural/industrial, and was also linked with sugar cane production [30] (p. 473) [28] (p. 113). Here sugar pots were found during the excavation of a filling of the lake of Mareddolce [30,31]. They were dated to an earlier phase of sugar production and consumption, before the end of the 13th century [16].

(2) The excavation of Palazzo Steri–Chiaramonte (STE), in the current Piazza Marina in Palermo, by Tusa [32], revealed a long sequence of occupation of the site, which was the residence of many Sicilian rulers from the 14th century. In layers corresponding to the phase from the end of the 15th century to the beginning of the 16th century [33,34], some sugar pots were found, probably related to sugar consumption in the palace, which at that time was the residence of the Viceré.

(3) A large sugar cone was also found in the storeroom of the archaeological museum of Palermo “A. Salinas”, and is related to an underwater finding (UND) in Palermo’s waters.

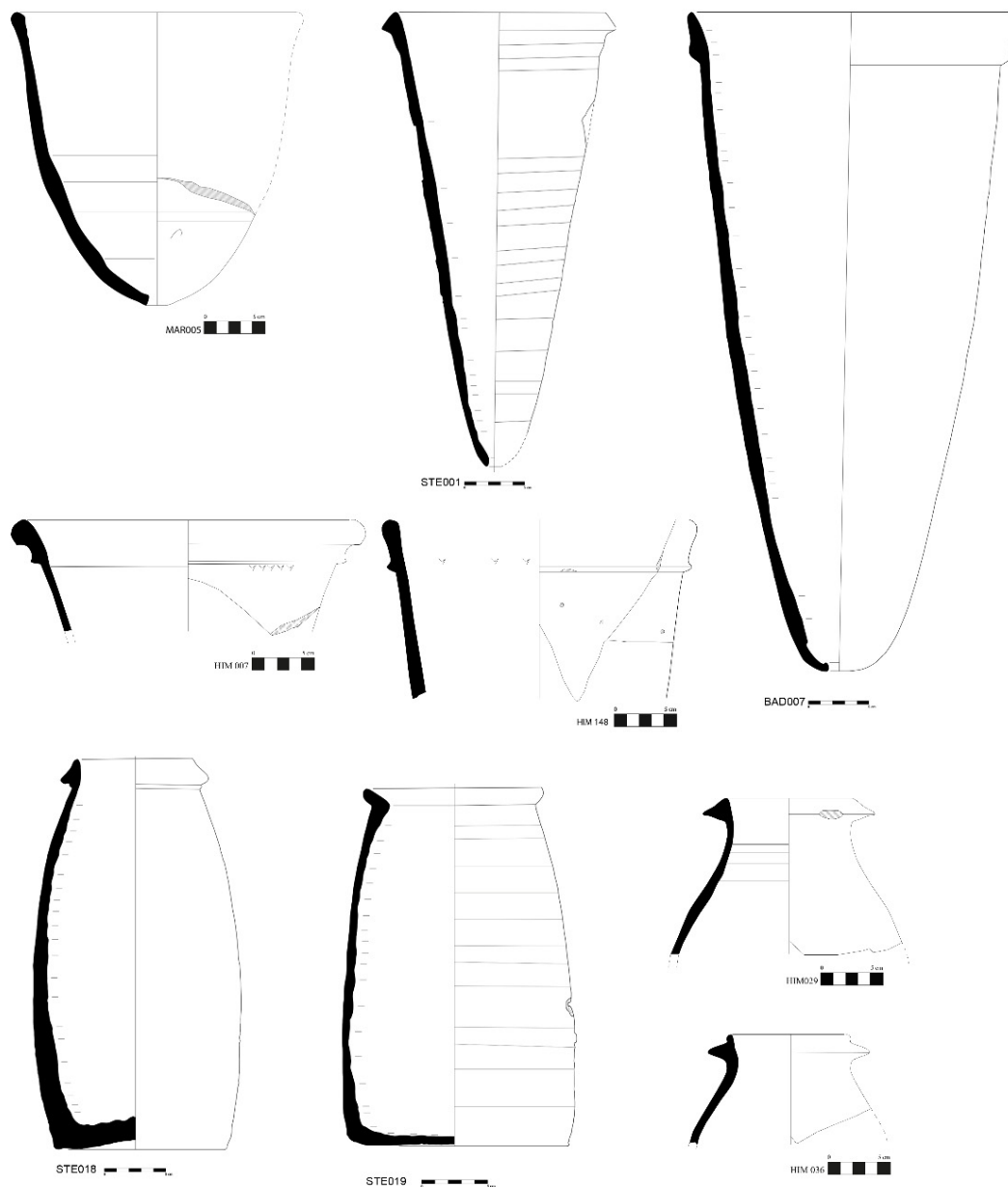
(4) Another seven cones were found in the same museum; these were retrieved during the restoration of the Convento di San Giovanni of Baida (BAD), where the cones were used as the filling material of the vaults. The latter may tentatively be dated to before the end of the 15th century [16].

(5) West of Palermo, the area of Partinico (PAR) was intensively dedicated to wine and sugar cane plantations since the end of the 14th century [35] (pp. 41–42) [27] (pp. 101–111). Here, some sugar pots were recovered during a survey and, therefore, only dated to after the end of the 14th century, which is the first known date of archive sources for sugar production in the area.

(6) Lastly, during the excavation of the Greek colony of Himera (HIM), near the present-day town of Termini Imerese, conspicuous traces of a sugar production site were found, with numerous sherds of sugar pots only partly recovered [36,37]. The few glazed ceramic sherds allow us to date these vessels to between the end of the 15th century and the beginning of the 16th century [16,38].

In summary, the sugar pots examined in this paper belong to different chronological phases: one between the 11th and 13th centuries, to which only Castello della Favara a Mareddolce could be placed; and another from the end of the 14th to the beginning of the 16th centuries, where all the other contexts belong, most of them to the range from the end of the 15th century to the beginning of the 16th century.

Sugar pots from these sites were measured and grouped into types based on their rim features and the typology previously used by Falsone for molasses jars [32] (Figure 3). A total of 87 sugar pots (26 molasses jars and 62 sugar cones), in addition to five vessels belonging to other types for comparison, were sampled for analytical study as representative of each site, chronological phase, and type (Table 1) (These comparison types were noria vessels and cantaro. Noria vessels are usually bell-shaped vessels, with a pointy bottom, used as water buckets on a waterwheel (noria), whereas a cantaro is a two-handled cylindrical vessel. Both these shapes were found in conspicuous quantities at the Palazzo Steri–Chiaramonte site [33,34]). Individuals were labelled with an acronym indicating the location where they were found and a progressive number (Table S1). The complete list of the individuals studied is published and openly accessible [39].



**Figure 3.** Representative sugar cones and molasses jars for each type: sugar cone type 1 (MAR005), type 2 (STE001), type 3 (BAD007), type 4 (HIM007), type 5 (HIM148); molasses jar type A.1 (STE018), type A.2 (HIM029), type A.3 (HIM036), type B (STE019). (Drawings of STE001, BAD007, STE018 and STE019 by S. Arrabito, others by R. Mentasana).

**Table 1.** Archaeological sites studied and sampled for this study.

Site	Vessel Shape			Tot. Site
	Molasses Jar	Sugar Cone	Others	
Underwater, Palermo (UND) sampled		1 1		1 1
Castello della Favara in Mareddolce, Palermo (MAR) sampled	2 2	8 8		10 10
Convento di Baida, Palermo (BAD) sampled		7 5		7 5
Palazzo Steri–Chiaramonte, Palermo (STE) sampled	5 2	7 7	7 5	19 14
San Giovanni degli Eremiti? (PAM) sampled		1 0		1 0
Himera–Buonfornello (HIM) sampled	50 19	126 34		176 53
Partinico (PAR) sampled	3 3	8 7		11 10
Tot. studied	60	156	7	225
Tot. sampled	26	62	5	93

Geological deposits near the sites under study were sampled to compare them with the raw materials of the archaeological individuals, and to make the experimental briquettes needed for the mechanical and thermal tests (Table 2). DHIM01 was collected at the present-day tile industry of Later Siciliana (Collesano, Termini Imerese), where deposits of Terravecchia formation clay can be found. Two deposits of Ficarazzi formation were sampled: DPAM01 was collected on the beach of Ficarazzi, Palermo; DPAM02 was gathered on the beach of Santa Flavia (Palermo) near the archaeological site of Solunto. Lastly, for Partinico, some deposits were sampled at the Baia di San Cataldo; only one resulted in being adapted for ceramic making, and corresponds to a Numidian flysch formation. Except for the deposit from Partinico, those of Ficarazzi and Terravecchia formations have been extensively characterised [40,41].

**Table 2.** Geological deposits sampled for this study.

ID	Location	Geological Formation
DHIM01	Collesano (PA) 37°57'48.8" N 13°50'58.8" E	Terravecchia
DPAM01	Ficarazzi (PA), 38°05'44.1" N 13°27'23.3" E	Ficarazzi
DPAM02	Santa Flavia (PA) 38°04'53.1" N 13°32'14.1" E	Ficarazzi
DPAR01	Baia di San Cataldo, cala dei Muletti (PA), 38°05'06.0" N 13°05'02.0" E	Numidian flysch

### 3. Methods

#### 3.1. Theoretical Framework

Sugar pots started to be produced with the introduction of sugar cultivation in Sicily. The design and the property requirements of these vessels were unknown to potters before this time. Sugar pots were made with the same intended function as in other places in the Mediterranean where sugar was produced; it may thus be wondered whether this implies a similarity in the material requirements, and therefore, the choices of potters. The link between material properties, shape, and function has been advocated in many

studies: choices were directed towards creating the best-fitting, best-performant solution [42–46]. It has been argued that material culture is adapted to different natural or cultural circumstances, and survives and is transmitted according to its *fittingness* [47]. The evolutionary explanation has been successfully adopted to explain changes in the ceramic making in different contexts [48–50]. Many studies interpret their findings in this way, even if it is not clearly stated. Some of the authors share some aspects with the systemic approach [51], whereas others consider that this approach does not encompass other reasons that come into play during manufacturing processes. Technological choices, as formulated by Lemonnier [52], represent the conscious and unconscious adoption of certain technical features, and the dismissal others, based on multiple intermingled factors, such as material properties, ways of doing, the environment, beliefs, and, in short, the entire socio-cultural system of the individual and the group. This concept goes past the division between technique and technology, and the functional and style aspects of material culture, thus allowing an understanding of the material culture as a whole. However, it becomes difficult to translate the technological choice approach into a methodology for examining these choices, especially if it implies analytical techniques. Jones [53], amongst other authors [54,55], discusses the challenges of interpreting human actions starting from analytical data, but he argues that the finer the analytical technique used (i.e., chemical characterisation), the greater the tendency to interpret the results within the framework of general histories (macroscale); and the coarser the technique (i.e., macro-observations), the more the results will be interpreted as a local development (microscale). It has been argued elsewhere [56] that, rather than the analytical techniques, the research objectives define the scale of analyses—macro or micro—and that *chaîne opératoire* [57] can be one of the best operational frameworks to overcome the issue of merging different data types and scales of research. The *chaîne opératoire* approach helps in following a structured reconstruction of the sequence of ceramic manufacture, which goes from raw material selection and manipulation, to forming, surface treatment, and firing, and is able to incorporate elemental to macroscopic data [58]. The *chaîne opératoire* approach is a useful framework to understand the manufacturing sequence, but becomes meaningful only when embedded in the learning context of *practice*. This concept, created by Bourdieu [59,60] and transformed by Lave and Wegner into the *community of practice* [61,62], allows us to understand the way in which technological choices are generated and reproduced by people in their everyday practical activities. In our case study, dealing with an input external to ceramic manufacture, the communities of practice approach can help understand how individuals and collective choices are created and negotiated through the already existing ceramic manufacturing practices.

### 3.2. Analytical Approach

Petrographic examination (PE), wavelength dispersive X-ray fluorescence (WD-XRF), and powder X-ray diffraction (PXRD) analyses were used to characterise the petrographic, chemical, and mineralogical composition of the paste. PE was also used to infer forming techniques coupled with a macroscopic examination of forming traces [63]. Scanning electron microscopy with energy-dispersive X-ray spectroscopy (SEM-EDX) enabled the study of the microstructure, estimation of the vitrification stage, and microanalysis of features of interest [64,65]. The combination of these different techniques allowed the study of provenance, raw material manipulation, forming, firing regimes, and surface treatments. All the ceramic samples and the fired geological deposits were analysed by WDXRF, PE, and PXRD. In addition, in a multiphase sampling strategy, a subsample of 20 previously analysed individuals was sampled for study under SEM-EDX, according to the classification revealed by the XRF, PE, and XRD analyses in terms of meaningful compositional groups and mineralogical fabrics [51]. Both archaeological and experimental ceramics were characterised and tested for mechanical and thermal properties to investigate textural and microstructural variables and their impact on material performance. Sample

preparation and instrumental conditions are available in the Supplementary Material 2 [20–22,35,40,41,65–77].

#### 4. Results

##### 4.1. Macroscopic Examination, Chemical, Mineral-Petrological, and Microstructural Results

The results of elemental concentrations of the individuals analysed by WD-XRF [78] correspond with a special case of the projective  $d + 1$ -dimensional space where the projective points are projected into the simplex  $\mathbb{S}^d$ . Points are represented by homogeneous coordinates that have a constant sum  $k$  ( $k \in \mathbb{R}_+$ ):

$$C(\mathbf{w}) = \mathbf{x} = [x_1, \dots, x_d, x_{d+1}] \mid x_i \geq 0 \ (i = 1, \dots, d, d+1), x_1 + \dots + x_d + x_{d+1} = k,$$

(in this case,  $k = 100$ ). The projective points' vector space is the positive orthant. Hence, for the statistical data treatment, the raw concentrations were additive log-ratio (alr) transformed, according to:

$$\mathbf{x} \in \mathbb{S}^d \rightarrow \mathbf{y} = \ln\left(\frac{x_d}{x_{d+1}}\right) \in \mathbb{R}^d$$

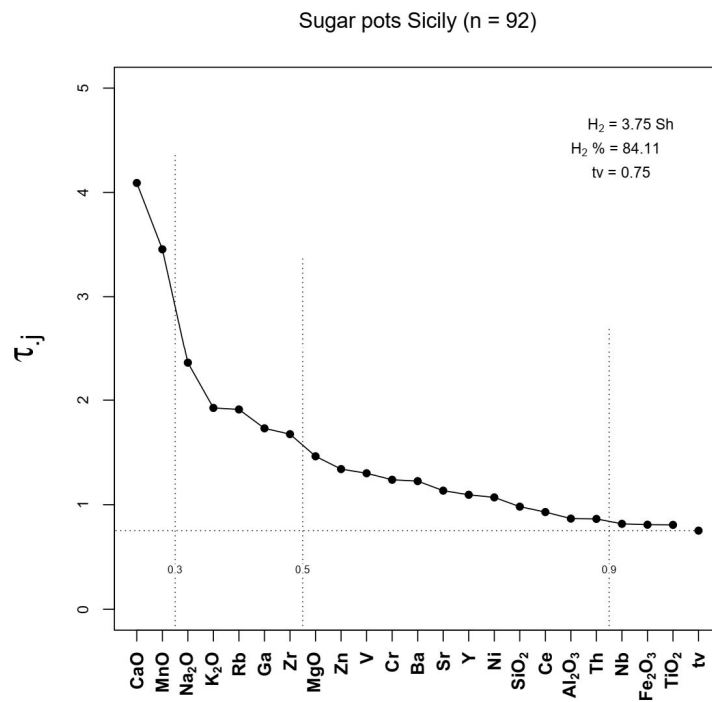
where  $\mathbb{S}^d$  is the  $d$ -dimensional simplex and  $\mathbf{x}_d = [x_1, \dots, x_d]$ . They were also centred log-ratio (clr) transformed following the equation:

$$\mathbf{x} \in \mathbb{S}^d \rightarrow \mathbf{z} = \ln\left(\frac{\mathbf{x}}{g(\mathbf{x})}\right) \in \mathbb{H} \subset \mathbb{R}^{d+1}$$

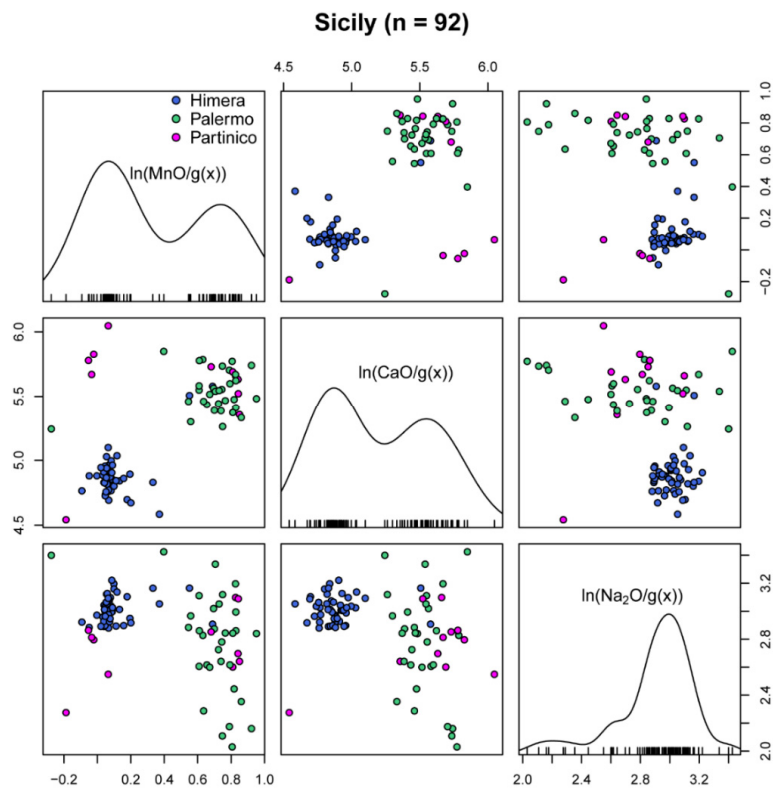
where  $\mathbb{S}^d$  is the  $d$ -dimensional simplex,  $g(\mathbf{x})$  the geometric mean of all  $d + 1$  components of  $\mathbf{x}$ , and  $\mathbb{H} \subset \mathbb{R}^{d+1}$  a hyperplane vector subspace of  $\mathbb{R}^{d+1}$  [67,79–81].

The statistical treatment was performed on 88 archaeological individuals (HIM015, 029, 070, 072, 146 were removed as only major and minor elements were measured) and the four geological deposits, for a total of 92 individuals. The statistical data treatment of the chemical data was performed on the retained values using R [82], and the first step was to measure the existing variability in the dataset. This variability results from the difference in the chemical data, and how evenly the chemical differences relate to the retained components [51,83]. In this case, total variation ( $tv = 0.75$ ) was higher than expected for a monogenetic set [84]. Focusing our attention on the compositional evenness graph (Figure 4), most of the variability is linked to the relative concentrations of CaO, MnO ( $tv/\tau_{j} < 0.3$ ), and to a lesser extent, to Na<sub>2</sub>O, K<sub>2</sub>O, Rb, Ga, and Zr ( $0.3 < tv/\tau_{j} < 0.5$ ). The compositional evenness was measured according to information entropy ( $H_2$ ), also known as the Shannon index [85], on the  $\tau_{j}$  values in decreasing order [51]. Looking at the scatterplot matrix using the three clr-transformed components that introduce more variability, CaO, MnO, and Na<sub>2</sub>O (Figure 5), the distribution of samples into two groups seems clear; one of these corresponds to the samples recovered from Himera–Buonfornello, and the other from the different sites in Palermo. In addition, the plot  $\ln(\text{CaO}/g(\mathbf{x}))$  vs.  $\ln(\text{MnO}/g(\mathbf{x}))$  also shows a few samples placed together that may form a small group related to Partinico.





**Figure 4.** Compositional evenness graph of all the measured individuals according to the entropy value ( $H_2$  and its relative value from the maximum attainable,  $H_2$  %) of the elements considered for the statistical treatment of data.  $tv$  = total variation.  $\tau_{j,j}$ : trace of the variance-covariance matrix following the alr transformation using that  $j$  element as the divisor. Vertical dotted lines express different  $tv/\tau_{j,j}$  values.

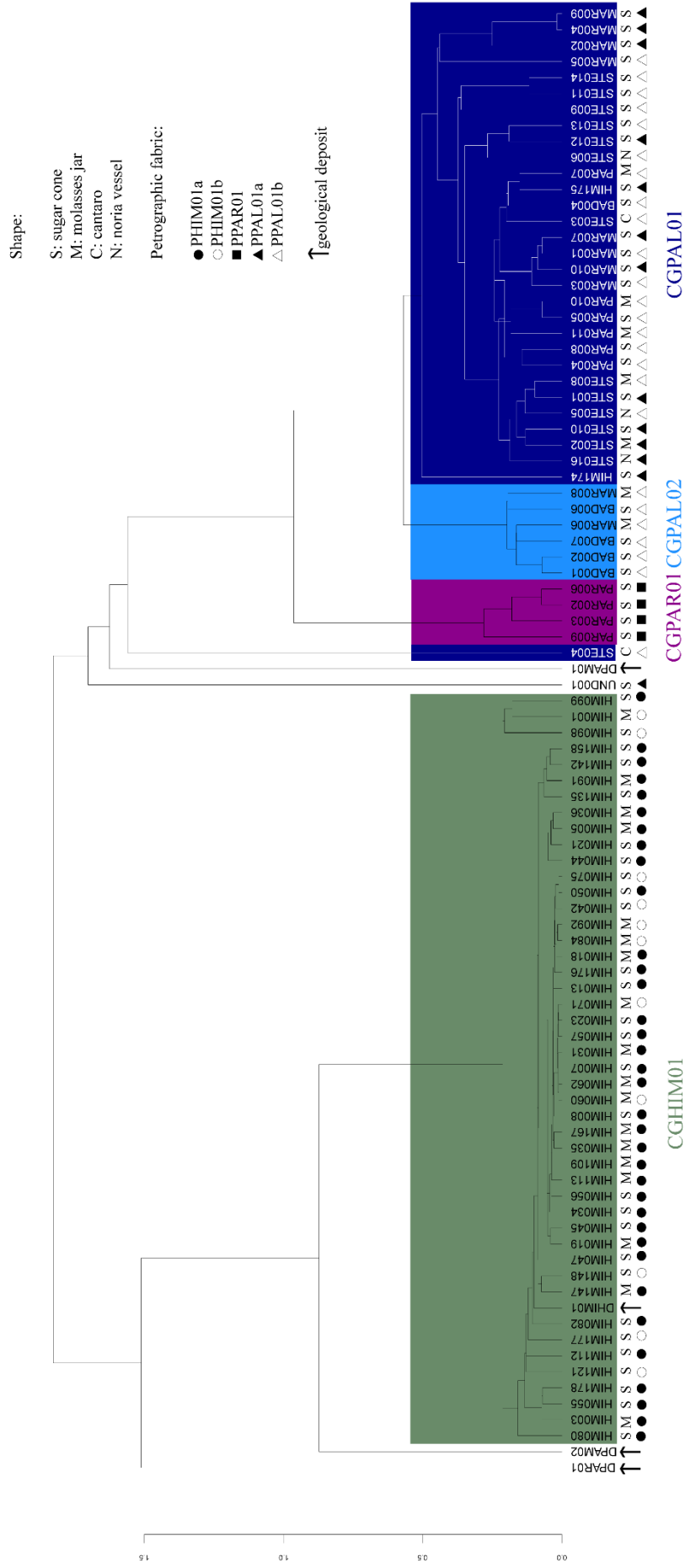


**Figure 5.** Scatterplot matrix on clr-transformed data using the three components that introduce most variability: MnO, CaO, and Na<sub>2</sub>O. In the diagonal, KDE of these clr-transformed components. Individuals are grouped by site found.

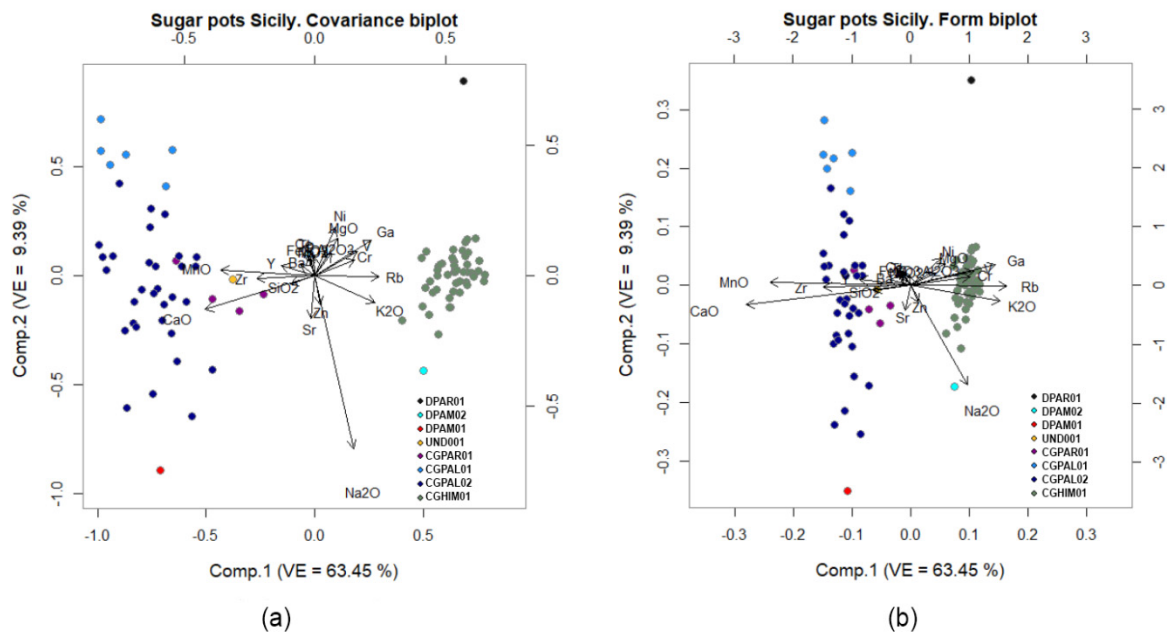
As a second step of exploring chemical data, we provide the dendrogram from the cluster analyses (Figure 6) and the form and covariance biplots (Figure 7). The dendrogram presents results from the clr-transformed data, using the square Euclidean distance and the centroid agglomerative algorithm; whereas the form and covariance biplots present results from the singular value decomposition of the double-centred clr transformation [86–88]. The resulting form and covariance biplots of the first two principal components explain more than 70% of the variance ( $VE = 72.84\%$ ). Both in the dendrogram and the biplots, a structure of four groups and five ungrouped individuals can be observed: CGHIM01, CGPAR01, CGPAL01, and CGPAL02. The same structure of groups is observed when treating the data independently by finding location, that is, individuals recovered in Palermo and Partinico together separated from those from Himera–Buonfornello. According to the biplots, the most significant components in this discrimination are those already revealed by the compositional evenness graph of Figure 4. The first component exhibits the opposition of CaO, MnO, and Zr in the negative values, and K<sub>2</sub>O, Rb, and Ga in the positive values, which is responsible for the distinction of CGHIM01 from the other groups. For the second component, mainly Na<sub>2</sub>O, Zn, and Sr in the positive values are responsible for the discrimination of groups CGPAL01 from CGPAL02, and for the intra-group differences of the group CGPAL02. Regarding the ungrouped individuals, those corresponding to the clay samples DPAR01, DPAL01-02 remain isolated, whereas the one from underwater recovery is plotted close to CGPAR01 and CGPAL02, indicating compositional similarities (Table 3).

**Table 3.** Mean ( $\bar{x}$ ), standard deviation (s), and total variation (tv) of the groups of more than two samples and values of the loners (as normalised values). Major and minor elements (expressed as oxides) in *w*%. Trace elements in  $\mu\text{g/g}$ .

	DPAR01	DPAM02	DPAM01	UND001	CGPAR01 ( <i>n</i> = 4)		CGPAL01 ( <i>n</i> = 6)		CGPAL02 ( <i>n</i> = 31)		CGHIM01 ( <i>n</i> = 47)	
					$\bar{x}$	s	$\bar{x}$	s	$\bar{x}$	s	$\bar{x}$	s
Na <sub>2</sub> O	0.48	1.6	1.25	1.19	0.73	0.13	0.46	0.08	0.88	0.2	1.16	0.11
MgO	1.99	2.14	1.24	6.28	2.18	0.06	2.33	0.19	1.87	0.28	2.66	0.17
Al <sub>2</sub> O <sub>3</sub>	17.97	17.33	9.59	14.93	12.76	0.54	14.35	0.93	13.96	0.85	17.77	0.62
SiO <sub>2</sub>	64.04	58.42	66.42	57.8	60.00	1.08	59.24	1.18	61.51	1.44	59.91	1.28
K <sub>2</sub> O	2.24	2.29	1.42	1.65	1.78	0.16	1.64	0.11	1.73	0.31	2.92	0.30
CaO	4.61	10.1	14.13	10.17	15.79	1.83	14.18	1.57	12.62	1.5	7.37	0.79
TiO <sub>2</sub>	0.97	0.93	0.64	0.85	0.72	0.03	0.81	0.04	0.79	0.05	0.90	0.03
V	147	143	87	100	101	7	96	5	86	6	134	9
Cr	125	121	88	89	81	11	87	4	83	8	125	7
MnO	0.04	0.04	0.06	0.11	0.05	0.00	0.11	0.01	0.10	0.01	0.06	0.01
Fe <sub>2</sub> O <sub>3</sub>	7.52	7.00	5.13	6.88	5.85	0.29	6.74	0.38	6.39	0.37	7.08	0.21
Ni	39	35	20	42	30	2	40	2	37	4	49	3
Zn	91	88	52	78	70	6	78	3	96	27	104	4
Ga	21	19	9	14	13	1	14	1	13	2	22	1
Rb	108	101	62	62	68	5	73	2	71	10	124	7
Sr	181	344	348	290	340	18	312	57	274	37	322	29
Y	27	26	20	27	23	1	30	2	30	2	27	1
Zr	251	225	287	248	232	12	265	14	276	13	212	10
Nb	29	26	18	23	22	1	24	2	23	1	25	1
Ba	304	224	216	284	370	55	326	41	345	52	363	44
Ce	105	104	49	80	72	12	87	9	85	7	90	6
Th	15	15	11	14	14	1	16	1	14	1	16	1
tv						0.12		0.13		0.33		0.08

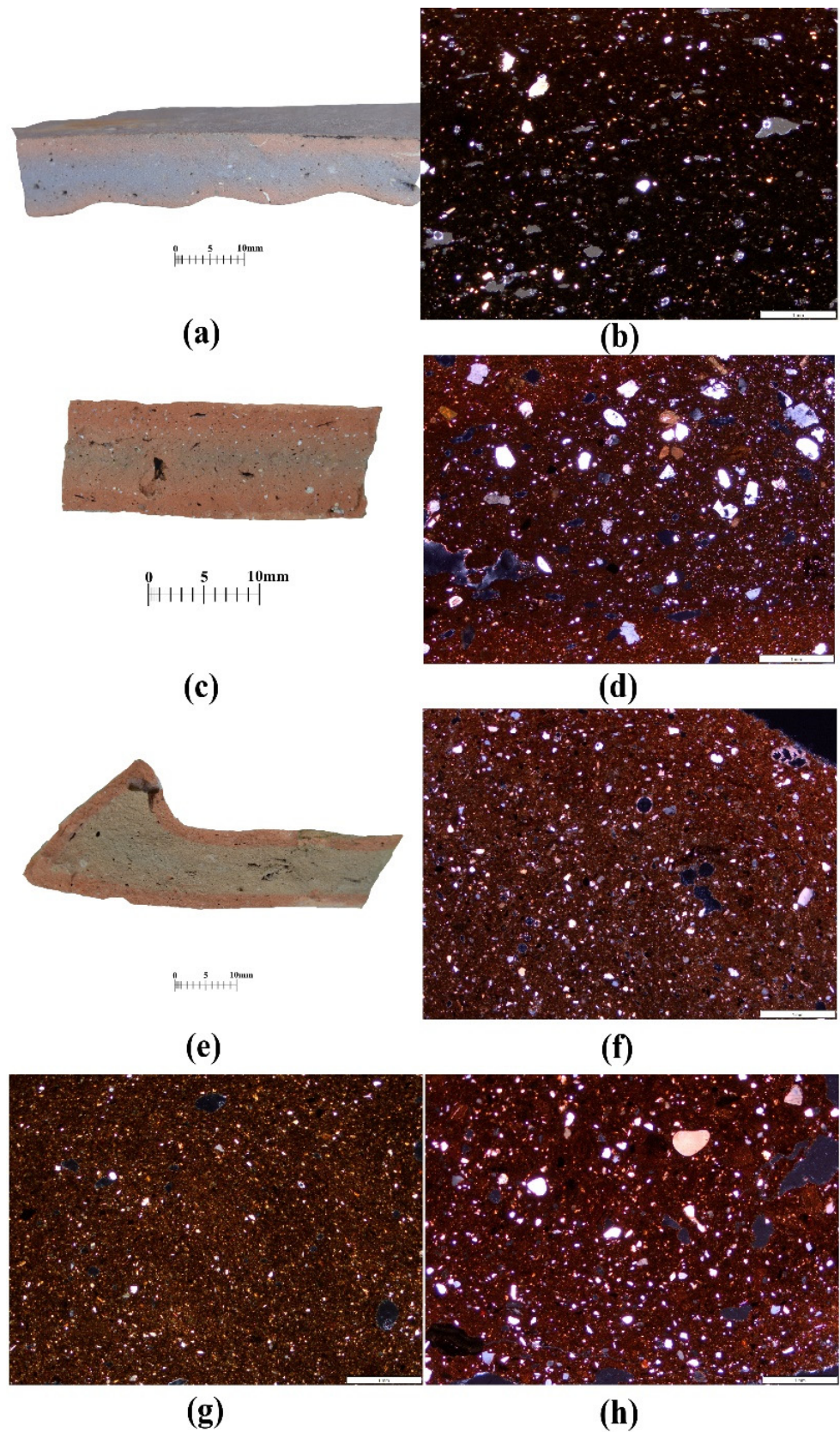


**Figure 6.** Dendrogram resulting from the analysis of the 92 individuals on the sub-composition Na<sub>2</sub>O, MgO, Al<sub>2</sub>O<sub>3</sub>, SiO<sub>2</sub>, K<sub>2</sub>O, CaO, TiO<sub>2</sub>, V, Cr, MnO, Fe<sub>2</sub>O<sub>3</sub>, Ni, Zn, Ga, Rb, Sr, Y, Zr, Nb, Ba, Ce, and Th, clr transformed, using the square Euclidean distance and the centroid agglomerative algorithm.



**Figure 7.** Covariance (a) and form (b) biplots of the principal component analysis using the singular value decomposition of the double-centred clr-transformed sub-composition  $\text{Na}_2\text{O}$ ,  $\text{MgO}$ ,  $\text{Al}_2\text{O}_3$ ,  $\text{SiO}_2$ ,  $\text{K}_2\text{O}$ ,  $\text{CaO}$ ,  $\text{TiO}_2$ ,  $\text{V}$ ,  $\text{Cr}$ ,  $\text{MnO}$ ,  $\text{Fe}_2\text{O}_3$ ,  $\text{Ni}$ ,  $\text{Zn}$ ,  $\text{Ga}$ ,  $\text{Rb}$ ,  $\text{Sr}$ ,  $\text{Y}$ ,  $\text{Zr}$ ,  $\text{Nb}$ ,  $\text{Ba}$ ,  $\text{Ce}$ , and  $\text{Th}$ .

The first large group on the left of the dendrogram is composed of 47 individuals recovered from the production centre of Himera–Buonfornello, except one individual that corresponds to a geological deposit (DHIM01), collected near the site. This group is very homogeneous and can be considered calcareous, although the  $\text{CaO}$  content is not very high (around 7 w%, Table 3). PE confirmed this grouping, as all these individuals were grouped in fabric PHIM01 (Supplementary Material 2). This is a fine- to medium-grained fabric composed mainly of monocrySTALLINE quartz, feldspars, and mica in both the fine and coarse fraction; some sedimentary rocks (quartzarkose to quartzwacke, limestone, and chert) and metamorphic rock fragments (quartzite) are frequently to scarcely present in the coarser fraction. This fabric was divided into two sub-fabrics on the basis of the size distribution and frequency of the coarse fraction, larger and more homogeneously distributed in PHIM01b (Figure 8a,b). These differences may reasonably be due to intra-source variation rather than to technological reasons, as the sample shows a continuum of this feature, sometimes without a clear division amongst the two subgroups. This subdivision is not mirrored in the dendrogram resulting from the statistical manipulation of chemical data (Figure 6). The five individuals from the same site for which only major and minor elements were measured fit into this group both chemically (related only to these elements) and petrographically. The fabric is highly compatible with Terravecchia formation deposits available near the site [41] and the collected one, DHIM01, is strongly comparable with the ceramic samples, especially with subgroup PHIM01a (Figure 8g), as chemical data previously showed. Both sugar cone and molasses jars are included in this group (Tables S2 and S3).



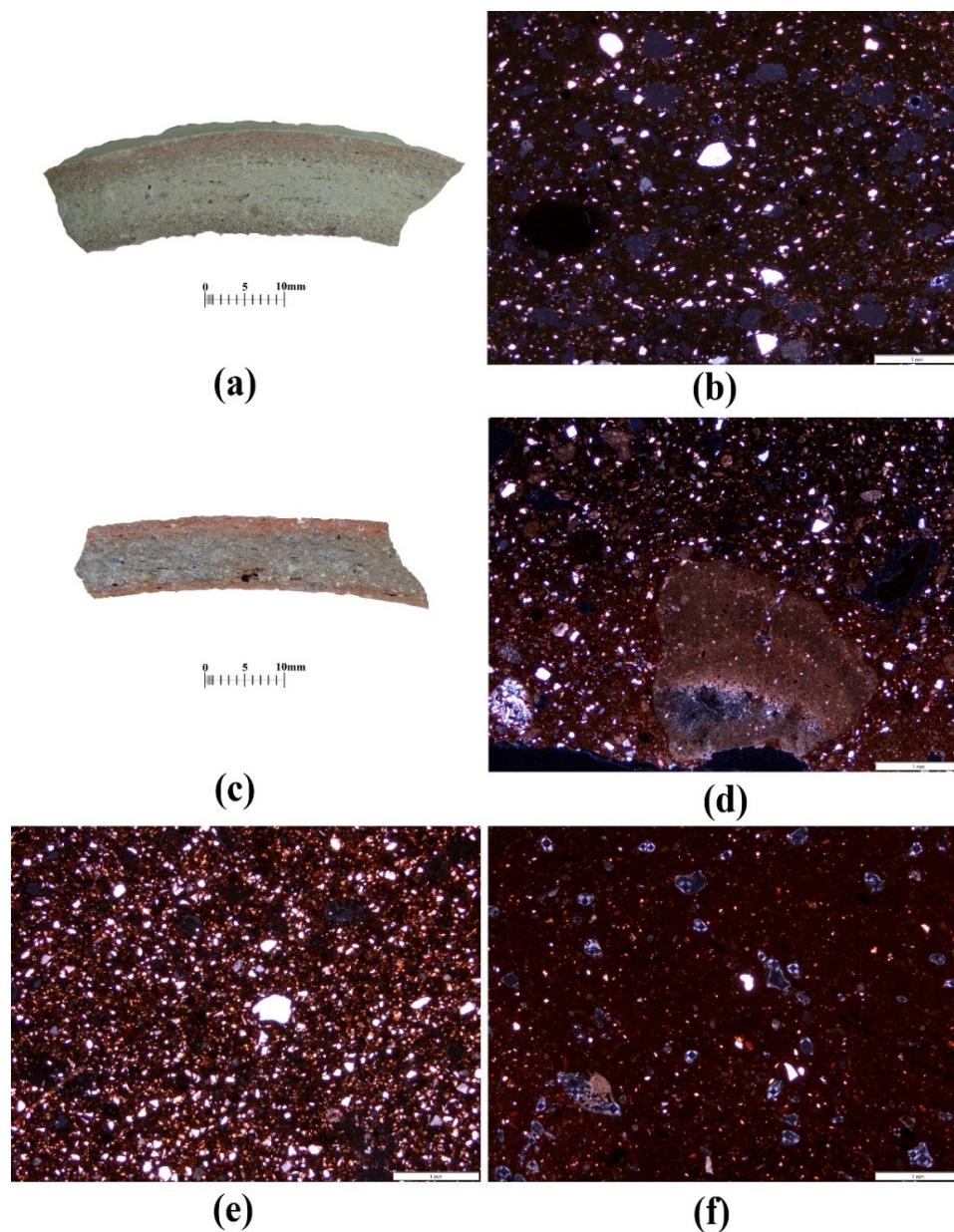
**Figure 8.** Fabric PHIM01a: macrophotograph (a) and photomicrograph in XP (b) of individual HIM178; fabric PHIM01b: macrophotograph (c) and photomicrograph in XP (d) of individual HIM078; fabric PPAR01: macrophotograph (e) and photomicrograph in XP (f) of individual PAR002; photomicrograph of DHIM01 (g) and DPAR01 (h) fired at 850 °C.



A group of four of the nine individuals from Partinico included in this study join together in the centre of the dendrogram (CGPAR01), showing clear differences from Palermo individuals, placed to the right (Figure 6). Covariance and form biplots confirm the discrimination of this small group, although its similarities with the individuals from Palermo, especially in the CaO content, placed both groups very close to each other. These individuals were grouped in the fabric PPAR01, which is a fine-grained fabric, mainly characterised by quartz and feldspars in both the fine and coarse fractions with a coarser fraction, when present, characterised also by chert, quartzite, and limestone; microfossils are common (Figure 8e,f; Supplementary Material 2). The fabric may be compatible with some deposits present in the area of Partinico [75]. However, the Numidian flysch geological sample, DPAR01, did not provide a clear matching fabric for the archaeological individuals in terms of composition and grain size distribution (Figure 8h). In addition, chemical results show that this deposit differs in multiple elemental concentrations from individuals in CGPAR01, amongst which it strikes the lower concentration in CaO and Sr, and the highest in Cr and Ce, compared to the archaeological individuals (Table 3). The composition of this deposit matches other Numidian flysch deposits analysed from western Sicily [40,41] which differs from the archaeological individuals grouped in this study. Montana et al. [41] (p. 96) note that the clay deposits collected in Palermo show a higher concentration of CaO but they differ from the CGPAR01 individuals. The Marnoso-Arenacea del Belice formation, present in the area of Partinico, is excluded as a possible source of raw materials as being highly calcareous, in addition to other differences in composition [40]. Therefore, the area of Partinico would need further investigation to locate possible raw material sources. In this group, only sugar cones are present (Tables S2 and S3).

At the right side of the dendrogram (Figure 6), calcareous individuals with the highest CaO content (12–15 w%) show a structure divided into two groups along with three isolated individuals. The latter correspond to the underwater recovery (UND001), one of Palermo's geological deposits (DPAM01), and an individual (STE004) from the site of Palazzo Steri-Chiaramonte (Palermo). Another ungrouped individual can be found on the extreme left of the dendrogram and corresponds to the other geological deposits from Palermo (DPAM02). Some individuals from Palermo join in a small group, labelled CGPAL01, composed of four sugar cones from Convento di San Giovanni at Baida (BAD) and two molasses jars from Castello della Favara a Mareddolce (MAR). Finally, the largest group plotted on the right, labelled CGPAL02, includes 14 individuals recovered from Palazzo Steri-Chiaramonte (STE), eight from Castello della Favara a Mareddolce (MAR), and one from Convento di Baida (BAD), all at Palermo; it also includes two individuals from Himera (HIM174–HIM175) and six from Partinico (PAR). Sugar cones, molasses jars, noria vessels, and cantaros are present in this large group (Tables S2 and S3). Moreover, in this case, PE shows the grouping of these individuals in one fabric, PPAR01 (Supplementary Material 2), although with an internal variability, as also seen in the biplots discussed above. PPAR01 is a fine- to medium-grained fabric composed mainly of quartz with a minor frequency of feldspars, mica, and pyroxenes, and a variable presence of a coarser fraction composed of limestone, chert, and sandstones (Figure 9a,b). The coarse fraction is larger and more frequent in subgroup PPAR01b. In most of the individuals grouped in this fabric, voids are filled by micritic inclusions, such as those described by Cau Ontiveros et al. as micritic clots and fringes along pores [76] due to the recrystallisation after firing of residual CaO already present in the paste. This fabric is compatible with the characteristics of Ficarazzi deposits available in the Palermo area [40]. Its chemical and fabric variability, although not matching, may be due to intra- and inter-variability of the clay deposits. Compared to the Ficarazzi formation deposits previously characterised by Montana et al. [41], the concentration of MnO, Zr, Ba, and Zn is higher in the archaeological individuals. Moreover, the two geological deposits analysed, DPAM01 and DPAM02, differ from the published dataset for the same elements. These two share similar rock fragments with the archaeological material but are also dissimilar regarding different points. DPAM01 is well packed with silt size inclusions, whereas DPAM02 has a finer groundmass with heterogeneously distributed

sand size inclusions (Figure 9e,f). From the chemical perspective, DPAM01 has a lower concentration of many elements, mostly in  $\text{Al}_2\text{O}_3$ , Ce, Rb, and Ga, and a high concentration of  $\text{SiO}_2$  compared to DPAM02. Our archaeological group fits in the middle of these two extremes, both from a fabric and chemical point of view. Nevertheless, DPAM01 was chosen for the mechanical and thermal performance test as the one more resembling the archaeological individuals for the grain size distribution and packing.

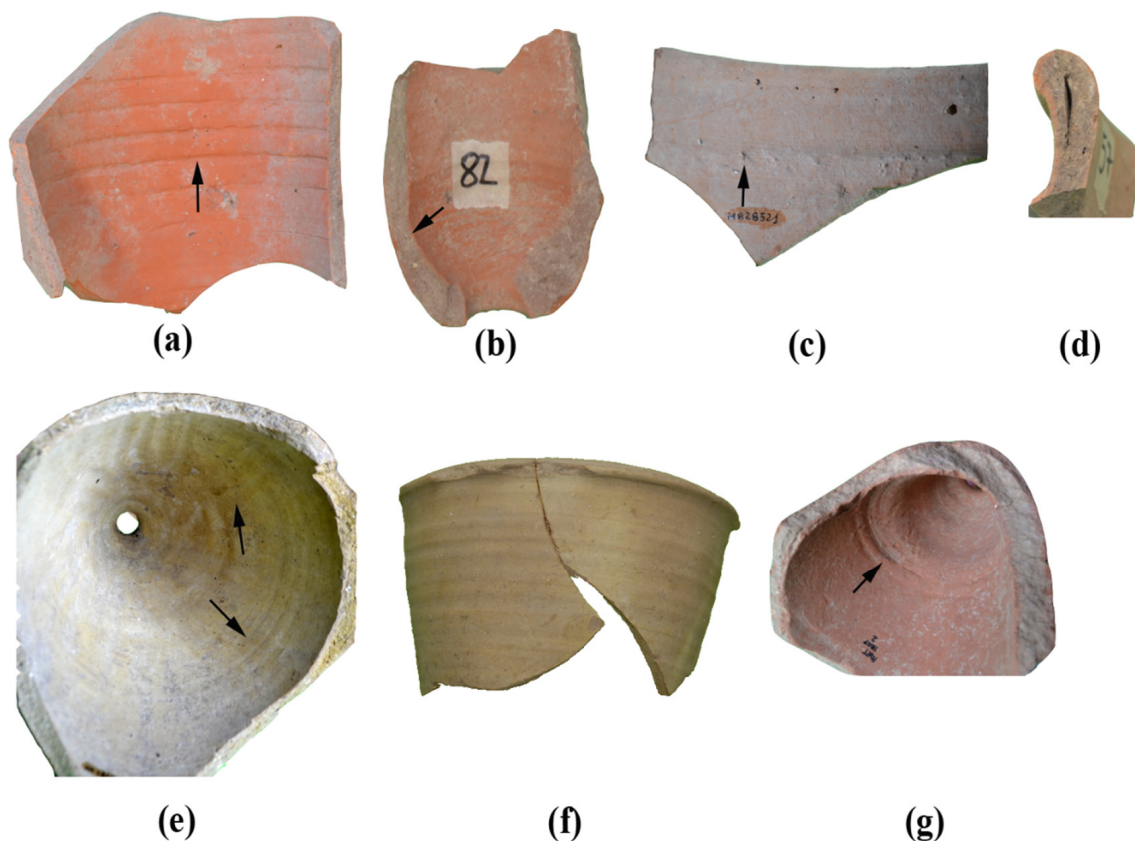


**Figure 9.** Fabric PPAL01a: macrophotograph (a) and photomicrograph in XP (b) of individual HIM174; fabric PPAL01b: macrophotograph (c) and photomicrograph in XP (d) of individual BAD007; photomicrograph of briquettes DPAM01 (e) and DPAM02 (f) fired at 850 °C.

Regarding the isolated individuals, STE004 suffers severe contamination of Pb because of analytical interference caused by Pb, in addition to other chemical elements (Rb, Y, Ce, Th) [89,90]; however, by removing these elements from the statistical treatment, it groups with CGPAM02, and PE confirmed this grouping [91].

PE allows hypotheses to be drawn regarding formation [69,70], although macroscopic observations are, in this case, most suited due to the large size of these vessels. Individuals

of PHIM01-CGHIM01 seem wheel-thrown (Figure 8b), probably in segments; in some cases, the joint of the section is visible by the change in the preferred orientation of voids and inclusions. These features can be better observed macroscopically for the clear traces of a wheel on the body (Figure 10a), and by areas of depressions in the vessel's body (so-called Y marks) [63] on the possible junction with the rim part (Figure 10c). Moreover, the bottom part of the cones shows a variation of thickness towards the hole, probably due to the fact that the bottom part was thrown upside down (Figure 10b). External cordons seem rolled up and outwards from the rim (Figure 10d). Strong orientations of voids and inclusions that may be due to wheel throwing were found in a few individuals grouped in fabric PPAR01 (especially BAD001-007), but the majority show no to poor preferred orientation of voids and inclusions. Moreover, individuals in PPAR01 show poor orientation of voids and inclusions. Macroscopically, these individuals show uneven wall thicknesses along the two sides of the cones, in addition to traces of the wheel on the surface, suggesting the use of hand-forming methods and possibly rotary devices only for finishing (Figure 10d,e); holes are not always centred and also here there are signs of the bottom part being added (Figure 10f), probably upside down as a variation in thickness towards the hole can be observed. A systematic study of the forming traces coupled with experimental reproduction will support these initial hypotheses.

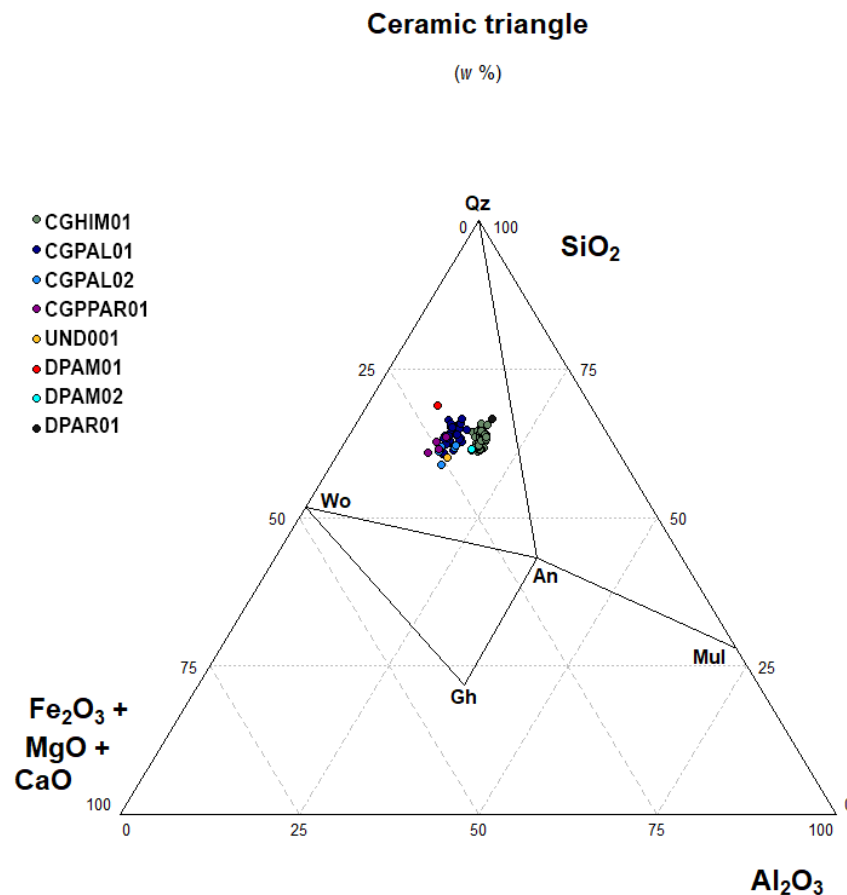


**Figure 10.** Some examples of the forming macro-traces observed on the sugar cones: (a) body of an individual from Himera (not numbered), rings produced by the wheel; (b) bottom part of HIM082, change in wall thickness towards the hole; (c) inside part of the upper part of HIM172, Y marks; (d) section of the rim of HIM057, rolling and folding of the clay outwardly; (e) inside bottom part of HIM175, wheel ring, and traces of finger pulling clay towards the hole; (f) outside upper part of HIM175 showing wheel rings; (g) inside bottom part of PAR005, change in thickness towards the hole, and joint of two sections of the vessel. Arrows indicate points where the features described can be observed. Not to scale.



Regarding firing strategies, PE suggests that most of the individuals from PHIM01 and PPAM01 show signs of being fired at a high temperature according to the micro-mass optical activity. Individuals in PPAR01 seem to have been fired at a low temperature and in oxidising conditions. Individuals of each group were mineralogically and microstructurally characterised by means of XRD and SEM to verify these initial observations.

In order to contribute to the knowledge of technical aspects of the production of the artefacts considered in this study, chemical results show that the analysed individuals are ceramics considered as being calcareous ( $5\text{--}6\% < \text{CaO} < 20\text{--}25\%$ ). Accordingly, calcareous ceramics commonly develop high-temperature phases and a light microstructure with a progressive formation of a vitreous phase [65,92,93]. The ceramic phase triangle ( $\text{CaO} + \text{Fe}_2\text{O}_3 + \text{MgO}$ )- $\text{Al}_2\text{O}_3$ - $\text{SiO}_2$  (Figure 11) shows how all the individuals analysed in this study are positioned in the quartz–anorthite–wollastonite triangle, which is characteristic of calcareous ceramics. With this in mind, mineralogical and microstructural characterisation is explained below based on the chemical and petrographic results. The complete set of XRD diffractograms and SEM photomicrographs was previously published [94,95].



**Figure 11.** Ternary diagram of the system  $(\text{CaO} + \text{Fe}_2\text{O}_3 + \text{MgO})\text{-Al}_2\text{O}_3\text{-SiO}_2$ . An: anorthite ( $\text{Ca}[\text{Al}_2\text{Si}_2\text{O}_8]$ ); Gh: gehlenite ( $\text{Ca}_2\text{Al}[\text{AlSiO}_7]$ ); Mul: mullite ( $\text{Al}_6[\text{Si}_2\text{O}_{13}]$ ); Qz: quartz ( $\text{SiO}_2$ ); Wo: wollastonite ( $\text{CaSiO}_3$ ) (abbreviations according to [96]).

The study of the XRD diffractograms of the 47 individuals of the CGHIM01 chemical group allowed the identification of four fabrics (F1 to F4), i.e., different categories of association of crystalline phases, representing four different equivalent firing temperatures (EFT) (Table 4). F1 (HIM001, 015, 070, 99, and 121) presents the three characteristic peaks of illite-muscovite at lower angles, quartz, plagioclase, alkali feldspar, an intense peak of calcite, and hematite (Figure 12a, HIM099). Amongst these phases, only the presence of the three illite-muscovite peaks, which are usually present in EFT up to  $950\text{--}1000\text{ }^\circ\text{C}$ ,

points to an EFT below this range for F1. Hematite is observed in individuals of all fabrics and therefore fails to provide indications to estimate the EFT. The microstructural study of HIM099 shows a generally no-vitrification (NV) microstructure with a few areas on the margins that are starting the vitrification process (Figure 13a). These observations allow us to estimate an EFT of below 800 °C for these individuals. Diffractograms of F2 (HIM036, 042, 044, 047, 080, 091, 098, 135, 142, 146, and 158) show a decrease in the peaks of calcite, a clear development of plagioclase, and the development of gehlenite and initial peaks of pyroxene, firing phases that crystallise above 800 or 850 °C. The three peaks of illite-muscovite are still present, which indicates an EFT in the range of (850–950/1000) °C (Figure 12a, HIM091). Two individuals were examined by SEM from this group, HIM091 and 142, revealing an extensive vitrification stage (Vc) (Figure 13b). The EFT may be in the range proposed. F3 (HIM013, 21, 35, 50, 75, 112, 148, 176 and 177) shows the almost complete decomposition of illite-muscovite, which preserves only one peak visible for most of the cases, and of calcite, which is completely decomposed or showing a very reduced peak. On the other side, pyroxene, plagioclase, and alkali feldspar are now well-developed phases. Gehlenite is still present but with significantly reduced peaks (Figure 12a, HIM075). All this evidence enables us to estimate an EFT of around 950 °C. SEM examination of individuals HIM035 and 075 reveals a well-developed vitrified microstructure with many areas having micro- and macro-pores (Figure 13c). According to this microstructure, the EFT is estimated at around 950–1000 °C. Finally, illite-muscovite and calcite completely disappear in the diffractograms of fabric F4, and gehlenite peaks are greatly reduced or decomposed for most of the cases (HIM003, 005, 7, 8, 18, 19, 23, 29, 31, 34, 45, 55, 56, 57, 60, 62, 71, 72, 82, 84, 92, 109, 113, 147, 167, and 178). In addition, an important development of plagioclase, hematite, and pyroxene is observed (Figure 12a, HIM178). These characteristics indicate an EFT above 950/1000 °C. From SEM, both HIM031 and 178 showed a total vitrified microstructure with macro-pores (Figure 13d); this suggests a higher EFT than the previous groups, probably in the range of 1000–1100 °C. Sugar cones and molasses jars can be found in all the fabrics but most of the molasses jars (13 over 17) are included in the highest EFT fabric, F4.

**Table 4.** Table of the estimated equivalent firing temperature (EFT) according to X-ray diffraction (XRD) fabrics and vitrification stages by scanning electron microscopy (SEM, in bold individuals, examined). Afs: alkali feldspar; Cal: calcite; Px: pyroxene; Gh: gehlenite; Hem: hematite; Ilt: illite-muscovite; Pl: plagioclase; Qz: quartz; Spl: spinel (abbreviations according to Whitney and Evans, 2010). NV: no vitrification; IV: initial vitrification; Vc: extensive vitrification; TV: total vitrification. low calc.: low calcareous, calc: calcareous.

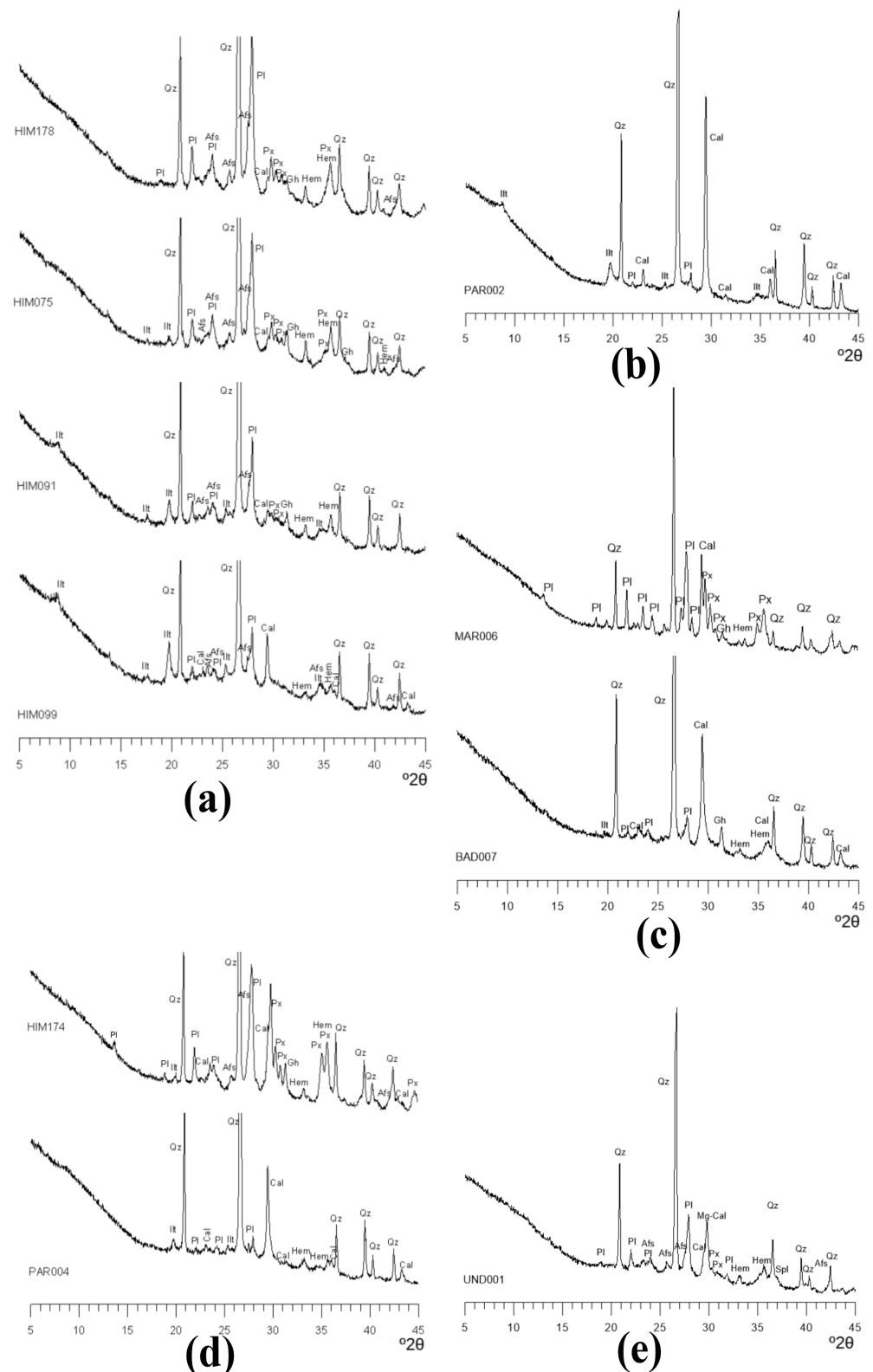
XRF Group	Petrographic Fabric	XRD Fabric	Individuals	Vitrification Stage Core/Margins	Calcareous/Low Calcareous	EFT °C
UND001	PPAL01	F1—Afs, Cal, Mg-Cal, Hem, Pl, Px, Qz, Spl	UND001	/	low calc.	>950–1000
		F1—Afs, Cal, Hem, Ilt, Pl, Qz	HIM001, 015, 070, <b>099</b> , 121	NV	calc.	<800
		F2—Cal, Px, Hem, Ilt, Gh, Pl, Qz	HIM036, 042, 044, 047, 080, <b>091</b> , 098, 135, <b>142</b> , 146, 158	Vc	calc.	(850–950/1000)
CGHIM01	PHIM01	F3—Afs, Di, Hem, Ilt (1-2/3), Gh, Pl, Qz	HIM013, 021, <b>035</b> , 050, <b>075</b> , 112, 148, 176, 177	Vc+	calc.	(950/1000)
		F4—Afs, Cal, Gh, Px, Hem, Pl, Qz	HIM003, 005, 007, 008, 018, 019, 023, 029, <b>031</b> , 034, 045, 055, 056, 057, 060, 062, 071, 072, 082, 084, 092, 109, 113, 147, 167, <b>178</b>	TV	calc.	(1000–1100)

Table 4. Cont.

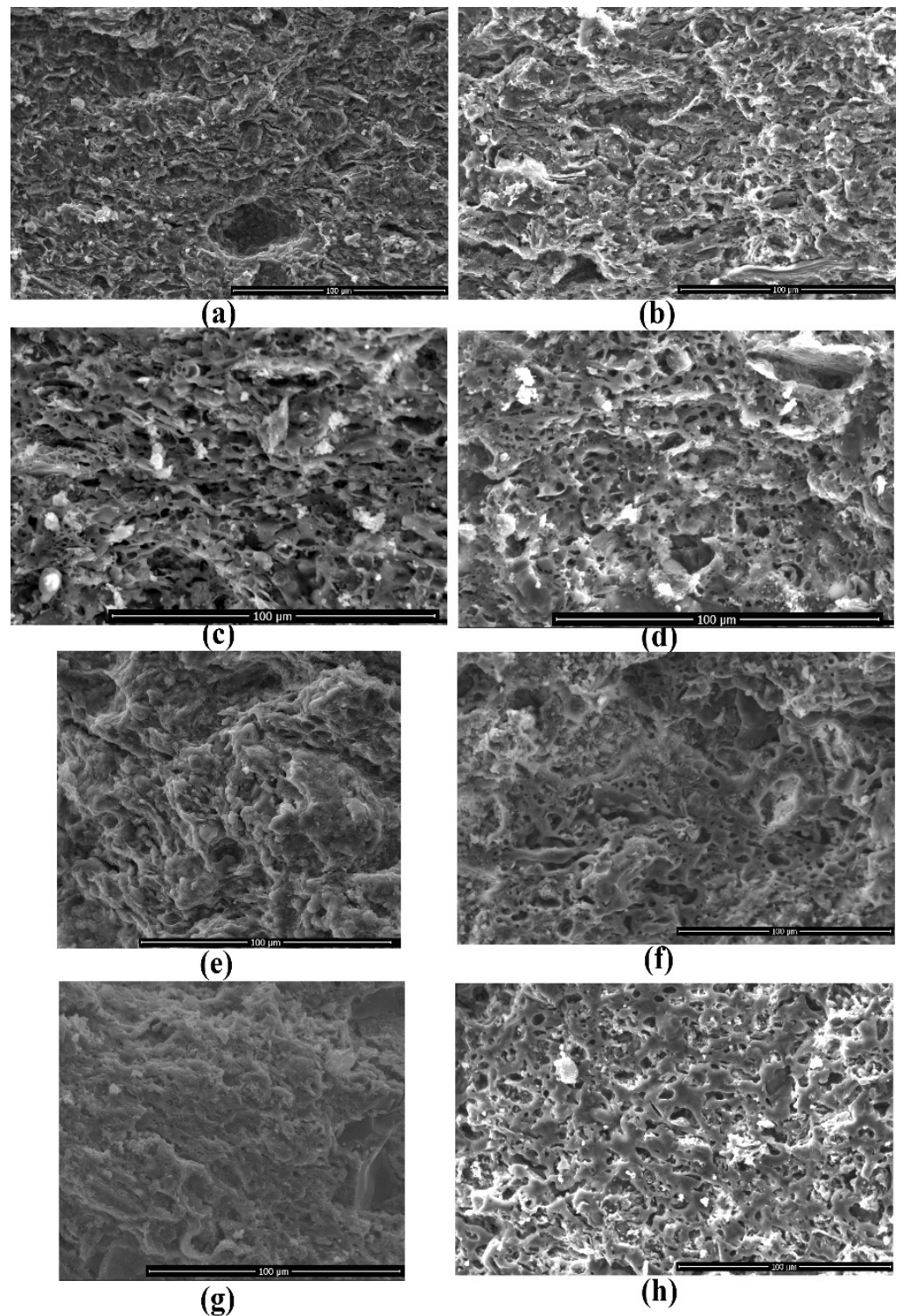
XRF Group	Petrographic Fabric	XRD Fabric	Individuals	Vitrification Stage Core/Margins	Calcareous/Low Calcareous	EFT °C
CGPAR01	PPAR01	F1—Cal, Ill, Pl, Qz	PAR002, 003, 006, 009	NV	calc.	<800
CGPAL01	PPAL01	F1—Cal, Hem, Ill (2/3), Gh, Pl, Qz	BAD001, 02, 006, 007 MAR008	Vc	calc.	(950–1000)
		F2—Cal, Px, Hem, Pl, Qz	MAR006	TV	calc.	(1000–1100)
CGPAL02	PPAL01	F1—Cal, Ill (1/3), Pl, Qz	STE011, 013, 014, PAR005	NV/IV	calc.	800
		F2—Cal, Ill (1/3), Hem, Pl, Qz	STE003, MAR005, PAR004	NV/IV	calc.	800
		F3—Cal, Gh, Ill (1/3), Hem, Pl, Qz	STE012, PAR007, 008, 010, 011	V	calc.	(950–1000)
		F4—Afs, Cal, Px, Gh, Ill (1/3), Hem, Pl, Qz	STE001, 002, 005, 006, 008, 009, 016, BAD004, HIM174, 175	TV	calc.	(1000–1100)
		F5—Afs, Cal, Px Ill (1/3), Hem, Pl, Qz	MAR009 MAR001, 004, 007, STE004	TV	calc.	(1000–1100)
		F6—Afs, Cal, Px, Hem, Pl, Qz	MAR003 and MAR010	/	calc.	(1000–1100)
		F7—Cal, Px, Hem, Pl, Qz, Gh	STE010	TV	calc.	(1000–1100)
		F8—Afs, Di, Pl, Qz	MAR002	TV+	calc.	(1000–1100)

The four individuals belonging to the CGPAR01 group are four sugar cones that exhibit peaks of illite-muscovite, quartz, calcite, and plagioclase (Figure 12b) (Table 4). No firing phases are present, which would indicate an EFT below 800 °C. SEM examination of PAR002 confirms this interpretation by showing an NV microstructure (Figure 13e). In spite of the small number of individuals from this group, a low temperature can be characteristic of these products.

Regarding the six individuals in CGPAL01, the examination of the diffractograms allowed the identification of two fabrics (Table 4). F1, which includes most of the individuals (BAD001, 002, 006, 007, and MAR008), exhibits two of the three peaks of illite-muscovite at lower angles, calcite, quartz, plagioclase, hematite, and gehlenite and, in some instances, the low-intensity peaks of pyroxene are observed (Figure 12c). By SEM, BAD006 and 007 show a Vc core with micro-bloating in a few areas at the core of the section (Figure 13f). The only individual corresponding to F2 (MAR006) shows the total decomposition of illite-muscovite, the decrease in the gehlenite peak, and development of pyroxenes; the high peak of calcite is due to post-firing crystallisation, as was verified by PE (Figure 12c). According to these results, an EFT in the range of 950–1000 °C can be proposed for F1 and around 1000–1100 °C for F2. SEM examination of MAR006 shows a TV microstructure and confirms the higher temperature proposed for F2. Therefore, it would seem that high temperatures would be the option preferred by the potters in this case, for both sugar cones and molasses jars.



**Figure 12.** Diffractograms of some of the archaeological individuals discussed by the chemical groups. (a) CGHIM01: individual HIM099, F1; individual HIM091, F2; individual HIM075, F3; individual HIM178, F4. (b) CGPAR01: individual PAR002, F1. (c) GCPAL01: individual BAD007, F1; individual MAR006, F2. (d) GCPAL02: individual PAR004, F1; individual HIM174, F4; (e) individual UND001. Afs: alkali feldspars; Cal: calcite; Gh: gehlenite; Hem: hematite; Ill: illite-muscovite; Hem: hematite; Mg-Cal: magnesium calcite; Pl: plagioclase; Px: pyroxene; Qz: quartz; Spl: spinel (abbreviations according to [96]).



**Figure 13.** SEM photomicrograph (SE) of some of the archaeological individuals discussed. Chemical group CGHIM01: (a) HIM099, F1, NV microstructure; (b) HIM091, F2, V microstructure; (c) HIM075, F3, V+ microstructure; (d) HIM178, F4, TV microstructure. Chemical group CGPAR01: (e) PAR002, F1, NV microstructure. Chemical group CGPAL01: (f) BAD007, F1, V microstructure. Chemical group CGPAL02: (g) PAR004, F2, IV microstructure; (h) HIM174, F4, TV microstructure. Photomicrograph taken at  $\times 2000$ , except for (c,d) at  $\times 1000$  taken with a JEOL J6510.

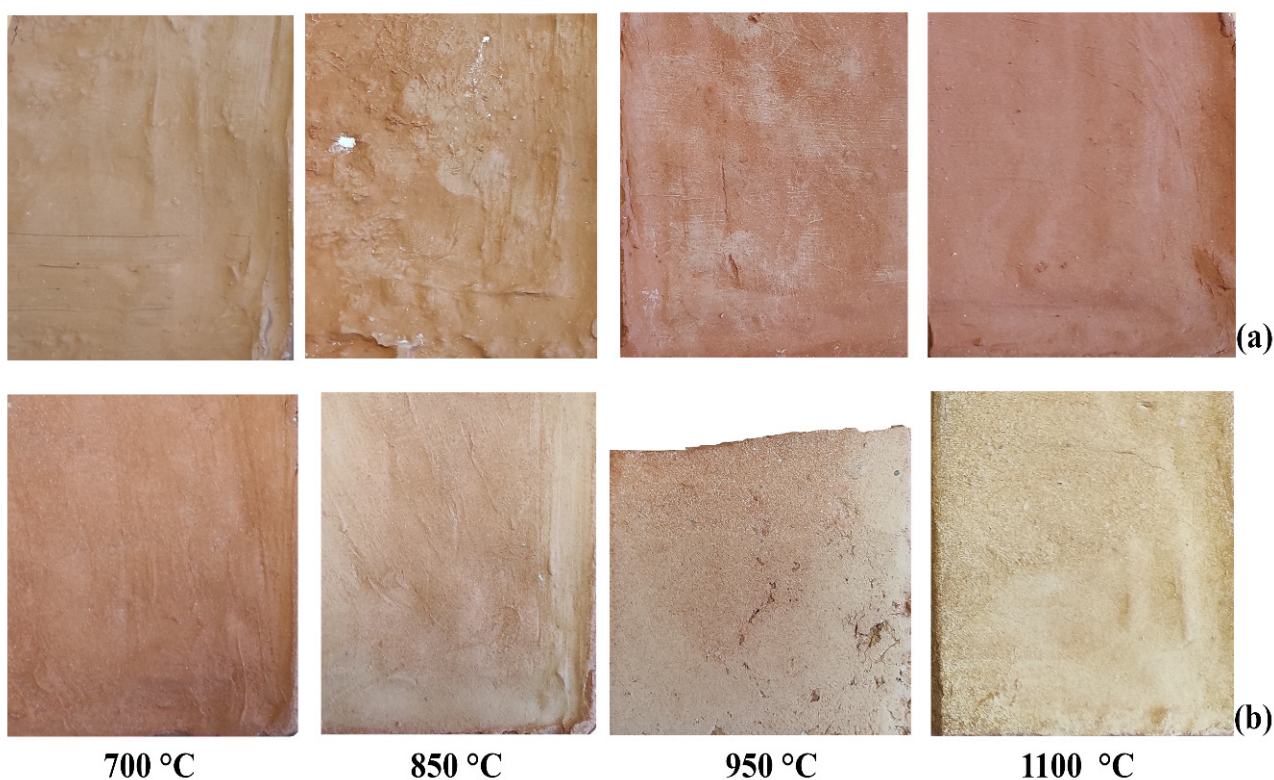
The second group related to Palermo, CGPAL02, is the second-largest group identified in this study, formed by 31 individuals. Their diffractograms show up to eight fabrics

indicating a wide range of EFT from  $<800\text{ }^{\circ}\text{C}$  to  $>950/1000\text{ }^{\circ}\text{C}$  (Table 4). The F1 (STE011, 013, 014, PAR005) and F2 (STE003, MAR005 and PAR004) exhibit the same mineral phases: illite-muscovite, quartz, calcite, and plagioclase, with the exception of hematite, which is only present in F2 (Figure 12d, PAR004). In both cases, only the illite-muscovite peak of  $4.5\text{ \AA}$  is visible, a fact that might lead us to think about the decomposition of primary minerals of clay and calcite and the crystallisation of firing phases. According to the mineralogical characterisation of other Ficcarazzi formation deposits [41], these are not as rich in illite-muscovite as in other clays and therefore the development of illite-muscovite peaks may not be an explanation for firing temperature changes. In addition, the presence of the peak of calcite, which is prominent in both fabrics, cannot be used for the estimation of a low EFT; PE indicates that almost all these individuals show the presence of calcite recrystallised after firing. In the samples examined by SEM from these two fabrics, a similar microstructure can be observed: STE011 and 014 are generally NV but with a few spots showing IV; PAR004 shows an NV core and IV margins (Figure 13g). According to these observations, an EFT  $\sim 800\text{ }^{\circ}\text{C}$  is estimated. The next three fabrics, F3 (STE012, PAR007, 008, 010, and 011), F4 (STE001, 002, 005, 006, 008, 009, 016, BAD004, MAR001, 004, 007, and HIM174, 175), and F5 (MAR009) still show the peak of  $4.5\text{ \AA}$  of illite-muscovite, but now the clear crystallisation of gehlenite is observed for F3 together with an important development of plagioclase and hematite. Some individuals present an initial development of pyroxenes, clear for F4 (Figure 12d, HIM174) and more developed for F5, a fabric in which gehlenite is not present. All the individuals from these three fabrics present a peak of calcite to a greater or lesser extent. Consequently, an EFT  $>850\text{ }^{\circ}\text{C}$  is clear for the three fabrics and an EFT around  $950/1000\text{ }^{\circ}\text{C}$  can be estimated for F4 and F5. SEM examination allows this temperature to be increased to the  $950\text{--}1100\text{ }^{\circ}\text{C}$  range; PAR011 from F3 shows a Vc microstructure with some areas at the core showing an advanced state of Vc<sup>+</sup>; both individuals from F4 (BAD004, HIM174) show dense vitreous masses (TV, Figure 13h), whereas individual MAR009 has an over-vitrified microstructure. Finally, three more fabrics were identified: F6 (MAR003 and MAR010), F7 (STE010), and F8 (MAR002), which would be clearly fired above  $950/1000\text{ }^{\circ}\text{C}$ . None of the individuals from these fabrics show the presence of the illite-muscovite peaks; the peak of gehlenite is absent in F6 and F8, and the peak of calcite is completely decomposed in F8. The microstructure of STE010 is characterised by total vitrification, whereas in the MAR002 the microstructure is very disturbed but areas totally vitrified are recognisable. The variety of microstructures and XRD fabrics encountered in this group does not seem correlated to ceramic shape or archaeological context. Only the five molasses jars and the three *norja* vessels of this group are included in F3 and F4, which are the products fired at a high temperature, as was observed for Himera; however, the number of these is too small compared to that of sugar cones to consider this result significant.

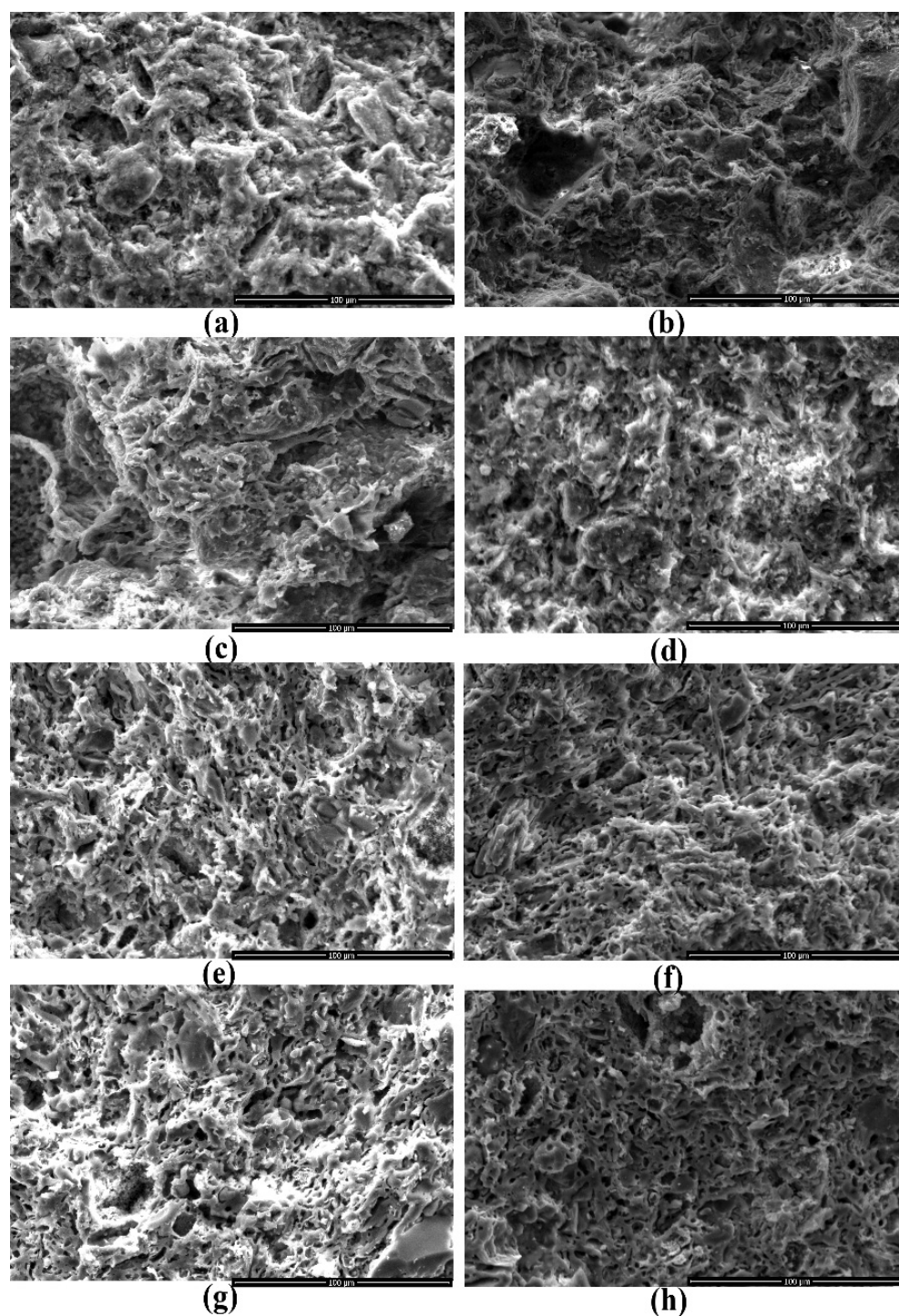
The underwater individual UND001 was included in fabric PPAM01 (Supplementary Material 2), but chemically it seems that it does not match the other individuals from CGPAL01-02. Compared to these groups, UND001 shows clear chemical changes that typically are found in sherds from marine environments [97–105]: a high concentration of MgO, which often occurs in underwater findings, causing a decrease in CaO, although in this case, CaO is still high (around  $10\text{ }w\%$ ). The diffractogram of UND001 shows the absence of hydrotalcite, a mineral phase reported as usually developing in seawater environment, but the presence of magnesium calcite has also reported as being formed in the same environment; a peak of spinel is also evident (Figure 12e). This suggests that the significant amounts of both MgO and CaO are allochthonous, and fixed by secondary phases, and that UND001 is a low calcareous individual. In addition to the CaO and MgO content, UND001 has strong similarities to other CGPAL01-02 individuals, and when removing MgO and CaO from the statistical treatment of the data, it fits within the CGPAL02 group. However, as CGPAL01-02 individuals usually bear higher CaO content, UND001 is considered a loner at present. The firing temperature of this individual is probably in the higher range due to the absence of any of the illite-muscovite peaks and the presence of spinel. The pyroxene peak is probably due to its primary presence in the paste.



Based on the chemical and petrographic results, two geological deposits were chosen to further perform mechanical and thermal tests on experimental briquettes fired at different temperatures (Figure 14). DHIM01 perfectly matches the archaeological individuals in group CGHIM01, whereas DPAM01 was considered the closest to the individuals in groups CGPAL01-02. DPAM01 is the closest to the CaO content, which influences the microstructure development, and the packing and grain size of inclusions that also affect the thermal and mechanical properties. SEM examination of these experimental briquettes allows the consideration of the development of the microstructure of these fabrics at different temperatures (Figure 15). In both DHIM01 and DPAM01, a major change occurs between 950 and 1100 °C when areas with a denser mass are formed. In DPAM01, one can see some areas where macro- and micro-pores are still present, whereas in DHIM the latter prevail. The difference in CaO content between the two deposits (around 7 and 14 *w%*, respectively) is the cause of this different development. Comparing microstructures, a good correspondence between the experimental briquettes and those of the archaeological ceramics is observed.



**Figure 14.** Experimental briquettes of DHIM01 (a) and DPAM01 (b) fired at different temperatures.

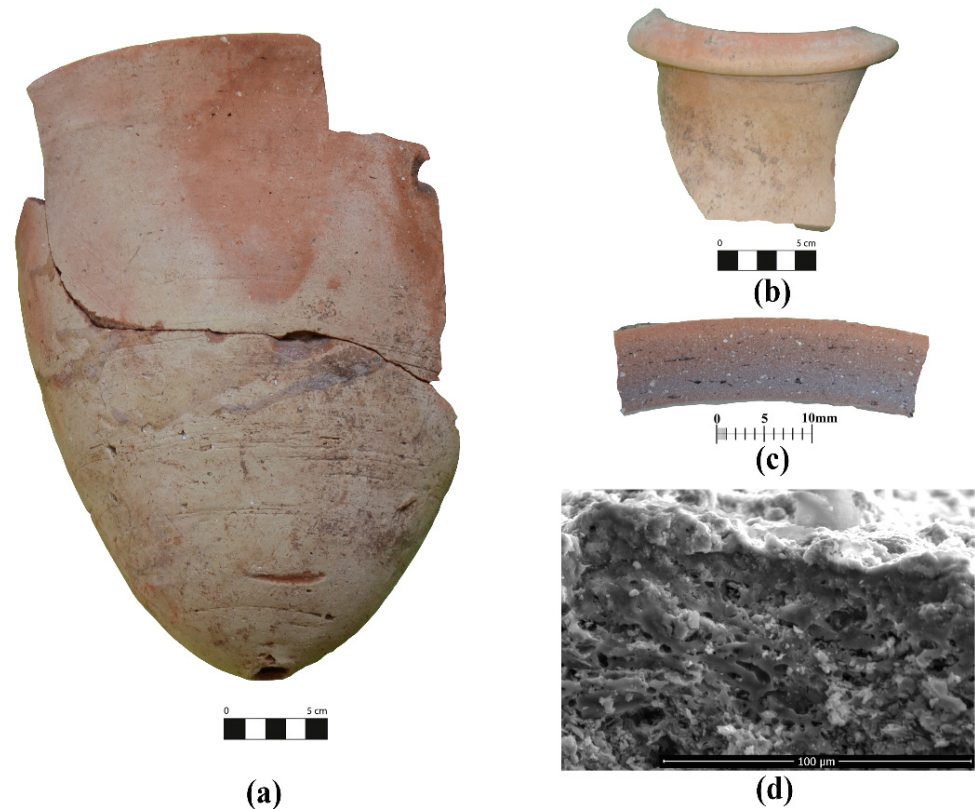


**Figure 15.** SEM photomicrographs (SE) of the microstructure developed by the experimental briquettes of the two geological deposits sampled: (a) DHIM01 and (b) DPAM01 fired at 700 °C showing an NV microstructure; (c) DHIM01 and (d) DPAM01 fired at 850 °C, IV microstructure; (e) DHIM01 and (f) DPAM01 fired at 950 °C, Vc microstructure; (g) DHIM01 and (h) DPAM01 fired at 1100 °C, TV microstructure. Magnification:  $\times 2000$ .

In terms of surface treatment, sugar pots present a heterogeneously distributed white appearance, which is clearer when examining complete vessels (Figure 16a,b). Macroscopic examination of the surface and section suggests that vessels were not slipped with a calcareous material; the white area is found in patches on the surface, and in the section the white is very thin, almost invisible (Figure 16c) or fading into the margins. SEM exami-



nation confirmed this hypothesis because no significant microstructural or compositional differences could be detected between the body and the surface (Figure 16d). A similar heterogeneous white layer was observed in the experimental briquettes of DPAM01, visible only on those fired at 850 and 950 °C (Figure 14b). In the archaeological materials, however, it is not clearly related to temperatures because it could be observed on individuals fired at low to high temperatures.



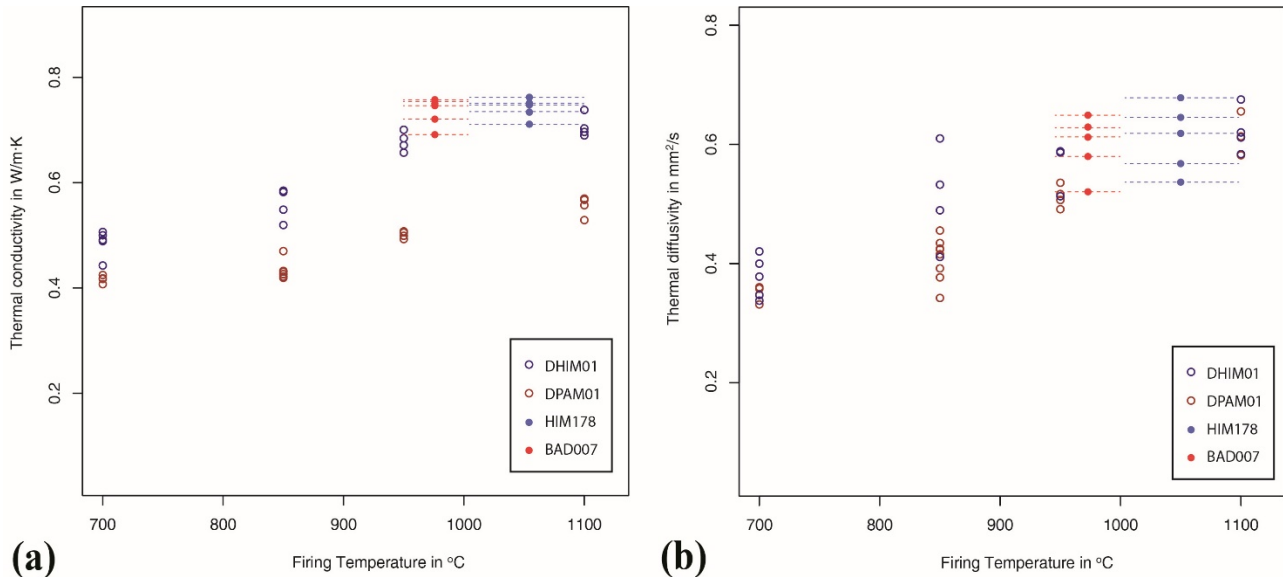
**Figure 16.** (a) Sugar cone MAR005 showing heterogeneously distributed white patches on the surface; molasses jar HIM031: (b) showing similar white patches on the rim and body, (c) in section showing a very thin layer of whitish colour on the surface, (d) SEM photomicrograph showing the surface and the body ( $\times 1000$ , SE).

#### 4.2. Mechanical and Thermal Properties

##### 4.2.1. Heat Transfer Properties

As expected, the fired geological deposit samples presented thermal conductivities correlated with the firing temperature (Figure 17). This can be explained by the densification of the ceramic matrix during firing and the increasing degree of vitrification (Figure 15) [19]. The specimens of the fired geological deposit sampled close to Himera–Buonfornello (DHIM01), however, presented higher thermal conductivity compared to the fired geological deposit from Palermo (DPAM01), particularly at firing temperatures of above 950 °C. This might be related to the higher CaO content in the paste from Palermo, which apparently results in a higher porosity of the ceramic fabric. The two archaeological individuals measured, HIM178 (CGHIM01, F4) and BAD007 (CGPAL01, F1) presented thermal conductivity values at a level comparable to that of the Himera clay (DHIM01) fired at 1100 °C. Although the EFT of BAD007 is estimated to be lower on the basis of the mineral phases developed, the micromorphology observed under the SEM of both the archaeological samples (Figure 13d,f) resembles the micromorphology of the Himera clay fired at 1100 °C. The thermal diffusivity, which describes the rate of heat transfer, indicates a similar correlation with firing temperature, although in the case of the clay from Palermo (DPAM01) the specimens fired at 950 and 1100 °C are at the same level as the fired clay

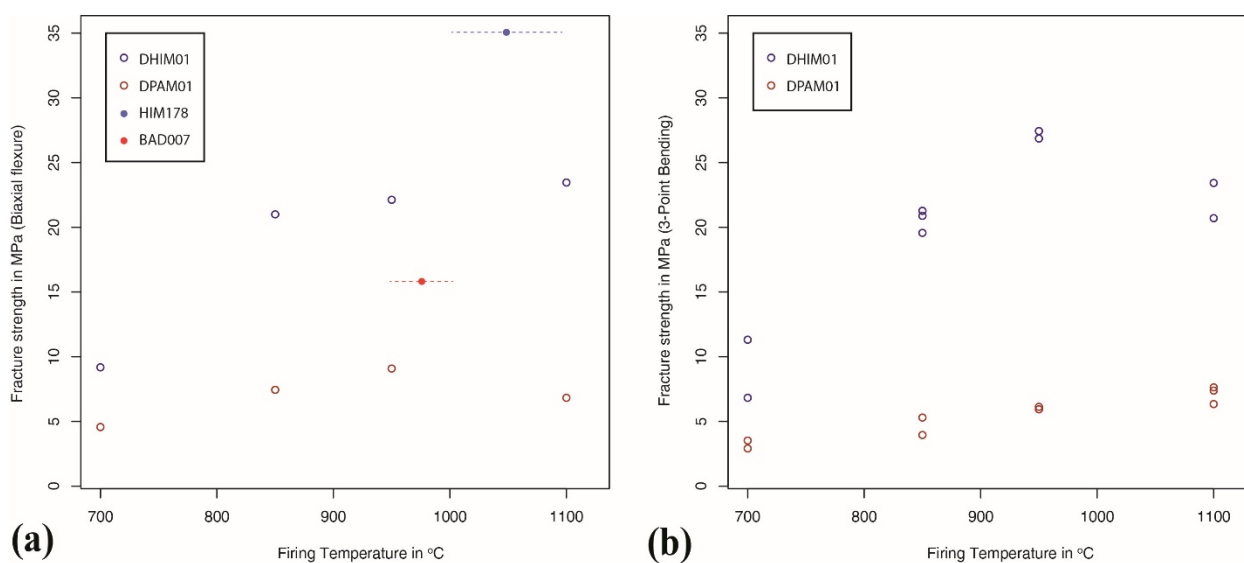
from Himera (DHIM01). Hence, ceramics fired from these two clays will transfer heat at the same rate, which concerns, for example, the capability to withstand thermal stress and thermal shock, or the rate at which the content of the vessel exchanges heat with the environment.



**Figure 17.** Thermal conductivity (a) and thermal diffusivity (b) measured in the fired geological specimens and in the two archaeological individuals HIM178 and BAD007: the values are plotted versus firing temperature and the EFT estimated for the two archaeological individuals. Raw data are available in [106].

#### 4.2.2. Fracture Strength

The fracture strength measured in biaxial flexure tests and three-point bending tests also indicates, as expected, a correlation with firing temperature (Figure 18). Particularly in the case of the Himera clay (DHIM01) a significant increase at firing temperatures from 700 to 850 °C can be observed, which can be explained with the development of the microstructure and the increase in vitrification in the ceramic fabric [20]. The geological deposit sampled at Palermo (DPAM01) presents comparably lower fracture strength, probably due to the higher content of non-plastic inclusions observed, which introduce flaws and imperfections in the ceramic matrix [21]. By comparison, the recorded load-displacement curves indicated a potentially increased toughness, which can be expected based on the coarser microstructure [20]. The archaeological specimen from Himera HIM178 presents increased fracture strength even in comparison with the Himera clay specimen (DHIM01) fired at 1100 °C. For this, an efficient clay paste preparation and refinement can be assumed before this clay was possibly used for ceramic manufacture. The same may apply to the archaeological specimen from Palermo (BAD007). Although it presents a lower fracture strength than the fired clay specimens from Himera, its fracture strength is increased compared to the fired clay specimens sampled at Palermo.



**Figure 18.** Fracture strength measured in the fired clay specimens and in the two archaeological individuals HIM178 and BAD007: the values are plotted versus firing temperature and the EFT estimated for the two archaeological individuals. The left plot presents the results of the biaxial flexure tests (a) and the right plot the results of the 3-point bending tests (b). Raw data are available in [106].

## 5. Discussion

### 5.1. Sugar Pots Production Areas and Circulation

The results of the chemical and petrographic analyses of the archaeological and geological deposits at least three production areas to be suggested for sugar pots: Palermo, Himera–Buonfornello, and another that we might provisionally assign to Partinico. Further research is needed on archaeological ceramics and local geology in this last case. Palermo production seems more varied than that of Himera, which is most probably due to two factors. First, the sugar pots from Palermo cover a larger chronological range, at least from the 11th to the beginning of the 16th century A.D.; therefore, a certain variability within the same source is expected [107], considering that all the workshops in the city use this source for this entire period. By comparison, Himera–Buonfornello production is dated within a smaller timescale, from the end of the 15th century to the beginning of the 16th century A.D. For this latter case, we are dealing with a sugar production centre, which probably included a ceramic workshop for sugar cones and other wares in its premises [16,38]. In the second instance, regarding Palermo, none of the contexts examined can be considered a production centre *per se*; the production of sugar probably occurred in the surroundings of Palazzo Steri–Chiaramonte and Castello della Favara a Maredolce, as historical studies confirmed [28] (p. 67) [18] (p. 283), but these were mainly residential areas during the phases under study [30,31,34]. Castello della Favara a Maredolce seems to have been transformed from a residential agricultural function, probably in the mid-13th century [30]. In a second phase, probably by the 15th century, part of its activity was devoted to sugar production, as a larger quantity of sugar cones and molasses jars were found in contact with the four kilns [108]. The ceramics pertaining to this last phase were not examined in this project, however [16]. In addition, the sugar cones found at Convento di San Giovanni di Baida were reused there as building materials [16]. By not being primary production places, sugar pots were probably produced in different workshops operating within the city of Palermo, and reaching the contexts in our study for consumption or secondary purposes. These differences between the two areas are also visible in the vessel design, which is much varied in terms of dimensions and profiles in Palermo compared to Himera–Buonfornello (Figure 3, [16]). This variability can only in part be explained by differences in chronology, and is related to the context of the production of these vessels.

From this study, it emerges that ceramics needed for sugar production were mainly produced in the surroundings of the sugar production centres. In the cases of Himera–Buonfornello and Partinico, the archival record refers to the construction of kilns by sugar production owners to cut the high transport costs and to facilitate the production of large quantities of the vessels [29] (p. 245) [18] (p. 279). Nevertheless, sugar pots produced in Palermo reached the other two areas. In the case of Partinico, although this study concerned survey material, half of the vessels retrieved there match those of Palermo production. Moreover, in terms of design, these vessels resemble those from Palazzo Steri–Chiaromonte [16]. Similarly, two sugar cones found at Himera–Buonfornello belong to the same typology and, indeed, it was found that they were produced in Palermo. In contrast, the circulation of sugar pots from these sugar production centres to Palermo, one of the main consumption and distribution centres, is missing from the archaeological point of view. On the one hand, sugar pots were re-used in their production and their use as transport vessels is not common. On the other hand, the archival record refers to the transport of sugar within sugar cones, for example, from Carini to Palermo [18] (p. 265). The cone found underwater, which was produced in a yet to be defined location in Sicily, suggests that these vessels were circulating, even over long distances. Further archaeological research may contradict this hypothesis but, at present, the only indication we have from archaeological data is that sugar pots from Palermo reached Partinico and Himera–Buonfornello, but not the opposite. It may be wondered whether these were circulating with sugar or empty, to be filled and returned to Palermo; at present, however, we do not possess enough data to discriminate amongst these two scenarios.

### 5.2. Sugar Cones Material Properties across Phases and Contexts

In terms of raw material choices and manipulation, generally calcareous fine-grained pastes were used. At least for Palermo and Himera–Buonfornello, we do not have evidence of those manipulation processes, such as the addition or removal of rock fragments or organics that would drastically alter the properties of the raw materials available. The calcareous content of the two pastes is, nevertheless, different, which may create differences in the microstructure developed during firing and, therefore, in the final properties of the vessel [65,92,93].

Regarding forming techniques, the present evidence suggests that most of the sugar pots were wheel-thrown. Sugar cones have traces of being wheel-thrown in a different section, that is, first the body, then the rim, and finally the bottom part. By comparison, some of the cones found in Partinico and Castello della Favara a Mareolce, and the two found at Himera–Buonfornello but produced in Palermo, show signs of a combination of hand-building and wheel-forming/finishing techniques. These belong to different phases of sugar production and sites; therefore, it is unclear whether we can assign these differences to an earlier phase of sugar pot production or to a different means of forming.

Regarding surface treatment, the whitening effect on the surface is not obtained by applying a calcareous slip. A known method of obtaining the same effect is by mixing seawater with the paste or by smoothing the surface of the vessel with it as a finishing method; during drying and firing, the water evaporates, causing the migration of sodium chloride to the margins and/or the surface, which causes the whitening [99,109]. This method was used since prehistory in the Near East [109] and in Sicily, at least since the 8th century AD [110]. Rye [111] (pp. 35–36) reports that the use of seawater mitigates the effect of calcite decomposition during firing, also lowering the temperature of vitrification. In the case of the sugar pots from Himera–Buonfornello, the addition of seawater may have led to the production of a white surface, rather than mitigate the presence of calcium-rich inclusions, which are not very common in the paste. In contrast, the paste used in Palermo is richer in calcareous content due to the presence of large limestone inclusions. However, in this case it cannot be confirmed that potters always added seawater; the experimental briquette shows the development of this effect without the addition of seawater, probably because this paste is naturally rich in soluble salt. Rather than adding seawater to produce

this surface effect, potters may have chosen those clay deposits which allowed them to produce the desired final result.

Finally, the study of the mineralogical and microstructural development in the examined individuals allows us to discuss some patterns. An EFT in the range of 950–1100 °C is most commonly encountered in individuals from the Himera–Buonfornello group and is probably the intended one to be reached by the potters. A few sugar cones seem to be fired at lower temperatures, and this may have occurred accidentally or resulted from different firings within the same production area. In the case of Palermo production, a variety of EFTs was reconstructed; most of the individuals were in the high ranges of firing temperature (950–1100 °C) and some were fired at lower temperatures. The molasses jars and the noria vessels seem to be fired at high temperatures; otherwise, however, no clear correlation could be found between the estimated EFT and the site, chronology, or vessel shape. This diversity in firing may have resulted from the presence of several workshops in the production of these artefacts, using a technique probably related to their own way of operating. In addition to the diversity in EFT, the microstructure developed between Palermo and Himera–Buonfornello individuals fired at high temperatures is similar, although larger pores could be observed in Palermo individuals. Conversely, all the individuals from Partinico were fired at low temperatures (EFT below 800 °C). As only four individuals belong to this group, it is unsure whether this may be considered a dissimilarity or just the result of an information gap.

These technological profiles were tested for their mechanical and thermal properties. Our results on experimental and archaeological individuals show that, when individuals are fired at high temperature (>950 °C), similar capabilities to transfer heat and to reduce the liability to thermal stress and thermal shock can be observed. Below this firing temperature, the results from the two pastes diverge more, with the Himera sample showing higher thermal conductivity. Similarly, resistance to crack initiation (mechanical strength) and propagation (toughness) changes as a function of the temperature and the developed microstructure. The paste from Himera shows higher fracture strength. By comparison, the Palermo paste appears to show a tough behaviour, enabling the ceramic fabric to absorb energy even after initial crack development. The frequency and size of inclusion in the Palermo paste surely plays a role in this different behaviour [21].

### 5.3. Sugar Pots in the Context of Ceramic Manufacture in Sicily in the Medieval and Post-Medieval Phases

As mentioned above, the sugar pots examined here belong to different phases. Although detailed knowledge of ceramic production is not available for all of these phases, we can try to situate the sugar pots in their manufacturing context. For the first phase (11–13th century AD), the most detailed study available comes from Testolini's research of the operational sequence of 8–11th century ceramics in Sicily [110]. Her reconstruction suggests that, in the 11th century, the glazed and unglazed wares in Palermo were produced with the local Ficarazzi clay, but then differed in terms of the other steps of the manufacturing sequence, thus creating distinguishable final products; she also referred to the whitening of the surfaces on the same wares [110] (pp. 180–202). Of interest is the case of cooking pots, which are made with the same clay with the addition of chert fragments, but then wheel-thrown or coil-built, and fired at high or low temperatures in an oxidising or reducing atmosphere; each *chaîne opératoire* corresponds to a specific shape which, according to Testolini, is a link to the different workshops manufacturing cooking pots in Palermo [110] (pp. 177–179). Previous works on medieval ceramics confirmed the use of Ficarazzi clay for the production of amphorae [112], glazed and unglazed wares for later phases [113–115], and the addition of chert for cooking pots [113,116]. Giarrusso and Mulone [113] also found that a low calcareous paste, probably of Numidian flysch formation, to which chert was added, was also used for cooking pots. Sugar pots, therefore, were manufactured in Palermo, at least with the same paste used for glazed and unglazed materials, but not cooking wares; the whitening on the surface seems to be present also



in other wares, both glazed and unglazed, and both hand and wheel-forming techniques co-existed. Unfortunately, not much knowledge of production processes is available for the 15–16th century phase in Palermo. In contrast, the spatial organisation of the manufacture of the city has been tackled by many scholars [117–120]. In the 10–12th century phase, the ceramic manufacturing activities were located mainly within the city’s urban area and along the river Kemonia, with some extension outside the city near the river Oreto, where the clay was extracted [117,120]. These areas continued to be devoted to ceramic manufacture, even in a later phase (from the end of the 13th century to the 14th century), when a southern part of the city walls also seemed to be dedicated to ceramic manufacture [120]. It is not clear from the archive sources whether there was a specialisation of workshops for the manufacturing of specific wares, but craftspeople working with clay for ceramics or tiles were clustered in this part of the city, and were therefore in close contact [118]. A few *trapeti* in Palermo were also located between the Kalsa and the Albergheria neighbourhoods, on the eastern side of the city, but most of the others were in the western part of the city [18] (p. 283). Although the topography of the ceramic and sugar production areas need further research, at first glance it seems that the two forms of production were not concentrated in the same areas (Figure 19).



**Figure 19.** Map of Palermo with the sites sampled (1: Castello della Favara in Mareddolce, 2: Convento di Baida, 3: Palazzo Steri–Chiaromonte), and the areas of sugar production according to archival sources [18,28] and the areas of ceramics production according to archival and archaeological sources [117–120]. The localisation of the areas has to be considered to be broad.

In contrast, in the case of Himera–Buonfornello, the production of sugar cones took place within the premises of the *trapetum* [29] (p. 245), as was common in this second phase of sugar production on the island, when it spread outside the urban boundaries of Palermo. Termotto [121] describes in detail the organisation and the labour division of the *trapetum* of Galbinogara, one of the biggest sugar production centres, and which was not far from that of the Himera–Buonfornello. He mentions that the clay sources of Collesano, a nearby town, may have been used to produce the sugar pots, which were most probably fired at the *trapetum*. Around this place grew a number of crafts and structures linked with the lives of the workers connected with the sugar production, who were often from other territories and worked seasonally in the *trapetum* [122]. In the case of Himera–Buonfornello, different potters moved their production near the *trapetum*, where the vessels were immediately used and where potters worked in the same restricted area with the other workers of the *trapetum*. Regarding our knowledge of ceramic production in

the area, the use of Terravecchia formation deposits has been attested to since the Greek phases [123,124]. In contrast, for the chronological range, the only available study is that of D'Angelo et al. [125], which indicates that this clay was used for the production of the polychrome glazed Polizzi ware. Kiln wasters of this ware were retrieved together with sugar pots at Himera–Buonfornello, suggesting that the production was performed by the same craftspeople manufacturing the sugar pots. The individuals examined came from Polizzi and not from Himera–Buonfornello, but they share the same type of raw material. However, D'Angelo et al. [125] reported that Polizzi ware was slipped with a different material compared to that used for sugar pots. Future research should examine whether the Polizzi ware vessels made at Himera–Buonfornello share the same characteristics.

#### 5.4. One Function, Multiple Choices

In the reconstructed *chaîne opératoire* of sugar pots from the three areas considered, some common patterns were identified: the conical shape with a hole at the bottom; the use of calcareous raw material, and a raw material used for other wares (but not for cooking pots); a whitened surface; the use of the wheel-throwing method, at least for some part of the manufacture; the manufacture of the cones by sequential section. Some of these choices are directly related to the function of these pots. Their conical shape provides an easier release of the crystallised sugar loaf, and the hole at the bottom enables the discharge of the excess liquid. The use of the wheel-throwing method allows faster production and vessels having more standardised dimensions. A calcareous raw material produces a microporosity that may have favoured heat dissipation [22]. Conversely, some features were not related to the function of sugar pots; rather, they were part of the *habitus* of the potters; for example, the use of whitening the vessel surface can be also encountered in other wares and for more or less calcareous pastes. Some of these choices are linked to the manufacturing context in which these vessels were made, and cannot be explained only with regard to their function. In addition to these commonalities, the examined sugar pots diverge in terms of the characteristics of the clays (more or less calcareous), the firing strategy (generally fired at high temperatures, but also at low temperatures), the means of obtaining the white surface (use of seawater, or perhaps a raw material naturally rich in soluble salt), and the choice of the dimensions and design of the vessels, which were the most visible aspects [16]. These differences have a geographical correlation, i.e., sugar pots in Palermo are distinct from those made at Himera–Buonfornello and from those of Partinico, but are also site related. In Palermo, we can observe a variety of choices in the making of sugar pots, which can only in part be explained by a chronological aspect, and may be related to the organisation of the production of these pots. Although this point needs further research to integrate our results with archival sources, we can suggest two different scenarios. In the case of Palermo, the ceramic manufacture area is separated from that of the sugar production: sugar pots from different workshops reached the *trapetum*, but there was no immediate feedback to the potters about their product (Figure 19). In the case of Himera–Buonfornello, ceramic production took place in the *trapetum*: although potters did not neglect the production of other wares, as the case of ware produced in Polizzi shows, their production was focused on the needs of the sugar industry, and they may have worked together with other craftspeople in the *trapetum*. Although a certain degree of variability is observed in the production of in Himera–Buonfornello, the design and manufacturing sequences are strikingly more homogeneous than those of Palermo. It may be suggested that the community of practice at Himera–Buonfornello was focused on sugar production, whereas that in Palermo was focused on ceramic production itself.

## 6. Conclusions

Due to the pioneering research of archaeologists and historians who have shed light on many aspects of sugar production in Sicily, this project could move forward and consider the archaeological evidence from a different point of view, aided with an analytical examination. Three main areas of production of sugar pots were defined: Palermo, Himera–Buonfornello,

and one, for the present time, labelled Partinico. Completing the information from archival sources that refer to sugar pots circulating from other places to Palermo, this study revealed that sugar pots also circulated from Palermo to the other two areas. Further research is needed to discern whether these sugar pots were travelling filled with sugar to be consumed, or empty, to be filled with sugar and then returned to Palermo. The underwater discovery, probably also made in Sicily, shows that sugar pots were also circulating by sea.

The ways in which sugar pots were designed and manufactured followed some common features, such as the conical shape, the forming methods, and the adoption of calcareous pastes. The specific function of these vessels clearly constrained some potters' choices. Conversely, some technological characteristics were specific to each area, such as the firing strategies, the vessel profile, and the means of obtaining a white surface. In terms of the analysis, vessels showed similar heat transfer properties when fired at high temperatures; however, the vessel of Himera–Buonfornello were more capable of resisting thermal shock and crack initiation, whereas Palermo's vessels were probably tougher. When considering the forces these were subjected to during use, sugar cones from Himera and Palermo would perform in the same way when the hot syrup was poured inside, but those of Himera would remain stronger during continuous handling and travelling. Sugar cones produced in Palermo, in contrast, would crack more easily but withstand longer use after use. These differences reinforce the hypothesis that there does not seem to be a "standard" for sugar pot design and technology; rather, a local re-interpretation of common and generic requirements can be observed [16]. These idiosyncrasies may have originated in the context of manufacture; that is, the choices made by potters in making other wares and in the production organisation. The community of practice of potters in Palermo working on a wide range of ceramic products may have been very different from that of Himera–Buonfornello, where sugar pot manufacture was closely related to sugar production. The variety observed in Palermo sugar pots compared to those of Himera–Buonfornello may be explained by the different levels of connection of the ceramic manufacture to the sugar production. For Partinico, we cannot generate any hypotheses on this aspect at present due to the scarcity of the materials found.

As in the example of the can opener, would the reconstructed design and technological differences have a consequence for the actual performance of the vessels? Would their utilisation differ? Finite element analyses have been used in other cases to solve these questions [24,25], and will be further applied to the sugar pot case study.

Robertson argues that the terms globalisation and glocalisation should not be seen as opposing. He also argues that these terms involve the 'simultaneity and the interpenetration of what are conventionally called the global and the local or ... the universal and the particular' [1] (p. 30). We do not argue in this paper whether sugar production and consumption in the Mediterranean can be considered a 'globalised' phenomenon; however, this concept also fits well in explaining the response of local potters to the particular demands for specific vessels from the sugar industry: potters thought globally but acted locally.

**Supplementary Materials:** The following supporting information can be downloaded at: <https://www.mdpi.com/article/10.3390/min12040423/s1>, Supplementary Material 1: Table S1 List of individuals examined and the analyses performed; Table S2 Correlation of vessel shape by context with the petrographic fabric as defined in Supplementary Materials 2; Table S3 Correlation of vessel shape by context with the chemical groups. Supplementary Material 2: Sample preparation and instrumental conditions and the petrographic descriptions.

**Author Contributions:** Conceptualization, R.M.; methodology, R.M., M.M.i.F., A.H., V.K. and J.B.i.G.; validation, R.M., M.M.i.F. and A.H.; formal analysis, R.M., M.M.i.F., A.H., V.K. and J.B.i.G.; investigation, R.M.; resources, R.M.; data curation, V.K. and J.B.i.G.; writing—original draft preparation, R.M., M.M.i.F. and A.H.; writing—review and editing, R.M., M.M.i.F., A.H., V.K. and J.B.i.G.; visualization, R.M., M.M.i.F. and A.H.; supervision, R.M., J.B.i.G. and V.K.; funding acquisition, R.M., J.B.i.G. and V.K. All authors have read and agreed to the published version of the manuscript.



**Funding:** This research is part of the project “Sugar Pot manufacture in western Europe in the medieval and post-medieval period (11–16th centuries AD)”, funded under the Horizon 2020 Marie Skłodowska-Curie actions (grant agreement: 797242).

**Data Availability Statement:** The raw data presented in this study are openly available in the CORA, Research Data Repository.

**Acknowledgments:** For their support, their feedback and to provide access to the materials, we would like to thank L. Arcifa of Università di Catania; F. D’Angelo, medieval archaeologist; E. Pezzini, F. Spatafora, C. Greco of Museo A. Salinas di Palermo; S. Vassallo, G. Battaglia e M.R. Cucco of Soprintendenza ai BBCCAA di Palermo; M.R. Panzica of Museo P. Marconi di Himera; G. Falsone of Università di Palermo; A. Molinari of Università La Sapienza di Roma; M. Gasparo and G. Montana of Università di Palermo for helping in identifying and collecting the clays from Partinico. The CCTIUB of Universitat de Barcelona for performing the analyses with special mention to M. Romero. G. Vekinis, head of the Advanced Ceramics and Composites Laboratory of the NCSR Demokritos for facilitating the use of the INSTRON 5982. The Labstone laboratory for preparing the thin sections. Judith, Julia, Marta and Cristina of the ARQUB and Maria and Dimitra of the NCSR Demokritos team for their scientific and, more importantly, human support. V. Testolini, V. Anicetiand S. Valenzuela for providing feedback and support since the first stages of the project.

**Conflicts of Interest:** The authors declare no conflict of interest. The funders had no role in the design of the study; in the collection, analyses, or interpretation of data; in the writing of the manuscript, or in the decision to publish the results.

## References

- Robertson, R. Glocalization: Time-space and homogeneity-heterogeneity. *Glob. Mod.* **1995**, *2*, 25–44.
- Horden, P.; Purcell, N. *The Corrupting Sea: A Study of Mediterranean History*; Blackwell: Oxford, UK, 2000.
- Broodbank, C. *The Making of the Middle Sea: A History of the Mediterranean from the Beginning to the Emergence of the Classical World*; Thames & Hudson: London, UK, 2013.
- Mintz, S.W. Sweetness and Power. In *The Place of Sugar in Modern History*; Penguin: New York, NY, USA, 1986; pp. 48–52.
- Galloway, J.H. The Mediterranean Sugar Industry. *Geogr. Rev.* **1977**, *67*, 177–194. [CrossRef]
- Watson, A. The Arab Agricultural Revolution and Its Diffusion, 700–1100. *J. Econ. Hist.* **1974**, *34*, 8–35. [CrossRef]
- Decker, M. Plants and Progress: Rethinking the Islamic Agricultural Revolution. *J. World Hist.* **2009**, *20*, 187–206. [CrossRef]
- Squatriti, P. Of Seeds, Seasons, and Seas: Andrew Watson’s Medieval Agrarian Revolution Forty Years Later. *J. Econ. Hist.* **2014**, *74*, 1205–1220. [CrossRef]
- Fuks, D.; Amichay, O.; Weiss, E. Innovation or preservation? Abbasid aubergines, archaeobotany, and the Islamic Green Revolution. *Archaeol. Anthr. Sci.* **2020**, *12*, 50. [CrossRef]
- Berthier, P. *Les Anciennes Sucrieries du Maroc et Leurs Réseaux Hydrauliques: Étude Archéologique et D’histoire Économique*; Impr. Française et Marocaines: Rabat, Morocco, 1966.
- Abulafia, D. Sugar in Spain. *Eur. Rev.* **2008**, *16*, 191–210. [CrossRef]
- Politis, K.D. (Ed.) Origins of the Sugar Industry and the Transmission of Ancient Greek and Medieval Arab Science and Technology from the Near East to Europe. In *Proceedings of the International Conference Athens 23 May 2015*; National and Kapodistriaki: Athens, Greece, 2015.
- Jones, R.E. *Sweet Waste: A View from the Mediterranean and from the 2002 Excavations at the Tawahin es-Sukkar (Safi), Jordan*; Pottingair Press: Glasgow, UK, 2017.
- Bronstein, J.; Stern, E.J.; Yehuda, E. Franks, locals and sugar cane: A case study of cultural interaction in the latin kingdom of Jerusalem. *J. Mediev. Hist.* **2019**, *45*, 316–330. [CrossRef]
- Shapiro, A.; Stern, E.J.; Getzov, N.; Waksman, S.Y. Ceramic Evidence for Sugar Production in the ‘Akko Plain: Typology and Provenance Studie. In *Multidisciplinary Approaches to Food and Foodways in the Medieval Eastern Mediterranean*; Waksman, S.Y., Ed.; Archéologie(s) 4, MOM Éditions: Lyon, France, 2020; pp. 163–189.
- Tullio, A. *Mentesana et al. forthcoming*. Archaeological evidences of Medieval Sugar Production in Sicily: A Reassessment. 2022; Submitted for publication.
- Banqueri, J.A. *Ibn al-‘Awwām, Libro de Agricultura*; García Sánchez, E., Hernández Bermejo, J.E., de Ministerio, A.P.A., de Ministerio, A.A., Eds.; EE: Madrid, Spain, 1988; Volume 2.
- Ouerfelli, M. *Le Sucre. Production, Commercialisation et Usages Dans la Méditerranée Médiévale*; Brill: Leyde-Boston, MA, USA, 2008.
- Hein, A.; Müller, N.S.; Day, P.M.; Kilikoglou, V. Thermal Conductivity of Archaeological Ceramics: The effect of Inclusions, Porosity and Firing Temperature. *Thermochim. Acta* **2008**, *480*, 35–42. [CrossRef]
- Müller, N.S.; Kilikoglou, V.; Day, P.M.; Vekinis, G. The influence of temper shape on the mechanical properties of archaeological ceramics. *J. Eur. Ceram. Soc.* **2010**, *30*, 2457–2465. [CrossRef]

21. Müller, N.S.; Vekinis, G.; Day, P.M.; Kilikoglou, V. The influence of microstructure and texture on the mechanical properties of rock tempered archaeological ceramics. *J. Eur. Ceram. Soc.* **2015**, *35*, 831–843. [CrossRef]
22. Kilikoglou, V.; Vekinis, G.; Maniatis, Y.; Day, P.M. Mechanical Performance of Quartz Tempered Ceramics: Part I, Strength and Toughness. *Archaeometry* **1998**, *40*, 261–279. [CrossRef]
23. Müller, N.S. Mechanical and Thermal Properties. In *The Oxford Handbook of Archaeological Ceramic Analysis*; Hunt, A., Ed.; Oxford University Press: Oxford, UK, 2016; pp. 602–624.
24. Kilikoglou, V.; Vekinis, G. Failure Prediction and Function Determination of Archaeological Pottery by Finite Element Analysis. *J. Archaeol. Sci.* **2002**, *29*, 1317–1325. [CrossRef]
25. Hein, A.; Kilikoglou, V. Breaking Pots—Simulating design failures of transport amphorae by using the finite element method (FEM). In *Archaeological Research in the Digital Age. Proceedings of the 1st Conference on Computer Applications and Quantitative Methods in Archaeology Greek Chapter (CAA-GR), Rethymno, Greece, 6–8 March 2014*; Papadopoulos, C., Paliou, E., Chrysanthi, A., Kotoula, E., Sarris, A., Eds.; Institute for Mediterranean Studies—Foundation of Research and Technology (IMS-Forth): Rethymno, Greece, 2015; pp. 187–190.
26. Sillar, B.; Tite, M.S. The Challenge of ‘Technological Choices’ for Materials Science Approaches in Archaeology. *Archaeometry* **2000**, *42*, 2–20. [CrossRef]
27. Morreale, A. *Insula Dulcis: L’industria Della Canna da Zucchero in Sicilia*; Edizioni Scientifiche Italiane: Napoli, Italy, 2006; Volume 8.
28. Trasselli, C. *Storia Dello Zucchero Siciliano*; Sciascia ed.: Caltanissetta-Roma, Italy, 1982.
29. Bresc, H. *Un Monde Méditerranéen: Economie et Société en Sicile 1300–1450*; Accademia di Scienze, Lettere e Arti di Palermo ed.: Palermo, Italy, 1986.
30. Tullio, A. Strumenti per la lavorazione dello zucchero a Maredolce. *Archeol. Territ.* **1997**, 471–479.
31. Tullio, A. *L’indagine Archeologica (2000–2001)*; Complesso di Maredolce: Roma, Italy, 2002; pp. 661–667.
32. Tusa, V. Scavi medioevali a Palermo. *Sicil. Archeol.* **1973**, *23*, 57–61.
33. Falsone, G. Forme e cantarelli: I vasi per la raffinazione dello zucchero alla luce dei recenti rinvenimenti dello Steri. *Sicil. Archeol.* **1974**, *24–25*, 103–112.
34. Falsone, G. Gli scavi del 1973. Sequenza cronologica e culturale. In *Lo Steri dei Chiaromonte a Palermo*; Lima, M.I., Ed.; Plumelia ed.: Palermo, Italy, 2015; pp. 420–435.
35. Lo Cascio, P. Due trappeti della cannamela dell’area palermitana. *Sicil. Archeol.* **2002**, XXXV, 35–71.
36. Bonacasa, N. I Saggi di Scavo. In *Himera 2. Campagne di Scavo 1966–1973*; Allegro, N., Belvedere, O., Bonacasa, N., Bonacasa-Carra, R.M., Epifanio, E., di Stefano, C., Elda, A.J., Manni-Piraino, M.T., Schmiedt, G., Tullio, A., et al., Eds.; L’Erma di Bretschneider: Roma, Italy, 1976; pp. 627–664.
37. Vassallo, S. Scavi della Soprintendenza Beni Culturali di Palermo nella città bassa e nelle necropoli di Himera. *Kokalos* **2017**, LIV, 159–202.
38. D’Angelo, F. “Forme” da zucchero e ceramiche invetrate dipinte “tipo Polizzi” della fine XV–inizio XVI secolo rinvenute a Buonfornello (comune di Termini Imerese). *Not. Archeol. Soprintend. Palermo* **2021**, *130*, 115x28.
39. Montesana, R.B. Medieval sugar pots from Sicily: Archaeological, typological and morphometric data. *Repos. Dades Recer.* **2022**. [CrossRef]
40. Montana, G.; Caruso, A.; Lavore, A.T.; Polito, A.M.; Sulli, A. Definizione Compositiva Delle “Argille Ceramiche” Presenti Nella Sicilia Nord-Occidentale: Inquadramento Geologico E Ricadute Di Carattere Archeometrico. *Il Quat.* **2006**, *19*, 279–298.
41. Montana, G.; Polito, A.M.; Sulli, A. *Le «Argille Ceramiche» Sicilia Occidentale e Centrale*; IlionBooks: Enna, Italy, 2011.
42. Dunnell, R.C. Evolutionary theory and archaeology. *Adv. Archaeol. Method Theory* **1980**, *3*, 35–99.
43. Neff, H. Ceramics and evolution. In *Archaeological Method and Theory, 4*; Schiffer, M.B., Ed.; University of Arizona Press: Tucson, AZ, USA, 1992; pp. 141–193.
44. Neff, H. Theory, sampling, and technical studies in archaeological pottery analysis. *Am. Antiq.* **1993**, *58*, 23–44. [CrossRef]
45. O’Brien, M.J.; Holland, T.D.; Hoard, R.J.; Fox, G.L. Evolutionary implications of design and performance characteristics of prehistoric pottery. *J. Archaeol. Method Theory* **1994**, *1*, 259–304. [CrossRef]
46. Leonard, R.D. Evolutionary Archaeology. In *Archaeological Theory Today*; Hodder, I., Ed.; Blackwell Publishers: Oxford, UK, 2001; pp. 65–97.
47. Hodder, I. *Entangled: An Archaeology of the Relationships between Humans and Things*; John Wiley and Sons: Hoboken, NJ, USA, 2012.
48. Steponaitis, V.P. Technological studies of prehistoric pottery from Alabama: Physical properties and vessel function. In *The Many Dimensions of Pottery*; van der Leeuw, S.E., Pritchard, A.C., Eds.; University of Amsterdam: Amsterdam, The Netherlands, 1984; pp. 79–127.
49. Bronitsky, G.; Hamer, R. Experiments in Ceramic Technology: The Effects of Various Tempering Materials on Impact and Thermal-Shock Resistance. *Am. Antiq.* **1986**, *51*, 89–101. [CrossRef]
50. Manem, S. Modeling the Evolution of Ceramic Traditions through a Phylogenetic Analysis of the Chaînes Opératoires: The European Bronze Age as a Case Study. *J. Archaeol. Method Theory* **2020**, *27*, 992–1039. [CrossRef]
51. Buxeda i Garrigós, J.; Madrid i Fernández, M.M. Designing Rigorous Research: Integrating Science and Archaeology. In *The Oxford Handbook of Archaeological Ceramic Analysis*; Hunt, A.M.W., Ed.; Oxford University Press: Oxford, UK, 2016; pp. 19–47.
52. Lemonnier, P. Introduction. In *Technological Choices: Transformations in Material Cultures Since the Neolithic*; Lemonnier, P., Ed.; Routledge: London, UK, 1993; pp. 1–35.

53. Jones, A. *Archaeological Theory and Scientific Practice*; Cambridge University Press: Cambridge, UK, 2004.
54. Day, P.M. Technology and Ethnography in Petrographic Studies of Ceramics. In *Archaeometry: Proceedings of the 25th International Symposium (Athens, Greece 1986)*; Maniatis, Y., Ed.; Elsevier: Amsterdam, The Netherlands, 1989; pp. 138–147.
55. Hilditch, J. Reconstruction of Technological Choice, Social Practice and Networks of Exchange from a Ceramic Perspective in the Middle Bronze Age Cyclades. Ph.D. Thesis, University of Exeter, Exeter, UK, 2008.
56. Mentasana, R. The Final Neolithic-Early Bronze Age Transition in Phaistos, Crete: An Investigation of the Continuity and Change in Pottery Manufacture. Ph.D. Thesis, University of Sheffield, Sheffield, UK, 2016. Available online: <https://etheses.whiterose.ac.uk/15354/> (accessed on 1 February 2022).
57. Cresswell, R. Transferts de techniques et chaînes opératoires. *Tech. Cult.* **1983**, *2*, 143–163. [CrossRef]
58. Roux, V. Anthropological interpretation of ceramic assemblages: Foundations and implementations of technological analysis. In *Archaeological Ceramics: A Review of Current Research*; Scarcella, S., Ed.; BAR International Series 2193; Archaeopress: Oxford, UK, 2011; pp. 80–88.
59. Bourdieu, P. *Outline of a Theory of Practice*; Cambridge University Press: Cambridge, UK, 1977.
60. Bourdieu, P. *Distinction: A Social Critique of the Judgment of Taste*; Harvard University Press: Harvard, MA, USA, 1984.
61. Lave, J.; Wenger, E. *Situated Learning: Legitimate Peripheral Participation*; Cambridge University Press: Cambridge, UK, 1991.
62. Wenger, E. *Communities of Practice: Learning, Meaning and Identity*; Cambridge University Press: Cambridge, UK, 1998.
63. Roux, V. *Des Céramiques et des Hommes: Décoder les Assemblages Archéologiques*; Presses Universitaires de Paris Ouest: Paris, France, 2016.
64. Maggetti, M. Phase Analysis and Its Significance for Technology and Origin. In *Archaeological Ceramics*; Olin, J.S., Franklin, A.D., Eds.; Smithsonian Institution Press: Washington, WA, USA, 1982; pp. 121–133.
65. Tite, M.S.; Freestone, I.C.; Meeks, N.D.; Bimson, M. The use of scanning electron microscopy in the technological examination of ancient ceramics. In *Archaeological Ceramics*; Olin, J.S., Franklin, A.D., Eds.; Smithsonian Institution Press: Washington, WA, USA, 1982; pp. 109–120.
66. Madrid i Fernández, M.; Sinner, A.G. Analysing technical choices: Improving the archaeological classification of Late Republican Black Gloss pottery in north-eastern Hispania consumption centres. *Archaeol. Anthropol. Sci.* **2019**, *11*, 3155–3186. [CrossRef]
67. Buxeda i Garrigós, J. Alteration and Contamination of Archaeological Ceramics: The Perturbation Problem. *J. Archaeol. Sci.* **1999**, *26*, 295–313. [CrossRef]
68. Whitbread, I.K. A Proposal for the Systematic Description of Thin Sections towards the Study of the Ancient Ceramic Technology. In *Archaeometry: Proceedings of the 25th International Symposium (Athens, Greece 1986)*; Maniatis, Y., Ed.; Elsevier: Amsterdam, The Netherlands, 1989; pp. 127–138.
69. Whitbread, I.K. Appendix III. In *Greek Transport Amphorae: A Petrological and Archaeological Study*; Whitbread, I.K., Ed.; British School at Athens: London, UK, 1995.
70. Whitbread, I.K. Fabric Description of Archaeological Ceramics. In *the Oxford Handbook of Archaeological Ceramic Analysis*; Hunt, A., Ed.; Oxford University Press: Oxford, UK, 2016; pp. 199–216.
71. Log, T.; Gustafsson, S.E. Transient plane source (TPS) technique for measuring thermal transport properties of building materials. *Fire Mater.* **1995**, *19*, 43–49. [CrossRef]
72. Shetty, D.K.; Rosenfield, A.R.; Duckworth, W.H.; Held, P.R. A Biaxial Flexure Test for Evaluating Ceramic Strengths. *J. Am. Ceram. Soc.* **1983**, *66*, 36–42. [CrossRef]
73. Shetty, D.K.; Rosenfield, A.R.; McGuire, P.; Bansal, G.K.; Duckworth, W.H. Biaxial Flexure Tests for Ceramics. *Am. Ceram. Soc. Bull.* **1980**, *59*, 1193–1197.
74. Morrell, R. *Biaxial Flexural Strength Testing of Ceramic Materials, Measurement Good Practice Guide No. 12.*; Middlesex: National Physical Laboratory: Teddington, UK, 1998.
75. Catalano, R.; Basilone, L.; Di Maggio, C.; Gasparo Morticelli, M.; Agate, M.; Avellone, G. *Note Illustrative Della Carta Geologica D'Italia alla Scala 1:50.000, Foglio 594–585*; Partinico–Mondello: Ispra, Italy, 2013.
76. Cau Ontiveros, M.A.; Day, P.M.; Montana, G. Secondary calcite in archaeological ceramics: Evaluation of alteration and contamination processes by thin section study. In *Modern Trends in Scientific Studies on Ancient Ceramics. Papers presented at the 5th European Meeting on Ancient Ceramics, Athens 1999*; Kilikoglou, V., Hein, A., Maniatis, Y., Eds.; BAR International Series: 1011; Archaeopress: Oxford, UK, 2002; pp. 9–18.
77. Polizzi, G.; Ducati, F. Fornaci e produzioni del Golfo di Castellammare (Sicilia nord-occidentale), *Mélanges de l'École française de Rome. Antiq. Open Ed.* **2020**, *132*, 403–428. [CrossRef]
78. Mentasana, R.B.; Buxeda i Garrigós, J.; Madrid i Fernández, M. Medieval sugar pots from Sicily: Chemical data. *Repos. Dades Recer.* **2022**. [CrossRef]
79. Egozcue, J.J.; Pawlowsky-Glahn, V. Basic concepts and procedures. In *Compositional Data Analysis*; Pawlowsky-Glahn, V., Buccianti, A., Eds.; Theory and Applications; Wiley: Chichester, UK, 2011; pp. 12–28.
80. Martín-Fernández, J.A.; Buxeda i Garrigós, J.; Pawlowsky-Glahn, V. Logratio Analysis in Archaeometry: Principles and Methods. In *Mathematics and Archaeology*; Barceló, J.A., Bogdanovic, I., Eds.; CRC Press: Boca Raton, FL, USA, 2015; pp. 178–189.
81. Buxeda i Garrigós, J. Compositional Data Analysis. In *The Encyclopedia of Archaeological Sciences*; Varela, S.L.L., Ed.; John Wiley & Sons: Oxford, UK, 2018; pp. 1–5.

82. R Core Team. *R: A Language and Environment for Statistical Computing*; R Foundation for Statistical Computing: Vienna, Austria, 2021. Available online: <http://www.R-project.org/> (accessed on 1 February 2022).
83. Aitchison, J. *The Statistical Analysis of Compositional Data*; Monographs on Statistics and Applied Probability; Chapman and Hall: London, UK, 1986.
84. Buxeda i Garrigós, J.; Kilikoglou, V. Total variation as a measure of variability in chemical data sets. In *Patterns and Process: A Festschrift in Honor of Dr. Edward V. Sayre*. van Zelst, L., Ed.; Smithsonian Center for Materials Research and Education: Washington, DC, USA, 2003; pp. 185–198.
85. Shannon, C.E. A mathematical theory of communication. *Bell Syst. Tech. J.* **1948**, *27*, 379–423. [CrossRef]
86. Aitchison, J.; Greenacre, M. Biplots of compositional data, applied statistics. *J. R. Stat. Soc. Ser. C* **2002**, *51*, 375–392. [CrossRef]
87. Greenacre, M. *Biplots in Practice, BBVA Foundation Manuals*; Fundación BBVA: Bilbao, Spain, 2010.
88. van de Boogaart, K.G.; Tolosana-Delgado, R. *Analysing Compositional Data with R*; Springer: Berlin/Heidelberg, Germany, 2013.
89. i Garrigós, J.B.; Fernández, M.M.; Gurt i Esaparraguera, J.M. Provenença i Tecnologia de les Ceràmiques de “Pisa” i d’Obra de Manises” del Dipòsit de la Plaça Gran de Mataró. In *La Ceràmica Catalana del Segle XVII Trobada a la Plaça Gran (Mataró)*; Mellado, J.A.C.i., Ed.; Associació Catalana de Ceràmica Decorada i Terrissa: Barcelona, Spain, 2001; pp. 155–170.
90. Iñañez, J.G. Caracterització Arqueomètrica de la Ceràmica Vidrada Decorada de la Baixa Edat Mitjana al Renaixement dels Principals Centres Productors de la Península Ibèrica. Ph.D. Thesis, Universitat de Barcelona, Barcelona, Spain, 2007. Available online: <http://hdl.handle.net/10803/2596> (accessed on 1 February 2022).
91. Montesana, R.B. Medieval sugar pots from Sicily: Petrographic photomicrographs. *Repos. Dades Recer.* **2022**. [CrossRef]
92. Heimann, R.B.; Maggetti, M. *Ancient and Historical Ceramics. Materials, Technology, Art, and Culinary Traditions*; Schweizerbart Science Publishers: Stuttgart, Germany, 2014.
93. Maniatis, Y.; Tite, M.S. Technological examination of Neolithic- Bronze Age pottery from Central and Southeast Europe and from the Near East. *J. Archaeol. Sci.* **1981**, *8*, 59–76. [CrossRef]
94. Montesana, R.B.; Buxeda i Garrigós, J.; Madrid i Fernández, M. Medieval sugar pots from Sicily: Mineralogical data. *Repos. Dades Recer.* **2022**. [CrossRef]
95. Montesana, R.B.; Buxeda i Garrigós, J.; Madrid i Fernández, M. Medieval sugar pots from Sicily: Microstructural data. *Repos. Dades Recer.* **2022**. [CrossRef]
96. Whitney, D.L.; Evans, B.W. Abbreviations for names of rock-forming minerals. *Am. Mineral.* **2010**, *95*, 185–187. [CrossRef]
97. Lemoine, C.; Poupet, P.; Barrandon, J.N.; Borderie, B.; Meille, E. Étude de quelques altérations de composition chimique des céramiques en milieu marin et terrestre. *Rev. D’Archéométrie* **1981**, *1*, 349–360. [CrossRef]
98. Maritan, L. Ceramic abandonment. How to recognise post-depositional transformations. *Archaeol. Anthropol. Sci.* **2020**, *12*, 199. [CrossRef]
99. Béarat, H.; Dufournier, D.; Nouet, Y. Alterations of ceramics due to contact with seawater. *Archaeol. Pol.* **1992**, *30*, 151–162.
100. Amadori, M.L.; Baldassari, R.; Lanza, S.; Maione, M.; Penna, A.; Acquaro, E. Archaeometric study of Punic amphorae from the underwater recoveries of Pantelleria Island (Sicily). *Rev. Archéométrie* **2002**, *26*, 79–91. [CrossRef]
101. Buxeda i Garrigós, J.; Madrid i Fernández, M. Sobre un Individu de Ceràmica Grisà Monocroma del Derelict de Cala Sant Vicenç i la Seva Contrastació Amb la Producció de la Palaia Polis D’Empúries: La Seva Caracterització Arqueomètrica. In *El Vaixell Grec Arcac de Cala Sant Vicenç*; Nieto, X., Santos, M., Eds.; Monografies del CASC, 7; Museu d’Arqueologia de Catalunya-Barcelona/Centre de Cultura Contemporània de Barcelona: Barcelona, Spain, 2008; pp. 347–354.
102. Buxeda i Garrigós, J.; Tsantini, E. Les Àmfores Ibèriques del Derelict de Cala Sant Vicenç i la Seva Contrastació Amb les Àmfores de la Palaia Polis d’Empúries. Evidències des de la Seva Caracterització Arqueomètrica. In *El Vaixell Grec Arcaic de Cala*; de Cala, E.V.F., Vicenç, S., Nieto, X., Santos, M., Eds.; Monografies del CASC 7; Museu d’Arqueologia de Catalunya-Barcelona/Centre de Cultura Contemporània de Barcelona: Barcelona, Spain, 2008; pp. 373–395.
103. Buxeda i Garrigós, J.; Cau Ontiveros, M.A.; Madrid, M.; Toniolo, A. Roman Amphorae from the Iulia Felix Shipwreck: Alteration and Provenance. In *Proceedings of the 33rd International Symposium on Archaeometry, Amsterdam, The Netherlands, 22–26 April 2002*; Hars, H., Burke, E., Eds.; Institute for Geo-and Bioarchaeology of the Vrije Universiteit in Amsterdam: Amsterdam, The Netherlands, 2005; pp. 149–151.
104. Buxeda i Garrigós, J.; Ferreras, V.M.; Socias, L.V. Caracterització arqueomètrica de les àmfores Pascual 1 del derelict Culip VIII. In *Culip VIII i les àmfores Haltern 70*; Carreras, C., Aguilera, A., Berni, P., Garrote, E., Marimón, P., Morais, R., Moros, J., Nieto, X., Puig, A., Remesal, J., et al., Eds.; Monografies del CASC 5: Girona, Spain, 2005; pp. 167–188.
105. Pradell, T.; Vendrell-Saz, M.; Krumbein, W.; Picon, M. Altérations de céramiques en milieu marin: Les amphores de l’épave romaine de la Madrague de Giens (Var). *Rev. Archéométrie* **1996**, *20*, 47–56. [CrossRef]
106. Hein, A.; Montesana, R.B.; Kilikoglou, V. Medieval sugar pots from Sicily: Mechanical and thermal properties test data. *Repos. Dades Recer.* **2022**. [CrossRef]
107. Hein, A.; Day, P.M.; Quinn, P.S.; Kilikoglou, V. The geochemical diversity of Neogene clay deposits in Crete and its implications for provenance studies of Minoan pottery. *Archaeometry* **2004**, *46*, 357–384. [CrossRef]
108. Canzonieri, E.; Vassallo, S. Insemediamenti Extraurbani A Palermo: Nuovi Dati Da Maredolce. In *Les Dynamiques de L’islamisation en Méditerranée Centrale et en Sicile: Nouvelles Propositions et Découvertes Récentes*; Nef, A., Ardizzone, F., Eds.; Edipuglia: Roma-Bari, Italy, 2014; pp. 271–277.

109. Matson, F.R. The study of temperatures used in firing ancient Mesopotamian pottery. In *Science and Archaeology*; Brill, R., Ed.; The Massachusetts Institute of Technology Press: Cambridge, MA, USA, 1971; pp. 65–79.
110. Testolini, V. Ceramic Technology and Cultural Change in Sicily from the 6th to the 11th Century AD. Ph.D. Thesis, University of Sheffield, Sheffield, UK, 2018.
111. Rye, O.S. Pottery Technology. In *Principles and Reconstruction*; Taraxacum: Washington, DC, USA, 1981.
112. Alaimo, R.; Giarrusso, R.; Montana, G.G. Indagini mineralogiche e petrografiche su materiale ceramico proveniente dal palazzo medievale della Zisa. *Mélanges L'école Française Rome Moyen-Âge* **1999**, *111*, 45–50.
113. Giarrusso, R.; Mulone, A. L'analisi dei Materiali. In *Les bains de Cefalà (Cefalà Diana, prov. de Palerme): La Campagne de Fouilles de Septiembere 2006*; Bagnera, A., di Liberto, R., Nef, A., Pezzini, E., Eds.; Mélanges de L'école Française de Rome; Edipuglia: Roma-Bari, Italy, 2007; pp. 493–517.
114. Giarrusso, R.; Mulone, A. Caratterizzazione Mineralogico-Petrografica di Campioni Ceramici Provenienti da Castello-S. Pietro, Dalla Chiesa Della Gancia (Palermo) e da Castello Della Pietra (Castelvetrano). In *Les Dynamiques de L'islamisation en Méditerranée Centrale et en Sicile*; Nef, A., Ardizzone, F., Eds.; Collection de L'école Française de Rome; Edipuglia: Roma-Bari, Italy, 2014; pp. 191–195.
115. Gioia, C.; D'Angelo, F. Analisi minero-petrografiche sui reperti dello scarico di fornaci di Palazzo Lungarini a Palermo (fine XI-inizio XII secolo). *Archeol. Mediev.* **2007**, *34*, 337–343.
116. Alaimo, R.; Giarrusso, R. Indagini Mineralogiche Petrografiche su Materiale Ceramico Medievale Rinvenuto a Palermo in Via Torremuzza. In *La Ceramica Altomedievale in Italia. Atti del V Congresso di Archeologia Medievale, Roma, 2001*; Uggeri, S.P., Ed.; All'Insegna del Giglio: Firenze, Italy, 2004; pp. 372–374.
117. D'Angelo, F. Influenze Straniere Nella Ceramica Medievale di Palermo. In *Atti del VI Convegno Internazionale della Ceramica; Centro Ligure per la Storia Della Ceramica: Albisola, Italy, 1976*; pp. 107–116.
118. D'Angelo, F. Maestranze e processi produttivi nei quartieri della Palermo Medievale (Sec. XI–XIV). *Not. Archeol. Soprintend. Palermo* **2016**, *10*, 1–12.
119. Battaglia, G.; Canzonieri, E. Fornaci e Scarichi di età Islamica alla Stazione Centrale e Presso Porta Sant'Agata (Palermo). In *La Città che Produce: Archeologia della Produzione Negli Spazi Urbani: Atti delle Giornate Gregoriane, X Edizione (10–11 December 2016)*; Caminacci, V., Parello, M.C., Rizzo, M.S., Eds.; Edipuglia: Bari, Italy, 2018; pp. 215–222.
120. Pezzini, E. Questioni sulle produzioni ceramiche palermitane tra fine XII e XIV secolo: Un confronto tra fonti scritte e dato ceramico. *Arch. Stor. Per La Sicil. Orient. IV* **2020**, *1*, 28–37. [CrossRef]
121. Termotto, R. Una industria zuccheriera del Cinquecento: Galbinogara. *Mediterr. Ric. Stor.* **2005**, *3*, 45–74.
122. Termotto, R. Contratti di lavoro e migrazioni stagionali nell'industria zuccheriera siciliana. *Mediterr. Ric. Stor.* **2012**, *25*, 253–284.
123. Alaimo, R.; Giarrusso, R.; Iliopoulos, I.; Montana, G. Coppe Tipo Iato K480: Indagini Archeometriche Finalizzate Alla Individuazione del Centro di Produzione. In *Atti del Io Congresso Nazionale di Archeometria*; Martini, M., D'Amico, C., Fassani, L., Garagnani, G.L., Improta, S., Milazzo, M., Sabbioni, F.P.C., Eds.; Verona, Dicembre 1999; Pàtron Editore: Bologna, Italy, 2000; pp. 413–425.
124. Montana, G.; Randazzo, L.; Bechtold, B. The Beginning of Western Greek Amphorae Production in Western Sicily: Archaeometric and Archaeological Studies on 6th–5th Centuries BCE Amphorae Manufactured in Himera. *Minerals* **2020**, *10*, 762. [CrossRef]
125. D'Angelo, F.; Gioia, C.; Reginella, M. La Ceramica Ingobbata, Invetriata e Dipinta del XV Secolo di Polizzi (PA). In *Atti del XLIV Convegno Internazionale della Ceramica; Centro Ligure per la Storia della Ceramica: Albisola, Italy, 2012*; pp. 313–323.

## Article

# Archaeometric Study on Roman Painted Terracottas from the Sanctuary of Hercules in Alba Fucens (Abruzzo, Italy)

Gilda Russo<sup>1</sup>, Emanuela Ceccaroni<sup>2</sup>, Aida Maria Conte<sup>3</sup>, Laura Medeghini<sup>3,4</sup>, Caterina De Vito<sup>3,4</sup> and Silvano Mignardi<sup>3,4,\*</sup>

- <sup>1</sup> Science and Technology for the Conservation of Cultural Heritage, Faculty of Mathematical, Physical and Natural Sciences, Sapienza University of Rome, Piazzale Aldo Moro 5, 00185 Rome, Italy; russo.1674343@studenti.uniroma1.it
  - <sup>2</sup> Soprintendenza Archeologia, Belle Arti e Paesaggio per le Province di Chieti e Pescara, Via degli Agostiniani 14, 66100 Chieti, Italy; emanuela.ceccaroni@beniculturali.it
  - <sup>3</sup> Department of Earth Sciences, CNR—Istituto di Geologia Ambientale e Geoingegneria, Sapienza University of Rome, Piazzale Aldo Moro 5, 00185 Rome, Italy; aidamaria.conte@igag.cnr.it (A.M.C.); laura.medeghini@uniroma1.it (L.M.); caterina.devito@uniroma1.it (C.D.V.)
  - <sup>4</sup> Department of Earth Sciences, Faculty of Mathematical, Physical and Natural Sciences, Sapienza University of Rome, Piazzale Aldo Moro 5, 00185 Rome, Italy
- \* Correspondence: silvano.mignardi@uniroma1.it; Tel.: +36-0649914155

**Abstract:** In a period spanning from the 7th to the 1st century BC, the exterior surfaces of civil and sacred buildings in Italy were mainly decorated with terracottas. The aim of this study is to determine the skills and technological level reached by ancient manufacturers of painted ceramics from the sanctuary of Hercules in the archaeological site of Alba Fucens (Abruzzo, Central Italy). A multi-analytical approach including X-ray Powder Diffraction (XRPD),  $\mu$ -Raman and portable X-ray fluorescence (pXRF) was applied to determine the mineralogical composition of terracotta samples and to identify the pigments decorating the ceramics. The studied terracottas were decorated using valuable pigments such as Egyptian blue as well as a palette of colors common in the Roman period from the 3rd to the 1st century BC. The mineralogical composition of the ceramics allows estimating a firing temperature lower than 800 °C. Finally, a local origin of raw materials is suggested by the presence of alluvial and lake deposits outcropping in the Fucino area.

**Keywords:** architectural terracottas; production technology; archaeometry; Alba Fucens

**Citation:** Russo, G.; Ceccaroni, E.; Conte, A.M.; Medeghini, L.; De Vito, C.; Mignardi, S. Archaeometric Study on Roman Painted Terracottas from the Sanctuary of Hercules in Alba Fucens (Abruzzo, Italy). *Minerals* **2022**, *12*, 346. <https://doi.org/10.3390/min12030346>

Academic Editors: Daniel Albero Santacreu, José Cristóbal Carvajal López and Adrián Durán Benito

Received: 14 February 2022

Accepted: 9 March 2022

Published: 11 March 2022

**Publisher's Note:** MDPI stays neutral with regard to jurisdictional claims in published maps and institutional affiliations.



**Copyright:** © 2022 by the authors. Licensee MDPI, Basel, Switzerland. This article is an open access article distributed under the terms and conditions of the Creative Commons Attribution (CC BY) license (<https://creativecommons.org/licenses/by/4.0/>).

## 1. Introduction

Ceramic artifacts are particularly common in archaeological sites as they are generally resistant to alteration and weathering. Therefore, archaeometric analysis on ancient ceramics can provide significant data for reconstructing the cultural and technological development of the context in which they were produced [1–3].

Ancient ceramics had different functions: cult objects, decorations, vessels, refractory materials, and building materials [4,5].

Between the Archaic and the Late Republican period (7th–1st century BC) in Italy, terracotta (or fired clay) was the main material used for decorating the exterior surfaces of civic and sacred buildings. Painted revetment plaques in terracotta were nailed to facades in stone or wood, and the material was also used to cover ceiling beams or columns. On roofs, terracotta was used for tiles, *antepagmentum*, *antefixes*, and *simas*, which often carried lavish figural schemes too. In preparation for painting, but also as a protection against weathering, the upper surfaces of architectural terracottas were usually refined with a fine slip of diluted clay. After air-drying, clay-based colors (essentially colored slips) were applied to the visible surface with brushes. Some pieces also show a thin white slip of clay minerals as a primer for the color layers. After the final firing, the surfaces could be

further refined with pigments, dyes, and gold leaf attached with an organic binder. The Italic tradition of using terracotta as a surface material was particularly strong, and it only decreased during the late 1st century BC, when *stucco* and marble became predominant [6].

In this perspective, the present work is the first archaeometric study aimed at reconstructing the technological knowledge reached by the ancient manufacturers of painted ceramic materials (3rd–2nd century BC) collected from the sanctuary of Hercules in the Latin colony of Alba Fucens (Abruzzo, Central Italy) [7].

The terracottas belong to different phases of the architectural decoration of the sanctuary. The main interest behind this research is the absence of previous archaeometric studies on these ceramics characterized by extraordinary craftsmanship. Moreover, such materials are not easily found in archaeological contexts and for this reason their characterization could significantly contribute to reconstruction of the skills and material knowledge of ancient artisans.

The goal of this study was achieved by means of a multi-analytical approach including X-ray Powder Diffraction (XRPD) analysis to investigate the mineralogical composition of terracotta samples and the combination of  $\mu$ -Raman and portable X-ray fluorescence (pXRF) analysis for the identification of the pigments decorating the ceramics.

## 2. Archaeological Context

The archaeological area of Alba Fucens, located in the current municipality of Massa d'Albe (Abruzzo, Central Italy), a few kilometers north of the city of Avezzano, preserves the remains of the Latin colony founded by Romans at the end of the 4th century BC [6].

The toponym Alba comes from the Indo-European root and means “high ground”, while the adjective Fucens is linked to the name of the ancient Fucino lake (in Latin Fūcinus), at that time the third largest lake in Italy. The first work of reclamation of the lake was carried out by the Emperor Claudius (41–52 AD) and the final drainage occurred in the second half of the 19th century [6].

The central area of the city is occupied by a series of public buildings: the Basilica, the *macellum* (market) with *tabernae*, the baths, and the sanctuary of Hercules. Other preserved public buildings are the theater and the amphitheater, while the church of St. Peter was built on the temple of Apollo [7]. The abandonment of the city was gradual and due to several causes. First of all, the violent earthquake that occurred between 484 and 508 AD [8] followed by floods and colluviums of the plain, along with the decadence of the Roman Empire.

Since 2006, the Soprintendenza for Archaeological Heritage of Abruzzo carried out some excavations in the square of the Sanctuary of Hercules. The excavations brought to light hundreds of fragments of painted terracotta (3rd–2nd century BC), which had been used as filling material below the pavement slabs [9]. In 2011, the excavations brought to light a large well (1st century BC) where numerous fragments of terracotta have been found [9,10]. Four different types of antefixes were identified: (a) with satyr's head, (b) with head of *maenad*, (c) with *potnia* (Mediterranean goddess that feeds all beings that inhabit the Earth), and (d) with winged victory.

Besides the antefixes, different types of *antepagmentum* and *sime* have been brought to light. Although these terracottas are attributable to the presence of a building, no structures have been identified to date referable to it, traced back to the “Etruscan-Italic” model and suggested by the remains of the ceramics found [9,10].

## 3. Geological Context

Alba Fucens was founded on a hill of pre-Pliocene carbonate rocks, Plio-Pleistocene clayey-sandy deposits and carbonate breccias, overlooking the ancient Fucino lake [7]. This is the largest intramontane basin (20 × 15 km) of the Apennines chain, a fold-and-thrust belt developed during the Alpine orogeny [11]. The Fucino Basin is surrounded by mountains comprising Triassic-middle Miocene carbonate platform, slope, and ramp sequences. The



Plio-Pleistocene and Holocene alluvial fan and lacustrine deposits of the ancient Fucino lake largely cover the carbonate sequences [11].

The sanctuary of Hercules is located on Pliocene colluvial sediments, above which a thick soil evolved during the Holocene. Peaty levels were found beneath the lake sediments, evidence of stagnant water and the presence of a marshy environment. On the top of the marsh sediments a thin pedogenetic layer is identified, connected to the reclamation of the area before the urbanization. To obtain the floor of the Roman city, it was necessary to fill the lake depression with a considerable thickness of yellow silt-clay and large limestone blocks. The origin of these limestone blocks could be linked to the works at the base of the western flank of the eastern hill (Pettorino) for the building of the theater.

#### 4. Materials and Methods

Thirteen samples (A, 2, C, 4, E, F, G, H, I, L, M, N, O) were selected from different types of architectural elements (slabs, antefixes, and frames), based on macroscopic analysis of the color of the matrix, the abundance and nature of inclusions of terracotta, and decorative pigments.

All these samples were recovered from the large well, except the sample M (Figure 1) that comes from the square of the Sanctuary.



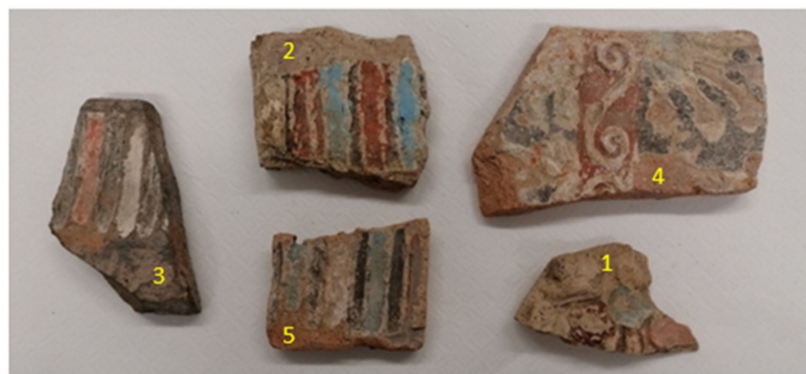
**Figure 1.** The 13 samples analyzed by XRPD (front and back). Labels (A–O) indicate the studied samples.

The pigments decorating the terracotta of five selected samples (1, 2, 3, 4, 5) were analyzed by pXRF and  $\mu$ -Raman (Figure 2).

The sample 1 comes from the square of the Sanctuary while the remaining ones from the well.

The samples were analyzed by a multi-analytical approach, including portable X-ray fluorescence (pXRF), X-ray powder diffraction (XRPD), and  $\mu$ -Raman spectroscopy.





**Figure 2.** The five samples analyzed by  $\mu$ -Raman and pXRF. Labels 1–5 refer to the studied samples.

For pXRF analysis, a portable X123 Amptek Inc. tool was used to analyze the back and the painted side of the samples. It consists of a cooled thermoelectric detector with an area of 6–25 mm<sup>2</sup>, resolution between 139 and 260 eV, and FWHM at 5.9 keV, a PC for signal processing, a pulse generator, and an X-ray source Moxtek 10–50 kV Bullet. The spectra were processed with the Winaxil 4.0.1 software. Spectra were normalized, making the ratio of the relative counts of each peak compared to the total counts. pXRF has a small stage, that can scan areas up to 20 × 20 cm<sup>2</sup> with a lateral resolution of 1 mm. The focus between the scanning head and sample was set manually with the aid of a laser triangulation system. Spot size was dictated by the X-ray focusing optics chosen (collimator). At about 1 cm from the sample's surface, it was roughly 2 mm diameter for both tubes.

$\mu$ -Raman measurements were performed with a RenishawInVia Raman spectrometer equipped with a 532 nm laser (used for all pigments except pink) and one UV at 355 nm (used for pink pigment) (ICT Laboratory, LFoundry, Avezzano). The instrument uses two gratings, one at 1800 rows/mm (green) and one at 2400 rows/mm (UV). Wtics used were 50× for green and a special NUV 40× lens for UV. The baseline and the background noise were subtracted by the WirETM Software available in Ranishaw Raman instrument [12].

pXRF data (Tables S1 and S2) were easily visualized through principal component analysis (PCA), a multivariate technique that summarizes the information of a dataset by means of a smaller set of “summary indices” emphasizing the differences among data [13]. The intensity of pXRF peaks (X) and the number of samples (N) were arranged in a matrix (N, X). The PCA aims to compress the original hyperspace into a new principal component (PC) space of reduced dimensionality, while retaining as much of the data variation as possible. In general, the PC space contains a total of 2 or 3 principal axes (called score plot) to be easily visualized. A second plot called loadings plot is reported too. The loadings express the magnitude (large or small correlation) and manner (positive or negative correlation) in which the original variables contribute to the scores or PC. In such a plot, high positive correlations are indicated by small angles between vectors, no correlation is indicated by right angles and inverse correlations are indicated by angles close to 180. PCA, ternary diagram, and scatter plot were carried out using algorithms in the JMP Pro software package from SAS Institute [14].

Finally, a fragment of terracotta from the back of each sample was collected and analyzed by XRPD to determine the mineralogical composition, to estimate firing temperatures, and to infer the provenance of the raw materials. A small part of the sample (about 5–10 mg) was ground with agate mortar and pestle. The ceramic powder was then analyzed using a Bruker D8 focus diffractometer (Department of Earth Sciences, Sapienza University of Rome, Italy) with Cu K $\alpha$  radiation, operating at 40 kV and 30 mA. The following instrumental set-up was chosen: 3–60° 2 $\theta$  range, scan step of 0.02° 2 $\theta$ /2s. Semiquantitative analysis based on the “Reference Intensity Ration Method” was performed using X PowderX© software. The International Centre for Diffraction Data Powder Diffraction Files (ICDD-PDF) were used for the identification of the mineral phases by XRPD.

## 5. Results

### 5.1. Ceramic Body

For the ceramic body analysis, XRPD,  $\mu$ -Raman, and XRF were applied. The last two, the main purpose of which was the pigment analysis, were applied on the ceramic body to better identify the pigment's spectra peaks.

#### 5.1.1. XRPD Analysis

The XRPD analysis allowed the identification of the minerals that compose the ceramic body. All samples reported in the Table 1 showed a high content of quartz and the common presence of plagioclase. Only some samples showed the presence of calcite, augitic clinopyroxene, and illitic clay, while muscovite is present only in sample A.

**Table 1.** Semiquantitative summary of the mineralogical phases present in the terracotta. Legend: XXX = abundant (100–50 wt%); XX = common (50–30 wt%); X = scarce (30–5 wt%). (Qtz: quartz; Cal: calcite; Plg: plagioclase; Cpx: augite; Ill: illite, Ms: muscovite).

Sample	Qtz	Cal	Plg	Cpx	Ill	Ms
A	xxx	xx	x	x		x
2	xxx	xxx	x	x	x	
C	xxx	xx	x	x	x	
4	xxx	x	xx	x	x	
E	xxx		xx		x	
F	xxx	xx	x	xx	xx	
G	xxx	xx	xx	x	x	
H	xxx		x	xx	x	
I	xxx	x	x	x	x	
L	xxx	xx	x	x		
M	xxx	xx	x	x	xx	
N	xxx	x	x	x	x	
O	xxx	xx	x	x	x	

#### 5.1.2. $\mu$ -Raman Analysis

The ceramic body of sample 5 was analyzed to investigate the composition of architectural terracottas on which the pigments were applied. The spectrum (Figure 3g) shows the peaks of quartz ( $\text{SiO}_2$ ) and calcite ( $\text{CaCO}_3$ ). Specifically, quartz was identified thanks to the peak around  $470\text{ cm}^{-1}$  due to the symmetric bending vibration of Si-O-Si [15], and calcite because of the peaks at  $290$  and  $1100\text{ cm}^{-1}$  connected to the symmetric stretching of the carbonate group [16].

#### 5.1.3. pXRF Analysis

The pXRF analyses of the matrices of the samples 1, 2, 3, 4, and 5 show high intensity lines, related to Fe ( $E = 6.40\text{ keV}$  and  $E = 7.06\text{ keV}$ ) and Ca ( $E = 3.69\text{ keV}$  and  $E = 4.01\text{ keV}$ ) [17], while Mn, Ti, and Sr are only present in traces (Table S1).

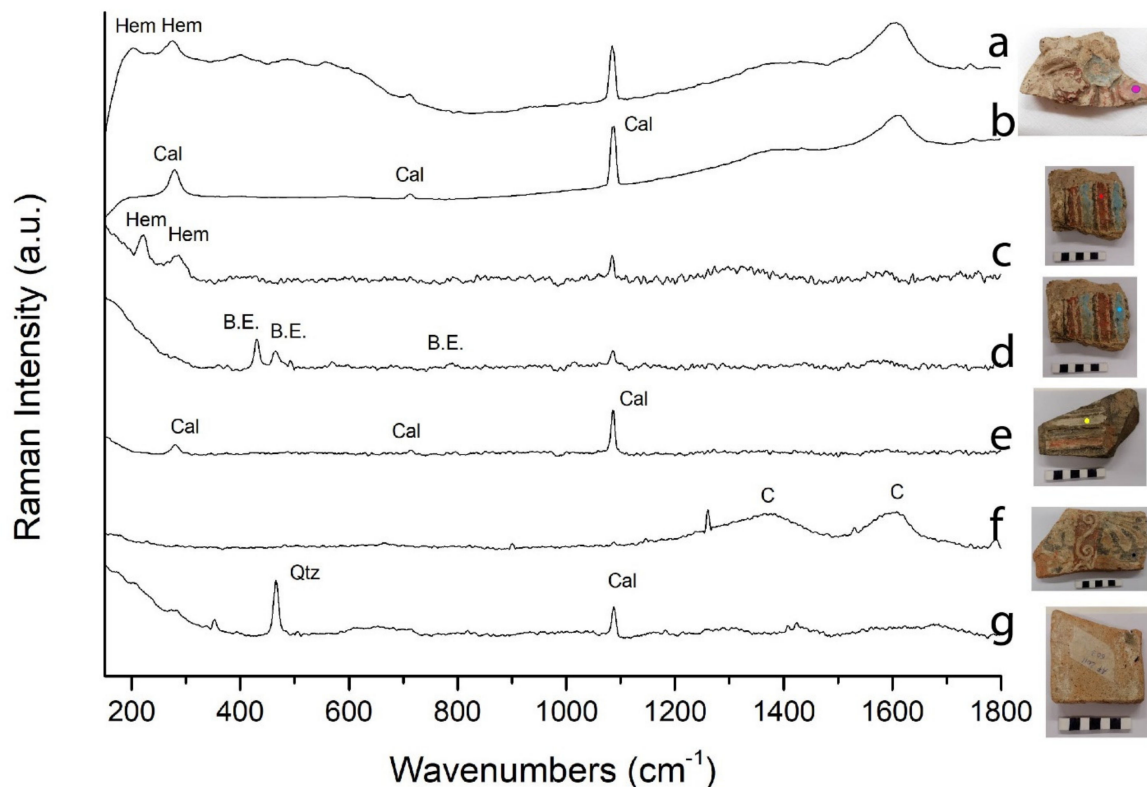
## 5.2. Pigments

### 5.2.1. $\mu$ -Raman Analysis

The  $\mu$ -Raman spectroscopy was used to identify the nature of the different pigments on the surfaces of terracottas (samples 1, 2, 3, 4, and 5). All the pigment spectra were compared to the ceramic body to better identify the characteristic peaks of each pigment.

Sample 1 was used to analyze the pink layer. The first granule analyzed appeared whitish (Figure 3b) and the relative  $\mu$ -Raman peaks are characteristic of calcite. The band at about  $1086\text{ cm}^{-1}$  is associated with the symmetrical stretching of the  $(\text{CO}_3)^{2-}$  group, while the band at about  $710\text{ cm}^{-1}$  is due to the bending vibration of the same group. There is another weaker band, at about  $275\text{ cm}^{-1}$ , linked to the vibration of the lattice [18]. A second granule analyzed appeared red under the microscope (Figure 3a), with peaks characteristic

of hematite ( $\text{Fe}_2\text{O}_3$ ). Specifically, the band at  $222\text{ cm}^{-1}$  is due to the symmetrical stretching of Fe-O, the band at  $410\text{ cm}^{-1}$  to the bending vibration of O-Fe-O, while the band at  $612\text{ cm}^{-1}$  is due to the symmetric bending [15].



**Figure 3.**  $\mu$ -Raman spectra of the Alba Fucens samples and relative peak identification (compound abbreviations: Cal-calcite; Hem-hematite; Qtz-quartz; B.E-Egyptian blue [ $\text{CaOCuO}(\text{SiO}_2)_4$ ]; C-carbon). (a) Pink pigment layer; (b) background of pink pigment; (c) red pigment layer; (d) light blue pigment layer; (e) white pigment layer; (f) black pigment layer; (g) matrix.

Sample 2 was used to analyze the red pigment. The spectrum (Figure 3c) shows bands around  $275$  and  $1100\text{ cm}^{-1}$ , attributed to calcite, whereas those at  $222$  and  $290\text{ cm}^{-1}$  were attributed to hematite. The  $222\text{ cm}^{-1}$  band is due to symmetric Fe-O stretching, while the  $290\text{ cm}^{-1}$  band is due to symmetric Fe-O bending [15].

Sample 2 was used also to analyze the light blue layer. The Raman spectrum allowed the identification of Egyptian blue,  $\text{CaOCuO}(\text{SiO}_2)_4$  [19,20] (Figure 3d). In particular, the peak at  $430\text{ cm}^{-1}$  is due to the bridging O breathing [21], that at  $475\text{ cm}^{-1}$  is related to the stretching and rocking bending of Si-O, whereas the peak at  $570\text{ cm}^{-1}$  is due to scissoring bending of O-Si-O. Finally, the peaks at  $780$  and  $1084\text{ cm}^{-1}$  are connected to the stretching of Si-O [22].

Sample 3 was used to investigate the white pigment identified on several of the architectural terracottas analyzed. The peaks in the spectrum (Figure 3e) at about  $290$ ,  $720$ , and  $1100\text{ cm}^{-1}$  are all attributed to calcite [16].

Sample 4 was analyzed to investigate the black pigment. The spectrum (Figure 3f) shows the characteristic peaks of amorphous carbon at  $1370$  and at  $1600\text{ cm}^{-1}$  [23].

### 5.2.2. pXRF Analysis

The chemical composition of the pigments was determined using pXRF analysis.

Pink pigment is only present in sample 1 and it is mainly composed of Ca and Fe. In addition, Sr occurs in traces (Table S1).

Red pigment occurs in samples 1, 2, 3, 4, and 5. The main chemical components are Fe and Ca, except for sample 5 which also shows the presence of Cu. In addition, in some of these samples Mn, Ti, Cu, and Pb were identified in traces (Table S1).

The light blue pigment is present in samples 1, 2, 4, and 5. It contains mainly Cu and Ca. In addition, Fe, Pb, Sr, and Mn are identified in traces (Table S1).

White pigment is present in samples 2, 3, 4, and 5. The main constituent present in all samples is Ca. Fe is present as the main component in sample 5, while in the other samples it is present only in traces. Sample 2 only shows traces of As (Table S1). The As could be related to the proximity of the sample to a wooden object restored and protected with compounds containing As or from the presence of burying soil traces on the surface of the analyzed pigment.

The black pigment is present in samples 2, 3, and 4. The main constituents of this pigment are Ca and Fe. In addition, in some samples, traces of Mn, Pb, and Cu were also identified (Table S1).

## 6. Discussion

### 6.1. The Terracotta: Production Technology and Provenance

For the first time a detailed mineralogical characterization of the architectural ceramic materials from the Sanctuary of Hercules in Alba Fucens has been carried out.

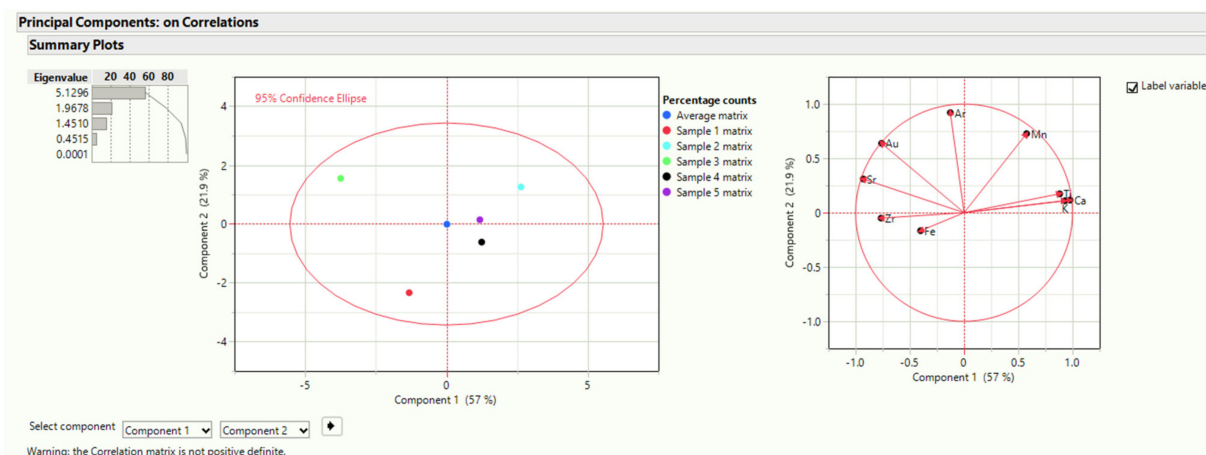
Two terracotta samples (F and O) showed a greyish color of the matrix whereas the others were mainly reddish. Red and brown colors are usually associated to an oxidizing atmosphere of firing, whereas firing in reducing conditions generally results in the grey color of the ceramics [24].

The XRPD analysis allowed the identification of the minerals constituting the ceramic body and then to estimate the firing temperature. All studied samples contain quartz and plagioclase, while only some of them show the presence of calcite, augite, and illite. Muscovite is only present in sample A (Table 1). The presence of illite and calcite suggests a firing temperature of the clays below about 800 °C [25]. Among the clayey minerals, in fact, kaolinite is the first to destabilize due to dehydration, below 550 °C, followed by illite, chlorite, and smectite that are dehydrated at a temperature between 459 and 900 °C [26]. At higher temperature, around 850–950 °C [27,28], carbonate-free CaO reacts with silica and alumina from the degradation of clayey minerals, resulting in the formation of calcium silicates or aluminum and calcium silicates, such as gehlenite, diopside, and wollastonite [29–31].

A further confirmation of the low firing temperature is the absence of neo-formation phases such as gehlenite and diopside in the terracotta matrix [26]. Indeed, gehlenite is formed from about 850 °C and remains stable up to 1100 °C [26]. The diopside, on the other hand, begins to enucleate at about 900 °C and it remains stable up to 1100 °C [26]. The absence of these mineral phases in the analyzed samples allows to suppose a firing temperature lower than about 800 °C. The presence of illite-muscovite and the scarce presence of plagioclase further supports this hypothesis.

The presence of augite can be related to the numerous volcanoclastic levels intercalated in the lake and alluvial deposits of the Fucino Basin. The archaeometric analyses carried out in this work support the hypothesis of a local origin of the raw materials as in the Fucino area, alluvial and lake deposits (rich in clay) are the main outcropping lithologies [11].

The pXRF spectra of the ceramic body show similar chemical composition for all the analyzed samples (1, 2, 3, 4, and 5), with high Fe and Ca contents. A similar pXRF pattern seems to suggest similar starting raw materials used for the realization of the architectural elements. The homogeneity of the analyzed matrices is further reinforced by the PCA elaboration of pXRF data [13] that shows all the samples within the “ellipse score” at 95% confidence limit (CL at 2 $\sigma$ ) (Figure 4). For this reason, the mean value of the elements of all the analyzed samples (Average Matrix) was used for comparison between the peaks of the colored pigments and those of the matrices (Table S2).



**Figure 4.** Principal component analysis of terracotta matrices.

The ceramic body  $\mu$ -Raman spectroscopy analysis showed the presence of quartz and calcite (Figure 3g), confirming the results of XRPD (Table 1). The Fe component (presumably its oxide), highlighted by the pXRF analysis, was not identified by the XRPD, most likely due to a low concentration below the instrument detection limit, nor by  $\mu$ -Raman analysis, most likely because of the difficulty in locating granules within the matrix.

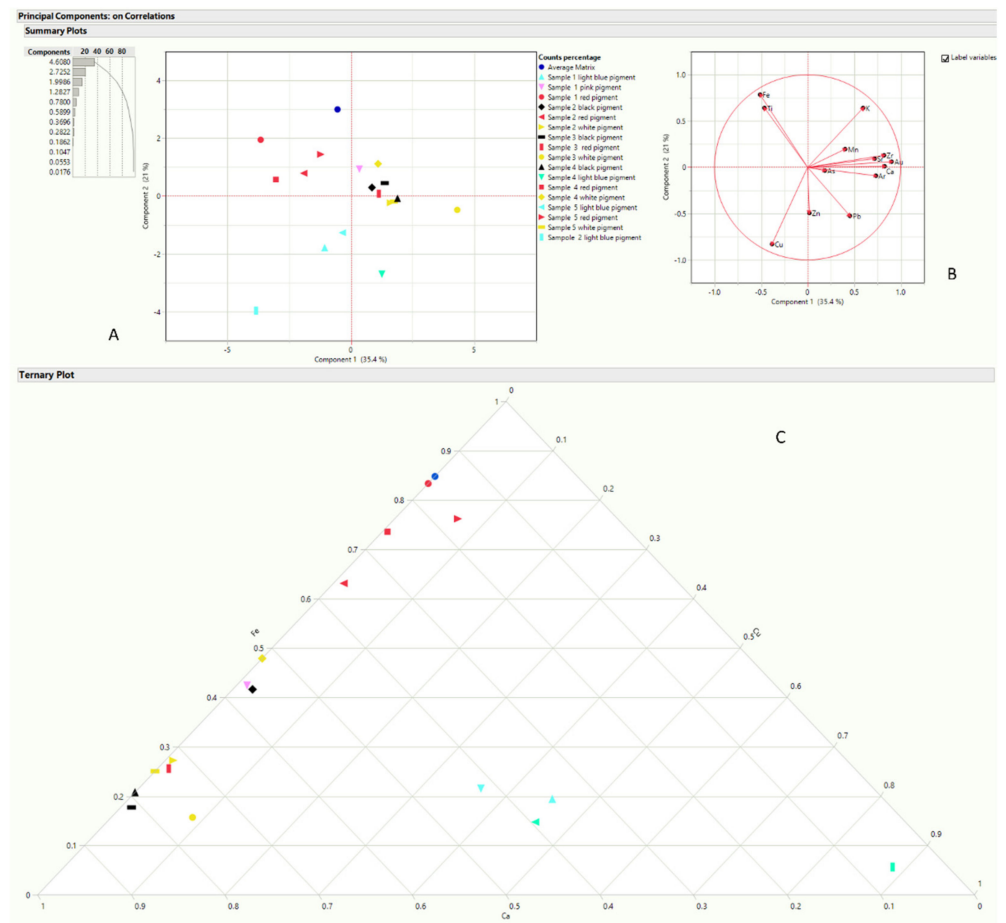
#### 6.2. The Pigments: Identification of Pigments' Palette

The red pigments analyzed on all the surfaces of architectural terracotta by pXRF show similar chemical composition, with the exception of sample 3. The majority of samples, located in the 2nd square of PCA plot (Figure 5A) (explaining more than 60% of data variability), are characterized by a consistent component of Fe (Figure 5A,B). On the contrary, sample 3 is closer to the pink of sample 1, influenced by a high content of Ca and a low content of Fe. The ternary diagram Ca-Fe-Cu (Figure 5C) further confirms that the red pigment of sample 3 has a chemical composition much closer to pink, black, and white, than to the other reds. This pigment, in fact, shows a higher amount of Ca than the others and a minor component of Fe.

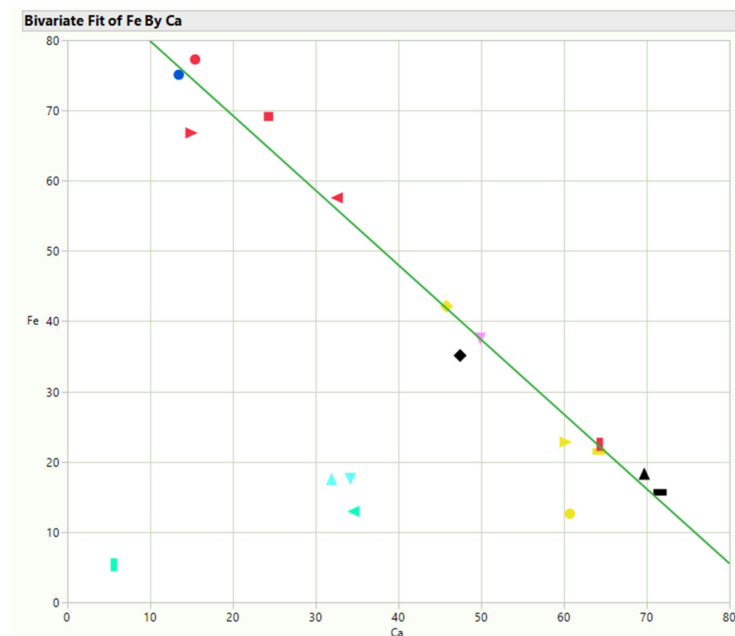
The  $\mu$ -Raman analysis confirmed the presence of calcite and hematite in the red analyzed samples. Unfortunately, in the absence of a stratigraphic analysis of the pigment, it is impossible to determine whether calcite was mixed with hematite, or it was related to a preparation layer. However, it should be noted that the architectural terracottas were sometimes coated with a relatively thick white layer that was used as a background to obtain a brighter and more nuanced polychromy [32]. The presence of Pb in traces in almost all pigments analyzed with pXRF technique could reinforce the hypothesis of a coat with an additional white pigment based on Pb.

All pigments analyzed in this study, except for light blue, are placed along a straight line in the Fe-Ca plane (Figure 6). Red pigments tend to have an excess of Fe compared to Ca, while in the white and black pigments the Ca becomes predominant at the expense of Fe as expected. Light blue pigment forms a cluster outside the line because of its Cu nature.

The Fe/Mn ratio gives an idea of the mixture of iron oxides and manganese oxides used to obtain different shading of the color by the artist. The red pigments, in fact, show the presence of Mn with different ratios, most likely due to the artist's desire to darken the shade of red, given by the mixture of calcite and hematite. An example is the red pigment of sample 5, which has a Fe/Mn = 31 [33] (Table S3).



**Figure 5.** (A,B) Principal Component Analysis plot and (C) ternary diagram of all pigments analyzed with pXRF.



**Figure 6.** Fe-Ca correlation for all pigments analyzed with the pXRF technique. Symbols as in Figure 5.

The white pigments result very similar to each other and to the black and pink pigments (Figure 5A,B), as confirmed by the ternary diagram Ca-Fe-Cu (Figure 5C). The main constituent of the white pigment is Ca, linked to calcite, whose presence has also been confirmed by  $\mu$ -Raman spectra (Figure 3e). The presence of Fe most likely is due to the clay matrix. In addition, Pb is present, although at limited concentrations, which would allow hypothesizing the use of a mixture of white lime and white lead. Only the white pigment of sample 3 showed traces of Cu, which may suggest the artist's possible intention to obtain different color tones [34].

The black pigments show a homogeneous nature (Figure 5A), mainly composed of Ca (Table S1) and amorphous carbon (Figure 3f). The presence of Ca contents higher than in red pigments and in the ceramic matrix seems to indicate that the black pigment is of animal origin. However, the presence of Ca could also derive from the underlying matrix, and therefore it cannot be excluded at all that the black is of vegetable origin. Comparing the Fe/Mn ratio of the three samples, a low Mn content in the pigment of sample 4 was found, compared to those of samples 2 and 3. Again, the lower Mn content of sample 4 could indicate a different shading of black voluntarily obtained by the artist [33] (Table S1). Traces of Cu (samples 2 and 3) could suggest the use of Egyptian blue pigment, probably to give different shades to the black. The presence of Pb may be linked to the presence of a layer of white lead below the pigment, as discussed above.

The difference in the sample 2 pigment is clearly visible in Table S1 because of a higher percentage of Cu with respect to Ca and the higher Fe contents with respect to the Mn (~50 vs. ~15). It is worth noting the presence of small amounts of Zn in the pigments of samples 1 and 4. Deviations from the ideal compositions of the Egyptian blue, in general, may be due to inclusions present in the source material or from the matrix in which the pigment was incorporated. This often results in additional elements in the compositional analysis such as Na, K, Mg, Al, Fe, Ti, and Zn [35].

The analyzed pink pigment is only present in sample 1. The  $\mu$ -Raman analysis showed the presence of calcite and hematite (Figure 3a) confirmed by the identification of Ca and Fe in the pXRF spectrum (Table S1). The ratio Ca/Fe = 1.3 of the pink pigment, when compared to the matrix equal to Ca/Fe = 0.17, allows to hypothesize that it may be a color of earth (clay) with a higher content of Ca than that of terracotta. As there is the possibility of the use by ancient manufacturers of a white layer of calcite to cover the terracotta before painting, it is not excluded that the pink pigment was obtained from the combination of calcite and hematite, laid on the layer of calcite. Unfortunately, since a stratigraphic analysis of the sample is not available, it is impossible to determine the presence of calcite below the pink pigment. The elemental composition of the pink color is very similar to that of the red pigment of sample 3 (Figure 5A). Both colors have a Ca/Fe ratio greater than 1, while the red pigments have a value well below 1. This leads to the conclusion that the red of sample 3 attributed on the basis of a visual analysis, is to be considered a lighter red pigment, tending to pink, compared to other red pigments.

## 7. Conclusions

This first archaeometric study of painted architectural terracotta, dating back to the 3rd–2nd century BC, from the archaeological site of Alba Fucens (Italy, L'Aquila), allowed the identification of the production technologies, the provenance, and the nature of pigments used.

The studied materials are characterized by a good manufacture, probably coming from an Etruscan-Italic temple, built immediately after the establishment of the colony. The analytical results of this study highlighted the use of valuable pigments such as Egyptian blue. The other analyzed pigments confirmed the use of a palette typical of the Roman period from the 3rd century BC to the 1st century BC. The red pigment was obtained by using hematite, the hue of which was modified using lime white and perhaps also white lead. Regarding the black pigment, the analytical results did not allow to determine its origin (animal or vegetable). Despite the few colors used, it was noted that for the same



color different shading was used. In the case of Egyptian blue, for example, we can see how the artist went from a bright shade to an opaquer one, by modulating the Egyptian blue with white (white lead or calcite) or black (manganese oxide).

The analysis of terracotta showed a firing temperature lower than 800 °C, due to the presence of illite-calcite and the absence of neoformation phases such as gehlenite and diopside. The presence of augite is related to the numerous volcanoclastic levels intercalated in the lacustrine and alluvial deposits of the Fucino Basin. The archaeometric analyses, conducted in this study, allow the suggestion of a local origin of the raw materials, since alluvial and lake deposits (rich in clay) are the main lithologies emerging in the Fucino area. However, more in-depth analyses are needed to establish the source.

Finally,  $\mu$ -Raman and pXRF analyses seem to indicate the presence of a white layer of calcite and lead as primers before applying the pigments, even though a stratigraphic analysis of the pictorial layer of terracotta is essential to confirm it.

The preliminary results of this study are part of a larger project and will be validated hereafter.

**Supplementary Materials:** The following are available online at <https://www.mdpi.com/article/10.3390/min12030346/s1>, Table S1: pXRF counts (%) for all pigments of samples 1–5, Table S2: pXRF counts (%) for all ceramic bodies of samples 1–5, Table S3: pXRF counts (%) of Mn and Fe for red pigments.

**Author Contributions:** Conceptualization, G.R., E.C., L.M. and S.M.; formal analysis, G.R.; investigation, E.C., L.M. and S.M.; data curation, G.R., A.M.C., C.D.V., L.M. and S.M.; writing—original draft preparation, G.R. and E.C.; writing—review and editing, A.M.C., C.D.V., L.M. and S.M.; visualization, G.R.; supervision, L.M. and S.M. All authors have read and agreed to the published version of the manuscript.

**Funding:** This research was funded by Sapienza University of Rome, grant number 000047\_18.

**Data Availability Statement:** The data are available within the article or its Supplementary Materials.

**Acknowledgments:** The authors would like to thank the anonymous reviewers for their constructive comments and suggestions. The authors thank the “MUSÉ-Nuovo Museo Paludi di Celano-Centro di restauro” for having made available the terracottas analyzed in this work, Stefania Montanaro for the sampling of materials analyzed with XRPD, and the company LFoundry of Avezzano for their cooperation in  $\mu$ -Raman analysis. Finally, we are grateful to Stefano Ridolfi for having made available the portable instrumentation XRF of Ars Mensurae laboratory.

**Conflicts of Interest:** The authors declare no conflict of interest.

## References

1. Padeletti, G.; Fermo, P. A scientific approach to the attribution problem of renaissance ceramic productions based on chemical and mineralogical markers. *Appl. Phys. A* **2010**, *100*, 771–784. [CrossRef]
2. Medeghini, L.; Mignardi, S.; De Vito, C.; Macro, N.; D’Andrea, M.; Richard, S. New insights on Early Bronze Age IV pottery production and consumption in the southern Levant: The case of Khirbat Iskandar, Jordan. *Ceram. Int.* **2016**, *42*, 18991–19005. [CrossRef]
3. Giannossa, L.C.; Acquaviva, M.; De Benedetto, G.E.; Acquafredda, P.; Laviano, R.; Mangone, A. Methodology of a combined approach: Analytical techniques to identify the technology and raw materials used in thin-walled pottery from Herculaneum and Pompeii. *Anal. Methods* **2014**, *6*, 3490–3499. [CrossRef]
4. Tite, M.S. Ceramic production, provenance and use—A review. *Archaeometry* **2008**, *50*, 216–231. [CrossRef]
5. De Vito, C.; Medeghini, L.; Mignardi, S.; Ballirano, P.; Peyronel, L. Technological fingerprints of the early Bronze Age clay figurines from tell Mardikh-Ebla (Syria). *J. Eur. Ceram. Soc.* **2015**, *35*, 3743–3754. [CrossRef]
6. Zink, S. Polychromy, architectural, Greek and Roman. In *Oxford Classical Dictionary*; Goldberg, S., Ed.; Oxford University Press: New York, NY, USA, 2019; Available online: <http://oxfordre.com/classics> (accessed on 4 January 2022).
7. Ceccaroni, E. La colonia latina. In *Poco Grano, Molti Frutti. Cinquant’Anni di Archeologia ad Alba Fucens*; Campanelli, A., Strazzulla, M.J., Galadini, F., Eds.; Synapsi: Sulmona, Italy, 2006; pp. 57–65.
8. Galadini, F.; Ceccaroni, E.; Falcucci, E. Archaeoseismological evidence of a disruptive Late Antique earthquake at Alba Fucens (central Italy). *Boll. Geofis. Teor. Appl.* **2010**, *51*, 143–161.
9. Liberatore, D. Alba Fucens. Il santuario di Ercole (scavi 2006–2009). *Quad. Archeol. D’Abruzzo* **2009**, *1*, 214–220.

10. Ceccaroni, E. Alba Fucens: Gli interventi della Soprintendenza per i Beni Archeologici dell’Abruzzo nell’isolato di via del Miliario e nel piazzale del Santuario di Ercole. *Atti Pontif. Accad. Romana Archeol. III Rend.* **2014**, *85*, 245–277.
11. Cavinato, G.P.; Carusi, C.; Dall’Asta, M.; Miccadei, E.; Piacentini, T. Sedimentary and tectonic evolution of Plio-Pleistocene alluvial and lacustrine deposits of Fucino Basin (central Italy). *Sedim. Geol.* **2002**, *148*, 29–59. [CrossRef]
12. Ranishaw Apply Innovation™. Available online: <https://www.renishaw.com/en/automatic-intelligent-background-removal-25934> (accessed on 25 February 2022).
13. Holakhoeei, P.; Tessari, U.; Verde, M.; Vaccaro, C. A new look at XRD patterns of archaeological ceramic bodies. *J. Therm. Anal. Calorim.* **2014**, *118*, 165–176. [CrossRef]
14. JMP Statistical Discovery. Available online: [https://www.jmp.com/it\\_it/home.html](https://www.jmp.com/it_it/home.html) (accessed on 22 January 2022).
15. Olivares, M.; Zuluaga, M.C.; Ortega, L.A.; Murelaga, X.; Alonso-Olazabal, A.; Urteaga, M.; Amundaray, L.; Alonso-Martina, I.; Etxebarria, N. Characterisation of fine wall and eggshell Roman pottery by Raman spectroscopy. *J. Raman Spectrosc.* **2010**, *41*, 1543–1549. [CrossRef]
16. Sánchez-Pastor, N.; Oehlerich, M.; Astilleros, J.M.; Kaliwoda, M.; Mayr, C.C.; Fernández-Díaz, L.; Schmahl, W.W. Crystallization of ikaite and its pseudomorphic transformation into calcite: Raman spectroscopy evidence. *Geochim. Cosmochim. Acta* **2016**, *175*, 271–281. [CrossRef]
17. Zava, A. Analisi Elementale Non Distruttiva di Campioni di Interesse Storico con Tecniche di Spettroscopia XRF. Bachelor’s Thesis, Università degli Studi di Padova, Padova, Italy, 2016/2017.
18. De Carlo, T.M. Characterizing coral skeleton mineralogy with Raman spectroscopy. *Nat. Commun.* **2018**, *9*, 5325. [CrossRef] [PubMed]
19. Baraldi, P.; Bondioli, F.; Fagnano, C.; Ferrari, A.; Tinti, A.; Vinella, M. Study of the vibrational spectrum of cuprorivaite. *Ann. Chim.* **2001**, *91*, 679–692. [PubMed]
20. Pagès-Camagna, S.; Colinart, S.; Coupry, C. Fabrication processes of archaeological Egyptian blue and green pigments enlightened by Raman microscopy and scanning electron microscopy. *J. Raman Spectrosc.* **1999**, *30*, 313–317. [CrossRef]
21. Gagliano Candela, R.; Lombardi, L.; Ciccola, A.; Serafini, I.; Bianco, A.; Postorino, P.; Pellegrino, L.; Bruno, M. Deepening inside the pictorial layers of Etruscan sarcophagus of Hasti Afunei: An innovative micro-sampling technique for Raman/SERS analyses. *Molecules* **2019**, *24*, 3403. [CrossRef] [PubMed]
22. Bordignon, F.; Postorino, P.; Dore, P.; Trojsi, G. Raman identification of green and blue pigments in Etruscan polychromes on architectural terracotta panels. *J. Raman Spectrosc.* **2007**, *38*, 255–259. [CrossRef]
23. Tomasini, E.P.; Halac, E.B.; Reinoso, M.; Di Liscia, E.J.; Maier, M.S. Micro-Raman spectroscopy of carbon-based black pigments. *J. Raman Spectrosc.* **2012**, *43*, 1671–1675. [CrossRef]
24. Rathossi, C.; Pontikes, Y. Effect of firing temperature and atmosphere on ceramics made of NW Peloponnese clay sediments. Part I: Reaction paths, crystalline phases, microstructure and colour. *J. Eur. Ceram. Soc.* **2010**, *30*, 1841–1851. [CrossRef]
25. Jordan, M.M.; Sanfeliu, T.; de la Fuente, C. Firing transformations of Tertiary clays used in the manufacturing of ceramic tile bodies. *Appl. Clay Sci.* **2001**, *20*, 87–95. [CrossRef]
26. Guarino, V.; De Bonis, A.; Faga, I.; Giampaola, D.; Grifa, C.; Langella, A.; Liuzza, V.; Pierbon Benoit, R.; Romano, P.; Morra, V. Production and circulation of thin walled pottery from the Roman port of Neapolis, Campania (Italy). *Period. Mineral.* **2016**, *85*, 95–114.
27. Riccardi, M.P.; Messiga, B.; Duminuco, P. An approach to the dynamics of clay firing. *Appl. Clay Sci.* **1999**, *15*, 393–409. [CrossRef]
28. Trindade, M.J.; Dias, M.I.; Coroado, J.; Rocha, F. Mineralogical transformations of calcareous rich clays with firing: A comparative study between calcite and dolomite rich clays from Algarve, Portugal. *Appl. Clay Sci.* **2009**, *42*, 345–355. [CrossRef]
29. Aras, A. The change of phase composition in kaolinite and illite-rich clay-based ceramic bodies. *Appl. Clay Sci.* **2004**, *24*, 257–269. [CrossRef]
30. Barone, G.; Crupi, V.; Longo, F.; Majolino, D.; Mazzoleni, P.; Tanasi, D.; Venuti, V. FT-IR spectroscopic analysis to study the firing processes of prehistoric ceramics. *J. Mol. Struct.* **2011**, *993*, 147–150. [CrossRef]
31. Raneri, S.; Barone, G.; Mazzoleni, P.; Tanasi, D.; Costa, E. Mobility of men versus mobility of goods: Archaeometric characterization of Middle Bronze Age pottery in Malta and Sicily (15th–13th century BC). *Period. Mineral.* **2015**, *84*, 23–44.
32. Baccheschi, E.; Dufour Bozzo, C.; Franchini Guelfi, F.; Gallo Colonna, G.; Gavazza, E.; Giubbini, G.; Leva Pistoia, M.; Parma Armani, E.; Pesenti, F.R.; Sborgi, F. La lavorazione delle terre. In *Le Tecniche Artistiche*; Maltese, C., Ed.; Mursia: Milano, Italy, 2016; pp. 101–102.
33. Marchiafava, V.; Luzzatto, L. *Colore e Colorimetria. Contributi Multidisciplinari*; Gruppo del Colore—Associazione Italiana Colore: Milano, Italy, 2019.
34. Aliatis, I.; Bersani, D.; Campani, E.; Casoli, A.; Lottici, P.P.; Mantovan, S.; Marino, I.G. Pigments used in Roman wall paintings in the Vesuvian area. *J. Raman Spectrosc.* **2010**, *41*, 1537–1542. [CrossRef]
35. Wiedemann, H.G.; Berke, H. Chemical and physical investigations of Egyptian and Chinese blue and purple. In *The Polychromy of Antique Sculptures and the Terracotta Army of the First Chinese Emperor. Studies of Materials, Techniques and Conservation, Proceedings of the International Conference in Xi’an, China, 22–28 March 1999*; Yonggi, W., Tinghao, Z., Petzet, M., Emmerling, E., Blansdorf, C., Eds.; UNESCO International Council on Monuments and Sites: Paris, France, 2001; pp. 154–171.

## Article

# Supergene Copper and the Ancient Mining Landscapes of the Atacama Desert: Refining the Protocol for the Study of Archaeological Copper Minerals through the Case Study of *Pukara de Turi*

Pía Sapiains <sup>1,\*</sup>, Valentina Figueroa <sup>2</sup>, Frances Hayashida <sup>3</sup>, Diego Salazar <sup>4</sup>, Andrew Menzies <sup>5</sup>, Cristián González <sup>6</sup>, Rodrigo Loyola <sup>7</sup>, Beau Murphy <sup>3</sup>, Juan González <sup>8</sup>, César Parcerro-Oubiña <sup>9</sup> and Andrés Troncoso <sup>4</sup>

**Citation:** Sapiains, P.; Figueroa, V.; Hayashida, F.; Salazar, D.; Menzies, A.; González, C.; Loyola, R.; Murphy, B.; González, J.; Parcerro-Oubiña, C.; et al. Supergene Copper and the Ancient Mining Landscapes of the Atacama Desert: Refining the Protocol for the Study of Archaeological Copper Minerals through the Case Study of *Pukara de Turi*. *Minerals* **2021**, *11*, 1402. <https://doi.org/10.3390/min11121402>

Academic Editors: Daniel Albero Santacreu, José Cristóbal Carvajal López and Adrián Durán Benito

Received: 6 November 2021  
Accepted: 8 December 2021  
Published: 11 December 2021

**Publisher's Note:** MDPI stays neutral with regard to jurisdictional claims in published maps and institutional affiliations.



**Copyright:** © 2021 by the authors. Licensee MDPI, Basel, Switzerland. This article is an open access article distributed under the terms and conditions of the Creative Commons Attribution (CC BY) license (<https://creativecommons.org/licenses/by/4.0/>).

- <sup>1</sup> Doctorado en Ciencias Mención Geología, Departamento de Ciencias Geológicas, Universidad Católica del Norte, Antofagasta 1240000, Chile
  - <sup>2</sup> Instituto de Investigaciones Arqueológicas y Museo (IIAM), Universidad Católica del Norte, San Pedro de Atacama 1410000, Chile; vfigueroa@ucn.cl
  - <sup>3</sup> Department of Anthropology, University of New Mexico, Albuquerque, NM 87131, USA; fmh@unm.edu (F.H.); bgm10@unm.edu (B.M.)
  - <sup>4</sup> Departamento de Antropología, Universidad de Chile, Santiago 7800284, Chile; dsalazar@uchile.cl (D.S.); atroncos@uchile.cl (A.T.)
  - <sup>5</sup> Bruker Nano GmbH, 12489 Berlin, Germany; andrew.menzies@bruker.com
  - <sup>6</sup> MPhil/Ph.D. Programme, Institute of Archaeology, University College London, 31-34 Gordon Square, London WC1H 0PY, UK; c.gonzalez-rodriguez@ucl.ac.uk
  - <sup>7</sup> Instituto de Investigaciones Arqueológicas y Museo (IIAM), Universidad Católica del Norte—UMR 7055 Prehistoire et Technologie (PreTéch), Université Paris Ouest Nanterre La Défense, 92000 Nanterre, France; rodarkeo@gmail.com
  - <sup>8</sup> Department of Civil Engineering, Universidad Católica de la Santísima Concepción, Concepción 4090541, Chile; jgonzal@ucsc.cl
  - <sup>9</sup> Instituto de Ciencias del Patrimonio (Incipit), Consejo Superior de Investigaciones Científicas (CSIC), 15705 Santiago de Compostela, Spain; cesar.parcerro-oubina@incipit.csic.es
- \* Correspondence: psg004@ucn.cl

**Abstract:** Northern Chile is home to the world's largest copper ore deposits, which have been exploited for thousands of years by different groups, at varying scales and for different purposes. In this context, it is important to develop new protocols to characterise the mineralogical variability of archaeological copper ores. A comprehensive and representative methodology in the analysis of minerals, the application of non-destructive analytical techniques, and the combination of insights from geological, archaeological and local knowledge are key to developing a copper mineral repository of the Atacama Desert area. Geochemical analyses were applied to the study of 568 samples from the archaeological site *Pukara de Turi*, with different techniques such as micro-XRF, XRD, QEMSCAN, Raman spectroscopy and technological studies. This exhaustive analysis allowed for the recognition of two mineralogical associations: atacamite/brochantite (99%) and azurite/chrysocolla (1%). The study of various minerals allows data to be interpreted more reliably and to trace the likely geological sources of these minerals. The azurite/chrysocolla samples appear to belong to the same mineral association found in the Cerro Verde district, which is probably the source of these samples. The atacamite/brochantite samples appear to come from more than one geological source, including, but not limited to, Chuquicamata-Radomiro Tomic and El Abra-Conchi.

**Keywords:** copper minerals; micro-XRF; archaeometry

## 1. Introduction

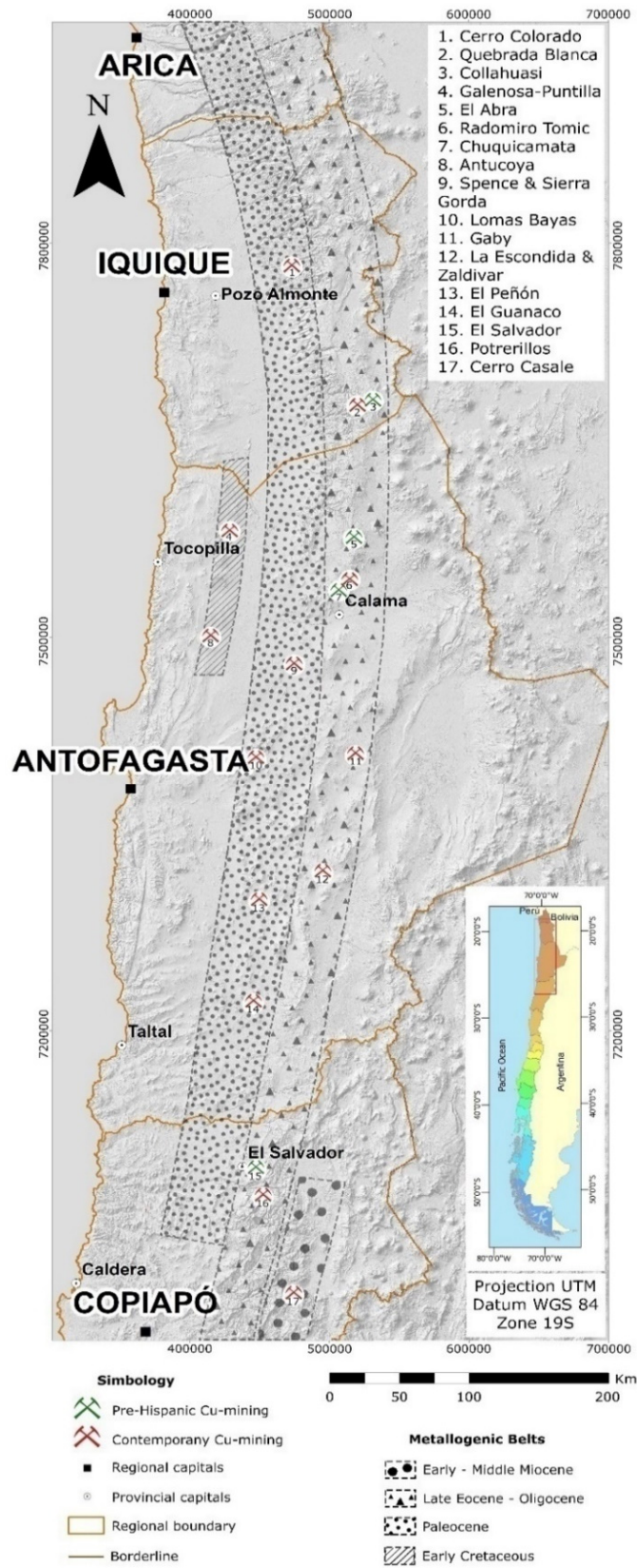
The Atacama Desert is home to the world's largest copper deposits, which have been exploited for thousands of years by different groups, at varying scales and for dif-

ferent purposes (Figure 1). Since pre-Hispanic times, a mining economy in the Atacama Desert supplied regional and interregional demand for copper ore uses such as metallurgy, lapidary, pigmentary and ores (in the form of powder, nodules and fragments).

Copper mining has a deep-rooted history dating back to the Formative Period (ca. 1500 BC–400 AD) to the Inca Horizon (ca. 1400–1540 AD) [2–4]. Mining districts in the Atacama Desert were exploited by the Incas from the mid-15th century, who kept their technology and reorganised mining activity [5–9]. However, these activities almost entirely ceased after the Hispanic Conquest and the installation of the colonial system. Nonetheless, the production and use of copper continued during colonial times, the Republican Period and is even carried out today by local indigenous communities [10]. Unlike in other regions of the South-Central Andean Area, where complex metallurgical industries developed [11,12], on the western side of the Circumpuna, metallurgy was a secondary activity during prehistory [13,14]. The bulk of mining production was destined for lapidary uses and, particularly, to supply the needs of local ritual ceremonies, in which copper ores played a prominent role as offerings. In the Andean world, the geological and mineral landscape was not part of an inert mineral world—since time immemorial, Andean peoples have personified the landscape, considering it alive. Copper minerals were offered in various contexts, identified in a range of settings: residential, agricultural (terraces, water holes, springs and wells), rock art (in paintings or offerings to them), funerary (nodules, beads, powders, pigments), monumental (tumuli), in paraphernalia (tablet and inhalation tube inlays, mortars, pylons and spoons), on top of certain hills, on ceremonial tables (walls and boxes) and in passageways, openings and routes (e.g., [15–22]). Given this variety of uses, copper minerals are among the most ubiquitous remains to be found in archaeological sites throughout the Atacama Desert.

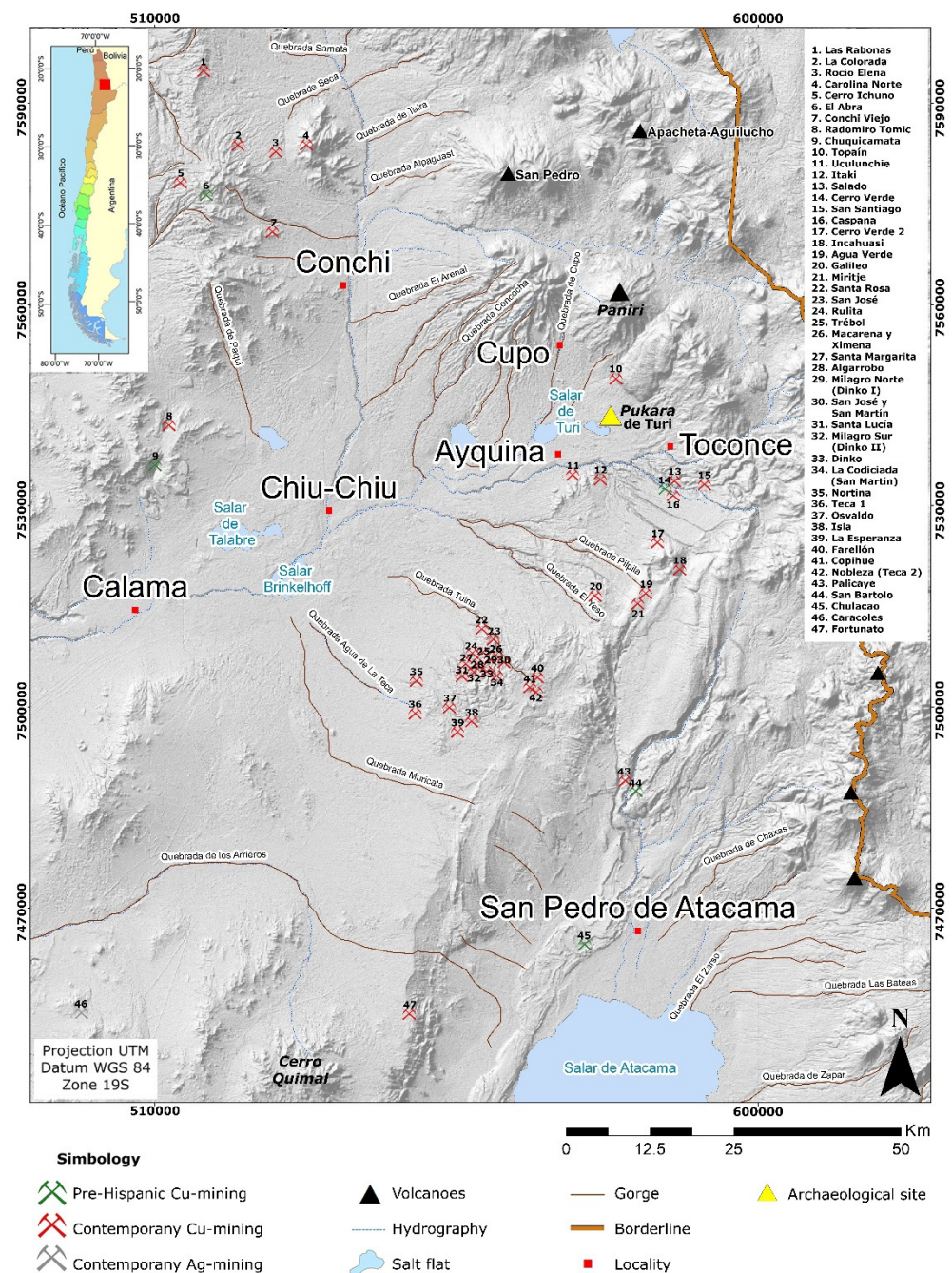
The abundance of mineral sources in the area has also led to deep levels of local knowledge and expertise in the fields of mineralogy and geochemistry [23–25] among others; therefore, the Atacama Desert is a privileged place to research copper ores and their uses over long timescales of human civilisation. Since the variability and complexity of copper deposits in the area make them challenging to characterise, many researchers have developed different mineral study methodologies based on this zone [26–29], among others. In addition, there is an extensive body of archaeological literature on the problems of copper mineral source characterisation and the limitations of such approaches.

In this study, samples were collected from the *Pukara* de Turi, an extensive 4 ha archaeological site from the Late Intermediate and Inca Periods (ca. 11th–16th centuries), located in northern Chile (Figure 2). We analysed 568 samples with geochemical analyses using micro-X-ray fluorescence ( $\mu$ -XRF). In addition, the following analyses were performed: X-ray diffraction (XRD), Raman spectroscopy and QEMSCAN, which allowed us to improve the understanding of pre-Hispanic copper ore technologies in the Atacama Desert in the context of mineral raw materials, as well as knowing how they were used in archaeological times through the recognition of mineral paragenesis. In addition, we carried out a technological study of the mineral assemblages. This was intended to characterise the diversity of copper ores from the *Pukara* de Turi and its diverse uses within the site. The analyses detailed in Sections 4.1–4.4 were carried out at Unidad de Equipamiento Científico-MAINI, at Universidad Católica del Norte, Antofagasta, Chile.



**Figure 1.** Metallogenic belts in northern Chile, mining districts and copper mines. Metallogenic belts were modified from [1].





**Figure 2.** Location map, showing the copper and silver deposits in the area. Pre-Hispanic copper mines are highlighted with a green symbol and modern copper mines with a red symbol.

## 2. Geochemical Characterisation of Pre-Hispanic Copper Ores in the Atacama Desert

The regional extent and distribution of the mining landscapes of the Atacama Desert can be characterised by considering the distances between populated nodes, based on water availability from rivers and oases, and mining districts [9], whose location is controlled by the underlying geology. Over the course of prehistoric times, Atacama societies developed an understanding of regional geography based on the needs of their social, technological and ritual systems that required access to mining districts to extract minerals and then redistribute them in their various contexts of use. To understand these mining landscapes, studies must, therefore, take into consideration the location and characteristics of mining districts and their relation to the areas where minerals were used.

The *Pukara* de Turi archaeological study sites lie within the Upper Eocene–Oligocene metallogenic belt (43–31 Ma) defined by [1,25,30], among others (Figure 1), where several pre-Hispanic mines have been identified and studied [6,7,9,14,31–38]. Copper deposits have a geochemical signature that is strongly dependent on the geological context of their formation [39]. Supergene ores form from the reaction of hydrothermally derived ores with near-surface meteoric water. The paragenesis of copper oxide minerals reveals that a specific series of progressive mineralogical changes take place during supergene oxidation, transport and precipitation [40]. Thus, to determine the sources of copper, it is important to define the paragenesis of minerals from pre-Hispanic mining districts and their impurities, which can be expressed as minor elements (comprising 0.1–1% of the rock mass) or as trace elements (<0.1%). These signatures are unique to each deposit and thus correspond to markers of the sample's geochemical origin [39]. Oxidised copper minerals may also have visible variations in their macroscopic characteristics which indicate the heterogeneity of their mineralisation [41]. In summary, the detailed study of trace element geochemistry allows each mineral type to be characterised in copper ore samples, thus delimiting their probable origin [42].

In the past 10 years, several analytical techniques have been used to characterise a range of mineral samples from archaeological sites in northern Chile. These include techniques such as X-ray diffraction (XRD) [43,44], X-ray fluorescence (XRF) [43,45], Particle-Induced X-Ray Emission (PIXE) [46,47], Scanning Electron Microscopy with Energy Dispersive Spectrometers (SEM-EDS) [48,49], Raman Spectroscopy [20] and automated mineralogical analysis (QEMSCAN) [6,28]. Copper ores primarily exploited by pre-Hispanic miners correspond to those found in the oxidised zone (i.e., antlerite ( $\text{Cu}_3\text{SO}_4(\text{OH})_4$ ), atacamite ( $\text{Cu}_2\text{Cl}(\text{OH})_3$ ), brochantite ( $\text{Cu}_4\text{SO}_4(\text{OH})_6$ ), chrysocolla ( $(\text{Cu},\text{Al})_2\text{H}_2\text{Si}_2\text{O}_5(\text{OH})\cdot n\text{H}_2\text{O}$ ), pseudomalachite ( $\text{Cu}_5(\text{PO}_4)_2(\text{OH})_4$ ) and turquoise ( $\text{CuAl}_6(\text{PO}_4)_4(\text{OH})_8\cdot 4\text{H}_2\text{O}$ ), among others), which precipitate close to the surface [40] and whose exploitation was possible with pre-Hispanic mining technology [2].

On the basis of these previous studies, we attempted to gain new insights into the geochemical characterisation of pre-Hispanic copper ores. In particular, although several analytical techniques have recently been used to characterise mineral samples from archaeological contexts in northern Chile with increasing precision, we suggested that the study of archaeological copper minerals requires an integrated approach, taking into account other variables (e.g., ore deposition, distribution, gravity, gangue, technology, ritual, etc.). Such an approach is crucial to develop a broader understanding of copper production in this context, such as contemporary technology, mobility and exchange.

### 3. Selection and Description of Samples

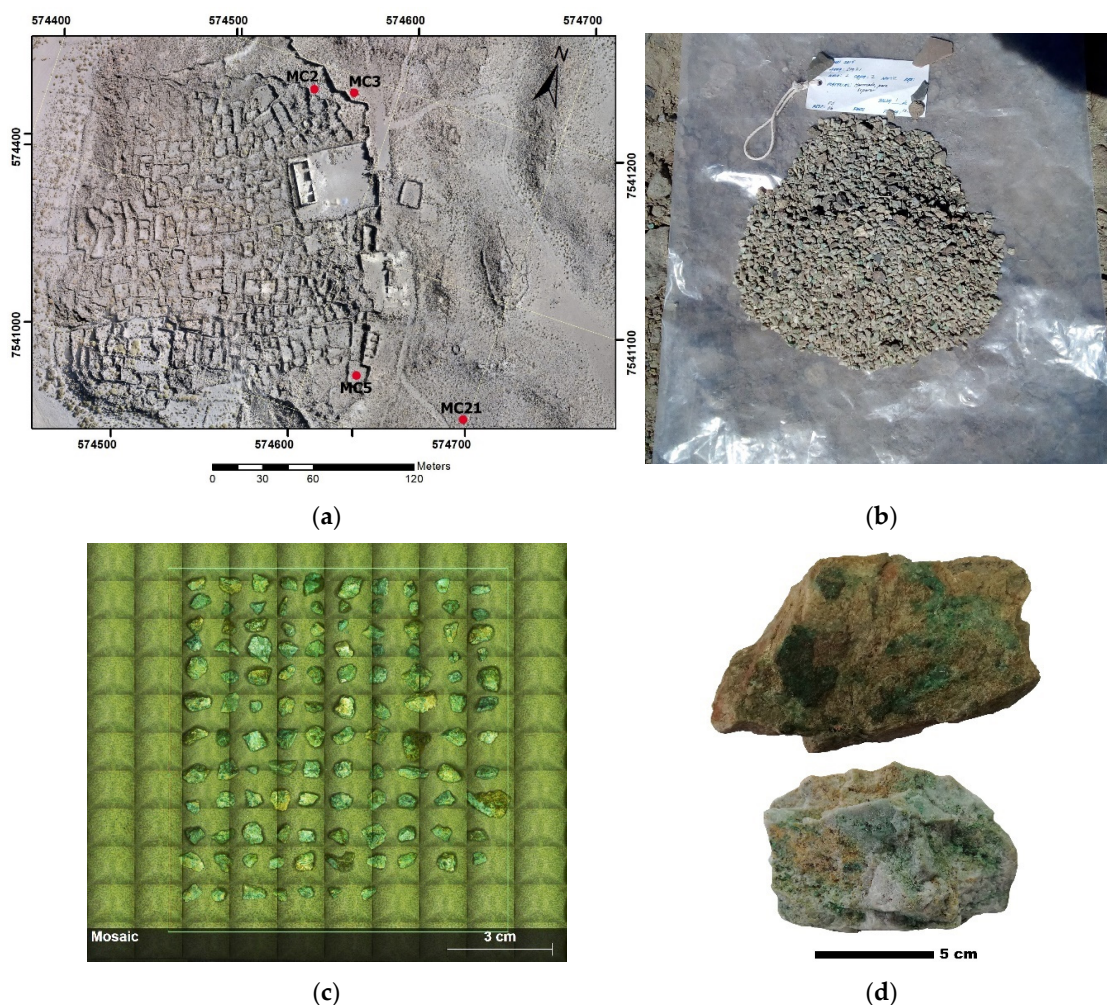
Turi was a residential and administrative centre, occupied in the Late Intermediate Period (LIP) (ca. 1000–1400 AD) through the Inca (ca. 1400–1540 AD) period and early colonial times (16th and with a small 17th century occupation [50]). *Pukara* de Turi has many copper ore concentrations (mineral concentrations) both inside and outside the site. The enclosures studied correspond to both the LIP and Inca occupation of the site.

Some of the concentrations correspond to stocks of copper mineral offerings. In this work, MC2, MC3, MC5 and MC21 (Figure 3a) were excavated and studied (Figure 4). Our proposed methodology starts from the excavation itself since the selection of samples will affect the subsequent results. In this study, each excavation unit measured  $50 \times 50$  cm and was excavated following natural strata. Strata exceeding 5 cm of thickness were divided into arbitrary 5 cm levels. Sediments were passed through a 1/8" screen and minerals and other cultural material was recovered. Minerals from each concentration were then labelled, and the total bulk material collected was then separated into samples, each comprising 1/8 by weight of each level by units, which were sent to the geochemistry laboratory (Table 1). The samples from the excavation were observed using a geological magnifying glass (14× magnification) to identify fragments that showed copper mineralisation, including partially or fully mineralised rock fragments (Figure 3b).



The samples were small angular fragments of copper ore between 3 and 5 mm in length. The fragments can be described as (i) small fragments of pure minerals, (ii) quartz fragments that are green in appearance due to traces of copper mineralisation and (iii) minerals with little gangue. In some fragments, the mineralisation appears as a patina on the rock and with intergrowth textures.

For the analytical techniques mentioned above, the archaeological samples did not need to be specifically prepared. Using this approach, 568 mineral fragments were selected and analysed via  $\mu$ -XRF (Figure 4). To confirm the mineralogy, we used XRD to analyse four of the samples previously examined with  $\mu$ -XRF. The use of XRD is a destructive approach as it was necessary to pulverise the mineral fragments. In addition, we applied automated mineralogy (QEMSCAN) to seven mineral fragments from the MC samples of *Pukara de Turi*, and, in addition, to four mineral fragments relatively close to the possible geological sources from the AB-20, Chu-2 and Chu-4 mining sites [7] (located close to El Abra-Conchi and Chuquicamata-Radomiro Tomic mining districts, respectively (see Figure 2, mines mentioned are identified with symbology of the mining districts and numbers 6–9 on the map). Additionally, we analysed a sample from a vein composed of quartz and feldspar with copper mineralisation. The vein fragment was a core (a mass of raw material fractured to obtain flakes or blanks through knapping) and was found in a typical building of the Inca architecture called a Compound Perimeter Enclosure (also known by the Spanish acronym RPC (Recinto Perimetral Compuesto)) (Figure 3d).



**Figure 3.** (a) Location of the samples in the place where mineral concentration (MC) was excavated on the site. (b) Sediments and minerals collected in the grid. (c) Samples selected for analytical analysis in  $\mu$ -XRF from MC21 (layer 2, level 3). (d) Core sample collected in Inca building (RPC); the two sides of the sample can be seen, one weathered and the other a fresh side.

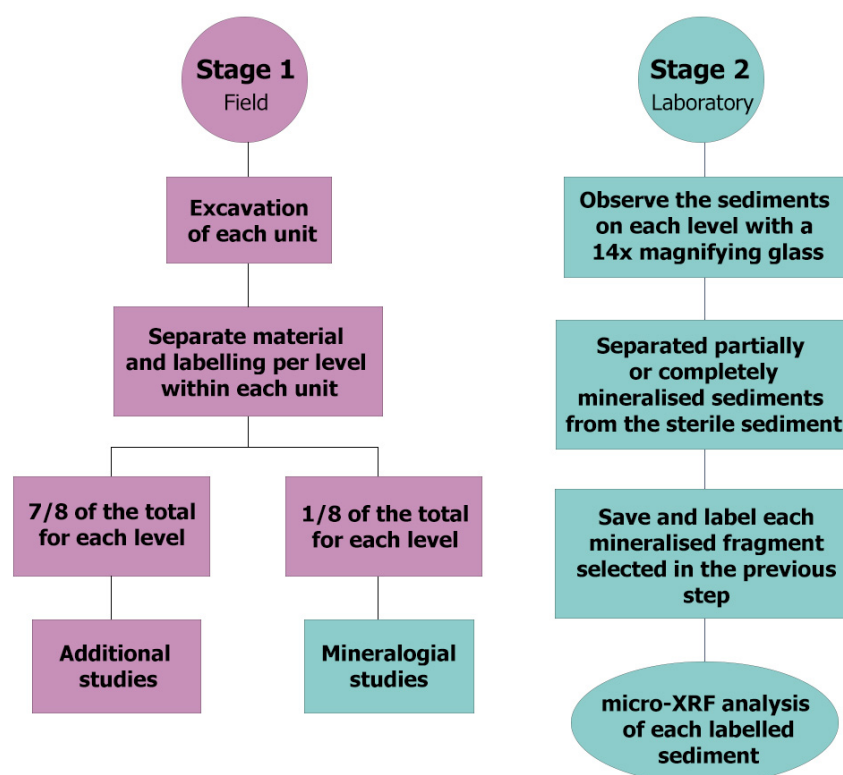


Figure 4. Outline of the analytical protocol.

Table 1. Excavated units (MC2, MC3, MC5 and MC21) by layer and level. In the code, U means a unit, C means layer and N means level.

Unit	Code	Weight (1/8 Total Weight)	Samples Analysed
MC2	U1C1N1	35.29 g	21
	U1C2N1	19.31 g	14
	U1C2N2	41.35 g	36
	U1C2N3	56.13 g	26
	U1C2N4	27.64 g	12
	U1C2N5	42.52 g	50
MC3	U1C1N1	18.74 g	6
	U1C2N1	24.14 g	21
	U1C3N1	6.43 g	5
MC5	U1C1N1	107.24 g	50
	U1C2N1	47.86 g	26
	U1C3N1	77.65 g	40
	U1C3N2	32.45 g	25
	U1C3N2-rasgo	11.28 g	9
	U1C3N3	100.34 g	17
MC21	U2C1N1	105.67 g	31
	U2C2N1	14.78 g	48
	U2C2N2	114.33 g	11
	U2C2N3	76.08 g	120

#### 4. Analytical Methodology

##### 4.1. Micro-X-ray Fluorescence ( $\mu$ -XRF)

Automated mineralogy, mineral element maps and major trace element mineral chemistry were obtained using a Bruker M4 Tornado<sup>AMICS</sup>  $\mu$ -XRF (Berlin, Germany). All these techniques could be acquired during a single analysis, with post-processing

conducted using the Bruker M4 and ESPRIT software. We selected the  $\mu$ -XRF analysis technique because this approach allows for the analysis of many samples, providing fast and detailed mineralogical information, and it is a non-destructive technique that does not require sample preparation. For high precision of elemental data, we carried out supplementary individual point analyses. Analytical conditions and times vary depending on the information required and the sample type, among other factors. The Bruker  $\mu$ -XRF allows the distribution of elements with  $Z \geq 11$  (i.e., Na and above) and trace elements (down to 20  $\mu\text{g/g}$ ) to be characterised; due to its polycapillary optics, an X-ray spot size of less than 20  $\mu\text{m}$  can be achieved. To optimally utilise this spot size, the stage has a step size resolution of 4  $\mu\text{m}$  [51].

The  $\mu$ -XRF instrument was equipped with dual XFlash<sup>®</sup> energy-dispersive silicon drift detectors (SDD) with 60 mm<sup>2</sup> active areas and Be windows with parallel signal processing (for maximum throughput). Standard instrument conditions for X-ray beam excitation of the Rh target tube are 50 kV and 600  $\mu\text{A}$ , without a primary filter. For the 60 mm<sup>2</sup> setup, this resulted in total input count rates of  $\sim$ 500 kcps on heavier elements (such as copper) and  $\sim$ 60 kcps on lighter elements (such as silicon). The current was adjusted depending on sample type and detector setup or size; the tube current could commonly range from 100 to 600  $\mu\text{A}$ . The measurement dwell time per pixel was approximately 50 ms and was based on the pulse throughput on silicates (ideally quartz) to obtain a minimum of 2000 counts per pixel for mineral identification. This requirement resulted in dwell times typically in the range of 20 to 50 ms; for the throughput of the XSPV 130 spectroscopic amplifier (equivalent to 0.8  $\mu\text{s}$  shaping time), the intensity was approximately 50 kcps for quartz and maintained a spectrometric energy resolution of 145 eV at Mn K $\alpha$ . The X-ray spot size was approximately 15  $\mu\text{m}$  and the samples were analysed using a variety of stepping intervals, e.g., 100, 50 or 20  $\mu\text{m}$ . The source X-rays interacted with the sample at a fixed position, and analytical measurements were performed by moving the highly precise and rapid servo stage [51]. The analytical conditions applied in point analyses for the protocol were also used for the next measurements, namely a time of 60 s per point analysis, tube current of 200  $\mu\text{A}$ , a polycapillary value of 50 kV and total input count rates of 130 kcps.

#### 4.1.1. Mineral Classification Using $\mu$ -XRF Data

Each of the mineral definitions in the M4 TORNADO<sup>AMICS</sup> mineral list contains numerous sub-definitions for different specific minerals. For example, the Cu-sulphides group contains definitions for chalcopyrite ( $\text{CuFeS}_2$ ), bornite ( $\text{Cu}_5\text{FeS}_4$ ), chalcocite ( $\text{Cu}_2\text{S}$ ), etc., each of which has a fixed composition and, thus, a relatively robust classification in the standard mineral library. In other cases, minerals or mineraloids must be added to the database due to their rarity, e.g., black-Cu and green-Cu ores [51], or due to variable compositions as a result of solid solution, e.g., silicates such olivine, pyroxenes, feldspars, etc. This classification is important if the  $\mu$ -XRF results are to be used to calculate elemental concentrations or behaviour. When examining spectra for trace elements, quantifying solid solutions or confirming stoichiometric minerals, the standardised parameter quantification in the M4 software provided precise results. However, for higher accuracy, the imperial or Polynomial methods were also used with a large pure element and mineral standard database acquired with the instrument.

#### 4.1.2. Elemental Maps and Point Analyses Using $\mu$ -XRF

To characterise the samples, an elemental map was made to gain a general overview of each sample's major and trace elements, and individual point analysis was used to refine the results. The samples were observed macroscopically and based on the macroscopic features of the minerals, we selected the point upon which to conduct the analysis. The point analyses were made on the predominant mineral in each sample. This decision does not exclude the fact that some samples contained a mixed association of minerals; however, if a sample visually contained  $>50\%$  of a particular mineral phase, the point analysis was conducted on this mineral and the sample was classified as this mineral type.

#### 4.2. X-ray Diffraction (XRD)

XRD is an analytical technique that allows the crystalline phases of a solid to be determined by bombarding the sample with an X-ray beam at varying angles [52]. To determine the mineralogy of a sample, the sample must first be pulverised and then placed in a briquette. In our analytical protocol, this technique was used in addition to  $\mu$ -XRF to confirm the mineralogy of the samples. Samples were prepared in the Applied Geochemistry Laboratory, Geological Sciences Department, Universidad Católica del Norte, Chile. The analytical conditions are presented in Table 2.

**Table 2.** The operating conditions of an automatic and computerised X-ray Diffractometer, Bruker brand, Model D8 Advance, are presented.

Analytical Parameter	Selection
Goniometer	Vertical Bragg–Brentano
Radiation	Cu Ka1 ( $\lambda = 1.5406 \text{ \AA}$ )
Voltage	40 kv
Intensity	30 mA
Detector	Scintillation counter
Secondary monochromator	Not applicable
Slits	1 mm/1 mm/0.2 mm
Scan range	3–70° $2\theta$
Step size	0.020° $2\theta$
Step time	1.10 s
Data base	ICDD (International Centre for Diffraction Data)
Quantification program	TOPAS (Total Pattern Analysis Software)

#### 4.3. Raman Spectroscopy

Raman spectroscopy is based on the interaction of light from a laser with chemical bonds in a sample. Raman spectra are unique to each chemical composition and provide qualitative and quantitative information about a material. The Raman spectra of minerals are very well defined, as they have a specific crystalline structure. These spectra can be found in freely accessible databases. Like  $\mu$ -XRF, this technique is advantageous in that it is non-destructive, which is particularly important in some archaeological contexts. In our protocol, we applied Raman spectroscopy to confirm the mineralogy of the anomalous samples, which corresponded to 5 out of 568 (i.e., <1% of the total number of samples analysed); this non-destructive approach was favoured as the preservation of these archaeological samples is essential for future studies. The samples were analysed using the He-Ne 633 nm laser.

#### 4.4. Automated Mineralogy (QEMSCAN)

QEMSCAN<sup>®</sup> (Quantitative Evaluation of Materials by Scanning Electron Microscopy) analysis measures the mineralogical variability of a sample based on its micrometre-scale geochemistry. The analytical results obtained through the automated mineralogy approach are received and analysed in the form of spectra signals, where each mineral has a specific spectrum according to its chemical composition. This technique provides information relating to mineralogy, mineral textures and the relative content of chemical elements through mineralogical maps [28]. Each sample was mounted in a 30 mm circular epoxy resin briquette; the briquettes were then cured, polished and carbon-coated prior to conducting the automated mineralogical analysis. The equipment was used in Field Scan mode [28] with the following parameters: field size 2500  $\mu\text{m}$ , point spacing 5.0  $\mu\text{m}$  and 500 points across the field.

#### 4.5. Technological Study

To understand the diversity of minerals in the social context of their production, we also carried out a technological study regarding the Turi assemblages, adapting the

methodologies that are typically used for lithic industries [53]. The study was aimed at understanding the manufacturing techniques and *chaîne opératoire* [53] of the final products. In the first stage, the assemblages were separated according to the variability of their minerals; subsequently, they were classified into general technological categories (cores, blanks, gangue-waste and final products), and the pieces were then measured and weighed. By comparing archaeological artifacts with the results of our experimental analyses, the production techniques were identified, and the different stages of the operational chains were reconstructed.

In order to identify the reduction technique, we carried out experimental tests on minerals. These tests were aimed at distinguishing the use of grinding (used in metallurgical industries and “challa” offerings of minerals) from knapping techniques, generally used in lapidary industries. As raw materials, chrysocolla, atacamite, turquoise and green onyx from local sources were employed. The following techniques were performed on these minerals: (1) hard mineral percussion (stone hammer); (2) hard mineral percussion supported on an anvil (bipolar percussion or split fracture); (3) organic soft tangential percussion with a wooden hammer (carob or algarrobo); and (4) pressure with a bone compressor (vicuña metapodium) [54,55]. A pumice pebble was used for platform preparation. In addition, we ground the minerals on a basalt stone anvil, using a hand-prepared granite grinding approach to reduce the mineral to fragments of 5 mm diameter.

Through a comparison of the technical stigmas (impact point, percussion cone, bulb, waves, lancets and lip) of the debris and negatives based on both experimental references and the archaeological samples, the different reduction techniques were recognised. In addition, taphonomic processes such as macroscopic fractures and abrasion were evaluated using a microscope.

## 5. Results

### 5.1. Mineralogy of Samples with Micro-X-ray Fluorescence, X-ray Diffraction and Raman Spectroscopy

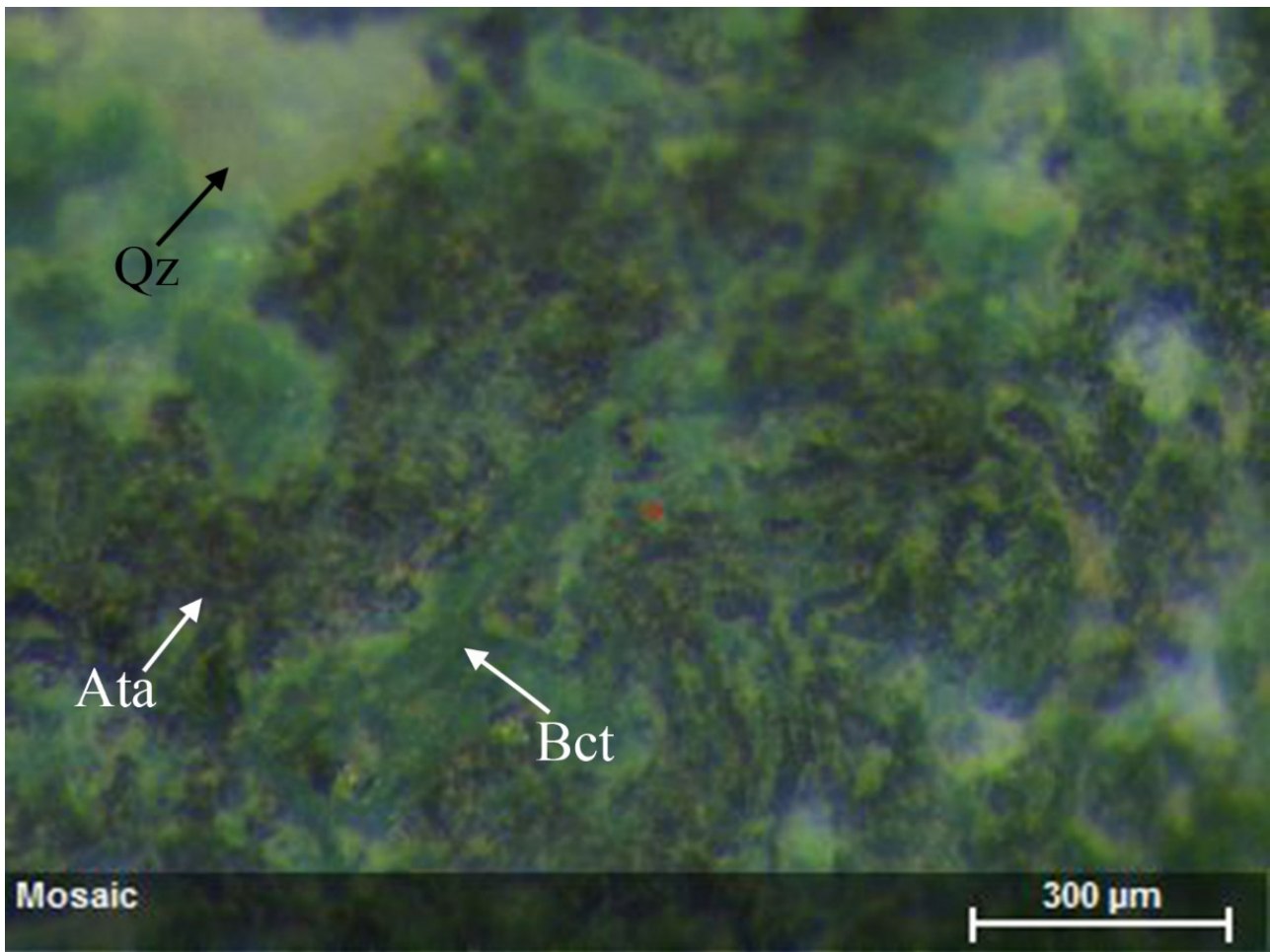
The predominant mineralogy corresponds to an association between atacamite ( $\text{Cu}_2\text{Cl}(\text{OH})_3$ ) and brochantite ( $\text{Cu}_4\text{SO}_4(\text{OH})_6$ ), dominated by atacamite (Figure 5).

In addition, some samples were classified as gangue (188 out of 568; i.e., quartz and feldspars with copper mineralisation or dyed blue or green). These samples were analysed to understand the source of the copper ores more precisely and thoroughly. In the point analysis of samples classified as atacamite, two peaks in the spectrum were clearly observed, i.e., Cl and Cu (Figure 6b). These samples are not characterised by any distinctive trace elements. For the samples classified as brochantite, two peaks were observed in the spectrum, corresponding to S and Cu (Figure 7b).

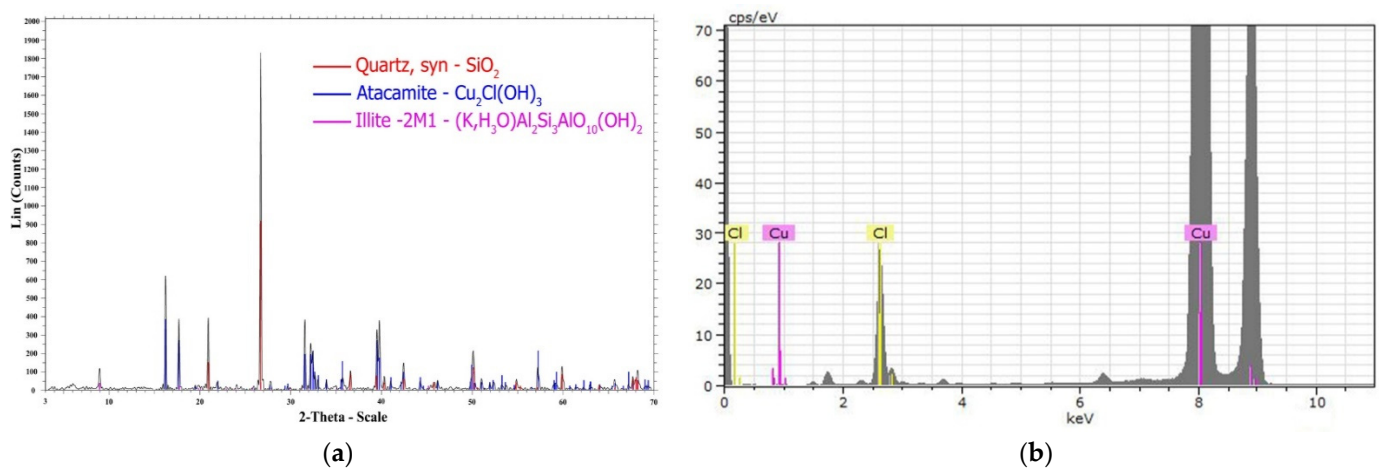
The mineralogy of both minerals was confirmed with XRD (Figures 6a and 7a). The mineral gangue is almost exclusively composed of quartz; the corresponding point analyses indicated that quartz contains Sr and Zn as trace elements. In all excavated units (i.e., MC2, MC3, MC5 and MC21), the mineralised samples represent the highest percentage of the analysed samples. Layer 2 contains the highest proportion of copper ore samples (>60% of the total samples). In all units, the layers are numbered with increasing depth, with layer 1 being the shallowest and 3 being the deepest.

In unit MC2, there are two natural layers, from which a total of 159 samples were analysed. In layer 1 (superficial), a total of 21 samples were analysed, of which eight samples were classified as atacamite and six as brochantite; the remaining seven samples correspond to gangue minerals. In layer 2, a total of 138 samples were analysed, of which 78 were classified as atacamite, 21 were classified as brochantite and 39 samples were gangue minerals (Figure 8a).

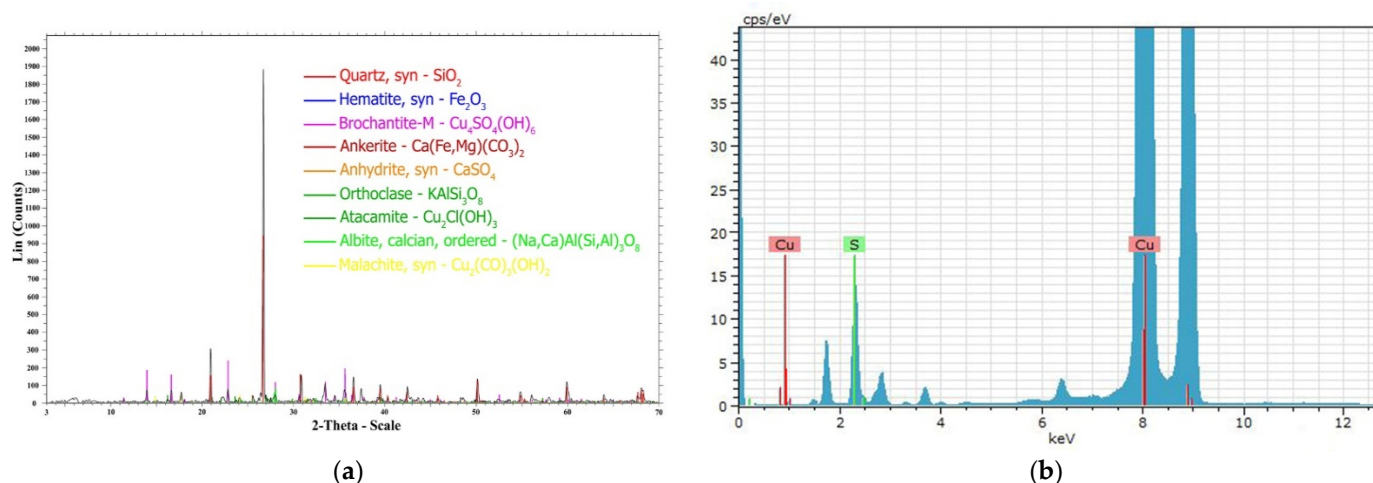




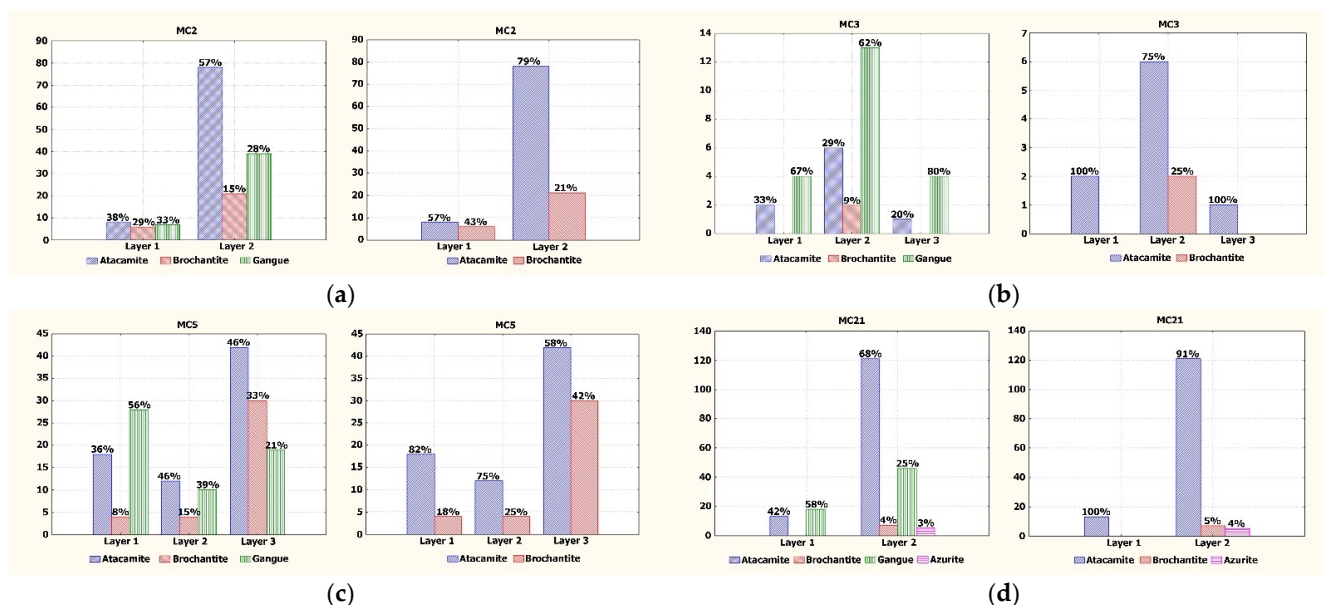
**Figure 5.** Atacamite/brochantite association common in the samples. Atacamite is the dominant copper mineral. Dark green is atacamite and light green is brochantite. Code sampleTu\_U1C1N1\_x11 from mineral concentration MC2, layer 1, level 1. Abbreviations: Qz: quartz, Ata: atacamite, Bct: brochantite.



**Figure 6.** Atacamite sample, code Turi\_U2\_C2\_N3\_m10 from mineral concentration unit MC21, layer 2, level 3. (a) XRD spectrum of atacamite. (b)  $\mu$ -XRF spectrum of Cl and Cu.



**Figure 7.** Brochantite sample, code Turi\_U2\_N3\_m76 from mineral concentration unit MC21, layer 2, level 3. (a) XRD spectrum of brochantite. (b)  $\mu$ -XRF spectrum of S and Cu.



**Figure 8.** Abundance of minerals in each mineral concentration. (a) Unit MC2. On the left: percentages of mineralogical results including gangue are shown. In layer 1 and layer 2, atacamite predominates over brochantite and gangue. On the right: the percentages of minerals excluding gangue are shown. In layer 1, the percentage of samples classified as atacamite and brochantite is similar. On the other hand, in layer 2, there is a significant presence of atacamite over brochantite. (b) Unit MC3. On the left: layers 1, 2 and 3 show a predominance of sediments classified as gangue, i.e., quartz stained blue or with very little mineralisation in the form of patina. On the right, excluding the gangue, there is a predominance of atacamite in all the layers of the unit. (c) Unit MC5. On the left: layer 1 shows a predominance of gangue over mineralised samples. In layers 2 and 3, the percentage of gangue decreases, and the predominant mineralisation is atacamite. On the right: excluding gangue, the predominance of atacamite over brochantite is observed in all the layers of the unit. (d) Unit MC21. Right: in layer 1, gangue is more abundant than atacamite. In layer 2, there is a predominance of atacamite over gangue and, in addition, samples of azurite/chrysocolla were found, representing 3% of the total samples analysed from the layer. On the right: the graphs excluding gangue show that in both layers, atacamite is the predominant mineral. The representation of azurite/chrysocolla mineralisation is very low with respect to atacamite/brochantite and is therefore considered anomalous.

The MC3 unit contains three layers in which a total of 32 samples were analysed. In layer 1 (surface level), a total of six samples were analysed, of which two samples were



classified as atacamite and the rest were gangue minerals. In layer 2, a total of 21 samples were analysed, six of which were classified as atacamite, two as brochantite and thirteen samples were gangue minerals. In layer 3, a total of five samples were analysed, one of which was classified as atacamite, and the other four samples were gangue minerals (Figure 8b).

The MC5 unit comprises three layers, with a total of 167 samples analysed. In layer 1 (surface level), a total of 50 samples were analysed, of which 18 samples were classified as atacamite and 4 as brochantite; the remaining 28 samples were gangue minerals. In layer 2, a total of 26 samples were analysed, of which 12 were classified as atacamite, 4 as brochantite and 10 as gangue minerals. In layer 3, 91 samples were analysed, of which 42 were classified as atacamite, 30 samples were classified as brochantite, and 19 samples were gangue minerals (Figure 8c).

The MC21 unit has two layers, and a total of 210 samples were analysed. In layer 1 (surface level), a total of 31 samples were analysed, of which 13 samples were classified as atacamite and the remaining 18 samples were gangue minerals. In layer 2, a total of 179 samples were analysed, 121 of which were classified as atacamite, 7 were classified as brochantite, 5 were classified as azurite and 46 samples were gangue minerals (Figure 8d). Notably, only this unit contained azurite. In addition, in macroscopic observations of the azurite samples, chrysocolla and a dark mineral phase were recorded. To confirm these macroscopic observations, we used Raman spectroscopy and found that the samples contained azurite (Figure 9a), malachite (Figure 9b), manganosite (Figure 9c) and amorphous chrysocolla (Figure 9d).

### 5.2. Mineralogical Maps with Automated Mineralogy (QEMSCAN)

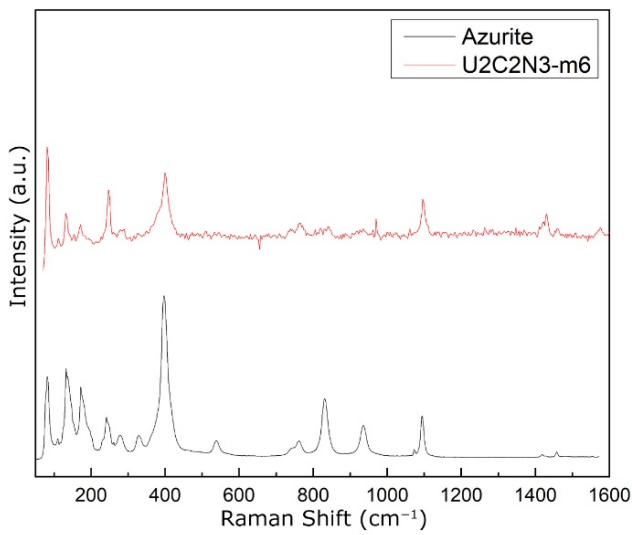
The modal mineralogy is summarised graphically in Figure 10 and numerically in Table 3. The samples contain a mixture of copper mineralisation and gangue minerals (e.g., silicates). Cu mineralisation extent varies between 0.43% (CDG960Q3) and 47.51% (CDG960Q5) and the mineral species present are mostly chrysocolla, atacamite and brochantite, except in sample CDG960Q5, where Cu mineralisation is mainly attributed to minerals such as cuprite/tenorite and chalcocite/digenite (Figure 11, Table 4). The content of other minerals is varied, with some samples containing Fe oxides, for example, CDG960Q1, which has an Fe oxide content of 0.31% (Figure 12, Table 5).

**Table 3.** QEMSCAN<sup>®</sup> modal mineralogy: grouped by Cu-bearing mineral and common gangue minerals.

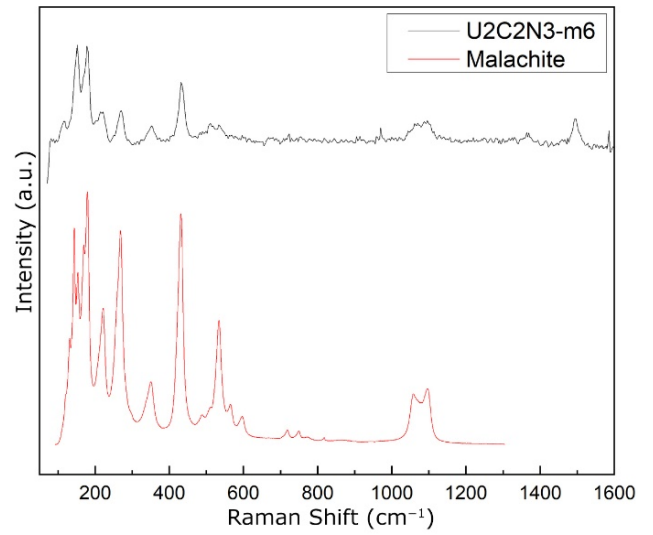
Mineral Mass (%)	CDG960Q01	CDG960Q02	CDG960Q03	CDG960Q04	CDG960Q05
Chalcocite/Digenite	0.34	0.02	0.00	0.43	7.67
Covellite	0.00	0.00	0.00	0.03	0.38
Native Copper	0.00	0.00	0.00	0.00	2.00
Chrysocolla	0.22	1.96	0.65	2.86	5.07
Cuprite/Tenorite	0.00	0.00	0.08	0.00	17.52
Malachite/Azurite	0.00	0.01	0.06	0.01	1.24
Brochantite	0.00	0.00	0.11	2.36	32.56
Atacamite	0.30	0.00	0.00	2.38	0.17
Other Cu Minerals	0.14	0.01	0.02	0.17	0.66
Cu-bearing Phyllosilicates	0.40	0.33	0.19	1.56	8.24
Cu-bearing Fe Oxide/Hydroxides	0.02	0.04	0.09	0.10	0.07
Cu-bearing Wad	0.23	0.24	0.11	0.97	5.62

Table 3. Cont.

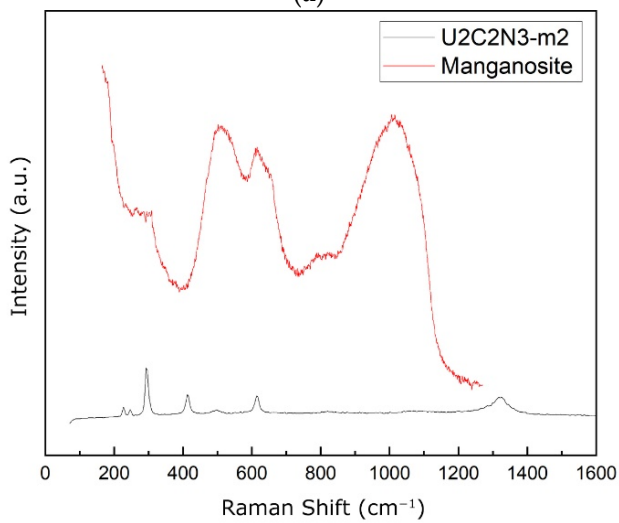
Mineral Mass (%)	CDG960Q01	CDG960Q02	CDG960Q03	CDG960Q04	CDG960Q05
Hematite	0.22	0.00	0.00	0.00	0.01
Other Fe Oxides/Hydroxides	0.02	0.00	0.01	0.00	0.00
Gypsum/Anhydrite/Bassanite	4.95	0.23	0.01	0.01	0.01
Alunite	20.43	0.01	0.01	0.01	0.81
Quartz	43.14	92.05	90.96	56.42	8.86
Feldspars (Orthoclase, Plagioclase)	11.72	0.63	0.65	27.27	0.81
Kaolinite Group	5.56	0.01	0.01	0.43	0.14
White Micas (Muscovite, Sericite and Illite)	5.57	4.23	6.71	4.62	7.83
Smectite Group (Montmorillonite, Nontronite)	3.91	0.01	0.02	0.10	0.07
Pyrophyllite/Andalusite	2.51	0.01	0.01	0.03	0.04
Others	0.32	0.22	0.29	0.26	0.20
Total	100.00	100.00	100.00	100.00	100.00



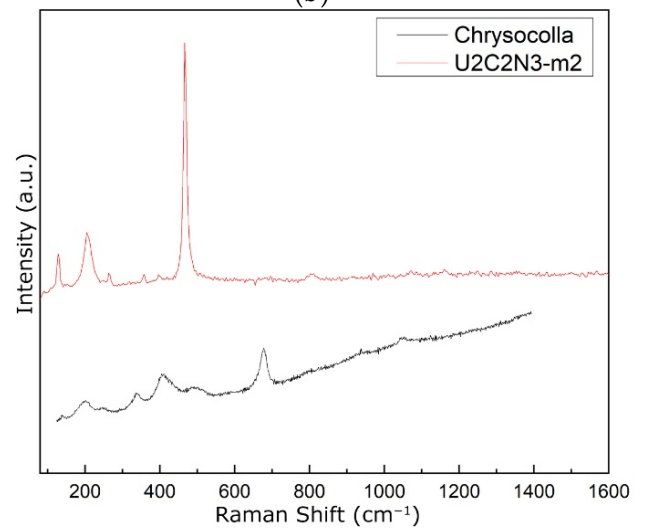
(a)



(b)

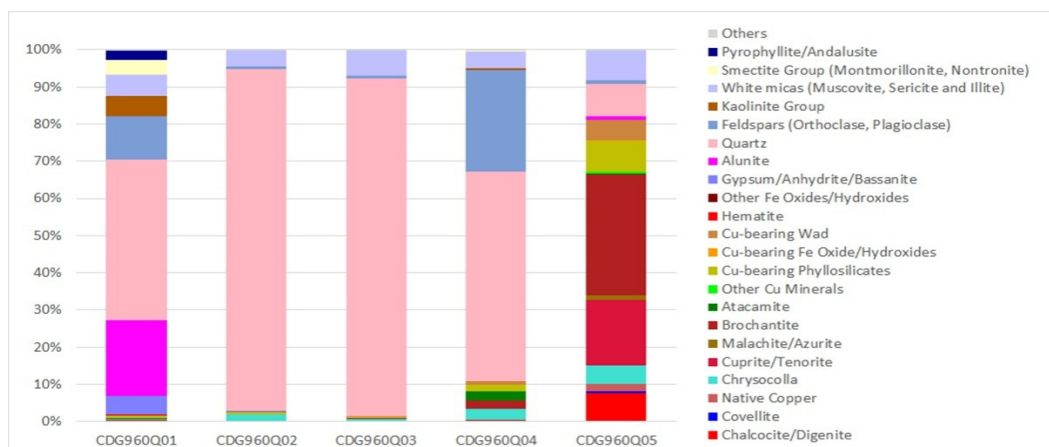


(c)

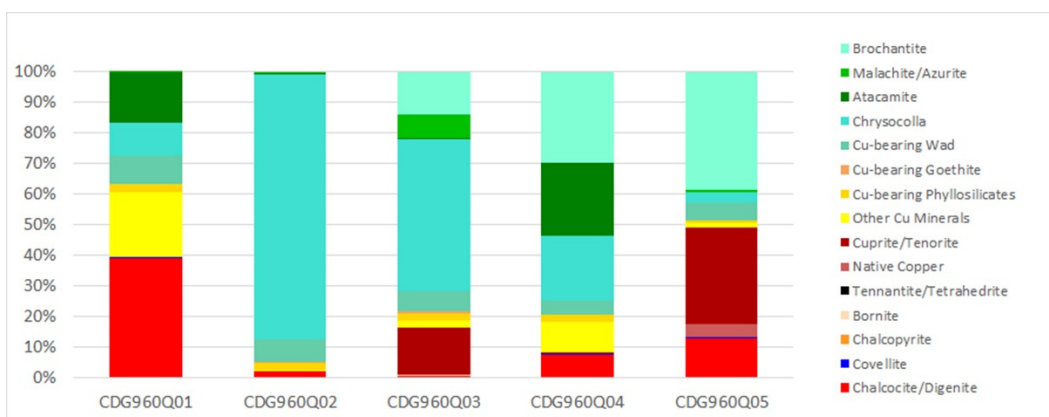


(d)

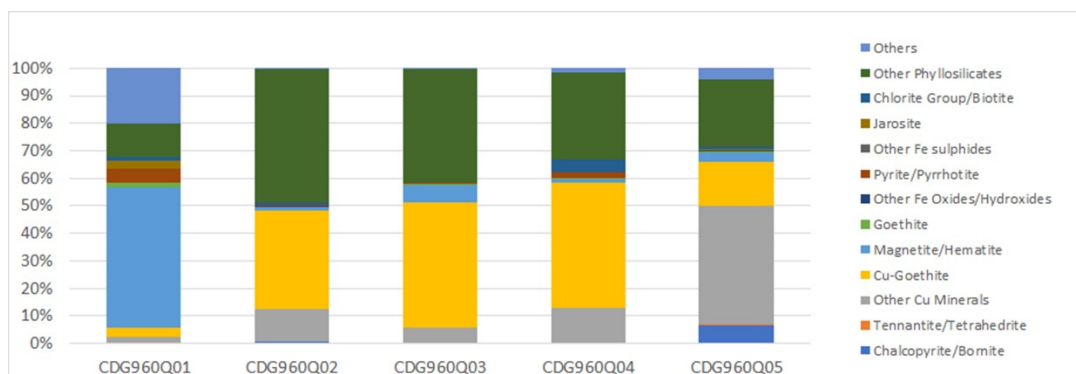
Figure 9. Raman spectrum. (a) azurite; (b) amorphous malachite; (c) manganosite; (d) amorphous chrysocolla.



**Figure 10.** QEMSCAN modal mineralogy: grouped by Cu-bearing mineral and common gangue minerals. Samples came from the following sites: CDG960Q01: Chu-2 (located close to Chuquicamata-Radomiro Tomic mining district). CDG960Q02: Chu-4 (located close to Chuquicamata-Radomiro Tomic mining district). CDG960Q03: RPC (*Pukara de Turi*). CDG960Q04: MC2 (*Pukara de Turi*). CDG960Q05: AB-20 (located close to El Abra-Conchi mining district).



**Figure 11.** QEMSCAN modal mineralogy: distribution of Cu supply by mineral species. Samples came from the following sites: CDG960Q01: Chu-2 (located close to Chuquicamata-Radomiro Tomic mining district). CDG960Q02: Chu-4 (located close to Chuquicamata-Radomiro Tomic mining district). CDG960Q03: RPC (*Pukara de Turi*). CDG960Q04: MC2 (*Pukara de Turi*). CDG960Q05: AB-20 (located close to El Abra-Conchi mining district).



**Figure 12.** QEMSCAN modal mineralogy: distribution of Fe supply by mineral species. Samples came from the following sites: CDG960Q01: Chu-2 (located close to Chuquicamata-Radomiro Tomic mining district). CDG960Q02: Chu-4 (located close to Chuquicamata-Radomiro Tomic mining district). CDG960Q03: RPC (*Pukara de Turi*). CDG960Q04: MC2 (*Pukara de Turi*). CDG960Q05: AB-20 (located close to El Abra-Conchi mining district).

**Table 4.** QEMSCAN modal mineralogy: distribution of Cu supply by mineral species.

Mineral Mass (%)	CDG960Q01	CDG960Q02	CDG960Q03	CDG960Q04	CDG960Q05
Chalcocite/Digenite	0.27	0.01	0.00	0.34	6.06
Covellite	0.00	0.00	0.00	0.02	0.26
Chalcopyrite	0.00	0.00	0.00	0.00	0.01
Bornite	0.00	0.00	0.00	0.00	0.00
Tennantite/Tetrahedrite	0.00	0.00	0.00	0.00	0.02
Native Copper	0.00	0.00	0.00	0.00	2.00
Cuprite/Tenorite	0.00	0.00	0.07	0.00	14.97
Other Cu Minerals	0.14	0.00	0.01	0.45	0.68
Cu-bearing Phyllosilicates	0.02	0.02	0.01	0.10	0.47
Cu-bearing Goethite	0.00	0.00	0.00	0.00	0.00
Cu-bearing Wad	0.06	0.06	0.03	0.21	2.67
Chrysocolla	0.07	0.66	0.22	0.95	1.61
Atacamite	0.11	0.00	0.00	1.07	0.10
Malachite/Azurite	0.00	0.00	0.03	0.01	0.36
Brochantite	0.00	0.00	0.06	1.32	18.30
Total	0.69	0.76	0.43	4.48	47.51

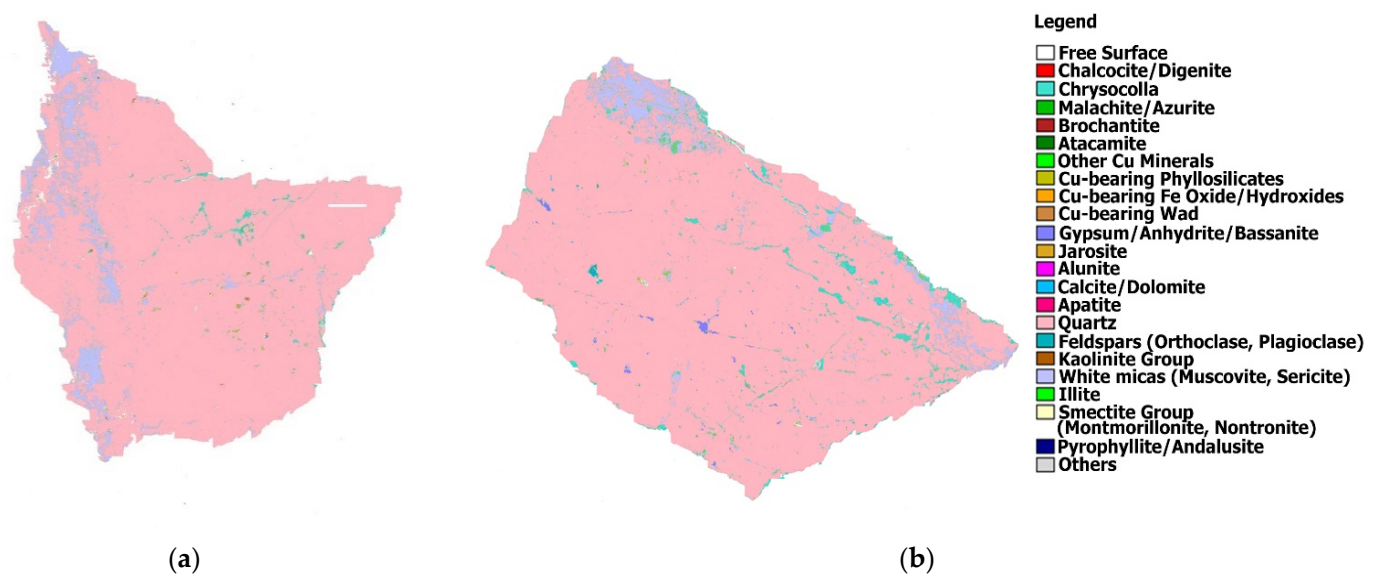
**Table 5.** QEMSCAN modal mineralogy: distribution of Fe supply by mineral species.

Minerals	CDG960Q01	CDG960Q02	CDG960Q03	CDG960Q04	CDG960Q05
Chalcopyrite/Bornite	0.00	0.00	0.00	0.00	0.02
Tennantite/Tetrahedrite	0.00	0.00	0.00	0.00	0.00
Other Cu Minerals	0.01	0.01	0.01	0.01	0.11
Cu-Goethite	0.01	0.02	0.05	0.05	0.04
Magnetite/Hematite	0.16	0.00	0.01	0.00	0.01
Goethite	0.00	0.00	0.00	0.00	0.00
Other Fe Oxides/Hydroxides	0.00	0.00	0.00	0.00	0.00
Pyrite/Pyrrhotite	0.02	0.00	0.00	0.00	0.00
Other Fe Sulphides	0.00	0.00	0.00	0.00	0.00
Jarosite	0.01	0.00	0.00	0.00	0.00
Chloride Group/Biotite	0.00	0.00	0.00	0.01	0.00
Other Phyllosilicates	0.04	0.03	0.04	0.04	0.06
Others	0.06	0.00	0.00	0.00	0.01
Total	0.31	0.06	0.11	0.12	0.25

Mineral fragments collected from the mining sites have textures and mineralogies which are macroscopically very similar to those found in the *Pukara* de Turi excavations. These findings were confirmed by analytical results using automated mineralogy (QEMSCAN).

The samples exhibit a wide range of copper minerals as well as gangue mineralogy. Although these results do not indicate the mineralisation percentages of the parent sources, they can, nonetheless, be used as a clear guide for comparison.

Through this technique, we verified that the mineralised rock fragment found in the RPC site has the same texture and mineralogy as a fragment from the archaeological site Chu-4 [7,56], located very close to the active Chuquicamata mine, one of the largest copper mines in the world. The fragment from the RPC site (Figure 13a) is dominated by quartz (90.9%); in addition, the sample contains 0.65% feldspars, 0.65% chrysocolla and 6.71% white micas (muscovite, sericite and illite). In comparison, the sample from the Chu-4 site (Figure 13b) shows very similar mineral content, specifically 92.05% quartz, 0.63% feldspars, 1.96% chrysocolla and 4.23% white micas.



**Figure 13.** QEMSCAN results (2500  $\mu\text{m}$  scale view). Both samples show similar percentages of mineralisation in quartz, feldspars, white micas and chrysocolla. (a) Sample CDG960Q03, which corresponds to a fragment found in an Inca architecture of the *Pukara de Turi* (RPC). (b) Sample CDG960Q02 corresponding to a mineral found in the Chu-4 (located close to Chuquicamata-Radomiro Tomic mining district).

In addition, we analysed one mineral fragment from the archaeological site AB-20 [7] (located very close to the pre-Hispanic mining district El Abra-Conchi) and two mineral fragments from the MC2 excavation of *Pukara de Turi*. The selected samples are macroscopically very similar (Figure 14a,b). Both show evident copper mineralisation (brochantite (18.30%); cuprite/tenorite (14.97%); chalcocite/digenite (6.06%); Cu-bearing wad (2.67%); native copper (2.00%); chrysocolla (1.61%) in a quartziferous host rock with iron oxides. The samples mineralogy was confirmed using QEMSCAN automated mineralogy (Figure 14c).

Finally, we analysed a sample from Chu-2 (located close to the Chuquicamata-Radomiro Tomic mining district [7,56]) (Figure 15b(2)) and compared it with a sample from the MC2 excavation of *Pukara de Turi* (Figure 15b(1)), as both are macroscopically very similar (Figure 15a(1),(2)). The sample from *Pukara de Turi* has a high percentage of gangue minerals (27.27% feldspars and 56.42% quartz), whereas the sample from the Chu-2 site also contains alunite (11.72% feldspars, 43.14% quartz and 20.43% alunite). Therefore, although both samples macroscopically resemble each other, their mineralogies differ. However, a relationship between the two samples cannot be ruled out; alunite is an alteration mineral formed by the reaction of acid with a rock rich in potassium feldspars or orthoclase. This suggests that the two samples may be genetically similar; the rock from the archaeological excavation at MC2 in *Pukara de Turi* is the fresh, unaltered rock, while the rock from the Chu-2 site is the same rock type but with a degree of alteration, where a percentage of the feldspars are altered to alunite.

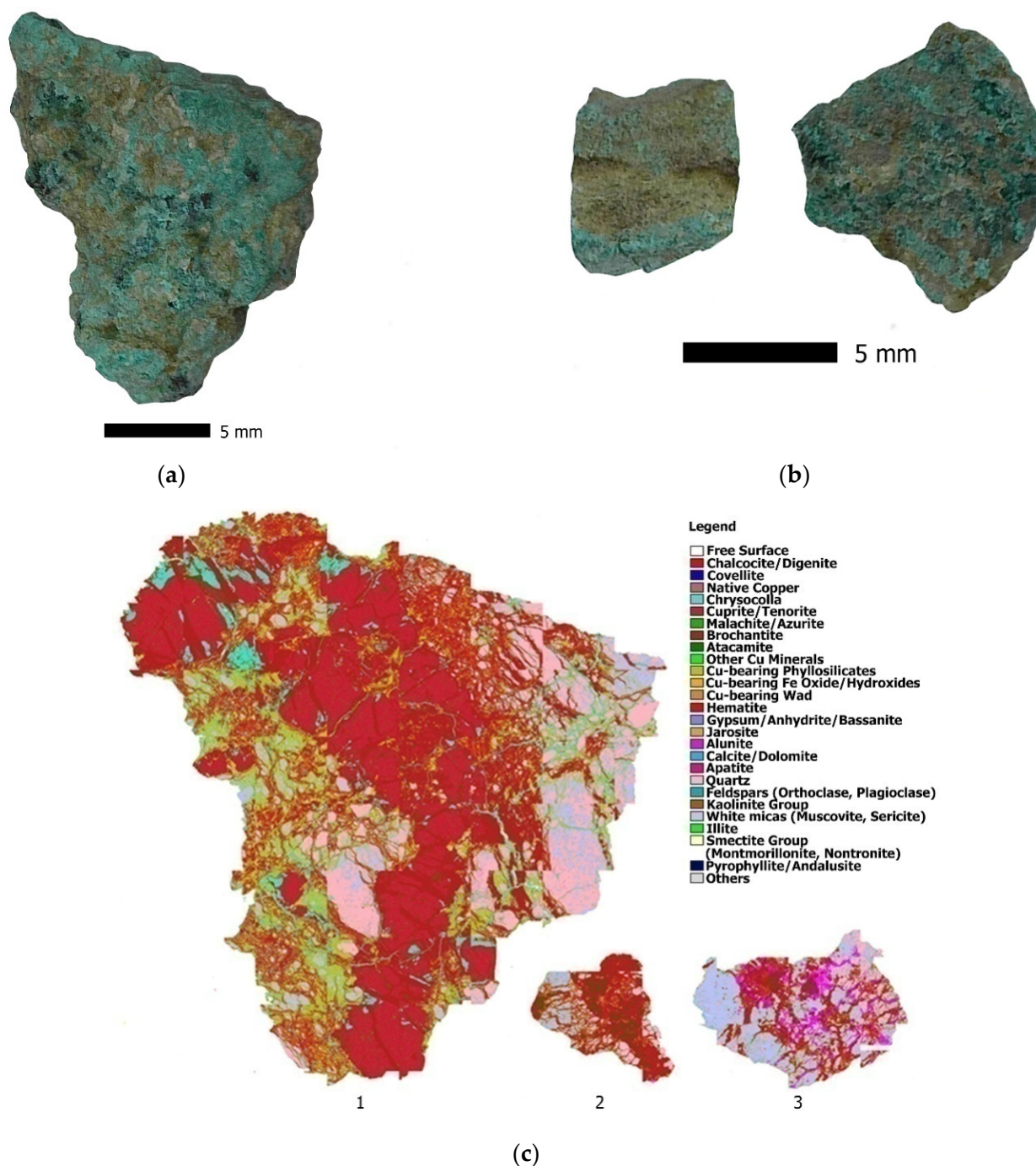
### 5.3. Technological Study of the Copper Minerals

After a technological study, it was found that the main objective of the production appeared to obtain small angular fragments of atacamite/brochantite up to 5 mm in length.

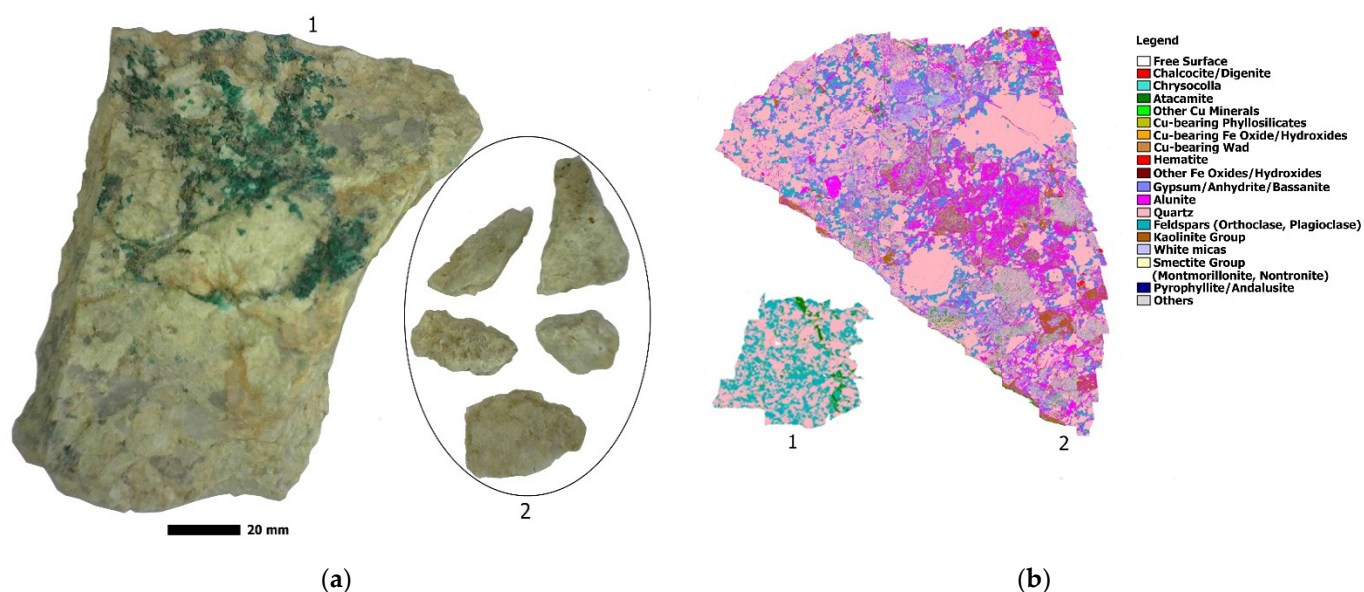
The exceptional finding of a core in this raw material (Complex 11, Room 279) suggests that the production modes were based on the roughing of single-platform cores with an orthogonal *débitage* surface distributed along one of the faces (Figure 16). The technical negatives of the detachments on this piece, as in the related knapping debris, suggest that the predominant technique of detachment was direct hard percussion, probably on an anvil at an angle between  $80^\circ$  and  $90^\circ$ . This mode of processing allows split fractures of the raw material to be obtained (also known as bipolar knapping in the Anglo-Saxon literature [53,57]).



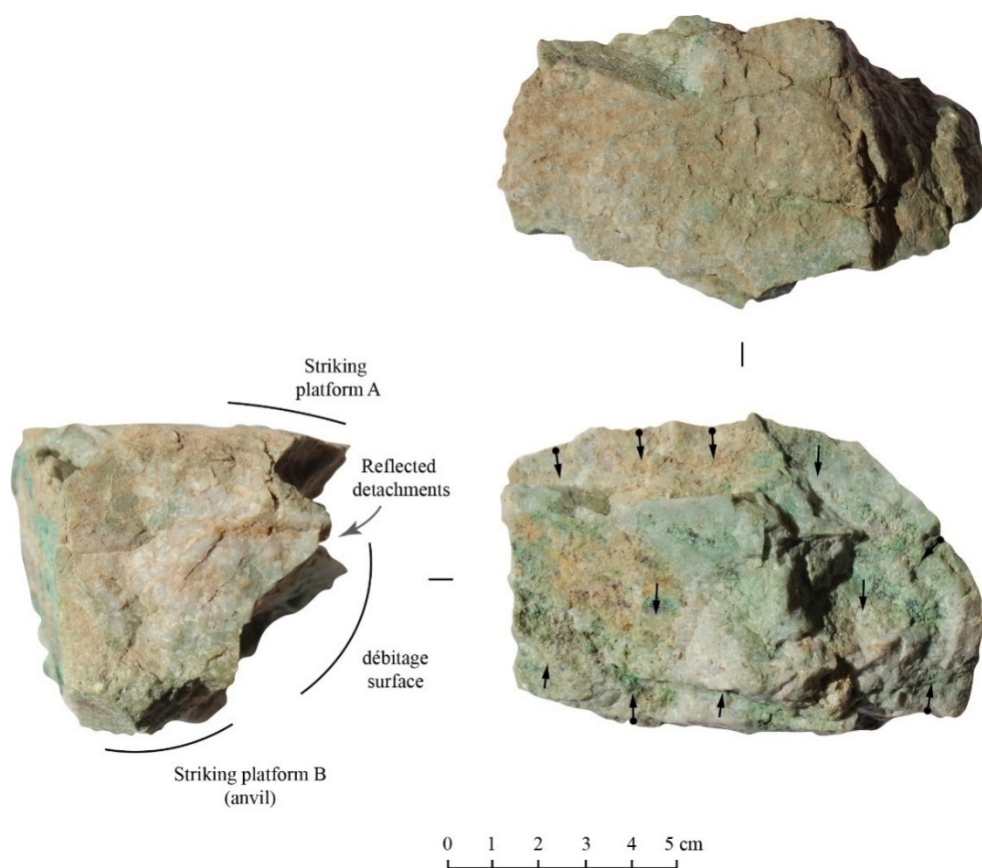
Based on our experimental tests, despite the scarce samples, this technique appears to be the most suitable for working on heterogeneous rocks with high crystal content.



**Figure 14.** QEMSCAN results for the samples from AB-20 (located close to El Abra-Conchi mining district) and from the MC2 excavation of the *Pukara* de Turi. The samples macroscopically present similarities that were corroborated by the analyses carried out. (a) Macroscopic photograph of sample CDG960Q05 from site AB-20. (b) Macroscopic photographs of sediments from MC2. (c) Mineralogical maps: (1) sample CDG960Q05 (sample of approximately 2 cm in its maximum dimension, 2500  $\mu\text{m}$  scale), (2) sample Turi\_U1C2N5\_x16 (sample of approximately 0.5 cm in its maximum dimension, 2500  $\mu\text{m}$  scale), (3) sample Turi\_U1C2N2\_3 (sample approximately 0.7 cm in maximum dimension, scale 2500  $\mu\text{m}$ ).



**Figure 15.** QEMSCAN results for samples from Chu-2 (located close to Chuquicamata-Radomiro Tomic mining district) and from the MC2 excavation of the *Pukara* de Turi. (a) Samples macroscopically present similarities that were corroborated by the analyses carried out: (1) macroscopic photograph of sample CDG960Q01 from site Chu-2, (2) macroscopic photographs of sediments from MC2. (b) Mineralogical maps: (1) sample CDG960Q04 (sample from MC2 of approximately 0.2 cm in its maximum dimension, 2500  $\mu\text{m}$  scale), (2) sample CDG960Q01 (sample from Chu-2 of approximately 1 cm in its maximum dimension, 2500  $\mu\text{m}$  scale).



**Figure 16.** Simple platform core with split fractures and reflected detachments.

The blanks obtained were mainly backed flakes or slices that provided more manageable raw material volumes. However, both the detachment technique and the heterogeneity



of the raw material led to a high fracture rate and reflected and step damage, along with a large amount of small and medium debris. The blanks and resulting fragments were subsequently crushed and ground on a hard surface using a grinding stone, with the aim of selecting and isolating the areas with the highest percentage of ore and separating them from the less productive areas. In this phase of the operational chain, the final products were obtained. The abrasion and rounding of angles, in addition to the cracked surfaces observed in most fragments under a magnifying glass, may have originated during this processing phase and, therefore, could serve as discriminant criteria. However, taphonomic processes should not be ruled out; mechanical weathering may have occurred during transport due to the percussion of fragments or due to post-depositional factors such as trampling and wind abrasion.

## 6. Discussion

Throughout the total samples analysed, a consistent atacamite/brochantite ratio is observed in all the layers of the units. This association of minerals is a common paragenesis recorded in the copper veins of the Atacama Desert. Quartz fragments with atacamite and/or brochantite are part of the gangue contained in mineralised veins. The size of the samples is homogeneous with a maximum dimension not exceeding 10 mm, indicating that these fragments were previously crushed. The 568 samples analysed indicate that those selected from the vein were atacamite and that the quartz was a waste product. The results also indicate that the atacamite/brochantite mineral association is present in all the mineralised samples analysed, suggesting that the crushed minerals from the *Pukara de Turi* come from the same mineral source. Furthermore, the vein sample found in Complex 11 is compositionally identical to the crushed material from the units and allows some of the characteristics of the source to be inferred. Although these results do not represent samples from an in situ mine, they can, nonetheless, be used as a guide to relate the samples to their exact source.

To constrain the geographical origin of the samples, specific analytical techniques (i.e., PIXE, Radiogenic and Stable Isotopy) are required to understand the geochemical markers of specific mineral sources. However, recent studies have shown that isotopes in veins do not necessarily match those obtained in the porphyry copper ore; there may also be no large isotopic variations between geographically distant locations [58]. Instead, the analytical techniques applied in this study represent an adequate tool to search for other characteristics in the studied minerals. First, it is necessary to establish the mineral associations—generally, these characteristics will allow us to rule out possible geological sources and narrow down potential provenances. Although mineral–source correlations could not be found in all cases, thanks to the mineralogical study and analytical techniques usually applied in geology, we were able to infer archaeological conclusions that allowed us to determine the minerals' raw materials and understand their consumption. In provenance studies, it is necessary to compare more than one sample from the same deposit. Furthermore, there is the potential that veins from large mines may no longer exist; thus, it is necessary to access museum collections that may hold samples of old veins from the 19th or early 20th century to make comparisons with ores from pre-Hispanic mining sites. This aspect is essential—contemporary mining does not necessarily represent the minerals that were mined in ancient times. There are few pre-Hispanic mines that have not been destroyed with the advancement of modern mining. El Abra and Cerro Verde are exceptional, and their conservation is no small feat for pre-Hispanic mining archaeology. However, the mineral wealth of the Atacama Desert presents a great challenge, as copper deposits are not an anomaly. For example, atacamite and brochantite are common minerals in the supergene zones of different deposits in northern Chile, such as those at El Abra, Mantos Blancos, Chuquicamata, Radomiro Tomic, La Escondida, among others [23,24,59–63]. While the geological literature is a guide and a first start in the search for provenance, the integration of these constraints with archaeological information will allow us to come closer to defining the minerals' geological sources.

### 6.1. Atacamite/Brochantite Association

Some aspects of mineral formation are relevant to understanding the nature of the atacamite/brochantite ratio. Atacamite is a copper hydroxy-chloride mineral ( $\text{Cu}_2\text{Cl}(\text{OH})_3$ ) present in the supergene mineralisation zone; its formation, as a result of supergene enrichment, requires a hyper-arid climate, and the water filtering through the deposit must also be relatively saline [61,62]. Atacamite/brochantite paragenesis is fairly common as both minerals precipitate under alkaline conditions [40,62]. There is a consistent relationship observed between atacamite/brochantite in all units (~80%/20%, respectively) and the vein fragment examined in this study. This ratio is consistent with the stability fields of atacamite, which are wider than those of brochantite [62]; therefore, more atacamite is present than brochantite because the precipitation of brochantite is limited to certain conditions, whereas atacamite precipitates in a wider range of conditions. Another important factor is that atacamite and brochantite are intergrown—this suggests co-precipitation; thus, the ratio of these minerals would more likely result from a specific ratio of chlorite to sulphate in the meteoric water. Both minerals display intergrowth textures, meaning that it would be exceedingly difficult to manually separate these them, supporting the hypothesis that although they are crushed fragments, the relationship between the two mineral phases is natural rather than anthropic in origin. However, the copper content in both minerals is similar, i.e., 59.51% in atacamite and 56.20% in brochantite; therefore, if manual separation had taken place, it would not have been related to the grade of the minerals.

### 6.2. Azurite/Chrysocolla Association

For the precipitation of copper carbonates, such as azurite or malachite, the circulation of carbonate-rich, copper sulphate-bearing waters is required. These minerals precipitate, for example, in sedimentary environments where carbonate sources exist under pH-neutral or alkaline conditions [40]. These carbonates, along with mineraloids such as chrysocolla, commonly occur together and comprise paragenetically late-maturing minerals.

The stability field of azurite does not match or overlap with those of atacamite and brochantite [62]; therefore, these minerals have different formation conditions. This suggests that the samples showing an atacamite/brochantite mineral association belong to a different source from those with the azurite/chrysocolla association. The azurite/chrysocolla-associated samples found in the MC21 unit are, therefore, anomalous compared to the bulk of the samples we examined and likely do not originate from the same source as the other minerals studied.

Recent associative surveys with the indigenous community of Caspana in their territory allowed us to review mineralogy present in four mining pits. Three of them were recently exploited (Rio Pila pit, San Santiago mine and the current Cerro Verde mine), and one of them was originally exploited during pre-Hispanic times (Cerro Verde mine) [47]. Macroscopic study of the rocks in these locations and Raman spectroscopy confirmed that all the pits present rocks with azurite/chrysocolla as their main mineral association, in addition to manganosite, which is a characteristic mineral of these samples.

We suggest that the geological source of the minerals with the azurite/chrysocolla association is a mining pit similar to those observed around Caspana. This mineral paragenesis is representative of this mining district and matches well with the pre-Hispanic mine at Cerro Verde [63,64].

### 6.3. The Known Pre-Hispanic Ores of Atacama La Baja

Pre-Hispanic mining districts corresponding to Late Intermediate and Late Period times have been identified at El Abra, Conchi Viejo, Cerro Verde and, possibly Chuquicamata and San Bartolo. In terms of straight-line distance, El Abra is located 68 km from Turi and Cerro Verde is 15 km from Turi, whereas Chuquicamata is located at a distance of 65 km, Conchi Viejo at 62 km and San Bartolo at 54 km (Figure 2).

The Inca mines of El Abra are famous for their turquoise veins [14,33]; however, they are not as well known for their atacamite; a similar situation is recorded at Chuquicamata-

Radomiro Tomic [7]. However, some samples of atacamite/brochantite in Turi may have originated from these districts. The arguments in favour of this interpretation are mainly based on the bulk macroscopic observations of all the sediments extracted from the mineral concentrations of *Pukara de Turi*, i.e., not only the sediments with copper mineralisation, but also of the sediments with little or no mineralisation. Based on their mineralogy and textures (Figures 13–15), these samples are comparable with some samples from the AB-20, Chu-2 and Chu-4 excavations, all of them sites associated with the pre-Hispanic exploitation of El Abra-Conchi and Chuquicamata-Radomiro Tomic. Notably, no turquoise was analysed in any of the Turi samples of the structures we studied in this work, a mineral in high demand during pre-Hispanic times for lapidary work, which is characteristic of the El Abra, Chuquicamata and San Bartolo pits. A little further south, the pre-Hispanic district of San Bartolo does present atacamite/brochantite. However, the occurrence and host rock of the mineral is different. Specifically, the copper mineralisation is disseminated and hosted in sandstones; in addition, native copper and cuprite are found in these locations. It would appear that the material targeted in Turi was specifically high-grade ores, such as atacamite, rather than turquoise-type ores. It is also important to note that the sediments with mineralisation in *Pukara de Turi* are not eroded; therefore, they do not seem to have arrived there by transport, but rather, they have straight edges, indicating that they may have undergone a previous grinding process.

The observation of minerals with an azurite/chrysocolla association in Turi is the first direct evidence of the presence of minerals from one Inca mining district in another Inca site. Although the azurite specimens only comprise a few samples and do not represent the majority mineral of Turi, they are nonetheless an important finding. In this context, the nature of the Cerro Verde site is of particular interest. This site was one of the most important provincial centres built by the Incas in the Loa River basin and has a direct relationship with mining [65]. The mining settlements are connected to the *ushnu*, the ceremonial area of Cerro Verde, via the Inca Road, and there is also a pre-Hispanic mining camp. As noted by [65], the *ushnu* has a direct relationship with the mining areas and it is proposed that this characteristic may be interpreted as a mining centre and its corresponding *wak'a* (*sensu* [66]). The ritual dimension of the raw material and its precise location in the territory was a potentially crucial aspect of Inca mining activities that should be addressed in the future in the context of *Pukara de Turi*.

#### 6.4. Copper Mineral Technologies and the Production Context

Unlike the lapidary industries of Atacama, no evidence of direct percussion (hard and soft) or pressure were recorded. Objects such as mineral beads, pendants or carved figures are absent from the enclosures studied in this work; however, these are probably present in other specialised areas of Turi. Considering the evidence, we suggest that the technological structure of the assemblages was related to a single operational chain that focused on the production of small angular fragments of atacamite/brochantite. The fact that only a few cores were recorded in situ, together with the absence of blanks, suggests that the initial stages of the operational chains (i.e., acquisition of the raw material, initial reduction and roughing of cores) were performed in the extraction areas themselves or in intermediate workshops.

The reduction of blocks through split fracturing did not necessarily require greater skill in technique and had the objective of obtaining blanks of a determined morphology according to the final product. We consider that this was likely an intermediate stage to obtain more suitable volumes of raw material for transport and to facilitate grinding in the workshops where small angular fragments were obtained. According to our study, only the final stages of production were carried out in Turi, i.e., those related to grinding, selection and use in offerings, implying a high spatial segmentation of the operational chains probably related to a social division of the production process.

In this context, copper mineral technology would be considered a ritual technology (production rituals, *sensu* [67]), which was an integral part of the productive technologies

in the Andes. Enabling the non-human agents that inhabit the Andean world was seen as fundamental to the success of daily and productive activities. In this sense, copper technology was a true ritual technology, as the mineral constituted a central substance used in the various production rituals of the Atacameño Andean agro-pastoralists, miners and caravaners to ensure the success of their various activities and needs.

## 7. Conclusions

By systematically evaluating the characteristics, chronology, contextual associations, architecture and spatial distributions of the main areas where copper minerals were offered in the *Pukara* de Turi, we can confirm that a minimum of two entirely different types of mineralisation were used: a vein of atacamite/brochantite and another of azurite/chrysocolla. In the first case, mineralisation occurs in veins. Such mineralised quartz veins are characteristic of small-scale mining in northern Chile and their associated mineralisation generally originates from the circulation of hydrothermal fluids.

The azurite/chrysocolla association appears to belong to the same mineral association found in the Cerro Verde district [47], which is probably the source of these samples. The study of copper mineral powder from an Inca site in Caspana (a few kilometres from Cerro Verde) yielded atacamite [48]. The origin of the atacamite/brochantite may lie within the Late Eocene–Oligocene Metallogenic belt where the districts of Chuquicamata–Radomiro Tomic and El Abra–Conchi are located and where atacamite/brochantite veins have been described. Some mineral products from Turi are similar to those of Chuquicamata–Radomiro Tomic and El Abra–Conchi, based on our analysis of copper minerals from AB-20, Chu-2 and Chu-4. However, based on the macroscopic characteristics of the samples, from *Pukara* de Turi, there is undoubtedly at least a third set of minerals that originate from a vein of translucent quartz with vetiform atacamite. This mineral association does not present similarities with those of known mining sites, so we must continue searching for pits (for example, in the Salado River area) that present similarities to these minerals, which would allow us to make comparisons to get closer to the geological source.

Complementarily, the use of an extensive categorical database (~380 samples) of mineral types (atacamite, brochantite and azurite) as an exploratory random sampling technique can reveal unobserved mineral associations in the analysed archaeological batch. As an example, following a basic analysis of categorical data proposed by [68], the minimum number of samples needed to satisfy the dominant proportion of atacamite/brochantite (~80%/20%) is ~400 samples with a maximum error of  $\pm 5\%$  at the 99% confidence level, suggesting a reasonable adjustment to the preliminary sampling design proposed.

Our systematic research in the *Pukara* de Turi documented various indigenous ritual practices associated with copper minerals. To understand the types of copper minerals that were consumed and how they circulated, the starting point of the study was the development of a comprehensive methodology, developed based on archaeological and geochemical perspectives in addition to constraints from indigenous geology, in one of the largest copper-producing environments in the world. This protocol will help contribute to understanding the production, demand and consumption of minerals through an improved understanding of the changes and continuities in the mining districts and pre-Hispanic circulation areas of copper minerals in the Atacama Desert.

The development of an ad hoc methodology for mineral analysis in archaeological sites allows data to be interpreted more reliably. In particular, the application of non-destructive analyses is paramount for samples originating from archaeological sites. The description of such minerals allows improved future comparisons to be made with copper minerals from candidate source areas in the Atacama Desert. As noted above, although there are many copper veins in the region, integrating constraints from a combination of a broad selection of samples, both geological and archaeological, and the traditional geological knowledge of indigenous communities allows improved correlations to be made between districts. Although it is not the focus of this article, it is necessary to emphasise the relevance of traditional ecological knowledge specifically related to Andean geologies.

As part of the scientific practice of contemporary geological research, it is essential to find common ground with traditional ecological knowledge through horizontal scientific partnerships with local communities, in particular, those that preserve the indigenous mining heritage, especially from contemporary mining extractivism.

The geological study of archaeological samples is important to adequately reconstruct the long history of human interaction with minerals, how these interactions developed, and changes in the know-how needed to identify, process and use these geological resources. Working on provenance is a matter of patience, so while there is hope in this, there is still a long life for mineralogical studies.

**Author Contributions:** Conceptualisation, P.S. and V.F.; methodology, P.S. and A.M.; formal analysis, J.G. and C.G.; investigation, P.S., V.F., F.H., B.M. and R.L.; resources, F.H., D.S., C.P.-O., A.T., P.S. and V.F.; writing—original draft preparation, P.S.; writing—review and editing, P.S., V.F., D.S., F.H. and R.L.; project administration, F.H., D.S., C.P.-O., A.T. and V.F. All authors have read and agreed to the published version of the manuscript.

**Funding:** Field study of the *challas* was supported by an IIE Fulbright award to Frances Hayashida and funds from the University of New Mexico Snead-Wertheim Endowed Lectureship in Anthropology and History. The analyses were supported by the Agencia Nacional de Investigación y Desarrollo (ANID)/BECA DOCTORADO NACIONAL/2018-21181070, Proyecto FONDECYT 1201603 “*Paisajes mineros prehispánicos en el desierto de Atacama: hacia un estudio del uso de los minerales de cobre y su vinculación con la producción de tecnologías rituales*” and Grant CONICYT-USA 2013/0012 “*Water management and agrohydraulic systems in desert environments: the upper Loa from A.D. 1000–1500*”.

**Data Availability Statement:** All data derived from this research are presented in the enclosed figures and tables.

**Acknowledgments:** The analyses presented were conducted at Unidad de Equipamiento Científico-MAINI at Universidad Católica del Norte, Antofagasta, Chile. In addition, we would like to thank the directive of the Comunidad Atacameña de Caspana (2020-2021) and of the community of Ayquina-Turi (2018). Special thanks to Lautaro Núñez for the Abra/Chuquicamata samples. In addition, thanks to Mariela Pino, César Borie y Pastor Fábregas-Alvarez, who are part of the Turi-Topaín project. Finally, the support of doctoral grant ANID/BECA DOCTORADO NACIONAL/2018-21181070, Proyecto FONDECYT 1201603 “*Paisajes mineros prehispánicos en el desierto de Atacama: hacia un estudio del uso de los minerales de cobre y su vinculación con la producción de tecnologías rituales*” and the postdoctoral grant ANID/FONDECYT 3200772 is acknowledged.

**Conflicts of Interest:** The authors declare no conflict of interest. The funders had no role in the design of the study; in the collection, analyses, or interpretation of data; in the writing of the manuscript, or in the decision to publish the results.

## References

1. Camus, F.; Dilles, J.H. A Special Issue Devoted to Porphyry Copper Deposits of Northern Chile. *Econ. Geol.* **2001**, *96*, 233–237. [CrossRef]
2. Figueroa, V.; Salazar, D.; Salinas, H.; Núñez-Regueiro, P.; Manríquez, G. Pre-hispanic mining ergology of northern Chile: An archaeological perspective. *Chungara* **2013**, *45*, 61–81. [CrossRef]
3. Vaughn, K.J.; Tripcevich, N. An introduction to mining and quarrying in the ancient Andes: Sociopolitical, economic and symbolic dimensions. In *Mining and Quarrying in the Ancient Andes: Sociopolitical, Economic and Symbolic Dimensions*; Tripcevich, N., Vaughn, K., Eds.; Springer: New York, NY, USA, 2013; pp. 3–19. [CrossRef]
4. Zori, C. Extracting Insights from Prehistoric Andean Metallurgy: Political Organization, Interregional Connections, and Ritual Meanings. *J. Archaeol. Res.* **2019**, *27*, 501–556. [CrossRef]
5. Berenguer, J.; Salazar, D. Territorialización del modelo minero inkaico en el río Salado: Una aglomeración productiva entre Lípez y San Pedro de Atacama. *Bol. del Mus. Chil. Arte Precolomb.* **2017**, *22*, 51–69. [CrossRef]
6. Figueroa, V.; Mille, B.; Salazar, D.; Berenguer, J.; Menzies, A.; Sapiains, P.; Cifuentes, A.; Joly, D. A major Prehispanic copper production center identified at Collahuasi, Southern Tarapacá Altiplano (Chile). *Chungara* **2018**, *50*, 557–575. [CrossRef]
7. Núñez, L. Valoración minero-metalúrgica circumpuneña: Menas y mineros para el Inka Rey. *Estud. Atacameños* **1999**, *18*, 177–222. [CrossRef]
8. Núñez, L.; Grosjean, M.; Cartajena, I. The expansion of the Inka empire into the Atacama Desert. In *23°S Archaeology and Environmental History of the Southern Deserts*; Smith, M., Hesse, P., Eds.; National Museum of Australia Press: Canberra, Australia, 2005; pp. 324–332.

9. Salazar, D. La producción minera en San José del Abra durante el Período Tardío Atacameño. *Estud Atacameños* **2008**, *36*, 43–72. [CrossRef]
10. Melero, D.; Salazar, D. Historia colonial de Conchi Viejo y San José del Abra, y su relación con la minería en Atacama, Norte de Chile. *Rev. Hist. Indígena* **2003**, *7*, 55–86.
11. González, L.R. El Arte Del Cobre En Los Andes Prehispánicos: Historias de Poder, Brillos y Colores. In *El Arte del Cobre en el Mundo Andino*; Berenguer, J., Ed.; Museo Chileno de Arte Precolombino: Santiago, Chile, 2003; pp. 8–59.
12. Lechtman, H. Andean Metallurgy in Prehistory. In *Archaeometallurgy in Global Perspective: Methods and Syntheses*; Roberts, B., Thornton, C., Eds.; Springer: New York, NY, USA, 2014; pp. 361–422. [CrossRef]
13. Cifuentes, A.; Figueroa, V.; Salazar, D.; Mille, B. Producción metalúrgica local y coexistencia de tecnologías metalúrgicas en San Pedro de Atacama durante el Período Medio (400–1000 DC). *Chungará* **2018**, *50*, 423–439. [CrossRef]
14. Salazar, D. El complejo Minero San José del Abra, II Región (1450–1536 d.C.). Una Aproximación a la Arqueología de la Minería. Tesis Para Optar al Grado de Magíster en Arqueología, Universidad de Chile, Santiago, Chile, 2002.
15. Angiorama, C.I. Producción y circulación de objetos de metal en la Quebrada de Humahuaca en momentos prehispánicos tardíos. Unpublished. Ph.D. Thesis, Universidad Nacional de Tucumán, San Miguel de Tucumán, Argentina, 2003.
16. Berenguer, J. *Caravanas, Interacción y Cambio En El Desierto de Atacama*; Sirawi Ediciones: Santiago, Chile, 2004; p. 604. [CrossRef]
17. Nielsen, A. Armas significantes: Tramas culturales, guerra y cambio social en el Sur Andino prehispánico. *Boletín del Mus Chil Arte Precolomb* **2007**, *12*, 9–41.
18. Pimentel, G. Redes viales prehispánicas en el Desierto de Atacama. Viajeros, Movilidad e Intercambio. Unpublished. Ph.D. Thesis, Universidad Católica del Norte and Universidad de Tarapacá, San Pedro de Atacama, Chile, 2012.
19. Rees, C. Elaboración, distribución y consumo de cuentas de malaquita y crisocola durante el Período Formativo en la Vega de Turi y sus inmediaciones, subregión del río Salado, norte de Chile. In *Los Tres Reinos: Prácticas de Recolección En El Cono Sur de América*; Aschero, C., Korstanje, A., Vuoto, P., Eds.; Instituto de Arqueología y Museo, Universidad Nacional de Tucumán: Tucumán, Argentina, 1999; pp. 85–98.
20. Sepúlveda, M.; Figueroa, V.; Cárcamo, J. Pigmentos y pinturas de mineral de cobre en la región de Tarapacá, norte de Chile: Nuevos datos para una tecnología pigmentaria prehispánica. *Estud Atacameños* **2014**, *1*, 23–37. [CrossRef]
21. Sinclair, C. Los sitios de “Muros y Cajas” del río Loa y su relación con el tráfico de caravanas. In *Taller de Costa a Selva*; Albeck, M.E., Ed.; Instituto Interdisciplinario Tilcara, Universidad de Buenos Aires: Buenos Aires, Argentina, 1994; pp. 51–76.
22. Soto, C. Tipología de cuentas de collar en la Quebrada de Tulan (Salar de Atacama): Nueva línea de evidencia para la transición arcaico-formativo. In Proceedings of the Actas Del XVII Congreso Nacional de Arqueología Chilena, Valdivia, Chile, 9 October 2006; Ediciones Kultrún: Valdivia, Chile, 2010; Volume 2, pp. 1123–1134.
23. Ulriksen, C.E. *Mapa Metalogénico de Chile Entre Los 18° y 34°S, Escala 1:1.000.000*; Servicio Nacional de Geología y Minería: Santiago, Chile, 1990; Volume 42, p. 112.
24. Boric, R.; Díaz, F.; Makshev, V. *Geología y Yacimientos Metalíferos de La Región de Antofagasta*; Servicio Nacional de Geología y Minería: Santiago, Chile, 1990; Volume 40, p. 246.
25. Sillitoe, R.H.; Mckee, E.H. Age of Supergene oxidation and enrichment in the Chilean porphyry copper province. *Econ. Geol.* **1996**, *91*, 164–179. [CrossRef]
26. Brimhall, G.H.; Levi, B.; Nyström, J.O.; Enrique, T.F. Atacamite inclusions in rock-forming feldspars and copper-bearing smectites from the Radomiro Tomic mine, Chile: Copper-insoluble mineral occurrences. *Econ. Geol.* **2001**, *96*, 401–420. [CrossRef]
27. Campos, E.; Menzies, A.; Sola, S.; Hernández, V.; Riquelme, R.; Barraza, M. Mineral resources in a sustainable world, Session 10, Concentration processes in sub-surface environments, Understanding Exotic-Cu Mineralisation: Part I—Characterization of Chrysocolla. In Proceedings of the 13th SGA Biennial Meeting, Nancy, France, 24–27 August 2015; André-Mayer, A.S., Cathelineau, M., Muchez, P., Pirard, E., Sindern, S., Eds.; Volume 3, p. 1153.
28. Sapiains, P.; Menzies, A.; Figueroa, V.; Wilke, H.G.; Mille, B.; Salazar, D.; Berenguer, J. Estudio arqueomineralógico de las menas de cobre prehispánicas en Collahuasi, norte de Chile. *Estud Atacameños* **2020**, *66*, 83–103. [CrossRef]
29. Kahou, Z.S.; Brichau, S.; Poujol, M.; Duchêne, S.; Campos, E.; Leisen, M.; d’Abzac, F.X.; Riquelme, R.; Carretier, S. First U-Pb LA-ICP-MS in situ dating of supergene copper mineralization: Case study in the Chuquicamata mining district, Atacama Desert, Chile. *Miner. Depos.* **2021**, *56*, 239–252. [CrossRef]
30. Sillitoe, R.H. Epochs of intrusion-related copper mineralization in the Andes. *J. S. Am. Earth Sci.* **1988**, *1*, 89–108. [CrossRef]
31. Salazar, D. Investigaciones arqueológicas sobre la minería incaica en San José del Abra (II región, norte de Chile). *Xama* **2002**, *15*, 101–117.
32. Salazar, D.; Salinas, H. Tradición y transformaciones en la organización de los sistemas de producción mineros en el norte de Chile prehispánico: San José del Abra, siglos I al XVI DC. In *Mina y Metalurgia En Los Andes Del Sur Desde La Época Prehispánica Hasta El Siglo XVII*; Cruz, P., Vacher, J.J., Eds.; Instituto Francés de Estudios Andinos: Sucre, Bolivia, 2008; pp. 163–200.
33. Salazar, D.; Salinas, H.; McRostie, V.; Labarca, R.; Vega, G. Cerro Turquesa: Diez siglos de producción minera en el extremo norte de Chile. In Proceedings of the Actas Del XVII Congreso Nacional de Arqueología Chilena, Valdivia, Chile, 9 October 2006; Ediciones Kultrún: Valdivia, Chile, 2010; Volume 2, pp. 1085–1097.
34. Salazar, D.; Borie, C.; Oñate, C. Mining, Commensal Politics, and Ritual under Inca Rule in Atacama, Northern Chile. In *Mining and Quarrying in the Ancient Andes: Sociopolitical, Economic, and Symbolic Dimensions*; Tripcevich, N., Vaughn, K., Eds.; Springer: New York, NY, USA, 2013; pp. 253–274. [CrossRef]



35. Aldunate, C.; Castro, V.; Varela, V. San Bartolo. Retazos de una historia de la minería en Atacama. In Proceedings of the Actas Del XVI Congreso Nacional de Arqueología Chilena, Concepción, Chile, 13–17 October 2003; Ediciones Escaparate: Concepción, Chile, 2005; pp. 213–224.
36. Aldunate, C.; Castro, V.; Varela, V. San Bartolo y Cobija: Testimonios de un modo de vida minero en las tierras altas y la costa de Atacama. *Estud Atacameños* **2008**, *35*, 97–118. [CrossRef]
37. Westfall, C.; González, C. Mina Las Turquesas: Un asentamiento minero lapidario preincaico en el extremo meridional circumpuneño, Región de Atacama, Chile. In *Proceedings of the Actas Del XVII Congreso Nacional de Arqueología Chilena*; Valdivia, Chile, 9 October 2006, Ediciones Kultrún: Valdivia, Chile, 2010; Volume 2, pp. 1073–1084.
38. Cantarutti, G.E. Mining Under Inca Rule in North-Central Chile: The Los Infieles Mining Complex. In *Mining and Quarrying in the Ancient Andes*; Springer: New York, NY, USA, 2013; pp. 185–211. [CrossRef]
39. Bourgarit, D.; Mille, B. Provenance du cuivre et alliages. In *Circulation et Provenance Des. Matériaux Dans Les Sociétés Anciennes*; Dillmann, P., Bellot-Gurlet, L., Eds.; Éditions des Archives Contemporaines: Paris, France, 2014; pp. 103–132. [CrossRef]
40. Chavez, W. Supergene oxidation of copper deposits: Zoning and distribution of copper oxide minerals. *Soc. Econ. Geol. Newsl.* **2000**, *41*, 1–21. [CrossRef]
41. Thibodeau, A.M. Isotopic Evidence For The Provenance of Turquoise, Mineral Paints, And Metals in the Southwestern United States. Ph.D. Thesis, University of Arizona, Tucson, AZ, USA, 2012.
42. Kim, J.; Simon, A.W.; Ripoché, V.; Mayer, J.W.; Wilkens, B. Proton-induced x-ray emission analysis of turquoise artefacts from Salado platform Mound sites in the Tonto Basin of central Arizona. *Meas Sci Technol.* **2003**, *14*, 1579–1589. [CrossRef]
43. González, C.; Westfall, C.; Castells, C. Mina las turquesas: Lapidaria, secuencia alfarera prehispánica e interrelaciones culturales en un espacio internodal del Desierto de Atacama, Chile. *Estud Atacameños* **2017**, *56*, 225–251. [CrossRef]
44. Van Hoesen, J.; Arriaza, B.; Ryan, P.; Grady, C. A multianalytical approach for identifying a manganese source for the black pigment of the Chinchorro mortuary palette. *Geoarchaeology* **2019**, *34*, 322–335. [CrossRef]
45. Carrión, H. Producción e identidad: Cuentas de Mineral de Cobre durante el Periodo Medio en San Pedro de Atacama. Tesis para optar al Título de Arqueólogo, Universidad de Chile, Santiago, Chile, 2015.
46. Figueroa, V.; Salazar, D.; Mille, B.; Manríquez, G. Metal Use and Production among Coastal Societies of the Atacama Desert. *Archaeometry* **2015**, *57*, 687–703. [CrossRef]
47. Coquinot, Y.; (Centre de Recherche et de Restauration des Musées de France, Paris, France). Field Observations and Results of Sample Analysis of Two Secondary Copper Mineral Deposits from: 1) the El Abra Turquoise-Rich Deposit and 2) Cerro Verde, Caspana “Chrysocolla-Azurite-Malachite-Cryptomelane”, Deposit. Report on File. Proyecto Arqueológico El Abra, 2013. Unpublished work.
48. Sepúlveda, M.; Figueroa, V.; Pagés-Camagna, S. Copper Pigment-Making in the Atacama Desert (Northern Chile). *Lat. Am. Antiq.* **2013**, *24*, 467–482.
49. Sepúlveda, M.; Valenzuela, D.; Cornejo, L.; Lienqueo, H.; Rousselière, H. Óxidos de manganeso en el extremo norte de Chile: Abastecimiento, producción y movilidad del color negro durante el Período Arcaico. *Chungará* **2013**, *45*, 143–159. [CrossRef]
50. Aldunate, C. El pukara de Turi: Un testimonio monumental de continuidad cultural en la subárea Circumpuneña (s. XI al XVII). In *Actas Del XII Congreso Nacional de Arqueología Chilena*; Museo Regional de la Araucanía: Temuco, Chile, 1991; Volume 2, pp. 61–78.
51. Scheller, S.; Tagle, R.; Gloy, G.; Barraza, M.; Menzies, A. Advancements in Minerals Identification and Characterization in Geo-Metallurgy: Comparing E-Beam and Micro-X-ray-Fluorescence Technologies. *Microsc Microanal.* **2017**, *23*, 2168–2169. [CrossRef]
52. Garrison, E. X-Ray diffraction (XRD): Applications in Archaeology. In *Encyclopedia of Global Archaeology*; Smith, C., Ed.; Springer: New York, NY, USA, 2014; pp. 7929–7933.
53. Inizan, M.-L.; Reduron-Ballinger, M.; Roche, H.; Tixier, J. *Technology and Terminology of Knapped Stone*; CREP: Nanterre, France, 1999.
54. Pelegrin, J. Les techniques de débitage laminaire au Tardiglaciaire: Critères de diagnose et quelques réflexions. *Mémoires du Musée préhistoire d’Ile-de-France* **2000**, *7*, 73–86.
55. Pelegrin, J. Remarks about archaeological techniques and methods of knapping: Elements of a cognitive approach to stone knapping. In *Stone Knapping: The Necessary Conditions for a Uniquely Hominin Behaviour*; McDonald Institute for Archaeological Research: Cambridge, UK; pp. 23–33.
56. Núñez, L.; Agüero, C.; Cases, B.; de Souza, P. El campamento minero Chuquicamata-2 y la explotación cuprífera prehispánica en el Desierto de Atacama. *Estud Atacameños* **2003**, *25*, 7–34. [CrossRef]
57. Faivre, J.-P.; Geneste, J.-M.; Turq, A. La fracturation en split, une technique de production dans l’industrie lithique des Tares (Sourzac, Dordogne). *Paléo* **2010**, 133–142. [CrossRef]
58. Kahou, Z.S.; Duchêne, S.; Brichau, S.; Campos, E.; Estrade, G.; Poujol, M.; Kathirgamar, J.; Testa, H.; Leisen, M.; Choy, S.; et al. Mineralogical and chemical characterization of supergene copper-bearing minerals: Examples from Chile and Burkina Faso. *Ore Geol. Rev.* **2021**, *133*, 104078. [CrossRef]
59. Camus, F. *Geología de Los Sistemas Porfíricos En Los Andes de Chile*; Servicio Nacional de Geología y Minería: Santiago, Chile, 2003; p. 267.
60. Cuadra, C.P.; Rojas, S.G. Oxide mineralization at the Radomiro Tomic porphyry copper deposit, Northern Chile. *Econ. Geol.* **2001**, *96*, 387–400. [CrossRef]

61. Cuadra, P.; Camus, F.; Porter, T.M. The Radomiro Tomic Porphyry Copper Deposit, Northern Chile. In *Porphyry and Hydrothermal Copper and Gold Deposits: A Global Perspective*; PGC Publishing: Adelaide, Australia, 1998; pp. 99–110.
62. Reich, M.; Palacios, C.; Vargas, G.; Luo, S.; Cameron, E.M.; Leybourne, M.I.; Parada, M.A.; Zúñiga, A.; You, C.F. Supergene enrichment of copper deposits since the onset of modern hyperaridity in the Atacama Desert, Chile. *Miner. Depos.* **2009**, *44*, 497–504. [CrossRef]
63. Cameron, E.M.; Leybourne, M.I.; Palacios, C. Atacamite in the oxide zone of copper deposits in northern Chile: Involvement of deep formation waters? *Miner. Depos.* **2007**, *42*, 205–218. [CrossRef]
64. Adán Alfaro, L. Aquellos antiguos edificios. Acercamiento arqueológico a la arquitectura prehispánica tardía de Caspana. *Estud Atacameños* **1999**, *18*, 13–34. [CrossRef]
65. Salazar, D.; Berenguer, J.; Vega, G. Paisajes minero-metalúrgicos incaicos en Atacama y el Altiplano Sur de Tarapacá (norte de Chile). *Chungará* **2013**, *45*, 83–103. [CrossRef]
66. Bovisio, M.A. Acerca de la naturaleza de la noción de wak'a: Objetos y conceptos. In *Wak'as, Diablos y Muertos: Alteridades Significantes En El Mundo Andino*; Bugallo, L., Vilca, M., Eds.; Universidad Nacional de Jujuy & Instituto Francés de Estudios Andinos: Jujuy, Argentina; Lima, Perú, 2016; pp. 73–110.
67. van Kessel, J. Ritual de Producción y Discurso Tecnológico. *Chungara* **1989**, *23*, 73–91.
68. Drennan, R. *Statistics for Archaeologists: A Common Sense Approach*, 2nd ed.; Springer: Dordrecht, The Netherlands; Heidelberg, Germany, 2009. [CrossRef]



## Article

# Pitfalls and Possibilities of Patinated Bronze: The Analysis of Pre-Roman Italian Armour Using pXRF

Joshua Emmitt <sup>1,\*</sup> , Andrew McAlister <sup>1</sup> and Jeremy Armstrong <sup>2</sup>

<sup>1</sup> School of Social Sciences, University of Auckland, Auckland 1010, New Zealand; andrew.mcalister@auckland.ac.nz

<sup>2</sup> Classics and Ancient History, University of Auckland, Auckland 1010, New Zealand; js.armstrong@auckland.ac.nz

\* Correspondence: josh.emmitt@auckland.ac.nz

**Abstract:** Despite the importance of weapons and armour as part of material culture in the Mediterranean during the first millennium BCE, such objects have generally not been studied beyond stylistic analyses. Bronze was extensively used in the construction of these materials; however, its characterisation is complicated due to patination and the different manufacturing techniques used. We used portable XRF (pXRF) to non-destructively characterise bronze material in a way that mitigates the distorting effects of patina. Analysis was conducted on 23 pieces of pre-Roman Italian bronze armour. Assays were taken using two different techniques; ‘single point’ assays and ‘cluster’ assays. There is variability visible across assays both on and between items, grouped both geographically and chronologically. We highlight significant trends visible in the results over time and different object types and discuss the utility of pXRF on ancient bronze with recommendations for best practice.

**Keywords:** Italy; military equipment; bronze; pXRF; museum collections; non-destructive analysis

**Citation:** Emmitt, J.; McAlister, A.; Armstrong, J. Pitfalls and Possibilities of Patinated Bronze: The Analysis of Pre-Roman Italian Armour Using pXRF. *Minerals* **2021**, *11*, 697. <https://doi.org/10.3390/min11070697>

Academic Editors: Daniel Albero Santacreu, José Cristóbal Carvajal López and Adrián Durán Benito

Received: 10 June 2021  
Accepted: 25 June 2021  
Published: 29 June 2021

**Publisher’s Note:** MDPI stays neutral with regard to jurisdictional claims in published maps and institutional affiliations.



**Copyright:** © 2021 by the authors. Licensee MDPI, Basel, Switzerland. This article is an open access article distributed under the terms and conditions of the Creative Commons Attribution (CC BY) license (<https://creativecommons.org/licenses/by/4.0/>).

## 1. Introduction

Given the generally accepted cultural significance of weapons and armour within the societies of the ancient Mediterranean during the first millennium BCE (e.g., [1,2]), it is perhaps surprising that the actual physical properties of weapon and armour finds from this region and period remain largely unexplored by modern scholars. Although long studied for their stylistic and artistic merits, very few analyses have been conducted on the physical nature and composition of equipment finds from the ancient Mediterranean during the first millennium BCE beyond the recording of their basic dimensions and the identification of material used, which are typically described as simply ‘bronze’ or ‘iron’ (e.g., [3–5]; notable exceptions include [6,7], see [8] for discussion, and more recent work [9]). This is despite the fact that the ancient literary sources themselves explicitly discuss the use of different types of alloys in the production of items—most notably Pliny (esp. *NH* 34) but also Cicero (*Tusc. Disp.* 4.32) amongst others—and the obvious differences in technology, construction, and performance which the use of different alloys and materials would entail. Admittedly, the lack of work in this area is partly due to the relative difficulty in analysing such objects, as we discuss below. The items under investigation are often heavily patinated, repaired, or conserved, and the vast majority of ancient military equipment finds have long been housed in museums and private collections, which necessitates the use of non-destructive analytic methods. However, this has not stopped others (e.g., [10]) from exploring similar issues in earlier weapons and armour from the European Bronze Age.

The elemental characterization of military equipment has the potential to reveal variations in manufacturing processes over time and space as well as differences between and within specific categories of items (e.g., helmets, cuirasses, etc.). Comparison of elemental compositions across an object, and on its different components, may also highlight how different alloys were used in the manufacturing process. Likewise, comparison of the

elemental compositions of objects in a particular depositional context (such as a tomb), between different tomb assemblages, and between different regions, may identify local and regional variations as well as indicate trade and distribution patterns. Differences in production techniques may be observed, as well as the differential sourcing of materials and changes in material use over time. Variations in these processes have the potential to inform on the nature, development, supply, and maintenance of bronze military equipment.

To this end we examine military equipment from the Gaudo Necropolis (Paestum), Necropoli dell'Osteria (Vulci), Necropoli di Malpasso (Gualdo Tadino, Umbria), Casal del Fosso (Veii), Cava della Pozzolana (Cerveteri) (Figure 1) to explore these issues in central Italy from c. 900–300 BCE.



**Figure 1.** Location of the provenances where military equipment examined in this paper are from (Squares) and the location of Rome and Naples for reference (Circles).

## 2. Elemental Characterization of Bronze

As noted above, non-destructive characterization of bronze alloys (defined here as being composed of predominantly copper (Cu) and tin (Sn), typically with other trace elements) from archaeological contexts is notoriously difficult, primarily because non-destructive techniques are limited to analyses near the surfaces of objects, which often are patinated. Patina has a different elemental signature from the base metal it forms on, and its formation varies over time; starting fast, gradually slowing, and eventually stabilizing [11]. The composition of patina is variable, depending on original composition of the metal and the post-depositional environment, and is formed when an alloy is exposed to the corrosive effects of soil, water, and air. The chemical composition of the depositional environment, its pH level, and resistivity all play a part in its formation, as does the thickness of the alloy and how it was formed. The formation of patina alters the elemental signature of the alloy in a number of ways, and specifically the structure of the surface, the form of which is influenced by the aforementioned factors [11]. Most notably, the formation of patina can often result in depletion of copper and the surface enhancement of a range of other

elements pulled from both the depositional environment and the core metal [12]. Due to the patination process, elements such as Sn often appear in increased percentages in surface readings, even on cores/bases which were initially composed of medium-to-low Sn alloys. Indeed, Sn at the surface can sometimes reach levels comparable to those found in items that had undergone tinning, therefore rendering the two processes indistinguishable from each other [11,13–15]. Patinas also often vary across a single object, forming localised or non-uniform areas of corrosion due to a range of different factors related to both the alloy and the depositional context [16].

Another related factor which complicates this sort of work is the fact that ancient bronzes are themselves rarely uniform in composition [17,18], even within a single item (let alone across a context, site, or culture), and often feature a complex array of trace elements found in varying ratios across the item. Trace elements can also be introduced in a range of different ways. In a study of ancient copper, and the potential analyses of it to determine provenance, Pernicka [19] investigated changes in trace elements during the smelting processes. Elements were classified as either remnants from the original ore, a result of metallurgical practices (incl. patination), or a combination of the two [20]. Elements such as iron (Fe) and sulphur (S) can either be a result of the smelting process, intentional additions, or form part of a corrosion layer during deposition [19]. Lighter elements, such as oxygen (O), carbon (C), and chlorine (Cl), were found to relate to corrosion processes (i.e., patina formation). Elements like Sn are often overrepresented as a result of patination and studies have also demonstrated that concentrations of other elements, such as Fe, reduce when copper is re-melted and recycled [21,22]. The aim of the studies by Pernicka and Merkel was to investigate the feasibility of determining the provenance of different copper sources by elemental composition alone, which could be used to discuss larger processes of resource availability and trade and exchange. Complications caused by patination, both on the surface and in the core of the metal, meant that this was largely ineffective and there are more suitable methods, such as lead isotope analysis, that can be used for these purposes (e.g., [23]). However, the work of Pernicka and Merkel clearly demonstrates the range of issues and complexities which arise during all stages of the life-cycle of, not only a bronze artefact, but also the ore it is made from and where and how it is deposited. Further, the widespread evidence for the recycling of bronze items in the ancient Mediterranean, and particularly Italy [24], complicates provenancing items by elemental signature and hints that this sort of analysis may only be useful for very specific artefacts and contexts.

Due to the issues caused by patina, elemental characterization of bronze alloys has therefore often been a destructive process, where items are cleaned to remove the patina or the item is cut or drilled to access the core or 'base alloy' (e.g., [25]). As is often the case and often cited as the case (e.g., [23]), the destructive sampling of objects from antiquity is not possible (or indeed desirable) due to the aesthetic value of the object, or indeed the object's integrity, both physically and as an excavated item existing in its modern context. The value of destructive analysis is therefore often debatable and its utility certainly depends on what the investigator wishes to discover, as well as the nature of the object itself. For artefacts made from thin bronze sheets, there may be little effective difference between destructive and non-destructive, 'surface based' techniques. Patinas often form quickly on exposed bronze, reaching thicknesses of 0.1 mm within the first three months, although slowing in subsequent periods, only reaching 0.13 mm after two years [26]. Additionally, while patinas start on the surface, they are not strictly surface phenomena and typically penetrate the metal along grain boundaries and may ultimately convert the entire core to cuprite [27] (p. 5). This is particularly true for thin sheets (under 0.5mm, which is typical for archaic bronze armour), with the result that there often appears to be no untouched core of metal left to test even if destructive techniques were employed. Perhaps ironically, to confirm this, destructive metallographic analyses would need to be carried out.

PXRF has increasingly been touted as a quick, affordable, non-invasive, surface-based technique, which might be able to provide a non-destructive method by which to elementally characterise an object. As a consequence, it has been regularly deployed in a wide

range of situations (e.g., [25,28,29] etc.). This work is complicated by the aforementioned difficulties in determining what is being measured, the patina or core metal, and in determining a measure from the 'original' surface of the object. Indeed, it is clear that for many bronze items, and for many research questions (which require any degree of objective specificity in the results), pXRF is decidedly ill-suited [30]. However, as Pearce noted in his critique of the wider use of pXRF on corroded bronze, "portable XRF is a useful tool for the preliminary analysis of metal artefacts" ([30], p. 84). Similar issues have previously been raised with the use of pXRF on other materials which largely argue between 'scientific precision' versus internal consistency of readings, which can still be deployed in pursuance of appropriate research questions (see debate between [31,32] for an example with obsidian sourcing). Further, depending on the items being investigated and their level of patination, the benefits of destructive techniques over pXRF can also vary.

As pXRF analyses are often carried out on unmodified artefact surfaces, the results do not necessarily represent the bulk composition of the core metal alone but also include the composition of surface patinas, which can vary considerably in extent. When compared to other methods, such as multicollector inductively coupled plasma mass spectrometry (MC-ICP-MS) and electron probe microanalyser (EPMA), the measurement of some materials, such as copper, by pXRF has still demonstrated similar accuracy under certain conditions [23,28,33,34]. Cleaned copper has shown to provide similar results between destructive methods and pXRF [23,28]. Dussubieux and Walder [34] were able to distinguish American native copper from European copper fragments using pXRF alone and on uncleaned surfaces. Some success has also come with the use of pXRF through the implementation of Monte Carlo simulations, as a way to circumvent the effects of patina [35–39]. Monte Carlo simulations are often tested on experimental data and, when implemented on artefacts, are accompanied by a contrasting destructive analysis. The issue with the implementation of Monte Carlo simulations is that it currently still requires knowledge of the cross-section of a corroded alloy. The thickness and composition of a patina are required to simulate the original bronze alloy [36]. In the absence of a comparative assay taken on a clean surface, it is not possible to verify the results of the analysis. One is effectively comparing a surface reading with a hypothesised ideal reading, without any firm way to confirm the hypothesised ideal is correct. Future work may remove this barrier, but as yet it does not provide the answer to the long-standing issue of patination.

Another approach to the issue of elemental characterisation of bronze alloys with pXRF, and in particular bronze alloys with varying degrees of patina, is to examine the signatures from the patina itself [40]. The aim of such an analysis is to investigate what the patina can say about the post-depositional environment of the artefacts. With enough data about the patina, and enough readings from the item, it may be possible to 'filter out' or compensate for this layer of material to achieve at least a qualified and comparative set of results. The risk with such an approach is that equifinality arguments are likely, but in such cases more information is known than was previously. Given patina and cuprified material forms the vast majority, if not totality, of many of the thin items explored, in addition to the fact that the items are currently housed in museums and private collections and were therefore unavailable for destructive sampling, we apply such an approach here. However, as will be described, within this approach some methodologies are more illuminating than others.

### 3. Case studies

Twenty-three items of bronze armour were examined, from nine contexts that come from five sites across central and southern Italy (Figure 1, Table 1). The objects are dated between 750–350 BCE (Table 2) and generally come from what may be considered as primary sealed contexts (i.e., tombs). Little is known about the specific provenance of most of the objects beyond what is reported here, and, as is often the case, the details which do exist do not include sufficient information about the specific depositional contexts in



which the objects were found to make informed inferences regarding the formation of their patinas.

**Table 1.** Provenances and descriptions of the objects analysed.

Site	Tomb	Item(s)	Date (BC)	Location
Paestum/Poseidonia: Gaudio Necropolis [41–44]	Tomb 136: Male, 25–30 y/o Figure S1.1	• Triple disc cuirass (P001). ID#: 103957	420–400	National Archaeological Museum of Paestum
	Tomb 164: Male, 17–20 y/o Figures S1.2–6	• Samno-Attic Helmet (P005) ID#: 104106 • Triple disc cuirass (P004). ID#: 104110 • Belt (P006). ID# 104108 • Left greave (P003) ID# 104110 • Right greave (P002) ID# 104110	380–370	
	Tomb 197: Adult male Figure S1.7	• Triple disc cuirass (P008) ID#: 104376		
Cerveteri: Cava della Pozzolana [45,46]	Tomb 72 Figure S1.12	• Belt (VG006) ID#4999	c.700	
Gualdo Tadino, Umbria: Necropoli di Malpasso [47]	Tomb 12 Figure S1.9–11	• Negau Helmet (VG002) ID# 44429 • Negau Helmet (VG003) ID# 44430 • Seven pieces of a single shield boss/decoration (VG004a-g) ID# 44434	400–350	
Veii: Casale del Fosso [48–50]	Tomb 871 Figures S1.18–19	• Crested helmet (VG015) ID#61913 • Shield (VG013) ID#36455	730–720	National Etruscan Museum of Villa Giulia, Rome
	Tomb 1036 Figure S1.17,20–23	• Crested helmet (VG012) • Armour discs (VG016, VG019) ID#37391-2 • Composite shield (VG017, VG018) ID#37393-6	750–730	
Vulci: Necropoli dell'Osteria [51]	Tomb 47 Figures S1.13–16	• Negau helmet (VG010) ID#63579 • Left greave (VG008) ID#63575 • Right greave (VG009) ID#63575 • Shield (VG011)	530–510	
	Tomb 55 Figure S1.8	• Etrusco-Thracian helmet (VG001) ID#63688	400–350	

**Table 2.** Location and date of the different tomb assemblages examined here across time.

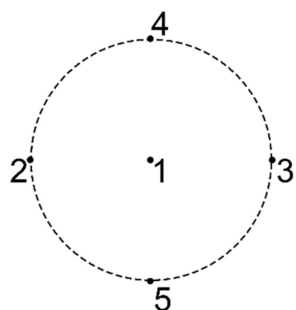
BCE	Paestum	Vulci	Gualdo Tadino	Veii	Cerveteri
750				Tomb 871	Tomb 1036
700					Tomb 72
650					
600					
550		Tomb 47			
500					
450	Tomb 136				
400	Tomb 164	Tomb 197	Tomb 55	Tomb 12	
350					

Most of the objects examined were made from a single piece of bronze, although some (most notably helmets) featured some additions. These include decorative pieces, flanges, cheekpieces, and attachments which may be of a different material, or attached via a different material (e.g., solder) but these are visually distinguishable. Cuirasses represent a rather different set of items as well, as they are consistently composed of multiple large pieces (e.g., front and back plates, along with shoulder straps, side plates, etc.), and the materials and alloys of the different components may be different. In addition, clasps, hooks, rings, and rivets may all have slightly different compositions. This creates another potential complication when distinguishing the compositions of metal objects, as when variability is sought between assemblages, it first needs to be investigated across single objects. Museum identification numbers were also often found to be insufficient to clearly

identify the objects, as a single item may have no clear identification number or multiple numbers depending on how and when it was found, reconstructed, and classified. Many items are conventionally described in scholarship using tomb contexts and not museum inventory number. Identifiers localised to this study were assigned to each object and are presented in Table 1 with the provenance information for the objects and museum identification numbers where possible. Objects are patinated to varying degrees, which caused some issue during the analysis and is discussed with the results below. It was not possible to clean or destructively sample the objects that were examined, and as discussed it is questionable what merit there would be in doing so.

#### 4. Methods

In this study we used a Tracer III-SD portable X-ray Fluorescence (pXRF) analyser (Bruker, Billerica, MA, USA; see Appendix A for calibration details, Supplementary Materials for the locations of assays on each object). pXRF assays were taken for 60 s each, and their locations were recorded on annotated photographs and transcribed to a photogrammetric model of each object. At the first level, assays were compared across single objects. This involved the analysis of a combination of single assays as well as clusters of five assays (as proposed by Ferretti [52]) that were taken in a circular fashion across a 1cm diameter circle on an object (Figure 2). The aim of these cluster assays was to measure variation over a relatively contained surface area, where both the core metal and depositional conditions should have been largely consistent. Microscale heterogeneity remains a problem with any ancient bronze alloy, and this type of approach falls into the category of “area mapping”, as proposed by Karydas et al. [53], to ascertain mean values of elemental intensities across an area. Assays were targeted at the cleanest areas possible (i.e., those with perceived low surface roughness caused by patina) and other areas of interest, as determined from a visual analysis, including decorative sections, rivets, areas of potential repair, rings, and separate sheets of metal.



**Figure 2.** Example of a cluster of five assays and the order they were recorded in. The circle is 1cm in diameter. This is represented as a cross-hair symbol on object figures.

#### 5. Results

The results of each assay are presented by item and location in Table S1, with accompanying figures in the Supplementary Materials Figure S1 for where assays were taken on each object. Due to the heterogeneous nature of the artefacts in their current state, the percentages of the elements recorded do not add up to 100%. Cu-Sn bronzes develop patinas consisting of various copper salts which feature significant amounts of carbon (C) and oxygen (O), along with chlorine (Cl) amongst other elements [54]. These elements are not within the detectable limits of current pXRF devices. In addition, patinas are not only surface phenomena and alter the elemental signature of the metal, a point we return to below. As a result, even given what might be considered ‘almost optimal’ conditions, between 4 and 20% of the elements in the material will not be calibrated for. Working on the assumption that uncalibrated elements must be part of the patina requires caution as the character of the ‘actual bronze’ being measured can be skewed by both the calibration standards used and the underlying assumptions of the normalization.

Data from the patinated items from museum collections suggests that patina might account for up to 70% of the elements in some assays, and this fact very likely skews the remaining elements as well. Some measurements provided an even lower total percentage, although these were from areas which were visually identifiable as being composed of other elements, often Fe rivets or Pb attachments.

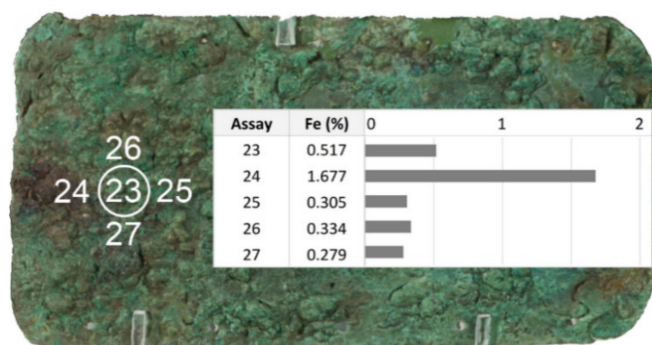
An interesting feature of the study was the variation visible in the measurements across each item. This confirms the work from other studies on ancient bronzes (e.g., [18]) which shows ancient bronze items, and particularly weapons and armour, typically do not have uniform compositions – even across a single item. It is noteworthy, though, that the vast amount of the variability occurred in the levels of Cu identified in each assay, which likely relates to cuprification. Levels of other key elements, most notably Sn, Pb, Fe, zinc (Zn), and arsenic (As), stayed largely stable within clusters.

It is clear that increased levels of patina exacerbated many of the factors visible in the assays on relatively clean items – albeit in largely predictable ways. Looking at the total amount of material which fell within the calibrated elements, this varied by wider amounts depending on the amount and type of patina on the items, ranging up to 40% on a single item. However, again, the vast majority of this variation was due to the amount of Cu. Other elements stayed largely stable, varying by less than 2%, across individual pieces of bronze, for all elements except for tin (Sn). Measurements for tin (Sn) varied by up to c. 10% across single pieces. Although, much of this may have been due to the impact of patination and readings from assay clusters typically revealed more stable numbers (within a range of  $\pm 3\%$  from the average), which is supported by results from comparable studies [55].

#### Cluster Assays

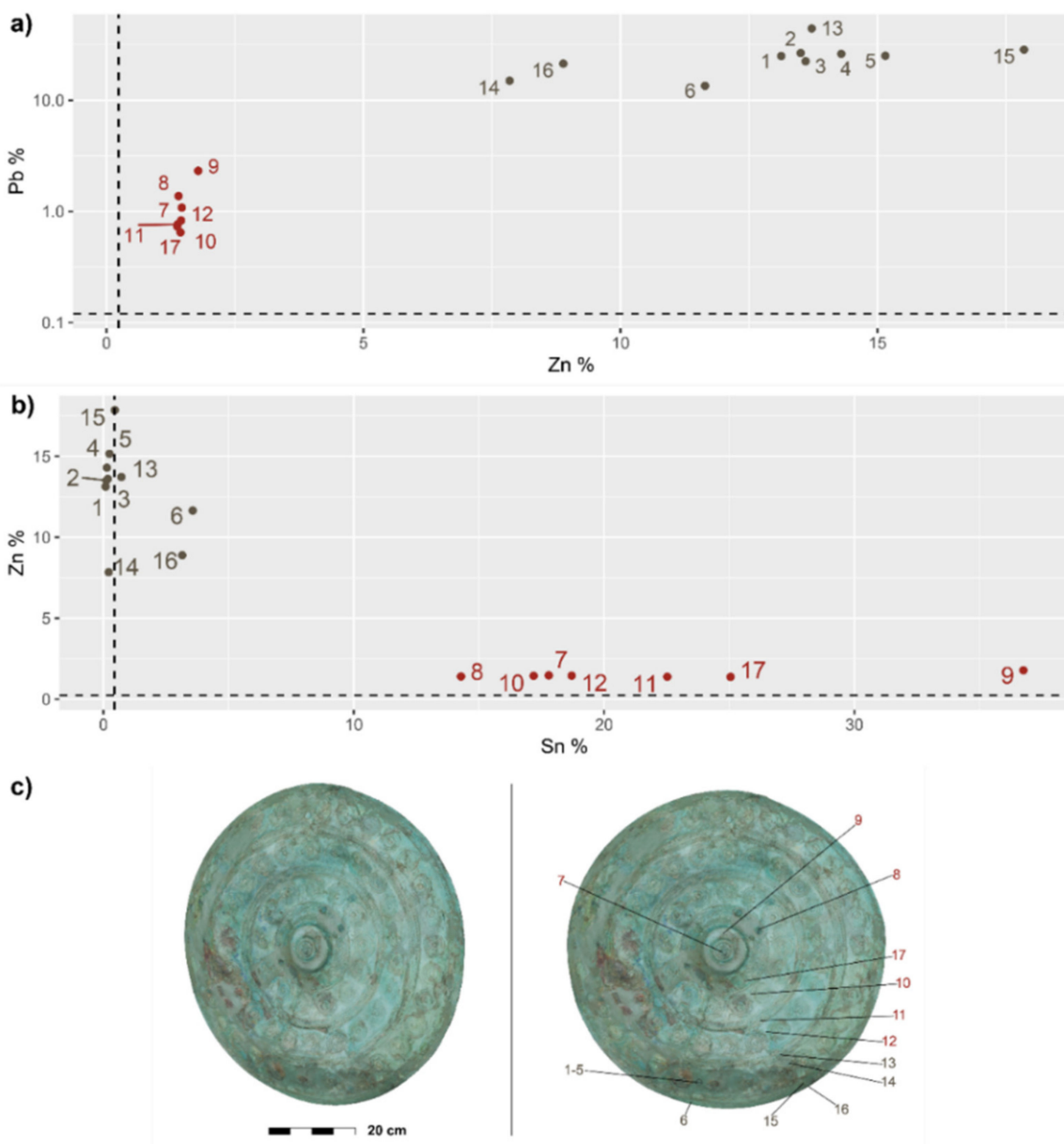
Values for the cluster assays are the mean values of the five readings in each cluster. Only elements determined ‘stable’ across the item and by the calibration were used in this process; Mn, Fe, Zn, As, Sn, Pb. Copper was found to be too variable across objects in both percentage and composition. It was concluded that Cu is affected too much and too variably by patina formation, and so was excluded from the analysis of the cluster assays.

The cluster assays provide a method by which the relative homogeneity of the material may be identified. Again, it must be noted that these readings include the patina and are not strictly a result of the base of metal, however, given the thinness of the items (c. 0.1mm) they can be taken as roughly indicative of patina and base combination. The analyses show low variation within each cluster, demonstrating the roughly homogenous nature of the materials (patina and base), with the exception of one. One example from P004 (P004\_4—assays 23–27) has three of the five assays with relatively homogenous readings, and two have higher Fe concentrations (Figure 3). In the case of P004\_4, the remains of a visually identified rivet were the target of analysis, but the area was so small that multiple readings were undertaken. The fortuitous result being that the assays which ‘missed’ the rivet resulted in the identification of it due to their differential composition.



**Figure 3.** Location of cluster assay P004\_4 (assays 23–27) on the right flap of P004 with values of Fe.

The cluster assays can also help to reveal modern interventions. On item VG013, a heavily reconstructed shield from tomb 871 of the Casale del Fosso necropolis at Veii, individual (6, 13–16) and cluster assays (1–5) revealed a markedly different material, featuring much higher levels of Pb and much lower levels of Sn, from that measured by most of the various single assays (7–12, 17) taken at other points on the artefact (Figure 4). This particular area encompassed by assays 1–5 was targeted for a cluster of assays as it appeared to be, from an initial visual examination, a roughly representative section of the artefact. However, upon reviewing the totality of the results, alongside macro photography and earlier publications, it was clear that it was likely in fact a heavily reconstructed section, along with assays 6 and 13–16 (Grey in Figures 4 and 5). For this reason, this particular cluster, as well as others shown to group with it, has been removed from the wider analysis of ancient materials, although it is illustrative of the effectiveness of pXRF for identifying modern repair (Figure 4).



**Figure 4.** (a) Scatter plot of Pb and Zn, (b) scatter plot of Zn and Sn, (c) Assay locations on VG013 (shield from Veii, Casale del Fosso, tomb 871). Grey represents assays on reconstructed material. Red represents assays represent assays on ‘original’ material. Dashed lines indicate the limits of detection.

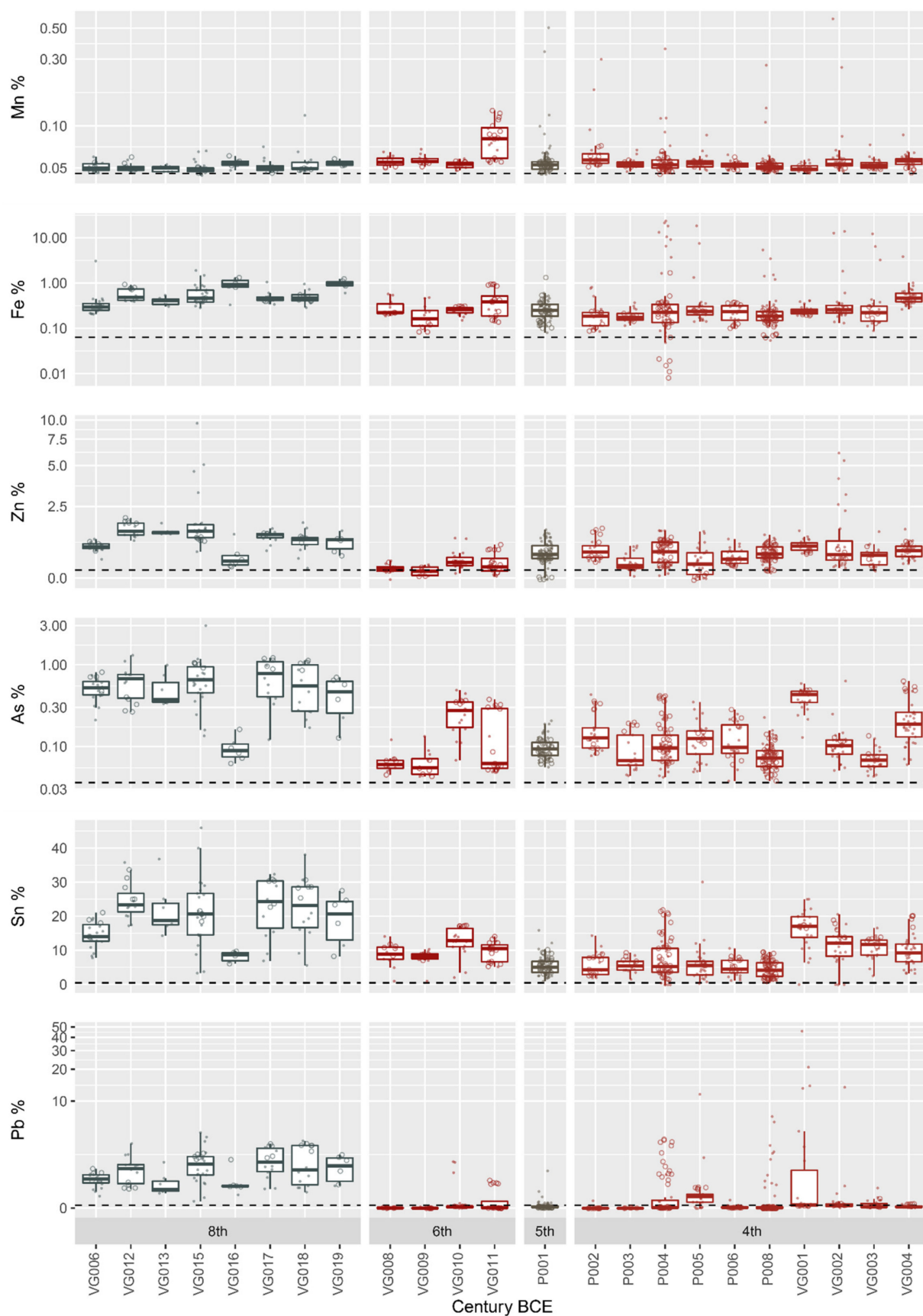


**Figure 5.** Detail photograph of the cluster assay location on VG013 (shield from Veii, Casale del Fosso, tomb 871).

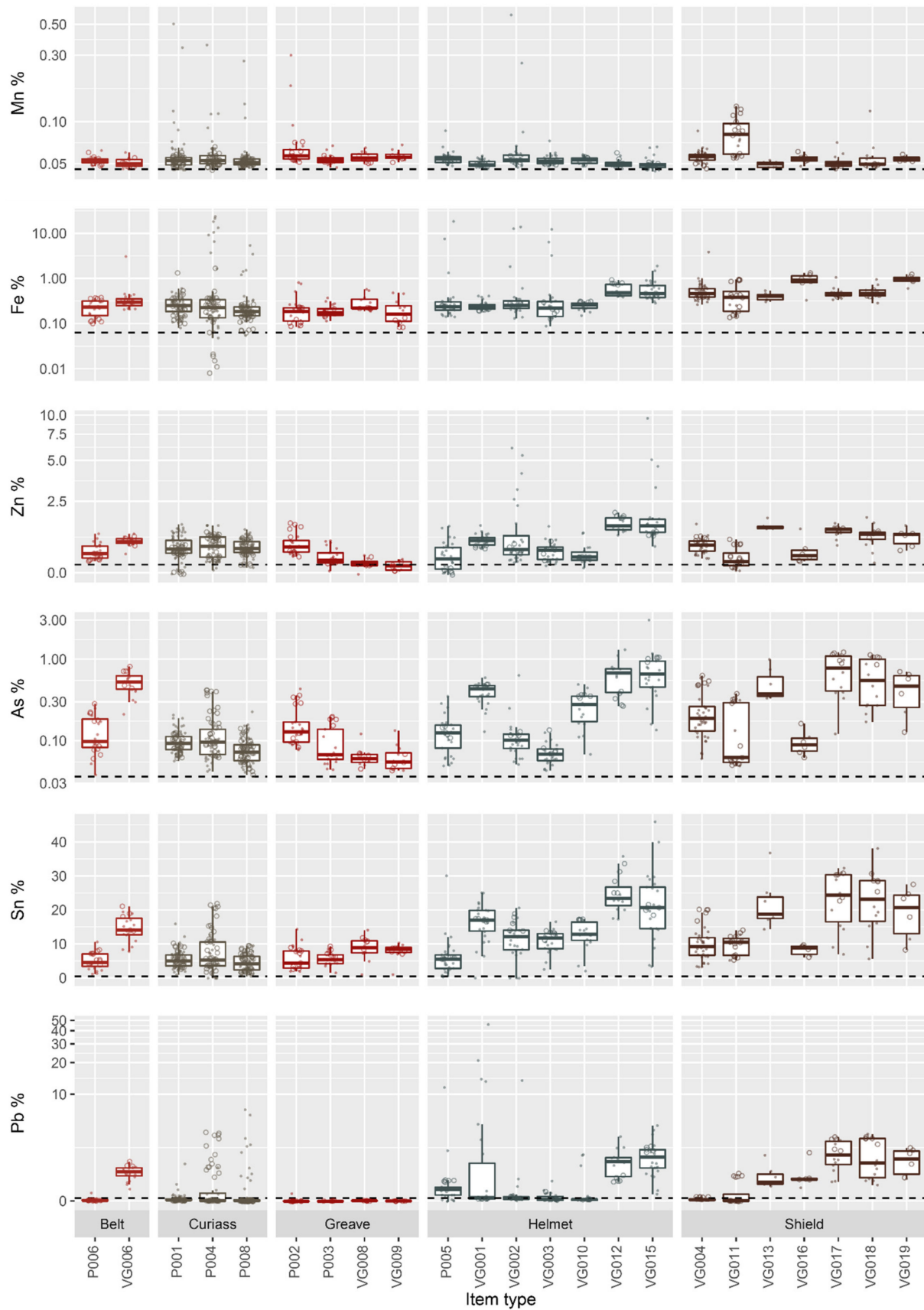
Examination of the composition of all objects by century identified some trends (Figure 6). On average, the amount of Fe tends to decrease over time, with some outliers. The general trend towards less Fe and other trace elements in the objects may suggest the recycling of bronze, which allows for the gradual removal of unwanted elements with each iteration [21,22,56], while the outliers may represent objects where new sources of bronze were introduced or where Fe was perhaps even purposely added. Arsenic generally decreases over time as well, as does Sn and Pb. Additionally, the range within which these elements appear also seems to shrink, suggesting less variability in (and perhaps more control over) the alloy over time. Mn and Zn remain largely stable over time, with one outlier from the eighth century BCE, which is the shield VG013 commented on above. However, as Mn in particular could not be reduced to the metallic state with ancient smelting technologies (modern techniques require a blast or electric furnace), this likely relates to corrosion. There is also some variation in As and Sn in objects from the fourth century which is related to their geographic distribution.

When the averaged elements are viewed by the type of object, patterns are also observed (Figure 7). In general, objects which have more embellishment, and which seem to represent more decorative pieces (including belts and shields), tend to have less consistency within the elements measured. This suggests a range of manufacturing processes were practiced and that different elements may have been added to achieve different visual impacts. It is possible that this is also reflected in the relatively variable, and often high, levels of As present in those objects, as As could be used to create a more ductile medium for manipulation which was more conducive for producing thin sheets [57]. This suggestion is complicated by the fact that it is uncertain whether As had actually been identified as a discrete element/metal during this period, although the qualities of high-As bronze, whether produced deliberately or accidentally, were certainly known [58].





**Figure 6.** Box-plots of elements organised by century BCE. ○ denotes assay used in cluster assays. · denotes non-cluster assay. Dashed lines indicate the limits of detection.



**Figure 7.** Box-plots of elements organised by type. ○ denotes assay used in cluster assays. · denotes non-cluster assay. Dashed lines indicate the limits of detection.



It is possible that As was added, along with elements like antimony (Sb) and nickel (Ni), through the addition of fahlore, or fahlerz ores or the recycling of high-As items. Conversely, items like greaves, which seem to have seen little innovation or variation in either form or production techniques across the period in question, remained remarkably consistent and stable in terms of the chemical composition of the alloy used.

## 6. Discussion

Both single pXRF assays and cluster assays seem to have merit and value independently. However, they can be best deployed in tandem. Clustered assays provide a base characterisation for the item by which other single assays can be validated. Single assays seem to give an accurate reading of the material at the specific point which is measured, but given variability across items, caused by both the natural heterogeneity of the bronze and variations in corrosion and patina, it can be difficult to use any single measurement as a standard reading. The above being noted, results from the analysis reveal that pXRF on ancient bronze can currently, at best, be used to make relative comparisons. This is particularly true if the item is heavily patinated. Indeed, even within a relative context and on relatively 'clean' pieces, levels of Cu vary significantly, suggesting they should not be seen as consistently reliable. However, certain other elements (Mn, Zn, As, Sn, Pb, and we would suggest Fe), offer more stable readings and, again taken relatively, can be understood to function with minimal variability across a single piece of bronze.

Fe has, to date, represented something of a problem for bronze analyses, and is usually seen as either an impurity if found in the alloy (given the typically negative characteristics it brings to bronze) or a part of the patina derived from the soil [10]. Fe (like Mn and Ni, as lighter elements with lower x-ray energy) is only detectable to a depth of between 0.05–0.1 mm in bronze matrices and their associated patinas (e.g., cuprite, atacamite), compared to 0.2–0.4 mm for heavier elements like Cu and Zn. When these lighter metals are detected, particularly on heavily corroded pieces, it is more likely that they come from the patina. Our work has suggested that Fe may sometimes be included in the more stable readings typically associated with the alloy, although this must be done carefully. Destructive analyses have indicated that Fe does often appear in higher quantities in the upper layers of patinas on many bronze objects, suggesting it may originate in the soil and not the alloy in some contexts [59]. However, in our samples, Fe variations followed patterns similar to other alloy-based elements with a general decrease over time and no significant variation due to location. In later periods (c. 400 BCE), there appear to be shifts in the use of Fe in ancient bronze in Italy, which is detectable via pXRF on both cleaned and patinated pieces (this is explored further in a forthcoming publication). Although not conclusive, it is suggestive that we should perhaps pay more attention to temporal variability in Fe in future studies.

In addition to Fe, our study indicates decreasing concentrations of As, Pb, and Sn over time (Figure 6). In particular, the eighth century BCE pieces possess both higher concentrations and increased variability of these elements, which may suggest a lower degree of standardization at that time. Sn varies slightly more than other elements (apart from Cu), likely due to making up a slightly higher percentage of the initial core metal and its tendency to appear in higher quantities in many patinas [60]. It is also worth noting that some types of armour seem to have distinctive chemical signatures, no matter where they are from or their period, likely by virtue of their means of construction and function. For instance, greaves were shown to consistently have low levels of Pb. This is likely a result of both their creation through extensive hammering and the need for them to maintain a degree of spring tension to be equipped.

Accordingly, it is also important to understand the depositional environment in which objects were found. For instance, an oxygenated corrosive environment adjusts the distribution of some elements [37]. This is an area where changes in conservation practice could help with future work, as an analysis of the soil removed from excavated bronzes during the initial cleaning of an artefact and from various sections of the excavated bronze

would be useful in understanding the patination process and how it may have impacted the readings. There is also some opacity about conservation practices, particularly in earlier periods of modern cultural heritage management, due to the different objectives of academic and heritage institutions [61]. Since the 1980s, conservation often includes being cleaned mechanically and being treated for bronze disease using benzotriazole, before any fragments are jointed together, gaps filled with plasticine *vel sim* and modelling paste, and then being painted [62]. However, practices vary over time and location, as do the compounds used, and all known methods would involve leaving some residue or material on the surface which would be detected by the pXRF.

Repairs and interventions on ancient items are relatively easy to identify when analyzed with pXRF. This is evident in the analysis of shield VG013 discussed above. This shield is certainly ancient, with a secure archaeological provenance (excavated in the early 20th century [48,50,63]), but was heavily reconstructed and restored multiple times post-excavation (Figure 8). The cluster reading taken was initially thought to be on an ancient part of the shield, although closer analysis of the results combined with detailed visual analysis of the macrophotography and previous photographs and line drawings, revealed it to be a partially restored section. The pXRF readings, however, were not wholly out of line from what one might expect from a decorative piece of ancient bronze, which seems to underlie the repair—i.e., this location contained a layer of restoration over an ancient core. This is visible in the lower levels of Cu and Sn measured in these sections, compared to other sections where the original material was exposed (e.g., assays 7–12 and 17), coupled with higher levels of Zn and Pb. While all of these elements are often impacted by the patination processes, the ratios here are abnormal. With a normal piece of patinated bronze, and indeed on other sections of this shield, both Pb and Sn are typically enhanced, while Zn is depleted [55].

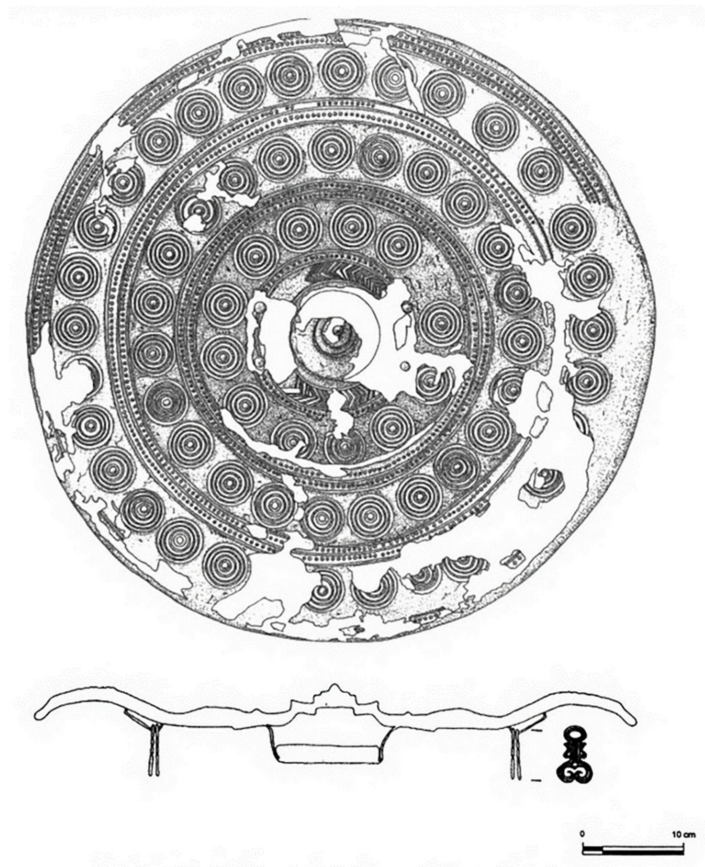


Figure 8. Example of the early reconstruction on VG013, after Drago Troccoli [64] (p. 102).

The lower Sn, but higher Pb and Zn, seen in these readings on VG013 may therefore relate to the compound used to reconstruct the artefact, an interpretation also supported by the lower Cu which may be a result of an extra material on top of the bronze. Cluster assays using pXRF, and particularly when done across the totality of an artefact, are therefore most beneficial for identifying repairs, but although perhaps not outright forgery. Again, they are best used for relative readings within a single piece. The technique could be usefully combined with radiography, which has long been deployed to detect reconstructed section of artefacts [65], as a quicker technique which can occur 'on site'.

Although it is difficult to compare readings outside of a single piece, due to the variability noted above, some basic trends were also visible. For instance, given the significant differences visible in the readings from items from individual contexts, and even from different components of a single piece, our work supports the suggestion that ancient craftspeople were using particular alloys for particular items, and even for particular aspects of a single, composite item [66]. The use of specific bronze alloys for specific items is attested in Italy going back to the Eneolithic [67], while bronze alloys seem to standardise during the Bronze Age, there is evidence that they began to diversify again in the Iron Age [68]. There is also evidence for, again stretching back to the Bronze Age, using different alloys for helmet caps and knobs. As Mödlinger noted ([69], p. 188), referring to helmets from the European Bronze Age: "Whereas all caps show an alloy composition with tin ranging from 7 to 12 wt.%, the smaller components of the helmets (such as the knobs) were cast from much more heterogeneous tin alloys." It is likely that these differences related to production practices, with the higher tin content of the caps explained by the desire to create a thinner, harder, and stronger sheets.

In the items analysed in this study, the most obvious examples of the use of specific alloys and materials for specific purposes is the use of rivets. In later items these are often made of Fe, although in earlier pieces they are made from different types of bronze alloys. Many decorations, which appear to have been cast and then soldered on (as solder is often still visible around the base of items and in places where pieces have broken off – as on the Samno-Attic Helmet (P005)), are also composed of a different alloy. For instance, the earpieces on VG001 contain a significantly higher percentage of lead (Pb), presumably in order to lower the melting temperature, increase fluidity, and make casting easier. The same is true for the decorative attachments to VG010. One can also clearly identify locations where pieces were soldered on, typically using Sn.

Our work confirms the current *communis opinio*, that accurate pXRF measurements of the original or core metal (if it still exists in its original form) are effectively impossible on patinated bronze. If one is attempting to get an accurate elemental signature of the core metal, destructive techniques must be employed. However, it is worth considering whether this is advisable in all cases. As noted above, even on a cleaned piece of bronze, patination processes (esp. intercrystalline corrosion) can change the elemental composition of what might appear to be the core metal, meaning that not only will the resultant readings be variable, but they will not reflect the original material. This is particularly problematic with items produced from thin sheets, like the armour examined in this study, where a thick core of untouched alloy is not available. Additionally, as demonstrated by the range visible in the readings taken across a single (even cleaned) artefact, the inherent variability of ancient bronze means that an 'accurate' reading, taken using destructive techniques, may not be indicative of the overall composition of an item rather that of the specific point analysed. The patina certainly causes significant issues in interpretation and the level of uncertainty it introduces is greater than that which comes with destructive testing, but not by orders of magnitude.

We suggest that non-destructive, surface-based, elemental analysis (pXRF) is a viable technique for analysing ancient bronzes particularly where destructive analyses are not possible. Complimentary information from methods such as radiography, multimodal images, and the trained eye of a conservator are also useful. Both destructive and non-destructive, surface-based techniques return results which must be understood as approximate, given

both the inherent variability within ancient bronze and the variable nature of mineralization and patination processes across an artefact. While the patina certainly increases the range and nature of this variability for non-destructive, surface-based techniques – particularly with regards to Cu and Sn—we would suggest that the benefits do not outweigh the myriad issues involved in damaging or destroying an artefact. Additionally, when working with ancient items made from thin bronze sheets, there is little to be gained from destructive testing as there is often no core metal left to test due to cuprification. This being noted, the issues involved in surface-based techniques must be accounted for. First, we would recommend taking a series of assays across each individual piece of bronze analysed. A single assay will not allow the comparison required to understand the relatively variability. These assays should include areas of low patina if possible. They should also include areas where the patina is visually different. If practical, multiple readings (in a grid or cruciform pattern) should be taken of each area (Figure 2). The goal is to gain as comprehensive an understanding of the elemental signature of the surface across the entire piece as possible. This set of readings can then be compared and contrasted. In the analysis, reading for Cu should be largely discounted and patination processes always considered when looking at trace elements. However, initial results suggest that some relative measurements may be achievable, both within a single piece and assemblage, and across multiple pieces and assemblages.

## 7. Conclusions

The elemental characterization of ancient bronze, although problematic, still offers potential benefits for scholars. When exploring issues of provenance, production, or use, the evidence pXRF offers does add to the dataset of these items. In particular, its ability to give an indication of trace elements within ancient bronze can add to our understanding of how specific alloys were deployed in particular contexts and periods. For instance, in the items analysed in this study there is a decrease in Sn and Fe concentrations over time, possibly due to recycling and purification of the alloy over time. The results also suggest the use of specific materials and different bronze alloys for different items and aspects of ancient military equipment, particularly shields and helmets. It is evident that for ancient smiths, all bronze was not the same. While they might not have been able to achieve the same levels of homogeneity and exactness in their mixtures and recipes which are available today, pXRF data suggests that they were consciously manipulating their alloys to achieve specific results with specific aspects of the equipment and that these aims and methods changed over time. Clearly more work needs to be done on this, but we are confident that, if the techniques are appropriately deployed and the results appropriately interpreted, there is much more we can learn.

**Supplementary Materials:** The following are available online at <https://www.mdpi.com/article/10.3390/min11070697/s1>, Figure S1: Assay Locations, Table S1: Assay data.

**Author Contributions:** Conceptualization, J.E. and J.A.; Methodology, J.E., A.M. and J.A.; Validation, J.E., A.M. and J.A.; Formal Analysis, J.E., A.M.; Investigation, J.E. and A.M.; Resources, J.E. and J.A.; Data Curation, J.E. and A.M.; Writing—Original Draft Preparation, J.E., A.M., J.A.; Writing—Review & Editing, J.E., A.M. and J.A.; Visualization, J.E., A.M.; Supervision, J.A.; Project Administration, J.A.; Funding Acquisition, J.A. All authors have read and agreed to the published version of the manuscript.

**Funding:** This work was supported by the Royal Society of New Zealand Marsden Fund project “Blood and Money: The ‘Military Industrial Complex’ of Archaic Central Italy” [17-UOA-136].

**Data Availability Statement:** The calibrated assays used in this study along with their locations on the objects and calibration procedures are available as Supplementary Materials to this paper.

**Acknowledgments:** The authors wish to thank the directors and curators from the Teece Museum, Museo Nazionale Etrusco di Villa Giulia and Museo Archeologico Nazionale di Paestum for facilitating access to their collections and allocating staff, space, and time to help us during our visit, and for granting us permission to publish the data. In particular we would like to thank Giulia Bison and

Gabriel Zuchriegel for their help. We are very grateful for the feedback provided on a draft of this article by Marianne Mödinger—all errors and omissions remain our own. Finally, thanks is also due to Tim Mackrell helped to facilitate transport of the equipment from Auckland to Italy and back.

**Conflicts of Interest:** The authors declare no conflict of interest.

## Appendix A. Portable X-ray Fluorescence Calibration Procedures

One approach for ancient bronze studies has been to use the in-built factory calibrations supplied with some instruments (e.g., [25,70]). These types of calibrations are, however, generally intended for the rapid identification of modern bronze and brass alloys and, as such, are not necessarily optimised for ancient alloys. For this reason, Heginbotham and colleagues [71] developed the CHARM set of reference materials especially for the analysis of heritage copper alloys. Unfortunately, the CHARM set is not currently in production, which necessitated the use of nine modern copper-based alloy reference standards instead (Table A1). Although these standards have a similar range of elemental concentrations as the CHARM set, the range of elements is more limited.

In this study we used a Bruker Tracer III-SD portable X-ray Fluorescence (pXRF) analyser. The instrument employs an x-ray tube with a Rh target and a 10 mm<sup>2</sup> silicon drift detector (SDD) with a typical resolution of 145 eV at 100,000 cps. For analysis of copper-based alloys, we found that operating the x-ray tube with a setting of 40 keV at 5.0 µA in an air-path and through a window composed of 12 mil Al and 1 mil Ti filters (Bruker's Yellow filter) provided a good count rate for the elements of interest. Assays of artefacts were taken for 60 seconds each, which was sufficient time for the count rates to stabilise, and is in line with other researchers using similar instruments [25,72,73]. Each reference standard was analysed twice and the results averaged. Assays of artefacts were taken using the same instrument and settings outlined above, and their locations were recorded on annotated photographs and transcribed to a photogrammetric model of each object.

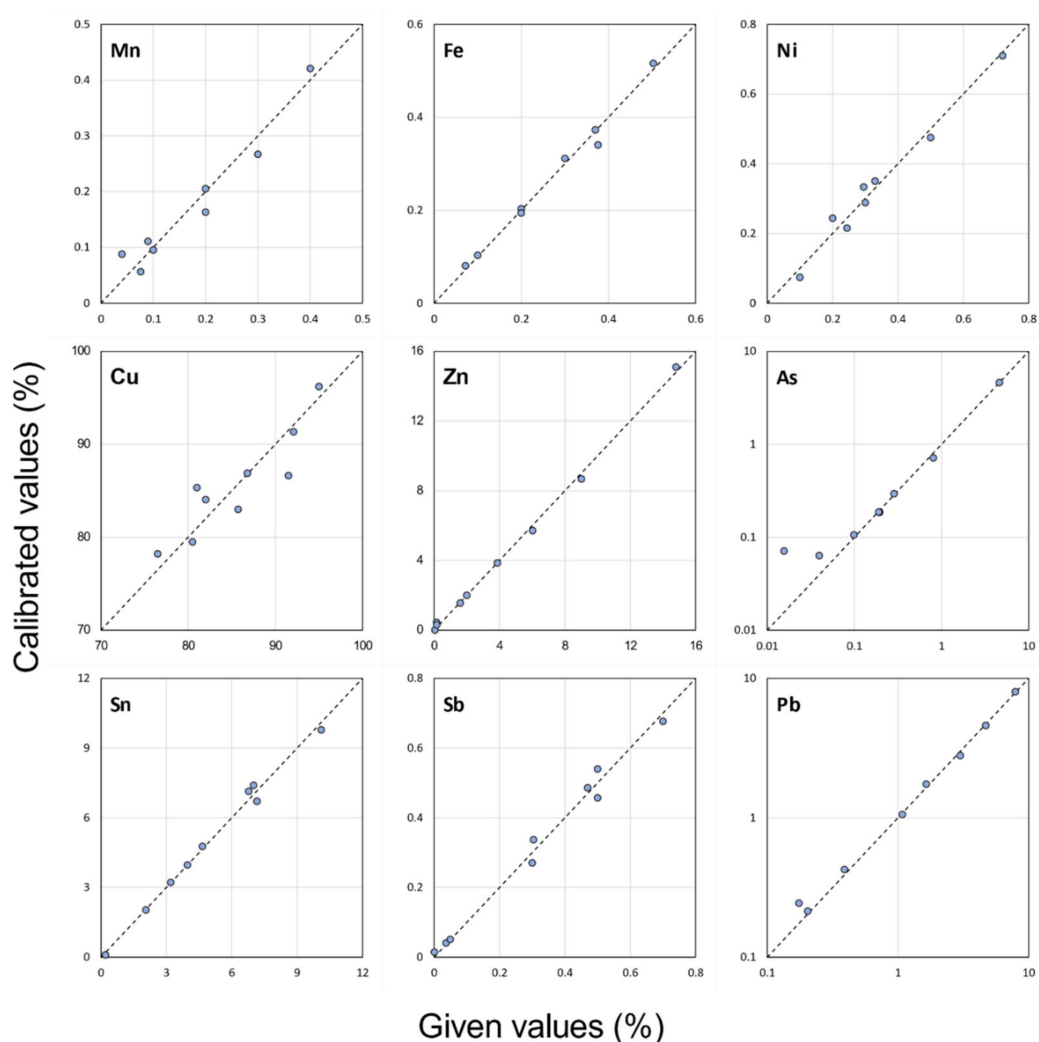
Given the relatively small number of standards available, the calibration procedure was kept as simple as possible. Linear regressions on the net characteristic element peaks (normalised to counts-per-second) were employed, and corrections for interference peaks were included in the regression formulas where necessary (Table A2, Figure A1). For example, the escape K $\alpha$  peak of Cu (6.306keV) overlaps with the characteristic K $\alpha$  peak of Fe (6.405keV) and introduces error if not accounted for in the regression equation.

**Table A1.** Reference standards used for the calibration with given values (%). Uncertified values are underlined. <sup>1</sup> Outlier removed from calibration.

	Mn	Fe	Ni	Cu	Zn	As	Sn	Sb	Pb
	<b>Given Values</b>								
BCR-691-A	<u>0.20</u>	<u>0.20</u>	<u>0.10</u>	<u>76.50</u>	6.02	0.19	7.16	0.50	7.90
BCR-691-B	<u>0.40</u>	<u>0.50</u> <sup>1</sup>	<u>0.20</u>	<u>81.00</u>	14.80	0.10	2.06	-	0.39
BCR-691-C	<u>0.20</u>	<u>0.20</u>	-	<u>95.00</u>	0.06	4.60	0.20	0.50	0.18
BCR-691-D	<u>0.10</u>	<u>0.10</u>	<u>0.30</u>	<u>80.50</u>	0.15	0.29	10.10	0.30	9.20 <sup>1</sup>
BCR-691-E	<u>0.30</u>	<u>0.30</u>	<u>0.50</u>	<u>91.50</u>	0.16	0.19	7.00	0.70	0.20
MBH-32X PB11	0.04	0.37	0.72	92.09	1.60	0.19	3.20	0.47	1.08
MBH-32X SN6B	0.09	0.38	0.30	85.73	2.00	0.80	6.78	0.30	1.64
MBH-33X 54400A	-	0.07	0.24	86.79	3.87	0.02	3.97	0.04	4.69
MBH-33X RB2 B	0.08	0.50	0.33	82.02	9.01	0.04	4.65	0.05	2.99
	<b>Calibrated Values</b>								
BCR-691-A	0.17	0.21	0.07	78.21	5.72	0.19	6.72	0.46	8.00
BCR-691-B	0.42	-	0.25	85.34	15.10	0.11	2.04	-	0.43
BCR-691-C	0.21	0.20	-	96.21	-0.01	4.62	0.10	0.54	0.25
BCR-691-D	0.10	0.11	0.29	79.50	0.46	0.30	9.79	0.27	-
BCR-691-E	0.27	0.32	0.48	86.63	0.31	0.19	7.40	0.68	0.22
MBH-32X PB11	0.09	0.37	0.71	91.33	1.56	0.19	3.22	0.49	1.06
MBH-32X SN6B	0.11	0.34	0.34	83.00	2.00	0.72	7.14	0.34	1.75
MBH-33X 54400A	-	0.09	0.22	86.89	3.86	0.07	3.97	0.04	4.59
MBH-33X RB2 B	0.06	0.52	0.35	84.04	8.68	0.07	4.77	0.05	2.80

**Table A2.** Calibration parameters. <sup>1</sup> Detection limit calculated as  $3.3 \times (\sigma/S)$ .

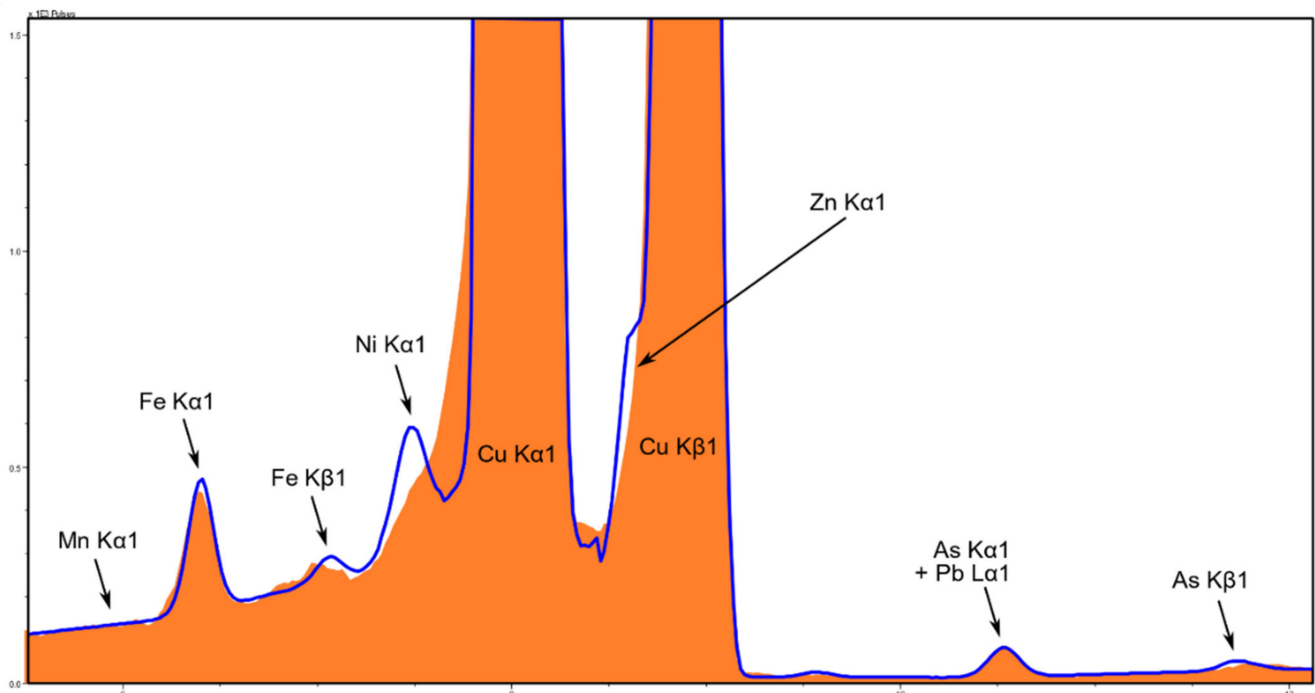
Element	Conc.	R <sup>2</sup>	RMS	Mean Abs.	Det.	Element	Interference
	Range (%)						
Mn	0.04–0.40	0.944	0.03	0.02	0.05	Mn Kα1	-
Fe	0.07–0.50	0.989	0.02	0.01	0.06	Fe Kα1	Cu Kα1 (Escape peak)
Ni	0.10–0.72	0.976	0.03	0.03	0.05	Ni Kα1	Cu Kα1 (Peak overlap)
Cu	76.50–95.00	0.806	2.59	2.08	34.84	Cu Kα1	-
Zn	0.06–14.80	0.998	0.21	0.17	0.24	Zn Kα1	Cu Kβ1 (Peak overlap)
As	0.02–4.60	0.999	0.04	0.02	0.04	As Kβ1	-
Sn	0.20–10.10	0.992	0.26	0.20	0.44	Sn Kα1	-
Sb	0.01–0.70	0.987	0.03	0.02	0.06	Sb Kα1	-
Pb	0.18–7.90	0.999	0.10	0.08	0.12	Pb Lβ1	-



**Figure A1.** Scatterplots of given versus calibrated values for the reference standards. The dashed black lines show the ideal 1:1 *x-y* line. As and Pb are shown with logarithmic axes.

In the case of three elements (Ni, Sb and Pb) slightly negative values were occasionally obtained from the calibration. Examination of typical spectra indicates that, at low concentrations, the peaks for these elements are swamped by the tails of the much larger Cu Kα and Kβ peaks at low concentrations (Figure A2).





**Figure A2.** Spectrum of a typical bronze piece, showing the Cu K $\alpha$  peak overlap on Ni and the Cu K $\beta$  overlap Zn. The spectrum is shown in orange and the fitted peaks (using Bruker's Artax v.8.0 software) as a blue line.

## References

1. Burns, M. *The Cultural and Military Significance of the South Italic Warrior's Panoply from the 5th to the 3rd Centuries BC*; University College London: London, UK, 2005.
2. Kagan, D.; Viggiano, G.E. (Eds.) *Men of Bronze: Hoplite Warfare in Ancient Greece*; Princeton University Press: Princeton, NJ, USA, 2017.
3. Egg, M. *Studien zu den Ätereisenzeitlichen Helmen Italiens und der Alpen*; Verlag des Römisch-Germanischen Zentralmuseums: Mainz, Germany, 1986; Volume 1–2.
4. Bottini, A.; Egg, M.; von Hase, F.; Pflug, H.; Schaff, U.; Schauer, P.; Waurick, G. *Antike Helme. Sammlung Lipperheide und andere Bestände des Antikenmuseums Berlin mit Beiträgen*; Verlag des Römisch-Germanisches Zentralmuseums: Mainz, Germany, 1988.
5. Paddock, J. *The Bronze Italian Helmet: The Development of the Cassis from the Last Quarter of the Sixth Century B.C. to the Third Quarter of the First Century A.D.* Ph.D. Thesis, University of London, London, UK, 1993.
6. Born, H. Antike Herstellungstechniken: Gegossene Brustpanzer und Helme aus Italien. *Acta Praehist. Archaeol.* **1989**, *21*, 99–115.
7. Born, H. Zur Herstellung der etruskischen Bronzehelme mit Scheitelknauf. *Archäologisches Korresp.* **1991**, *21*, 73–78.
8. Mattusch, C. Corinthian Bronze: Famous, but Elusive. In *Corinth Volume 20, Corinth, the Centenary: 1896–1996*; Williams, C.K., II, Bookidis, N., Eds.; The American School of Classical Studies at Athens: Princeton, NJ, USA, 2003; pp. 219–232.
9. Riccucci, C.; Ingo, G.M.; Faustoferri, A.; Pierigè, M.I.; Parisi, E.I.; Di Carlo, G.; De Caro, T.; Faraldi, F. Micro-chemical and metallurgical study of Samnite bronze belts from ancient Abruzzo (central Italy, VIII–IV BC). *Appl. Phys. A* **2013**, *113*, 959–970. [CrossRef]
10. Mödlinger, M. *Protecting the Body in War and Combat: Metal Body Armour in Bronze Age Europe*; Austrian Academy of Sciences Press: Vienna, Austria, 2017.
11. Robbiola, L.; Mlengino, J.-M.; Fiaud, C. Morphology and mechanisms of formation of natural patinas on archaeological Cu–Sn alloys. *Corros. Sci.* **1998**, *40*, 2083–2111. [CrossRef]
12. Moreau, J.-F.; Hancock, R.G.V. L'anatomie d'un chaudron. In *L'archéologie Sans la Loupe. Contributions à l'Archéométrie*; Moreau, J.-F., Ed.; Recherches Amérindiennes au Québec: Montréal, QC, Canada, 1999; Volume Paléo-Québec 29, pp. 73–86.
13. Scott, D. An Examination of the Patina and Corrosion Morphology of Some Roman Bronzes. *J. Am. Inst. Conserv.* **1994**, *33*, 1–23. [CrossRef]
14. Manti, P. *Shiny Helmets: Investigation of Tinning, Manufacture and Corrosion of Greek Helmets (7th–5th c. BC)*. Ph.D. Thesis, Cardiff University, Cardiff, UK, 2012.
15. Nicholas, M.; Manti, P. Testing the applicability of handheld portable XRF to the characterisation of archaeological copper alloys. In *Proceedings of the ICOM-CC 17th Triennial Conference Preprints*, Melbourne, VIC, Australia, 15–19 September 2014; Bridgland, J., Ed.; International Council of Museums: Paris, France, 2014.

16. Piccardo, P.; Mille, B.; Robbiola, L. Tin and copper oxides in corroded archaeological bronzes. In *Corrosion of Metallic Heritage Artefacts—Investigation, Conservation and Prediction for Long-Term Behaviour*; Dillmann, P., Beranger, G., Piccardo, P., Matthiesen, H., Eds.; Woodhead Publishing: Cambridge, UK, 2007; pp. 239–262.
17. Adriaens, A.; Dowsett, M. Electrochemical analysis of metallic heritage artefacts: Time-lapse spectroelectrochemical techniques. In *Corrosion and Conservation of Cultural Heritage Metallic Artefacts*; Dillmann, P., Watkinson, D., Angelini, E.A.A., Eds.; Woodhead Publishing: Cambridge, UK, 2013; pp. 149–164.
18. Dolfini, A.; Crellin, R.; Horn, C.; Uckelmann, M. Interdisciplinary Approaches to Prehistoric Warfare and Violence: Past, Present, and Future. In *Prehistoric Warfare and Violence: Quantitative and Qualitative Approaches*; Dolfini, A., Crellin, R., Horn, C., Uckelmann, M., Eds.; Springer: Cham, Switzerland, 2018; pp. 1–20. [CrossRef]
19. Pernicka, E. Trace element fingerprinting of Ancient Copper: A Guide to Technology or Provenance? In *Metals in Antiquity*; Young, S.M.M., Pollard, A.M., Budd, P., Ixer, R.A., Eds.; B.A.R.: Oxford, UK, 1999; pp. 163–171.
20. Pernicka, E. Provenance Determination of Archaeological Metal Objects. In *Archaeometallurgy in Global Perspective*; Roberts, B., Thornton, C., Eds.; Springer: New York, NY, USA, 2014; pp. 239–268. [CrossRef]
21. Merkel, J. Experimental reconstruction of Bronze Age copper smelting based on archaeological evidence from Timna. In *The Ancient Metallurgy of Copper*; Rothenberg, B., Ed.; Institute of Archaeo-Metallurgical Studies: London, UK, 1990.
22. Merkel, J. Summary of experimental results for Late Bronze Age copper smelting and refining. *Mus. Appl. Sci. Cent. J.* **1983**, *2*, 173–179.
23. Holmqvist, E.; Wessman, A.; Mänttari, I.; Lahaye, Y. Lead isotope and geochemical analyses of copper-based metal artefacts from the Iron Age water burial in Levänluhta, Western Finland. *J. Archaeol. Sci. Rep.* **2019**, *26*, 101854. [CrossRef]
24. Iaia, C. Handicrafts, 10th cent.-730 BCE. In *Etruscology*; Naso, A., Ed.; DeGruyter: Berlin, Germany, 2017; pp. 739–758.
25. Charalambous, A.; Kassianidou, V.; Papassavas, G. A compositional study of Cypriot bronzes dating to the Early Iron Age using portable X-ray fluorescence spectrometry (pXRF). *J. Archaeol. Sci.* **2014**, *46*, 205–216. [CrossRef]
26. Letardi, P. Laboratory and field tests on patinas and protective coating systems for outdoor bronze monument. In *Metal 04, Proceedings of the International Conference on Metals Conservation, Canberra Australia, 4–8 October 2004*; Ashton, J., Hallam, D., Eds.; National Museum of Australia: Canberra, Australia, 2004; pp. 379–387.
27. Hughes, R. Artificial patination. In *Metal Plating and Patination: Cultural, Technical and Historical Developments*; Niece, S., Craddock, P., Eds.; Butterworth-Heinemann: Oxford, UK, 2013; pp. 1–18.
28. Orfanou, V.; Rehren, T. A (Not So) Dangerous Method: PxrF Vs. Epma-Wds Analyses of Copper-Based Artefacts. *Archaeol. Anthropol. Sci.* **2015**, *7*. [CrossRef]
29. Tykot, R.H. Investigating Ancient Bronzes: Non-Destructive Analysis of Copper-Based Alloys. In *Artistry in Bronze: The Greeks and Their Legacy. Sixth International Congress on Ancient Bronzes*; Daehner, J.M., Lapatin, K., Spinelli, A., Eds.; The J. Paul Getty Museum and the Getty Conservation Institute: Los Angeles, CA, USA, 2017; pp. 289–299.
30. Pearce, M. The Curse of the pXRF: The Negative Consequences of the Popularity of Handheld XRF Analysis of Copper-Based Metal Artefacts. *Metalla* **2019**, *24*, 81–85.
31. Speakman, R.J.; Shackley, M.S. Silo science and portable XRF in archaeology: A response to Frahm. *J. Archaeol. Sci.* **2013**, *40*, 1435–1443. [CrossRef]
32. Frahm, E. Is obsidian sourcing about geochemistry or archaeology? A reply to Speakman and Shackley. *J. Archaeol. Sci.* **2013**, *40*, 1444–1448. [CrossRef]
33. Šatović, D.; Desnica, V.; Fazinic, S. Use of Portable X-Ray Fluorescence Instrument for Bulk Alloy Analysis on Low Corroded Indoor Bronzes. *Spectrochim. Acta Part B At. Spectrosc.* **2013**, *89*, 7–13. [CrossRef]
34. Dussubieux, L.; Walder, H. Identifying American native and European smelted coppers with pXRF: A case study of artifacts from the Upper Great Lakes region. *J. Archaeol. Sci.* **2015**, *59*, 169–178. [CrossRef]
35. Brunetti, A.; Golosio, B.; Melis, M.G.; Mura, S. A high-quality multilayer structure characterization method based on X-ray fluorescence and Monte Carlo simulation. *Appl. Phys. A* **2014**, *118*, 497–504. [CrossRef]
36. Manso, M.; Schiavon, N.; Queralt, I.; Arruda, A.M.; Sampaio, J.M.; Brunetti, A. Alloy characterization of a 7th Century BC archaeological bronze vase—Overcoming patina constraints using Monte Carlo simulations. *Spectrochim. Acta Part B At. Spectrosc.* **2015**, *107*, 93–96. [CrossRef]
37. Bottaini, C.E.; Brunetti, A.; Montero-Ruiz, I.; Valera, A.; Candeias, A.; Mirão, J. Use of Monte Carlo Simulation as a Tool for the Nondestructive Energy Dispersive X-ray Fluorescence (ED-XRF) Spectroscopy Analysis of Archaeological Copper-Based Artifacts from the Chalcolithic Site of Perdigões, Southern Portugal. *Appl. Spectrosc.* **2017**, *72*, 17–27. [CrossRef]
38. Giurlani, W.; Berretti, E.; Innocenti, M.; Lavacch, A. Coating Thickness Determination Using X-ray Fluorescence Spectroscopy: Monte Carlo Simulations as an Alternative to the Use of Standards. *Coatings* **2019**, *9*, 79. [CrossRef]
39. Trojek, T. Iterative Monte Carlo procedure for quantitative X-ray fluorescence analysis of copper alloys with a covering layer. *Radiat. Phys. Chem.* **2020**, *167*. [CrossRef]
40. Karydas, A. Application of a portable XRF spectrometer for the non-invasive analysis of museum metal artefacts. *Ann. Chim.* **2007**, *97*, 419–432. [CrossRef]
41. Sestieri, P.C. La necropoli preistorica di Paestum. *Riv. Sci. Preistoriche* **1946**, *1*, 245–266.
42. Sestieri, P.C. Nuovi risultati dagli scavi nella necropoli preistorica di Paestum. *Riv. Sci. Preistoriche* **1947**, *2*, 283–290.

43. Sestieri, P.C. Primi risultati degli scavi nella necropoli preistorica di Paestum. *Rendiconli Accad. Archeol. Lellere Belle Arti Napoli* **1946**, *23*, 251–308.
44. Voza, G. Ultimi scavi della necropoli del Gaudio. In Proceedings of the Atti Della IX Riunione Scientifica, Calabria, Italy, 6–8 April 1964; Istituto Italiano di Preistoria e Protostoria: Florence, Italy, 1965; pp. 265–274.
45. Pallottino, M. *La Necropoli di Cerveteri*; La Libreria dello Stato: Rome, Italy, 1939.
46. Pace, B.; Vighi, R.; Ricci, G.; Moretti, M. *Cerveteri. Scavi di Raniero Mengarelli*; Ulrico Hoepli: Milan, Italy, 1955.
47. Stefani, E. Gualdo Tadino: Scoperte varie. *Not. Scavi* **1935**, *1935*, 155–173.
48. Colini, A.M. Veio. Scavi nell’area della città e della necropolis. *Not. Scavi* **1919**, *1919*, 3–12.
49. Bianco Peroni, V. *Die Schwerter in Italien: Le Spade Nell’Italia Continentale*; Beck: Munich, Germany, 1970.
50. Buranelli, F.; Drago, L.; Paolini, L. La Necropoli di Casale del Fosso. In *Le Necropoli Arcaiche di Veio: Giornata di Studio in Memoria di Massimo Pallottino*; Pallottino, M., Bartoloni, G., Eds.; Università degli Studi di Roma “La Sapienza”, Dipartimento di scienze Storiche, Archeologiche e Antropologiche dell’antichità: Rome, Italy, 1997; pp. 63–83.
51. Ricciardi, L. La necropoli settentrionale di Vulci. resoconto di un’indagine bibliografica e d’archivio. *Boll. Arte* **1989**, *58*, 27–52.
52. Ferretti, M. The investigation of ancient metal artefacts by portable X-ray fluorescence devices. *J. Analytical At. Spectrom.* **2014**, *29*, 1753–1766. [CrossRef]
53. Karydas, A.G.; Anglos, D.; Harith, M.A. Mobile Micro-XRF and LIBS Spectrometers for Diagnostic Micro-Analysis of Ancient Metal Objects. In *Metals and Museums in the Mediterranean: Protecting, Preserving and Interpreting*; Argyropoulos, V., Ed.; Department of Conservation of Antiquities and Works of Art: Athens, Greece, 2008; pp. 141–177.
54. Nørgaard, H.W. Portable XRF on Prehistoric Bronze Artefacts: Limitations and Use for the Detection of Bronze Age Metal Workshops. *Open Archaeol.* **2017**, *3*, 101–122. [CrossRef]
55. Castelle, M.; Dillmann, P.; Vega, E.; Blanc-Riehl, C.; Vilain, A.; Chastang, P.; Anheim, E. Seal the deal: An extensive study of European historical copper-based seal matrices using a multimodal protocol. *J. Archaeol. Sci.* **2020**, *113*, 105061. [CrossRef]
56. Mödlinger, M.; Calderon, E.d.O.; Haubner, R. Arsenic Loss During Metallurgical Processing of Arsenical Bronze. *Archaeol. Anthropol. Sci.* **2019**, *11*, 133–140. [CrossRef]
57. Lechtman, H. Arsenic Bronze: Dirty Copper or Chosen Alloy? A View from the Americas. *J. Field Archaeol.* **1996**, *23*, 477–514. [CrossRef]
58. Lechtman, H. The Production of Copper–Arsenic Alloys (Arsenic Bronze) by Cosmelting: Modern Experiment, Ancient Practice. *J. Archaeol. Sci.* **1999**, *26*, 497–526. [CrossRef]
59. Oudbashi, O.; Naseri, R.; Malekzadehet, M. Technical Studies on the Bronze Age Metal Artefacts from the Graveyard of Deh Dumen, South-Western Iran (Third Millennium BC). *Archaeometry* **2016**, *58*, 947–965. [CrossRef]
60. Chiavari, C.; Rahmouni, K.; Takenouti, H.; Joiret, S.; Vermaut, P.; Robbiola, L. Composition and electrochemical properties of natural patinas of outdoor bronze monuments. *Electrochim. Acta* **2007**, *52*, 7760–7769. [CrossRef]
61. Jones, C.; Duffy, C.; Gibson, A.; Terras, M. Understanding multispectral imaging of cultural heritage: Determining best practice in MSI analysis of historical artefacts. *J. Cult. Herit.* **2020**, *45*, 339–350. [CrossRef]
62. Tuttle, P. Conservation of the Bronze Cuirass and Helmet. *J. Paul Getty Mus. J.* **1982**, *10*, 141–144.
63. Stefani, E. Veio. Saggi E Scoperte Fortuite Nella Necropolis. *Not. Scavi* **1929**, *1929*, 326–349.
64. Humphreys, E. How to spot a fake. *Mater. Today* **2002**, *5*, 32–37. [CrossRef]
65. Drago Troccoli, L. Una coppia di principi nella necropoli di Casale del Fossa a Veio. In *Dinamiche di Sviluppo delle Città Nell’Etruria Meridionale: Veio, Caere, Tarquinia Vulci, Proceedings of the Atti del XXIII Convegno di Studi Etruschi ed Italici, Roma, Veio, Cerveteri/Pyrgi, Tarquinia, Tuscania, Vulci, Viterbo, 1–6 Ottobre 2001*; Paoletti, O., Ed.; IEPI: Pisa, Italy, 2005; Volume 23, pp. 87–124.
66. Molloy, B.; Mödlinger, M. The Organisation and Practice of Metal Smithing in Later Bronze Age Europe. *J. World Prehistory* **2020**, *33*, 169–232. [CrossRef]
67. De Marinis, R.C. Aspetti della metallurgia dell’età del Rame e dell’antica età del Bronzo nella penisola italiana. *Riv. Sci. Preist.* **2006**, *56*, 211–272.
68. Esposito, A.; Petitti, P.; Ferretti, M.; Gorghinian, A.; Rossi, F. The production of metal artefacts in Southern Etruria (Central Italy): Case studies from copper to Iron Age. *STAR Sci. Technol. Archaeol. Res.* **2019**, *5*, 64–84. [CrossRef]
69. Mödlinger, M. Body Armour in the European Bronze Age. In *Prehistoric Warfare and Violence: Quantitative and Qualitative Approaches*; Dolfini, A., Crellin, R., Horn, C., Uckelmann, M., Eds.; Springer: Cham, Switzerland, 2018; pp. 177–198. [CrossRef]
70. Chen, D.; Yang, Y.; Du, J.; Tang, X.; Luo, W. Alloy ratio and raw material sourcing of Warring States Period bronze bracelets in Huili County, Southwest China by pXRF and MC-ICP-MS. *Herit. Sci.* **2020**, *8*, 69. [CrossRef]
71. Heginbotham, A.; Bassett, J.; Bourgarit, D.; Eveleigh, C.; Glinsman, L.; Hook, D.; Smith, D.; Speakman, R.J.; Shugar, A.; Van Langh, R. The copper CHARM set: A new set of certified reference materials for the standardization of quantitative X-ray fluorescence analysis of heritage copper alloys. *Archaeometry* **2015**, *57*, 856–868. [CrossRef]
72. Roxburgh, M.A.; Heeren, S.; Huisman, D.J.; van Os, B.J.H. Non-Destructive Survey of Early Roman Copper-Alloy Brooches Using Portable X-Ray Fluorescence Spectrometry. *Archaeometry* **2019**, *61*, 55–69. [CrossRef]
73. Zararsiz, A.; Zimmermann, T. The Missing Jigsaw Piece—PxrF Bulk Analysis of the Karaburun Dagger and Some General Considerations on Metalwork in Early Bronze Age Western Anatolia. *Cedrus* **2020**, *8*, 65–74. [CrossRef]

Article

# Aqua Traiana, a Roman Infrastructure Embedded in the Present: The Mineralogical Perspective

Michela Botticelli , Laura Calzolari , Caterina De Vito, Silvano Mignardi  and Laura Medeghini \* 

Department of Earth Sciences, Sapienza University of Rome, Piazzale A. Moro, 5, 00185 Rome, Italy; michela.botticelli@uniroma1.it (M.B.); laura.calzolari@uniroma1.it (L.C.); caterina.devito@uniroma1.it (C.D.V.); silvano.mignardi@uniroma1.it (S.M.)

\* Correspondence: laura.medeghini@uniroma1.it; Tel.: +39-064991-4926

**Abstract:** Construction materials from the internal ducts of *Aqua Traiana*, a still operative Roman aqueduct built in 109 AD to supply water to Rome, were characterized by optical microscopy (OM), scanning electron microscopy (SEM-EDS), X-ray powder diffraction (XRPD) and electron microprobe analysis (EMPA). Petrographic analysis and XRPD revealed that mortar aggregates are compatible with Vitruvius' *harena fossicia* and allowed the distinction of the original mortars from those of the 17th-century papal restoration. The first showed an amorphous binder while the latter have a typical lime binder. By SEM-EDS and EMPA, the microstructure of mortar aggregates was analyzed and the composition of specific minerals quantified. Microanalysis testifies the Romans' great expertise in the selection of pozzolanic building materials, giving evidence of the possible use of local tuffs from the Sabatini Volcanic District. It also confirms the exploitation of red pozzolan from the Roman Magmatic Province, specifically from the Alban Hills district. OM also proves a high compatibility with local supplies for bricks and *cocciopesto*. Of these, the first were fired at moderately low temperature, while the latter show an amorphous binder as in the original Trajan mortars. All building materials thus stand for similar technological choices and a coeval production.

**Keywords:** Roman mortars; aqueduct; microanalysis; red pozzolan; Sabatini Volcanic District

**Citation:** Botticelli, M.; Calzolari, L.; De Vito, C.; Mignardi, S.; Medeghini, L. *Aqua Traiana*, a Roman Infrastructure Embedded in the Present: The Mineralogical Perspective. *Minerals* **2021**, *11*, 703. <https://doi.org/10.3390/min11070703>

Academic Editors: Daniel Albero Santacreu, José Cristóbal Carvajal López and Adrián Durán Benito

Received: 2 June 2021  
Accepted: 26 June 2021  
Published: 29 June 2021

**Publisher's Note:** MDPI stays neutral with regard to jurisdictional claims in published maps and institutional affiliations.



**Copyright:** © 2021 by the authors. Licensee MDPI, Basel, Switzerland. This article is an open access article distributed under the terms and conditions of the Creative Commons Attribution (CC BY) license (<https://creativecommons.org/licenses/by/4.0/>).

## 1. Introduction

Knowledge on ancient societies develops through the study of customs, traditions, beliefs and relationships with other populations. Important information can be obtained by the analysis of the materials these societies produced. In this perspective, archaeometry has recently paid increasing attention to the mineralogical and chemical study of geomaterials [1–10] to reconstruct technological knowledge and skills acquired by ancient populations.

Roman aqueducts are the greatest expression of these competencies, material awareness being merged with the creation of architectural solutions to ensure survival over time. Although these monuments reflect the set of engineering knowledge of the past, historical sources dealing with their raw materials and supplies are few: Vitruvius' *De Architectura*, Pliny the Elder's *Naturalis Historia* or Strabo's *Geographica* [11]. Similarly, archaeometric studies taking into consideration material analysis on aqueducts are rare. Mortars and bricks from the Antioch aqueduct of Syria (Turkey) have been most recently analyzed to identify their production technology and deterioration [12]; mortars and plasters from the aqueduct of Naxos island (Greece) have been studied to define their hydraulic features [13]; finally, mortars, pilasters and arches of the ancient aqueduct of Carthage have been characterized [14]. Even the Italian literature is scarce: in the Roman aqueduct of Padua only stone materials were characterized [15]; Rizzo et al. [16] characterized the hydraulic mortars used in Pantelleria aqueducts and finally ceramic pipes of the Roman aqueduct of Raiano (L'Aquila) were analyzed to identify its raw materials [17].

*Aqua Traiana* is one of the few still functioning Roman aqueducts and the characterization study hereby presented is a unique opportunity to document its building materials.

The aqueduct, with its 57-km route from Lake Bracciano to Rome and the strong difference in height between the starting and arrival point (from 320 to 72 m asl), is a perfect example of Roman engineering skills (Figure 1a). Inaugurated in 109 AD, *Aqua Traiana* was built to supply energy to the mills located on the Janiculum (eastern part of the city of Rome). The main duct is variable, both in size and height, and it is characterized by a mixture of construction methods and materials. During barbarian invasions, the aqueduct was damaged several times. It was finally restored by Pope Paul V, between 1609 and 1612 [18–20]. Since that moment, it has never stopped functioning and supplying water to Rome.

The present study evaluates the mineralogical and physicochemical composition of mortars, *cocciopesto* and bricks from the *Aqua Traiana* to define the building technology. Of these, *cocciopesto* is the term applied to a mortar containing either crushed terracotta or pozzolan [21]. A multianalytical approach was applied including optical microscopy (OM) in thin section and X-ray powder diffraction (XRPD). Scanning electron microscopy with energy dispersive X-ray spectroscopy (SEM-EDS) and electron microprobe analysis (EMPA) were then applied to determine chemical composition and microstructure of the mortars.

The results obtained from the different samples allow a complete characterization of the materials used in the monument and the comparison among those used in the Trajan Era and the ones related to the restoration of Pope Paul V.

#### *Brief Geological Setting*

Lake Bracciano is part of the Sabatini Volcanic District, which belongs to the Roman Comagmatic Province [22]. The high-K feature of these products has been related to a metasomatized mantle source, i.e., to a phlogopite-bearing peridotite recording subduction-related fluids and/or melting processes [23–25]. The occurrence of silica-undersaturated ultrapotassic rocks (e.g., leucite-bearing) is related to the subduction of carbonate-rich pelites [26]. Volcanic activity was mainly characterized by widespread pyroclastic flows and sub-Plinian to Plinian fallout, the activity area (ca. 1800 Km<sup>2</sup>) having originated the Bracciano system (W) and the Sacrofano system (E) [22,27].

The Sabatini Volcanic District is characterized by volcanic rocks ranging from leucite-tephrites to leucite- and hauyne-phonolites. The activity of the area can be divided in five main phases, which generated the volcanic products shown in Figure 1a.



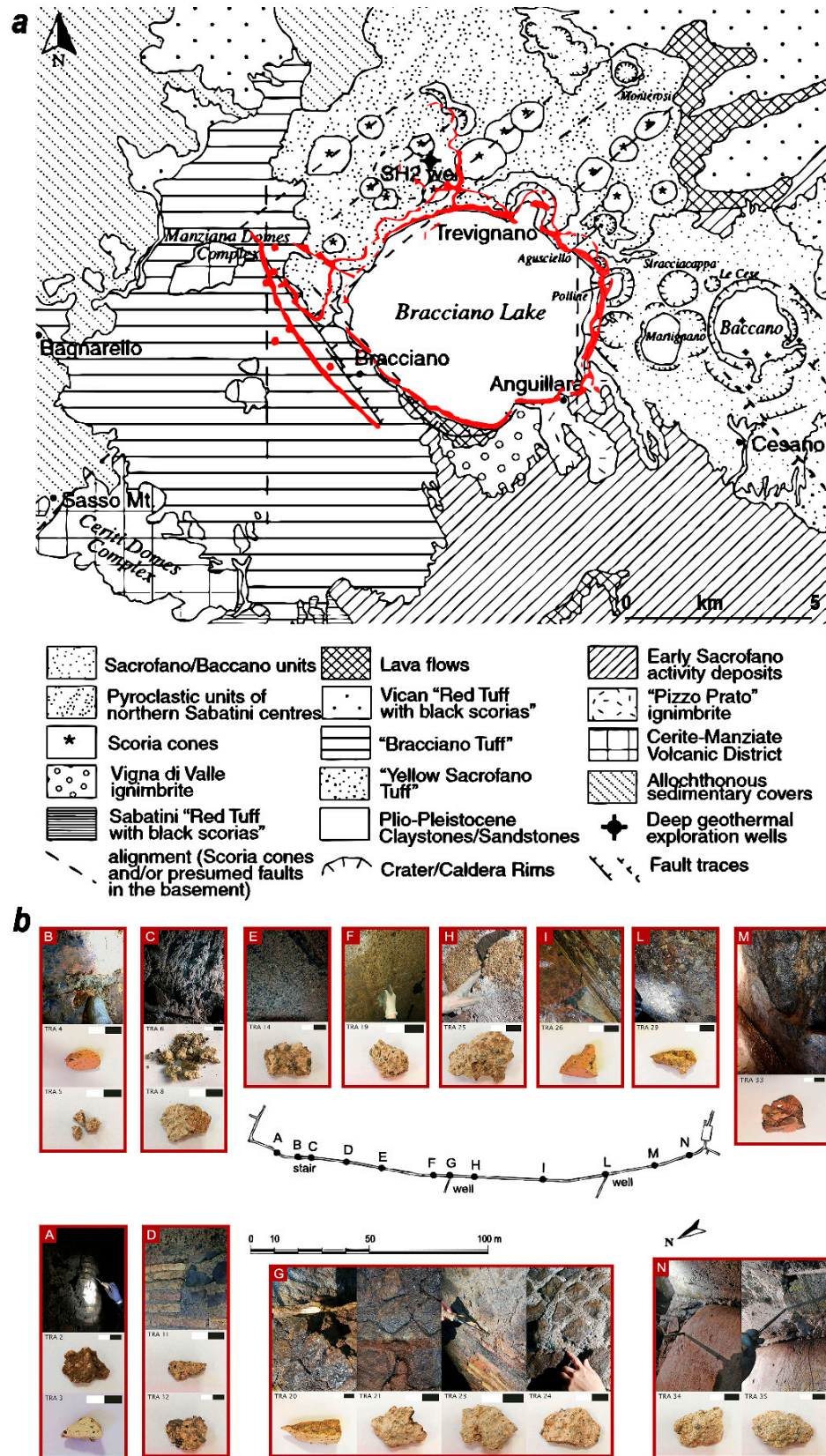


Figure 1. (a) Geological map of the Sabatini Volcanic District, modified after [28]: the light red line represents the path of the Trajan aqueduct around Lake Bracciano; (b) segment of the aqueduct with the location of each sampling point (A–N) and corresponding sample (Table 1).

Among them, the Tufo Giallo della Via Tiberina (yellow tuff of Via Tiberina, TGdVT) leucite phono-trachytic pyroclastic succession includes lower (LTGdVT) and upper (UT-GdVT) sequences, Tufo Giallo di Prima Porta (yellow tuff of Prima Porta, TGdPP) and the Grottarossa Pyroclastic Sequence [22,29]; above it the emplacement of extensive airfall tuffs and ashes interbedded with surges and minor pyroclastic flow units corresponds to the Sacrofano stratified tuffs, alternating with sporadic lava flows; a large pyroclastic-flow forms the Tufo Rosso a Scorie Nere (red tuff with black scoria, TRaSN); finally, a succession of pumice and scoria fall deposits underlies the Tufo Giallo di Sacrofano (yellow tuff of Sacrofano, TGdS) [30].

**Table 1.** List of samples analyzed, with the reference period and sampling point.

Sample	Dating	Description
mortars		
TRA 2	Trajan Age	Mortar between bricks
TRA 5	Trajan Age	Mortar between the bricks of the stairs near TRA 4
TRA 6	Papal restoration	Mortar of the vault that covers the access stair
TRA 8	Trajan Age	Mortar between leucitite blocks (between the stair and the vault)
TRA 11	Trajan Age	Mortar in the junction between leucitite blocks and <i>opus latericium</i>
TRA 12	Trajan Age	Mortar of the vault, over sample TRA 11
TRA 14	Trajan Age	Mortar of the vault
TRA 19	Trajan Age	Mortar of the vault
TRA 21	Trajan Age	Mortar between leucitite blocks in the well
TRA 23	Trajan Age	Mortar between the bricks
TRA 24	Trajan Age	Mortar between leucitite blocks in the well
TRA 25	Trajan Age	Mortar of the vault
TRA 34	Papal restoration	Plaster on the wall
TRA 35	Papal restoration	Mortar of the vault over TRA 34
<i>cocciopesto</i>		
TRA 29	Trajan Age	<i>Cocciopesto</i> from the wall
TRA 33	Trajan Age	<i>Cocciopesto</i> from the floor
brick		
TRA 3	Trajan Age	Brick near TRA 2
TRA 4	Trajan Age	Brick of the stairs
TRA 20	Trajan Age	Brick from the floor of the well
TRA 26	Trajan Age	Bipedal brick from the floor

## 2. Materials and Methods

### 2.1. Samples

Samples of ancient mortars, bricks and *cocciopesto* (Table 1, Figure 1b) were collected inside a secondary duct of Trajan's aqueduct, at Settebotti-Trevignano Romano, in the northern area of Lake Bracciano (Rome, Italy). Fourteen mortar samples belong to different types of masonry (mortars between bricks in *opus latericium*, mortars between stone blocks in *opus reticulatum* or the hydraulic plaster). They are also representative of different building phases (Trajan Age and papal restoration), as recognized by the archaeologists based on macroscopic features, stratigraphic context and construction phase; two *cocciopesto* (or *opus signinum*) fragments were collected from the covering of the duct, whereas four brick fragments were sampled from both the masonry and the bipedal bricks used on the floor.

### 2.2. Experimental Methods

A preliminary macroscopic analysis was performed by the naked eye on dried samples to define the colour and size of the aggregates and the possible presence of additives.



Thin sections were then analyzed by a Zeiss D-7082 Oberkochen polarized optical microscope. Microscopic analysis in both parallel (PPL) and crossed polarized light (XPL) was performed according to Pecchioni et al. [31] and the normal 12/83 [32] for mortars, through which it was also possible to qualitatively estimate the binder/aggregate ratio and porosity by visual comparison. Whitbread's criteria [33] were indeed used for brick and *cocciopesto* fragments.

The identification of material providing hydraulicity is easy by OM. However, if this component is finely ground or interference colours are similar to that of the matrix, microstructural analysis combined with chemical investigations can help [31]. Hence, SEM-EDS investigation was carried out on representative mortar samples. Based on microscopic analysis, macroscopic features and discrimination given by the archaeologists, two Papal samples (TRA 6 and TRA 35) and five Trajan samples (TRA 2, TRA 11, TRA 12, TRA 21 and TRA 23) were analyzed. A FEI Quanta 400 scanning electron microscope coupled with energy dispersive spectroscopy was used to define the microstructure of the samples and chemical composition of the aggregates and possibly highlight different microchemical features between original and restoration materials.

EMPA was also carried out on samples representative of the different function of the mortar: in the junction between leucite blocks and *opus latericium* (TRA 11); between leucite blocks in the well (TRA 21) and between bricks (TRA 23). A Cameca SX50 microprobe was used, equipped with five wavelength-dispersive spectrometers and operating at 15 kV accelerating voltage, 15 nA beam current and 10  $\mu\text{m}$  beam size. Element peaks and background were measured with counting times of 20 s and 10 s respectively. Wollastonite was used as a reference standard for Si (TAP, thallium (acid) phthalate crystal) and Ca (XET, pentaerythritol crystal), augite for Mg (TAP), corundum for Al (TAP), jadeite for Na (TAP), rutile for Ti (XET), fayalite for Fe (LIF, lithium fluoride), rhodonite for Mn (LIF), orthoclase for K (XET), chalcopyrite for Cu (LIF), galena for Pb (XET), cassiterite for Sn (XET), apatite for P (XET), barite for Ba (XET) and sphalerite for Zn (LIF). Matrix corrections were calculated by the PAP method with software supplied by the Microbeams Services [34,35]. The relative analytical error was 1% for major elements and it increased as their concentration decreased [36,37]. The detection limits under the specified working condition ranged between 0.01 and 0.1 wt %.

Finally, a small amount of each mortar sample was finely ground in an agate mortar for XRPD analysis by a Bruker D8 focus diffractometer with  $\text{CuK}\alpha$  radiation, operating at 40 kV and 30 mA. The following instrumental set-up was chosen: 3–60° 2 $\theta$  range and a scan step of 0.02° 2 $\theta$ /2 s. Data processing, including semiquantitative analysis based on the "Reference Intensity Ration Method", was performed using X PowderX software.

### 3. Results and Discussion

#### 3.1. Mortars

The preliminary macroscopic analysis highlighted that the mortars samples are hard and compact, i.e., resistant and not friable. They are characterized by a binder fraction varying in colour from beige to yellow and a pozzolan-based aggregate with tuff-ash fragments. Grains vary in size and shape (from rounded to subrounded) and are mainly represented by dark, reddish and yellow tuff fragments. Specifically, Trajan samples present a light-grey, whitish colour binder fraction.

Optical microscopy first permitted to distinguish the microstructure of the binder: a carbonate one with micritic texture and high birefringence for the papal samples and an amorphous gel-like cementing matrix in the Trajan mortars. In addition, OM analysis allowed the estimation of the binder/aggregate ratio. Papal samples show a ratio of 1:2, whereas Trajan Age samples have a binder/aggregate ratio of 1:3 or near this value.

XRPD spectra of papal restoration samples show very abundant calcite related to the binder. Minerals mainly related to the aggregate, which are possibly linked to a volcanic origin, are present in variable amount: clinopyroxene; K-feldspar, anorthoclase or sanidine; and zeolites, like analcime. Clay minerals are absent. On the contrary, most of the samples,

which correspond to the original Trajan Age samples, are characterized by the absence of calcite and a more abundant presence of clinopyroxene, clay minerals being present or in trace (Table 2). Specifically, the absence of calcite in these samples could be due to a complete portlandite consuming during the pozzolanic reaction (preventing calcite formation) or connected to alteration processes [38].

**Table 2.** Mineral assemblage of mortar samples and relative abundances (++++ very abundant; +++ abundant; ++ common; + present; t trace; - not detected), calculated by the reference intensity ratios (RIR) method in X PowderX. Anl: analcime, Cpx: clinopyroxene, Bt: biotite, Cal: calcite, Fsp: feldspar, Lct: leucite, Qtz: quartz, Cbz: chabazite, Pl: plagioclase, Amp: amphibole.

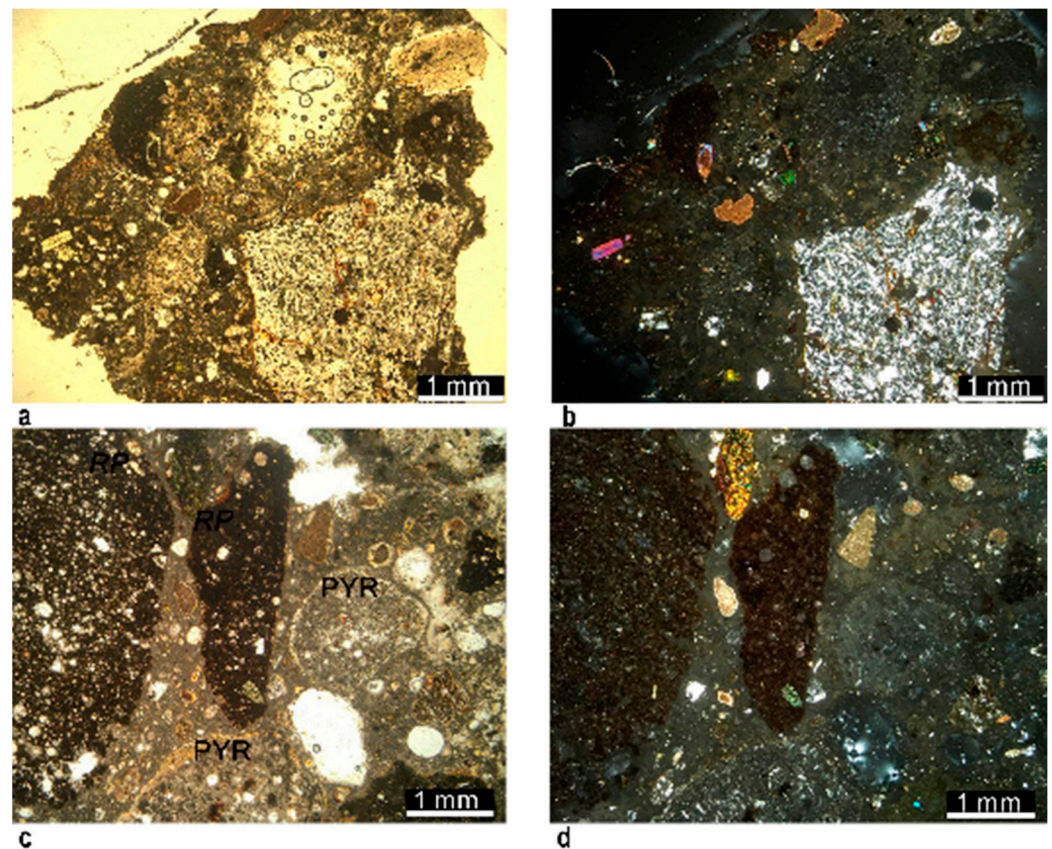
Sample	Anl	Cpx	Bt	Cal	Fsp	Clays	Lct	Qtz	Cbz	Pl	Amp
TRA 2	+++	++	+	-	++	+	-	t	t	-	-
TRA 5	+++	++++	t	-	+	t	-	-	-	t	-
TRA 6	-	+	+	++++	+	-	+	t	-	-	-
TRA 8	++++	++++	t	-	t	-	-	-	-	-	-
TRA 11	+++	++++	++	-	t	t	-	-	-	-	-
TRA 12	+++	++	t	-	++++	t	t	-	-	-	-
TRA 14	++++	+	++	-	+++	t	-	-	-	+	-
TRA 19	+++	++	t	-	++++	t	-	-	-	-	-
TRA 21	++	t	t	-	++++	t	-	-	-	-	-
TRA 23	+++	++++	t	-	++	t	-	-	tr	-	-
TRA 24	++	t	t	-	++++	t	-	-	-	-	t
TRA 25	+++	++	+	-	+	+	-	-	-	+++	-
TRA 34	t	+	t	++++	+	-	-	-	-	-	-
TRA 35	++	++	t	+++	+++	-	-	-	-	-	-

Additionally, based on the amount of alkali feldspars, two subgroups of Trajan samples can be described. One subgroup has K-feldspars generally very abundant in samples coming from the vault or between leucitite blocks in proximity of the first wall (see Figure 1b, samples TRA 12, TRA 14 and TRA 19 from the vault and TRA 21, TRA 23 and TRA 24 between leucitite blocks in the well or bricks nearby). Another subgroup indeed shows K-feldspars as present or in trace, mainly coming from the stairs (TRA 2, TRA 5 and TRA 8 in Figure 1b). Micaceous minerals, specifically biotite, are ubiquitous in lower amount. A feldspathoid typical of the Roman volcanic activity, leucite, was identified only in sample TRA 6, as already found by OM. Traces of clinopyroxene were found in TRA 14 and quartz in sample TRA 11.

Petrographic and SEM-EDS analysis highlighted that the aggregate is mainly composed of volcanic rock fragments, such as pyroclastic rock fragments with pozzolanic behavior. The pozzolanic material mainly consists of pumice clasts, tuff and lava fragments with primary phenocrysts surrounded by a vitreous fine-ash matrix. Porosity, size, shape and distribution of the aggregate are highly variable among the samples (Figure 2).

Specifically, it was possible to identify different inclusions belonging to the aggregate fraction. The pyroclastic rock fragments with porphyritic texture, variable porosity, sphericity, shape and colour ranging from brown to red or rarely yellow can be defined as pozzolanic tuff-like materials (Figure 2). This type of aggregate is the most abundant in all samples and less diffusive in samples TRA 6 and TRA 34. They are either highly porphyritic, with augite-crystals, or sometimes surrounded by illuvial clays (PYR Figure 2c).

Some big porous reddish-brown fragments with a very low porphyritic character and leucite microcrystals showing star-like habit were also recognized by OM as red pozzolan (RP in Figure 2c), especially in the original Trajan samples coming from the vaults (samples TRA 14, TRA 19, TRA 24 and TRA 25). Dark brown-to-black scoria fragments are also common in all samples, showing lower porphyritic texture, high porosity (subrounded vesicles are predominant) and colour comparable to the matrix by OM. They are characterized by the diffuse presence of elongated crystals of sanidine. Pores are either filled with acicular zeolite crystals or show reaction rims only.



**Figure 2.** Optical Microscopy micrographs of two Trajan mortars in thin section (parallel (left) and crossed polarized light (right)): (a,b) sample TRA 5; (c,d) sample TRA 25; PYR = pyroclastic rock fragment surrounded by illuvial clay; RP = red pozzolan.

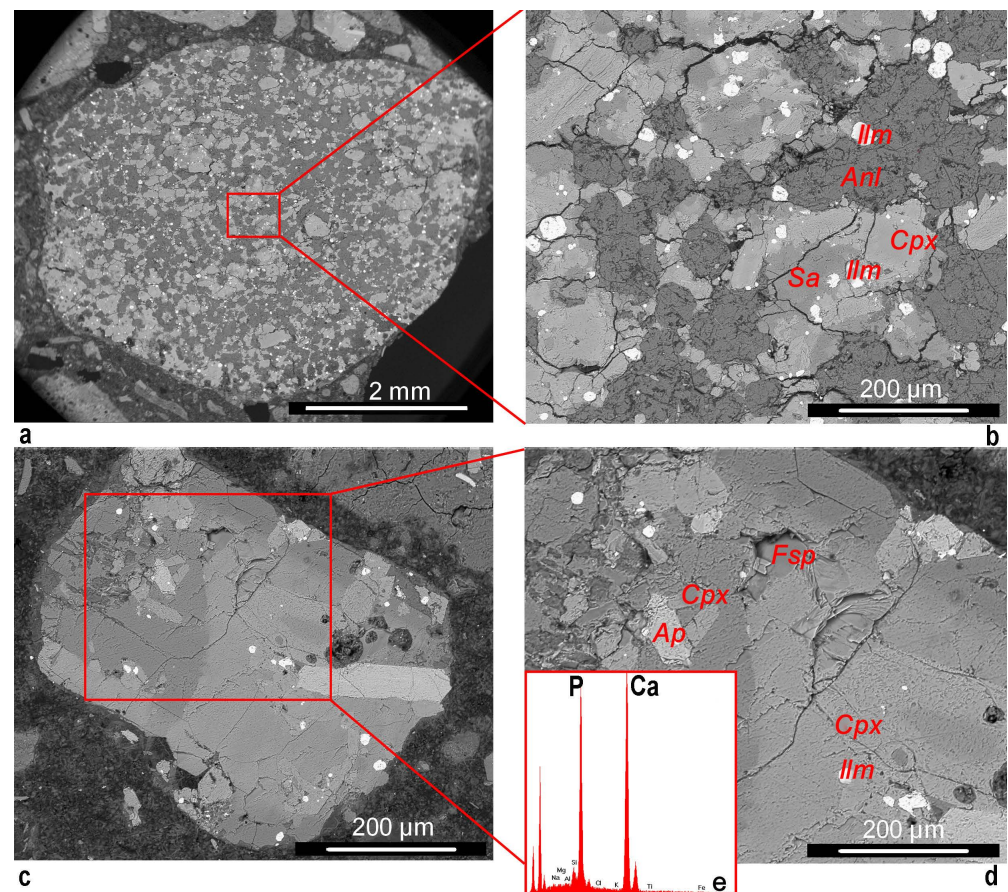
Additionally, some lava fragments showing analcime replacing leucite, feldspar, sanidine, ilmenite microcrystals and small volcanic rock fragments exhibiting apatite inclusions (Figure 3) were also identified.

Both original and restoration mortars are hydraulic and they are characterized by pozzolanic aggregates that favored the hydraulic reaction [39–41], as constantly found in Roman architecture [31]. In particular, the use of pozzolan is attested starting from 250 BC and the masonry technique of *cocciopesto* has been used since ancient times, probably the 2nd century BC [21,40]. Granular volcanic aggregates are either sand-sized or gravel-sized tephra and they correspond to Vitruvius' *harena fossicia* as described by Jackson et al. [42]. Raw materials at *Aqua Traiana* in fact correspond to highly altered volcanic glass scoriae, hard lavas, dispersed crystals and glassy fragments, frequently highly altered. Even the binder/aggregate ratio (1:3), estimated by petrographic analysis, suggests that Trajan mortars have been produced following Vitruvius' instructions for *harena fossicia*. However, it is now proposed for the first time that *harena fossicia* could possibly be exploited not only from the lithostratigraphic units of the Alban Hills volcano, but also from the deposits of Sabatini Volcanic District.

Trajan samples do not show high porosity (lower than 40%), suggesting that wet concrete could have been pressed to obtain a coherent, well-cemented final product [42]. Additionally, their grey-to-white colour may suggest the washing of pozzolanic aggregates to remove dirt and dust before their addition to the mortar [21]. These features are comparable with the original description by Van Deman [43], later confirmed by Jackson et al. [41], of high-quality mortars produced for monumental buildings during the Trajan era, such as the Trajan Market and the Baths. Moreover, lime lumps do not occur in the Trajan Age mortars of the present study, testifying great knowledge of the manufacturing process and high control of each step [44]. This considerable expertise is even attested by a deep knowledge

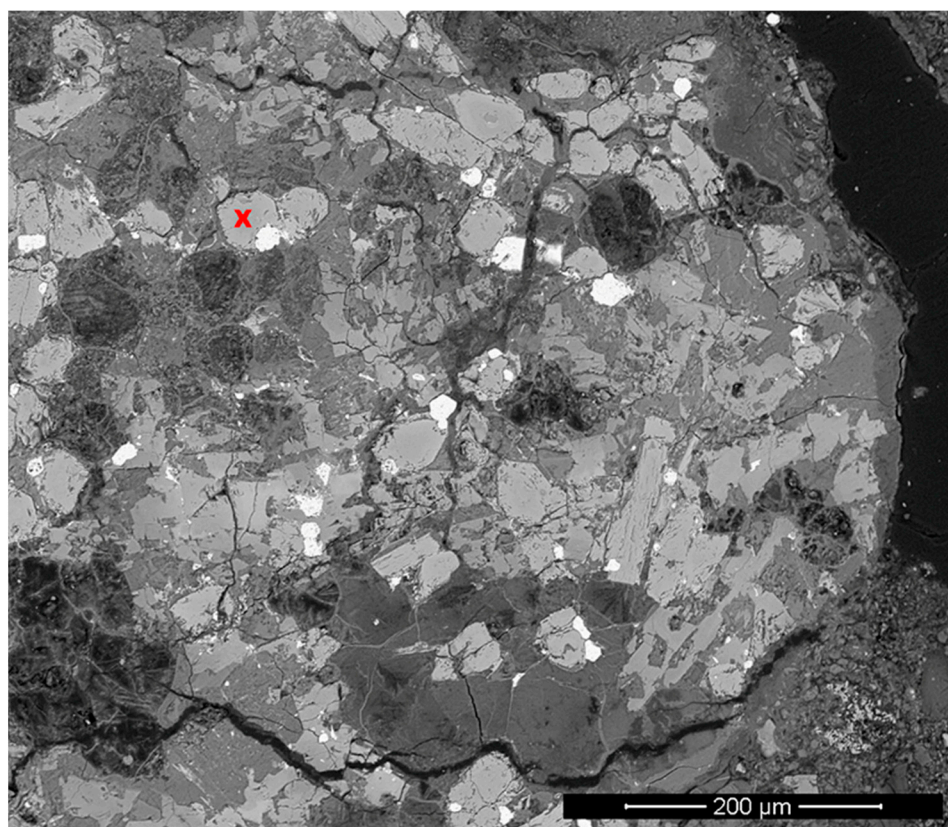


of supplies and by precise mixing and selection of the raw materials, strongly depending on the mortar function: lighter aggregates in fact predominate on the vaults. Specifically, the occurrence of red pozzolan (dark-red scoria fragments with starry leucite) was only documented in the Trajan mortars used to build the upper elements of *Aqua Traiana*. This is in agreement with coeval technological choices: at the Trajan's Baths, which indeed followed Domitian's building procedures [42,45,46], but also in the lightened mortars of the vault of "Aula Grande" at the Markets of Trajan [47] and of the "Sala Trisegmentata" at the Forum of Trajan [48].



**Figure 3.** Scanning Electron Microscopy (SEM) micrographs from sample TRA 23: lava fragment (a) and a magnified view of the red area (b) showing analcime (Anl) replacing leucite, clinopyroxene (Cpx), sanidine (Sa) and ilmenite (Ilm) microcrystals; volcanic rock fragment (c) and the red area (d) at a higher magnification, with microcrystals of clinopyroxene (Cpx), apatite (Ap), recognized by the contemporary presence of P and Ca in the Energy Dispersive X-ray Spectroscopy spectrum (e), feldspar (Fsp) and ilmenite (Ilm).

EMP analysis was performed to identify specific mineral phases that could be useful to characterize the aggregate and reconstruct the possible provenance of raw material. Therefore, aggregates were analyzed to obtain the chemical composition of specific minerals. Particularly, augite crystals analyzed in representative samples highlighted enrichment in Fe. Figure 4 shows an augite crystal in the Trajan sample TRA 11, whose composition (Table 3) is representative of the augite crystals also found and analyzed in the other samples.



**Figure 4.** Representative augite crystal in a volcanic rock fragment of the Trajan sample TRA 11 identified by SEM (red cross, see Table 3 for chemical data); in the same micrograph, acicular crystals filling porosities can be also seen.

**Table 3.** Chemical composition of the representative augite crystal of Figure 4 The relative formula was calculated on 6 oxygens from Electron Microprobe analysis (EMPA).

Oxide	wt% *		apfu
SiO <sub>2</sub>	44.66	Si	1.680
Al <sub>2</sub> O <sub>3</sub>	7.64	Al	0.339
MgO	10.10	Mg	0.567
Cr <sub>2</sub> O <sub>3</sub>	0.00	Cr <sup>+3</sup>	0.000
TiO <sub>2</sub>	1.37	Ti	0.039
FeO	11.27	Fe <sup>+2</sup>	0.086
Fe <sub>2</sub> O <sub>3</sub>	0.00	Fe <sup>+3</sup>	0.268
MnO	0.27	Mn	0.009
CaO	24.02	Ca	0.968
Na <sub>2</sub> O	0.53	Na	0.038
K <sub>2</sub> O	0.13	K	0.006
Total	100	Cat. Sum	4.000

\* normalized to 100.

Additionally, in these pyroclastic rock fragments, secondary minerals also occurred (analcimised leucite) and porosities were filled with recrystallized zeolite. These crystals were very fine, with a thickness lower than 5  $\mu\text{m}$ , therefore only one measurement could be performed on each crystal. However, numerous (more than three for each sample) point analyses were performed to evaluate the chemical composition of zeolites, according to [49]. By EMPA, these acicular crystals were identified as Mg-enriched chabazite (Table 4).

**Table 4.** Chemical composition and relative formula, calculated on 24 oxygens and 12 H<sub>2</sub>O molecules, of different representative chabazite crystals identified in different pyroclastic rock fragments.

	TRA 23	TRA21	TRA11		TRA 23	TRA21	TRA11
Oxide		<i>wt %</i>		<b>Element</b>		<i>apfu</i>	
SiO <sub>2</sub>	46.807	51.835	55.020	Si	7.962	8.959	8.971
Al <sub>2</sub> O <sub>3</sub>	21.280	15.019	16.684	Al	4.272	3.063	3.210
				<b>Z-site</b>	<b>12.234</b>	<b>12.022</b>	<b>12.182</b>
CaO	6.553	5.336	4.707	Ca	1.196	0.989	0.823
Na <sub>2</sub> O	0.166	0.271	0.205	Na	0.027	0.045	0.032
K <sub>2</sub> O	2.023	2.411	2.350	K	0.440	0.532	0.489
MgO	0.888	0.726	0.582	Mg	0.225	0.187	0.142
<b>Total</b>	<b>77.717</b>	<b>75.598</b>	<b>79.548</b>	<b>X-site</b>	<b>1.888</b>	<b>1.754</b>	<b>1.487</b>

Pumice clasts in the mortars have a round shape and high porosity, with colour ranging from white to yellow or grey in PPL.

Single crystals such as amphiboles, pyroxenes and feldspars (plagioclase—mainly albite—orthoclase, anorthoclase and sanidine), all attributable to volcanic rock fragments, are dispersed in the binder. Some of them, especially pyroxene and feldspar crystals, sometime show alterations, such as partial dissolution or fractures with recrystallizations.

Fragments of volcanic rocks (leucite type), with big crystals of leucite, clinopyroxene and plagioclase, were only present in TRA 6 and TRA 34, which were both related to the papal restoration and may imply a slightly different supply.

Grog, namely crushed ceramic fragments, is the only artificial material with pozzolanic behavior identified in the sole sample TRA 34 as predominant, while natural materials with pozzolanic behavior are less common in this sample. The use of ceramic fragments as aggregates in ancient mortar is widely attested [40,50]. The role of ceramics is comparable to that of pozzolan, the vitreous or amorphous fraction reacting with the binder to produce a hard and waterproof material, even if the reaction is not as strong as with pozzolan [38].

The strong compositional difference between papal and Trajan Age samples allows an easy differentiation of the two building phases.

Our results show that the original bedding mortars of the Trajan aqueduct were produced from a mixture of lime, water and fine-grained material with pozzolanic behavior. The aggregate is exclusively constituted by the natural material of volcanic origin, while artificial components are absent. These major components are typical in the volcanism of the Roman Magmatic Province [51] and compatible with the geological setting of the Sabatini Volcanic District with rocks ranging from leucite-tephrites to leucite- and haüyne-phonolites. Analcime characterizes the secondary assemblage of these volcanic products, being leucite subjected to analcimation [52], as it is commonly found in lithified deposits of this area [53,54]. Microsubhedral ilmenite has been also described as a typical, ubiquitous accessory mineral in the Sabatini dark-grey porphyritic lava fragments [55]. The black fragments in our mortars may indeed correspond to the description given for glassy clasts from the upper lithified deposit of Tufo Rosso a Scorie Nere (red tuff with black scoria) [56]. Finally, the recognition of apatite in some vitreous fragments corroborates the hypothesis of local supply. In fact, apatite occurs as an accessory mineral in the tephriphonolite, latite and phonotephrite of the Martignano Units [57]. The use of this kind of supply is expressed by the compatibility in chemical composition of the clinopyroxenes calculated in the present work and those provided by the literature [55,57,58] in leucite-tephrites from the middle Martignano Unit. However, it must be remarked that apatite has been also found in the low porphyritic scoriae of Pozzolane Nere and Pozzolanelle formations of the Alban Hills [59]. Indeed, the concomitant presence of pozzolanic aggregates from further areas of the Roman Magmatic Province is possible, especially if we consider that in the Roman imperial period the supply from far away quarries had become common [41]. For example, sanidine-bearing pumices, which are frequent aggregates in the mortars from



*Aqua Traiana*, are also described in the San Paolo formation, deposited by the Tiber River and its tributaries at the base of the Capitoline Hill [41,48].

Independently of the nature of the aggregate and binder, needle-shaped recrystallizations occurred in the pores. These recrystallizations were also found in local tuffs [60,61]. However, chabazite in the present work showed a slightly higher Mg content and less K and Na, suggesting the presence of zeolite (phillipsite and chabazite) as the secondary weathering mineral or related to the hydraulic reaction [62–64].

### 3.2. Bricks and Cocciopesto

Brick samples are characterized by fine grain-sized inclusions and a clayey matrix. The nature of the inclusions, their packing and mean size were considered to distinguish two petrographic fabrics (Table 5).

**Table 5.** Microscopic characteristics of brick and *cocciopesto* fragments.

Sample	Porosity	Matrix		Inclusions
TRA 3	5% Meso–macrovesicles	90% non calcareous brown-green activity	5% Equant–elongated; angular–subrounded; open spaced; not aligned	Predominant: quartz (0.1–0.3 mm), feldspars (0.2–0.3 mm) Common: pyroxene (0.3–1.2 mm) Frequent: iron oxide nodules (0.2–1 mm)
TRA 4	10% Micro–macrovesicles Macrovoids	85% non calcareous brown-green activity	5% Equant–elongated; angular–subrounded; open-spaced; not aligned	Predominant: quartz (0.1–0.2 mm) Common: pyroxene (0.5–1.2 mm) Few: iron oxide nodules (0.2–1 mm), quartz (0.3–1.2 mm) Very rare: siliceous rock fragments (1 mm)
TRA 20	5% Meso–microvesicles	90% non calcareous brown-green activity	5% Equant–elongated; angular–subrounded; open-spaced; not aligned	Predominant: quartz (0.1 mm), feldspars (0.2–0.3 mm) Dominant: pyroxene (0.4–1.3 mm) Few: quartz (0.5–1 mm) Very rare: volcanic rock fragments (5 mm)
TRA 26	5% Meso–microvesicles	55% non calcareous red-brown activity	40% Equant–elongated; angular–subrounded; open-spaced; not aligned	Predominant: quartz (0.1–0.3 mm), Few: quartz (0.6–1.3 mm) Rare: pyroxene (0.3–0.5 mm), iron oxide nodules (0.3–0.8 mm)
TRA 29 *	5% Microvesicles	90% non calcareous brown-green activity	5% Equant–elongated; angular–subangular; single-spaced; not aligned	Predominant: quartz (0.1–0.3 mm), Common: pyroxene (0.7–0.8 mm) Few: quartz (0.7 mm) Very rare: fragments of siliceous rocks (1.0 mm), iron oxide nodules (0.3–0.5 mm)
	5% Microvesicles	90% non calcareous brown-green activity	5% Equant–elongated; angular–subangular; single-spaced; not aligned	Predominant: quartz (0.1–0.3 mm), Common: pyroxene (0.6 mm) Very rare: iron oxide nodules (0.3–0.5 mm)

Table 5. Cont.

Sample	Porosity	Matrix	Inclusions
TRA 33 *	3% Microvesicles	92% non calcareous brown-green activity	5% Equant–elongated; angular–subangular; single-spaced; not aligned
	3% Microvesicles meso–macrovoids	87% non calcareous brown-green activity	10% Equant–elongated; angular–subangular; single-spaced; not aligned
	5% Microvesicles meso–macrovoids	90% non calcareous brown-green activity	5% Equant–elongated; angular–subangular; single-spaced; not aligned

\* TRA 29 and TRA 33 are *cocciopesto* samples where three different brick fragments were recognized and described.

The first *fabric A-matrix* is characterized by a low percentage of inclusions (5%), equant and elongated, from angular to subrounded, open-spaced and not aligned with respect to the margin of the sample. Predominant fine quartz and plagioclase, common pyroxene crystals and iron oxide nodules were identified. In addition, some very rare fragments of rocks were also present. The porosity was estimated to be between 5 and 10% and was mainly represented by mesovesicles and voids, not aligned and without any secondary calcite. The non-calcareous matrix ranged in colour from beige to brown-green and it was optically active. The results obtained for the samples belonging to *fabric A-matrix* suggest that the starting raw material consisted of a purified clay containing fine quartz, plagioclase and pyroxene inclusions. The material underwent a selection process to remove the coarser fraction, as suggested by the absence of coarse inclusions. This process had good efficiency, as testified by the low percentage of inclusions and by the very fine grain size.

The second *fabric B-inclusions*, including only bipedal samples, was distinguished by the higher percentage (40%) of very fine grain-sized inclusions. Fine quartz is predominant in the samples, whereas coarser crystals were few in the matrix; rare pyroxene and nodules of iron oxides were also identified. The low porosity was represented by meso- and microvesicles without any secondary recrystallization. The non-calcareous matrix had a red-brownish colour and optical activity.

Concerning the *cocciopesto* fragments, the matrix was similar to the amorphous gel-like cementing matrix identified in mortar samples. It was impossible to distinguish crystals and it had very low colours ranging from green to brown. The aggregate was only represented by grog. Its inclusions show a clayey matrix with a brown-greenish colour, optically active. Predominant fine quartz and rare coarser crystals of pyroxene and quartz were identified among aggregates. The porosity was low and both inclusions and pores did not exhibit a preferred alignment. In addition, porosities were filled by secondary calcite.

*Fabric B-inclusions* could have been produced with a different clay respect to *fabric A-matrix*, the first being characterized by a higher amount of fine quartz and subjected to a lighter purification step during the production.

The difference in the granulometry and percentage of inclusions is probably connected to the end-use of the materials. The *fabric A-matrix* includes brick samples used in the masonry, which are not subjected to continuous attrite, whereas bipedal bricks in *fabric B-inclusions* are typical, squared, Roman bricks with a 60-cm side, used for flooring.

The strong optical activity of the matrix observed in both fabrics gives preliminary information about the firing temperature, which is suggested to be lower than 850 °C [17], in agreement with the literature [65].

The rest of the minerals identified are compatible with the volcanic geological setting of the area, suggesting a local supply of the clay.

*Cocciopesto* fragments show a matrix similar to the amorphous binder of mortar samples dated to the Trajan Age. The inclusions, only represented by grog, are comparable to the bricks of *fabric A-matrix*. Therefore, a supply of similar raw materials is suggested, and comparable technology and contemporary production are hereby hypothesized.

#### 4. Conclusions

The current research for the first time permitted a complete characterization of the building materials of the ancient *Aqua Traiana* aqueduct.

Concerning the mortars, they are all hydraulic, with fine aggregates of volcanic origin. Specifically, Trajan Age samples are characterized by a calcite-free amorphous binder, while a lime binder characterizes the samples of the papal restoration.

The compatibility of the pozzolanic aggregate with local supplies from the Bracciano area is for the first time inferred; however, supplies from more distant areas of the Roman Magmatic Province are co-occurrent. Raw materials are likely described as Vitruvius' *harena fossicia* and their use is highly compatible with the building technology of the Trajan Era, with specific aggregates for different parts of the masonry.

The great differences among Trajan and papal samples documented in this study may allow the future dating of other parts of the aqueduct, based on mineralogical and chemical characterization. Indeed, an increased number of mortar samples will allow collecting a systematic overview of the mineralogical assemblage in the mortars from *Aqua Traiana*. In addition, a multivariate statistical analysis using chemical data may be planned, investigating the role of the elements with lower mobile behavior in surface environments, such as K, Sc, Ga, Rb, Cs, REE and other elements such as Hf, Ta and Th, for a deeper differentiation of mortars.

Concerning ceramic components, bricks were produced with local materials and fired at a low temperature, with specific features connected to the end-use. *Cocciopesto* fragments showed a matrix similar to the amorphous binder of Trajan mortar samples and fragments of bricks as inclusions.

The compatibility of materials used in the production of Trajan mortars, bricks and *cocciopesto* suggests similar technological choices and may be explained by a coeval production. However, further investigation is ongoing and it will include samples from the main ducts of the aqueduct.

**Author Contributions:** M.B.: Data curation, Investigation, Writing—Original Draft. L.M.: Conceptualization, Funding acquisition, Supervision, Writing—Original Draft. L.C.: Data Curation, Investigation. C.D.V.: Formal analysis, Writing—review and editing. S.M.: Writing—review and editing. All authors have read and agreed to the published version of the manuscript.

**Funding:** Financial support was provided by “Sapienza” University of Rome—Progetto Ateneo 2019 Medeghini.

**Institutional Review Board Statement:** Not applicable.

**Informed Consent Statement:** Not applicable.

**Data Availability Statement:** All data derived from this research are presented in the enclosed figures and tables.

**Acknowledgments:** The authors want to express their gratitude to Sovrintendenza Capitolina ai Beni Culturali, in particular to Francesco Maria Cifarelli and Marina Marcelli, who allowed the research on the hydraulic mortars of Trajan's aqueduct; to ACEA ATO 2, Antonio Grosso and Armando Zitelli; to Roma Sotterranea speleological association, and in particular to Elettra Santucci, who lead us inside the aqueduct for the sampling. The authors thank the five anonymous reviewers for the useful comments and suggestions on ways to improve the manuscript.

**Conflicts of Interest:** The authors declare no conflict of interest.

## References

1. Botticelli, M.; Mignardi, S.; De Vito, C.; Liao, Y.; Montanari, D.; Shakarna, M.; Nigro, L.; Medeghini, L. Variability in pottery production at Khalet al-Jam'a necropolis, Bethlehem (West Bank): From the Early-Middle Bronze to the Iron Age. *Ceram. Int.* **2020**, *46*, 16405–16415. [CrossRef]
2. Rispoli, C.; Esposito, R.; Guerriero, L.; Cappelletti, P. Ancient Roman mortars from Villa del Capo di Sorrento: A multi-analytical approach to define microstructural and compositional features. *Minerals* **2021**, *11*, 469. [CrossRef]
3. Botticelli, M.; Maras, A.; Candeias, A.  $\mu$ -Raman as a fundamental tool in the origin of natural or synthetic cinnabar: Preliminary data. *J. Raman Spectrosc.* **2020**, *51*, 1470–1479. [CrossRef]
4. Bandiera, M.; Verità, M.; Lehuédé, P.; Vilarigues, M. The technology of copper-based red glass sectilia from the 2nd century AD Lucius Verus Villa in Rome. *Minerals* **2020**, *10*, 875. [CrossRef]
5. Sanjurjo-Sánchez, J.; Trindade, M.J.; Blanco-Rotea, R.; Garcia, R.B.; Mosquera, D.F.; Burbidge, C.; Prudêncio, M.I.; Dias, M.I. Chemical and mineralogical characterization of historic mortars from the Santa Eulalia de Bóveda temple, NW Spain. *J. Archaeol. Sci.* **2010**, *37*, 2346–2351. [CrossRef]
6. Sánchez-Pardo, J.C.; Blanco-Rotea, R.; Sanjurjo-Sánchez, J.; Barrientos-Rodríguez, V. Reusing stones in medieval churches: A multidisciplinary approach to San Martiño de Armental (NW Spain). *Archaeol. Anthropol. Sci.* **2019**, *11*, 2073–2096. [CrossRef]
7. Ricca, M.; Paladini, G.; Rovella, N.; Ruffolo, S.A.; Randazzo, L.; Crupi, V.; Fazio, B.; Majolino, D.; Venuti, V.; Galli, G.; et al. Archaeometric characterisation of decorated pottery from the archaeological site of Villa dei Quintili (Rome, Italy): Preliminary study. *Geosciences* **2019**, *9*, 172. [CrossRef]
8. Maltoni, S.; Silvestri, A. A mosaic of colors: Investigating production technologies of Roman glass tesserae from Northeastern Italy. *Minerals* **2018**, *8*, 255. [CrossRef]
9. Rahim, N.S.A. Analytical study and conservation of archaeological terra sigillata ware from Roman period, Tripoli, Libya. *Sci. Cult.* **2016**, *2*, 19–27. [CrossRef]
10. Maritan, L. Archaeo-ceramic 2.0: Investigating ancient ceramics using modern technological approaches. *Archaeol. Anthropol. Sci.* **2019**, *11*, 5085–5093. [CrossRef]
11. Jackson, M.; Marra, F. Roman stone masonry: Volcanic foundations of the ancient city. *Am. J. Archaeol.* **2006**, *110*, 403–436. [CrossRef]
12. Benjelloun, Y.; de Sigoyer, J.; Dessales, H.; Garambois, S.; Şahin, M. Construction history of the aqueduct of Nicaea (Izник, NW Turkey) and its on-fault deformation viewed from archaeological and geophysical investigations. *J. Archaeol. Sci. Rep.* **2018**, *21*, 389–400. [CrossRef]
13. Marvelaki-Kalaitzaki, P.; Galanos, A.; Doganis, I.; Kallithrakas-Kontos, N. Physico-chemical characterization of mortars as a tool in studying specific hydraulic components: Application to the study of ancient Naxos aqueduct. *Appl. Phys. A* **2011**, *104*, 335–348. [CrossRef]
14. Figueiredo, M.O.; Veiga, J.P.; Silva, T.P. Materials and reconstruction techniques at the Aqueduct of Carthage since the Roman period. *Hist. Constr. Guimarães* **2001**, *1*, 391–400.
15. Maritan, L.; Mazzoli, C.; Sassi, R.; Speranza, F.; Zanco, A.; Zanovello, P. Trachyte from the Roman aqueducts of Padua and Este (north-east Italy): A provenance study based on petrography, chemistry and magnetic susceptibility. *Eur. J. Miner.* **2013**, *25*, 415–427. [CrossRef]
16. Rizzo, G.; Ercoli, L.; Megna, B.; Parlapiano, M. Characterization of mortars from ancient and traditional water supply systems in Sicily. *J. Therm. Anal. Calorim.* **2008**, *92*, 323–330. [CrossRef]
17. Medeghini, L.; Ferrini, V.; Di Nanni, F.; D'Uva, F.; Mignardi, S.; De Vito, C. Ceramic pipes of the Roman aqueduct from Raiano village (L'Aquila, Italy): A technological study. *Constr. Build. Mater.* **2019**, *218*, 618–627. [CrossRef]
18. Dembskey, E.J. The Aqueducts of Ancient Rome. Ph.D. Thesis, University of South Africa, Pretoria, South Africa, 2009.
19. Cifarelli, F.M.; Marcelli, M. L'Aqua Traiana: Infrastruttura della città antica e moderna. In *Traiano: Costruire L'Impero, Creare L'Europa*; Parisi Presicce, C., Milella, M., Pastor, S., Eds.; De Luca Editori d'Arte: Rome, Italy, 2017; pp. 221–226.
20. O'Neill, E. L'Acquedotto di Traiano tra il ninfeo di S. Fiora e il Lago di Bracciano. *Atlante Temat. Topogr. Antica* **2014**, *24*, 197–214.
21. Lancaster, L.C. *Concrete Vaulted Construction in Imperial Rome: Innovations in Context*; Cambridge University Press: New York, NY, USA, 2005; ISBN 9780511610516.
22. Marra, F.; Sottili, G.; Gaeta, M.; Giaccio, B.; Jicha, B.; Masotta, M.; Palladino, D.M.; Deocampo, D.M. Major explosive activity in the Monti Sabatini Volcanic District (central Italy) over the 800–390 ka interval: Geochronological–geochemical overview and tephrostratigraphic implications. *Quat. Sci. Rev.* **2014**, *94*, 74–101. [CrossRef]
23. Conticelli, S.; Peccerillo, A. Petrology and geochemistry of potassic and ultrapotassic volcanism in central Italy: Petrogenesis and inferences on the evolution of the mantle sources. *Lithos* **1992**, *28*, 221–240. [CrossRef]
24. Peccerillo, A. Multiple mantle metasomatism in central-southern Italy: Geochemical effects, timing and geodynamic implications. *Geology* **1999**, *27*, 315–318. [CrossRef]
25. Conticelli, S.; D'Antonio, M.; Pinarelli, L.; Civetta, L. Source contamination and mantle heterogeneity in the genesis of Italian potassic and ultrapotassic volcanic rocks: Sr-Nd-Pb isotope data from Roman Province and Southern Tuscany. *Mineral. Petrol.* **2002**, *74*, 189–222. [CrossRef]
26. Conticelli, S.; Avanzinelli, R.; Ammannati, E.; Casalini, M. The role of carbon from recycled sediments in the origin of ultrapotassic igneous rocks in the Central Mediterranean. *Lithos* **2015**, *232*, 174–196. [CrossRef]



27. Masotta, M.; Gaeta, M.; Gozzi, F.; Marra, F.; Palladino, D.M.; Sottili, G. H<sub>2</sub>O- and temperature-zoning in magma chambers: The example of the Tufo Giallo della Via Tiberina eruptions (Sabatini Volcanic District, central Italy). *Lithos* **2010**, *118*, 119–130. [CrossRef]
28. Buttinelli, M.; De Rita, D.; Cremisini, C.; Cimarelli, C. Deep explosive focal depths during maar forming magmatic-hydrothermal eruption: Baccano Crater, Central Italy. *Bull. Volcanol.* **2011**, *73*, 899–915. [CrossRef]
29. Sottili, G.; Palladino, D.M.; Marra, F.; Jicha, B.; Karner, D.B.; Renne, P. Geochronology of the most recent activity in the Sabatini Volcanic District, Roman Province, central Italy. *J. Volcanol. Geotherm. Res.* **2010**, *196*, 20–30. [CrossRef]
30. Marra, F.; Anzidei, M.; Benini, A.; D’Ambrosio, E.; Gaeta, M.; Ventura, G.; Cavallo, A. Petro-chemical features and source areas of volcanic aggregates used in ancient Roman maritime concretes. *J. Volcanol. Geotherm. Res.* **2016**, *328*, 59–69. [CrossRef]
31. Pecchioni, E.; Fratini, F.; Cantisani, E. *Atlas of the Ancient Mortars in Thin Section under Optical Microscope*; Nardini Editore: Firenze, Italy, 2017.
32. Consiglio Nazionale delle Ricerche; Istituto Centrale del Restauro. *Normal 12-83-Aggregati Artificiali di Clasti e Matrice Legante non Argillosa*; COMAS Grafica: Rome, Italy, 1983.
33. Whitbread, I.K. *Greek Transport Amphorae: A Petrological and Archaeological Study*; British School at Athens: Athens, Greece, 1995; Volume 4, ISBN 0-904887-13-8.
34. Pouchou, J.L.; Pichoir, F. “PAP”  $\phi(\rho z)$  procedure for improved quantitative microanalysis. In *Microbeam Analysis*; Armstrong, J.T., Ed.; San Francisco Press Inc.: San Francisco, CA, USA, 1985.
35. De Vito, C.; Medeghini, L.; Garruto, S.; Coletti, F.; De Luca, I.; Mignardi, S. Medieval glazed ceramic from Caesar’s Forum (Rome, Italy): Production technology. *Ceram. Int.* **2018**, *44*, 5055–5062. [CrossRef]
36. Lifshin, E.; Gauvin, R. Minimizing Errors in Electron Microprobe Analysis. *Microsc. Microanal.* **2001**, *7*, 168–177. [CrossRef]
37. Poole, D.M. Progress in the correction for the atomic number effects. In *Quantitative Electron Probe Microanalysis*; Heinrich, K.F.J., Ed.; National Bureau of Standards, Spec. Pub. 298: Washington, WA, USA, 1968; pp. 93–131.
38. Moropoulou, A.; Bakolas, A.; Aggelakopoulou, E. Evaluation of pozzolanic activity of natural and artificial pozzolans by thermal analysis. *Thermochim. Acta* **2004**, *420*, 135–140. [CrossRef]
39. Chiari, G.; Santarelli, M.L.; Torraca, G. Caratterizzazione delle malte antiche mediante l’analisi di campioni non frazionati. *Materiali Strutt. Probl. Conserv.* **1992**, *2*, 111–137.
40. Torraca, G. *Lectures on Materials Science for Architectural Conservation*; Getty Conservation Institute: Los Angeles, CA, USA, 2009; ISBN 978-0-9827668-3-5.
41. Jackson, M.; Deocampo, D.; Marra, F.; Scheetz, B. Mid-Pleistocene pozzolanic volcanic ash in ancient Roman concretes. *Geoarchaeology* **2010**, *25*, 36–74. [CrossRef]
42. Jackson, M.; Marra, F.; Deocampo, D.; Vella, A.; Kosso, C.; Hay, R. Geological observations of excavated sand (harenae fossiciae) used as fine aggregate in Roman pozzolanic mortars. *J. Rom. Archaeol.* **2007**, *20*, 25–53. [CrossRef]
43. Van Deman, E.B. Methods of determining the date of Roman concrete monuments. *Am. J. Archaeol.* **1912**, *16*, 230–251. [CrossRef]
44. Moropoulou, A.; Bakolas, A.; Anagnostopoulou, S. Composite materials in ancient structures. *Cem. Concr. Compos.* **2005**, *27*, 295–300. [CrossRef]
45. Freda, C.; Gaeta, M.; Giaccio, B.; Marra, F.; Palladino, D.M.; Scarlato, P.; Sottili, G. CO<sub>2</sub>-driven large mafic explosive eruptions: The Pozzolane Rosse case study from the Colli Albani Volcanic District (Italy). *Bull. Volcanol.* **2011**, *73*, 241–256. [CrossRef]
46. Marra, F.; Danti, A.; Gaeta, M. The volcanic aggregate of ancient Roman mortars from the Capitoline Hill: Petrographic criteria for identification of Rome’s “pozzolans” and historical implications. *J. Volcanol. Geotherm. Res.* **2015**, *308*, 113–126. [CrossRef]
47. Jackson, M.D.; Logan, J.M.; Scheetz, B.E.; Deocampo, D.M.; Cawood, C.G.; Marra, F.; Vitti, M.; Ungaro, L. Assessment of material characteristics of ancient concretes, Grande Aula, Markets of Trajan, Rome. *J. Archaeol. Sci.* **2009**, *36*, 2481–2492. [CrossRef]
48. Bianchi, E.; Brune, P.; Jackson, M.; Marra, F.; Meneghini, R. Archaeological, structural, and compositional observations of the concrete architecture of the Basilica Ulpia and Trajan’s Forum. *Comm. Hum. Litt.* **2011**, *128*, 73–95.
49. Campbell, L.S.; Charnock, J.; Dyer, A.; Hillier, S.; Chenery, S.; Stoppa, F.; Henderson, C.M.B.; Walcott, R.; Rumsey, M. Determination of zeolite-group mineral compositions by electron probe microanalysis. *Mineral. Mag.* **2016**, *80*, 781–807. [CrossRef]
50. Izzo, F.; Arizzi, A.; Cappelletti, P.; Cultrone, G.; De Bonis, A.; Germinario, C.; Graziano, S.F.; Grifa, C.; Guarino, V.; Mercurio, M.; et al. The art of building in the Roman period (89 B.C.–79 A.D.): Mortars, plasters and mosaic floors from ancient Stabiae (Naples, Italy). *Constr. Build. Mater.* **2016**, *117*, 129–143. [CrossRef]
51. Jackson, M.D.; Marra, F.; Hay, R.L.; Cawood, C.; Winkler, E.M. The judicious selection and preservation of tuff and travertine building stone in ancient Rome. *Archaeometry* **2005**, *47*, 485–510. [CrossRef]
52. Giampaolo, C.; Godano, R.F.; Di Sabatino, B.; Barrese, E. The alteration of leucite-bearing rocks: A possible mechanism. *Eur. J. Mineral.* **1997**, *9*, 1277–1292. [CrossRef]
53. Cappelletti, P.; Petrosino, P.; de Gennaro, M.; Colella, A.; Graziano, S.F.; D’Amore, M.; Mercurio, M.; Cerri, G.; de Gennaro, R.; Rapisardo, G.; et al. The “Tufo Giallo della Via Tiberina” (Sabatini Volcanic District, Central Italy): A complex system of lithification in a pyroclastic current deposit. *Mineral. Petrol.* **2015**, *109*, 85–101. [CrossRef]
54. Hay, R.L.; Sheppard, R.A. Occurrence of zeolites in sedimentary rocks: An overview. *Rev. Mineral. Geochem.* **2001**, *45*, 217–234. [CrossRef]
55. Cundari, A. Petrogenesis of leucite-bearing lavas in the Roman volcanic region, Italy-The Sabatini lavas. *Contrib. Mineral. Petrol.* **1979**, *70*, 9–21. [CrossRef]

56. Bear, A.N.; Giordano, G.; Giampaolo, C.; Cas, R.A.F. Volcanological constraints on the post-emplacement zeolitisation of ignimbrites and geoarchaeological implications for Etruscan tomb construction (6th–3rd century B.C.) in the Tufo Rosso a Scorie Nere, Vico Caldera, Central Italy. *J. Volcanol. Geotherm. Res.* **2009**, *183*, 183–200. [CrossRef]
57. Del Bello, E.; Mollo, S.; Scarlato, P.; von Quadt, A.; Forni, F.; Bachmann, O. New petrological constraints on the last eruptive phase of the Sabatini Volcanic District (central Italy): Clues from mineralogy, geochemistry, and Sr–Nd isotopes. *Lithos* **2014**, *205*, 28–38. [CrossRef]
58. Sottili, G.; Palladino, D.M.; Gaeta, M.; Masotta, M. Origins and energetics of maar volcanoes: Examples from the ultrapotassic Sabatini Volcanic District (Roman Province, Central Italy). *Bull. Volcanol.* **2012**, *74*, 163–186. [CrossRef]
59. Marra, F.; Karner, D.B.; Freda, C.; Gaeta, M.; Renne, P. Large mafic eruptions at Alban Hills Volcanic District (Central Italy): Chronostratigraphy, petrography and eruptive behavior. *J. Volcanol. Geotherm. Res.* **2009**, *179*, 217–232. [CrossRef]
60. Cappelletti, P.; Langella, A.; Colella, A.; De' Gennaro, R.D.E. Mineralogical and technical features of zeolite deposits from northern Latium volcanic district. *Period. Mineral.* **1999**, *68*, 127–144.
61. Lombardi, G.; Meucci, C. Il Tufo Giallo della Via Tiberina (Roma) utilizzato nei monumenti romani. *Rend. Lincei* **2006**, *17*, 263–287. [CrossRef]
62. Jackson, M.D.; Mulcahy, S.R.; Chen, H.; Li, Y.; Li, Q.; Cappelletti, P.; Wenk, H.R. Phillipsite and Al-tobermorite mineral cements produced through low-temperature water-rock reactions in Roman marine concrete. *Am. Mineral.* **2017**, *102*, 1435–1450. [CrossRef]
63. Jackson, M.D.; Chae, S.R.; Mulcahy, S.R.; Meral, C.; Taylor, R.; Li, P.; Emwas, A.-H.; Moon, J.; Yoon, S.; Vola, G.; et al. Unlocking the secrets of Al-tobermorite in Roman seawater concrete. *Am. Mineral.* **2013**, *98*, 1669–1687. [CrossRef]
64. Jackson, M.D.; Moon, J.; Gotti, E.; Taylor, R.; Chae, S.R.; Kunz, M.; Emwas, A.-H.; Meral, C.; Guttman, P.; Levitz, P.; et al. Material and elastic properties of Al-tobermorite in ancient Roman seawater concrete. *J. Am. Ceram. Soc.* **2013**, *96*, 2598–2606. [CrossRef]
65. Cairolì, F.G. *L'Edilizia Nell'Antichità*; Carocci Editore: Rome, Italy, 2018.



Article

# Calle Horno del Vidrio—Preliminary Study of Glass Production Remains Found in Granada, Spain, Dated to the 16th and 17th Centuries

Inês Coutinho <sup>1,\*</sup>, Isabel Cambil Campaña <sup>2</sup>, Luís Cerqueira Alves <sup>3</sup> and Teresa Medici <sup>4</sup>

<sup>1</sup> Department of Conservation and Restoration and VICARTE Research Unit, FCT NOVA, 2829-516 Caparica, Portugal

<sup>2</sup> Independent Researcher, 18500 Granada, Spain; isabelcambil@gmail.com

<sup>3</sup> C2TN, Instituto Superior Técnico, Universidade de Lisboa, 2695-066 Bobadela LRS, Portugal; lcalves@ctn.tecnico.ulisboa.pt

<sup>4</sup> VICARTE Research Unit, FCT NOVA, 2829-516 Caparica, Portugal; teresa.medici@gmail.com

\* Correspondence: icoutinho@fct.unl.pt

**Abstract:** A set of 14 glass fragments and production remains dated to the 16th and 17th centuries was collected during rescue archaeological works conducted in Granada, Spain, and was characterised by  $\mu$ -PIXE. This preliminary study constitutes the first analytical approach to glass manufacturing remains from a Spanish production dated to the early-modern period.  $\mu$ -PIXE allowed for the quantification of major, minor and some trace elements of the glass fragments. It also allowed mapping the elemental distribution on the fragments that were identified as an interface of crucible/glass. This analysis constitutes an evaluation of the ionic exchange between glass and crucible. The glass colours vary from the natural green and blue hues to completely colourless samples. The results show that the majority of the glass samples are of soda-lime-silicate composition, and only one proved to be of a potassium-rich composition. From this, one can hypothesise that glass rich in sodium (following the Mediterranean tradition) and potassium-rich glass (following a central and north European tradition) were both locally produced. Since this location was known as *la Calle Horno del Vidrio* (Glass Furnace Street) and several production evidences were found, it is highly probable that an artisanal glass production existed in this area.

**Citation:** Coutinho, I.; Cambil Campaña, I.; Cerqueira Alves, L.; Medici, T. *Calle Horno del Vidrio—Preliminary Study of Glass Production Remains Found in Granada, Spain, Dated to the 16th and 17th Centuries*. *Minerals* **2021**, *11*, 688. <https://doi.org/10.3390/min11070688>

Academic Editors: Daniel Albero Santacreu, José Cristóbal Carvajal López and Adrián Durán Benito

Received: 14 May 2021

Accepted: 23 June 2021

Published: 26 June 2021

**Publisher's Note:** MDPI stays neutral with regard to jurisdictional claims in published maps and institutional affiliations.



**Copyright:** © 2021 by the authors. Licensee MDPI, Basel, Switzerland. This article is an open access article distributed under the terms and conditions of the Creative Commons Attribution (CC BY) license (<https://creativecommons.org/licenses/by/4.0/>).

**Keywords:** glass production; Spain; 16th century;  $\mu$ PIXE; glass kiln; production remains; objects

## 1. Introduction

Glass manufacturing in Spain during the 16th and 17th centuries was a well-established and flourishing craft. The existence of glass production in the Peninsula is explicitly referred to by written sources from the 12th century onward and the making of luxury glass in Barcelona, Murcia, Malaga and Almería is frequently mentioned by documents. The rapid diffusion of the innovations of the art in the Muslim-ruled area of the Peninsula and the role played by Barcelona in the import and sale of enamelled glass from Syria and Egypt were probably relevant factors for the development of a local production, which ended up being influenced by these imports. The allusions to glass in “Damascus style” appearing in Catalan documents dated to the end of the 14th century and to the first half of the 15th century have been interpreted in this sense [1,2]. Glass production has also been recorded in Valencia and the Balears, territories that, in the 13th and 14th centuries, formed a political unit with Catalonia, under the Crown of Aragon. A few archaeological objects dated to the 14th century are known, including those found in a kiln excavated at Sant Fost de Campsentelles (Barcelona). They consist mainly of glass of everyday use, with few enamelled fragments [3–5].

At the beginning of the 15th century, the most important technical developments in European glassmaking were achieved in Venice. The accurate selection of raw materials

and the purification processes allowed for Venetian glassmakers to produce very fine colourless glass, exported to the rest of Europe and to the East. The success of the Venetian production soon led several manufactures in many countries to adopt a Venetian-style production, often employing expatriated Venetian glassmakers, even if they were not legally allowed to work outside the island of Murano. These manufactures attempted to imitate shape and colours, producing the so called *façon-de-Venise* glass [6].

*Façon-de-Venise* was a term that first appear in a document in Antwerp dated to 1549, to describe glass objects made outside Venice but following the Venetian tradition in terms of shapes and decorative features [7]. To achieve the quality of the Venetian glass was a desire that rapidly spread through Europe, especially the ability of the Venetian glassmakers to attain a perfectly colourless glass, the *cristallo*, which became the ultimate object of fascination by the wealthiest collectors [8].

From Venice, luxurious and rare glass objects were also brought to the Iberian Peninsula and the first Venetian glassmakers are documented in Spain already during the first half of the 16th century. The spread of Venetian glassmaking techniques greatly enhanced the 16th and 17th century glass production in the country and the many pieces preserved in the collections of important museums are clear proof of the great value of these creation [2,9].

According to the literature, the two main regions producing *façon-de-Venise* glass in Spain were Catalunya and Castile [1,2]. The Catalan production during the 16th and the first half of the 17th century was particularly significant. Chalice, footed cups, serving dishes and jugs were blown in thin, high quality colourless or coloured glass. They were often gilded and enamelled or decorated with applied white glass. Among the most common decorative features were the green enamelling and the diamond-point engraving. The colourless glass of Catalan origin appears to have a different hue when compared with other *façon-de-Venise* European production centres, with shades of smoky yellow or amber [1,2]. Most of these objects had mainly a decorative purpose. They were produced to satisfy the well-known passion for collecting glass that characterised the kings and the nobility [2,9]. The data revealed by archaeology, although scarce, provide a more varied picture of the glass circulating in the region, where the more exquisite pieces are accompanied by objects of common use [2]. No kilns connected to the production of the 16th and 17th century are known; the written documents locate two main settings for them, Barcelona and Matarò, a centre in the province of Barcelona [1]. The existence of an important glass activity was recorded in Majorca, which benefitted from the arrival of Venetian masters on the island [5].

In Castile, there is a record of glass furnaces active from the 15th century onward. None of them have been located so far. The Castilian glass preserved in the collections is generally accredited to originate from Cadalso de los Vidrios (Madrid) and Recuenco (Guadalajara). The Venetian style was reinterpreted here in peculiar ways, with singular shapes and using glass with a special hue, especially in the objects identified as coming from the Recuenco's production [1,2,10].

A different character, markedly distinct from the glassware until now examined, is evident in the Andalusian (southern Spain) production. Together with Almería, the main furnaces were in the area of Granada, known for the production of glass since at least the 17th century. Documentary sources refer to furnaces in Castril de la Peña, a municipality located in the province of Granada. Castril production was considered among the most significative in the region [1,11–13]. Castril glasses were exhumed in an archaeological excavation in Murcia, but most information on them stems from written sources and objects preserved in museums collections [2,11,14].

In Almería and Castril, glass of everyday use was produced, such as cups, mugs, jars and bottles. The Andalusian glass is characterised by bright colours: mainly green and yellow (believed to be due to the unintentional presence of iron in the sands), brownish-black, purple and shades of blue. The many bubbles indicate some technological constraint during the fining processes of the melt. Applied decorative elements abound, such as

threads, ribbons and crested handles [1,2,15]. The glass objects attributed to a Granada provenance are often composed of two coloured glasses combined in one object, for instance, green and amber tonalities. This colourful glass, usually blown with thick walls and considered a direct revivalism of the Islamic repertoire, has been related to Syrian glass dated to the 14th century [1].

It is generally acknowledged that Andalusian glassmakers inherited the Islamic glass manufacturing traditions, including shapes, decorative features and techniques. In Almeria and Granada, the Islamic Al-Andalus influence was present and reflected in the glass production long after the end of the Islamic occupation, that began in the 8th century and lasted until the end of the 15th century. Moreover, the permeability between Christians and Muslims was dynamic and the Islamic influence in the production technology of other materials is undeniable, as is the case with lusterware. As already noted [16], this interconnection and transfer of technology is never restricted to one sole craft.

In the Iberian Peninsula, considering the Portuguese territory, no *façon-de-Venise* production location has so far been identified. However, a great number of archaeological remains has been unearthed from the north to the south of the territory. Due to the typological and compositional characteristics that some of these objects present, it was proposed that some of the pieces were locally produced [17–19].

Concerning archaeometric studies applied to glass unearthed in Spain, more systematic work is being done to older chronologies, namely to glass assemblages dated to between the 5th and the 12th centuries [20–26], although singular case-studies can also be found for later chronologies [27]. With regard to the southern regions, it was concluded that the glass was of a soda-rich nature; however, glass rich in lead has been systematically identified, which appears to constitute a characteristic of local production, believed to be the result of Islamic influence. During the Nasrid period (roughly dated to between 1230 and 1492), glass production from the Córdoba region appears to be more homogeneous in terms of glass colour and composition, which can be related to a higher control from the authorities and also to the existence of a guild [26]. When traveling south, in Málaga, one faces a different reality, where recycling was very important within the glass production line and in terms of colours the variety is greater. This has been attributed to the position that this city has in the trading routes in the Mediterranean Sea [26]. This shows that even within the Al-Andalus region, one cannot assume an organised and homogeneous production of glass.

The assemblage under study allows for an outstanding opportunity to examine a later chronology, after the Islamic occupation. This research will combine the study of the archaeological context together with historical data, the glass formal characteristics and the determination of its chemical composition in major, minor and some trace elements. Provenance suggestions will be based on the relation of all these aspects. With this study, we hope to contribute to enrich the knowledge about glass production in Europe, specifically the Spanish territory, during the late medieval/early modern periods.

### 1.1. Archaeological Context and Description of the Glass Fragments

A set of 14 glass fragments and production remains was collected during rescue archaeological works conducted in Granada (Spain), at a location known as *Calle Horno del Vidrio* (Glass Furnace Street). Excavations revealed continuous occupation of the area between the 11th and the 17th–18th centuries, with scant traces of domestic buildings. No evidence of structures related to furnaces was discovered so far. Thus, the massive concentrations of glass wastes led archaeologists to suppose the presence of a glass production site in the immediate surroundings of the excavated parcels (Figure 1). The finds were stratigraphically dated between the 16th and 17th centuries [12].

Considering the 14 fragments under study, three fragments can be identified as probably belonging to objects and nine belong to production remains. Two fragments were collected very close to the crucible walls and will be discussed separately because of the different compositional characteristics (see Table 1).



**Figure 1.** Example of the glass remains found during the excavation at Calle del Horno del Vidrio in Granada, Spain.

**Table 1.** Description of the fragments under study and the respective photography.

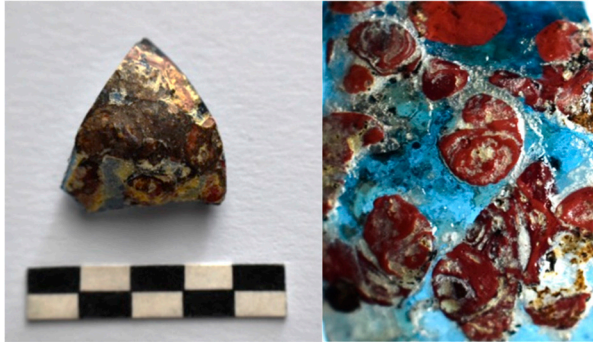
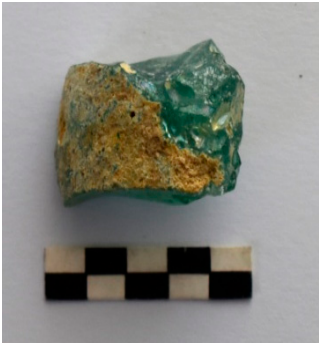

Inventory Number	Fragment Description	Photography
HV-1	<p>Fragment of <i>Millefiori</i> decorated glass. It belongs to the lower part of the object's body, possibly a small globular vase. The body is of a transparent blue glass decorated with an opaque red pick-up decoration. The degradation layers do not allow for an appreciation of the colour nor to interpret the appearance of the applied murrine.</p>	
HV-2	<p>Glass sample collected very close to the crucible wall. It is a fully melted fragment of frit. The colour is a transparent bluish green.</p>	
HV-3	<p>Production waste. It may be a pontil knock-off. The glass is transparent green.</p>	

Table 1. Cont.

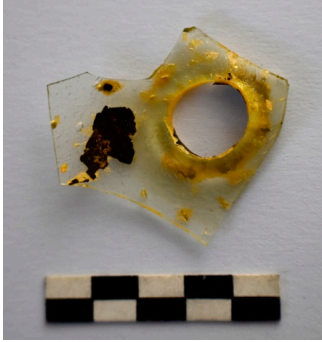
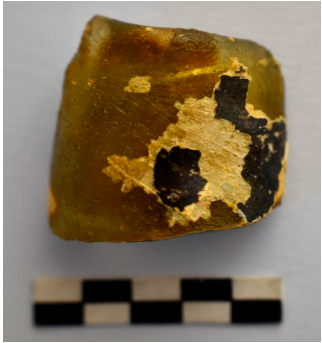

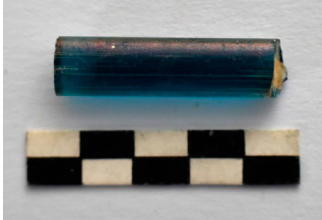
Inventory Number	Fragment Description	Photography
HV-4	<p>Object or production waste? Transparent colorless glass with a slight yellowish green tone that can be perceived in the thickest parts. The minimum thickness is half a millimeter.</p> <p>It is not clear if this fragment belongs to an object; the circular opening does not seem to be part of a piece mouth.</p>	
HV-5	<p>The fragment could be the mouth of a piece. At the top, it ends as if it were a rounded, straight rim with a thickness less than 3 mm. The maximum thickness at the bottom is 6 mm. The glass is transparent olive green.</p> <p>The fragment is quite irregular and it seems that this was the result of a less cared for production.</p>	
HV-6	<p>Production waste. Glass can be seen attached on the two faces of a ceramic fragment that could belong to a crucible. The ceramic paste is blackened on the outside. A slightly purple interior of the ceramic paste is visible on the edges of recent cracks. On one side, the glass has an homogeneous layer that has cracked. The other glass layer looks very uneven. The glass is transparent bluish green.</p>	
HV-7	<p>Fragment of a transparent blue glass rod, with a turquoise blue hue. The rod is not perfectly cylindrical and it has a 5.5 mm of diameter at its widest part.</p>	



Table 1. Cont.







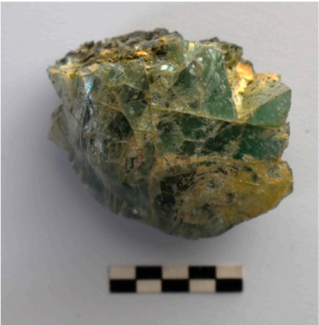
Inventory Number	Fragment Description	Photography
HV-8	Production waste. Opaque green glass. The narrowest part has a crack that shows a shiny glass interior. It appears to be a drop.	
HV-9	Production waste. Deformed glass chunk, fully melted, with a bottle green colour. On one side it has attached impurities that may have come from the furnace wall.	
HV-10	Production waste. Since on one side it has a central area that seems to correspond to a cylindrical shape, it may be of a pontil knock-off. The glass is transparent green with a slight yellowing hue. Inside one may see a medium-large bubble.	
HV-11	Possible production waste from the interface area where the molten glass gets mixed with the crucible wall. The batch is not fully melted.	
HV-12	Production waste. Glass fragment of transparent bluish colour, fully melted.	



Table 1. Cont.

Inventory Number	Fragment Description	Photography
HV-13	Production waste. Glass fragment of bluish green colour. Although homogeneous, it seems that the batch did not melt completely and it seems to present some opacity.	
HV-14	Production waste. It seems that this fragment might have been attached to the furnace walls. On one side it has the remains of material with a totally calcined aspect. The attached glass is cracked and presents a transparent bluish green colour.	

The production remains' samples belong to lumps of green/bluish glass, apparently at different degrees of melting; some show the mark left by the blowing cane or by the pontil. The colour of the glass can be compared and related to the glass manufactured during the 16th and 17th century at Castril de la Peña. Castril production is characterised by objects with thick walls in several shades of green and the typologies focus the daily utilitarian needs [1,13]. This seems to relate with the type of glass under study here.

The glass of the sampled objects differs. In particular, sample HV-4 is made of colourless glass, with very thin walls and it seems to have belonged to a delicate glass (see Table 1). Sample HV-5, on the other hand, probably belongs to a vessel (shape not identified) with thick walls and a green hue, which is very characteristic of the Castril production type [1,9,13]. The third object (sample HV-1) is a fragment of blue glass with red millefiori decoration.

It is more likely that sample HV-4 relates to objects from the Nasrid tradition [12]. Nasrid glass production is characterised by objects with thin walls and less tinted glass (some objects are close to transparent and colourless glass), which seems to indicate two hypotheses: glassmakers from the Nasrid tradition had a greater domain over raw materials and production techniques than the ones that followed and were part of the Castril-type production, or the Castril production was responding to a different taste from the market demand. When looking to the production wastes, apparently, no relation in terms of glass colour can be found between sample HV-4 and the remaining samples.

Finally, the millefiori fragment (sample HV-1) is likely to have been imported. Following what was said for sample HV-4, this fragment has no relation with the production remains recovered by the archaeological excavation. Since *façon-de-Venise* glass was known to be produced in the Catalonian region, it will be important to try to understand if this fragment was imported from abroad (from Italy for instance) or if it was coming from another Spanish region such as Catalonia.

The relation between the fragments' characteristics (such as glass colour) and compositional results will be explored. The results will be compared with published compositions of coeval glass from Spain and also from other production centres in order to try to propose a provenance for the samples. This will be especially relevant for samples HV-1 and HV-4.

Regarding the location of the furnaces, it is important to mention that *Calle Horno del Vidrio* was very close to the Palacio de Castril, a palace whose land was the property of Don Hernando de Zafra, the founder of the glass factory in Castril de la Peña. This location is characterised for having a series of streets with names related to what was being produced there, such as Horno de Vidrio (Glass Furnace) and Horno de Oro (Gold Furnace), among others. This may lead to the hypothesis that these were active crafts in the neighbourhood; however, apart from the glass production remains, no other material remains from these activities had been found so far. Don Hernando de Zafra was secretary of the catholic kings and played a central role during the conquest and organisation of the Granada kingdom [28]. According to M. Garzón Pareja, Don Hernando de Zafra was an entrepreneur, who travelled and got in contact with the Catalanian and the Gerona glass production traditions, which probably was one of the reasons for him to pursue the glass production business, which might have started in smaller furnaces and evolved after to a larger production in the Castril factory [29]. However, other authors believe that glass production at Castril probably started later, after the death of Don Hernando de Zafra [28]. In spite of this discussion, it is safer to assume that if this important figure had any relation with the beginning of glass production at Castril, following the example of other magnates of the time, it would have been as an entrepreneur [28]. It is relevant to clarify that the Castril property and surrounding lands stayed in the de Zafra family long after Don Hernando died [28], which leads to suggest that glass production at Castril may have started during the regency of the de Zafra family.

Noteworthy is the relation this important figure had with the royal family. At the end of the 15th century, glass collecting in Spain started to have some importance among royalty [9]. Later, in the 16th and 17th centuries, it evolved to a different level, where glass also had a prominent place related to its transformative nature. Glass (some produced in Spain) was present in the Spanish royal collections as early as the 15th century [9]; together with the trading and entrepreneurial spirit of Don Hernando de Zafra, this might somehow be related. Looking from different perspectives, it appears that the royal secretary was connected to glass, including trading it and probably establishing and financing its production.

### 1.2. Mineralogy of the Silica Source: Implication in the Study of Glass Production

Considering the archaeometric research that has been developed in glass studies, its main focus are the raw materials that compose this material. Raw materials are the group of basic components that are put together and submitted to a transformation process to obtain a final product, in this case glass. The raw materials out of which glass is made can come directly from nature, can be manufactured, or can result from previous recycling actions. In many cases, the combination of the three situations are observed when analysing glass compositions [30]. In the history of glass making, the most frequently used raw materials to obtain silica—the main component and vitrifying agent of glass—are quartz pebbles and sand. The quartz crystal structure is composed of silicon with an ionic valency of  $\text{Si}^{4+}$  that, although having a very small ionic size, still has the capacity of incorporating small amount of other elements, such as Al, Ti and Fe [31]. Additionally, apart from the silica, the sand used in the glass batch always contains different types of impurities or accessory minerals, among which one may find clay minerals, iron and titanium oxides, and more complex minerals such as zircon and pyroxenes, among others [31–33]. All these accessory components, including the rare earth elements (REE), will enter the glass batch and become part of the composition of the final pieces. Alumina, iron and titanium oxides are the main elements and trackers for sand, allowing discussion about the provenance of raw materials and, consequently, the provenance of the glass object [34].

## 2. Materials and Methods

### 2.1. Sample Selection and Preparation

Samples were selected from the set of production remains (represented in Figure 1), where all fragments presented the same morphological characteristics (such as the glass colour). Some fragments belonging to objects were also selected to be studied. For the choice of these fragments, the criterion was to select among those who presented similar characteristics to the production remains present in Figure 1. In addition, some objects that did not show any resemblance to the production remains from Figure 1 were also selected to be studied, since these may represent objects that might have been made elsewhere.

In order to avoid erroneous results by analysing and quantifying corrosion layers instead of the uncorroded bulk glass, it was decided to sample all selected objects. Small glass samples of 2–4 mm<sup>2</sup> were dry cut from the selected glass fragments with a diamond wire. Samples were embedded in an epoxy resin and polished with SiC sandpaper down to 4000 mesh. This sampling procedure was performed only on broken objects and on individual fragments without possible connections.

### 2.2. $\mu$ -PIXE

Quantitative results were achieved with the  $\mu$ -PIXE ion beam analytical technique using an Oxford Microbeams OM150 type scanning nuclear microprobe (the  $\mu$ -PIXE system is located at the Center for Nuclear Sciences and Technologies–C<sup>2</sup>TN, Lisbon University, Lisbon, Portugal) setup with the in-vacuum configuration. To allow efficient detection of low energy X-rays, such as the ones of Na, all the glass fragments were irradiated in vacuum with a focused 0.7 MeV proton beam and the produced X-rays collected by a 8  $\mu$ m thick Be windowed Si(Li) detector. In order to avoid or detect possible local glass heterogeneities, X-ray imaging (2D elemental distribution) and spectra were generally obtained from an irradiated sample area of 750  $\times$  750  $\mu$ m<sup>2</sup>. For trace elements quantification (typically elements with atomic number above the one of Fe), a 2 MeV proton beam was used with a 50  $\mu$ m thick Mylar foil positioned in front of the Si(Li) X-ray detector. Its use as an X-ray filter reduces the strong Si X-ray spectrum contribution, thus allowing an increase of the beam current and accumulated beam charge to attain higher sensitivity (lower detection limits) for elements such as Cu, As and Sb. The samples were also coated with a thin carbon layer in order to prevent sample beam-charging, and consequently, X-ray spectra degradation. Operation and basic data manipulation, including elemental distribution mapping, was achieved through the OMDAQ software code (version 5.1, Oxford Microbeams, Oxford, UK), and quantitative analysis with the GUPIX program (version 2.1.4, University of Guelph, Guelph, Ontario, Canada) [35]. The results are expressed in weight percentage of oxides and were normalised to 100%. To validate the obtained concentration results, a glass reference standard, Corning B, was also analysed. Those values are presented in Table 2. The measurements uncertainties were considered as the combined uncertainties of spectra counting statistics and spectra deconvolution fit uncertainty. This implies a relative uncertainty below 1% for SiO<sub>2</sub>, below 5% for Na (except for HV8 sample), Mg, Al, K and Ca oxides and below 30% for all the remaining oxides.

**Table 2.** Chemical composition of the samples from Horno del Vidrio, Granada, determined by  $\mu$ -PIXE, in weight percent of oxides.

Sample	Na <sub>2</sub> O	MgO	Al <sub>2</sub> O <sub>3</sub>	SiO <sub>2</sub>	P <sub>2</sub> O <sub>5</sub>	SO <sub>3</sub>	Cl	K <sub>2</sub> O	CaO	TiO <sub>2</sub>	MnO	Fe <sub>2</sub> O <sub>3</sub>	CoO	NiO	CuO	ZnO	As <sub>2</sub> O <sub>5</sub>	Rb <sub>2</sub> O	SrO	BaO	PbO
<i>Production remains and Glass fragments</i>																					
HV-1	14.2	4.0	2.1	59.4	0.24	0.16	0.61	6.09	10.04	0.14	1.28	0.93	0.08	0.076	0.06	0.01	0.23	0.01	0.11	0.10	0.03
HV-3	16.6	2.3	3.7	63.2	0.24	0.14	0.66	5.82	5.12	0.27	0.60	1.06	<0.01	0.01	0.01	0.01	<0.01	0.01	0.08	0.10	0.09
HV-4	15.5	4.2	3.0	60.2	0.44	0.16	0.66	6.93	6.39	0.21	0.92	1.22	<0.02	0.01	0.02	0.01	0.01	<0.01	0.07	0.09	<0.01
HV-5	15.2	3.9	2.9	57.9	0.24	0.25	0.51	6.50	10.41	0.19	0.68	1.07	<0.02	0.01	0.05	0.01	0.01	0.01	0.10	0.07	<0.01
HV-6	16.8	2.2	3.8	63.7	0.27	0.11	0.79	5.71	5.02	0.29	0.09	0.95	<0.01	0.01	0.01	0.01	<0.01	0.01	0.07	<0.06	0.02
HV-7	19.7	1.8	3.8	60.5	0.23	0.18	0.85	3.84	5.84	0.22	0.02	1.09	0.040	0.03	1.57	0.04	0.16	0.01	0.04	0.04	0.04
HV-8	1.2	1.4	4.2	71.0	0.27	<0.01	0.02	13.91	5.64	0.31	0.06	1.72	<0.02	<0.01	0.01	0.01	<0.01	0.01	0.05	0.07	<0.01
HV-9	15.5	2.1	3.7	64.7	0.23	0.16	0.64	6.62	4.94	0.30	0.04	0.96	<0.01	0.01	0.00	0.01	<0.01	0.01	0.07	<0.07	<0.01
HV-10	17.0	2.5	3.5	61.1	0.23	0.19	0.65	6.88	5.39	0.29	0.84	1.03	<0.02	0.01	0.03	0.01	<0.01	0.01	0.08	0.11	0.09
HV-12	16.1	2.3	3.6	63.3	0.23	0.13	0.69	5.84	5.51	0.33	0.59	0.99	<0.02	0.01	0.01	0.01	0.02	0.01	0.08	0.10	0.13
HV-13	16.7	2.2	3.6	63.9	0.21	0.13	0.83	5.91	5.07	0.34	0.08	0.94	<0.02	0.01	0.00	0.01	<0.01	0.01	0.06	0.03	<0.01
HV-14	15.6	2.2	3.6	64.5	0.19	0.13	0.82	5.95	5.38	0.31	0.04	1.11	<0.02	0.01	0.00	0.01	<0.01	0.01	0.07	0.04	<0.01
<i>Glass Waste and Crucibles</i>																					
HV-2	6.2	1.5	11.0	65.0	1.27	0.45	2.86	2.89	5.61	0.81	0.05	2.11	<0.02	<0.01	0.01	0.01	<0.01	<0.01	0.07	0.08	<0.01
HV-11 (Crucible/Glass interface, area richer in Al)	0.9	1.7	13.4	62.6	0.53	<0.02	<0.01	5.82	7.50	0.87	0.09	6.16	<0.05	0.01	0.01	0.02	<0.01	<0.02	0.08	<0.02	<0.02
HV-11 (Crucible/Glass interface, area richer in Si)	0.2	0.2	6.2	88.9	<0.04	<0.02	<0.01	1.90	0.22	0.32	<0.02	1.84	<0.02	<0.001	<0.004	<0.002	<0.004	<0.01	<0.01	<0.06	<0.01
<i>Glass Standard</i>																					
CMoG B-Measured	16.1	1.0	4.1	61.2	0.62			1.25	8.28	0.10	0.24	0.34	0.050		2.63	0.17			0.02	0.08	0.48
CMoG B-Certified [36]	17.00	1.03	4.36	62.0	0.82			1.00	8.56	0.09	0.25	0.34	0.05		2.66	0.19			0.02	0.12	0.61
Relative Error (%)	5	5	7	1	25			25	3	11	4	0.3	-		1	11			-	33	21

### 3. Results and Discussion

The studied material can be divided in: glass waste and glass remains attached to crucibles or furnace walls, production remains of loose glass and, finally, glass fragments from objects. The presentation and discussion of the results will be made following this division and a relation between production remains and the objects' fragments will be made.

From the 14 samples that were analysed, it was possible to determine the type of glass for 12 of the samples. For these 12 samples, 11 are of a soda-rich silica glass and only 1 (sample HV-8) was identified as being of a potassium-rich glass. Two samples, still attached to the crucible material, do not present alkali values that permit a glass type identification.

For the soda-lime-silica glass, the contents of MgO (1.5–4.2 wt%), K<sub>2</sub>O (3.8–6.9 wt%), P<sub>2</sub>O<sub>5</sub> (0.2–0.4 wt%) and the presence of chlorine (>0.5 wt%) are consistent with the use of coastal plant ashes, the usual alkali source identified for Mediterranean glass productions, such as the Venetian one [37,38].

Results and discussion are divided in a Glass Waste and Crucibles section and Production Remains and Glass Fragments section to help explore results and identify relations, similarities and differences among data. The obtained glass composition will be compared with coeval glass from Spain and from other production centres.

#### 3.1. Glass Waste and Crucibles

Samples HV-2 and HV-11 are the ones considered to belong to this category. Sample HV-2 was collected very close to the crucible wall and presents alkali values that prevent us to discuss its nature (see Table 2). This was confirmed by the very high level of alumina (11.0 wt%), and for this reason, no further conclusions were explored for sample HV-2.

Considering sample HV-11, due to the aspect of the fragment, it seemed to come from the interface area where the molten glass gets mixed with the crucible wall. It has a blackish/greyish colour and there was a great number of bubbles or pores present in the sample. A  $\mu$ -PIXE mapping was performed on the fragment in order to observe the distribution of some elements in the sample (Figure 2). It is possible to observe an area richer in Si, which is also richer in Ca and K. This area is probably the one closer to the crucible, which is the area more susceptible to ionic exchange [39].

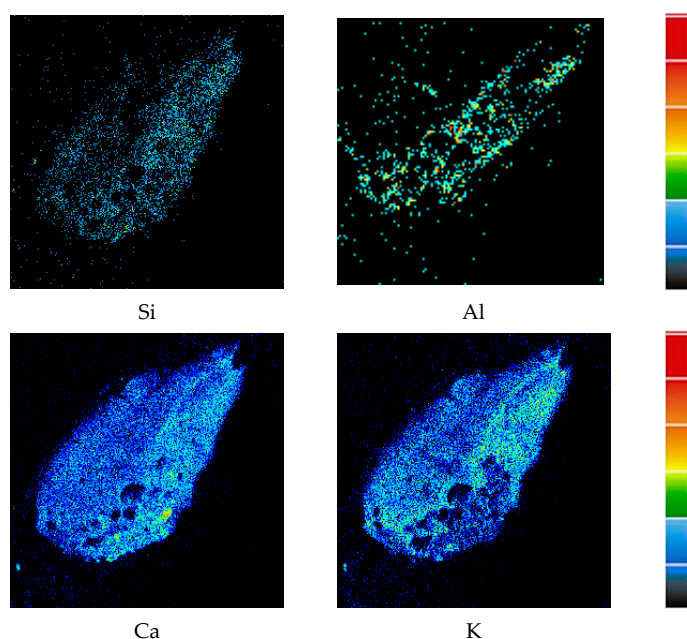
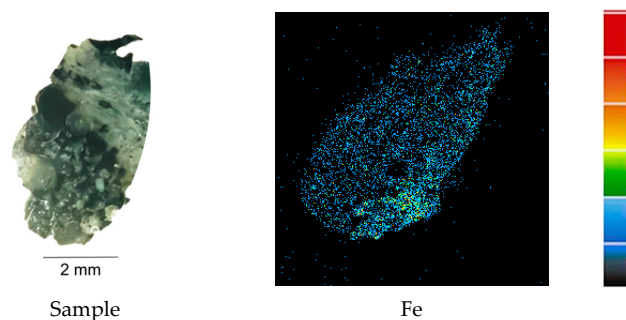


Figure 2. Cont.

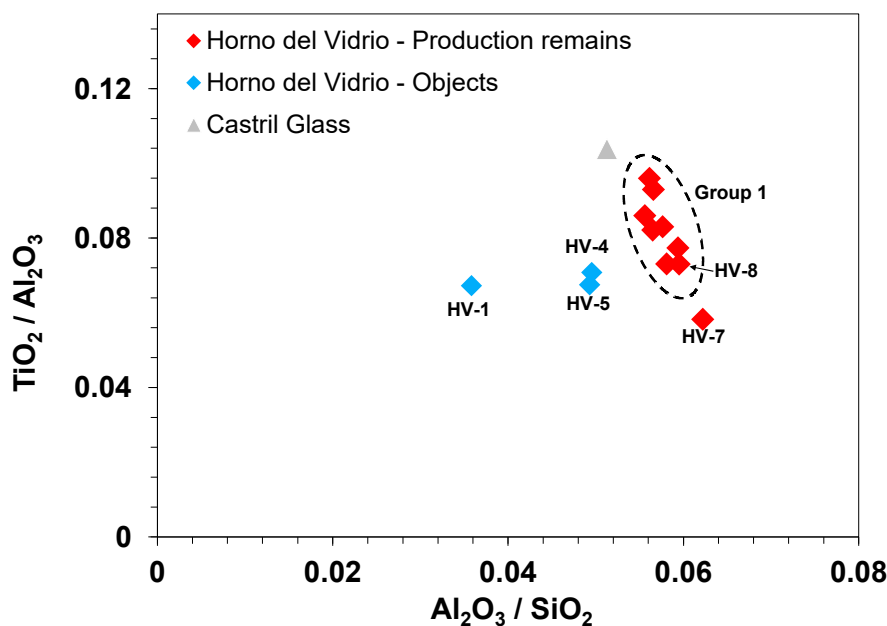


**Figure 2.**  $\mu$ -PIXE elemental distribution in sample HV-11 for elements Si, Al, Ca, K and Fe. The two maps on top row have dimensions of  $2.25 \times 2.25 \text{ mm}^2$  and were obtained with a 0.7 MeV proton beam and the remaining maps have dimensions of  $2.64 \times 2.64 \text{ mm}^2$  and were obtained with a 2 MeV proton beam.

### 3.2. Production Remains and Glass Fragments

#### 3.2.1. Silica Sources

Before looking at the samples of production remains and glass fragments separately, in Figure 3, the main components of the silica source for all these samples are plotted in order to verify if the assumptions made previously when looking to the glass colours and forms, could be verified.



**Figure 3.** Binary plot of weight ratios of  $\text{Al}_2\text{O}_3/\text{SiO}_2$  vs. the weight ratio of  $\text{TiO}_2/\text{Al}_2\text{O}_3$ . The Castril Glass values were taken from [13].

The plot shown in Figure 3 allows for the comparison of the mineralogy of the glassmaking sands. As mentioned previously, titania and alumina are among the most important oxides to study the origins of the silica source. With the presented combination of oxides, it is possible to create a chart where the mineralogical characteristics of the silica raw material is related to the glass composition, namely the quartz content ( $\text{SiO}_2$ ), the feldspar contribution ( $\text{Al}_2\text{O}_3$ ) and the heavy minerals contribution ( $\text{TiO}_2$ ) [40,41]. This relation suggests that the group of eight samples marked with an oval dashed line (designated Group 1) and which represents the majority of production remain samples with very similar green/bluish hues are also very similar in terms of the composition of the silica source, strongly suggesting that these glass samples were made from the same source of silica.



What is very interesting and noteworthy is that this group, composed of soda-lime-silica glass, includes a glass drop with the only potassium-rich composition (sample HV-8) found in the set, which seems to indicate that despite the fact that a different flux and consequently a different recipe were used, the silica source is the same used for the production of the batch with a sodium-rich composition. All samples within this group were identified as belonging to production remains (samples HV-3, HV-6-10 and HV-12-14) while presenting a greenish/bluish colour, which seems to be in accordance with the Castril production style [12].

Still looking to the binary plot represented in Figure 3, the composition of the glass samples retrieved from Granada were also compared with the published composition for Castril glass [13]. One can find a very straight relation between the Castril glass composition and the analysed samples shown within the oval dashed line of Figure 3. Together with the previously mentioned Castril characteristics, this group of eight samples can be clearly correlated to the Castril glass.

The second relation that can be identified is between samples HV-4 and HV-5. As one can see in Table 1, sample HV-4 was collected from a colourless and thin fragment (shape not identified), possible related to a Nasrid tradition. Sample HV-5, on the other hand, probably belongs to a vessel (shape not identified) with thick walls and a light green hue, very characteristic of the Castril production type. Due to the similarity of the two samples in terms of the mineralogic characteristics of the glass, it is proposed that for both samples, the same source of silica was employed. This seems to suggest that the same silica source was being exploited during different chronological periods, such as the Nasrid and the Castril ones. This hypothesis needs to be further explored, since it is not possible to fully understand such a relation with only two samples showing this behaviour. It is also important to notice that these two samples are somehow close to the group of samples previously described, which may indicate that, even though these two glasses were made with a different source of silica, these were not probably very distant (geographically) from each other.

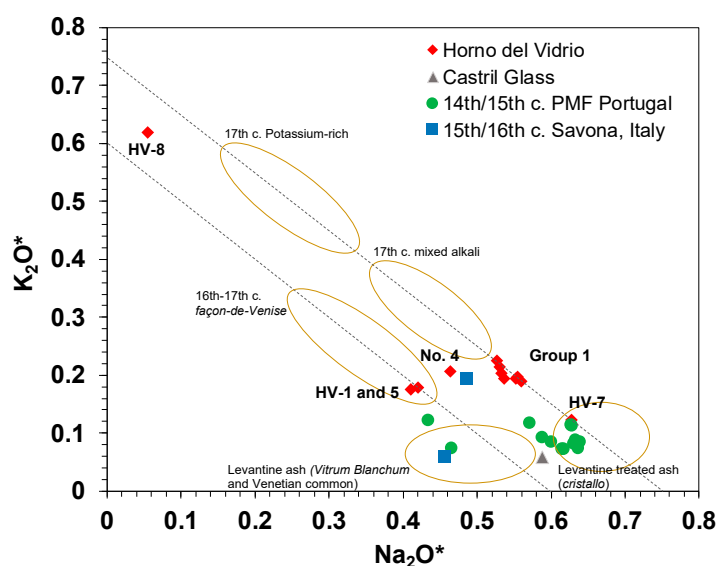
Looking now to the two samples that appear isolated on the chart from Figure 3, sample HV-7, which belongs to a blue rod, is similar to the main group of samples firstly described here. Following what was proposed previously for the group of two samples (HV-4 and HV-5), it seems that the silica source used for the making of sample HV-7 is geographically related to the one used for Group 1 samples. Regarding sample HV-1, this sample stands out on account of its decorative feature: a blue glass body with millefiori decoration in red glass. Concerning its composition, it also appears completely separated from all the other samples, showing no relation with the other glass, having the poorest content in alumina and titania from all characterised samples. However, despite these low values, the body glass has alumina and titania contents higher than the ones that have been measured for genuine Venetian glass so far, preventing in this way to attribute this fragment to a genuine Venetian production [42,43]. Two hypotheses can be considered: either the fragment is of local production or it was imported from elsewhere. When comparing the composition of this fragment with the other analysed remains, it is clear that it cannot be compared with any, which seems to indicate that the second hypothesis is more likely to be correct. It is, however, very interesting that a millefiori fragment was found amongst the glass production remains. This fragment might have been part of a piece from a habitational house and just got mixed with the furnace production remains or collected for recycling. Other *façon-de-Venise* glass were found during the excavations and these were considered imported products, either from Venice or from other Spanish locations such as Catalonia, known for its *façon-de-Venise* production of high quality, or as Castille, where during the 16th and 17th centuries, the production of *façon-de-Venise* glass was of outstanding quality and manufactured by immigrant glassmakers from Venetian and Flemish origins [12,44].

### 3.2.2. Alkali Sources

When studying the alkaline sources, the great majority of the analyzed glass is of a soda-rich composition, with the exception of one fragment which is of a potassium-rich composition (sample HV-8). Looking to Figure 4, the fractions of  $\text{Na}_2\text{O}$  and  $\text{K}_2\text{O}$  were normalised to the content of all alkaline and alkaline-earth oxides and plotted, in order to observe the distinct fractions of these oxides employed in the flux, and consequently, to distinguish amongst the different possible fluxes employed in the glass.

The two dashed lines marked on the chart (Figure 4) represent the use of unpurified ashes (correlation line of  $\text{Na}_2\text{O}^* + \text{K}_2\text{O}^* = 0.6$ ) and purified ashes ( $\text{Na}_2\text{O}^* + \text{K}_2\text{O}^* = 0.75$ ).  $\text{Na}_2\text{O}^*$  and  $\text{K}_2\text{O}^*$  values are obtained through the division of the respective oxide by every component introduced by the ash ( $\text{Na}_2\text{O}$ ,  $\text{MgO}$ ,  $\text{P}_2\text{O}_5$ ,  $\text{K}_2\text{O}$  and  $\text{CaO}$ ). The purification of vegetable ashes was introduced in glassmaking during the 15th century in Murano. The ashes were ground, dissolved in water and then boiled. The resulting solution was filtered and left to dry. These steps led to the formation of a white salt—*sale da cristallo*—that was mixed with the silica source in the right proportion, and calcined in order to obtain *Cristallo* glass [37]. This purification process resulted in the removal of iron compounds as well as calcium and magnesium, the presence of these last two being essential to the chemical stability of the glass. Unpurified ashes refer to the use of the same vegetable ashes with no treatment applied. In this period, the source of alkali used by the Venetians was imported from Levantine region; however, in the Spanish mediterranean coast line, barrilla (*Salsola soda*) was mostly likely the source for the ashes, with the Alicante barrilla being the most famous one for glass production [37,45].

Adding to the samples from the Granada glass furnace, the values for Castril glass for the 14th/15th century Portuguese glass from Beja (PMF) and the values for 1the 5th/16th century glass from Savona, Italy (two samples) were also plotted. The areas for Levantine treated ash (usually related to *Cristallo*), Levantine untreated ash (usually related to *Vitrum Blanchum* and Venetian common glass), 16th/17th century *façon-de-Venise* glass from different provenances, 17th century mixed alkali glass and 17th century potassium-rich glass, the latter two both made by employing purified raw materials, were marked on the chart to help visualising where the Granada glass samples would correlate the most.



**Figure 4.** Binary plot of  $\text{Na}_2\text{O}^*$  vs.  $\text{K}_2\text{O}^*$ .  $\text{Na}_2\text{O}^*$  and  $\text{K}_2\text{O}^*$  values are obtained through the division of the respective oxide by every component introduced by the ash ( $\text{Na}_2\text{O}$ ,  $\text{MgO}$ ,  $\text{P}_2\text{O}_5$ ,  $\text{K}_2\text{O}$  and  $\text{CaO}$ ). The two correlation lines represent the purified ash ( $\text{Na}_2\text{O}^* + \text{K}_2\text{O}^* = 0.75$ ) and the unpurified ash ( $\text{Na}_2\text{O}^* + \text{K}_2\text{O}^* = 0.6$ ) [46]. Samples from the Horno del Vidrio were plotted together with Castril glass [13], 14th/15th century PMF samples [17] and 15th/16th century glass from Savona, Italy [46].

Analysing the chart from Figure 4, it can be immediately observed that samples identified in Group 1 appear again all together aligned on the correlation line that belongs to the employment of purified ashes; however, in a different way than the Levantine ashes employed in the Venetian Cristallo glass. The purified Levantine ashes have a lower  $K_2O^*$  value, which implies higher soda contents. The ashes employed for the production of Group 1 samples have a higher  $K_2O^*$  value, and as far as we know, no other coeval samples showing this behaviour have been reported in the literature. One can hypothesise that local plants rich in sodium were being purified and employed in the production of this group of samples with similar characteristics to Castril glass. What is interesting to notice is that Castril glass appears much lower on the chart, very close to PMF samples, showing no relation with Group 1 Granada samples.

When looking to the other plotted samples from the Granada furnace, samples HV-1 and HV-5 appeared in close proximity to each other in the area identified for the 16th/17th century *façon-de-Venise* glass from different provenances. This is in accordance with what had already been verified when the silica sources were discussed. Sample HV-1, which belongs to millefiori glass, showed characteristics for the silica source not compatible with genuine Venetian glass. This is emphasised when studying the alkaline source, since no relation with the use of Levantine ashes (purified or non-purified) is identified and, on the other hand, the glass seems to be in accordance with the recipes used for *façon-de-Venise* glass produced throughout all Europe. Concerning sample HV-5, no shape or decoration feature is perceived that allows for a deeper discussion; however, one can suggest that a very similar source and recipe for alkaline content was used for both samples HV-1 and HV-5.

Regarding sample HV-7, it falls within the boundaries for Levantine treated ash. This fragment, which seems to belong to a glass rod, was made employing Levantine treated ashes. When crossing this information with the study of the silica source, it seems that this fragment was probably locally made (the silica source seems highly related to the Group 1 Si source).

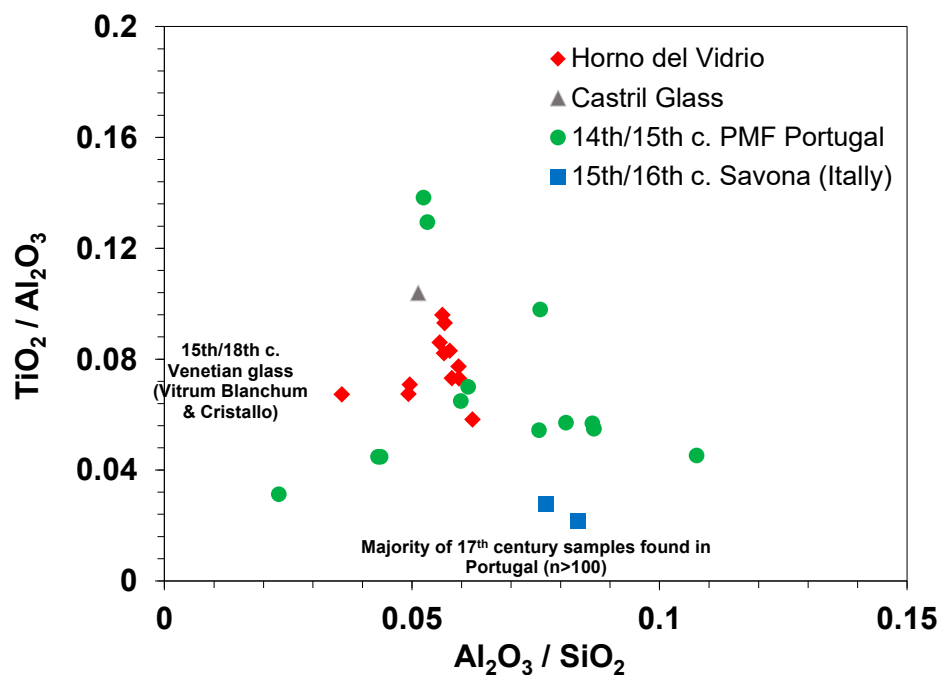
When looking at sample HV-4, it appears related to one sample from Savona, Italy. The Savona sample was identified as been made with a type of ash that was named as West Mediterranean Ash (WMA). This alkaline source is characterised by being produced with a soda-rich ash with a higher potassic content when compared with the Levantine one [46]. According to Cagno et al. (2012), there are different possibilities for the origin of this flux, with the most probable being a mixture of plant ashes from different origins.

Finally, sample HV-8 shows a very different behaviour than expected, since this sample has a potassium-rich composition. This sample appears in the upper part of the chart and does not relate with 17th century potassium-rich glass made using purified ashes. It is important to recall that this sample, in terms of silica source, falls within Group 1, which was identified as to probably have been made with a local source related to Castril glass.

In sum, raw materials from different sources were identified in the *Calle Horno del Vidrio* samples, especially with regards to alkaline sources. Not only different sources, but also different recipes were identified, showing that the knowledge circulation and also probably glassmakers' circulation was very active in this period. Additionally, the adaptation of recipes to local raw materials seems to be a normal procedure. However, more samples need to be analysed to further explore these results.

### 3.3. Iberian Peninsula and beyond

In Figure 5, a comparison between the production remains and the pieces from Granada furnace was made with coeval glass from other Spanish, Italian and Portuguese contexts to try to identify differences and similarities [13,18].



**Figure 5.** Binary plot of weight ratios of  $\text{Al}_2\text{O}_3/\text{SiO}_2$  vs. the weight ratio of  $\text{TiO}_2/\text{Al}_2\text{O}_3$  for the samples from the Horno del Vidrio together with the Castril glass, the 14th/15th century glass unearthed in Beja, Portugal (PMF) and the 15th/16th century glass from Savona, Italy [13,46,47].

Again, here, concerning Spanish contexts for this chronology, only the analytical results for Castril glass samples were used, since no other published compositions for glass from this chronology were found. As discussed before, one may find a straight relation between the cohesive group of eight samples and the Castril glass, indicating that probably, the same source of silica was used to produce the group of samples from Granada.

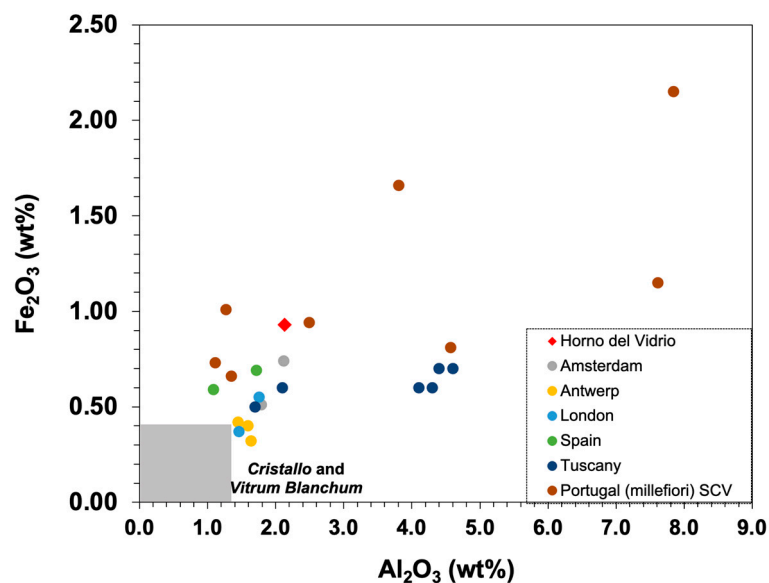
Concerning the comparison with glass found in Portugal, it was decided to compare with samples dated to the 14th up to the 17th century [18]. In Figure 5, one can see the ratios of alumina/silica versus titania/alumina for the Granada samples, the Castril glass [13] and for the 14/15th centuries Praça Miguel Fernandes (Beja) samples (PMF) [47]. Still, in Figure 5, a grey shadow was marked, which represents the area to which the great majority of the Portuguese samples dated to the 17th century belong (more than 100 samples) [18]. It is possible to propose that 17th century glass samples unearthed in Portugal and some samples from the 14/15th centuries from PMF assemblage were made with different silica sources that do not compare with the Granada samples or with Castril glass. The silica source employed in the glass found in Spain have different mineralogical characteristics when compared with the ones employed for 17th century glass found in Portugal.

What is striking when analysing the binary chart in Figure 5 is the resemblance of two samples dated to the 14th/15th century from PMF assemblage, with glass from Granada, more specifically from Group 1 samples. The two PMF samples are made of colourless glass, with very thin walls, resembling Nasrid glass. These fragments belong to two drinking glasses. Fragment PMF0401 is a colourless glass with a natural light yellow hue, and it belongs to a drinking glass with a cylindrical or cylindrical-conical body, with vertical ribs that resulted from mould-blowing, and has a string applied from the same glass that composes the body [19]. Some objects decorated with mould-blown ribs and applied glass strings were found among the Nasrid glass from the Alhambra Museum collection; however, these are not from drinking glasses but belong to jars instead [44]. Fragment PMF0691 is colourless with a natural light greenish hue, and it belongs to a drinking glass with a foot, blown into a mould, which gave the object vertical ribs. No parallel for this type of shape was found among Nasrid glass so far. Since these two PMF fragments are comparable with Group 1 samples (with Castril glass characteristics) and the same source

of silica was probably employed for the production of both PMF and Granada samples, this might indicate that this specific silica source was used for the production of glass with different characteristics and probably during a long period of time.

Finally, concerning sample HV-1, which belongs to a blue glass with millefiori decoration, in Figure 6, the contents of alumina and iron oxide for this sample were plotted and compared with *façon-de-Venise* glass from different production locations. It is possible to see that this millefiori sample is quite distant from the region defined for the genuine Venetian *Cristallo* and *Vitrum Blanchum* glass. This comes in accordance with what was said before about this sample not being of genuine Venetian provenance. Granada sample appears close to one of the millefiori samples that was found in the excavations performed to the Monastery of Santa Clara-a-Velha in Coimbra, Portugal [48]. Most studied millefiori fragments from the Monastery of Santa Clara-a-Velha in Coimbra were not compatible with genuine Venetian glass or even with known *façon-de-Venise* production centres. The millefiori fragment from Granada furnace seems to follow the same tendency, and even though it seems to be related to one of the Santa Clara-a-Velha monastery, Coimbra (SCV) millefiori samples, no probable provenance can currently be proposed for this fragment.

What is striking and worth mentioning is that, in the majority of the literature available about millefiori glass, this decorative technique is mainly attributed to a genuine Venetian provenance because of the complexity that its production involves. It is, however, clear that by looking into Figure 6, millefiori glasses found in Portugal, Amsterdam, Antwerp, London and Tuscany cannot be attributed to a Venetian production, which seems to suggest that the production of these glasses was more spread than one might expect, a hypothesis that has already been proposed elsewhere [49].



**Figure 6.** Binary chart of alumina versus iron oxide in weight percent of oxides. The grey shadow represents the values for genuine Venetian *cristallo* and *vitrum blanchum*. Samples from Amsterdam, Antwerp, London, Spain and Tuscany belong to *façon-de-Venise* glass that was locally produced and, finally, the Portuguese samples belong exclusively to millefiori fragments unearthed in the Santa Clara-a-Velha Monastery in Coimbra.

#### 4. Conclusions

A set of 14 glass fragments, including objects and production remains dated to the 16th and 17th century and unearthed in Granada, were studied and their chemical composition was characterised by  $\mu$ -PIXE, which allowed for the discussion of the nature and origin of the employed raw materials and types of produced glass.

The area where these glass production remains were excavated was known as *Calle Horno del Vidrio* (Glass Furnace Street), which in the past was the way used to indicate or designate the type of activity that was being developed in the street.

All the analysed glasses are soda-lime-silica glass, excluding sample HV-8, which is a potassium-rich glass. Concerning the silica sources, one group composed of eight samples was identified. This group presents cohesive characteristics allowing one to propose that these samples were made from the same source of silica, which is comparable with the so far analysed Castril glass. Within this very cohesive group, one may find one sample with a potassium-rich composition. This reinforces the suggestion that the furnaces were probably producing different glass types from the same silica source, meaning that for this specific sample, HV-8, the alkali source was different but the employed source of silica was not. However, with only one sample showing this behaviour, it is not possible to make any further conclusions. Still, analysing the silica sources, two samples, one showing Nasrid characteristics (HV-4) and the other with Castril characteristics (HV-5), are slightly different from the main group but appeared in close proximity to each other, leading one to propose that the same silica source (probably geographically close to the one employed for Group 1 samples) was used to produce both Nasrid and Castril glasses.

When crossing data from the Granada furnace with data from the analysis performed to glass excavated in Beja, Portugal (PMF), it is possible to strongly relate two PMF fragments with Group 1 samples. This could suggest that glass was already manufactured in Granada during the 14th/15th century, not only for local consumption, as the objects were also exported, at least to the south of Portugal. More data are needed in order to support this hypothesis.

Finally, when analysing the alkaline sources and apart from the K-rich sample, the same grouping observed for the silica sources is maintained. The whole set of samples is distributed along the previously defined groups in the literature as a function of the use of unpurified or purified ash treatment and the millefiori sample for instance appears in the area defined for *façon-de-Venise* glass from different provenances. What is striking is that Group 1 samples, which in the majority presents Castril characteristics, appear all together aligned in the region of purified ashes, forming a new group with characteristics not reported in the literature so far. We hope in the future, with further analysis, to be able to better explore this group, trying to disclose the followed recipe that implies the step of purifying the ashes.

This preliminary work reinforces the need to further study glass from the 14th to 17th century, chronologies that are not well explored. Moreover, glass from this period and from the Andalusian region is a ‘rough diamond’ with recipes and trading patterns yet to be found, which will probably change the current beliefs about glass production in the Iberian Peninsula.

**Author Contributions:** Conceptualisation, I.C. and T.M.; methodology, I.C., T.M. and L.C.A.; software, L.C.A. and I.C.; validation, I.C. and T.M.; formal analysis, I.C., I.C.C., L.C.A. and T.M.; investigation, I.C., I.C.C., L.C.A. and T.M.; resources, I.C., I.C.C., L.C.A. and T.M.; data curation, I.C., I.C.C., L.C.A. and T.M.; writing—original draft preparation, I.C. and T.M.; writing—review and editing, I.C., I.C.C., L.C.A. and T.M.; visualisation, I.C., I.C.C., L.C.A. and T.M.; supervision, I.C., I.C.C., L.C.A. and T.M.; project administration, I.C., I.C.C., L.C.A. and T.M.; funding acquisition, I.C. and L.C.A. All authors have read and agreed to the published version of the manuscript.

**Funding:** This work has been partially funded by the Fundação do Ministério de Ciência e Tecnologia de Portugal through the research unit VICARTE (UID/00729/2020) and through the research unit C<sup>2</sup>TN (UID/Multi/04349/2013).

**Data Availability Statement:** Not applicable.

**Acknowledgments:** The authors would like to thank to the reviewers, whose work helped improving the quality and readability of this paper.

**Conflicts of Interest:** The authors declare no conflict of interest.



## References

1. Frothingham, A.W. *Spanish Glass*; Faber: London, UK, 1963.
2. Domènech, I.V.I. El vidrio español de los siglos XVI a XVIII. In *Frágil Transparencia. Vidrios Españoles de Los Siglos XVI a XVIII*; Philippart, J.-P., Mergenthaler, M., Eds.; Verlag J.H. Röhl GmbH: Dettelbach, Germany, 2011; pp. 19–61.
3. Oliver, C.A. El taller de vidre medieval de Sant Fost de Campsentelles. *Acta Hist. Archaeol. Mediaev.* **1989**, *10*, 387–426.
4. Barrachina, J. El Vidre. In *El Castel de Llinars del Vallés*; Monreal, L., Barrachina, J., Eds.; Abadia de Montserrat: Barcelona, Spain, 1983; pp. 207–234.
5. Galmés, M.À.C. *ARS VITRARIA. Mallorca (1300–1700)*; UIB: Palma, Spain, 2015.
6. Liefkes, R. *Glass*; The Board of the Trustees of the Victoria and Albert Museum: London, UK, 1997.
7. Liefkes, R. Façon de Venise Glass in the Netherlands. In *Beyond Venice: Glass in Venetian Style, 1500–1750*; Page, J.-A., Ed.; The Corning Museum of Glass: Corning, NY, USA, 2004; pp. 227–249.
8. McCray, W.P. Glassmaking in renaissance Italy: The innovation of venetian cristallo. *JOM* **1998**, *50*, 14–19. [CrossRef]
9. García, J.L.G. El coleccionismo de vidrio artístico español en los siglos XVI y XVII. *Bol. del Mus. E Inst. Camón Aznar* **1998**, *73*, 111–139.
10. Moreno, M.J.S. La fabricación de vidrio en El Recuenco: Una industria olvidada. *Cuad Etnol Guadalaj.* **1997**, *29*, 205–270.
11. Barberán, V.G. Resumen histórico sobre la vidriera de Castril. In *Castril, Testimonio*; Mallorquín, A.T., Ed.; Diputacion Provincial De Granada: Castril, Granada, Spain, 1990; pp. 155–188.
12. Marcos, A.L.; Cobos, A.C.; Pertíñez, C.L. Excavación arqueológica de urgencia en la calle horno del vidrio, 16 (granada). *Anu. Arqueol. Andal.* **1998**, *3*, 275–286.
13. Martínez, J.F.R.; Linares, M.A.A.; Mondejar, F.G.; Milán, L.A. Estudio químico y mineralógico de un conjunto de vidrios de Castril (SS. XVII-XIX) (Granada). *MACLA Rev. Soc. Esp. Miner.* **2015**, *20*, 123–124.
14. García, J.M.C.; Martínez, J.M. Un lote de cerámica de Manises y vidrio de Castril (ss. XVII-XVIII) aparecido en la ciudad de Murcia. Estudio analítico de sus materiales. *Verdoly Rev. Mus. Arqueol. Murcia* **1991**, *3*, 141–162.
15. Doménech, I. Spanish Façon de Venise glass. In *Beyond Venice: Glass in Venetian Style, 1500–1750*; Page, J.-A., Ed.; The Corning Museum of Glass: Corning, NY, USA, 2004.
16. Govantes-Edwards, D.J.; Duckworth, C.N.; Córdoba, R.; De La Llave, R.C. Recipes and experimentation? The transmission of glassmaking techniques in Medieval Iberia. *J. Medieval Iber. Stud.* **2016**, *8*, 176–195. [CrossRef]
17. Coutinho, I.; Medici, T.; Alves, L.; Gratuze, B.; Vilarigues, M. Provenance studies on façon-de-Venise glass excavated in Portugal. *J. Archaeol. Sci. Rep.* **2016**, *7*, 437–448. [CrossRef]
18. Coutinho, I. *New Insights into 17th and 18th Century Glass from Portugal: Study and Preservation*; Universidade Nova de Lisboa: Carcavelos, Portugal, 2016.
19. Medici, T. *Vidros da Terra, o Vidro Tardomedieval e Moderno em Portugal (Séculos XIV-XVII). O Contributo da Arqueologia*; Faculdade de Letras da Universidade de Coimbra: Coimbra, Portugal, 2014.
20. Carmona, N.; Villegas, M.-A.; Jiménez, P.; Navarro, J.; García-Heras, M. Islamic glasses from Al-Andalus. Characterisation of materials from a Murcian workshop (12th century AD, Spain). *J. Cult. Heritage* **2009**, *10*, 439–445. [CrossRef]
21. Duckworth, C.N.; De La Llave, R.C.; Faber, E.W.; Edwards, D.J.G.; Henderson, J.C. Electron Microprobe Analysis of 9th–12th Century Islamic Glass from Córdoba, Spain. *Archaeometry* **2014**, *57*, 27–50. [CrossRef]
22. Ares, J.D.J.; Schibille, N. La Hispania antigua y medieval a través del vidrio: La aportación de la arqueometría. *Bol. Soc. Esp. Cerám. Y Vidr.* **2017**, *56*, 195–204. [CrossRef]
23. Ares, J.D.J.; Schibille, N. Glass import and production in Hispania during the early medieval period: The glass from Ciudad de Vascos (Toledo). *PLoS ONE* **2017**, *12*, e0182129. [CrossRef]
24. Heras, M.G. Estudio arqueométrico de los vidrios andalusíes procedentes del taller de la calle Puxmarina (Murcia). *Verdoly Murcia* **2008**, *11*, 277–302.
25. Ares, J.D.J.; Guirado, A.V.-E.; Gutiérrez, Y.C.; Schibille, N. Changes in the supply of eastern Mediterranean glasses to Visigothic Spain. *J. Archaeol. Sci.* **2019**, *107*, 23–31. [CrossRef]
26. Govantes-Edwards, D.; Duckworth, C.; de la Llave, R.C.; Aparicio Sánchez, L.; Camacho Cruz, C. El vidrio Andalusí su composición química: Primeros resultados y posibilidades de estudio. *Bol. Arqueol. Mediev.* **2014**, *18*, 31–49.
27. Murcia-Mascarós, S.; Roldan, C.; Falomir, C.; Domènech, I.; Carreras, J.; Ibáñez Puchades, R. Non-destructive analysis of enamelled ‘façon-de-venise’ glass discovered in morella (castelló, spain). In *ANNALES of the 17th Congress of the International Association for the History of Glass (Antwerp 2006)*; Janssens, K., Degryse, P., Cosyns, P., Caen, J., Van’t Dack, L., Eds.; University Press: Antwerp, Belgium, 2009; pp. 493–499.
28. Boyero, E.P. Hernando de zafra: Secretario real, oligarca granadino y señor de vasallos. *Misc. Mediev. Murc.* **2003**, 175–208. [CrossRef]
29. Pareja, M.G. Hernando de Zafra, cortesano y hombre de empresa de los Reyes Católicos. *Cuad. Estud. Mediev. Y Cienc. Y Téc. Hist.* **1974**, *2–3*, 127–147.
30. Navarro, J.M.F. *El Vidrio, Colección Textos Universitarios, No6, 3rd ed*; Consejo Superior de Investigaciones Científicas Sociedad Española de Cerámica y Vidrio: Madrid, Spain, 2003.
31. Brems, D.; Degryse, P. Trace Element Analysis in Provenancing Roman Glass-Making. *Archaeometry* **2013**, *56*, 116–136. [CrossRef]

32. Wedepohl, K.H.; Simon, K.; Kronz, A. Data on 61 chemical elements for the characterization of three major glass compositions in late antiquity and the middle ages. *Archaeometry* **2010**, *53*, 81–102. [CrossRef]
33. Moretti, C.; Hreglich, S. Raw Materials, Recipes and Procedures Used for Glass Making. In *Modern Methods for Analysing Archaeological and Historical Glass*; Wiley: Hoboken, NJ, USA, 2013; pp. 23–47.
34. Velde, B. Glass Compositions over Several Millennia in the Western World. In *Modern Methods for Analysing Archaeological and Historical Glass, Vol.I*; Janssens, K., Ed.; Wiley: Chichester, UK, 2013; pp. 67–78.
35. Vilarigues, M.; Coutinho, I.; Medici, T.; Alves, L.; Gratuze, B.; Machado, A. From beams to glass: Determining compositions to study provenance and production techniques. *Phys. Sci. Rev.* **2019**, *4*, 1–24. [CrossRef]
36. Adlington, L.W. The Corning Archaeological Reference Glasses: New Values for “Old” Compositions. *Pap. Inst. Archaeol.* **2017**, *27*, 1–8. [CrossRef]
37. Verità, M.; Zecchin, S. Thousand Years of Venetian Glass: The evolution of chemical composition from the origins to the 18th century. In *ANNALES of the 17th Congress of the International Association for the History of Glass*; Janssens, K., Degryse, P., Cosyns, P., Caen, J., Van’t Dack, L., Eds.; University Press: Antwerp, Belgium, 2009; pp. 602–613.
38. Verità, M. Venetian Soda Glass. In *Modern Methods for Analysing Archaeological and Historical Glass V.II*; Janssens, K., Ed.; John Wiley & Sons, Ltd.: West Sussex, UK, 2013; pp. 515–536.
39. Dungworth, D. Glass-ceramic reactions in some post-medieval crucibles. *Glass Technol. Eur. J. Glass Sci. Technol. Part A* **2008**, *49*, 157–167.
40. Schibille, N.; Sterrett-Krause, A.; Freestone, I.C. Glass groups, glass supply and recycling in late Roman Carthage. *Archaeol. Anthr. Sci.* **2017**, *9*, 1223–1241. [CrossRef]
41. Coutinho, I.; Medici, T.; Alves, L.; Perović, Š. Colourless Roman glass from the Zadar necropolis: An exploratory approach. *J. Archaeol. Sci. Rep.* **2017**, *15*, 194–202. [CrossRef]
42. Coutinho, I.; Alves, L.C.; Medici, T. The Broken Piece of a Larger Picture: A Renaissance Enameled Glass Fragment Depicting a Triumphal Procession. *J. Glass Stud.* **2019**, *61*, 87–95.
43. Biron, I.; Verità, M. Analytical investigation on Renaissance Venetian enamelled glasses from the Louvre collections. *J. Archaeol. Sci.* **2012**, *39*, 2706–2713. [CrossRef]
44. Campaña, I.C. *El Vidrio en La Alhambra—Desde el Period nazarí Hasta el Siglo XVII*; Junta de Andalucía: Granada, Spain, 2016.
45. Girón-Pascual, R.M. Cenizas, cristal y jabón. El comercio de la barrilla y sus derivados entre España e Italia a finales del siglo XVI (1560–1610). *eHumanista* **2018**, *38*, 215–232.
46. Cagno, S.; Badano, M.B.; Mathis, F.; Strivay, D.; Janssens, K. Study of medieval glass fragments from Savona (Italy) and their relation with the glass produced in Altare. *J. Archaeol. Sci.* **2012**, *39*, 2191–2197. [CrossRef]
47. Coutinho, I.; Medici, T.; Coentro, S.; Alves, L.C.; Vilarigues, M. First archaeometric study on medieval glass found in Beja (Southern Portugal). *J. Mediev. Iber. Stud.* **2016**, *8*, 148–175. [CrossRef]
48. Lima, A.; Medici, T.; De Matos, A.P.; Verità, M. Chemical analysis of 17th century Millefiori glasses excavated in the Monastery of Sta. Clara-a-Velha, Portugal: Comparison with Venetian and façon-de-Venise production. *J. Archaeol. Sci.* **2012**, *39*, 1238–1248. [CrossRef]
49. Valente, F.P.; Coutinho, I.; Medici, T.; Vilarigues, M. Glass colored by glass: Review of the pick-up decoration in early modern Europe. *J. Archaeol. Sci. Rep.* **2021**, *36*, 102832. [CrossRef]

Article

# Ancient Roman Mortars from *Villa del Capo di Sorrento*: A Multi-Analytical Approach to Define Microstructural and Compositional Features

Concetta Rispoli <sup>1,2,\*</sup>, Renata Esposito <sup>3</sup>, Luigi Guerriero <sup>1</sup> and Piergiulio Cappelletti <sup>1,2</sup>

- <sup>1</sup> Dipartimento di Scienze della Terra, dell' Ambiente e delle Risorse, Università di Napoli Federico II, Complesso Universitario Monte Sant' Angelo, Ed. L, Via Cintia 26, 80126 Naples, Italy; luigi.guerriero2@unina.it (L.G.); piergiulio.cappelletti@unina.it (P.C.)
- <sup>2</sup> Center for Research on Archaeometry and Conservation Science, CRACS, Ed. L, Via Cintia 26, 80126 Naples, Italy
- <sup>3</sup> Dipartimento di Studi Umanistici, Università degli Studi di Napoli Federico II, Via Porta di Massa 1, 80133 Naples, Italy; renataesp@libero.it
- \* Correspondence: concetta.rispoli@unina.it

**Abstract:** This research provides a characterization of ancient Roman mortars from “*Villa del Capo di Sorrento*” (commonly known as “*Villa di Pollio Felice*” or “*Bagni della Regina Giovanna*”). A deepened analysis of cementitious binding matrix and aggregates was conducted with the aims of determining possible sources of raw materials and the mix recipe, and to evaluate the minerogenetic secondary processes. Twenty samples taken from the *Villa* were investigated by means of a multi-analytical approach, including polarized optical microscopy on thin sections, X-ray powder diffraction, scanning electron microscopy analysis, energy dispersed spectrometry, simultaneous thermal analyses, and mercury intrusion porosimetry. Bedding mortars were made with slaked lime mixed with volcanic materials, whereas coating mortars were made adding to previous recipe as ceramic fragments. All samples were classified as hydraulic mortars. Cementitious binding matrix was characterized by gel-like C-A-S-H, calcite, hydrocalumite, and gypsum, deriving from lime/pozzolan material. Geomaterials used for mortar production had a local origin. Pozzolan materials, such as volcanic fragments, scoriae, pumice, and crystal fragments derived from both pyroclastic rocks of the *Campi Flegrei* district and from rocks of the *Somma-Vesuvio* complex; porosity test suggest that the products related to minerogenetic secondary processes, make mortars more resistant.

**Keywords:** ancient mortars; analytical characterization; Sorrento Peninsula

**Citation:** Rispoli, C.; Esposito, R.; Guerriero, L.; Cappelletti, P. Ancient Roman Mortars from *Villa del Capo di Sorrento*: A Multi-Analytical Approach to Define Microstructural and Compositional Features. *Minerals* **2021**, *11*, 469. <https://doi.org/10.3390/min11050469>

Academic Editors: Daniel Albero Santacreu, José Cristóbal Carvajal López and Adrián Durán Benito

Received: 8 April 2021  
Accepted: 27 April 2021  
Published: 29 April 2021

**Publisher's Note:** MDPI stays neutral with regard to jurisdictional claims in published maps and institutional affiliations.



**Copyright:** © 2021 by the authors. Licensee MDPI, Basel, Switzerland. This article is an open access article distributed under the terms and conditions of the Creative Commons Attribution (CC BY) license (<https://creativecommons.org/licenses/by/4.0/>).

## 1. Introduction

The Campania region was renowned during ancient times as *Campania felix*, thanks to its climate, beautiful landscapes, and fertile land. For these reasons, the region was among the favorite places to live in Roman times, with highly populated cities and *otium villae* on the coast [1].

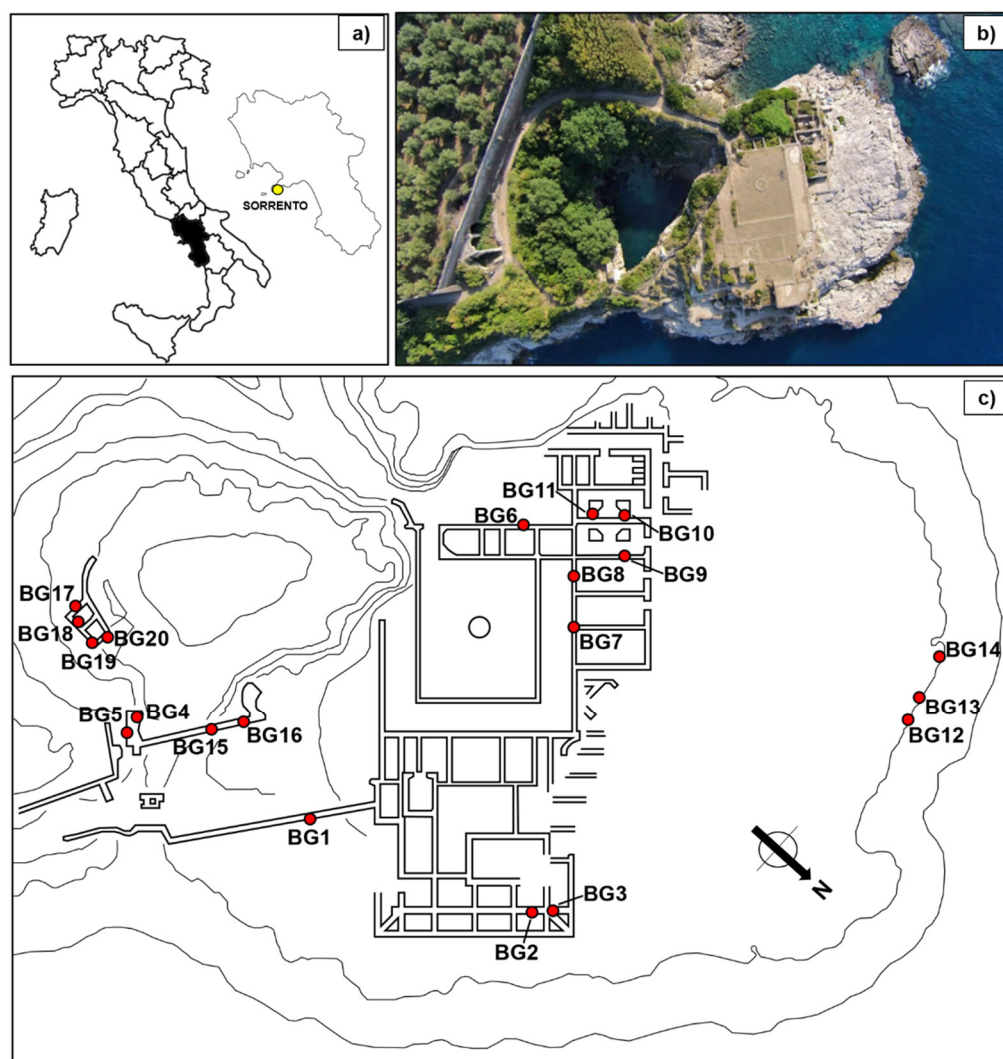
Nowadays, the region has plenty of major archeological sites, such as the eternal Vesuvian cities, *Pompeii*, and *Herculaneum*, the *Campi Flegrei*, which were often visited by rich Roman senators because of the natural baths and the stunning *villae maritimae*, found from *Posillipo* to *Punta Campanella* [2].

These sites, like other remarkable examples in the Campania region, are still preserved despite their location in an aggressive environment, such as the seaside, and the impact of waves and weathering, which is why they have been the object of many scientific studies.

The Department of Earth Sciences, Environment, and Resources (DiSTAR), Federico II University of Naples, for more than twenty years has been engaged in the application of mineralogical and petrographic studies of several ancient finds and monuments, especially of Campania region, such as Roman concrete, mortars, and ceramics, e.g., [3–7].

In this study the area of interest is the Sorrento Peninsula, between the village of *Aequa* (near *Vico Equense*) and the far side of the Sorrentine peninsula with its adjoining islets (Figure 1a). A total of 24 ruins have been identified as structures related to *villae maritimae*, commonly dated, based on their building techniques, between Late Republican period (133–21 B.C.) and the start of the 2nd c. A.D. [2]. In particular, we have focused the study on ancient roman mortars of one of the most remarkable *villa maritima* of the Sorrento Peninsula: *Villa del Capo* (commonly known as *Villa di Pollio Felice* or *Bagni della Regina Giovanna*; Figure 1).

Twenty lime-based mortars were carefully selected from different structures of *Villa del Capo* (Figure 1c) with the aim of characterizing them, especially regarding the cementitious binding matrix and aggregates, to determine the provenance of raw materials and mix recipe, improve the knowledge of Roman construction techniques, and study the secondary mineralogical processes affecting the investigated mortars.



**Figure 1.** (a) Map of Italy and location of Sorrento in the Campania region (Italy); (b) satellite picture of Villa of Capo; (c) sketch map of Villa del Capo with sampling points in red (modified after [8]).

## 2. Geological Context

*Villa del Capo* is located along the northwestern sector of the Sorrento Peninsula at the base of the north facing slope of the Corbo Mt. The ancient building is placed on the distal part of a small promontory that developing in NNW-SSE direction forms the so-called *Punta del Capo*. Being part of the Sorrento Peninsula horst, the Corbo Mt. is formed of Cretaceous

limestones, that widely crop out in the Sorrento Peninsula promontory, overlined by a transgressive Miocene succession, locally covered by quaternary rocks [9] (Figure 2). Forming a morphologic boundary between two semi-grabens located to the north and to the south (i.e., Gulf of Naples and Gulf of Salerno, respectively [9,10] (Figure 2), the Sorrento Peninsula is characterized by a structural setting dominated by NNW-SSE normal faults, resulting from the Plio-Quaternary transcurrent and extensional tectonics [10–12]. Less significant is the structural expression of the Late Miocene–Pliocene compressive tectonics. Similar to the Corbo Mt., the Lattari Mts. Range, forming the Sorrento Peninsula, is consistently mantled by pyroclastic soils representing the product of the activity of the *Somma-Vesuvio* and the *Campi Flegrei*. Such deposits have a thickness ranging from few centimeters to ten meters [12] and were mostly produced by the Holocenic Vesuvius eruption of 79 A.D. Between 18 ka ago and 79 A.D., the Lattari Mts. did not receive any significant fallout deposits, because during this time span, the *Vesuvio* Plinian eruptions were dispersed in other directions (NE to E; [13]. The pyroclastic cover has been subject to both mass wasting and fluvial denudation processes that completely removed it from steeper slopes.

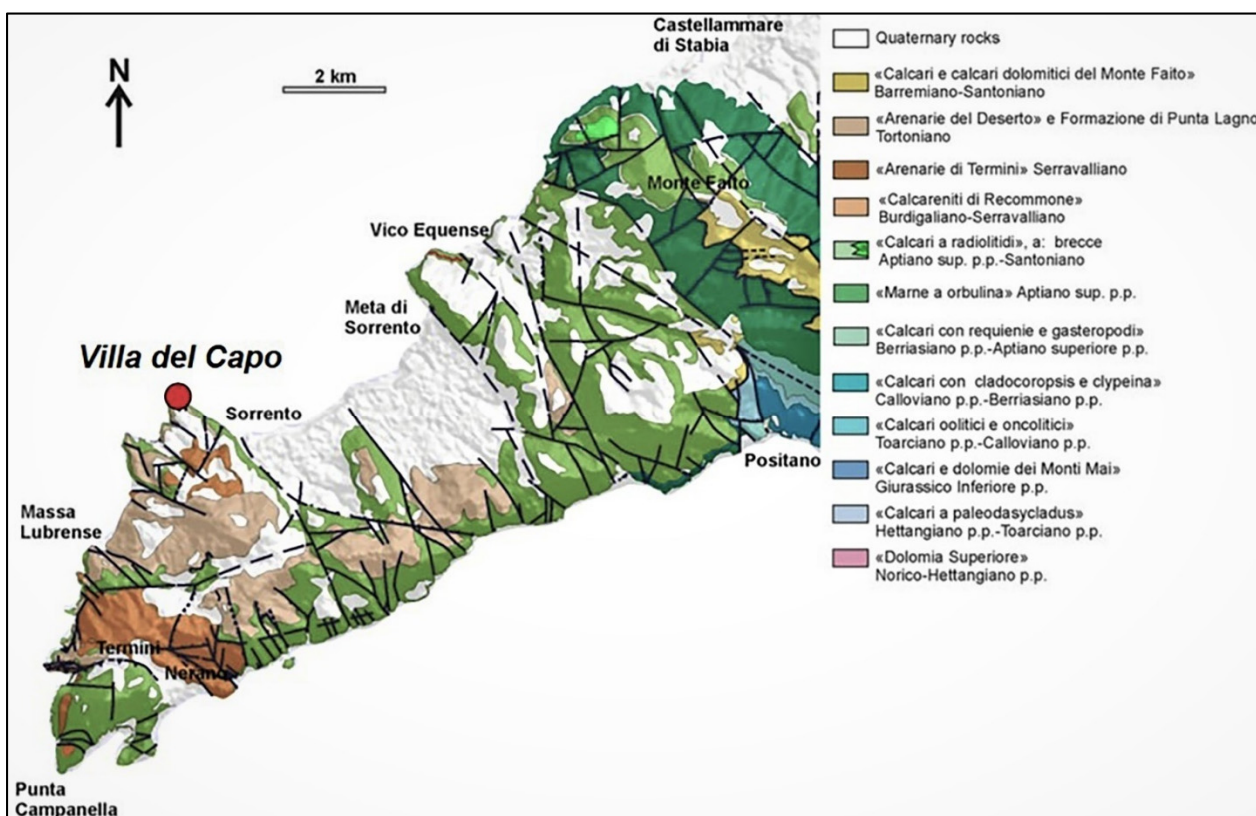


Figure 2. Geological sketch map of the Sorrento Peninsula (modified after [14]).

### 3. The Roman Villa del Capo

Roman *Villa del Capo*, which the popular tradition knew as *I bagni della regina Giovanna* (the baths of Queen Giovanna) or *Villa di Pollio Felice*, was identified by antiquarian tradition, since the sixteenth century, as well as by part of archaeological studies [15]. Located in a unique position, due to the presence of a circular basin, the *villa* is part of a dense network of maritime residences that studded the entire Gulf of Naples between the first century B.C. and the first century A.D. [16].

The Roman residence, organized with different living areas and services, was located on the top of the promontory, and characterized by several continuous terraces along the slope, about 200 m long, down to the sea where there were dockings [15]. The central



area was characterized by four levels with a compact nucleus of buildings; the presence of a peristyle with backyard and central basin on the upper terrace has been documented, where open rooms paved in opus sectile and a system of ramps and stairs linked this place with others. The structures of the *Villa*, facing the Sorrento side, due to the irregularly ascending shape of the area was leveled with the basis of the *Villa* made by *opus caementicium* foundations, exhibiting arches on the first floor and a covered porch with residential rooms at the second one [15]. The thermal area is identified by several rooms near the sea, where traces of their decoration survive, although partially destroyed by sea storms [2]. Finally, *Villa del Capo* continued to be inhabited for several centuries despite the damages caused by *Somma-Vesuvio* eruption of 79 A.D. [16].

#### 4. Materials and Methods

In the context of the ongoing collaboration and related authorization of the former *Soprintendenza archeologia della Campania* and to the assistance of archaeologists, who have carried out several studies on the investigated area, mortar samples were carefully collected in the most representative architectural structures of the archaeological site of *Villa del Capo* (Figure 1c, Table 1).

**Table 1.** Sample list, group, typology, and location.

Sample	Group	Typology	Location
BG1	C	floor mortar	external landing platform
BG2	A	bedding mortar	noble residential area
BG3	A	bedding mortar	noble residential area
BG4	B	coating mortar	bridge and input structures of sea bath
BG5	B	coating mortar	bridge and input structures of sea bath
BG6	A	bedding mortar	<i>quadriportico</i> of sea <i>Villa</i>
BG7	B	coating mortar	cistern of sea <i>Villa</i>
BG8	B	coating mortar	cistern of sea <i>Villa</i>
BG9	C	floor mortar	warehouses
BG10	A	bedding mortar	warehouses
BG11	A	bedding mortar	warehouses
BG12	A	bedding mortar	breakwater
BG13	A	bedding mortar	breakwater
BG14	A	bedding mortar	breakwater
BG15	A	bedding mortar	bridge and input structures of sea bath
BG16	A	bedding mortar	bridge and input structures of sea bath
BG17	B	coating mortar	cistern
BG18	B	coating mortar	cistern
BG19	B	coating mortar	cistern
BG20	B	coating mortar	cistern

The sampling of mortars was preceded by an accurate on-site survey to define the most suitable samples to collect in terms of archaeological and architectural significance. A total of 20 samples was collected comprising ten bedding mortars (Group A), eight coating mortars (Group B) and two floor mortars (Group C).

Samples were removed mechanically with hammers and chisels, ensuring to avoid external and clearly altered portions to study materials that are as close as possible to the original conservation state.

In order to achieve this study's goals, various analytical techniques were used to obtain a mortar's complete petrographic, mineralogical, and chemical characterization and degree of hydraulicity.

The first approach to the study of mortar samples was macroscopic observation, for: (1) identification of the materials and (2) planning of analytical procedures.

Polarized optical microscopy (POM) on polished thin section was performed to observe the textural features and the petrographic composition of the samples with a Leica DFC280 microscope (Leica Camera, Wetzlar, Germany). Percentage of binder and aggregate



was measured via modal analysis on four representative thin sections from each different sector of the investigated area, selected on the base of their macro- and microscopical features. 1500 points for each section were counted using a Leica Q Win image analysis software. Maximum uncertainty of percentage for a total amount of 1500 points is about 2.8% [17].

Qualitative mineralogical analysis was performed by X-Ray Powder Diffraction (XRPD) using a Panalytical X'Pert Pro diffractometer (Malvern PANalytical, Almelo, The Netherlands) equipped with a RTMS X'Celerator detector with Cu-K $\alpha$  radiation, operating at 40 kV and 40 mA. Scans were collected in the range 4–70° 2 $\theta$  using a step interval of 0.017° 2 $\theta$ , with a step counting time of 120 s. Panalytical Highscore Plus 3.0c software (Malvern PANalytical, Almelo, The Netherlands) and PDF-2/ICSD databases were used for identification.

Micro-textural observations and quantitative micro-chemical analyses were carried out by Scanning Electron Microscopy coupled and Energy Dispersive Spectroscopy (SEM/EDS; JEOL JSM-5310 (Jeol Ltd., Tokyo, Japan) coupled with Oxford Instruments Microanalysis Unit, INCA X-act detector (Oxford Instruments plc, Abingdon, Oxfordshire, UK). Measurements were performed with an INCA X-stream pulse processor (ETAS group, Stuttgart, Germany) using a 15-kV primary beam voltage, 50–100  $\mu$ A filament current, variable spot size, from 30,000 to 200,000 $\times$  magnification, 20 mm WD, and 50 s net acquisition real time). The INCA Energy software was employed, using the XPP matrix correction scheme, developed by Pouchou and Pichoir [18], and the Pulse Pile up correction. The quant optimization was carried out using cobalt (FWHM—full width at half maximum peak height—of the strobed zero = 60–65 eV).

Details of the utilized standard and precision and accuracy are provided in [19].

Micro-chemical analyses were performed to determine major chemical composition of binder, lime lumps and aggregates. Hydraulicity index (HI) of binder was calculated according to Boynton using the  $(\text{SiO}_2 + \text{Al}_2\text{O}_3 + \text{Fe}_2\text{O}_3)/(\text{CaO} + \text{MgO})$  ratio.

Thermal Analyses (TGA/SDTA) were carried out with a Mettler Toledo TGA/SDTA 851e instrument (Mettler Toledo, Columbus, OH, USA) and Mettler Toledo STARE SW 7.01 software, with the main goal of determining total (binder plus aggregates) hydraulic features of these materials. Samples were previously dried at 40 °C in a drying oven for 48 h. Thermal analysis was performed within the temperature range of 25–1000 °C, heating rate of 10 °C/min in nitrogen atmosphere (flow 60 mL/min).




Porosity was determined on fragments of mortar (binder and aggregate were not separated) and was evaluated using mercury intrusion porosimetry (MIP), according to ASTM D4404–18 [20]. Due to the scarce amount and small dimensions of samples, on the bases of macroscopic and microscopic features, three fragments were selected, approximately 1 cm<sup>3</sup> in size. Selected fragments were dried in an oven for 24 h at 105 °C, and then analysed on Thermo Scientific equipment PASCAL 140 (ThermoFischer, Waltham, MA, United States) with a maximum injection pressure of 0.4 MPa and PASCAL 240 with a maximum injection pressure of 200 MPa. Total volume of pores of radius between 3.75 nm and 800  $\mu$ m (expressed in mm<sup>3</sup>/g) was determined; open porosity (expressed in vol %); bulk density (g/cm<sup>3</sup>); apparent density (g/cm<sup>3</sup>), and specific surface (m<sup>2</sup>/g); graphical and numerical representation of the distribution of pore sizes were also determined.

## 5. Experimental Results and Discussion

### 5.1. Texture and Optical Microscopy

From a macroscopic point of view, some samples appear to be intact with respect to others that seem to be quite dusty and friable. In addition, they globally show grain size from fine to coarse sand [21]. A brief macroscopic description of mortar Groups (A, B, and C) along with representative sample images is summarized in Table 2.

**Table 2.** List and brief macroscopic description of the examined groups of mortar samples on archaeological site of *Villa del Capo*.

Group	Typology	Binder Color	Aggregate Size	Compactness	Photographic Representation
A (BG15 sample)	Bedding mortars	light grey color	Up to 10 mm	++	
B (BG18 sample)	Coating mortars	Light yellow to reddish	Up to 1.5 cm	+++	
C (BG9 sample)	Floor mortars	pale brown to greyish	Up to 10 mm	+++	

Degree of compactness: +: poor; ++: moderate; +++: high.

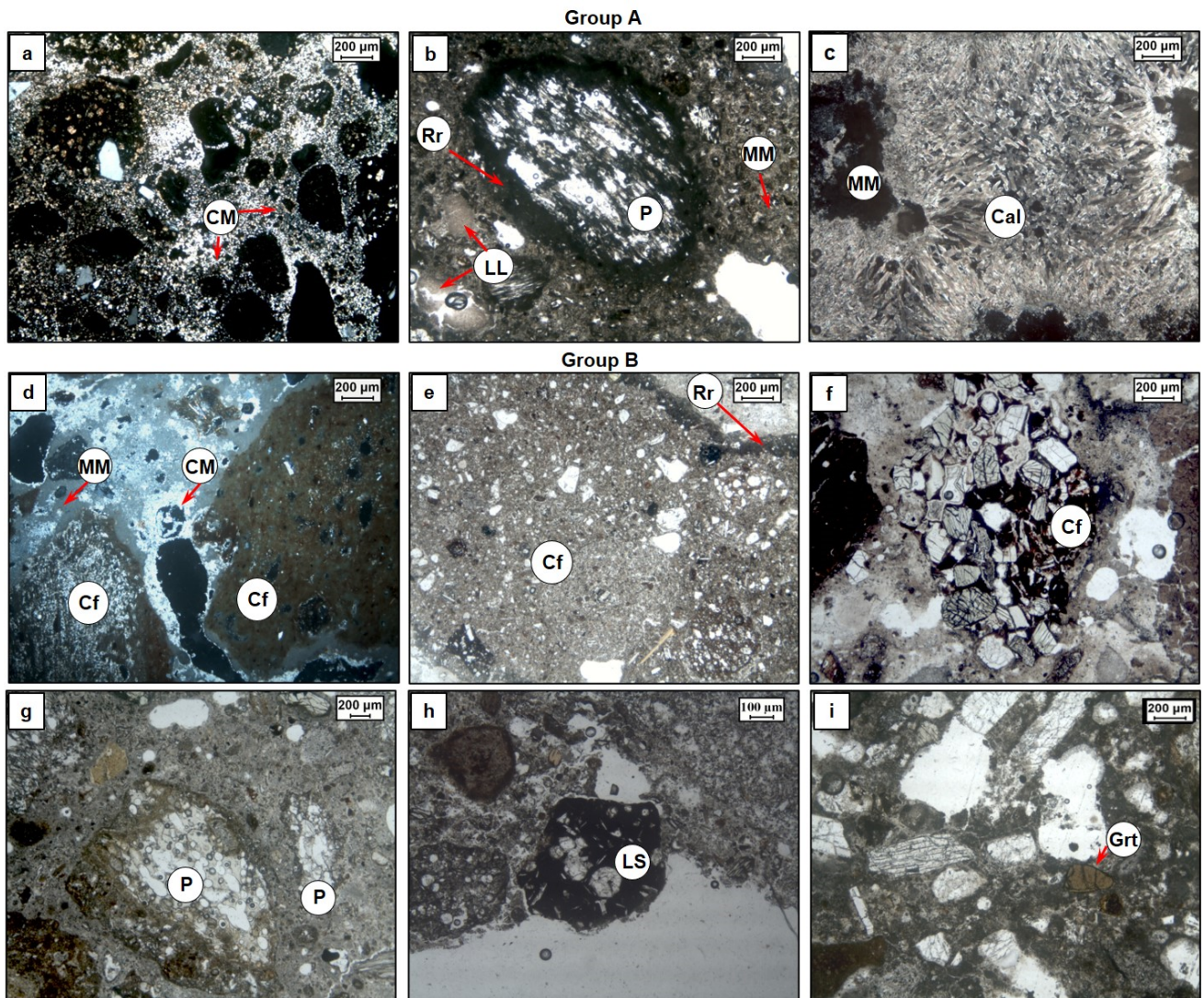
Optical microscopy shows that all mortars are characterized by presence of lime lumps (mm to cm). Their formation generally is related to lime binder not well mixed in mortars but sometimes they could be also formed due to not adequate slaking processes of lime or to non-homogeneous temperature in the kiln (under/over-burnt fragments of limestone) [22–24]. Secondary calcite on pore rims and pumice vesicles also occurs.

Binder phase in group A (bedding mortars) is characterized by pale brown/beige to grey color and shows various grades of crystallinity from cryptocrystalline (36.8 Vol.%; Figure 3a) to micritic (22.0 Vol.%; Figure 4b,c). The binder shows the presence of small and fractured lime lumps (5.5 Vol.%, Figure 3b) and few percentages of sparite grains (0.4 Vol.%). Aggregate is mainly composed by volcanic fragments (5.2 Vol.%), pumice (12.0 Vol.%; Figure 3b), and scoriae with clear reaction rims (1.7 Vol.%), mineral aggregates (0.1 Vol.%) formed by clinopyroxene, sanidine, plagioclase, biotite, and, sometimes, calcite, and crystal fragments of sanidine, plagioclase, and clinopyroxene (5.2 Vol.%). Volcanic fragments can be identified as volcanic tuff, characterized by pumice and obsidian fragments, lithics and crystal fragments of sanidine, clinopyroxene, biotite, and plagioclase set in an ashy matrix mainly constituted by volcanic glass shards, affected by secondary mineralization processes [25]. In sample BG12 presence of acicular crystals was also observed, apparently calcite, filling the vugs. (Figure 3c). The binder/aggregate ratio was about 2.7 (Table 3).

Group B (coating mortars) is characterized by a binder that ranges from greyish to brownish color and shows a cryptocrystalline (31.4 Vol.%) and micritic texture (18.9 Vol.%; Figure 3c), small and fractured lime lumps, with not well-defined edges (6.3 Vol.%), and very small percentage of sparite grains (0.4 Vol. %). Aggregate fraction is characterized mainly by ceramic fragments (21.5 Vol.%; Figure 3d–f) with occurrence of reaction rims. Petrographic observations revealed a certain variability in types of ceramic fragments. These sometimes contain temper of different mineralogical composition: for example, in sample BG17 (Figure 3e,f), ceramic fragments containing pumice, scoriae, and small crystals (Figure 3e), and other fragments presenting only crystals of different types (Figure 3f), can be recognized. Moreover, they have also different degrees of porosity and optical activity. The other secondary aggregates that characterize this Group (B) are volcanic and carbonate fragments (2.8 Vol.%–0.5 Vol.%), pumice, and scoriae with reaction rim (4.8 Vol.%; 2.2 Vol.%; Figure 3g) and crystal fragments of plagioclase, sanidine, and clinopyroxene (5.8 Vol.%). Particularly relevant is the presence of leucite-bearing scoriae in BG8 sample (Figure 3h) and the presence of crystal fragments of garnet in BG7 sample (Figure 3i).

Mortars from group B can be identified as *cocciopesto*, a typical building technique used in ancient Rome for waterproof structures, such as cisterns and floors [3,26]. The binder/aggregate ratio is of about 1.5 (Table 3).

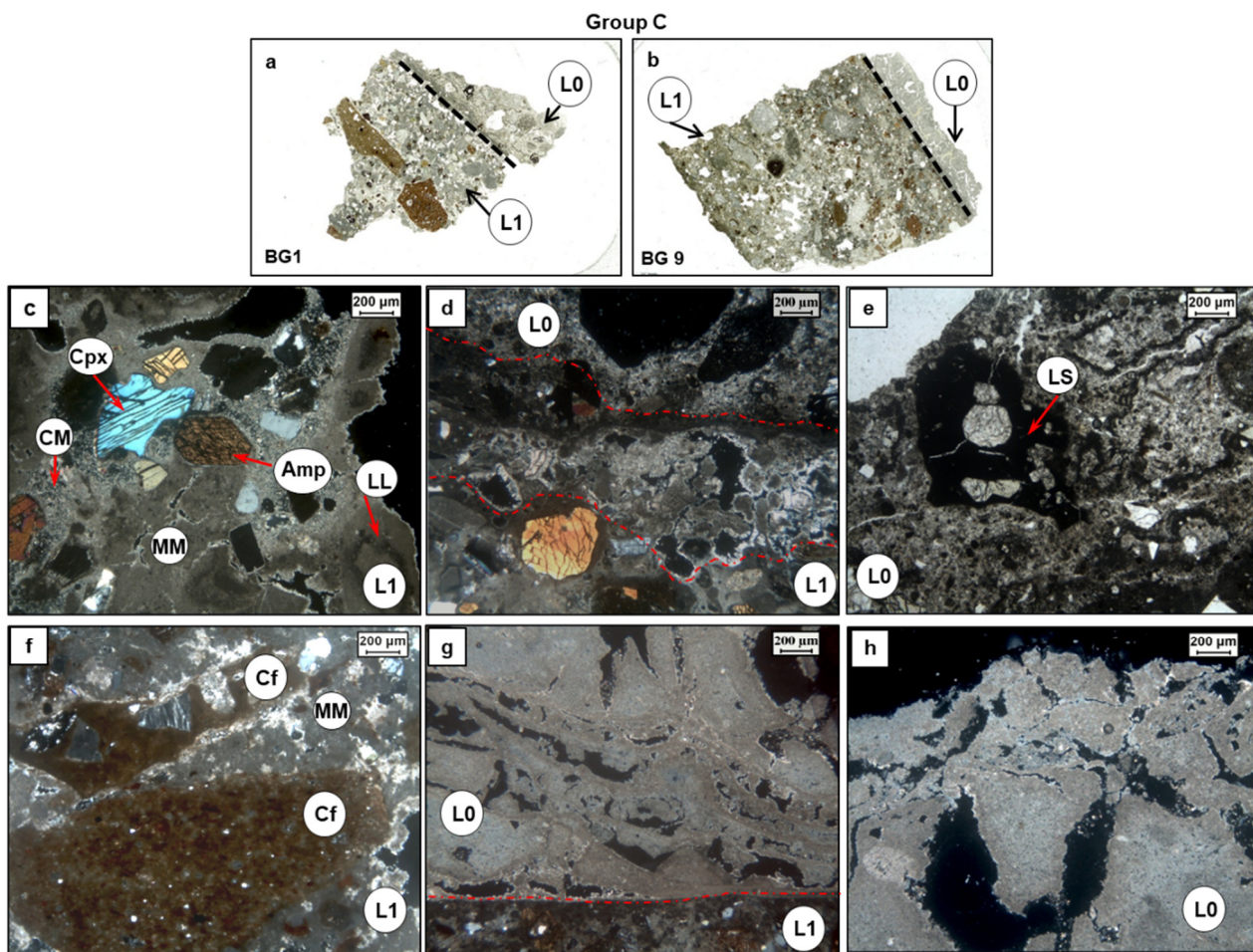




**Figure 3.** Microphotographs of mortar components (in CPL: cross polarized light; PPL: plane polarized light). Abbreviations: MM micritic matrix, CM cryptocrystalline matrix, Rr reaction rim, P pumice, Cf ceramic fragment, Cal calcite, Ls leucite-bearing scoriae, Grt garnet. Group A: (a) cryptocrystalline matrix (CPL) in sample BG3. (b) pumice with reaction rim, lime lumps, and micritic matrix in sample BG6 (PPL). (c) micritic matrix and acicular crystal calcite in sample BG12 (CPL). Group B: (d) cryptocrystalline matrix, micritic matrix, and ceramic fragments in BG19 sample (CPL). (e) ceramic fragment with reaction rim in BG17 sample (CPL). (f) ceramic fragment in BG17 sample (PPL). (g) pumice in BG20 sample (PPL). (h) leucite-bearing scoriae in BG8 sample (PPL). (i) crystal fragment of garnet in BG7 sample.

Floor mortars (Group C) are characterized by two different layers (1 and 0; Figure 4a,b). In BG1 sample, layer 1 (L1, internal layer) is characterized by beige color of binder, with cryptocrystalline to micritic aspect (27.5 Vol.%; 31.3 Vol.%; Figure 4c). Binder also shows presence of small and fractured lime lumps (5.5 Vol.%, Fig; Figure 4c). Aggregates are composed of different types of ceramic fragments (14.1 Vol. %), scoriae (6.2 Vol.%), leucite-bearing scoriae (1.5 Vol.%), and crystal fragments of clinopyroxene, amphibole, plagioclase, sanidine (5.9 Vol. %), and garnet (1.8 Vol.%). Between layers 1 and 0, carbonation processes are evident. (Figure 4d). Modal analysis was performed only in layer 1 and the resulting binder/aggregate ratio was about 2 (Table 3). Layer 0 (external layer) presents a grey color binder and cryptocrystalline aspect (Figure 4d,e). The aggregates are poorly sorted and composed by few leucite-bearing scoriae (Figure 4e), altered pumice, and rare crystal fragments of clinopyroxene.





**Figure 4.** Group C: (a) thin section scan of BG1 sample, L1 internal layer, L0 external layer, (b) thin section scan of BG9 sample, L1 internal layer, L0 external layer. (c–h) microphotographs of mortar components (in CPL: cross polarized light; PPL: plane polarized light). Abbreviations: MM micritic matrix, CM cryptocrystalline matrix, Cf ceramic fragment, Ls leucite-bearing scoriae, Cpx clinopyroxene, Amp amphibole. (c) cryptocrystalline matrix, micritic matrix, crystal of amphibole, and clinopyroxene (CPL) in L1 of BG1 sample, (d) transition between L1 and L0 (CPL) in BG1 sample, (e) leucite-bearing scoriae in L0 (PPL) of BG1 sample, (f) micritic matrix and ceramic fragments in L1 of BG9 sample (CPL), (g) transition of L1 and L0 in BG0 sample (CPL), (h) micritic aspect of L0 in BG9 sample (CPL).

In BG9 samples, Layer 1 is characterized by a brownish color of the binder and presents both micritic and cryptocrystalline texture (22.0 Vol.%; 38.0 Vol.%; Figure 4f). Binder phase also shows presence of lime lumps (1.4 Vol.%). Aggregates are composed by different types of ceramic fragments (10.3 Vol.%, Figure 4f), pumice and scoriae with clear reaction rims (10.1 Vol.%–2.9 Vol.%), volcanic fragments (2.1 Vol.%), and crystal fragments (8.2 Vol.%) of clinopyroxene, sanidine, and biotite. Volcanic fragments can be classified as volcanic tuff, characterized by the presence of microcrystals immersed in an altered ashy matrix [8].

Transition between layers 1 and 0 is well defined and evident (Figure 4g). Modal analysis, performed on layer 1, shows binder/aggregate ratio equal to 1.8.

Layer 0 (L0) is characterized by white color of the binder, with mainly micritic aspect with no aggregates (Figure 4h).

**Table 3.** Petrographic features of samples and their modal analysis. Mineral abbreviations from [27].

Mortars	Group A	Group B	Group C (BG1)	Group C (BG9)
<b>Constituents (Vol.%)</b>				
Feldspar (Sa, Pl)	3.7	3.6	4.5	5.3
Mafic Minerals (Cpx, Am, Bt)	1.5	2.2	1.4	2.9
Garnet	-	0.1	1.8	-
Volcanic fragments	5.2	2.8	-	2.1
Scoriae	1.7	2.1	6.2	2.9
Leucite-bearing scoriae	-	0.1	1.5	-
Pumice	12.0	4.8	-	10.1
Ceramic fragments	-	21.5	14.1	10.3
Carbonatic fragments	-	0.5	1.9	-
Sparite	0.4	0.4	0.1	-
Lime lumps	5.5	6.3	3.9	1.4
Micritic matrix	22.0	18.9	31.3	22.0
Cryptocrystalline matrix	36.8	31.4	27.5	38.0
Voids	11.1	2.4	4.7	4.7
Others	0.1	2.9	1.0	0.3
Total points %	100	100	100	100
Total Binder %	64.6	57.1	62.9	61.4
Total Aggregate%	24.1	37.6	31.4	33.7
Binder/Aggregate ratio	2.7	1.5	2.0	1.8

## 5.2. Mineralogy

Samples were separated in (1) binder and (2) aggregates (excluding ceramic fragments, due to their extreme variability) according to the UNI-EN 11305 [28] document (mortar characterization).

XRPD results confirmed occurrence of lime-based mortar with volcanic aggregate, as shown by semi-quantitative analyses reported in Table 4.

Regarding binder phases (Figure 5), calcite is the most abundant phase with subordinate gypsum  $[\text{CaSO}_4 \cdot 2(\text{H}_2\text{O})]$  and hydrocalumite  $\text{Ca}_2\text{Al}(\text{OH})_6[\text{Cl}_{1-x}(\text{OH})_x] \cdot 3(\text{H}_2\text{O})$ . Gypsum, since it is only in a few samples, could be ascribed to sulphation processes of calcite as a consequence of the decrease in pH value, caused by dissolution of atmospheric  $\text{SO}_2$  [29].

Hydrocalumite, also known as Friedel's salt or AFm phase in cement science, belongs to layered double hydroxides (LDHs) family [8,30,31]. LDHs are among the few oxide-based materials with permanent anion exchange capacity, developed through isomorphous substitution [30]. Hydrocalumite has not only an ordered Ca-Al distribution in the hydroxide layer, but well-ordered  $\text{Cl}^-$  and water in the interlayer space. The interlayer order is due to coordination of the water molecules to Ca in the hydroxide layer, which results in an unusual 7-coordinate Ca environment. This phase occurs naturally and generally forms by reaction of Cl-containing de-icing salts with the calcium aluminates of Portland cement [32]. In *Villa del Capo* mortars hydrocalumite is ascribable to the reaction between the  $\text{Ca}(\text{OH})_2$ , sea-water, and hydroxyaluminate derived from pozzolanic materials [31].

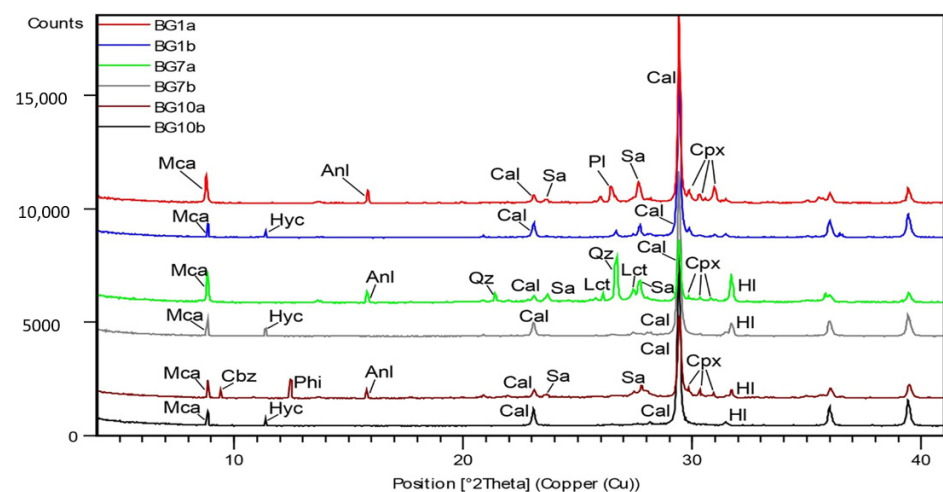
As far as volcanic aggregates fraction is concerned (Figure 5), XRPD analyses suggest that volcanic tuff fragments can be associated to *Campi Flegrei* ignimbrite products (Neapolitan Yellow Tuff and/or Campanian Ignimbrite), due to the presence of typical zeolitic association of this material, i.e.,: phillipsite, chabazite, and analcime [33,34]. In addition, presence of sanidine, clinopyroxene, and mica could be also associated to the *Campi Flegrei* ignimbrite formations.

All samples show the presence of halite, associated with marine aerosol.

XRPD analysis allowed to detect the presence of amorphous fraction, recognized by the rising of the pattern background, related to volcanic glass components and C-A-S-H (calcium, aluminum, silicate, hydrate) phases.

**Table 4.** Qualitative mineralogical composition of samples, XRPD analysis. Mineral abbreviations from [27].

Samples	Group	Main Binder Phases	Main Aggregates Phase
BG1	C	Cal, Hyc	Anl, Sa, Pl, Cpx, Mca, Cal
BG2	A	Cal, Gp, Hl	Anl, Sa, Pl, Mca, Hl, Cal
BG3	A	Cal, Hl	Phi, Anl, Sa, Pl, Cpx, Mca, Hl, Cal
BG4	B	Cal, Hl	Phi, Anl, Sa, Pl, Cpx, Mca, Cal
BG5	B	Cal	Phi, Anl, Sa, Pl, Cpx, Mca, Cal
BG6	A	Cal, Hyc, Hl	Phi, Pl, Cpx, Mca, Hl, Cal
BG7	B	Cal, Hyc, Hl	Anl, Pl, Qz, Cpx, Mca, Lct, Hl, Cal
BG8	B	Cal, Gp, Hyc, Hl	Anl, Sa, Pl, Qtz, Cpx, Lct, Mca, Hl, Cal
BG9	C	Cal	Phi, Cbz, Anl, Sa, Pl, Qtz, Cpx, Mca, Hl, Cal
BG10	A	Cal, Hyc, Hl	Phi, Cbz, Anl, Sa, Pl, Cpx, Mca, Hl, Cal
BG11	A	Cal, Hl	Phi, Anl, Sa, Pl, Mca, Hl, Cal
BG12	A	Cal, Gp, Hyc, Hl	Phi, Cbz, Anl, Sa, Pl, Cpx, Mca, Hl, Cal
BG13	A	Cal, Gp, Hyc, Hl	Phi, Cbz, Anl, San, Pl, Cpx, Mca, Hl, Cal
BG14	A	Cal, Hyc, Hl	Phi, Anl, Sa, Pl, Cpx, Mca, Hl, Cal
BG15	A	Cal, Hl	Phi, Anl, Sa, Pl, Cpx, Mca, Hl, Cal
BG16	A	Cal, Hyc, Hl	Phi, Anl, Sa, Pl, Cpx, Mca, Hl, Cal
BG17	B	Cal, Gp	Phi, Anl, Sa, Pl, Cpx, Qz, Mca, Cal
BG18	B	Cal	Phi, Cbz, Anl, Sa, Cpx, Pl, Mca, Cal
BG19	B	Cal	Phi, Cbz, Anl, Sa, Pl, Cpx, Mca, Cal
BG20	B	Cal, Gp	Phi, Anl, Sa, Pl, Cpx, Qz, Mca, Cal

**Figure 5.** XRPD patterns of selected mortars. BG1a: BG1 aggregate fraction (group C); BG1b: BG1 binder fraction (group C); BG7a: BG7 aggregate fraction (group B); BG7b: BG7 binder fraction (group B); BG10a: BG10 aggregate fraction (group A); BG10b: BG10 binder fraction (group A). Mineral abbreviations from [27], Cal calcite, Gp gypsum, Hyc hydrocalumite, Phi phillipsite, Cbz chabazite, Anl analcime, Sa sanidine, Pl plagioclase, Cpx clinopyroxene, Mca mica, Qz quartz, Hl halite.



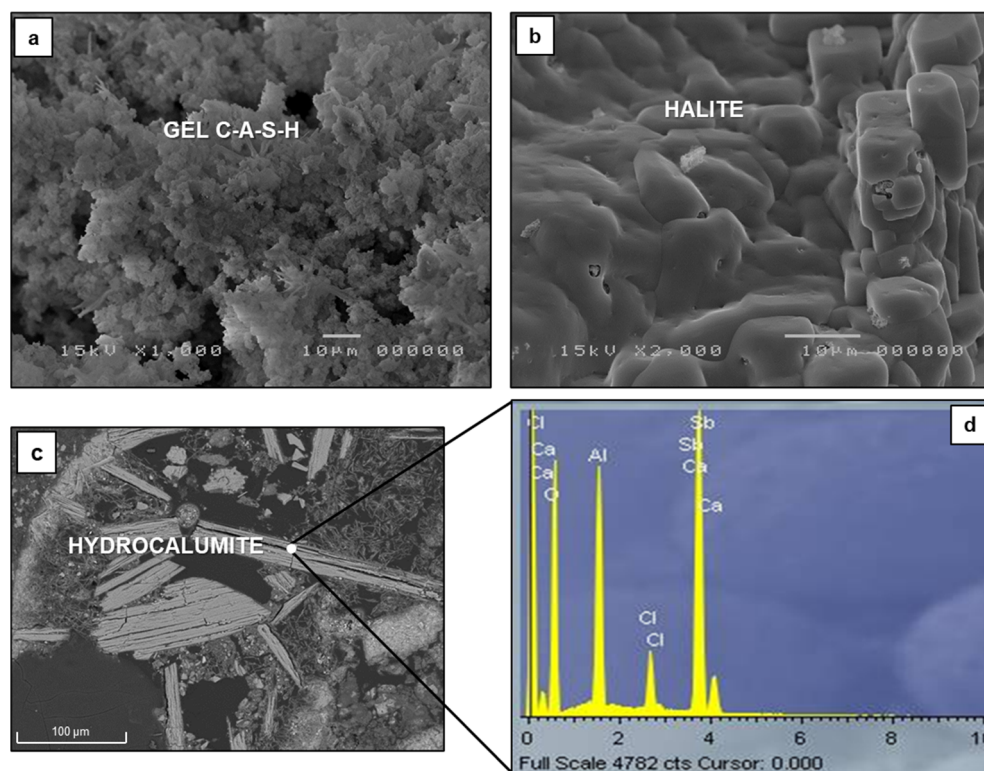
### 5.3. Micro-Morphology and Chemical Analysis (SEM-EDS)

#### 5.3.1. Binder and Lime Lumps

SEM-EDS analysis was carried out to obtain information about the type of lime used to produce the mortars, defining the Hydraulic Index (HI) of the binder and lime lumps.

SEM-EDS analysis of binder showed presence of newly formed hydraulic phases (C-A-S-H), and confirmed, as XRPD suggested, presence of halite and hydrocalumite (Figure 6). Gel C-A-S-H derived from reactions between lime and pozzolanic material (volcanic and ceramic materials). Pozzolanic materials consist predominantly of silica and alumina that are able to combine with slaked lime in the presence of water to produce new reaction products exhibiting a binding character, the so-called CASH phases [35]. Occurrence of hydrocalumite recognized in relict pores of *Villa del Capo* mortars, is associated to the migration of  $\text{Cl}^-$  anions from the sea-water saturated in  $\text{Ca}(\text{OH})_2$  to aluminum-rich sites along the edges of the relict lime clasts or in the voids of mortars [36].

EDS analyses on binder were realized averaging out four measurements for each investigated mortar sample and the results were considered as representative of chemical composition. Based on the mean values of the detected major elements (Table 5), binder results composed by  $\text{CaO} + \text{MgO}$  ranging from a minimum value of 78.31 wt% for sample BG17 to a maximum of 87.11 wt% for BG3 and values of  $\text{SiO}_2 + \text{Al}_2\text{O}_3 + \text{Fe}_2\text{O}_3$  varying from 10.39 wt% for BG1 to 18.77 wt% for BG20.



**Figure 6.** SEM images of (a) Gel C-A-S-H, BG17 binder sample; (b) halite crystals, BG10 binder sample; (c) BSE-SEM image of hydrocalumite, BG8 sample; (d) EDS spectrum of hydrocalumite, BG8 sample.

The Hydraulicity Index (HI), calculated according to Boynton's formula [37], showed values ranging between 0.12 and 0.25 wt%; in particular, mortar samples of Group A and C should be considered as weakly hydraulic lime ( $0.10 < \text{HI} < 0.15$  wt%; Figure 7); samples of Group B are moderately hydraulic limes ( $0.16 < \text{HI} < 0.31$  wt%; Figure 7). Regarding the investigation of lime lumps (Table 6), three measurements were performed for each detected lump and performed in their central portion, to reduce the level of contamination. Lime lumps were found to be composed mainly of  $\text{CaO}$ , with very high

values of CaO + MgO ranging from 90.56 wt% (BG9) to a maximum of 96.56 wt% (BG6) and low values of SiO<sub>2</sub> + Al<sub>2</sub>O<sub>3</sub> + Fe<sub>2</sub>O<sub>3</sub> all less than 5 wt%. The Hydraulicity Index related to lime lumps shows values from 0.01 and 0.05 wt% (0.03 < HI < 0.05 wt%; Figure 7), as a result of lumps with aerial properties (H.I. < 0.10). Considering these results, it is possible to infer that mortars became hydraulic by addition of aggregates (volcanic materials and ceramic fragments) with peculiar features. These aggregates, as said previously, produced a “pozzolanic reaction”, due to their silica and alumina content, that reacted with calcium hydroxide leading to the formation of calcium aluminum silicate hydrates, C-A-S-H phases [8,38,39], furtherly testified and confirmed by reaction rims around pumice, scoriae, and ceramic fragment (Figure 3).

**Table 5.** Average values of major oxides (wt%, recalculated to 100%, EDS) of lime lumps (L). SiO<sub>2</sub> + Al<sub>2</sub>O<sub>3</sub> + Fe<sub>2</sub>O<sub>3</sub>, CaO + MgO, HI (hydraulic index) is also shown.

Group	A	A	A	A	A	A	A	A	A	A	B	B	B	B	B	B	B	B	C	C
wt%	BG2 L	BG3 L	BG6 L	BG10 L	BG11 L	BG12 L	BG13 L	BG14 L	BG15 L	BG16 L	BG4 L	BG5 L	BG7 L	BG8 L	BG17 L	BG18 L	BG19 L	BG20 L	BG1 L	BG9 L
SiO <sub>2</sub>	1.95	1.55	1.34	2.87	1.91	1.79	2.34	2.46	1.52	2.14	3.73	1.25	0.52	1.92	1.72	2.88	1.93	2.83	2.34	2.21
TiO <sub>2</sub>	0.12	-	-	-	-	-	0.02	0.13	-	-	0.88	-	-	-	0.34	-	0.24	0.06	-	0.37
Al <sub>2</sub> O <sub>3</sub>	2.02	1.16	1.32	0.86	0.99	1.03	1.19	0.39	1.43	1.54	0.82	2.13	2.43	1.83	2.10	1.08	2.06	1.08	1.32	1.21
Fe <sub>2</sub> O <sub>3</sub>	0.09	0.20	-	0.37	0.38	0.31	-	0.34	0.50	0.10	-	0.37	0.50	0.44	-	0.41	-	0.21	-	-
MnO	-	-	-	-	-	0.12	-	0.09	0.42	0.06	0.15	0.22	0.42	0.32	0.41	0.20	0.42	0.11	-	0.19
MgO	0.56	1.14	1.87	2.48	2.45	0.56	1.87	2.80	0.55	1.73	1.28	0.60	0.55	0.46	2.13	0.26	1.12	0.36	1.87	2.19
CaO	92.78	94.80	94.68	91.12	93.04	94.28	93.80	91.89	93.11	93.61	91.09	94.23	93.11	93.47	92.07	93.36	93.79	93.70	93.68	88.38
Na <sub>2</sub> O	0.42	0.32	0.16	0.45	0.27	0.27	0.16	0.19	0.42	0.17	0.90	0.32	0.42	0.23	0.18	0.59	0.13	0.72	0.16	0.69
K <sub>2</sub> O	0.16	-	-	-	-	-	-	-	-	0.18	0.13	0.09	-	-	0.09	0.55	0.08	0.51	-	0.03
P <sub>2</sub> O <sub>5</sub>	0.05	-	-	-	-	-	-	-	-	-	-	-	-	-	-	-	-	-	-	0.48
BaO	0.49	-	0.49	-	-	0.09	0.49	0.05	-	0.09	0.00	-	-	-	-	-	0.06	-	-	0.49
SO <sub>3</sub>	0.12	0.19	0.13	0.99	0.10	1.13	0.13	0.62	1.16	0.23	0.29	0.44	0.40	0.10	0.02	0.24	-	0.29	0.13	0.30
Cl-	0.89	0.65	-	0.87	0.87	0.23	-	0.87	0.40	0.15	0.30	0.16	1.16	1.04	0.20	0.43	-	0.14	-	3.70
F-	0.34	-	-	-	-	0.18	-	0.16	0.47	0.00	0.42	0.18	0.47	0.18	0.75	-	0.17	-	-	0.25
Total	100.00	100.00	100.00	100.00	100.00	100.00	100.00	100.00	100.00	100.00	100.00	100.00	100.00	100.00	100.00	100.00	100.00	100.00	100.00	100.00
SiO <sub>2</sub> + Al <sub>2</sub> O <sub>3</sub> + Fe <sub>2</sub> O <sub>3</sub>	4.07	2.90	2.67	4.09	3.28	3.13	3.53	3.19	3.46	3.78	4.54	3.76	3.46	4.20	3.82	4.37	3.99	4.12	3.67	3.42
CaO + MgO	93.34	95.94	96.56	93.60	95.49	94.84	95.68	94.69	93.66	95.34	92.37	94.83	93.66	93.93	94.20	93.62	94.91	94.06	95.56	90.56
HI	0.04	0.03	0.03	0.04	0.03	0.03	0.04	0.03	0.04	0.04	0.05	0.04	0.04	0.04	0.04	0.05	0.04	0.04	0.04	0.04

**Table 6.** Average values of major oxides (wt%, recalculated to 100%, EDS) of binder (B). SiO<sub>2</sub> + Al<sub>2</sub>O<sub>3</sub> + Fe<sub>2</sub>O<sub>3</sub>, CaO + MgO, HI (hydraulic index) is also shown.

Group	A	A	A	A	A	A	A	A	A	A	B	B	B	B	B	B	B	B	C	C
wt%	BG2 B	BG3 B	BG6 B	BG10 B	BG11 B	BG12 B	BG13 B	BG14 B	BG15 B	BG16 B	BG4 B	BG5 B	BG7 B	BG8 B	BG17 B	BG18 B	BG19 B	BG20 B	BG1 B	BG9 B
SiO <sub>2</sub>	8.03	8.24	7.76	8.04	8.89	8.34	9.03	9.52	6.79	8.73	9.82	10.76	9.76	10.27	14.11	12.90	13.99	14.32	7.94	8.85
TiO <sub>2</sub>	0.19	0.22	-	0.33	0.13	-	0.05	0.21	-	-	-	-	-	-	0.26	0.24	0.28	0.14	-	0.40
Al <sub>2</sub> O <sub>3</sub>	2.69	2.41	3.07	2.34	2.15	3.76	3.13	2.03	3.77	2.92	3.19	3.27	3.07	2.82	3.70	3.82	3.17	3.59	2.24	2.65
Fe <sub>2</sub> O <sub>3</sub>	0.17	0.25	0.28	0.18	0.11	0.12	0.15	0.02	0.19	0.21	0.70	0.78	0.28	0.20	0.90	1.27	0.35	0.87	0.21	0.00
MnO	-	0.07	0.15	0.17	0.07	-	0.06	0.11	-	0.14	0.09	0.15	0.15	0.10	0.32	0.00	0.44	0.06	0.24	0.48
MgO	0.24	3.92	3.34	4.04	2.94	1.41	2.33	3.67	1.42	3.11	5.19	2.34	3.34	2.73	0.67	7.78	0.80	5.64	0.71	0.74
CaO	85.72	83.18	82.56	83.02	83.83	83.62	82.54	83.02	84.83	82.61	78.61	80.47	80.56	82.06	77.64	71.74	78.62	72.96	85.67	83.58
Na <sub>2</sub> O	0.82	0.68	0.91	0.71	0.45	0.81	0.97	0.71	0.89	0.39	0.86	0.52	0.91	0.72	1.07	0.53	1.06	0.63	1.20	1.37
K <sub>2</sub> O	0.20	0.15	0.22	0.19	0.09	0.24	0.14	0.14	0.43	0.22	0.13	0.22	0.22	0.13	0.74	0.30	0.58	0.40	0.35	0.94
P <sub>2</sub> O <sub>5</sub>	-	0.04	-	0.04	0.04	-	-	-	-	-	0.09	-	-	-	-	-	-	-	0.30	0.30
BaO	0.70	0.07	0.22	0.08	0.06	1.06	0.22	0.08	1.01	0.30	0.00	0.22	0.22	0.08	0.10	-	0.19	0.00	0.27	0.20
SO <sub>3</sub>	0.53	0.23	0.62	0.28	0.56	0.10	0.83	0.21	0.10	0.58	0.52	0.70	0.62	0.42	0.26	0.83	0.26	0.74	0.61	0.50
Cl-	0.21	0.53	0.24	0.58	0.68	0.53	0.15	0.28	0.56	0.19	0.80	0.24	0.24	0.13	0.23	0.60	0.25	0.66	0.26	-
F-	0.48	-	0.63	-	-	-	0.40	-	-	0.59	-	0.33	0.63	0.34	-	-	-	-	-	-
Total	100.00	100.00	100.00	100.00	100.00	100.00	100.00	100.00	100.00	100.00	100.00	100.00	100.00	100.00	100.00	100.00	100.00	100.00	100.00	100.00
SiO <sub>2</sub> + Al <sub>2</sub> O <sub>3</sub> + Fe <sub>2</sub> O <sub>3</sub>	10.89	10.91	11.11	10.57	11.15	12.22	12.31	11.58	10.76	11.87	13.71	14.81	13.11	13.29	18.71	17.99	17.51	18.77	10.39	11.49
CaO + MgO	85.96	87.11	85.89	87.06	86.77	85.03	84.87	86.69	86.25	85.72	83.80	82.81	83.89	84.79	78.31	79.52	79.42	78.60	86.38	84.32
HI	0.13	0.13	0.13	0.12	0.13	0.14	0.14	0.13	0.12	0.14	0.16	0.18	0.16	0.16	0.24	0.23	0.22	0.24	0.12	0.14

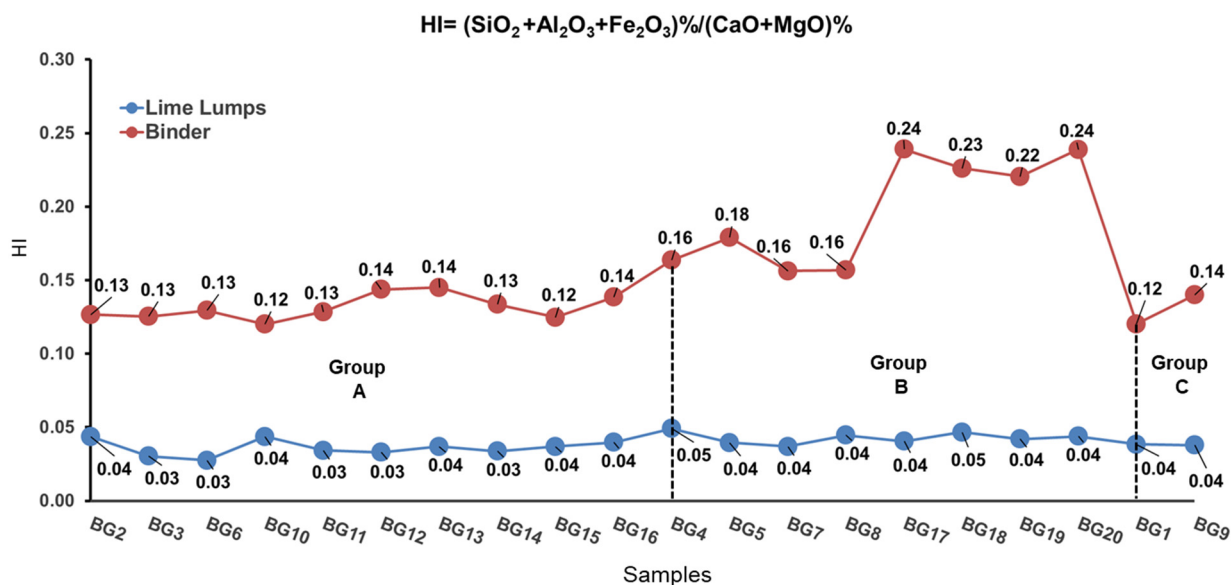
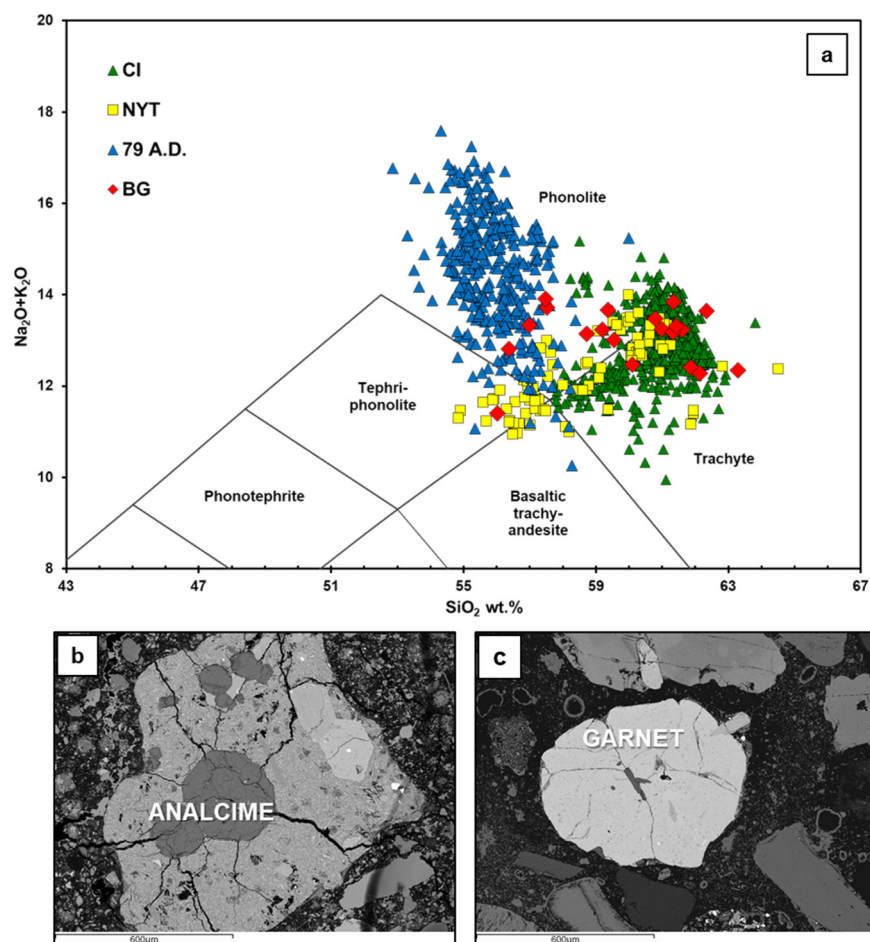


Figure 7. Hydraulicity index (HI) for lime lumps (blue line) and binder (red line) of analyzed mortars.

### 5.3.2. Volcanic Aggregates

SEM-EDS analysis of volcanic aggregates were performed to obtain additional information about the provenance of raw materials. Results confirmed the above-mentioned hypothesis of the employment of *Campi Flegrei* tuff aggregates, due to the presence of phillipsite with well-defined prismatic crystal habit and pseudo cubic crystals of chabazite [33].

EDS microanalysis was carried out on pumice from mortar samples (see Supplementary Materials Table S1). Using Total Alkali versus Silica diagram (TAS) for the effusive volcanic rocks [40], it is possible to observe that pumice fragments show trachytic compositions; their classification follows the compositional trend of *Campi Flegrei* products (Figure 8a). Results also suggested the use of geomaterials from the *Somma-Vesuvio* complex, due to the presence of volcanic scoriae containing analcime (typical product of leucite alteration; Figure 8b) and garnet fragments [13] typical of these materials. In support of this hypothesis, chemical composition of analyzed garnet (calculated following [41]; (see Supplementary Materials Table S2) shows similarity with garnets of *Somma-Vesuvio* (andradite 46–70 mol% and grossularia 16–45 mol%; taken by [42]; unpublished data on garnets from intrusive *Somma-Vesuvio* rocks. L. Melluso, personal communication).



**Figure 8.** (a) Total Alkali Silica (TAS) diagram [40] showing the composition of pumice fragments analyzed in the investigated samples (BG, *Villa del Capo*) and comparison with Phlegraean pumice (CI, Campanian Ignimbrite and NYT, Neapolitan Yellow Tuff; data from [43] and references therein). (b) BSE- SEM images of analcime bearing scoria in BG1 sample, (c) BSE- SEM images of garnet crystal in BG7 sample.

### 5.3.3. Ceramic Aggregates

Regarding ceramic fragments, SEM-EDS analysis allowed to confirm extreme differences occurring between them, even ones from the same mortar sample (Figure 9). These differences are testified by the different mineralogical composition, different texture, different porosity, and by the different chemical composition of matrix.

Chemical analysis on matrix of representative ceramic fragments (Table 7) showed different concentration in CaO ranging from 2.87 wt% for sample BG12 to a maximum of 19.08 wt% for BG4b.

The concentration of this oxide is a strong discriminant of ceramics in relation to their final use. When the percentage of this oxide is less than 6% [44] the clayey raw material used to produce ceramics is defined non calcareous, otherwise it is said calcareous ( $\text{CaO} > 6\%$ ). Non calcareous clays are best suited for making cookware, due to the better thermal shock resistance of the end products, whereas calcareous clays are generally employed to produce pottery used as containers [45].

Differences between ceramic fragments does not allow for defining provenance but represent a testimony of the re-use of ceramic waste materials in preparations of mortars. The relevant role played by ceramic fragments was to provide hydraulicity to the mortars, as pointed out by HI evaluation (Figure 7). Coating and floor mortars that contain both pozzolana and ceramics materials are characterized by highest HI values.

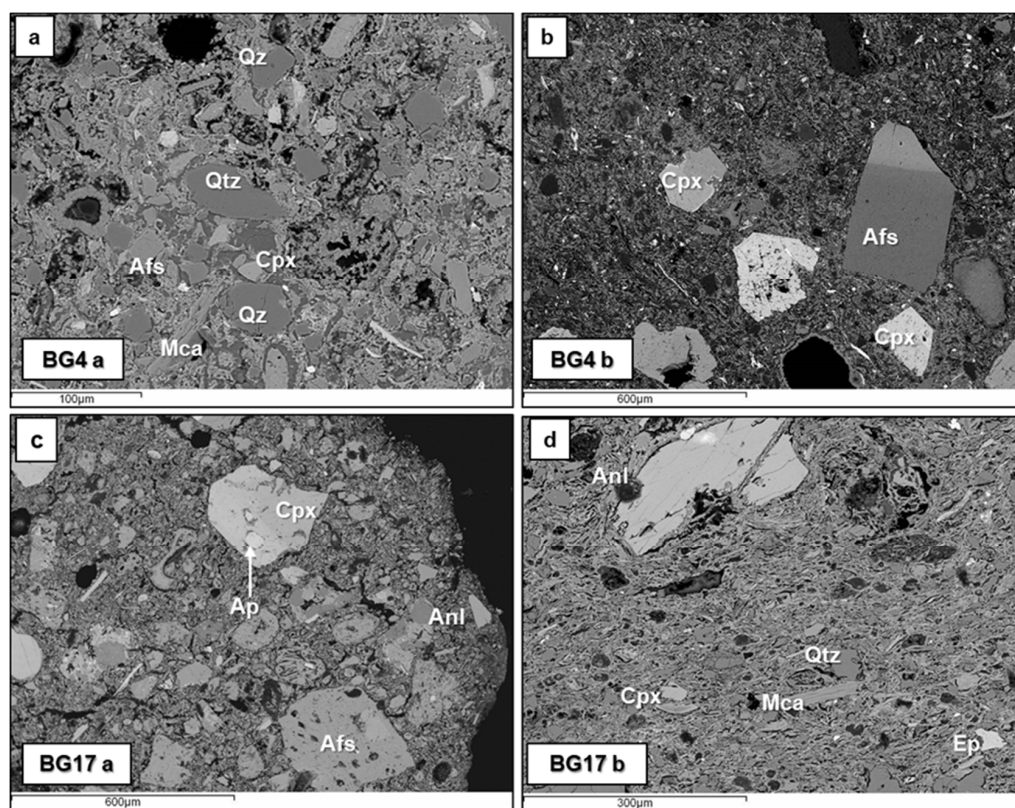


Figure 9. BSE-SEM images of different ceramic fragments: (a,b) BG4 sample; (c,d) BG17 sample. Abbreviations from [27], Qz quartz, Afs alkali-feldspar, Cpx clinopyroxene, Anl analcime, Mca mica, Ap apatite, Ep epidote.

Table 7. Average values of major oxides (wt%, recalculated to 100%, EDS) of matrix of ceramic fragments.

wt%	BG1a	BG4a	BG4b	BG7a	BG7b	BG7c	BG8a	BG8b	BG8c	BG9	BG12	BG17a	BG17b	BG17c	BG18a	BG18b	BG20
SiO <sub>2</sub>	57.68	54.18	51.00	50.00	56.07	54.07	55.58	53.90	53.84	51.36	50.94	54.31	57.63	54.94	60.57	52.53	58.77
TiO <sub>2</sub>	0.99	0.34	0.34	1.23	1.90	0.90	0.64	0.67	0.55	0.57	1.10	0.53	0.87	1.14	0.56	0.69	
Al <sub>2</sub> O <sub>3</sub>	17.77	13.72	15.13	13.88	18.23	17.23	15.47	18.70	15.27	14.56	21.72	32.37	18.42	21.41	15.98	17.64	19.54
Fe <sub>2</sub> O <sub>3</sub>	7.31	4.51	4.90	-	7.11	6.11	4.64	4.79	4.43	5.11	6.09	7.08	3.90	7.57	6.32	4.29	5.49
MnO	-	-	0.18	-	0.29	0.29	0.22	-	0.10	0.11	0.20	0.17	0.58	0.03	-	0.30	0.30
MgO	5.25	5.13	3.21	2.73	5.51	3.51	2.55	2.23	2.59	3.17	10.32	5.73	2.45	4.12	3.29	3.23	2.05
* CaO	5.27	17.43	19.08	19.04	5.83	12.83	11.78	4.98	16.96	17.47	2.87	4.04	9.98	5.65	4.30	13.46	3.93
Na <sub>2</sub> O	0.18	0.45	0.66	0.12	-	-	0.14	-	-	-	-	0.07	0.14	-	-	0.09	0.23
K <sub>2</sub> O	2.79	1.04	1.65	1.91	1.22	1.22	1.95	3.06	1.58	1.80	1.32	1.23	2.76	1.21	2.00	3.50	3.50
P <sub>2</sub> O <sub>5</sub>	2.17	2.48	2.95	3.43	2.18	2.18	3.72	2.95	2.46	2.52	2.62	2.54	3.42	3.58	4.55	3.20	4.42
V <sub>2</sub> O <sub>3</sub>	0.13	0.05	0.73	0.82	1.26	1.26	0.75	0.42	0.76	0.35	0.19	0.02	-	0.11	0.63	0.66	0.95
BaO	-	0.29	-	0.11	0.39	0.39	0.20	0.61	0.20	0.16	-	0.33	-	0.41	0.11	0.38	0.13
SO <sub>3</sub>	-	-	-	2.96	-	-	2.55	2.74	1.14	2.84	3.10	-	-	-	0.97	-	-
Cl <sup>-</sup>	0.45	0.38	0.16	3.62	-	-	-	-	-	-	0.07	-	0.19	0.11	0.15	0.16	-
Total	100.00	100.00	100.00	100.00	100.00	100.00	100.00	100.00	100.00	100.00	100.00	100.00	100.00	100.00	100.00	100.00	100.00

\* CaO < 6% non calcareous clay; CaO > 6% calcareous clay.

#### 5.4. Differential Thermal and Thermogravimetric Analysis

Simultaneous thermal analyses combined with mineralogical composition of the samples allowed to obtain further information about the hydraulic characteristics of mortar samples. Table 8 reports the percentage of weight loss estimated from the TG–DTG curves within the selected temperature ranges. In the temperature range from 25 to 120 °C the weight loss is due to dehydration of hygroscopic or adsorbed water (i.e., phyllosilicates), from 120 to 200 °C the weight loss of water from hydrated salts occurs, between 200 and 600 °C the weight loss is due to structurally bound water (SBW) from the hydraulic compounds and, finally, the loss of CO<sub>2</sub> as a consequence of the decomposition of calcium carbonate (CaCO<sub>3</sub>) takes place at temperature range between 600 and 900 °C [24,46,47].

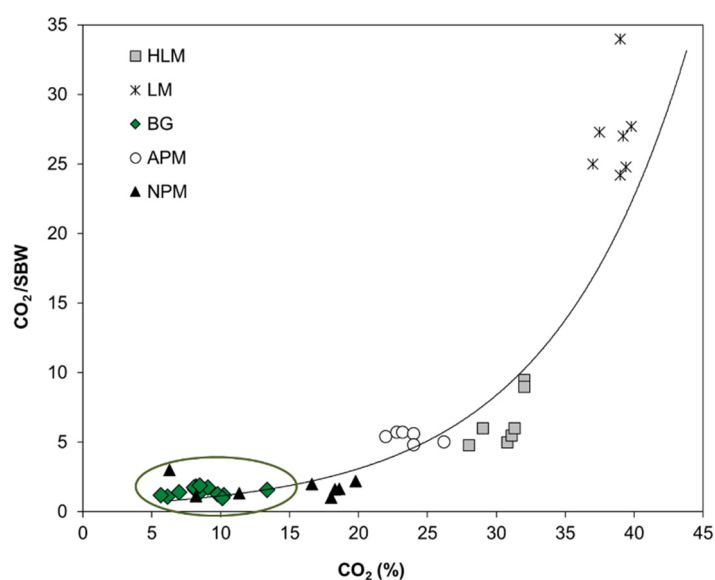
**Table 8.** TG–DTG weight losses as a function of the temperature range (wt%). Abbreviations: SBW structural boundary water, LOI loss on ignition.

Sample	Group	SBW% 200–600 °C	CO <sub>2</sub> % 600–800 °C	LOI%
BG1	C	6.30	8.43	25.89
BG3	A	5.72	6.15	27.83
BG4	B	8.60	1.023	23.69
BG6	A	8.42	13.38	37.68
BG7	B	5.21	9.08	31.00
BG8	B	7.81	9.78	37.03
BG9	C	10.13	10.12	29.33
BG10	A	4.92	8.15	17.51
BG12	A	5.70	7.97	22.68
BG13	A	4.57	8.21	23.45
BG15	A	4.75	5.64	22.06
BG18	B	4.62	8.06	20.67
BG19	B	4.50	8.49	18.27

Generally, lime mortars (or non-hydraulic mortars) are characterized by less than 3% of structural bound water (SBW) of the hydraulic components and high CO<sub>2</sub> amount (>32%), whereas mortars with higher amounts of water bound and proportionally small quantities of CO<sub>2</sub> are considered hydraulic [48].

All *Villa del Capo* mortars can be classified as hydraulic mortars, due to a weight loss at 200–600 °C (SBW values) greater of 3%, ranging from 5.64% (BG15) to 13.38 % (BG6) and CO<sub>2</sub> lower than 10 % (Table 8).

The CO<sub>2</sub> to structurally bound water ratio in relation to CO<sub>2</sub> percentage (% weight loss in the temperature range of 600–800 °C) is shown in Figure 10. The inverse trend of hydraulicity of mortars is being augmented exponentially with CO<sub>2</sub>. This representation allows a good classification of the mortar nature [24,46,48,49]. From the observation of Figure 10 and the values in Table 8 samples from *Villa del Capo* are highly hydraulic mortars and can be classified as natural pozzolanic mortars.



**Figure 10.** CO<sub>2</sub>/SBW vs. CO<sub>2</sub> diagram. Mortars from Villa del Capo (BG, green circle); NPM natural pozzolanic mortars, APM artificial pozzolanic mortars, HLM hydraulic lime mortars, and LM lime mortars from [24].



### 5.5. Porosity

Mercury intrusion porosimetry were performed on three selected samples: BG13 for Group A and BG13 and BG17 for Group B, due to the scarce amount of available material. Table 9 reports cumulative volume, bulk density, apparent density, open porosity, and specific surface, whereas Figure 11 shows representative pore size distribution.

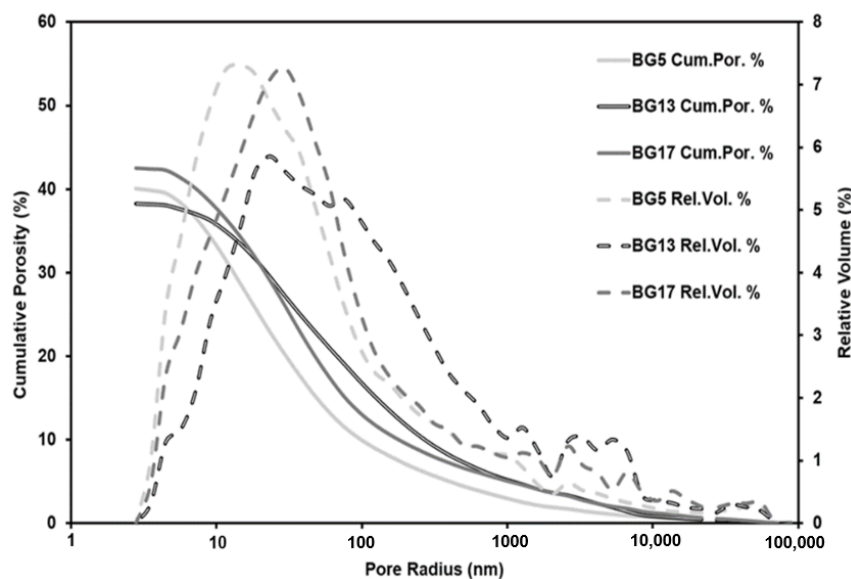
**Table 9.** Mercury intrusion data obtained for *Villa del Capo* mortars.

Sample	BG5 (Group B)	BG13 (Group A)	BG17 (Group B)
Cumulative volume (mm <sup>3</sup> /g)	300.25	254.53	296.64
Bulk density (g/cm <sup>3</sup> )	1.51	1.38	1.57
Open porosity (Vol. %)	40.03	38.25	42.27
Specific Surface (m <sup>2</sup> /g)	32.27	30.08	34.21
Apparent Density (g/cm <sup>3</sup> )	2.71	2.57	2.89

Open porosity of BG13 sample (Group A) was slightly lower (38.25%) than BG5 and BG17 (B group; 40.03%–42.27%), all analyzed mortars show unimodal and broadened shape of cumulative pore size distribution.

Bulk densities of samples were within the range of 1.38 g/cm<sup>3</sup> to 1.57 g/cm<sup>3</sup>, whereas apparent densities were within the range of 2.57 g/cm<sup>3</sup> to 2.89 g/cm<sup>3</sup>. Relative volume curves are positively skewed and highlighted that pore radii mainly range between 5 and 100 nm. Pore sizes of samples fall within the characteristic field of hydration product porosity, usually considered below 100 nm [50,51].

Comparing these results with those obtained for modern hydraulic mortars, reported in [3], it is clearly evident that *Villa del Capo* mortars, as well as other ancient roman pozzolanic mortars of previous study [3,19], possess very small pore size radii (5–100 nm), about one order of magnitude lower than modern hydraulic mortars (100–1000 nm). These differences are probably due to the vesicular structure of pozzolanic materials (i.e., pumice) that represents a fundamental feature of the complex pore structure of the cementitious matrix of ancient mortars. Secondary minerogenetic products, in this case hydrocalumite and C-A-S-H gels, fill pores, thus enhancing bonding of pumice clasts and making mortars less permeable [36,52]. These findings (1) decrease the possibility of alteration of the mortars; (2) increase mechanical resistance, and consequently, (3) also increase durability of manufactures.



**Figure 11.** Cumulative (continuous lines) and relative (dashed lines) pore size distribution *Villa del Capo* mortars (BG5; BG13; BG17).

## 6. Conclusions

This work presents an extensive multi-analytical characterization of ancient mortars from a very important Roman archaeological site: *Villa del Capo* in the Sorrento Peninsula.

A petrographical study of the investigated samples highlighted some important aspects regarding production technology of materials, suggesting different recipes for different mortar types.

Bedding mortars result from: (1) a mixture of slaked lime, water, fine grained volcanic materials, and aggregates of volcanic rocks, whereas, coating and floor mortars may be considered as (2) a mixture of slaked lime, water, fine grained volcanic, and ceramic materials with volcanic and ceramic aggregates.

The “recipe” of coating mortars is identified as *Cocciopesto* or *Opus signinum*, a typical building technique used in ancient Rome for lining of tanks, terraces, thermal environments, and flooring [26].

Geomaterials used for mortars production had local provenance and are very well consistent with the surrounding geological setting. In fact, volcanic fragments, scoriae, pumice, and crystal fragments (i.e., clinopyroxene, feldspar, and garnet) derived from both pyroclastic rocks of the *Campi Flegrei* district and from rocks of the *Somma-Vesuvio* complex, as inferred by optical microscopy, and mineralogical and chemical composition. In coating and floor mortars (group B and C) there is an addition of ceramic fragments that improve pozzolanic aptitude of the mortar. It was not possible to define their provenance, due to strong differences among samples, which likely suggest a recycling of materials.

Provenance of carbonate rocks used to produce lime for the investigated materials is still unknown, even if it is highly reasonable to assess that they were produced “on site” from carbonate deposits of Mesozoic age that border the Campanian plain (Figure 2).

SEM-EDS analysis and TGA investigation revealed that studied mortars can be classified as hydraulic mortars, which is also confirmed by reaction rims observed around pozzolanic materials.

XRPD and SEM-EDS analysis highlighted that binder fractions are characterized by different secondary products (reaction products), including amorphous C-A-S-H gel, calcite, gypsum, and hydrocalumite.

Results of porosity tests together with microstructural observations suggest the products related to minerogenetic secondary processes, especially gel C-A-S-H and hydrocalumite settling in the porous of pozzolanic materials, make mortars more resistant.

Studies like this, that entail meticulous characterization of all the components for the realization of the artificial geomaterials, paying special attention to secondary minerogenetic processes, are crucial in the perspective of future restoration works, and especially for the preservation of archaeological sites that cannot be independent from thorough knowledge of materials used for the construction and of their state of conservation, along with that of the building.

**Supplementary Materials:** The following are available online at <https://www.mdpi.com/article/10.3390/min11050469/s1>, Table S1: Major element concentrations of pumice fragments (wt%, recalculated to 100%, EDS). Na<sub>2</sub>O + K<sub>2</sub>O also shown; Table S2: Representative chemical composition (wt%, EDS) of garnets.

**Author Contributions:** Sampling, C.R. and R.E.; archaeological information, R.E.; formal analysis and data curation, C.R., L.G. and P.C.; writing—original draft preparation, C.R.; writing—review & editing, C.R., L.G. and P.C.; supervision, P.C. All authors have read and agreed to the published version of the manuscript.

**Funding:** This research received no external funding.

**Data Availability Statement:** All data derived from this research are presented in the enclosed figures and tables.

**Acknowledgments:** This paper stem from the doctoral thesis of one of the Authors (CR) in earth science, environment, and resources at DiSTAR of Federico II University of Naples. The analysis of

additional samples was supported by the following AIM projects [AIM18352321–1; AIM1835232–1, CUP: E66C18001140005]. The authors would like to thank Roberto de Gennaro for the invaluable assistance during EDS microanalyses, Sergio Bravi for his technical ability in thin sections preparation and Tommasina Budetta, former *Sovrintendenza archeologia della Campania* that provided authorization and useful support on sampling. Thanks, are also due to CTG Italcementi Heidelberg Group for supporting this research activity. The authors would like to thank the journal editors and the anonymous reviewers for their useful comments that helped us in the revision of this manuscript.

**Conflicts of Interest:** The authors declare no conflict of interest.

## References

1. D’Arms, J.H. Romans on the Bay of Naples. A Social and Cultural Study of the Villas and their Owners from 150 B.C. to A.D. 400. In *Romans on the Bay of Naples and Other Essays on Roman Campania*; Zevi, F., Ed.; Edipuglia: Bari, Italy, 2003; pp. 1–226.
2. Filser, W.; Fritsch, B.; Kennedy, W.; Klose, C.; Perrella, R. Surrounded by the Sea: Re-Investigating the Villa Maritima Del Capo Di Sorrento. *J. Roman Archaeol.* **2017**, *30*. [CrossRef]
3. Rispoli, C.; de Bonis, A.; Esposito, R.; Graziano, S.F.; Langella, A.; Mercurio, M.; Morra, V.; Cappelletti, P. Unveiling the Secrets of Roman Craftsmanship: Mortars from Piscina Mirabilis (Campi Flegrei, Italy). *Archaeol. Anthropol. Sci.* **2020**, *12*. [CrossRef]
4. Graziano, S.F.; Rispoli, C.; Guarino, V.; Balassone, G.; di Maio, G.; Pappalardo, L.; Cappelletti, P.; Damato, G.; de Bonis, A.; di Benedetto, C.; et al. The roman villa of positano (Campania region, Southern Italy): Plasters, tiles and geoarchaeological reconstruction. *Int. J. Conserv. Sci.* **2020**, *11*, 319–344.
5. Izzo, F.; Arizzi, A.; Cappelletti, P.; Cultrone, G.; de Bonis, A.; Germinario, C.; Graziano, S.F.; Grifa, C.; Guarino, V.; Mercurio, M.; et al. The Art of Building in the Roman Period (89 B.C.-79 A.D.): Mortars, Plasters and Mosaic Floors from Ancient Stabiae (Naples, Italy). *Constr. Build. Mater.* **2016**, *117*, 129–143. [CrossRef]
6. De Bonis, A.; Grifa, C.; Langella, A.; Mercurio, M.; Luisa Perrone, M.; Morra, V. Archaeometric Study of Roman Pottery from Caudium Area (Southern Italy). *Period. Mineral.* **2011**, *79*, 73–89.
7. Guarino, V.; de Bonis, A.; Grifa, C.; Langella, A.; Morra, V.; Pedroni, L. Archaeometric Study on Terra Sigillata from Cales (Italy). *Period. Mineral.* **2011**, *80*, 455–470. [CrossRef]
8. Rispoli, C. Ancient Roman Mortars: Mix Design, Mineralogical Composition and Minerogenetic Secondary Processes. Ph.D. Thesis, Federico II University of Naples, Naples, Italy, 2017.
9. Cinque, A.; Robustelli, G. Alluvial and Coastal Hazards Caused by Long-Range Effects of Plinian Eruptions: The Case of the Lattari Mts. After the AD 79 Eruption of Vesuvius. *Geol. Soc. Spec. Publ.* **2009**, *322*, 155–171. [CrossRef]
10. Aucelli, P.; Cinque, A.; Mattei, G.; Pappone, G. Historical Sea Level Changes and Effects on the Coasts of Sorrento Peninsula (Gulf of Naples): New Constrains from Recent Geoarchaeological Investigations. *Palaeogeogr. Palaeoclimatol. Palaeoecol.* **2016**, *463*, 112–125. [CrossRef]
11. Brancaccio, L.; Cinque, A.; Romano, P.; Roskopf, C.; Russo, F.; Santo, A.; Santangelo, N. Geomorphology and Neotectonic Evolution of a Sector of the Tyrrhenian Flank of the Southern Apennines, (Region of Naples, Italy). *Z. Geomorphol.* **1991**, *82*, 47–58.
12. Iannace, A.; Merola, D.; Perrone, V.; Amato, A.; Cinque, A.; Santacroce, R.; Sbrana, A.; Sulpizio, R.; Budillon, F.; Conforti, A.; et al. *Note Illustrative Della Carta Geologica d’Italia Alla Scala 1: 50.000 Fogli 466–485 Sorrento-Termini*; Servizio Geologico d’Italia: Ispra, Italy, 2015.
13. Santacroce, R.; Cioni, R.; Marianelli, P.; Sbrana, A.; Sulpizio, R.; Zanchetta, G.; Donahue, D.J.; Joron, J.L. Age and Whole Rock-Glass Compositions of Proximal Pyroclastics from the Major Explosive Eruptions of Somma-Vesuvius: A Review as a Tool for Distal Tephrostratigraphy. *J. Volcanol. Geotherm. Res.* **2008**, *177*, 1–18. [CrossRef]
14. Vitale, S.; Tramparulo, F.D.; Ciarcia, S.; Amore, F.O.; Prinzi, E.P.; Laiena, F. The Northward Tectonic Transport in the Southern Apennines: Examples from the Capri Island and Western Sorrento Peninsula (Italy). *Int. J. Earth Sci.* **2017**, *106*, 97–113. [CrossRef]
15. Mingazzini, P. *Forma Italiae: Latium et Campania*; De Luca Ed: Surrentum, Italy, 1946.
16. Budetta, T.; de Martino, R.; Franchino, R.; Frettoloso, C. The System of Environmental Networks for the Use of Archaeological Sites in Areas of Natural Beauty. *J. Sustain. Archit. Civ. Eng.* **2013**, *3*. [CrossRef]
17. Howarth, J. Improved Estimators of Uncertainty in Proportions, Point-Counting, and Pass-Fail Test Results. *Am. J. Sci.* **1998**, *298*, 594–607. [CrossRef]
18. Pouchou, J.L.; Pichoir, F. A simplified version of the PAP model for matrix corrections in EPMA. In *Microbeam Analysis*; San Francisco Press: San Francisco, CA, USA, 1988.
19. Rispoli, C.; De Bonis, A.; Guarino, V.; Graziano, S.F.; di Benedetto, C.; Esposito, R.; Morra, V.; Cappelletti, P. The Ancient Pozzolanic Mortars of the Thermal Complex of Baia (Campi Flegrei, Italy). *J. Cult. Herit.* **2019**, *40*. [CrossRef]
20. ASTM D4404–10. *Standard Test Method for Determination of Pore Volume and Pore Volume Distribution of Soil and Rock by Mercury Intrusion Porosimetry*; STM International: West Conshohocken, PA, USA, 2010.
21. Wentworth, C.K. A Scale of Grade and Class Terms for Clastic Sediments. *J. Geol.* **1922**, *30*, 377–392. [CrossRef]
22. Addis, A.; Secco, M.; Marzaioli, F.; Artioli, G.; Chavarría Arnau, A.; Passariello, I.; Terrasi, F.; Brogiolo, G.P. Selecting the Most Reliable <sup>14</sup>C Dating Material inside Mortars: The Origin of the Padua Cathedral. *Radiocarbon* **2019**, *61*, 375–393. [CrossRef]

23. Ricca, M.; Galli, G.; Ruffolo, S.A.; Sacco, A.; Aquino, M.; la Russa, M.F. An Archaeometric Approach of Historical Mortars Taken from Foligno City (Umbria, Italy): News Insight of Roman Empire in Italy. *Archaeol. Anthropol. Sci.* **2019**, *11*, 2649–2657. [CrossRef]
24. Moropoulou, A.; Bakolas, A.; Anagnostopoulou, S. Composite Materials in Ancient Structures. *Cement Concr. Compos.* **2005**, *27*, 295–300. [CrossRef]
25. Colella, A.; Di Benedetto, C.; Calcaterra, D.; Cappelletti, P.; D’Amore, M.; Di Martire, D.; Graziano, S.F.; Papa, L.; de Gennaro, M.; Langella, A. The Neapolitan Yellow Tuff: An Outstanding Example of Heterogeneity. *Constr. Build. Mater.* **2017**, *136*, 361–373. [CrossRef]
26. Colleparidi, M.; Colleparidi, S.; Troli, R. *Il Nuovo Calcestruzzo*, 5th ed.; Tintoretto: Treviso, Italy, 2009.
27. Whitney, D.L.; Evans, B.W. Abbreviations for Names of Rock-Forming Minerals. *Am. Miner.* **2010**, *95*, 185–187. [CrossRef]
28. UNI-EN 11305:2009. *Norme tecniche per i Beni Culturali. Malte Storiche: Linee Guida per La Caratterizzazione Mineralogico Petrografica, Fisica e Chimica Delle Malte*; CNR-ICR: Roma, Italy, 2009.
29. De Gennaro, M.; Colella, C.; Pansini, M. Hydrothermal Conversion of Trachytic Glass into Zeolite. II Reactions with High-Salinity Waters. *Neues Jahrb. Mineral. Mon.* **1993**, *3*, 97–110.
30. Tian, J.; Guo, Q. Thermal Decomposition of Hydrocalumite over a Temperature Range of 400–1500 °C and Its Structure Reconstruction in Water. *J. Chem.* **2014**, *2014*. [CrossRef]
31. Wei, G.; Germinario, C.; Grifa, C.; Ma, X. Characterization of Ancient Building Lime Mortars of Anhui Province, China: A Multi-Analytical Approach. *Archaeometry* **2020**, *62*, 888–903. [CrossRef]
32. Kalinichev, A.G.; Kirkpatrick, R.J.; Cygan, R.T. Molecular Modeling of the Structure and Dynamics of the Interlayer and Surface Species of Mixed-Metal Layered Hydroxides: Chloride and Water in Hydrocalumite (Friedel’s Salt). *Am. Mineral.* **2000**, *85*. [CrossRef]
33. De Gennaro, M.; Incoronato, A.; Mastrolorenzo, G.; Adabbo, M.; Spina, G. Depositional Mechanisms and Alteration Processes in Different Types of Pyroclastic Deposits from Campi Flegrei Volcanic Field (Southern Italy). *J. Volcanol. Geotherm. Res.* **1999**, *91*, 303–320. [CrossRef]
34. Langella, A.; Bish, D.L.; Cappelletti, P.; Cerri, G.; Colella, A.; de Gennaro, R.; Graziano, S.F.; Perrotta, A.; Scarpati, C.; de Gennaro, M. New Insights into the Mineralogical Facies Distribution of Campanian Ignimbrite, a Relevant Italian Industrial Material. *Appl. Clay Sci.* **2013**, *72*, 55–73. [CrossRef]
35. Moropoulou, A.; Cakmak, A.; Labropoulos, K.C.; van Grieken, R.; Torfs, K. Accelerated Microstructural Evolution of a Calcium-Silicate-Hydrate (C-S-H) Phase in Pozzolanic Pastes Using Fine Siliceous Sources: Comparison with Historic Pozzolanic Mortars. *Cem. Concr. Res.* **2004**, *34*, 1–6. [CrossRef]
36. Jackson, M.D.; Mulcahy, S.R.; Chen, H.; Li, Y.; Li, Q.; Cappelletti, P.; Wenk, H.R. Phillipsite and Al-Tobermorite Mineral Cements Produced through Low-Temperature Water-Rock Reactions in Roman Marine Concrete. *Am. Mineral.* **2017**, *102*, 1435–1450. [CrossRef]
37. Boynton, R.S. *Chemistry and Technology of Lime and Limestone*; Sons, J.W., Ed.; Interscience: New York, NY, USA, 1996.
38. De Luca, R.; Miriello, D.; Pecci, A.; Domínguez-Bella, S.; Bernal-Casasola, D.; Cottica, D.; Bloise, A.; Crisci, G.M. Archaeometric Study of Mortars from the Garum Shop at Pompeii, Campania, Italy. *Geoarchaeology* **2015**, *30*, 330–351. [CrossRef]
39. Columbu, S.; Sitzia, F.; Ennas, G. The Ancient Pozzolanic Mortars and Concretes of Heliocaminus Baths in Hadrian’s Villa (Tivoli, Italy). *Archaeol. Anthropol. Sci.* **2017**, *9*, 523–553. [CrossRef]
40. Le Bas, M.J.; Le Maitre, R.W.; Streckeisen, A.; Zanettin, B. A Chemical Classification of Volcanic Rocks Based on the Total Alkali-Silica Diagram. *J. Petrol.* **1986**, *27*, 745–750. [CrossRef]
41. Locock, A.J. An Excel Spreadsheet to Recast Analyses of Garnet into End-Member Components, and a Synopsis of the Crystal Chemistry of Natural Silicate Garnets. *Comput. Geosci.* **2008**, *34*, 1769–1780. [CrossRef]
42. Scheibner, B.; Wörner, G.; Civetta, L.; Stosch, H.G.; Simon, K.; Kronz, A. Rare Earth Element Fractionation in Magmatic Ca-Rich Garnets. *Contrib. Mineral. Petrol.* **2007**, *154*, 55–74. [CrossRef]
43. Morra, V.; Calcaterra, D.; Cappelletti, P.; Colella, A.; Fedele, L.; de Gennaro, R.; Langella, A.; Mercurio, M.; de Gennaro, M. Urban Geology: Relationships between Geological Setting and Architectural Heritage of the Neapolitan Area. *J. Virtual Explor.* **2010**, *36*. [CrossRef]
44. Maniatis, M.S.; Tite, Y. Technological Examination of Neolithic-Bronze Age Pottery from Central and Southeast Europe and from the Near East. *J. Archaeol. Sci.* **1981**, *8*, 59–76. [CrossRef]
45. De Bonis, A.; Cultrone, G.; Grifa, C.; Langella, A.; Morra, V. Clays from the Bay of Naples (Italy): New Insight on Ancient and Traditional Ceramics. *J. Eur. Ceram. Soc.* **2014**, *34*, 3229–3244. [CrossRef]
46. Genestar, C.; Pons, C.; Más, A. Analytical characterisation of ancient mortars from the archaeological Roman city of pollentia (Balearic Islands, Spain). *Anal. Chim. Acta* **2006**, *557*, 373–379. [CrossRef]
47. Izzo, F.; Grifa, C.; Germinario, C.; Mercurio, M.; de Bonis, A.; Tomay, L.; Langella, A. Production Technology of Mortar-Based Building Materials from the Arch of Trajan and the Roman Theatre in Benevento, Italy. *Eur. Phys. J. Plus* **2018**, *133*. [CrossRef]
48. Borsoi, G.; Santos Silva, A.; Menezes, P.; Candeias, A.; Mirão, J. Analytical Characterization of Ancient Mortars from the Archaeological Roman Site of Pisões (Beja, Portugal). *Constr. Build. Mater.* **2019**, *204*, 597–608. [CrossRef]
49. Moropoulou, A.; Bakolas, A.; Aggelakopoulou, E. Evaluation of Pozzolanic Activity of Natural and Artificial Pozzolans by Thermal Analysis. *Thermochim. Acta* **2004**, *420*, 135–140. [CrossRef]

50. Mehta, K.P.; Monteiro, P.J.M. *Concrete: Microstructure, Properties, and Materials*, 4th ed.; McGraw-Hill Education: London, UK, 2014.
51. Gotti, E.; Oleson, J.P.; Bottalico, L.; Brandon, C.; Cucitore, R.; Hohlfelder, R.L. A Comparison of the Chemical and Engineering Characteristics of Ancient Roman Hydraulic Concrete with a Modern Reproduction of Vitruvian Hydraulic Concrete. *Archaeometry* **2008**, *50*, 576–590. [CrossRef]
52. Brandon, C.J.; Hohlfelder, R.L.; Jackson, M.D.; Oleson, J.P. Building for eternity. In *The History and Technology of Roman Concrete Engineering in the Sea*; Oxbow Books: Oxford, UK, 2014; Volume 53, ISBN 9788578110796.





## Article

# Mineralogical Characterization of *Carreaux de Pavement* from Northern Spain (Tiebas, Navarre)

Iván Ruiz-Ardanaz, Esther Lasheras  and Adrián Durán \* 

Chemistry Department, University of Navarre, Irunlarrea 1, 31008 Pamplona, Spain; iruiz.23@alumni.unav.es (I.R.-A.); elasheras@unav.es (E.L.)

\* Correspondence: adrianduran@unav.es

**Abstract:** Several medieval tiles from Tiebas Castle in Navarre, classified as *carreaux de pavement*, were mineralogically analyzed. The aim was to add information to the very scarce analytical data available for *carreaux de pavement* in order to provide a quality primary work, mainly descriptive, in this topic. The characterization techniques applied were: optical microscopy (OM), colorimetry, Fourier transform infrared (FT-IR) spectroscopy, differential thermal analysis and thermogravimetry (DTA-TG), X-ray fluorescence (XRF) spectroscopy, petrographic microscopy (PM), X-ray diffraction (XRD), scanning electron microscopy coupled with energy dispersive X-ray spectroscopy (SEM-EDS). The tiles comprised three layers: a top glaze with mainly silicon and lead-based compounds; a thin layer of silicoaluminate (very possibly kaolinite) called *engobe* under it; and the pastes, composed of quartz, hematite, potassium feldspars and calcite. Honey glazes were richer in iron, being copper-based compounds responsible for dark green glazes. The orangish-reddish color of the pastes was provided by hematite. Although the tiles were found in three different locations within the castle, no significant differences were detected among them. The *carreaux de pavement* from Tiebas had similarities with that from the Bordeaux region. According to the composition data and thickness of tiles from other French *carreaux de pavement*, the Tiebas artifacts were dated to the 13th century.

**Citation:** Ruiz-Ardanaz, I.; Lasheras, E.; Durán, A. Mineralogical Characterization of *Carreaux de Pavement* from Northern Spain (Tiebas, Navarre). *Minerals* **2021**, *11*, 153. <https://doi.org/10.3390/min11020153>

Academic Editors: Petrus J Le Roux and Davide Lenaz

Received: 28 December 2020

Accepted: 28 January 2021

Published: 1 February 2021

**Publisher's Note:** MDPI stays neutral with regard to jurisdictional claims in published maps and institutional affiliations.



**Copyright:** © 2021 by the authors. Licensee MDPI, Basel, Switzerland. This article is an open access article distributed under the terms and conditions of the Creative Commons Attribution (CC BY) license (<https://creativecommons.org/licenses/by/4.0/>).

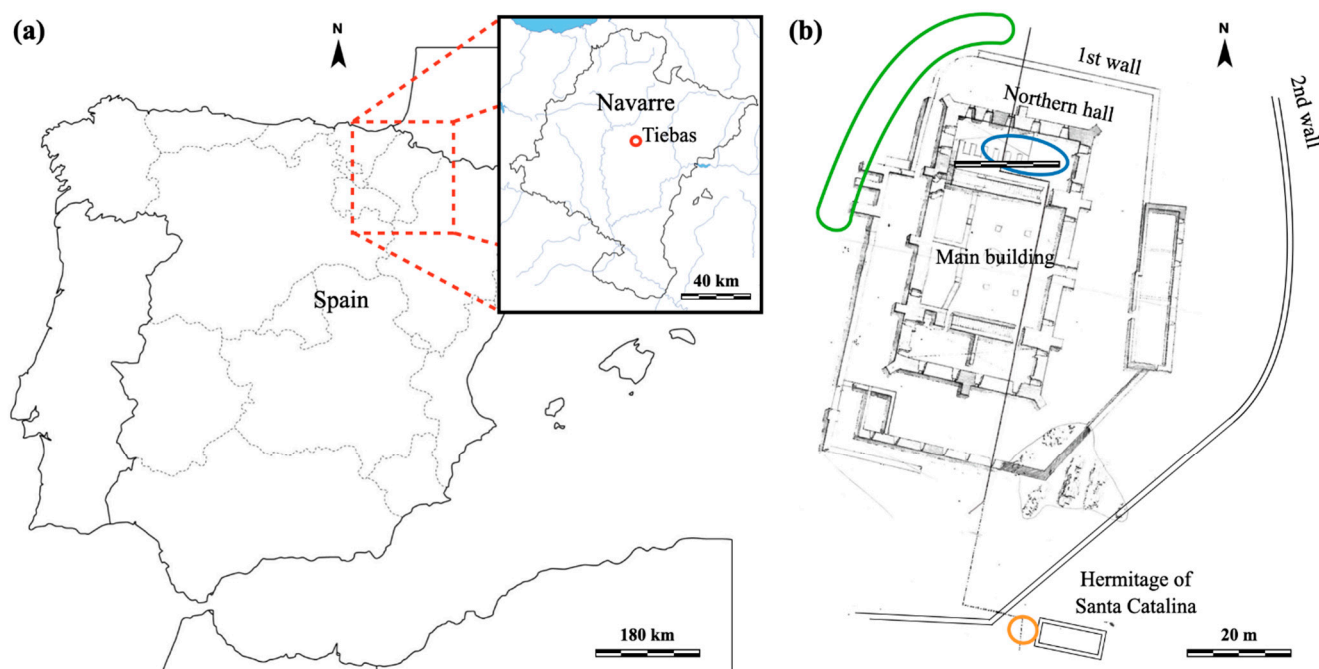
**Keywords:** *carreaux de pavement*; medieval pottery; archaeometry; mineralogical analysis; plumbiferous glaze; silicoaluminate *engobe*; reddish paste

## 1. Introduction

*Carreaux de pavement* is the French name given to a medieval type of glazed pottery, which has been referred to in several publications as inlaid tiles, encaustic tiles, *carreaux de pavage*, or *carrelages de sol* [1]. The most frequent are *carreaux de pavement* in the French lexicon and encaustic tiles in the English one [2]. This type of pottery is characterized by its inlaid decoration and three layers: the outer one is usually a very thin glaze with different color tones; another thin layer of paste under it that is called *engobe*, which fills gaps in the inner and thicker layer, named paste; and paste, which is normally reddish [1,2].

*Carreaux de pavement* appeared in Great Britain and northern France in the mid-12th century as an evolution of glazed monochromatic tiles used to luxuriously cover the floors of nobility and royal buildings (castles, palaces, cathedrals, churches, chapels, abbeys, monastic houses . . . ) [1–3]. An important role has been attributed to Cistercian monks in developing techniques for making terracotta, and more particularly, monochromatic tiles for paving their churches [2,3]. Monochromatic tiles led to dichromatic tiles at the beginning of the 13th century [1,2]. In the second half of the 13th century and especially in the 14th century, the expansion and use of these tiles increased, being set in a multitude of palaces, monasteries, abbeys, and churches, and also extended geographically to the south of France, Ireland, Belgium, and western Germany [1,2]. At the end of this period, the lead glaze began to be replaced by tin glaze. The tin glaze was extended mainly during the 15th century [2]. In the first half of the 19th century, the rise of English Neo-Gothic revived the production of *carreaux de pavement*, erroneously called encaustic tiles [1,2].

Tiebas Castle, located in Navarre (northern Spain) (Figure 1a), is the only place in the Iberian Peninsula where this type of tile has been found [4]. Due to their chronology and decoration, they were not related to the workshops of Bordeaux and Toulouse, but rather to the Champagne region [5,6]. The reason why these tiles appeared so far south was probably because the kingdom of Navarre was being ruled by the kings of the Champagne dynasty from 1234 to 1274 [7,8]. Theobald II of Navarre (1254–1270), the second king, ordered the construction of the castle of Tiebas at the beginning of his reign according to the stylistic models of that time [4,9–11].



**Figure 1.** (a) Location of Tiebas Castle in Navarre (northern Spain). (b) Modified early 19th century map of the Tiebas Castle with the locations of where the tiles were found: in situ Northern Hall (blue area), landfill (orange area), out-of-context fragments (green area).

The tiles analyzed in this work were recently found during an archaeological intervention. A pavement consisting of thousands of tiles with decorative motifs appeared in situ in the Northern Hall of Tiebas Castle (Figure 1b). These were dated to around 1256 thanks to the fact that they were covered by a layer of ash and rubble that was attributed to the fire of 1378 as well as their style and decorative motifs [4]. Similar tiles had already been found in previous archaeological surveys [9–11] such as those in the excavation of the Hermitage of Santa Catalina (ancient chapel close to Tiebas Castle). In this other location, fragments and complete tiles were found in a close landfill (Figure 1b) [11]. Other fragments also appeared out of the archaeological context on the slopes of the Castle hill (Figure 1b), which were not completely buried and were exposed to environmental agents and pollution [9,10]. The fragments and complete tiles ex situ were surely originally in the Northern Hall, but had been withdrawn and discarded at some later time [11].

Some studies have been performed on medieval artifacts of *carreaux de pavement*, mainly using scanning electron microscopy coupled to an energy dispersive X-ray detector (SEM-EDS) [5,6,12–14], inductively coupled plasma atomic emission spectroscopy (ICP-AES) [15], X-ray diffraction (XRD) [12], cathodoluminescence [12], differential thermal analysis-thermogravimetry analysis (DTA-TGA) [12], or petrographic microscopy (PM) [13]. These studies, although scarce, can be useful as references since they chemically analyzed samples of medieval *carreaux de pavement* (mainly dated to 13th and 14th centuries) from different zones of French geography. Some of these publications even made it possible to differentiate between materials from the 13th and 14th centuries. The coincidence

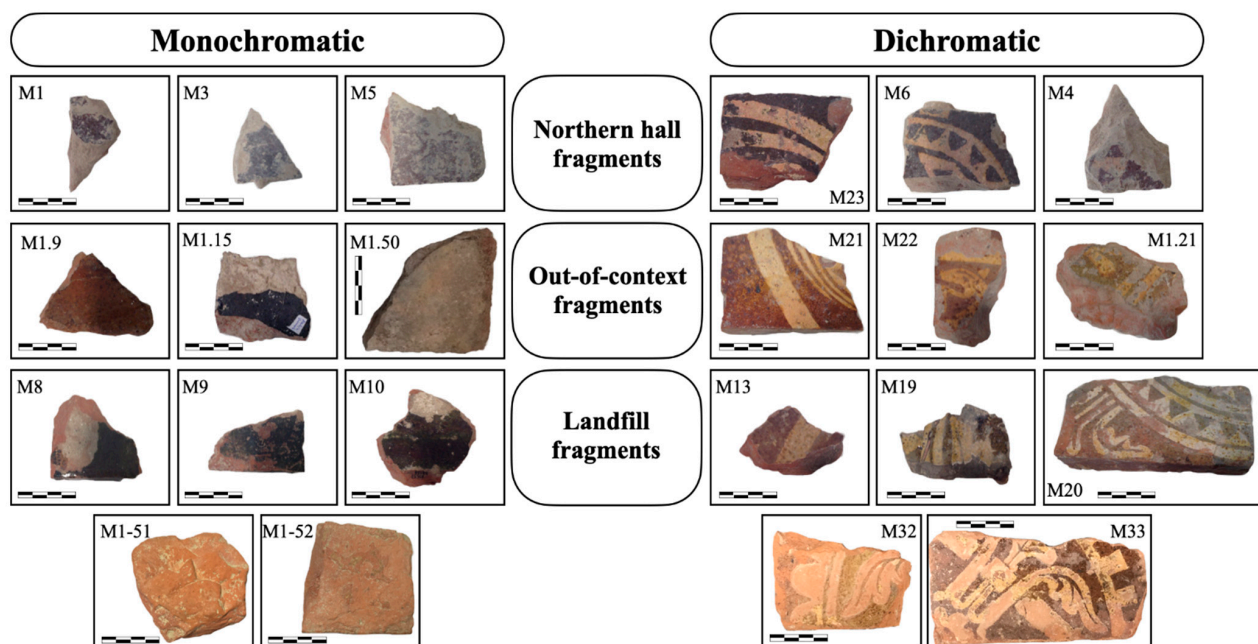
in typology (*carreaux de pavement*) [4], the geographical proximity, the linked historical context [7,8], and the dating within the same period [4] allowed the results of these studies to be compared with those obtained in this article. According to the information provided by these articles, the pastes could be classified in two types depending on the calcium oxide content: one pinkish or orangish with moderate percentage of CaO (mean values ca. 20%), and the other of reddish color and with a very low quantity of CaO (0.4–1.5%) [5,6,12,13,15]. The composition of the *engobe* layers was based on clay minerals or lime [5,6,12,14]. The glazes could also be classified depending on their light transmittance, so occurring opaque glazes were formed by a mixture of PbO, SnO, and clays, and transparent glazes with PbO and clays [5,6,12–14]. Metreau L et al. [13] classified the tiles found in *Sarzeau* in Northern France according to their thickness and the dates in which the tiles were made.

The investigation is mainly descriptive in nature with the main objective of adding information to the very scarce analytical data available for *carreaux de pavement*. In this sense, thanks to this study, the elemental and mineral compositions of the tiles from Tiebas Castle were determined as well as the possible differences between the tiles found in the different locations within the Castle and also with French production. The work will shed light on the raw materials used. The work presented did not aim to mainly address fundamental unsolved issues on the topic, but to provide meaningful, quality primary work to aid future workers in such efforts.

## 2. Materials and Methods

### 2.1. Materials

Around 7000–7500 tiles were installed in Tiebas Castle, most of them consisting of quadrangular tiles around 13–15 cm long, 13–15 cm wide, and 2–3 cm of thick; 62% of them were dichromatic and 38% were monochromatic [4,9]. Fragments of 22 tiles from *carreaux de pavement* were used in this research, most of them provided by the Registry, Movable, and Archeology Section of the Navarre Government. The samples were selected and classified (Figure 2, Table 1) according to the acceptable state of conservation of their three layers (paste, *engobe*, and glaze), type of decoration (monochromatic and dichromatic), and the archaeological location (Northern Hall, landfill, and out-of-context) (Figure 1b).



**Figure 2.** Analyzed tile fragments of *carreaux de pavement* from Tiebas Castle, classified by the type of decoration and archaeological location.

**Table 1.** Description of tile samples studied and the analytical techniques applied on each one. Abbreviations: e—engobe; g—glaze; p—paste; M—monochromatic tile; D—dichromatic tile; NH—Northern Hall fragment; LF—landfill fragment; OOC—out of context fragment; LHon—light honey glaze; DGre—dark green glaze; LGre—light green glaze.

Code	Type	Site	Glaze (color)	Thickness (mm)	Colorimetry	FTIR	DTA/TG	XRD	XRF	OM	PM	SEM/EDS
					p g e	p	p	p g e	p g e	a	p	a
M1	M	NH	DGre	23.6	✓✓-	✓	✓	✓✓-	✓✓-	✓	-	-
M3	M	NH	DGre	23.8	✓✓-	✓	✓	✓--	✓--	✓	-	-
M5	M	NH	DGre	25.7	✓✓-	✓	✓	✓✓-	✓--	✓	-	-
M8	M	LF	DGre	24.5	✓✓-	✓	✓	✓--	✓--	✓	-	-
M9	M	LF	DGre	23.2	✓✓-	✓	✓	✓--	✓--	✓	-	-
M10	M	LF	DGre	25.3	✓✓-	✓	✓	✓✓-	✓✓-	✓	-	✓
M1-15	M	OOC	-	23.4	✓--	✓	✓	✓--	✓--	✓	-	-
M1-50	M	OOC	DGre	22.4	✓✓-	✓	✓	✓--	✓--	✓	-	-
M1-9	M	OOC	LHon	20.8	✓✓-	✓	✓	✓--	✓--	✓	-	-
M6	D	NH	DGre	25.7	✓✓✓	✓	✓	✓✓-	✓✓-	✓	-	✓
M23	D	NH	DGre	28.3	✓✓✓	✓	✓	✓✓-	✓✓-	✓	-	-
M4	D	NH	DGre	24.9	✓✓✓	✓	✓	✓--	✓--	✓	-	-
M13	D	LF	LHon	24.8	✓✓✓	✓	✓	✓-✓	✓-✓	✓	-	-
M19	D	LF	LGre	23.6	✓✓✓	✓	✓	✓✓-	✓✓-	✓	-	✓
M20	D	LF	LGre	24.1	✓✓✓	✓	✓	✓--	✓--	✓	-	-
M21	D	OOC	LHon	25.2	✓✓✓	✓	✓	✓✓-	✓✓-	✓	-	✓
M22	D	OOC	LHon	24.4	✓✓✓	✓	✓	✓✓-	✓✓-	✓	-	✓
M1-21	D	OOC	LHon	25.4	✓✓✓	✓	✓	✓✓-	✓--	✓	-	-
M32	D	LF	LHon	22.8	-✓-	-	-	-✓-	-✓-	-	-	-
M33	D	LF	LHon	22.2	---	-	-	--✓	--✓	-	-	-
M1-51	-	OOC	-	-	---	-	-	---	---	-	✓	-
M1-52	-	OOC	-	-	---	-	-	---	---	-	✓	-

Two types of monochromatic tiles were recognized, some of them with a dark greenish glaze and others with a honey glaze. Honey, light green, or dark green glazes can be seen in the dichromatic tiles, covering a whitish decoration that fills the gaps of the pastes (Table 1).

## 2.2. Methods

For optical microscopy (OM) and SEM-EDS, small tile samples were cut vertically. The samples were laid in a mold of polymethyl methacrylate, which was filled with a resin. One of the faces of the samples was polished, in this form, cross-sections with the three layers (glaze, engobe and paste) were obtained. Optical PCE-MM200 and electronic Hitachi S4800 microscopes were employed for the investigation.

For the colorimetric analyses, a Konica Minolta CM-2300d spectrophotometer with D65 light was used. The measurements were carried out in triplicate directly on the surface of the tiles. Values of the  $L^*$ ,  $a^*$ , and  $b^*$  coordinates were measured.  $L^*$  represents lightness (100) to darkness (0);  $a^*$  gives information about reddish (positive  $a^*$  values) or greenish (negative  $a^*$  values) colors; and  $b^*$  about yellowish (positive  $b^*$ ) or bluish (negative  $b^*$ ).

To obtain the infrared spectra of the powder samples (after detaching the three different layers), a Shimadzu IRAffinity-1S spectrophotometer with a Golden Gate attenuated total reflectance (FTIR-ATR) accessory was employed (diamond-based ATR crystal with incidence angle of  $45^\circ$ ). The acquisition was in the wavelength range between 600 and  $4000\text{ cm}^{-1}$  with a resolution of  $4\text{ cm}^{-1}$  and 100 scans/sample.

A simultaneous TG-sDTA 851 Mettler Toledo apparatus was used for thermal analyses (DTA-TG) by heating the powder samples from ambient temperature to  $1000\text{ }^\circ\text{C}$  in an alumina crucible under a  $10\text{ }^\circ\text{C}/\text{min}$  heating rate and static air atmosphere.

For the analyses by XRD and X-ray fluorescence spectroscopy (XRF), the paste samples were crushed in an agate mortar. In the case of the engobes and glazes, laminar samples  $1\text{--}4\text{ cm}^2$  and 3 mm thick were prepared and measured in a non-destructive form. A Bruker S2 Puma instrument with a silver anode and helium atmosphere was used for the XRF analyses. The physical principle of acquisition was dispersion energy resource. A standard sample was measured before analyses to properly calibrate the energies' values.



For the mineralogical determination, PM and XRD were employed. For PM, a Zeiss polarizing petrographic microscope was used in two of the paste samples. For XRD, a Bruker D8 Advance diffractometer with Cu K $\alpha$  radiation was used and an LYNXEYE XE-T detector. The experimental conditions for XRD experiments were:  $2\theta$  range from  $5^\circ$  to  $70^\circ$ , 2 s per step, and step size of  $0.02^\circ$ .

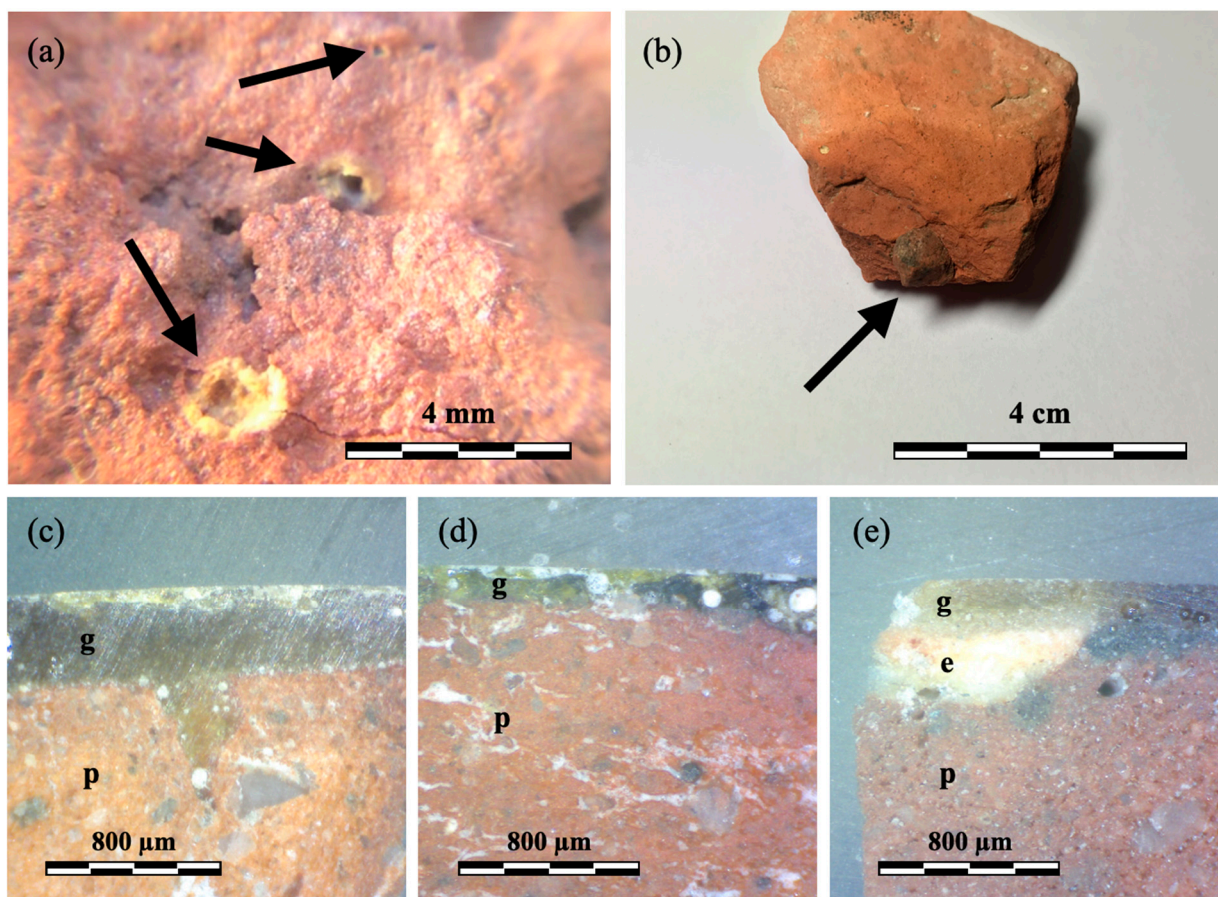
An EDS Bruker-X Flash-4010 analyzer coupled to a SEM microscope was used for elemental punctual analyses and mappings performed on some of the cross-sections. For the SEM-EDS analysis, the samples were previously metallized with gold.

All experiments performed on the 22 selected tiles are depicted in Table 1.

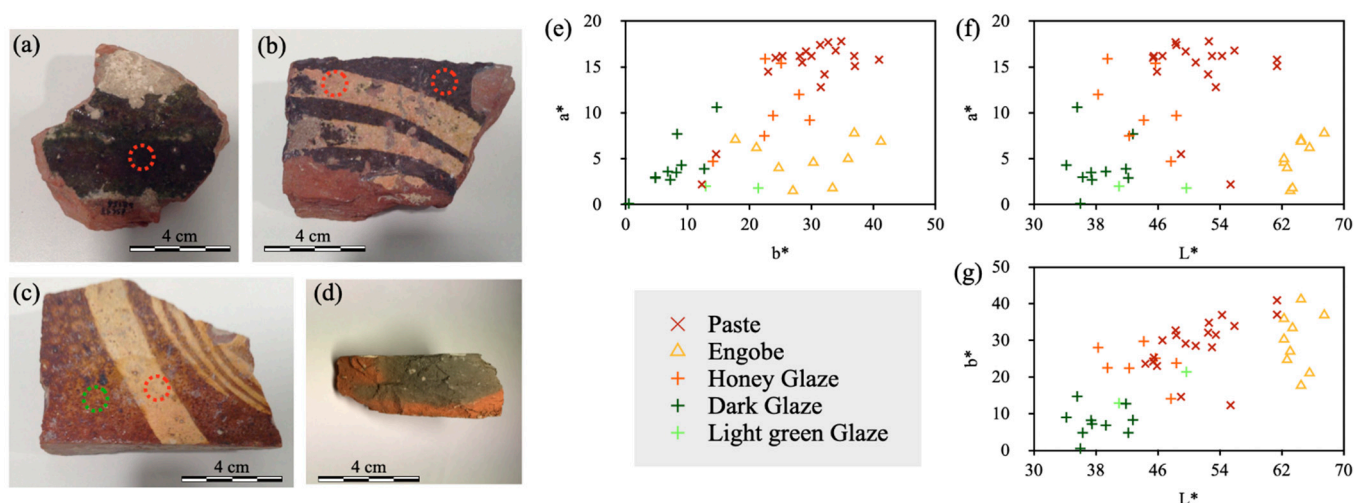
### 3. Results

#### 3.1. Naked-Eye Observation and Optical Microscopy (OM)

Some relevant macroscopic details were detected by looking properly at the tile pastes with the naked eye. Most tiles had a homogeneous paste, with no impurities or degreasers. Only in a few tiles were inclusions of small sandstone pebbles of diameters ca. 0.2–1 cm (M19, M1-15, M1-51), very tiny metal fragments of 0.5–3 mm (M1-51, M19), and air bubbles and cracks with diameters ca. 0.2–2 cm (M3, M21) filled with a yellowish powder (Figure 3a,b) detected. These irregularities were probably included during the production or molding of the clay. The pastes of two tiles, M19 and M20, showed an upper grey area and a lower reddish with an intermediate zone of mixed tones (Figure 4).



**Figure 3.** Images obtained by optical microscope ( $40\times$ ,  $200\times$ ) of the paste surface of the samples: (a) M21, and (b) M1-15. The arrows indicated air bubbles and sandstone pebble; and cross-sections of samples: (c) M22, (d) M8, and (e) M6. Abbreviations: p—paste; e—engobe; g—glaze.



**Figure 4.** (a–d) Zones in which the colorimetric experiments were done in some of the samples studied: M10, M23, M22 and M19. (e–g) Colorimetric study of the different layers of the fragments.

The observation of the cross-sections by means of an optical microscope allowed us to understand the morphology and thickness of the two thinnest layers, the glaze and *engobe* (Figure 3c,d). The glazes had thicknesses ranging from 500  $\mu\text{m}$  to 100  $\mu\text{m}$  (Figure 3c,d), and from 900  $\mu\text{m}$  to 300  $\mu\text{m}$  in the *engobes* (Figure 3e). Small air bubbles in the glazes had thicknesses of ca. 50  $\mu\text{m}$  (Figure 3c,d). The pastes were composed of a very fine reddish matrix that had a particle size of less than 50  $\mu\text{m}$ . In addition, crystals of light grey color (very possibly quartz) with an irregular shape and sizes ranging from 50 to 800  $\mu\text{m}$  were also observed (Figure 3c–e).

### 3.2. Colorimetry

A colorimetric analysis was carried in order to provide numerical values of the color variables ( $L^*$ ,  $a^*$ , and  $b^*$ ). These values were used to compare the different layers within the fragment and the different fragments to each other. The results found in this investigation will be available for future comparisons with other *carreaux de pavement*.

The color of the tile pastes and glazes is closely related to both their elemental composition and mineralogy [16]. One of the main characteristic properties of *carreaux de pavement* is the intense reddish color of its paste [4,15]. The red color of the pastes are usually related to either a high iron (III) oxide content, an oxidizing atmosphere during firing, or both [16–19]. The presence of carbonate based-compounds could lighten the pastes, and organic matter, carbon, or moisture darken them [16,17].

As an example, Figure 4a–d show some of the tile fragments in which different color measurements were carried out. In the sample M10, the measurements were performed on the dark greenish glaze (Figure 4a) and also on the paste; on the dark greenish glaze and whitish *engobe* in sample M23 (Figure 4b) and also in the paste; on the honey glaze and whitish *engobe* in sample M22 (Figure 4c) and also in the paste; and on the reddish and grey areas of the paste in sample M19 (Figure 4d).

Regarding the pastes, positive values of  $a^*$  and  $b^*$  were registered, ranging from 14 to 23 for  $a^*$  and from 23 to 41 for  $b^*$ . These values are characteristic of reddish-orange tones.  $L^*$  values oscillated between 44 and 62. In two of the studied tiles, M19 and M20, grey areas were present in the pastes (Figure 4d) as mentioned before, and consequently, the values of the  $a^*$  and  $b^*$  parameters were significantly reduced, especially for the pastes in sample M19 (Figure 4e–g and Table 2).



**Table 2.** Chromaticity values of each tile sample and layer. Each piece of data is the arithmetic mean of three experiments.

Sample	Glaze (Color)	Paste			Glaze			Engobe		
		L*	a*	b*	L*	a*	b*	L*	a*	b*
M1	DGre	44.4	22.8	23.6	39.3	3.6	6.8	-	-	-
M3	DGre	45.5	16.2	25.3	42.2	2.9	4.8	-	-	-
M4	DGre	49.6	16.7	29.1	42.8	7.7	8.3	64.5	7.1	17.7
M5	DGre	53	16.2	28.1	35.6	10.6	14.7	-	-	-
M6	DGre	45.4	16	24.2	37.5	2.7	7.2	65.6	6.2	21.1
M8	DGre	48.3	17.7	32.7	37.4	3.5	8.2	-	-	-
M9	DGre	48.4	17.4	31.4	36.3	3	4.8	-	-	-
M10	DGre	50.9	15.5	28.5	41.9	3.9	12.7	-	-	-
M23	DGre	45.9	14.5	23	34.2	4.3	9	62.7	4	24.7
M1-50	DGre	53.5	12.8	31.5	36.1	0.1	0.5	-	-	-
M19r	LGre	61.4	15.1	37	49.7	1.8	21.4	63.1	1.5	27
M19g	LGre	55.4	2.2	12.3	-	-	-	-	-	-
M20	LGre	49	5.5	14.6	41	2	12.9	63.4	1.8	33.4
M13	LHon	52.5	14.2	32.1	47.7	4.7	14.1	62.3	4.6	30.3
M21	LHon	52.6	17.8	34.8	48.4	9.7	23.8	67.5	7.8	36.9
M22	LHon	61.4	15.8	40.9	38.3	12	28	64.5	6.9	41.2
M32	LHon	-	-	-	45.7	15.4	25.1	-	-	-
M1-9	LHon	54.3	16.2	36.9	42.3	7.5	22.4	-	-	-
M1-15	-	46.6	16.2	30	-	-	-	-	-	-
M1-21	LHon	55.9	16.8	33.9	44.2	9.2	29.7	62.3	5	35.9

According to the whitish tone observed in the *engobe* layers (i.e., of sample M6, Figure 3e), the values of  $a^*$  were lower (between 1–8) and those of  $L^*$  higher (more clustered between 62 and 68) (Figure 4b,c, and Table 2) than those detected in the pastes.

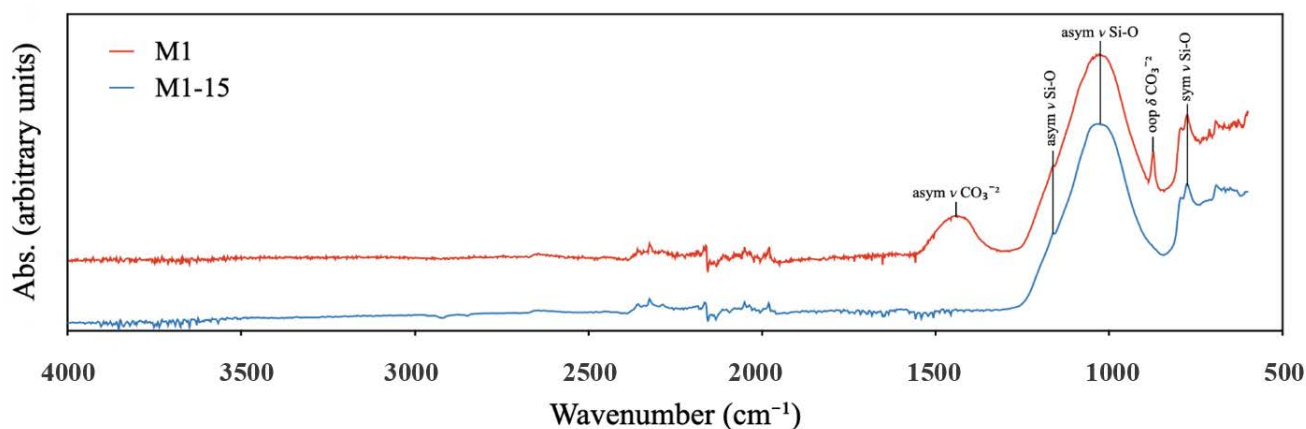
Conversely, the glaze was the layer with the greatest color parameter variability (Figure 4e–g and Table 2), very possibly due to their different compositions. Following the classification of types of glaze depending on color in Table 1, two major groups could be distinguished: dark green and light honey glazes. The first one stood out for having lower chromatic values than *engobes*, with  $L^*$  between 34 and 43,  $a^*$  between 0 and 11, and  $b^*$  between 0 and 15. The second type had intermediate values between the green glaze type and the color of the pastes, with  $L^*$  values between 38 and 49,  $a^*$  between 5 and 16, and  $b^*$  between 14 and 30. There was also a third type of glaze that was light green in color with shades in between the two glazes. The only two samples of this type (M19 and M20) had an  $L^*$  between 41 and 50,  $a^*$  between 1.8 and 2, and  $b^*$  between 13 and 21.

### 3.3. Fourier Transform Infrared (FTIR)

To facilitate the subsequent mineralogical characterization, a preliminary analysis of the pastes was carried out using infrared spectroscopy, in which the anionic groups (carbonates, silicates...) were identified in the samples.

The characteristic signals of quartz ( $\text{SiO}_2$ ) were identified in all of the spectra collected from the pastes: Si–O symmetric stretching band at  $780\text{ cm}^{-1}$  (sym  $\nu$  Si–O), asymmetric stretching at  $1050\text{ cm}^{-1}$  (asym  $\nu$  Si–O), and also a small band in the shoulder of the asymmetric stretching at  $1160\text{ cm}^{-1}$  (asym  $\nu$  Si–O) [20,21] (Figure 5). Carbonate signals were only present in a few of them and with low intensity (M1, M6, M8, M9, and M1-9 samples) (Figure 5). In these ones, out-of-plane  $\text{CO}_3^{-2}$  bending vibrations appeared at  $875\text{ cm}^{-1}$  (oop  $\delta$   $\text{CO}_3^{-2}$ ) and the asymmetric  $\text{CO}_3^{-2}$  stretching at  $1460\text{ cm}^{-1}$  (asym  $\nu$   $\text{CO}_3^{-2}$ ), which meant the presence of recarbonated calcite ( $\text{CaCO}_3$ ) [22,23] (Figure 5). There were no signals of other silicates or silicoaluminates such as plagioclase minerals ( $(\text{Na,Ca})(\text{Si,Al})_4\text{O}_8$ ), which usually appear between  $950$  and  $1150\text{ cm}^{-1}$ ; micas ( $\text{KAl}_2(\text{AlSi}_3\text{O}_{10})(\text{OH})_2$ ) around  $1000\text{ cm}^{-1}$ ; or potassium feldspars ( $\text{KAlSi}_3\text{O}_8$ ), between  $1040$  and  $1110\text{ cm}^{-1}$ , very possibly

due to the wide signal of the quartz [24]. In the following sections, additional mineralogical information will be provided.



**Figure 5.** Infrared spectra of samples M1 (red spectrum) and M1-15 (blue spectrum).

### 3.4. Differential Thermal Analysis-Thermogravimetry Analysis (DTA-TG)

The DTA-TG results corroborated the results by FTIR. Quantitative analyses were done using TG. Carbonates in a minimum proportion were detected in some of the pastes (M1, M6, M8, M9, and M1-9), since the mass loss of CO<sub>2</sub> between 600 and 1000 °C was on average 0.26%. The DTG peak of decarboxylation was recorded between 650–700 °C in all the cases, which could indicate that calcite is secondary [16]. The amount of organic matter and structural water (mass loss between 200 and 600 °C) was also very low, with 0.45% on average. These results matched with those by FTIR, in which neither free water H<sub>2</sub>O, OH<sup>−</sup> groups, nor organic molecule signals appeared between 3000 and 4000 cm<sup>−1</sup> (Figure 5). The scarcity of calcite, the fact of it being secondary, and also the lack of structural OH<sup>−</sup> groups could indicate that the pastes of the tiles were fired above 750–800 °C [17].

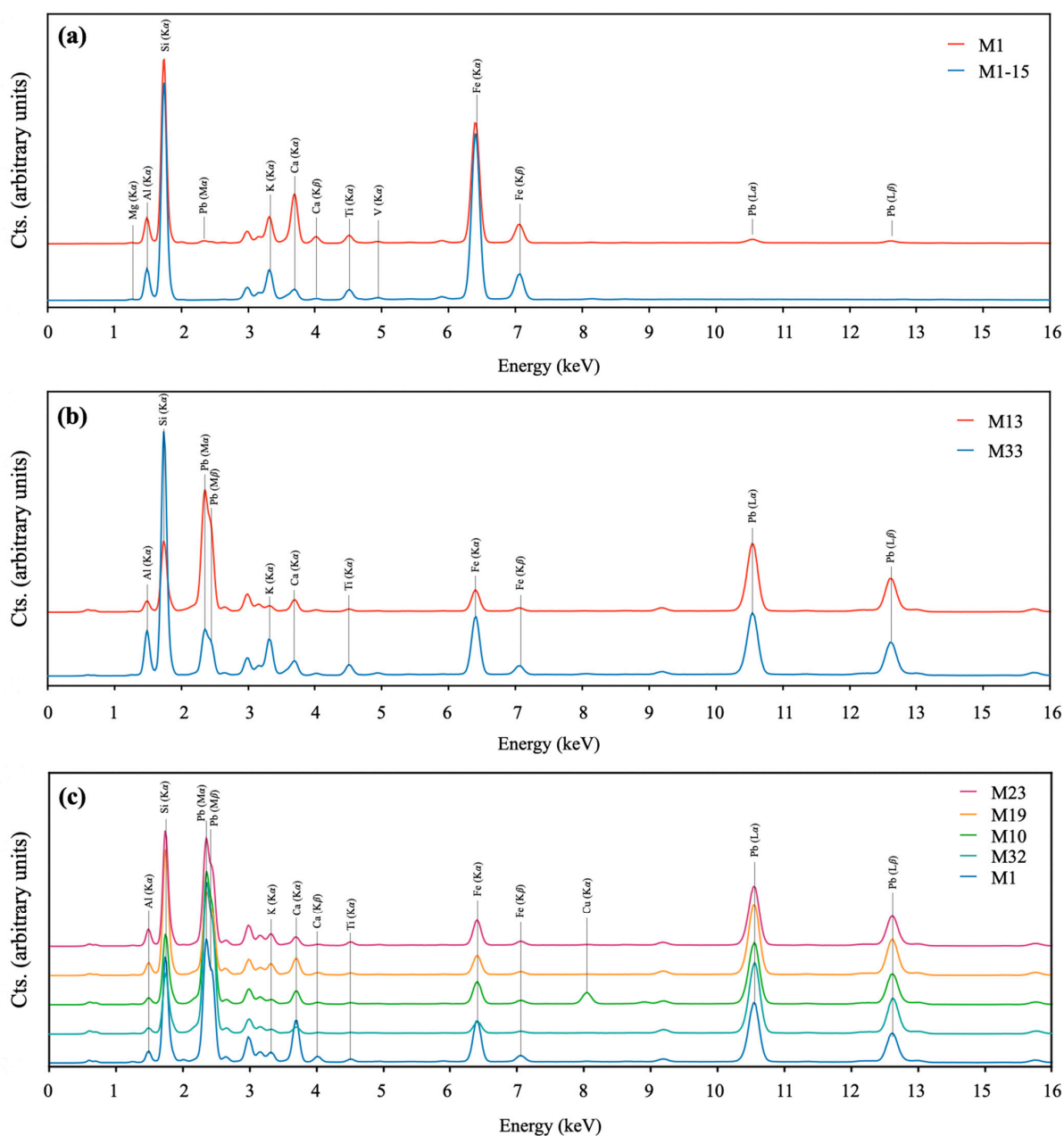
### 3.5. X-Ray Fluorescence (XRF) Spectroscopy

The identification of the major chemical elemental composition of each of the layers and the determination of their relative proportions are crucial for the classification of the *carreaux de pavement* as have been shown in the bibliography. Semiquantitative elemental chemical analyses also help in the identification of mineralogical phases and their amount.

The X-ray fluorescence spectra showed that the pastes had high relative contents of Si (K $\alpha$  at 1.74 keV), Fe (K $\alpha$  at 6.40 keV), Al (K $\alpha$  at 1.49 keV), Ca (K $\alpha$  signal at 3.69 keV), and K (K $\alpha$  signal at 3.31 keV). Mg, Pb, Ti, and V were also detected. The samples in which carbonates were detected by FTIR spectroscopy and DTA-TG had a higher proportion of Ca such as in sample M1 compared to M1-15 (Figure 6a). The high intensity of Si matched the presence of silicates (quartz) by FTIR.

The *engobe* stood out for its lower proportion of Fe and Ca and higher proportion of Si, Al, and especially Pb (L $\alpha$  and M $\alpha$  at 10.55 and 2.34 keV, respectively), probably coming from the layer of glaze that covered the *engobe* (Figure 6b showed the spectra of two of the samples, M13 and M33). Manual separation of both layers and separate analysis was not possible due to their low thickness and high fragility. Better results were achieved thanks to the analysis of the cross-sections by SEM-EDS.

The composition of the glazes was characterized by the significant proportion of lead and silicon (Figure 6c shows the spectra collected on some of the samples, M1, M10, M19, M23, and M32). None of the spectra of the glazes showed Sn. Furthermore, in sample M10 (with dark green color), a slight signal of Cu (K $\alpha$  at 8.05 keV) appeared.



**Figure 6.** XRF spectra of (a) the paste of samples M1 and M1-15; (b) glaze and *engobe* of samples M13 and M33; (c) glaze of samples M1, M10, M19, M23 and M32.

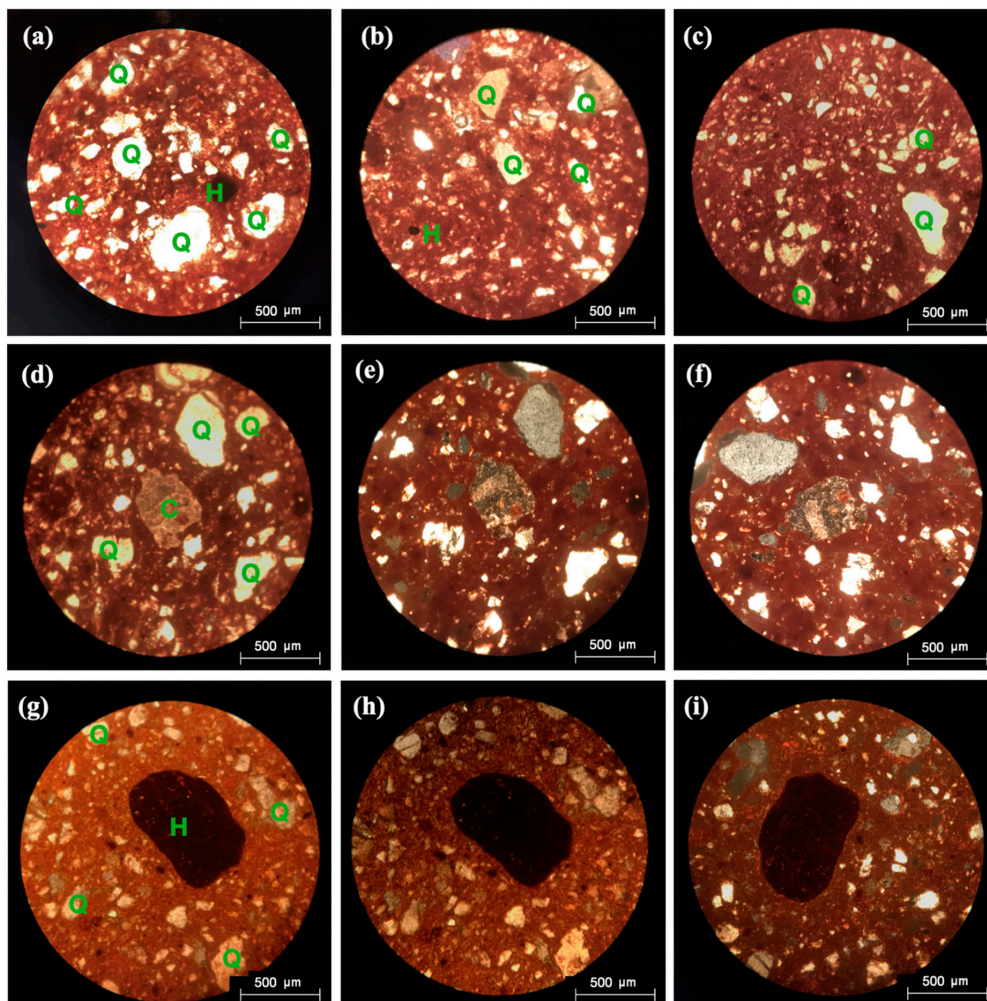
Semiquantitative analyses were performed taking into account the intensities of the peaks of each element ( $M\alpha$  for Pb and  $K\alpha$  for all the others) and the ratios with that from the Si  $K\alpha$  peak (Table 3). One of the main differences between the two main glaze groups (dark green and light honey) was their relative proportion of lead, which was greater in the honey glazes compared to the dark green in general terms. Some other slight differences were also found in the Fe/Si ratio, with being the honey glaze somewhat richer in Fe. In the Ca/Si and Al/Si ratios, there were no important differences between both types of glaze. As for the comparison between the three layers (glaze, *engobe*, and paste) (Table 3), glazes and *engobes* had much more lead and much less iron than the pastes; *engobes* and pastes had more potassium than the glazes; and the Al/Si ratios were higher in the *engobes* than in the glazes and pastes.

**Table 3.** Relative elemental semi-quantification of the samples taking into account the intensity (counts) of the peaks and comparing them with Si ( $K\alpha$  at 1.74 keV) as a reference.

Sample	Pb(M $\alpha$ )/Si	Al(K $\alpha$ )/Si	Fe(K $\alpha$ )/Si	K(K $\alpha$ )/Si	Ca(K $\alpha$ )/Si	Cu(K $\alpha$ )/Si
M1 glz DGre	1.1575	0.1109	0.3958	0.1004	0.4005	0.0157
M10 glz DGre	1.8962	0.0987	0.3264	0.0741	0.1933	0.1743
M6 glz DGre	0.9807	0.1187	0.3195	0.0852	0.0672	0.0142
M23 glz LGre	0.9333	0.1458	0.2244	0.1063	0.0799	0.0151
M19 glz LHon	0.6613	0.1	0.1556	0.0916	0.1365	0.0111
M21 glz LHon	1.4357	0.119	0.7653	0.0962	0.3346	0.0195
M22 glz LHon	2.1813	0.1416	0.4187	0.1128	0.3807	0.0209
M32 glz LHon	2.5358	0.1003	0.2036	0.0791	0.118	0.0217
Paste mean	0.0113	0.1368	0.6726	0.1326	0.1459	0.0077
Engobe mean	0.9472	0.1706	0.2749	0.121	0.118	0.0145

### 3.6. Petrographic Microscopy (PM)

The mineralogical identification of the pastes started with petrographic analyses performed on thin sections of 9  $\mu\text{m}$  thick, in which quartz, calcite, and hematite crystals were identified as embedded in a reddish matrix (Figure 7). Hematite was very possibly the compound responsible for the coloration of the pastes [25–27]. The most abundant mineral was quartz, as previously detected by FTIR.



**Figure 7.** Thin section of the pastes of the M1-51 (a,b,d–f) and M1-52 (c,g–i). Samples images collected under a petrographic microscope (100 $\times$ ). Aleatory captures for modal analysis (a–c). Capture of a region of a small crystal of calcite (d–f) and hematite (g–i), with parallel (d,g) and crossed nicols at 0 $^{\circ}$  (e,h) and 90 $^{\circ}$  (f,i).

The surface occupied by quartz crystals was large enough to be well defined and was approximated by modal analysis, resulting in 12–20%, whilst 80–88% corresponded to the reddish matrix. Regarding the granulometry of the minerals, quartz had a size of 50 to 800  $\mu\text{m}$  (similarly to those measurements by OM) and those of calcite and feldspar between 30 and 200  $\mu\text{m}$ . The reddish matrix particles had a grain size lower than 50  $\mu\text{m}$ . Therefore, in particle size terms, the tile pastes would be composed of a mixture of fine sand, silt, and clays [28].

### 3.7. X-Ray Diffraction (XRD)

In addition to the minerals identified in the pastes by PM, the XRD analyses showed the presence of other minor minerals phases such as dolomite ( $\text{CaMg}(\text{CO}_3)_2$ ), gehlenite ( $\text{Ca}_2\text{Al}(\text{SiAl})\text{O}_7$ ), potassium feldspars ( $\text{KAlSi}_3\text{O}_8$ ), and micas ( $\text{K}(\text{Al,Fe,Mg})_{2-3}(\text{AlSi}_3\text{O}_{10})(\text{OH})_2$ ) (Table 4). Quartz was the most abundant crystalline phase detected by XRD (Table 4). Hematite was present in all pastes. As aforementioned, this compound provided the reddish color to the pastes [25–27]. The mineralogical composition of the pastes was very similar in all tiles; therefore, the location of the artifacts (Northern Hall, landfill, or out of context) was not an important factor to differentiate among them. These results indicated a good homogeneity in the tile pastes from a compositional point of view and few affectation of the environment of the places where they were found. Samples M1, M6, M8, M9, and M1-9 showed the presence of calcite reflections at  $2\theta = 29.406, 39.402, 43.146$  (file 05-0586) (Figure 8a), matching the results provided by other techniques.

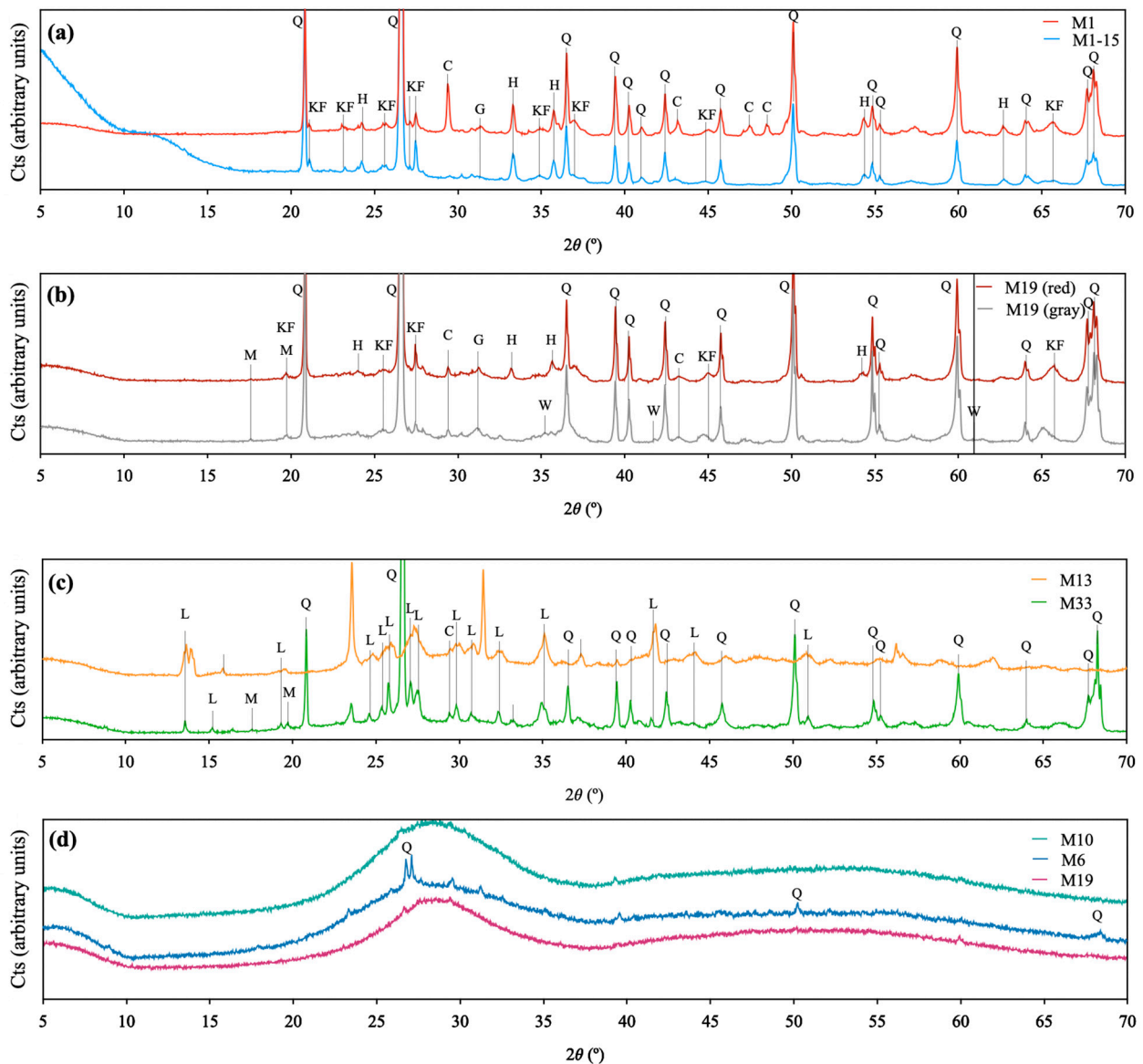
**Table 4.** Minerals phases identified in each sample of paste by x-ray diffraction (XRD) and its abundance (+++: abundant; ++: moderate; +: minority; nd: not detected). Abbreviations: Q—quartz (file 33-1161); C—calcite (file 05-0586); H—hematite (file 33-0664); KF—potassium feldspar (files 89-8673 and 19-0931); D—dolomite (file 36-0426); G—gehlenite (file 35-0755); M—mica (file 46-0741).

Sample	Q	C	H	KF	D	G	M	Sample	Q	C	H	KF	D	G	M
M1	+++	++	+	+	nd	+	nd	M13	+++	+	+	+	+	+	nd
M3	+++	+	+	nd	+	+	nd	M19	+++	+	+	+	nd	+	+
M5	+++	+	+	+	+	+	nd	M20	+++	+	+	+	nd	nd	+
M6	+++	++	+	+	+	nd	nd	M1.15	+++	nd	+	+	+	nd	nd
M23	+++	+	+	+	+	+	nd	M1-50	+++	+	+	+	nd	+	+
M4	+++	+	+	+	+	+	+	M1-9	+++	+	+	+	+	nd	+
M8	+++	++	+	+	+	nd	nd	M21	+++	+	+	+	+	+	+
M9	+++	++	+	+	+	nd	nd	M22	+++	+	+	+	+	nd	+
M10	+++	+	+	+	+	+	nd	M1-21	+++	+	+	+	+	nd	+

In the pastes of sample M19, some differences were observed between the red and grey zones. In the M19r (red) diffractogram, hematite appeared at  $2\theta = 33.153, 35.612, 57.091$  (file 33-0664), while in the M19g (grey), hematite was not detected (Figure 8b). However, in the XRF spectra, the Fe content in both zones was practically identical, so the difference must lie in a different mineralogical form of iron. In sample M19g, some of the main reflections of wüstite ( $\text{FeO}$ ) seemed to be distinguished at  $2\theta = 41.71, 60.92, 35.22$  (file 01-1223) [29–31].

The *engobes* (Figure 8c shows the XRD diagrams of samples M13 and M33) were formed by a lead silicoaluminate ( $\text{PbAl}_2\text{Si}_2\text{O}_8$ ) phase [32]. The main reflections of this phase appeared at  $2\theta = 35.02, 35.05, 34.90$  (file 25-0428). The high ratio Al/Si of this type of silicoaluminate matched the Al/Si ratio found by XRF spectroscopy in the *engobes* of the tiles. The mean value of the *engobes* was 0.17, higher than in the other two strata: 0.14 in pastes and 0.12 in the glazes (mean values). The absence of calcite in the *engobes* was also an important result since it allowed confirmation that the whitish color of the *engobe* was caused only by silicoaluminate. Furthermore, the *engobe* of sample M33 also showed a certain amount of quartz and mica.





**Figure 8.** X-ray diffraction patterns of: (a) paste samples M1 and M1-15; (b) the two paste colors of tile M19 (red and grey); (c) engobe samples M13 and M33; (d) glazes of M6, M10 and M19. Abbreviations: Q—quartz; C—calcite; H—hematite; KF—potassium feldspar; D—dolomite; G—gehlenite; M—mica; W—wüstite; L—lead silicoaluminate.

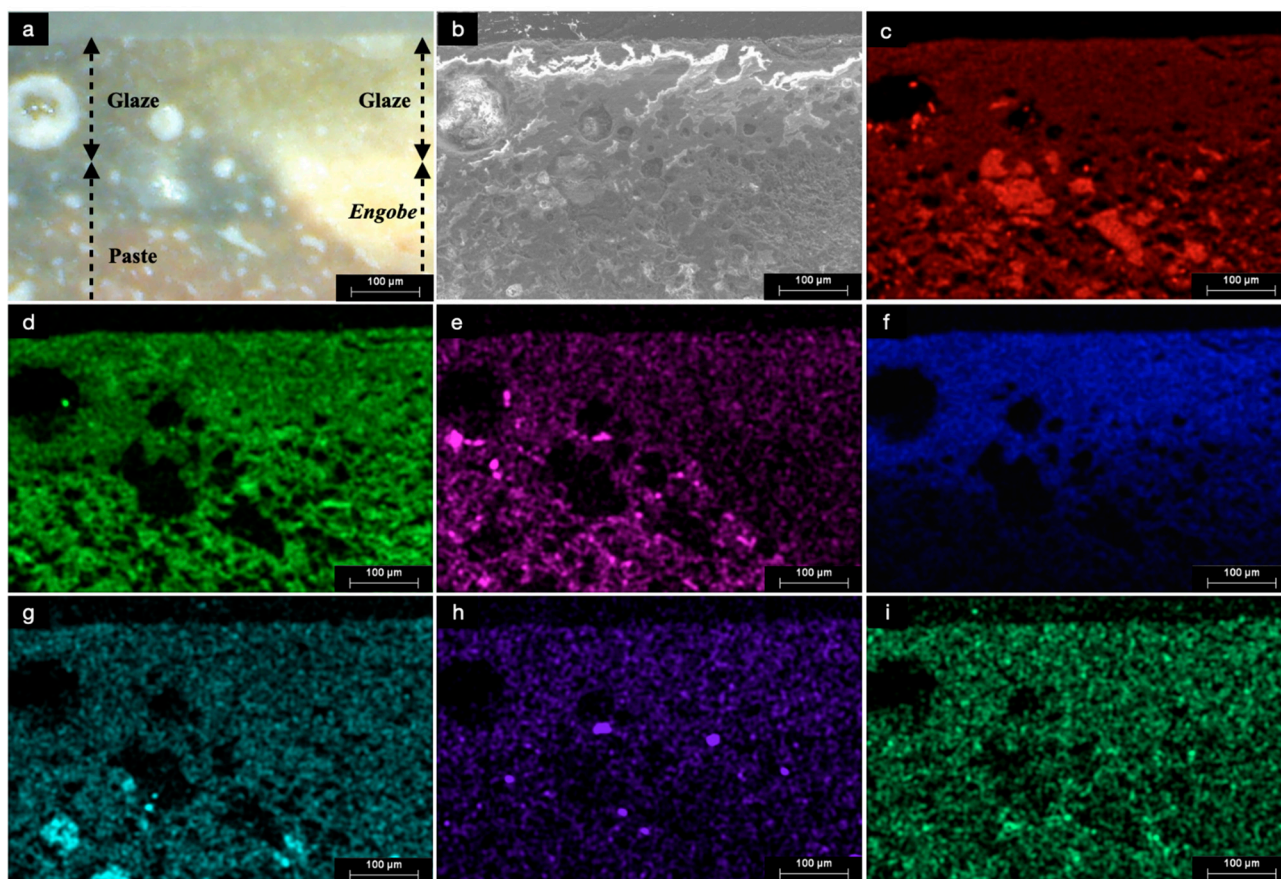
The XRD analysis of the glazes hardly provided any information on their composition since very wide signals appeared in the diffractograms (Figure 8d shows the XRD diagrams of samples M6, M10, and M19). The broad signals seen in the diffractogram indicated an amorphous arrangement. Lead oxide, used as a flux, reduces the melting point, thus creating a mixed amorphous vitreous layer (glaze). The absence of crystalline mineral phases could be also an indication that the firing temperature was high enough for the glaze to form a homogeneous vitreous layer. In the glaze of sample M6, some quartz peaks could be identified. Phases responsible for the honey and dark green glazes were not detected.

### 3.8. Scanning Electron Microscopy Coupled with Energy Dispersive X-Ray Spectroscopy (SEM-EDS)

According to the secondary electron images by SEM of the cross-sections, the glazes were seen as compact and homogeneous layers, except for the air bubbles of different sizes that were also clearly visible. As an example, the OM and SEM images of sample M6



and the EDX mappings corresponding to some elements (Si, Al, Fe, Pb, K, Ti and Ca) are shown in Figure 9. The glazes stood out for their high Pb content (Figure 9f), as previously indicated by the XRF analyses. Although the honey glaze color was assigned to iron-based compounds, the distribution of iron in the mapping was rather homogeneous within the cross-sections (Figure 9e) due to the presence of hematite (and wüstite) in pastes as detected by PM and XRD. From the mapping, the composition of glazes was based on Pb, Si, Al, and Fe-compounds.



**Figure 9.** Images (200×) collected using: (a) Optical microscopy (OM), (b) scanning electron microscopy (SEM); energy dispersive x-ray spectroscopy (EDS) mappings corresponding to: (c) Si, (d) Al, (e) Fe, (f) Pb, (g) K, (h) Ti, and (i) Ca.

The *engobe* and paste layers appeared more continuous and homogeneous, without air bubbles. The *engobes* showed compositions mainly based on Si and Al (Figure 9c,d). Quartz crystals also appeared, but smaller than those of the pastes (Figure 9c). The EDS mappings made a better determination of the composition of the *engobe* possible without the lead contamination coming from the upper glaze layers (as aforementioned in the XRF analyses). Therefore, a kaolinite-type silicoaluminate would be very possibly present in this layer.

The pastes appeared as a mixture of large Si-based crystals, assigned to quartz, previously observed by PM, XRD, FTIR, and XRF spectroscopy, but also Ti-based compounds (Figure 9h), which were not detected by XRD. In addition, some crystals rich in K (Figure 9g), which were assigned to the potassium feldspars detected by XRD; some areas with a higher distribution of Fe appeared throughout the pastes, matching with that described in the XRF spectroscopy section.

#### 4. Discussion

According to Metreau et al. [13], the tiles of the 13th century were thicker (2.3–2.7 cm) than those of the 14th century, which ranged from 1.6 to 2.2 cm, reducing mass and costs in the latter. The tiles of Tiebas Castle were dated to around 1256 [4] and their thicknesses ranged from 2.1 to 2.8 cm. Therefore, they matched the 13th century production of *carreaux de pavement*. This result provided a first datum about the possible date of manufacturing of the artifacts, which must be corroborated by other complementary techniques.

##### 4.1. Paste

The composition of the pastes of the Tiebas tiles turned out to be quite homogeneous. There were no significant differences in composition depending on the locations in which the tiles were found (Northern Hall, landfill, or out of context). It stood out mainly for its high quartz content, identified by most techniques (OM, FTIR spectroscopy, XRF spectroscopy, PM, XRD, SEM-EDS). This quartz had a variable grain size, from the largest grains observable by OM (ca. 800  $\mu\text{m}$ ) to the smallest observable by SEM-EDS (less than 50  $\mu\text{m}$ ). The appearance of sandstone pebbles and metallic inclusions by OM indicated a certain carelessness in kneading and modeling the pastes.

Another important characteristic of the Tiebas pastes was the low content of carbonates, especially calcite, detected by thermal analyses, PM, and XRD. Although some variability in the calcite content was detected, none of the samples exceeded 4.7% in mass. The vibrational frequency at which the asymmetric  $\text{CO}_3^{-2}$  stretching signal appeared in FTIR spectroscopy [16], together with the decarbonation maximum temperature of DTG, indicated that this calcite was very probably secondary [22]. These data allowed us to provide an approximate firing temperature above 750–800  $^{\circ}\text{C}$  [17]. The samples with recarbonated calcite and those without calcite showed an important difference in the relative content of CaO by XRF spectroscopy (Figure 6), which matched the FTIR results (Figure 5). The calcite formation probably originated from the inclusion of some limestone pebbles, as it could be seen by OM (Figure 3a) and PM (Figure 7d–f).

Literature about *carreaux de pavement*, devoted to mainly to French artifacts, distinguishes two types of tiles depending on the content of CaO in the pastes. The first type has high proportions of 13–30% [12] relative to a deposit in the Bourges region. The second, in contrast, reports low CaO concentrations in pastes: 1–2% in the region of Bordeaux [5,6], 1–3% in Alsace [15], and 1–2% for the 13th century and 0.2–1% for the 14th century, in Bretagne [13]. From the data provided by the thermal analysis in the Tiebas pastes, values of CaO between 0.1–2.6% were calculated. Therefore, the Tiebas samples would be similar to those of Bordeaux, Alsace, and Bretagne but different from those of Bourges.

The greyish color detected in two of the tile pastes (samples M19 and M20) contrasted with the reddish-orangish color observed in the majority of the tiles, which can be related to the absence of hematite (identified in the rest of the tiles by PM and XRD). Wüstite (iron II oxide that has a grayish color) was detected in these two tiles by XRD, very possibly due to the presence of a partial reducing atmosphere during the high temperature heating [29–31]. This heating with a reducing atmosphere could take place during the firing of the tiles in some areas inside the kiln, where oxygen is scarce. It is known that in the summer of 1378, the castle was burned down and the wooden ceilings over the tiled pavement burned down [4]. The abundance of burning wood and the absence of enough oxygen could cause the reducing atmosphere.

It was also possible to identify other more minor mineral phases such as titanium-based compounds by SEM-EDS (possibly titanium oxide), micas (PM, XRF spectroscopy), potassium feldspar (XRF spectroscopy, XRD, SEM-EDS), and gehlenite (XRD). The presence of these compounds did not coincide with the geology of the Pamplona Basin where Eocene marls and limestones predominate [33]. With the current data, it is most likely that the tiles were made in northern France, where this type of tile is typical [1–3]. From these results, a fluid trade between France regions and Northern Spain could be inferred. This subject will be deeply dealt with in another investigation in progress.

The presence of gehlenite would imply that the firing temperature was not higher than 1000 °C, since at this temperature it decomposes to anorthite. Another aspect to consider is that the gehlenite neoformation could occur from 800°, although it could already have been present in the raw clay [34].

#### 4.2. Engobe

The *engobe* was mainly composed of lead silicoaluminate ( $\text{PbAl}_2\text{Si}_2\text{O}_8$ ) (XRD), at least in its superficial part where *engobe* and glaze were hardly distinguishable. The assumption is that the original silicoaluminate compound forming the *engobes* was kaolinite ( $\text{Al}_2\text{Si}_2\text{O}_5(\text{OH})_4$ ), which transformed to metakaolinite ( $\text{Al}_2\text{Si}_2\text{O}_7$ ) after heating at 550 °C, and reacted with lead compounds of the glaze [34]. Cicuttini et al. [5] mentioned the use of kaolinite in the *engobes*. No significant differences were found between the *engobes* of the different locations within the Castle.

Depending on the *engobe* composition, two types of tiles were differentiated in the literature about the *carreaux de pavement*: those that used some type of silicoaluminate, with 68–73% of  $\text{SiO}_2$  and 19–22% of  $\text{Al}_2\text{O}_3$  [5,6]; or those that mainly employed CaO (30–40% of CaO [12] or 8% from Haute-Vienne [14]). The *engobe* of the analyzed samples from Tiebas would be again similar to those from the Bordeaux region.

#### 4.3. Glaze

Only dark glazes were found in the Northern Hall. The glazes found in the landfill were both dark green and honey and also included the only two samples with light glaze (M19 and M20). The tile fragments found out of archaeological context on the slopes of the castle hill were mostly the honey type, except for sample M1-15, which belonged to the dark green glaze type. In all cases, the glaze consisted of a compact (OM, SEM-EDS) and mostly amorphous (XRD) layer of about 100–500 µm thick (OM, SEM-EDS). The glazes appeared to have different thicknesses depending on whether they were on the paste or on the *engobe*, as can be seen in Figure 2e (OM). The thickness coincided with those described in [6].

High relative contents of lead and silicon (XRF spectroscopy, SEM-EDS) and the absence of tin (XRF spectroscopy, SEM-EDS) were detected. The presence of lead and the absence of tin allowed them to be classified as plumbiferous glazes [35–37], which are characteristic of a specific historical period [13]. As with the pastes and the *engobes*, the glazes can be classified into two types according to the information extracted from the articles published about the *carreaux de pavement*. The first type of glaze is that which uses only lead compounds as a flux. Lead oxide appeared in a concentration of 35–45% [12], 32–69% [5,6], 39–62% [13], and 51–65% [14]. The other type of glaze is that which uses a mixture of lead and tin compounds as a flux; the quantities of lead and tin oxides was respectively 20–42% and 7–36% [12], 50–68% and 0.2–1.4% [13], and 8–11% in tin oxide [14]. The lead glaze seems to be more characteristic of the 13th century *carreaux de pavement* [5,6,13,14], whilst the lead and tin glaze appeared only from the 14th century [12–14]. The tiles from Tiebas Castle would be within the first group, therefore, they could again be associated with manufacture in the 13th century [4] and with production in the Bordeaux area [5,6]. One drawback is that stylistically, it does not coincide with the decorative motifs of the sites in the Bordeaux region, but it does coincide with the Champagne region [1–3].

The two main sources of lead throughout history have been the roasting of galena (PbS) and the calcination of lead carbonates, generally cerussite ( $\text{PbCO}_3$ ) or hydrocerussite ( $\text{PbCO}_3 \cdot 2\text{H}_2\text{O}$ ) [38,39]. The small bubbles that appear in the glaze (Figures 2c–e and 9a,b) could indicate the use of lead carbonates as a source of lead for the glaze [39–42], since from 350–450 °C, it decomposes into  $\text{CO}_2$  and PbO [43]. These bubbles are frequent in glazes that do not reach a sufficient temperature (900–1000 °C), when the viscosity of the glaze is optimal [39].

Regarding the different types of glaze found in Tiebas, the dark glaze was characterized by a lower proportion of Pb (Table 3). The honey glaze, however, was much more transparent and had a higher Pb/Si ratio (Table 3). The remaining ratios of major elements

(Al/Si, Fe/Si, K/Si, Ca/Si) were similar between them, and were slightly lower than the ratios found in the pastes (Table 3). This could mean that similar clays were employed for the fabrication of glazes. Light green glazes appeared associated with the only two samples with grayish pastes (M19 and M20), which indicated that the color of the glazes were possibly influenced by those of the inner layers.

As aforementioned, a slight signal of Cu ( $K\alpha$  at 8.05 keV) appeared in one of the samples. The use of copper-based pigments has also been identified in other French tiles [5,6,13] in which copper is only applied on monochromatic tiles [13].

## 5. Conclusions

This study dealt with the unique *carreaux de pavement* found in the Iberian Peninsula. Thanks to an in-depth mineralogical investigation, the composition of the three layers of tiles from the Tiebas Castle was fully determined. The pastes were composed of quartz, potassium feldspar, mica, calcite, and hematite, the latter providing their characteristic orangish-reddish color. Silicoaluminate compounds (very probably kaolinite) were the main compound found in the *engobe*. Glazes were mainly composed of lead-based compounds and quartz. Honey glazes were richer in iron, and copper was detected in one of the dark green glazes. The heating temperature of the pastes was inferred above 750–800 °C and below 1000 °C. There were no important differences between the tiles found in the three locations within the Castle.

The *carreaux de pavement* tiles from Tiebas matched those manufactured in the Bordeaux region, which is relatively close to Navarre, more than those from other regions (Alsace, Bretagne, and Bourges). However, stylistically they did not coincide with them, being much more similar to those of the Champagne and Reims regions, of which, unfortunately, there have been no archaeological studies.

The comparison with the scarce articles devoted to *carreaux de pavement* has allowed for the dating of the Tiebas tiles to the 13th century, coinciding with the date of the construction of the castle that is given by historical and archaeological references. The dating was mainly possible thanks to the presence of plumbiferous glazes, characteristic of the *carreaux de pavement* of that century.

This article provides new information to include in the corpus of the *carreaux de pavement* made in Europe in medieval times and provides meaningful work to aid future researchers in this subject.

**Author Contributions:** Conceptualization: I.R.-A., E.L., and A.D.; Methodology: I.R.-A.; Software: I.R.-A.; Validation: I.R.-A., E.L., A.D.; Formal Analysis: E.L., A.D.; Investigation: I.R.-A., E.L., A.D.; Resources: I.R.-A., E.L., A.D.; Data Curation: I.R.-A., E.L., A.D.; Writing-Original Draft Preparation: I.R.-A., E.L., A.D.; Writing-Review & Editing: I.R.-A., E.L., A.D.; Visualization: I.R.-A.; Supervision: E.L., A.D.; Project Administration: I.R.-A., E.L., A.D.; Funding Acquisition: I.R.-A., E.L., A.D. All authors have read and agreed to the published version of the manuscript.

**Funding:** The reported study was funded by the Ayuntamiento de Tiebas-Muruarte de Reta, Fundación Sierra de Alaiz; and the Dirección General de Cultura-Institución Príncipe de Viana (Navarre Government) under the project *Thibalt. Caracterización arqueométrica de Carreaux de Pavement procedentes del Castillo de Tiebas (Navarra)*.

**Data Availability Statement:** The dataset is presented directly in the present study. Additional data (unpublished) are available upon request from the corresponding author (A.D.).

**Acknowledgments:** The authors wish to thank the staff from the Chemistry Department of the University of Navarre, especially to Cristina Luzuriaga and Iker Arrizabalaga, for their help in the experiments. We also thank M.C. Jimenez de Haro (ICMSE) for the SEM-EDS analyses, and the Service of Rock and Hard Materials Preparation of Zaragoza University.

**Conflicts of Interest:** The authors declare no conflict of interest.

## References



- Mayer, J.; Garrigou, P. Pavement. Carreaux de sol en champagne au moyen-âge et à la renaissance. *Editions du Patrimoine* **2000**, *4*, 393–394.
- Norton, C. *Carreaux de Pavement du Moyen Âge et de la Renaissance: Collections du Musée Carnavalet*; Editions Paris-Musées: Paris, France, 1992.
- Cailleaux, D.; Chapelot, O. *Carreaux de pavement du Moyen Âge et de la Renaissance: Catalogue des collections des Musées de Chaumont et de Saint-Dizier, Haute-Marne*; Musée Municipal de Chaumont et Musée Municipal de Saint-Dizier: Chaumont et Saint-Dizier, France, 1987.
- Ramos, M. Descubrimiento de un pavimento de baldosas decoradas en el castillo-palacio de Tiebas. *Trabajos de Arqueología de Navarra* **2009**, *21*, 317–324.
- Cicuttini, B.; Merat, A.; Ben Amara, A.; Bechtel, F. Étude stylistique et technologique des carreaux de pavement du château de Lormont (Gironde, XIII–XIV siècles). In Proceedings of the Actes du 4ème Congrès International d’Archéologie Médiévale et Moderne, Paris, France, 3–8 September 2007.
- Cicuttini, B.; Ben Amara, A.; Bechtel, F. An investigation into the ceramic technology of the two-colour tiles of “Prince Noir” castle (Bordeaux, France, Thirteenth to Fourteenth Centuries AD). In Proceedings of the 37th International Symposium on Archaeometry, Siena, Italy, 12–16 May 2008; pp. 55–60.
- García, M.R. *La Dinastía de Champaña en Navarra. Teobaldo I, Teobaldo II, Enrique I (1234–1274)*; Ediciones Trea: Gijón, Spain, 2010.
- García, M.R. *Teobaldo II*; Editorial Mintzoa: Pamplona, Spain, 2003.
- Castiella, A. Informe sobre los trabajos arqueológicos realizados en el Castillo de Tiebas (Navarra). *Trab. Arqueol. Navar.* **1998**, *13*, 247–286.
- Ramos, M. Excavaciones en el castillo de Tiebas (Navarra), primer informe provisional, 1998. *Trab. Arqueol. Navar.* **2001**, *15*, 167–213.
- Martínez, D.; Ruiz, F.J.; Vallejo, J.M. Algunas consideraciones en torno a unas baldosas góticas decoradas y vidriadas aparecidas en la ermita de Santa Catalina en Tiebas (Navarra). *Trab. Arqueol. Navar.* **2011**, *23*, 141–160.
- Ben Amara, A.; Gourdon-Platel, N.; Bechtel, F.; Schvoerer, M.; Bon, P. Carreaux glaçurés provenant d’un château du Duc de Berry (Mehun-sur-Yèvre, fin XIV siècle): Recherche d’indices techniques. *Arch. Sci.* **2005**, *29*, 21–34.
- Métreau, L.; Cantin, N.; Bechtel, F.; Rosen, J.; André, P. De Suscinio I à Suscinio II: Rupture ou continuité? Étude archéométrique des carreaux décorés à glaçure transparente des pavements médiévaux du château de Suscinio (Sarzeau, Morbihan). *Revue Archéol. l’Ouest* **2012**, *29*, 243–249. [CrossRef]
- Rouzeau, B.; Bocquet-Liénard, A.; Moulis, C. Les carreaux de pavement découverts à l’abbaye de Morimond (Haute-Marne): étude typologique, technique et archéométrique. *Revue Archéol. l’Est* **2013**, *62*, 343–366.
- Leon, Y.; Ben Amara, A.; Conte, P. Carreaux de pavement glaçurés du château du Haut Châlus (Haute-Vienne, XIII–XIV s.)—Inventaire et techniques de fabrication. In Proceedings of the Actes du 4ème Congrès International d’Archéologie Médiévale et Moderne, Paris, France, 3–8 September 2007; pp. 131–152.
- De Bonis, A.; Cultrone, G.; Grifa, C.; Langella, A.; Leone, A.P.; Mercurio, M.; Morra, V. Different shades of red: The complexity of mineralogical and physico-chemical factors influencing the colour of ceramics. *Ceram. Int.* **2017**, *43*, 8065–8074. [CrossRef]
- Jordanova, N.; Jordanova, D.; Barrón, V.; Lesigyski, D.; Kostadinova, M. Rock-magnetic and color characteristics of archaeological samples from burnt clay from destructions and ceramics in relation to their firing temperature. *Archaeol. Anthropol. Sci.* **2019**, *11*, 3595–3612. [CrossRef]
- Crupi, V.; D’Amico, S.; Denaro, L.; Donato, P.; Majolino, D.; Paladini, G.; Persico, R.; Saccone, M.; Sansotta, C.; Spagnolo, G.V.; et al. Mobile spectroscopy in archaeometry: Some case study. *J. Spectros.* **2018**, *2018*, 8295291. [CrossRef]
- Ricca, M.; Paladini, G.; Rovella, N.; Ruffolo, S.A.; Randazzo, L.; Crupi, V.; Fazio, B.; Majolino, D.; Venuti, V.; Galli, G.; et al. Archaeometric characterisation of decorated pottery from the archaeological site of Villa dei Quintili (Rome, Italy): Preliminary study. *Geosciences* **2019**, *9*, 172. [CrossRef]
- Daghmehchi, M.; Rathossi, B.; Omrani, H.; Emami, M.; Rahbar, M. Mineralogical and thermal analyses of the Hellenistic ceramics from Laodicea Temple, Iran. *Appl. Clay Sci.* **2018**, *162*, 146–154. [CrossRef]
- Medeghini, L.; Mignardi, S.; De Vito, C.; Conte, A.M. Evaluation of a FTIR data pretreatment method for principal component analysis applied to archaeological ceramics. *Microchem. J.* **2016**, *125*, 224–229. [CrossRef]
- Battcher, M.E.; Gehlken, P.L.; Steele, D.F. Characterization of inorganic and biogenic magnesian calcites by Fourier Transform infrared spectroscopy. *Solid State Ion.* **1997**, *101*, 1379–1385. [CrossRef]
- Crupi, V.; La Russa, M.F.; Venuti, V.; Ruffolo, S.; Ricca, M.; Paladini, G.; Albini, R.; Macchia, A.; Denaro, L.; Birarda, G.; et al. A combined SR-based Raman and InfraRed investigation of pigments used in wall paintings: The San Gennaro and San Gaudioso Catacombs (Naples, Italy) case. *Eur. Phys. J. Plus* **2018**, *133*, 369. [CrossRef]
- Măruțoiu, C.; Bratu, I.; Țiplic, M.I.; Măruțoiu, V.C.; Nemeș, O.F.; Neamțu, C.; Hernanz, A. FTIR analysis and 3D restoration of Transylvanian popular pottery from the XVI–XVIII centuries. *J. Archaeol. Sci. Rep.* **2018**, *19*, 148–154. [CrossRef]
- Torrent, J.; Schwertmann, U.; Fechter, H.; Alferez, F. Quantitative relationships between soil color and hematite content. *Soil Sci.* **1983**, *136*, 354–358. [CrossRef]
- Torrent, J.; Barrón, V. The visible diffuse reflectance spectrum in relation to the color and crystal properties of hematite. *Clays Clay Min.* **2003**, *51*, 309–317. [CrossRef]

27. Backes, C.J.; Cheetham, J.D.; Neff, H. The color of influence: A provenance study of hematite-based paints on early olmec carved pottery. *Cambridge Univ. Press.* **2012**, *23*, 70–92. [CrossRef]
28. Pye, K.; Blott, S.J. Particle size analysis of sediments, soils and related particulate materials for forensic purposes using laser granulometry. *Forens. Sci. Int.* **2004**, *144*, 19–27. [CrossRef] [PubMed]
29. Nagy, S.; Kuzmann, E.; Weiszburg, T.; Gyökeres-Tóth, M.; Riedel, M. Oxide transformation during preparation of black pottery in Hungary. *J. Radioanal. Nucl. Chem.* **2000**, *246*, 91–96. [CrossRef]
30. Yin, M.; Chen, Z.; Deegan, B.; O'Brien, S. Wüstite nanocrystals: Synthesis, structure and superlattice formation. *J. Mater. Res.* **2007**, *22*, 1987–1995. [CrossRef]
31. Maritana, L.; Nodarib, L.; Olivieric, L.M.; Vidale, M. Shades of black: Production technology of the black slip ware from Barikot, north-western Pakistan. *J. Cult. Herit.* **2020**, *43*, 342–355. [CrossRef]
32. Benna, P.; Tribaudino, M.; Bruno, E. The structure of ordered and disordered lead feldspar ( $\text{PbAl}_2\text{Si}_2\text{O}_8$ ). *Am. Min.* **1996**, *81*, 1337–1343. [CrossRef]
33. Del Valle, J. *Memoria de la hoja 141 (Pamplona). Mapa Geológico de España, E.1:50.000 (MAGNA)*, 1st ed.; IGME: Madrid, Spain, 1974; p. 26.
34. Pérez-Monserrat, E.M.; Fort, R.; López-Arce, P.; Álvarez de Buergo, M.; Varas-Muriel, M.J. Contribution of analytical techniques to determine the technologies used in the ceramic materials from the Former Workers Hospital of Maudes, Madrid (Spain). *J. Eur. Ceram. Soc.* **2013**, *33*, 479–491. [CrossRef]
35. Senvaitiene, J.; Smirnova, J.; Beganskiene, A.; Kareiva, A. XRD and FTIR characterisation of lead oxide-based pigments and glazes. *Acta Chim. Sloven.* **2007**, *54*, 185–193.
36. Schabbach, L.M.; Andreola, F.; Lancellotti, I.; Barbieri, L. Minimization of Pb content in a ceramic glaze by reformulation the composition with secondary raw materials. *Ceram. Int.* **2011**, *37*, 1367–1375. [CrossRef]
37. Thibodeau, A.M.; Habicht-Mauche, J.A.; Huntley, D.L.; Chesley, J.T.; Ruiz, J. High precision isotopic analyses of lead ores from New Mexico by MC-ICP-MS: Implications for tracing the production and exchange of Pueblo IV glaze-decorated pottery. *J. Archaeol. Sci.* **2013**, *40*, 3067–3075. [CrossRef]
38. Di Febo, R.; Molera, J.; Pradell, T.; Melgarejo, J.C.; Madrenas, J.; Vallcorba, O. The production of a lead glaze with galena: Thermal transformations in the  $\text{PbS-SiO}_2$  system. *J. Am. Ceram. Soc.* **2017**, *101*, 2119–2129. [CrossRef]
39. Tite, M.S.; Freestone, I.; Mason, R.; Molera, J.; Vendrell-Saz, M.; Wood, N. Lead glazes in antiquity—Methods of production and reasons for use. *Archaeometry* **2007**, *40*, 241–260. [CrossRef]
40. Hurst, D.; Freestone, I. Lead Glazing Technique from a Medieval Klin Site at Hanley Swan, Worcestershire. *Mediev. Ceram.* **1996**, *20*, 13–18.
41. Molera, J.; Pradell, T.; Salvadó, N.; Vendrell-Saz, M. Interactions between Clay Bodies and Lead Glazes. *J. Am. Ceram. Soc.* **2001**, *84*, 1120–1128. [CrossRef]
42. Ben Amara, A.; Schvoerer, M. Interactions between lead glazes and bodies: Research on the mode of application of the glazing mixture. *Institución Fernando el Católico. In Proceedings of the 34th International Symposium on Archaeometry, Zaragoza, Spain, 3–7 May 2006*; pp. 399–404.
43. Yonga, B.; Yanga, T.; Yanga, B.; Xu, B.Q.; Liua, D.C.; Zhang, W. Preparation of lead oxide from the recycled lead carbonate by vacuum T decomposition technology. *Vacuum* **2019**, *167*, 445–451. [CrossRef]



## Article

# Fernandina Wall of Lisbon: Mineralogical and Chemical Characterization of Rammed Earth and Masonry Mortars

Ricardo Infante Gomes <sup>1</sup>, António Santos Silva <sup>2,\*</sup> , Leandro Gomes <sup>3</sup> and Paulina Faria <sup>1,\*</sup> 

<sup>1</sup> Civil Engineering Research and Innovation for Sustainability (CERIS), Department of Civil Engineering, NOVA School of Science and Technology, NOVA University of Lisbon, 2829-516 Caparica, Portugal; ri.gomes@campus.fct.unl.pt

<sup>2</sup> National Laboratory for Civil Engineering, Av. do Brasil 101, 1700-066 Lisboa, Portugal

<sup>3</sup> Department of Civil Engineering, NOVA School of Science and Technology, NOVA University of Lisbon, 2829-516 Caparica, Portugal; lf.gomes@campus.fct.unl.pt

\* Correspondence: ssilva@lnec.pt (A.S.S.); paulina.faria@fct.unl.pt (P.F.)

**Abstract:** This paper aims to provide information on rammed earth and masonry mortars of the Fernandina defensive Wall of Lisbon, Portugal, which was built in the second half of the 14th century. No previous information exists concerning the materials and construction techniques used in this defensive structure, which is essential to increase knowledge and to define requirements for a reliable conservation. An experimental campaign was carried out on samples extracted in nine different sections of this structure, which were analyzed by X-ray diffraction, thermogravimetry and wet chemical analysis. Calcitic lime was employed as a binder in the stone masonry bedding mortars and was also identified in the rammed earth samples. The results obtained allowed us to verify the use of different binders and aggregates, with heterogeneous binder/aggregate ratios, in different sections of the Wall. To reduce time for lime preparation and to achieve a durable lime matrix, most probably quicklime was used and hydrated together with the moistened earth to produce rammed earth and masonry bedding mortars.

**Keywords:** defensive structure; stone masonry bedding mortar; rammed earth; air lime; architectural heritage

**Citation:** Gomes, R.I.; Santos Silva, A.; Gomes, L.; Faria, P. Fernandina Wall of Lisbon: Mineralogical and Chemical Characterization of Rammed Earth and Masonry Mortars. *Minerals* **2022**, *12*, 241. <https://doi.org/10.3390/min12020241>

Academic Editors: Daniel Albero Santacreu, José Cristóbal Carvajal López and Adrián Durán Benito

Received: 22 December 2021

Accepted: 6 February 2022

Published: 13 February 2022

**Publisher's Note:** MDPI stays neutral with regard to jurisdictional claims in published maps and institutional affiliations.



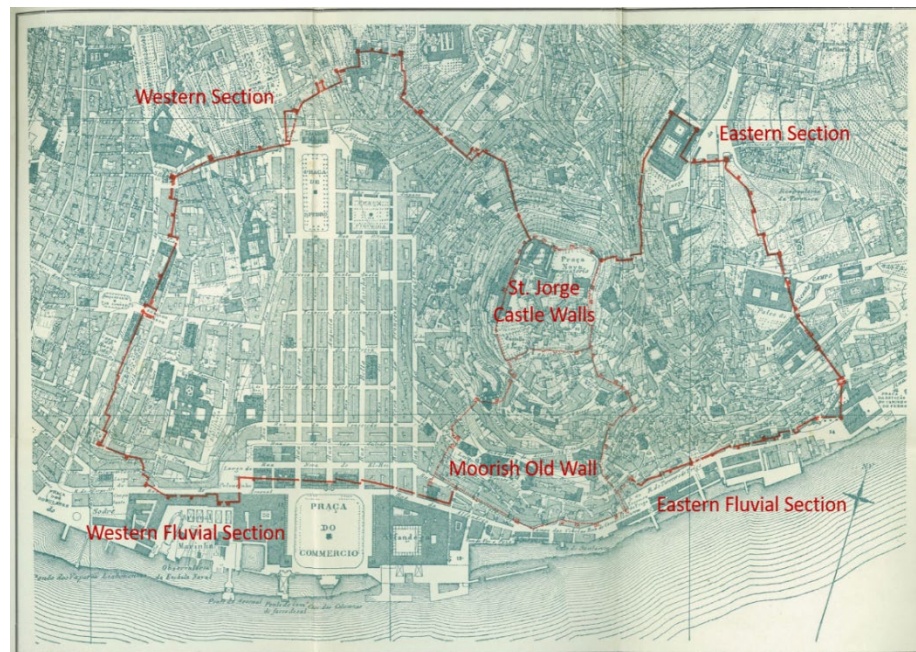
**Copyright:** © 2022 by the authors. Licensee MDPI, Basel, Switzerland. This article is an open access article distributed under the terms and conditions of the Creative Commons Attribution (CC BY) license (<https://creativecommons.org/licenses/by/4.0/>).

## 1. Introduction

The construction of the Fernandina Wall in Lisbon dates back to the second half of the 14th century [1,2]. It was built in response to the need to ensure the city's protection in a period of continuous and intense growth, but also in response to enemies' attacks. There was a previous defensive wall in the city, called the Moorish Wall of Lisbon, that was no longer able to accomplish the desired protection of the city due to city enlargement (Figure 1) [3,4]. Therefore, king Fernando I of Portugal (1367–1383) decided that a new defensive wall was needed and ordered its urgent construction. In addition to the main structure of walls, this rampart included several towers, turrets (*cubelos*), entrances and small entrances (*postigos*).

The layout of the Fernandina Wall developed in line with the dense growth seen in various surrounding areas of Lisbon, in the 14th century. The Wall can, therefore, be divided into four main sections: the Eastern Section, the Western Section and two Marginal or Fluvial Sections, having a total extension of 4.69 km (Figure 1). These main sections delineated two large pockets which enclosed the city's existing old walls—namely, the Moorish Wall of Lisbon (which formed the central pocket) and the walls of Saint Jorge Castle (Figure 1). The Fernandina Wall is, thus, defined to the East by the Eastern section, the first to be built, with an extension of about 1.38 km, and to the West by the Western section, extending 2.05 km. To the North, the layout of the Wall is contained between the

Eastern and Western sections and, to the South, the Eastern and Western Marginal and Fluvial sections extend around 0.72 km and 0.54 km, respectively [2] (Figure 1).



**Figure 1.** Surveying of St. Jorge Castle Walls, the Moorish Old Wall and the Fernandina Wall of Lisbon layouts carried out in 1956/58 (adapted from Vieira da Silva, 1987 [2]), with the location of its sections.

Regarding the type of construction and materials used to build the Fernandina Wall, the existing information is very scarce. According to Vieira da Silva [2], rubble stone masonry and rammed earth are the main materials. Complementary sections were composed by three-leaves, consisting of two parallel walls, each with a thickness of about 0.5 m, filled with a compacted earth core, presenting a total thickness of between 1.75 and 2.20 m.

Rammed earth (RE) consists of moistened earth compacted in consecutive layers within temporary frameworks, forming a monolithic wall. The chemically unstabilized RE technique functions with clay acting as the only binder; in stabilized rammed earth, other binders can be added to the earth mixture [5], generally to improve durability to weathering. With that aim, lime was frequently used to stabilize rammed earth in old structures with military and defensive purposes [6,7]. Therefore, the technique is called military RE. This technique was employed in several structures around the World, and in particular in the Iberian Peninsula, with still-existing structures such as the Castle of Paderne [6], the Juromenha Fortress [8] and the Silves Castle [9] in Portugal, and the Alcázar of King Don Pedro I [10], the Alcazaba or the ramparts of Málaga and the ramparts of Sevilla [11], the Castle of Atalaya [12] and the Monumental Complex of the Alhambra [13] in Spain. The compacted earth core of the three-leaf walls was similar to RE, but the exterior stone walls acted as permanent frameworks.

Geometrically, the Wall was composed of several elements that coordinated with the various sections of the walled structure, with prominence given to the imposing towers, turrets and gates. The Wall height varied depending on the type of architectural element used, 8 m being the most common, reaching a maximum of 15 m where the towers extend upwards [2].

According to Vieira da Silva [2], the Wall included 76 towers, one of the main constituent elements that played a key role in the city's defense, representing robust elements that, in most cases, exceeded the height and width of the adjacent walls. These towers were generally massive, except for those along the Eastern section flanking the river, some

of which are hollow inside, and each covered a base area of  $8\text{ m} \times 8\text{ m}$ . Most are now destroyed, but some were incorporated in buildings. In contrast, the smaller turrets (*cubelos*) covered a base area of  $5\text{ m} \times 5\text{ m}$  and, although of varying lengths, they never extended above the height of the Wall [14]. The turrets present three visible vertical surfaces projecting outwards and are attached to the Wall by their fourth side [15,16]. Some can still be found, mainly in the Eastern section, often integrated in residential buildings.

Being the main connecting axis between the entrances and exits of the city of Lisbon, the Fernandina Wall would have contained around 35 gates, in the form of robust, fortified large-scale entrances [2]. Many consisted of a square or rectangular walled enclosure with one or two openings, in the front and the back, the front-facing gate being embellished on both sides by defense towers. Many of these entrances were later demolished and turned into arches, often to overcome difficulties related to circulation and accessibility of the city [2]. The smaller gates (*postigos*) consisted of entrances located near one or two towers or between two turrets. They offered access to the city, facilitating security control in comparison with the larger gates. Not all were built when the walled structure was first constructed. Many were only opened after the construction was completed and are still visible today.

In 1910, the Fernandina Wall of Lisbon was recognized and classified as a national monument of public interest (Portuguese register: IPA PT031106120023). At present, remnants of the Fernandina Wall are still evident in several parts of Lisbon given the Wall's large-scale geometric characteristics, making it an important component of the city's architectural heritage.

The rapid growth in the rehabilitation of Lisbon's historical and urban center, and of its built heritage, is becoming increasingly noticeable. Faced with this trend, more rigorous and technical knowledge is required to ensure the conservation of archaeological heritage, namely that the materials and techniques used nowadays do not compromise the identity and originality of the old structures. It is, thus, of fundamental importance to consider the conservation interventions carried out to this day when proceeding with the characterization of the Fernandina Wall, in terms of its original materials and those used in subsequent interventions. Therefore, this article intends to collect and describe the interventions that were performed in some sections of the Wall over the past years, the description of some sections of the Wall, the collection of samples and the mineralogical characteristics that the materials employed in the construction of the Fernandina Wall of Lisbon present nowadays. That data is of fundamental importance in the conservation and maintenance of this type of architectural heritage.

## 2. Interventions in the Wall over the Last Years

The Wall has undergone several interventions in recent years, many of which have also targeted the old buildings confining it. Many of them are not (or not yet) documented. As a result, some sections of the Wall are now seen with new renders and plasters.

To the authors' knowledge, the interventions that were documented were carried out in the last 20 years. The first documented intervention took place in 1998, to the Western section of the Fernandina Wall, namely in the *Jogo da Péla* tower (Figure 2), near the *Martim Moniz* square. It was carried out by geologist Rui Brito in the context of his dissertation, in straight collaboration with the Lisbon City Council. It was intended to provide information on plastering and jointing mortars used between stone masonry blocks, as well as on the rocky substrate at the site of the tower. Laboratory tests revealed that the original mortars were mainly composed of air lime ( $\text{CaCO}_3$ ) and silica sand. Based on a macroscopic examination, the stones used for the masonry were classified into four different types: two sandstones, one fine-grained and the other very fine-grained, and marl and shell limestones [17].





**Figure 2.** Aerial mapping showing the locations where interventions were carried out (identified by capital letters) and of the section's location on the Wall (identified by numbers). Notation: A—*Jogo da Péla* tower; B—*António Maria Cardoso* street; C—*São Vicente de Fora* parish; D—*Graça* parish; E—*Chafariz de Dentro* square; F—*Terreiro do Trigo* street; 1—Independency Palace; 2—*Calçada de Santana*; 3—*Calçada do Jogo da Péla*; 4—Rose Palace; 5—*Bragança Terraces* complex; 6—*Corpo Santo* Hotel; 7—*Gil Vicente* school; 8—*Graça* square; 9—*Terreiro do Trigo* street.

The 2014 intervention on *António Maria Cardoso* street, in the historic center of Lisbon (Figure 2), focused on identifying the conservation state of the Western section of the Wall. Recommendations were made in order to preserve and restore the original characteristics of the walled structure. Inside one building, rammed earth main walls were identified in a reasonable state of preservation, including the concavities of the wooden needles inherent to its construction. Extending outside the building, one of the sections of the Wall presented a severe state of degradation, mainly owing to the impact of atmospheric agents. Air lime mortar and small pieces of bricks were, respectively, used to fill the existing smaller and larger gaps. After filling these gaps, the walls were rendered with two layers of natural hydraulic lime (NHL) mortar, the first layer with a proportion of 1:3 (NHL: sand) in mass, and the second of 1:4. In addition, the cement mortar render found in the interior of the building was removed and replaced with NHL mortars [18].

In 2016, several interventions were carried out to the Eastern section of the Wall, particularly in the *São Vicente de Fora* parish (Figure 2). The first intervention arose due to the construction of sanitary facilities in a tourist accommodation that was in direct contact with the Wall. Rammed earth was proven to be the construction technique used in this section. Although a visual analysis of the wall did not provide information concerning the composition of the plasters, which were possibly the original ones, the notorious exposure to which the rammed earth walls were subjected was very evident. It was also observed that there were gaps at the base of the RE walls which, due to the lack of protection, accentuated the material degradation of the structure. Therefore, it was proposed to reinforce the stone masonry basement of the rammed earth walls with a bedding NHL mortar. The application of an NHL mortar of a color similar to that of the existing ones was additionally recommended, aiming to fill and repair cracks, holes and joints. Once the RE showed signs of moisture, it was suggested that a hollow brick masonry wall (coated from the inside with tiles or other similar coat) should be constructed between the Wall and the compartments in contact with it, to prevent future moisture problems [19]. However, if the air layer between

the RE wall and the indoor masonry wall is not ventilated, this intervention can introduce high levels of relative humidity in that layer and damage the RE wall.

In another intervention, carried out in 2016 in the same Eastern section of the Wall, a preliminary visit was conducted to the site located in *Graça* parish, currently occupied by a car park (adjacent to the *Gil Vicente* School North Wall, not far from *Graça* square), which allowed for the performance of a visual analysis and several archaeological surveys (Figure 2). Some RE sections were found to be coated with non-original cement-based renders and, at the very top of the wall, brick capstones applied long after its construction were observed. The archaeological surveys found traces of a small entrance (postigo) and, through the analysis of a west facing Wall sector, it was possible to establish the settlement of the first layer of RE in the site's geological substrate [20].

The archaeological interventions to the Fernandina Wall involved four surveys. In the first, carried out in the west wall of this Eastern sector, the rocky substrate that constitutes the Wall was visibly altered. A lengthier survey of the same location revealed that it was a turret, the third present in this section of the Wall. The second survey confirmed the heterogeneity of the material composition of the Wall, namely in terms of the rendering mortars, with different constituent elements. Beneath the render, the original structure of the Wall revealed an RE construction, which presented four distinct layers of varying composition and thickness. The Wall's constructive system was, thus, visualized and identified, noting the upper and lower limits of the formworks, the joints and some voids left by the formworks [8]. In the third and fourth surveys carried out in the northern section of this Eastern sector and inside a small opening, respectively, the existence of RE was once again confirmed, this time in a turret, and in a small entrance made of rigged limestone masonry.

During the archaeological and urbanistic works carried out between 2007 and 2008 in the *Chafariz de Dentro* square, excavations allowed access to the Eastern fluvial section of the Fernandina Wall. One of the two towers in this section was identified by observation of a stairway path along the top of the Wall. The Wall's foundation ditches were also uncovered by these excavation works. It was found that wooden planks had been used as formworks and that timber had also been used to build other elements, such as scaffolding and shores (props) [21]. Hence, it was possible to gain greater knowledge on the methods employed in the construction of the Wall.

In 2016, main walls of the Eastern fluvial section were discovered during rehabilitation works on buildings located on *Terreiro do Trigo* street (Figure 2). Concerning the RE walls, chipping was performed, which permitted identification of the formworks used, as well as the voids left by the formworks' pieces at the time of the Wall's construction. Several mortars were identified, mostly lime mortars with ceramic fragments, siliceous sand and calcareous aggregates. Nevertheless, some of the identified materials are non-original, being applied over the years, sometimes without the necessary compatibility with the original materials. In the north-facing section of this Eastern fluvial section, the internal part of the Wall was noted as being composed of irregular stone masonry with mortars with ceramic and calcareous aggregates, pebbles and bone fragments [22].

Many of the interventions carried out were archaeological, to document the site and structures, and did not involve the characterization of materials. Therefore, it was intended to proceed to a material characterization of the employed mortars and the RE. In this paper, a chemical and mineralogical characterization is presented. In a forthcoming paper, it is foreseen to present a physical-mechanical characterization.

### 3. Samples Collection and Localization

Sections of the Wall are scattered throughout the city of Lisbon, with the authorization and support of the Directorate General for Cultural Heritage (DGPC) and Municipal Council of Lisbon. The intervention works described on Section 2 allowed for a preliminary assessment of the visual features of the Fernandina Wall in different sites.

Nine of these (Figure 2) were analyzed in the present work and are referred to in the following sub-sections.

### 3.1. *Palácio da Independência (Independency Palace)—Masonry Wall*

Built in 1467, the Independency Palace, classified as a national monument, is located in *São Domingos* square, just off *Rossio* square, at the very heart of the city of Lisbon (identified by “1” in Figure 2). This national monument is of great historical and political importance and houses several institutions and museums.

At the north of the palace, there is a garden, where a section of the Wall is located, of about 20 m length, and a staircase (most probably from a former round path) at its top. This remnant belongs to the Western section of the Wall, composed mainly by a rubble stone masonry intensely exposed to atmospheric action.

This may explain the degradation of the surface of the southern exposed Wall (Figure 3a), which lacks protective render and joint mortars. The various interventions carried out to this section, including the inclusion of the staircase and repair works using, eventually, inappropriate mortars, may also have contributed to the deteriorated conservation state of this original Wall section.



**Figure 3.** Case studies in Wall Western section: Independency Palace (a), *Calçada de Santana* (b), *Jogo da Péla* (c) and Rose Palace (d).

### 3.2. *Calçada de Santana—Turret*

This turret is integrated in a private building located on *Calçada de Santana* (Figure 2). The creation of this *Calçada* (name meaning sloping street) involved the destruction, in 1676, of the *Postigo de Santana*—an opening in the Wall, located between the *Santana* turret and the entrance.

The turret in limestone masonry, with an implementation area of 5.5 m × 9.0 m and a height of 11 m (Figure 3b) [23], contains, at its top, a 36 m<sup>2</sup> terrace with walls facing east and west. In the past, elements such as chicken coops and flower beds diminished the authenticity of the structure. As previously mentioned, the *Fernandina* turrets were as high as the walls, i.e., about 8 m tall. The fact that the *Santana* turret is taller suggests that an extension was added at a later date.



### 3.3. Jogo da Péla—Tower

The tower of *Jogo da Péla*, placed in the sidewalk with the same name, is located near *Martim Moniz* square, an important landmark of Lisbon located between *Arco da Graça* street and *Calçada do Jogo da Péla* (Figure 2). It is one of the better-preserved elements of the Wall, found in the Western section. Nowadays, it holds no visible continuity with other sections, either to the west or to the east. This tower, made with limestone masonry and air lime mortar, is the only completely isolated example that still preserves some of its original features (Figure 3c).

Several works have been carried out on it over recent years, such as the demolition of nearby old buildings and the renovation of infrastructures. However, some new buildings were also built nearby, causing a major impact on the surrounding area.

Regarding the tower geometry, its height varies between 8 m to the east and 17.5 m to the west [17]. At the top of the tower, there is an excavated area of approximately 2.5 m × 3.0 m and about 4 m high, executed during the archaeological interventions mentioned by Leitão, in 2014 [24].

A variety of projects involving the integration and musealization of the tower, which is currently property of the Municipal Council of Lisbon, are underway.

### 3.4. Palácio da Rosa (Rose Palace)—Masonry Wall

Rose Palace, classified as a monument of public interest, is located on the Western section of the Fernandina Wall, near Lisbon's *São Jorge* Castle (Figure 2). With its irregular L-shaped layout, the palace was architecturally modified and rehabilitated several times during the XVIII century [25].

A section of the Fernandina Wall in rubble stone masonry is present in the palace gardens (Figure 3d). Archaeological works being carried out in the palace exposed the foundations of the structure and discovered a tunnel dug inside the wall.

### 3.5. Terraços de Bragança Complex—Stone Masonry and Rammed Earth Walls

The *Terraços de Bragança* residential and commercial complex, located on Alecrim street (Figure 2), is composed of eight five-story buildings. Designed by the renowned Portuguese architect Siza Vieira, its construction began in 2003. During the construction works, a section of the Fernandina Wall was discovered and remains one of the most representative existing examples of the Western fluvial section of the Wall made in limestone masonry and RE (Figure 4a).



**Figure 4.** Case studies in Wall Western fluvial section: *Terraços de Bragança* Complex (a) and *Corpo Santo* Hotel (b).

### 3.6. Corpo Santo Hotel—Limestone Masonry

Located in the historic city center, close to the Tagus River (Figure 2), the *Corpo Santo* Hotel was built in 2015. During the archaeological works conducted previously to its

construction, a large number of archaeological remains, structures of the Fernandina Wall and surrounding structures were identified (Figure 4b) [26]. The most impressive is the *João Bretão* tower, built with limestone ashlar masonry. The concern with the preservation of Portuguese historical heritage by *Corpo Santo* Hotel has already been recognized with the achievement of several international awards.

### 3.7. Graças Square—Rammed Earth Wall

Located in the neighborhood of *Graça*, the square is one of the most visited touristic sites in the city of Lisbon. The square was outside the boundaries of the Old Moorish Wall; however, with the construction of the Fernandina Wall, it became part of the city and, thus, became protected. Remnants of the walled structure in RE are visible in the fire station, located close to the square, and in the square itself (Figure 5a).



**Figure 5.** Case studies in Eastern section: *Graça* square (a) and *Gil Vicente* school (b).

### 3.8. Gil Vicente School—Masonry and Rammed Earth Wall

The *Gil Vicente* School is located in *Graça* parish, one of the traditional neighborhoods of Lisbon, as previously mentioned. On the school north limit area, there is a 50 m long sector of the Eastern section of the Wall, well preserved and relatively protected (Figure 5b).

Several characteristic elements of the Wall can be found in this section, mainly walls and two turrets in RE, with the corners and base in regular limestone masonry [23].

### 3.9. Buildings Number 6–26 on Terreiro do Trigo Street—Masonry Wall

During the rehabilitation works on the buildings numbered 6 to 26 on *Terreiro do Trigo* street (Figure 2), several traces of the Fernandina Wall in rubble stone masonry were found, namely main walls, one tower and one small entrance. These buildings are located along the Eastern section of the Wall, close to Tagus River.

## 4. Materials and Experimental Methods

### 4.1. Materials

The samples were extracted manually or mechanically by core drilling, depending on the materials compactness. In five sites presented in Section 3, a total of 13 cylindrical cores were collected, namely in *Jogo da Péla* tower (3 cores), *Calçada de Santana* turret (1 core), *Gil Vicente* School (3 cores), *Bragança Terraces* complex (4 cores) and in the *Corpo Santo* Hotel (2 cores).

The terminology used for the samples' identification (Table 1) is based on the initials of the local designation: Independence Palace (IP), *Calçada de Santana* (CS), *Jogo da Péla* tower (JP), *Bragança Terraces* Complex (BT), *Corpo Santo* Hotel (CSH), *Gil Vicente* School (GVS), *Graça* square (GS) and *Terreiro do Trigo* street (TTS). The samples nomenclature also includes the identification of the Wall's element: M for main wall, T for tower, P for small gate (*postigo*) and C for turret (*cubelo*). Additionally, each sample was identified by a sequential number, which can include another number indicating the number of the specimen. For example, JP-T1-1 corresponds to the specimen 1 from sample JP-T1 collected in *Jogo da Péla* tower.

**Table 1.** Location of the samples collection and their identification.

Wall's Section	Location	Samples Identification
Western	Independency Palace <i>Calçada de Santana</i>	IP-M1
		CS-C1
	<i>Jogo da Péla</i> tower	JP-T1-1
		JP-T1-3
		JP-T3-3
		JP-T4
Rose Palace	RP-M3	
	RP-M6	
Western Fluvial	<i>Bragança Terraces</i>	BT-T1-2
		BT-M1-3
	<i>Corpo Santo</i> Hotel	BT-M2-4 CSH-T2-1
Eastern	<i>Graça</i> Square	GS-M1
	<i>Gil Vicente</i> School	GVS-M1-2
		GVS-M2-2
Eastern Fluvial	<i>Terreiro do Trigo</i> Street	TTS-T1
		TTS-M1
		TTS-P1

After collection, the samples identified in Table 1 were conditioned in a climatic room at a temperature of  $20 \pm 2$  °C and 65% relative humidity. After, the samples were prepared analysis by X-ray diffraction, thermogravimetry and wet chemical analysis.

#### 4.2. Methods

For analysis, two fractions were prepared as described by Santos Silva et al. [21]. A binder rich fraction, designated as BF, was obtained by disaggregating the sample, removing the aggregate particles without breaking them. The disaggregated portion of the paste was then milled and sieved through a 106 µm mesh sieve [22], and then stored. Additionally, to obtain the overall fraction (OF), a representative portion of the sample (about 20 g of the whole sample, without aggregate removal) was milled/grinded using a ball mill until all material passed a 106 µm sieve. After this process, the fraction obtained was homogenized using a spatula and was also stored.

A Philips PW3710 X-ray diffractometer was used to perform the mineralogical analysis. The XRD was operated at 35 kV and 45 mA with a scanning rate of  $0.05^\circ$   $2\theta/s$ . The two fractions of the sample were used: the fine fraction, to determine the mineralogical composition of the binder, and the overall one, which includes all mortar constituents.

The thermogravimetric analysis and differential thermal analysis (TGA/DTA) were carried out using simultaneous DTA-TGA thermal analyzer Setaram TGA92. The samples of the overall fraction were placed in a platinum crucible and heated from room temperature to 1000 °C at a uniform rate of 10 °C/min under argon atmosphere (3 L/h). By this analysis, it is possible to evaluate the mass variations associated with dehydration, dihydroxylation and decarbonation processes, occurring at specific temperature intervals. Decarbonation occurred in the temperature range of 550–900 °C, which enables one to obtain the carbonates content, expressed as a percentage of CaCO<sub>3</sub>, and which can be attributed, in the absence of limestone aggregates, to the carbonated lime content.

The siliceous aggregate content was obtained from the determination of the acid insoluble residue, which was performed by the attack of representative mortar sample with a hydrochloric acid solution with a ratio of 1:10 (H<sub>2</sub>O:HCl). The sample used was previously disaggregated, in an amount of 10–15 g of disaggregated fragments, taking care not to break the aggregate particles; the existence of limestone aggregates and/or shells was verified, and removed manually whenever present. Furthermore, a visual analysis was carried out to record the consistency and presence of lime lumps, coal, ceramics and fibers,

among other materials. Previously to the acid attack, the samples were dried in a ventilated oven at a temperature of 105 °C, for a period of time not less than 12 h. The material obtained in the insoluble residue, plus the coarse limestone grains manually separated, were then placed in a RETSCH electromagnetic sieve shaker equipment, for 10 min, with a series of ASTM sieves (4.5 mm to 0.063 mm), to obtain the granulometric curves of the aggregates [27].

## 5. Results and Discussion

### 5.1. XRD Analysis

A total of 18 samples were analyzed; the results are presented in Tables 2–4. The mineralogical qualitative composition of the mortars (Tables 2 and 3) is rich in quartz, feldspars and mica, therefore, indicative of the use of siliceous sands [23]. The quartz and feldspar ratio is quite variable among the different case studies analyzed, which is an indication of the use of different sand pits. The diffractograms are presented in Figure 6 and Figures S1–S17 in the Supplementary Materials.

**Table 2.** XRD composition of mortars from *Jogo da Péla* and Rose Palace.

Samples		Quartz	Feldspars	Mica	Calcite	Dolomite	Gypsum	Calcium Aluminate Hydrate	Ettringite	Tobermorite
JP-T1-1	OF	++/+++	tr	?	+++	-	-	-	-	-
	BF	+ /+++	tr	-	+++	-	-	-	-	-
JP-T1-3	OF	++/+++	tr	tr	+++	tr	-	-	-	-
	BF	+ /+++	+	tr/+	+++	-	-	-	-	-
JP-T3-3	OF	++/++	tr/+	tr	++	tr	-	+	?	-
	BF	+ /+++	+	tr	+++	-	-	+	+	-
JP-T4	OF	+++	+ /+++	+	++	tr	-	-	-	-
	BF	++	?	-	+++	-	-	-	-	-
RP-M3	OF	+++	++	+	++/+++	-	tr/+	-	-	-
	BF	+ /+++	+	?	+++	-	tr/+	-	-	-
RP-M6	OF	+++	++	+	++/+++	-	-	-	-	-
	BF	+ /+++	+	?	+++	-	tr	-	-	tr

Notation: OF—Overall Fraction; BF—Binder rich Fraction; +++ high proportion (predominant compound); ++ medium proportion; + low proportion; tr—traces; - undetected; ? doubts of the presence.

**Table 3.** XRD composition of mortars from Independence Palace, *Calçada de Santana*, *Terraços de Bragança* Complex, *Corpo Santo* Hotel and *Terreiro do Trigo* Street.

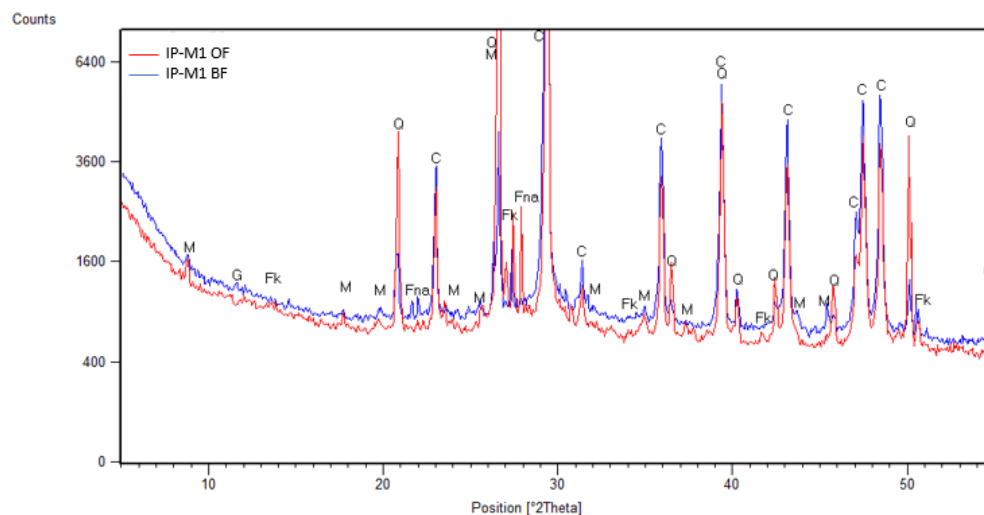
Samples		Quartz	Feldspars	Mica	Talco	Kaolinite	Calcite	Gypsum	Calcium Aluminate Hydrate	Ettringite	Weddellite
IP-M1	OF	+++	+	tr/+	-	-	+++	-	-	-	-
	BF	+ /+++	tr	tr	-	-	+++	?	-	-	-
CS-C1	OF	++/+++	+ /+++	+	-	-	+++	-	-	-	-
	BF	+ /+++	tr	-	-	-	+++	?	-	-	-
BT-T1-2	OF	++	tr/+	tr/+	-	?	+++	-	tr/+	tr	-
	BF	+ /+++	tr	-	-	?	+++	-	tr/+	+	+
CSH-T2	OF	+++	tr	tr	-	-	++/+++	-	-	-	-
	BF	+ /+++	?	?	tr	-	+++	-	-	-	-
TTS-T1	OF	++/+++	++	+	-	tr	++/+++	?	-	-	-
	BF	+ /+++	tr	tr	-	-	+++	-	-	-	-
TTS-M1	OF	+++	tr	tr	-	-	++/+++	-	-	-	-
	BF	++	+	tr	-	-	+++	tr	-	-	-
TTS-P1	OF	+++	+ /+++	tr	-	-	++/+++	-	-	-	-
	BF	+ /+++	+	tr	-	-	+++	-	-	-	-

Notation: OF—Overall Fraction; BF—Binder rich Fraction; +++ high proportion (predominant compound); ++ medium proportion; + low proportion; tr—traces; - undetected; ? doubts of the presence.

**Table 4.** XRD composition of the rammed earths from *Terraços de Bragança* Complex, *Graça* Square and *Gil Vicente* School.

Samples		Quartz	Feldspars	Mica	Kaolinite	Calcite	Dolomite	Anhydrous Calcium Silicates
BT-M1-3	OF	+++	+ / ++	+	tr	++ / +++	-	-
	BF	++	+	+	tr	++ / +++	-	-
BT-M2-4	OF	+++	++	+ / ++	tr	++ / +++	-	-
	BF	++	+ / ++	+	tr	++ / +++	-	-
GS-M1	OF	+++	+ / ++	+ / ++	-	+++	-	-
	BF	++	tr	+ / ++	-	+++	-	tr
GVS-M1-2	OF	+++	++	+	-	+++	tr	-
	BF	+++	+ / ++	+	-	++	tr	-
GVS-M2-2	OF	+++	+	+	-	+++	?	-
	BF	+++	+	+	-	+++	-	-

Notation: OF—Overall Fraction; BF—Binder rich Fraction; +++ high proportion (predominant compound); ++ medium proportion; + low proportion; tr—traces; - undetected; ? doubts in presence.

**Figure 6.** Diffractograms of sample IP-M1 (OF—overall fraction; BF—binder fraction). Notation: M—Mica, G—Gypsum, Fk—Potassium feldspar, C—Calcite, Q—Quartz.

Concerning the paste compounds of the mortars, the main compound detected was calcite (Figure 6), thus, confirming the use of air lime as a binder. Nevertheless, in some mortars, such as JP-T3-3, RP-M6 and BT-T1-2, some hydrated calcium silicates and calcium aluminates were detected, thus, suggesting the presence of a hydraulic binder. The origin of these hydraulic compounds is not possible to explain at this stage, but they could be attributed to recent interventions or due to the development of pozzolanic reactions between the binder and some siliceous constituents of the aggregates.

Mortars RP-M3, RP-M6 and TTS-M1 showed traces of gypsum, while BT-T1-2 present traces of weddellite; thus, both compounds indicated degradation processes [24].

Regarding RE samples (Table 4), the main compounds present are quartz, feldspars, mica and calcite. Hence, it can be confirmed that the use of siliceous aggregates also in the RE samples, most probably as earth component. The identification of calcite in the binder fraction confirms that the constructive technique used was the military RE [25], as the earth was stabilized with air lime. However, in terms of clayish minerals, such as mica and kaolinite, it can be seen the high variability of its proportion, thus confirming the employment of different earths in the areas analyzed, most probably picked in different

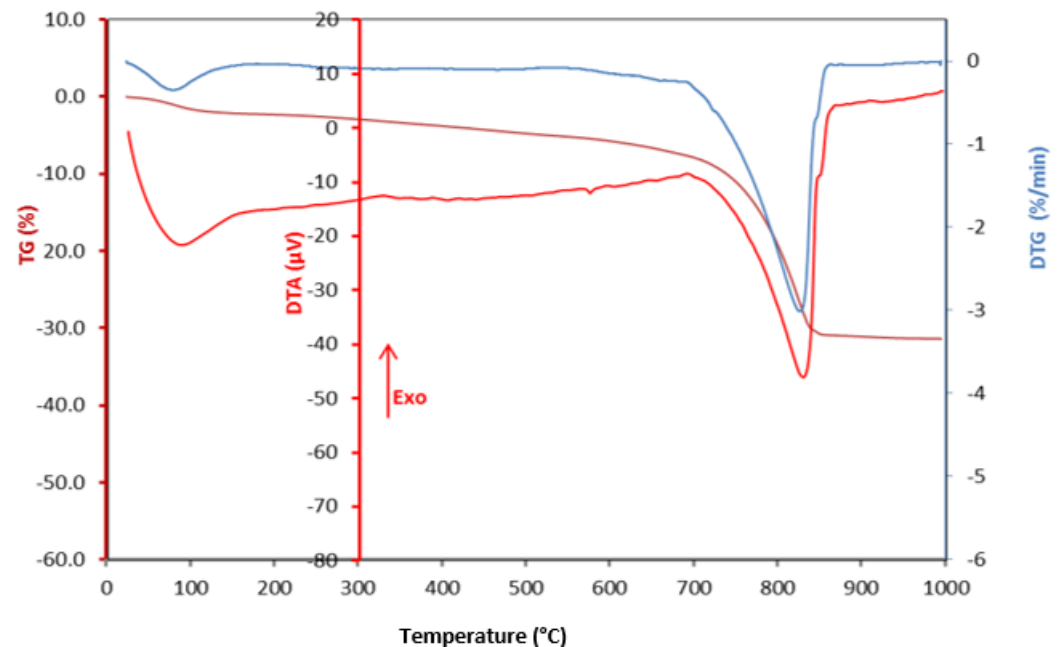
pits due to the urgent and fast building of the Wall (accomplished in very few years) and high raw materials consumption.

It is also worth mentioning the presence of anhydrous calcium silicates in the GS-M1 sample, compounds usually found in cement mortars. These silicates may be due to cement mortars that would have been applied in recent repairs, but that have presently been removed.

### 5.2. TGA/DTA Analysis

From the TGA/DTA charts obtained, presented in Figure 7 and Figures S18–S34 (Supplementary Materials), and according to the mineralogical compositions of the mortars, three mass losses ranges were considered [26] (Table 5):

- i. 25 to ~200 °C—mass loss due to dehydration of free or absorbed water, and hydration and zeolitic water;
- ii. ~200 to 500 °C—mass loss due essentially to the dihydroxylation of clay minerals and of calcium silicate hydrates;
- iii. 500 to 900 °C—mass loss due to the decarbonation of carbonates.



**Figure 7.** TGA/DTG/DTA charts of *sample* TTS-T1.

The TGA/DTA charts present a behavior in accordance with the mineralogical compositions previously obtained, with the main mass losses attributed to the dehydration of hydrated calcium silicates and calcium aluminates (e.g., samples JP-T3-3, BT-T1-2), and to the decarbonation of calcite and dolomite. The TTS\_T1 sample showed the highest mass loss, which is essentially related to its highest value in the decarbonation zone (500 to 900 °C)—Figure 7.

Regarding the RE samples, the same three temperatures ranges were considered for TGA analysis (Table 6). The higher mass losses were obtained in the decarbonation zone, as expected. The mass losses regarding the range covering ~200 to 500 °C, and according to XRD data obtained, are essentially due to the dihydroxylation of clay minerals [27]. Therefore, it is confirmed that main losses are due to the presence of hydrated and carbonated minerals.



**Table 5.** Sample mass losses obtained by TGA for mortar samples.

Samples	Mass Loss [%] per Temperature Range [°C]			Loss of Ignition * [%]
	25 to ~200	~200 to 500	500 to 900	
IP-M1	1.16	1.53	24.05	26.91
CS-C1	2.35	1.91	18.85	23.15
JP-T1-1	1.36	1.28	25.23	27.96
JP-T1-3	1.09	1.09	24.50	26.79
JP-T3-3	5.29	2.13	20.31	27.90
JP-T4	0.72	1.23	20.51	22.50
RP-M3	0.61	1.29	16.28	18.47
RP-M6	4.33	4.20	6.95	16.59
BT-T1-2	5.87	1.63	17.18	24.87
CSH-T2-1	1.98	0.94	21.13	24.08
TTS-T1	2.40	2.44	26.32	31.38
TTS-M1	1.34	1.60	22.26	25.17
TTS-P1	0.45	0.78	21.04	22.32

\* mass loss obtained between 25 and 1000 °C.

**Table 6.** Sample mass losses obtained by TGA for rammed earth samples.

Samples	Mass Loss [%] per Temperature Range [°C]			Loss of Ignition * [%]
	25 to ~200	~200 to 500	500 to 900	
BT-M1-3	8.21	2.12	7.22	17.84
BT-M2-4	3.09	2.18	7.03	12.74
GS-M1	0.69	0.54	9.17	10.38
GVS-M1-2	3.71	3.27	20.32	27.68
GVS-M2-2	7.27	4.91	18.46	29.64

\* mass loss obtained between 25 and 1000 °C.

### 5.3. Aggregate Content and Grain-Size Distribution

Tables 7 and 8 present the results of the insoluble residue (IR), corresponding to the siliceous and the total aggregate contents, respectively. It appears that the values of IR are quite heterogeneous, ranging from 30–80% for mortars and 42–78% for rammed earth samples. The total aggregate content is quite high and is mainly due to the siliceous sand. The grain-size distribution of the total aggregate of mortar and RE samples is presented in Figures 8 and 9, respectively.

By analyzing Figure 6, it is verified that mortar sample RP-M6 is the one with the highest percentage of coarse particles (4.75 mm), while samples JP-T1-3 and IP-M1 are those with the lowest percentages. The JP-T4 sample presents the highest percentage of constituent material between 150 µm and 1.18 mm. Of the remaining samples, the grain-size distributions of the aggregates are very similar.

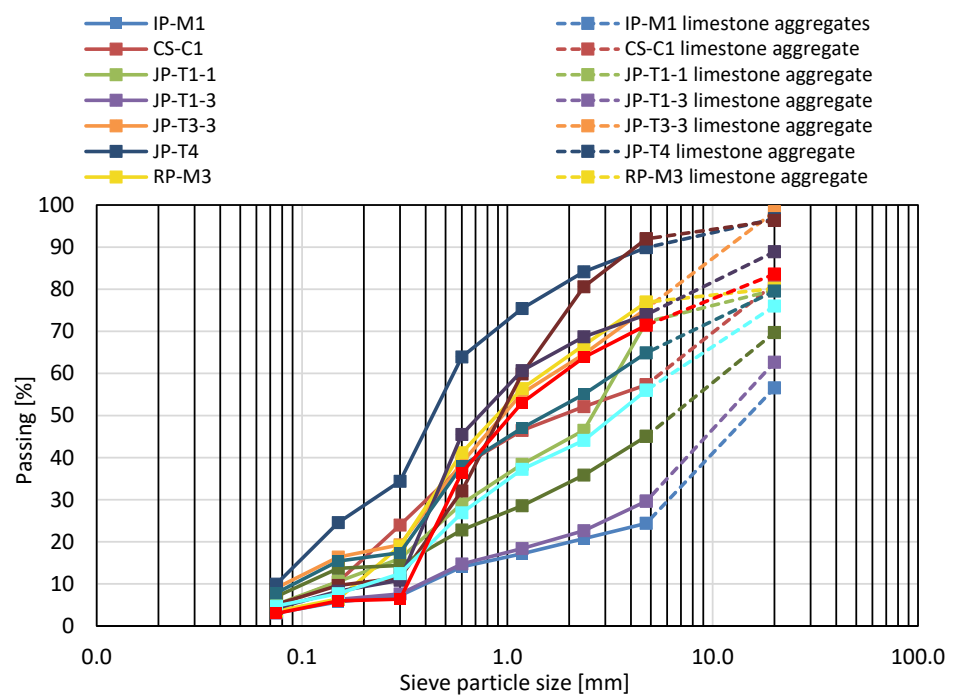
Concerning the grain-size distribution of the RE samples (Figure 9), sample BT-M2-4 presents the highest percentage of coarse particles among all others. Samples GVS-M1-2 and GVS-M2-2, although extracted in the same location, present different aggregate grain-size distributions, namely up to 300 µm, being similar in the coarse dimension. As each earth is composed by different types and contents of clay, silt and sand (apart from coarser aggregates), this suggests, as before, the use of different earths when building the RE wall. In turn, the GS-M1 sample contained the lowest percentages of finer and coarser particles.

**Table 7.** Insoluble residue and total aggregate content for mortar samples.

Sample	Insoluble Residue Content [%]	Total Aggregate Content (IR + Limestone Aggregate) [%]
IP-M1	37.9	77.2
CS-C1	49.6	59.0
JP-T1-1	46.7	54.3
JP-T1-3	30.5	56.8
JP-T3-3	73.6	74.7
JP-T4	56.3	57.7
RP-M3	46.8	56.3
RP-M6	79.0	82.0
BT-T1-2	42.7	65.5
CSH-T2-1	63.3	68.6
TTS-T1	35.1	45.5
TTS-M1	44.2	52.6
TTS-P1	65.7	79.3

**Table 8.** Insoluble residue and total aggregate content for rammed earth samples.

Sample	Insoluble Residue Content [%]	Total Aggregate Content [%]
BT-M1-3	59.2	65.6
BT-M2-4	77.8	81.8
GS-M1	56.7	74.7
GVS-M1-2	54.7	59.0
GVS-M2-2	42.9	61.5



**Figure 8.** Particle size distribution of the aggregates in mortar samples.

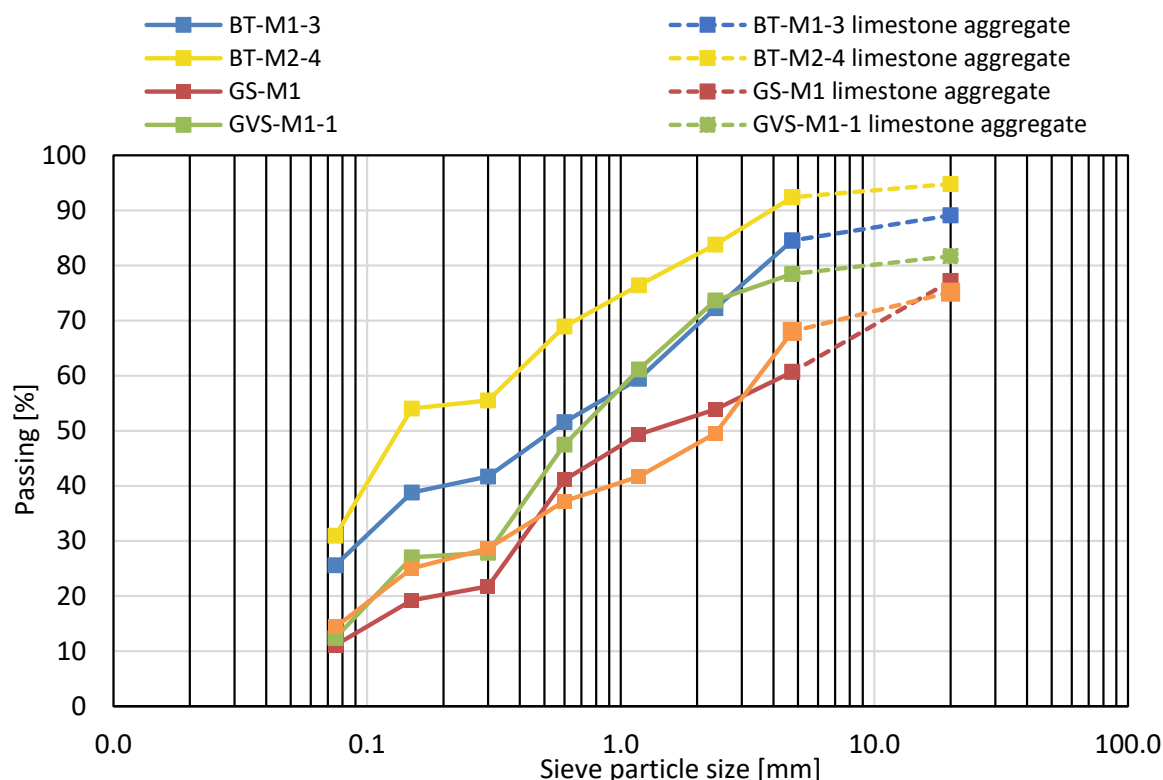


Figure 9. Particle size distribution of the aggregates in rammed earth samples.

5.4. Binder/Aggregate Ratio of Mortar and Rammed Earth Samples

Tables 9 and 10 present the mass contents of the different constituents and the binder/aggregate ratios [21] obtained for lime and RE samples, respectively. From these values, a great heterogeneity and diversity in constituents’ contents are visible. Even within the same case study, important differences are present, thus, implying the employment of heterogeneous materials in the Wall’s construction.

Table 9. Mortars constituents content and Lime:Aggregate (calcareous and siliceous separated or together) ratios.

Sample	Content [Mass%]			Lime:Calc. Aggr.:Silic. Sand (in Mass)	Lime:Aggregate (in Mass)
	Siliceous Sand <sup>1</sup>	Calcareous Aggregate <sup>2</sup>	Hydrated Calcic Lime <sup>3</sup>		
IP-M1	38	39	12	1:3.3:3.2	1:6.5
CS-C1	50	9	25	1:0.4:2	1:2.4
JP-T1-2	47	8	36	1:0.2:1.3	1:1.5
JP-T1-3	30	26	22	1:1.2:1.4	1:2.6
JP-T3-3	74	1	33	1:0.03:2.2	1:2.23
JP-T4	56	1	34	1:0.03:1.6	1:1.63
RP-M3	47	10	20	1:0.5:2.4	1:2.9
RP-M6	79	3	10	1:0.3:8.2	1:8.5
BT-T1-2	43	23	12	1:1.9:3.6	1:5.5
CSH-T2-1	63	5	32	1:0.2:2	1:2.2
TTS-T1	35	10	37	1:0.3:0.9	1:1.2
TTS-M1	44	8	32	1:0.3:1.4	1:1.7
TTS-P1	66	14	25	1:0.6:2.6	1:3.2

<sup>1</sup> Value corresponding to the insoluble residue content; <sup>2</sup> Value corresponding to the limestone grains manually separated during samples preparation; <sup>3</sup> Value obtained by TGA analysis.

**Table 10.** Rammed earth constituents content and Lime or Lime + Earth:Aggregate ratios.

Sample	Content [%]				Lime: Earth: Calc. Aggr: Silic. Sand (in Mass)	Lime + Earth: Aggr. (in Mass)
	Siliceous Sand <sup>1</sup>	Calcareous Aggregate <sup>2</sup>	Earth Fines (Clay + Silt) <sup>3</sup>	Hydrated Calcic Lime <sup>4</sup>		
BT-M1-3	59	6	17	7	1:2.3:0.8:8	1:2.7
BT-M2-4	78	9	26	9	1:2.9:0.5:8.8	1:2.4
GS-M1	57	18	8	2	1:3.7:8.1:25.7	1:7.2
GVS-M1-2	55	4	8	31	1:0.3:0.1:1.8	1:1.5
GVS-M2-2	43	4	8	31	1:0.6:1.14:3.2	1:2.7

<sup>1</sup> Value corresponding to the insoluble residue content; <sup>2</sup> Value corresponding to the limestone grains manually separated during samples preparation; <sup>3</sup> Value corresponding to the size fraction < 0.063 mm; <sup>4</sup> Value obtained by TGA analysis.

Furthermore, the visual observation has shown some lime lumps, thus indicating that to the moistened earth was added quick lime and then mixed, for hydration, resulting in RE stabilized with lime. Therefore, this mixture would allow for the aggregates surface to be attacked by the causticity of calcium oxide, leading to a better connection between the binder's matrix, earth and lime, and the coarser aggregates.

According to the results obtained, the lime content in the RE of the Fernandina Wall is very low when compared to the content of the aggregates and earth fines. This composition is also different from the composition employed in other RE structures, as is the case for the Castle of Paderne [6] in Portugal or the Walls of Cáceres [7] in Spain, where the lime content is much higher. This behavior may indicate that the use of lime was restricted in the sections of the Wall in RE, since there were other sections in rubble stone masonry more exposed to the action of water, or where there was a need for the construction to have more important defensive functions, in which lime was more necessary. On the other hand, it should be noted that the construction of the Wall took only two years, which required a great effort in terms of the construction materials to be used, which certainly also limited the use of lime in those sections of RE construction.

## 6. Conclusions

The existent rammed earth (RE) buildings and, particularly those in military RE, are an integral part of Lisbon's military, cultural, social and architectonic heritage. Hence, for their effective conservation and preservation, knowledge of the original techniques and materials employed is imperative. Nevertheless, and due to a neglect on these structures, it is also fundamental to have adequate information of the conservation interventions held over the years, namely to learn about the original characteristics, to ensure that previous conservation mistakes are not made again and that good practices can be disseminated.

The Fernandina Wall of Lisbon is an impressive defensive structure that was constructed in the second half of the 14th century. Its construction was carried out in a very short period of time, between 1373 and 1375, using limestone from the Lisbon region, air lime and earth. Several elements are visible in the 21st century around the old quarters of Lisbon, attesting to its greatness and durability, as its main walls, towers, turrets or former gates.

This work was focused on collecting and analyzing information about past interventions, its conservation state and the general composition of some Wall's sectors. Masonry mortars and RE samples were extracted from nine different sites of the Fernandina Wall, and mainly its chemical and mineralogical characterization assessed.

The sites analyzed in the Western Wall section are mainly constituted by rubble stone masonry, with the exception of the site closer to river Tagus in Bragança Terraces Complex, where both RE and limestone ashlar masonry were used. The limestone ashlars were also used in the eastern fluvial section of the Wall, where stone blocks were layered with a lime mortar. In opposition, in the Western section of the Wall, the RE was the main material used, while the rubble stone masonry was the most used material in the Western fluvial section.

Calcitic air lime was the binder used in masonry mortars. In some sites, traces of hydraulic binders were also found, their presence being attributed to 20th century interventions. With few exceptions, the grain size distribution of the aggregates is similar. However, their compositions vary according the wall sections analyzed.

RE samples shows also the use of air lime as additive, confirming that the construction technique used was the military rammed earth. Although, these RE are poorer in lime content when compared with others RE used in Iberian Peninsula in the same period.

As in the case of sands used for masonry mortars, the use of earths of different composition was also found in RE. Besides, siliceous sands and coarse limestone aggregates were also found in RE sections of the Wall. The heterogeneous grain size distribution of the aggregates confirms the use of different earth sources in the RE manufacture. One RE sample also contains traces of the use of a hydraulic binder, an indicator of 20th century repair works.

This work shows that materials with different composition and binder:aggregate ratios were employed in the construction of the Fernandina Wall of Lisbon. This variety and heterogeneity is observed not only in the different elements or Wall sections, as well as in the same site analyzed. That may be due to the limited construction period and the need of large contents of raw materials. The use of both RE and rubble stone sectors in different sections of the Wall can be due to the availability of materials, but also with the professional labor skills that were built the defensive Wall.

It is expected that the information obtained in this work about the composition and formulation of bedding mortars and RE used in the construction of the Fernandina Wall of Lisbon will be a contribution to carry out future conservation interventions properly supported and guarantying the compatibility with the original materials.

**Supplementary Materials:** The following supporting information can be downloaded at: <https://www.mdpi.com/article/10.3390/min12020241/s1>, Figures S1–S18: XRD diffractograms; Figures S19–S34: TGA/DTA charts.

**Author Contributions:** Conceptualization, P.F. and A.S.S.; methodology, A.S.S. and P.F.; validation, A.S.S., L.G. and R.I.G.; investigation, L.G.; resources, A.S.S. and P.F.; data curation, L.G.; writing—original draft preparation, R.I.G.; writing—review and editing, R.I.G., P.F. and A.S.S.; funding acquisition, A.S.S. All authors have read and agreed to the published version of the manuscript.

**Funding:** This research was funded by the Portuguese Foundation for Science and Technology by grant number PTDC/EPH-PAT/4684/2014: DB-HERITAGE—Data base of building materials with architectural heritage and historic importance, and UIDB/04625/2020: CERIS—Civil Engineering Research and Innovation for Sustainability.

**Data Availability Statement:** Data supporting reported results, including links to publicly archived datasets analysed or generated during the study can be found in the DB-Heritage database at: [http://db-heritage.lnec.pt/database\\_en.html](http://db-heritage.lnec.pt/database_en.html).

**Acknowledgments:** The authors acknowledge the Portuguese Foundation for Science and Technology for the financial support within the research project PTDC/EPH-PAT/4684/2014: DB-Heritage—Database of building materials with historical and heritage interest. A special acknowledge is due to the Manuela Leitão from the Cultural Heritage Department of the Lisbon City Council and to Maria José Sequeira and Maria Fernandes of the General Directorate of Cultural Heritage for their support in all field work and by sharing their knowledge in the context of the intervention sites. We would also like to thank António Valongo, Artur Rocha and Alexandra Krus, Carlos Sousa Valles and Luís Lamas, and Ana Proserpio of the Historical Society of the Independence of Portugal, Ana Duarte from the Gil Vicente School, Isabel Maria Lechner, Joni Silva and José Neiva Vieira, Nuno Almeida Pereira from VIPGEST, Pedro Pinto of Corpo Santo Hotel, Cheila Veloso and Carlos Mestre of Terraços de Bragança Complex for the shared information and facilities granted in the access to the sites.

**Conflicts of Interest:** The authors declare no conflict of interest.

## References

1. Oliveira, E. *Elements for the History of Lisbon Municipality*; Typografia Universal: Lisboa, Portugal, 1887. (In Portuguese)
2. Vieira da Silva, A. *The Fernandina Wall of Lisbon*, 2nd ed.; Publicações Culturais da Câmara Municipal de Lisboa: Lisboa, Portugal, 1987; Volume I. (In Portuguese)
3. Gomes Martins, M. *Lisbon and the War: 1367–1411*; Obras Clássicas da Literatura Portuguesa; Livros Horizonte: Lisboa, Portugal, 2001; ISBN 9789722411301. (In Portuguese)
4. Lopes, F. *Chronicles of D. Fernando*; Imprensa Nacional Casa da Moeda: Lisboa, Portugal, 1975; Volume II. (In Portuguese)
5. Bui, Q.B.; Morel, J.C.; Hans, S.; Walker, P. Effect of moisture content on the mechanical characteristics of rammed earth. *Constr. Build. Mater.* **2014**, *54*, 163–169. [CrossRef]
6. Parracha, J.L.; Silva, A.S.; Cotrim, M.; Faria, P. Mineralogical and microstructural characterisation of rammed earth and earthen mortars from 12th century Paderne Castle. *J. Cult. Herit.* **2020**, *42*, 226–239. [CrossRef]
7. Mota-López, M.I.; Maderuelo-Sanz, R.; Pastor-Valle, J.D.; Meneses-Rodríguez, J.M.; Romero-Casado, A. Analytical characterization of the almohad rammed-earth wall of Cáceres, Spain. *Constr. Build. Mater.* **2021**, *273*, 121676. [CrossRef]
8. Bruno, P. *The fortress of Juromenha: Contribution to the study and conservation of the Islamic Wall of militar rammed earth*. Master's Thesis, Universidade de Évora, Évora, Portugal, 2000. (In Portuguese)
9. Cravo, M. *Composition of a Rammed Earth Sample from Silves Castle*; Technical Note 024/3/303-DCM; LNEC: Lisbon, Portugal, 1898. (In Portuguese)
10. Canivell, J.; Rodríguez-García, R.; González-Serrano, A.; Romero-Girón, A. Assessment of Heritage Rammed-Earth Buildings: Alcázar of King Don Pedro I, Spain. *J. Archit. Eng.* **2020**, *26*, 05020003. [CrossRef]
11. Martín-del-Río, J.J.; Flores-Alés, V.; Alejandro-Sánchez, F.J.; Blasco-López, F.J. New Method for Historic Rammed-earth Wall Characterization: The Almohade Ramparts of Malaga and Seville. *Stud. Conserv.* **2019**, *64*, 363–372. [CrossRef]
12. Jaquin, P.A.; Augarde, C.E.; Gerrard, C.M. Chronological description of the spatial development of rammed Earth techniques. *Int. J. Archit. Herit.* **2008**, *2*, 377–400. [CrossRef]
13. De La Torre López, M.J.; Sebastián, P.E.; Rodríguez, G.J. A study of the wall material in the Alhambra (Granada, Spain). *Cem. Concr. Res.* **1996**, *26*, 825–839. [CrossRef]
14. Ferro, R.V. *In the limit of memory: The Fernandina Wall as catalyst for the rehabilitation of Encarnação Convent and surroundings*. Master's Thesis, Universidade Técnica de Lisboa, Lisboa, Portugal, 2017. (In Portuguese)
15. Vale, J.P. *The Fernandina Wall as a matrix for the New town of Lisbon evolution*. Master's Thesis, Universidade de Lisboa, Lisboa, Portugal, 2018. (In Portuguese)
16. Feliciano, M.; Leite, A. *The Fernandina Wall in Santana*. In Proceedings of the Seminário - Património Hospitalar de Lisboa, Lisboa, Portugal, 2–3 December 2010. (In Portuguese)
17. Brito, R. *Geological contribution for the recovery of Jogo da Péla Tower (Fernandina Wall of Lisbon)*. Master's Thesis, Universidade de Lisboa, Lisboa, Portugal, 1998. (In Portuguese)
18. Fernandes, M. *Section of Fernandina Wall Existing Inside the Building Located in Lisbon in 9-13 António Maria Cardoso Street*; Parecer de Proposta de Tratamento. Informação DGPC—Departamento de Estudos, Projetos, Obras e Fiscalização: Lisboa, Portugal, 2014.
19. Fernandes, M. *Report on the treatment of the Fernandina Wall in the Firefighters Headquarters of Graça Square/Verónica Street in Lisbon (S. Vicente de Fora)*; Informação N DGPC—Departamento de Estudos, Projetos, Obras e Fiscalização: Lisboa, Portugal, 2016. (In Portuguese)
20. Oliveira, J.; Manso, C. *Final Report: Archaeological Intervention—Graça Parking*; Lisbon City Council: Lisboa, Portugal, 2018. (In Portuguese)
21. da Silva, R.B.; Miranda, P.; Noronha Vieira, V.; Moreira Vicente, A.; Lopes, G.; Nozes, C. Largo do Chafariz de Dentro: Alfama em época moderna. *Velhos E Novos Mundos. Estud. Arqueol. Mod. Old New Worlds. Stud. Early Mod. Archaeol.* **2012**, *1*, 71–84.
22. Krus, A. *Final Report—Archaeological Works: 6-26 Terreiro do Trigo Street, Santa Maria Maior*; Centro de História de Além-Mar: Lisboa, Portugal, 2017. (In Portuguese)
23. Vieira da Silva, A. *The Fernandina Defensive Wall of Lisbon*, 2nd ed.; Publicações Culturais da Câmara Municipal de Lisboa: Lisboa, Portugal, 1987; Volume II. (In Portuguese)
24. Leitão, M. Walls of Lisbon. *Revista Rossio. Estudos* **2014**, *3*, 75–78. (In Portuguese)
25. Gonçalves, A. *Dictionary of Lisbon History: Rosa Palace*; Eduardo, S., Ed.; Guia de Portugal: Lisboa, Portugal, 1994. (In Portuguese)
26. Valongo, A.; Casimiro, T. *A Garbage in Noble Houses of Infantado*. *Arqueologia em Portugal*; José, A., Andrea, M., Eds.; Associação dos Arqueólogos Portugueses: Lisboa, Portugal, 2017; pp. 1835–1848. (In Portuguese)
27. ASTM. *ASTM C136/C136M: Standard Test Method for Sieve Analysis of Fine and Coarse Aggregates*; ASTM Standards: West Conshohocken, PA, USA, 2014. (In Portuguese)



MDPI  
St. Alban-Anlage 66  
4052 Basel  
Switzerland  
Tel. +41 61 683 77 34  
Fax +41 61 302 89 18  
[www.mdpi.com](http://www.mdpi.com)

*Minerals* Editorial Office  
E-mail: [minerals@mdpi.com](mailto:minerals@mdpi.com)  
[www.mdpi.com/journal/minerals](http://www.mdpi.com/journal/minerals)





MDPI  
St. Alban-Anlage 66  
4052 Basel  
Switzerland  
Tel: +41 61 683 77 34  
[www.mdpi.com](http://www.mdpi.com)



ISBN 978-3-0365-5677-2